30-95 JS②

DOE/ER-0313/17

Fusion Materials

Semiannual Progress Report for Period Ending September 30, 1994

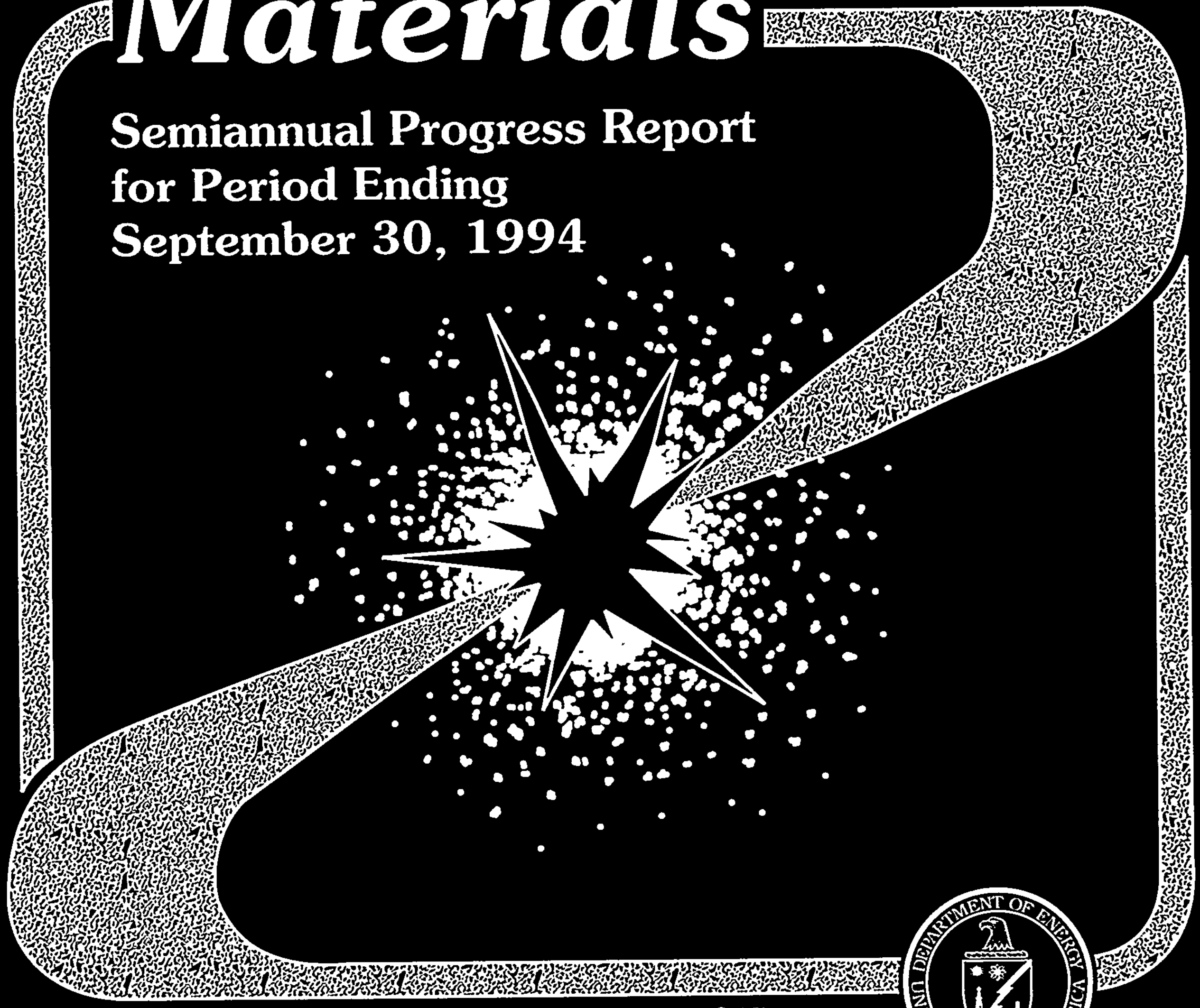

U. S. Department of Energy
Office of Fusion Energy

DISTRIBUTION OF THIS DOCUMENT IS UNLIMITED

This report has been reproduced directly from the best available copy.

Available to DOE and DOE contractors from the Office of Scientific and Technical Information, P.O. Box 62, Oak Ridge, TN 37831; prices available from (615) 576-8401, FTS 626-8401.

Available to the public from the National Technical Information Service, U.S. Department of Commerce, 5285 Port Royal Rd., Springfield, VA 22161.

This report was prepared as an account of work sponsored by an agency of the United States Government. Neither the United States Government nor any agency thereof, nor any of their employees, makes any warranty, express or implied, or assumes any legal liability or responsibility for the accuracy, completeness, or usefulness of any information, apparatus, product, or process disclosed, or represents that its use would not infringe privately owned rights. Reference herein to any specific commercial product, process, or service by trade name, trademark, manufacturer, or otherwise, does not necessarily constitute or imply its endorsement, recommendation, or favoring by the United States Government or any agency thereof. The views and opinions of authors expressed herein do not necessarily state or reflect those of the United States Government or any agency thereof.

DOE/ER-0313/17
Distribution
Categories
UC-423, -424

FUSION MATERIALS
SEMIANNUAL PROGRESS REPORT
FOR THE PERIOD ENDING
SEPTEMBER 30, 1994

Prepared for
DOE Office of Fusion Energy
(AT 15 05 01 0)

DATE PUBLISHED: April 1995

Prepared for
OAK RIDGE NATIONAL LABORATORY
Oak Ridge, Tennessee 37831
Managed by
MARTIN MARIETTA ENERGY SYSTEMS, INC.
for the
U.S. DEPARTMENT OF ENERGY
under Contract DE-AC05-84OR21400

FOREWORD

This is the sixteenth in a series of semiannual technical progress reports on fusion reactor materials. This report combines research and development activities which were previously reported separately in the following progress reports:

- Alloy Development for Irradiation Performance
- Damage Analysis and Fundamental Studies
- Special Purpose Materials

These activities are concerned principally with the effects of the neutronic and chemical environment on the properties and performance of reactor materials; together they form one element of the overall materials programs being conducted in support of the Magnetic Fusion Energy Program of the U.S. Department of Energy. The other major element of the program is concerned with the interactions between reactor materials and the plasma and is reported separately.

The Fusion Materials Program is a national effort involving several national laboratories, universities, and industries. The purpose of this series of reports is to provide a working technical record for the use of the program participants, and to provide a means of communicating the efforts of materials scientists to the rest of the fusion community, both nationally and worldwide.

This report has been compiled and edited under the guidance of A. F. Rowcliffe by G. L. Burn, Oak Ridge National Laboratory. Their efforts, and the efforts of the many persons who made technical contributions, are gratefully acknowledged.

F. W. Wiffen
Division of Advanced Physics
and Technology

Reports previously listed in this series are as follows:

DOE/ER-0313/1	Period ending September 30, 1986
DOE/ER-0313/2	Period ending March 31, 1987
DOE/ER-0313/3	Period ending September 30, 1987
DOE/ER-0313/4	Period ending March 31, 1988
DOE/ER-0313/5	Period ending September 30, 1988
DOE/ER-0313/6	Period ending March 31, 1989
DOE/ER-0313/7	Period ending September 30, 1989
DOE/ER-0313/8	Period ending March 31, 1990
DOE/ER-0313/9	Period ending September 30, 1990
DOE/ER-0313/10	Period ending March 31, 1991
DOE/ER-0313/11	Period ending September 30, 1991
DOE/ER-0313/12	Period ending March 31, 1992
DOE/ER-0313/13	Period ending September 30, 1992
DOE/ER-0313/14	Period ending March 31, 1993
DOE/ER-0313/15	Period ending September 30, 1993
DOE/ER-0313/16	Period ending March 31, 1994
DOE/ER-0313/100	Technical Evaluation of the Technology of Vanadium Alloys for Use as Blanket Structural Materials in Fusion Power Systems

CONTENTS

Capsules HFIR-MFE-JP9 through 16 were installed in the High Flux Isotope Reactor (HFIR) target July 20, 1990 for irradiation beginning with HFIR fuel cycle 289. Of these eight target capsules, JP10, 11, 13, and 16 accumulated 18 dpa and were removed from the reactor in September 1991. JP14 was removed from the reactor at the end of cycle 310 (September 1992) after achieving a peak of 34 dpa. Capsules JP9, 12, and 15 completed 35 cycles on April 1, 1994 and were removed from the target region. Each capsule had accumulated a peak of approximately 57 dpa.

Three additional capsules, HFIR-MFE-JP20, 21, and 22, have been designed to complete the original experiment matrix of the JP9 through JP16 series capsules. Irradiation began in December 1993 with the start of cycle 322. Capsule JP20 was removed from the reactor on June 3, 1994, after accumulating a peak of 8 dpa. As of September 16, 1994 (end of cycle 329), each of the other two capsules had achieved approximately 9.5 dpa.

The RB* experiments are the continuation of the ORR spectrally tailored experiments. In this stage, a hafnium liner is used to modify the spectrum to simulate the fusion helium to displacements per atom (He/dpa) ratio in the austenitic steel specimens. Of the four capsules in this set, two (60J-1 and 330J-1) have been disassembled and testing is in progress. Two capsules (200J-1 and 400J-1) are in the reactor and have accumulated 8 dpa.

To obtain early irradiation performance data on the new 500-kg production heat of the V-4Cr-4Ti material before the scheduled EBR-II shutdown, an experiment, X530, was expeditiously designed and assembled. Charpy, compact tension, tensile and TEM specimens with different thermal mechanical treatments (TMTs), were enclosed in two capsules and irradiated in the last run of EBR-II, Run 170, from August 9 through September 27. For comparison, specimens from some of the previous heats were also included in the test. The accrued exposure was 35 effective full power days, yielding a peak damage of ≈4 dpa in the specimens. The irradiation is now complete and the vehicle is awaiting to be discharged from EBR-II for postirradiation disassembly.

Calculations were performed to estimate damage and transmutation rates in vanadium irradiated in the ATR (Advanced Test Reactor) located in Idaho. The main focuses of the study are to evaluate the transmutation of vanadium to chromium and to explore ways to design the irradiation experiment to avoid excessive transmutation. It was found that the A-hole of ATR produces damage rate of ~15-30 dpa/full power year with a transmutation rate of ~0.2%/dpa of vanadium to chromium. A thermal neutron filter can be incorporated into the design to reduce the vanadium-to-chromium transmutation rate to low levels. A filter 1-2-mm thick of gadolinium or hafnium can be used.

2.2 NEUTRON FLUX SPECTRA AND RADIATION DAMAGE PARAMETERS FOR THE RUSSIAN BOR-60 AND SM-2 REACTORS – A. V. Karasiov (D. V. Efremov Scientific Research Institute of Electrophysical Apparatus, St. Petersburg, Russia) and L. R. Greenwood (Pacific Northwest Laboratory). 21

Neutron fluence and spectral information and calculated radiation damage parameters are presented for the BOR-60 (Fast Experimental Reactor - 60 MW) and SM-2 reactors in Russia. Their neutron exposure characteristics are comparable with those of the Experimental Breeder Reactor (EBR-II), the Fast Flux Test Facility (FFTF), and the High Flux Isotope Reactor (HFIR) in the United States.

2.3 NEUTRON DOSIMETRY, DAMAGE CALCULATIONS, AND HELIUM MEASUREMENTS FOR THE HFIR-MFE-60J-1 AND MFE-330J-1 SPECTRAL TAILORING EXPERIMENTS – L. R. Greenwood (Pacific Northwest Laboratory), C. A. Baldwin (Oak Ridge National Laboratory), and B. M. Oliver (Rockwell International). 28

Neutron fluence measurements and radiation damage calculations are reported for the joint U.S.-Japanese MFE-60J-1 and MFE-330J-1 experiments in the hafnium-lined removable beryllium (RB*) position of the High Flux Isotope Reactor (HFIR) at Oak Ridge National Laboratory (ORNL). These experiments were continuations of the ORR-6J and 7J irradiations performed in the Oak Ridge Research Reactor (ORR). The combination of irradiations was designed to tailor the neutron spectrum in order to achieve fusion reactor helium/dpa levels in stainless steel. These experiments produced maximum helium (appm)/dpa (displacement per atom) levels of 10.2 at 18.5 dpa for the ORR-6J and HFIR-MFE-60J-1 combination and 11.8 at 19.0 dpa for the ORR-7J and HFIR-MFE-330J-1 combination. A helium measurement in one JPCA sample was in good agreement with helium calculations.

2.4 PRELIMINARY REPORT ON THE IRRADIATION CONDITIONS OF THE HFIR JP-23 EXPERIMENT – A. M. Ermi (Westinghouse Hanford Company) and D. S. Gelles (Pacific Northwest Laboratory). 35

The JP-23 test capsule was irradiated in the HFIR during cycles 322 and 326. The capsule contained eight transmission electron microscopy (TEM) specimen holders, two each at irradiation temperatures of 300, 400, 500, and 600°C The test capsule was irradiated for a total of 110 effective full power days (EFPD), achieving estimated peak doses of 1.1 x 10^{22} n/cm^2 (E>0.1 MeV) and 8.8 dpa (in stainless steel).

3.0 MATERIALS ENGINEERING AND DESIGN REQUIREMENTS. 51

NO CONTRIBUTIONS

4.0 FUNDAMENTAL MECHANICAL BEHAVIOR. 53

4.1 CORRELATION BETWEEN SHEAR PUNCH AND TENSILE DATA FOR NEUTRON-IRRADIATED ALUMINUM ALLOYS – M. L. Hamilton and D. J. Edwards (Pacific Northwest Laboratory), M. B. Toloczko and G. E. Lucas (University of California-Santa Barbara), W. F. Sommer and M. J. Borden (Los Alamos National Laboratory), and J. F. Dunlap and J. F. Stubbins (University of Illinois). 55

Tensile specimens and TEM disks of two aluminum alloys in two tempers were irradiated at 90-120°C with neutrons from spallation reactions in the Los Alamos Spallation Radiation Effects Facility (LASREF) at the Los Alamos Meson Physics Facility (LAMPF). The materials were exposed to a fluence of 3.4-4 x 10^{20} n/cm^2. This work was part of a study to determine the potential for using aluminum alloys as structural components in accelerators used to produce tritium. Shear punch tests and tensile tests were performed at room temperature and at 100°C, a temperature characteristic of the operating temperature in the application of interest. Shear punch and tensile data from unirradiated specimens were used to develop a correlation between shear punch and tensile strengths. Using the shear punch data from the neutron irradiated TEM disks, the correlation predicted the tensile strength of the neutron irradiated condition reasonably well. Shear punch data on similar 760 MeV proton-irradiated specimens were used with the correlation in an attempt to predict uniaxial strength in the proton irradiated condition.

Transmission electron microscopy was used to examine the density and spatial distribution of defect clusters produced in copper and nickel as the result of fission neutron irradiation to damage levels of 0.01 to 0.25 displacements per atom (dpa) at irradiation temperatures between 50 and 230°C (0.24 to 0.37 T_M in Cu). A high density of small stacking fault tetrahedra (SFT) and dislocation loops was observed in both materials, and a moderate density of small voids was observed in the copper specimens irradiated at 230°C. The visible defect cluster density in both materials approached a saturation value at doses >0.1 dpa. The visible defect cluster density in nickel was a factor of 5 to 10 lower than that in copper at all damage levels. The defect clusters in Ni organized into {001} walls at damage levels >0.1 dpa, whereas defect cluster alignment was not observed in copper. A comparison with published results in the literature indicates that defect cluster wall formation occurs in nickel irradiated at 0.2 to 0.4 T_M in a wide variety of irradiation spectra. Defect cluster wall formation apparently only occurs in copper during low temperature irradiation with electrons and light ions. These results are discussed in terms of the thermal spike model for energetic displacement cascades.

The effects of H on the mixed-mode I/III critical *J*-integrals (J_{TQ}) and tearing moduli (*dJ/da*) were examined for a ferritic/martensitic stainless steel at ambient temperature. A H content of 4 ppm (wt) was attained after charging in a H_2 gas chamber (138 MPa) at 300°C for 2 weeks. Results showed that H decreased J_{TQ} and *dJ/da* values compared to steel tested without H. However, the presence of H did not change the dependence of J_{TQ} and *dJ/da* values on crack angle. Both J_{IQ} and *dJK/da* exhibited the highest relative values. The minimum values of both J_{TQ} and *dJ/da* occurred at a crack angle between 35 and 55° [*Piii* + *Pi*) /(*Piii* + *Pi*) = 0.4 and 0.6]. A mechanism of the combined effect of H and mixed-mode on J_{TQ} and *dJ/da* is discussed.

Mode I and mixed mode I/III fracture toughnesses were investigated in the range of -95°C to 25°C for a F82-H steel heat-treated in the following way; 1000°C/20 h/air-cooled (AC), 1100°C/7 min/AC, and 700°C/2 h/AC. Mode I fracture toughness (J_{IC}) was determined with standard compact tension (CT) specimens, and mixed-mode I/III fracture toughness (J_{MC}) was determined with modified CT specimens, which resulted in 0.41 ratio of

$P_{iii}/(P_{iii} + P_i)$. The F82-H was very tough at room temperature (RT), giving a J_{IC} value of about 284 kJ/m^2. Mixed-mode I/III loading dramatically lowered fracture toughness.. The J_{MC} value was only 150 kJ/m^2 at RT. J_{IC} values exhibited a strong temperature dependence and decreased rapidly with decrease of temperature. J_{IC} at -90°C was only 30 kJ/m^2. On the other hand, J_{MC} values depended much more weakly on temperature. J_{MC} at -95°C was 50kJ/m^2, about 70% higher than J_{IC} value at -90°C. At RT the mode I specimens fractured by microvoid coalescence. Mixed mode specimens also fractured by microvoid coalescence, but tortuosity and void size on fracture surfaces were significantly less than those in mode I specimens. Interestingly, at -90°C, a crack in a mode I specimen initiated and grew by quasi-cleavage fracture; but a crack in mixed mode specimen initiated and propagated a short distance (0.5 mm) by a mixture of intergranular fracture and ductile tearing. Then the crack turned to mode I and fractured by quasi-cleavage failure. Our results indicate that crack tip plasticity was increased by mixed mode loading, and suggest that at low temperature, mode I fracture toughness is the critical design parameter, but at temperatures above RT, especially concerning fatigue and creep-fatigue crack growth rate, a mixed mode loading may be more harmful than a mode I loading for this steel because a mixed mode loading results in lower fracture toughness and higher crack tip plasticity (or dislocation activity).

Subsize Charpy impact specimens of 9Cr-1MoVNb (modified 9Cr-1Mo) and 12Cr-1MoVW (Sandvik HT9) steels and 12Cr-1MoVW with 2% Ni (12Cr-1MoVW-2Ni) were irradiated in the High Flux Isotope Reactor (HFIR) at 300 and 400°C to damage levels up to 2.5 dpa. The objective was to study the effect of the simultaneous formation of displacement damage and transmutation helium on impact toughness. Displacement damage was produced by fast neutrons, and helium was formed by the reaction of 58Ni with thermal neutrons in the mixed-neutron spectrum of HFIR. Despite the low fluence relative to previous irradiations of these steels, significant increases in the ductile-brittle transition temperature (DBTT) occurred. The 12Cr-1MoVW-2Ni steel irradiated at 400°C had the largest increase in DBTT and displayed indications of intergranular fracture. A mechanism is proposed to explain how helium can affect the fracture behavior of this latter steel in the present tests, and how it affected all three steels in previous experiments, where the steels were irradiated to higher fluences.

The HFIR-MFE-RB* experiments are designed for irradiation in the removable beryllium (RB*) positions of the High Flux Isotope Reactor. A hafnium shield surrounds the capsules in order to reduce the thermal neutron flux and achieve a He/dpa level near that expected in a fusion reactor. The J316 austenitic alloy specimens irradiated in this experiment were in the solution annealed (SA) and 20% cold-worked (CW) condition. The specimens were irradiated at 60 and 330°C to a total of 19 dpa (11 appm He/dpa). For both irradiation temperatures, there was no significant difference between the strength properties of the CW J316 following irradiation to 7 dpa or 19 dpa. The strength properties saturate at a fluence less than 7 dpa. The same is true for the SA J316 irradiated at 60°C. However, at 330°C, there is a small but significant further increase in yield stress between 7 and 19 dpa. There is a marked difference in deformation behavior seen after irradiation at 60°C and 330°C. After irradiation to 19 dpa at 60°C, J316 maintains a uniform elongation greater than 20% while the uniform elongation of the 330°C material is less than 0.5%. The yield strength of the cold-worked material remains higher than that of the solution annealed material at both 7 and 19 dpa. The severe reduction in uniform elongation seen at 330°C is a synergistic effect of both the irradiation temperature and the test temperature.

Gas-metal reaction studies of V-5Cr-5Ti were conducted to determine the kinetics of reactions with H_2 and O_2, respectively, at 450-500°C. Reaction rates were determined through weight change measurements and chemical analyses, and effects on mechanical properties were evaluated by room temperature tensile tests. Exposures to hydrogen at 450°C and 0.1 torr pressure resulted in a significant loss in room temperature ductility in the case of alloys that has been annealed at 1125°C but not in the case of alloys annealed at 1050°C. Adding oxygen at 500°C at concentrations as low as 200 ppm seriously embrittled V-5Cr-5Ti specimens when the specimens were held for 100 h in vacuum at 500°C. A subsequent heat treatment in vacuum at 950°C restored the ductility. Exposure to air at 400°C and a subsequent vacuum heat treatment at 500°C caused ductility decreases similar to those observed after the small oxygen additions, and ductility again was restored by a 950°C vacuum anneal. However, similar heat treatments following air exposures at 450 and 500°C, respectively, resulted in ductility losses that were not recovered by the 950°C anneal. The latter exposures also resulted in the formation of thin oxide films.

The results of in-vacuum low cycle fatigue tests are presented for unirradiated V-5Cr-5Ti tested at room temperature (25), 250, and 400°C. A comparison of the fatigue data generated in rough and high vacuums shows that a pronounced environmental degradation of the fatigue properties exists in this alloy at room temperature. Fatigue life was reduced by as much as 84%. Cyclic stress range data and SEM observations suggest that this reduction is due to a combination of increases in rates of crack initiation and subsequent growth. The relative contribution of each difference is dependent upon the strain range.

In high vacuum, the fatigue results also show a trend of increasing cyclic life with increasing temperature between 25 and 400°C. From the limited data available, life at 250°C averages 1.7 times that at 25°C, and at 400°C, life averages 3.2 times that at room temperature. Like the environmental effects at 25°C, the effect of temperature seems to be a function of strain range at each temperature.
The total strain range and cycles to failure were correlated using a power law relationship and compared to 20% cold-worked 316 stainless steel and several vanadium-base alloys. The results suggest that V-5Cr-5Ti has better resistance to fatigue than 316-SS in the temperature range of 25 to 400°C. At 400°C, the data also show that V-5Cr-5Ti out performs Vanstar alloys 7 and 8 over the entire range of strains investigated. Furthermore, the fatigue properties of the V-5Cr-5Ti alloy compare favorably to V-15Cr-5Ti (at 25°C) and Vanstar 9 (at 400°C) at strains greater than 1%. At lower strains, the lower fatigue resistance of V-5Cr-5Ti is attributed to the higher strengths of the V-15Cr-5Ti and Vanstar 9 alloys.

The subsize charpy test results for electron beam weld metal from the V-5Cr-5Ti alloy have shown significant improvement in charpy fracture energy compared to both GTA weld metal and the base metal itself. These results are preliminary, however, and additional confirmation testing and analysis will be required to explain this improvement in properties.

6.3.4 DISLOCATION DEVELOPMENT IN V-5Cr-5Ti AND PURE VANADIUM – D. S. Gelles (Pacific Northwest Laboratory) and M. L. Grossbeck (Oak Ridge National Laboratory). 156

Microstructural examinations have been performed on deformed tensile specimens of V-5Cr-5Ti and pure vanadium in order to explain notch sensitivity noted in the candidate alloy V-5Cr-5Ti. SS-3 tensile specimens have been prepared, stress relieved and deformed to 5% strain. The resulting deformation structures have been examined by transmission electron microscopy. It is found that 5% deformation in V-5Cr-5Ti produces a higher dislocation density consisting of long straight dislocations, typical of Stage II, and many small loops, whereas in pure vanadium, the dislocation arrangements are more complex, typical of Stage III, and the small loops are at a lower density.

These results are interpreted in light of the tendency for enhanced notch sensitivity found in V-5Cr-5Ti.

6.3.5 EFFECT OF HEAT TREATMENT ON MICROSTRUCTURE AND FRACTURE TOUGHNESS OF A V-5Cr-5Ti ALLOY – H. Li (Associated Western Universities-Northwest Division), M. L. Hamilton and R. H. Jones (Pacific Northwest Laboratory). . 165

Fracture toughness and impact tests were performed on a V-5Cr-5Ti alloy. Specimens annealed at 1125°C for 1 h and furnace cooled in a vacuum of 1.33×10^{-5} Pa were brittle at room temperature (RT) and experienced a mixture of intergranular and cleavage fracture. Fracture toughness (J_{IQ}) at RT was 52 kJ/m^2 and the impact fracture energy (IFE) was 6J. The IFE at -100°C was only 1 J. While specimens exhibited high fracture toughness at 100°C (J_{IQ} is 485 kJ/m^2), fracture was a mixture of dimple and intergranular failure, with intergranular fracture making up 40% of the total fracture surface. The ductile to brittle transition temperature (DBTT) was estimated to be about 20°C. When some specimens were given an additional annealing at 890°C for 24 h, they became very ductile at RT and fractured by microvoid coalescence. The J_{IQ} value increased from 52 kJ/m^2 to ~1100 kJ/m^2. The impact test failed to fracture specimens at RT due to a large amount of plastic deformation. The IFE at -115°C was 4J, four times as much as when annealed only at 1125°C. The specimens became brittle at -50°C and fractured by cleavage, giving a J_{IQ} value of 50 kJ/m^2. The DBTT was estimated to be -40°C. Analysis of Auger electron microscopy showed significant sulfur segregation (6 at. %) on grain boundaries in the specimens annealed only at 1125°C, but only 0.9 at. % on grain boundaries if the additional annealing at 890°C was given. Moreover, significantly more second phase particles were found in the specimens annealed at 1125°C plus 890°C. The possible mechanism by which heat treatment affects fracture toughness is discussed.

6.3.6 FABRICATION OF 500-kg HEAT OF V-4Cr-4Ti – H. M. Chung, H.-C. Tsai, and D. L. Smith (Argonne National Laboratory) and R. Peterson, C. Curtis, C. Wojcik, and R. Kinney (Teledyne Wah Chang Albany). 178

A 500-kg heat of V-4C4-4Ti, and alloy identified previously as the primary vanadium-based candidate alloy for application in fusion reactor structural components, has been produced. The ingot was produced by electron-beam melting using screened high-quality raw materials of vanadium and titanium. Several ≈63.5-mm-thick bars were extruded from the ingot, and plates and sheets of various thicknesses ranging from 0.51 to 12.7 mm were fabricated successfully from the extruded bars. The chemical composition of the ingot and the secondary fabrication procedures, specified on the basis of experience and knowledge gained from fabrication, testing, and microstructural examination of a laboratory-scale heat, were found to be satisfactory. Charpy-impact tests showed that mechanical properties of the large-scale heat are as good as those of the laboratory-scale heat. This demonstrates a method of reliable fabrication of industrial-scale heats of V-4Cr-4Ti that exhibit excellent properties.

A 500-kg heat of V-4C4-4Ti, an alloy identified previously as the primary vanadium-based candidate alloy for application as fusion reactor structural components, has been produced successfully. Impact tests were conducted at -196 to 150°C on 1/3-size Charpy specimens of the scale-up heat after final annealing for 1 h at 950, 1000, and 1050°C. The material remained ductile at all test temperatures, and the ductile-brittle transition temperature (DBTT) was lower than -200°C. The upper-shelf energy of the production-scale heat was similar to that of the laboratory-scale (≈15-kg) heat. Effect of annealing temperature was not significant; however, annealing at 1000°C for 1 h produced impact properties slightly better than those from other annealing treatments. Effect of notch geometry was also investigated on the heat. Under otherwise similar conditions, DBTT increased ≈30°C when the notch angle was reduced from 45° (root radius 0.25 mm) to 30° (root radius 0.08 mm).

Annealing of 85% cold-worked unalloyed V and V-(1-18)Ti alloys for 1 hr at 180°C to 1200°C results in hardness maxima at 180-250°C, 420-600°C, and 1050-1200°C and in hardness minima at 280-360°C and, depending on Ti concentration in the alloy, at 850-1050°CC. Annealing of 85% cold-workedV-(4-15)Cr-(3-6)Ti alloys for 1 hr at 180-1200°C results in hardness maxima at 180-250°C, 420-800°C and 1050-1200°C, and in hardness minima at 280-360°C and 920-1050°C. Tentative interpretations are presented for the hardness maxima and minima. Annealing of specimens at 1200°C results in significant increase of VHNs upon removal of a 0.05-mm-thickness surface layer from the specimens.

Oxidation studies were conducted on V-5Cr-5Ti alloy specimens at 500°C in an air environment. The oxidation rates calculated from measurements of thermogravimetric testing are 10, 17, and 25 μm/y at 400, 450, and 500°C, respectively. Uniaxial tensile specimens were oxidized for several time periods in air at 500°C and subsequently tensile-tested at 500°C in air. The hardened layer in each of these oxidized specimens was confined to 75 μm after 1000 h exposure at 500°C. The influence of 1000 h oxidation is to increase the ultimate tensile strength of the alloy by ≈10% while decreasing the tensile rupture strain from 0.23 to 0.14.

One property of vanadium-base alloys that is not well understood in terms of their potential use as fusion reactor structural materials is the effect of simultaneous generation of helium and neutron damage under conditions relevant to fusion reactor operation. In the present Dynamic Helium Charging Experiment (DHCE), helium was produced uniformly in the specimen at linear rates of ≈0.4 to 4.2 appm helium/dpa by the decay of tritium during irradiation to 18-31 dpa at 425-600°C in the Li-filled DHCE capsules in the Fast Flux Test Facility. This report presents results of postirradiation tests of tensile properties of V-4Cr-4Ti, an alloy identified as the most promising vanadium-base alloy for fusion reactors on the basis of its superior baseline and irradiation properties. Effects of helium on tensile strength and ductility were insignificant after irradiation and testing at >420°C. Contrary to initial expectation, room-temperature ductilities of DHCE specimens were higher than those of non-DHCE specimens (in which there was negligible helium generation), whereas strengths were lower, indicating that different types of hardening centers are produced during DHCE and non-DHCE irradiation. In strong contrast to tritium-trick experiments in which dense coalescence of helium bubbles is produced on grain boundaries in the absence of displacement damage, no intergranular fracture were observed in any tensile specimens irradiated in the DHCE.

One property of vanadium-base alloys that is not well understood in terms of their potential use as fusion reactor structural materials is the effect of simultaneous generation of helium and neutron damage under conditions relevant to fusion reactor operation. In the present DHCE, helium was produced uniformly in the specimen at linear rates ranging from ≈0.4 to 4.2 appm helium/dpa by the decay of tritium during irradiation to 18-31 dpa at 425-600°C in Li-filled DHCE capsules in the Fast Flux Test Facility. Ductile-brittle transition behavior of V-4Cr-4Ti, recently identified as the most promising vanadium-base alloy for fusion reactor use, was determined from multiple-bending tests (at -196 to 50°C) and quantitative SEM fractography on TEM disks (0.3-mm thick) and broken tensile specimens (1.0-mm thick). No brittle behavior was observed at temperatures >-150°C, and predominantly brittle-cleavage fracture morphologies were observed only at -196°C in some specimens irradiated to 31 dpa at 425°C during DHCE. Ductile-brittle transition temperatures (DBTTs) were -200°C to -175°C for both types of specimens. In strong contrast to tritium-trick experiments in which dense coalescence of helium bubbles is produced on grain boundaries in the absence of displacement damage, no intergranular fracture was observed in the bend-tested specimens irradiated in the DHCE.

Combined effects of dynamically charged helium and neutron damage on density change, void distribution, and microstructural evolution of V-4Cr-4Ti alloy have been determined after irradiation to 18-31 dpa at 425-600°C in the DHCE, and the results compared with those from a non-DHCE in which helium generation was negligible. For specimens irradiated to ≈18-31 dpa at 500-600°C with a helium generation rate of 0.4-4.2 appm He/dpa, only a few helium bubbles were observed at the interface of grain matrices and some of the Ti(O,N,C) precipitates, and no microvoids or helium bubbles were observed at the interface of grain matrices and some of the Ti(O,N,C) precipitates, and no microvoids or helium bubbles were observed either in grain matrices or near grain boundaries. Under these conditions, dynamically produced helium atoms seem to be trapped in the grain matrix without significant bubble nucleation or growth, and in accordance with this, density changes from DHCE and non-DHCE (negligible helium generation) were similar for comparable fluence and irradiation temperature. Only for specimens irradiated to ≈31 dpa at 425°C, when helium was generated at a rate of 0.4-0.8 appm helium/dpa, were diffuse helium bubbles observed in limited regions of grain matrices and near ≈15% of the grain boundaries in densities significantly lower than those in the extensive coalescences of helium bubbles typical of other alloys irradiated in tritium-trick experiments. Density changes of specimens irradiated at 425°C in the DHCE were somewhat higher than those form non-DHCE irradiation. Microstructural evolution in V-4Cr-4Ti was similar for DHCE and non-DHCE except for helium bubble number density and distribution. As in non-DHCE, the irradiation-induced precipitation of ultrafine Ti_5Si_3 was observed for DHCE at >500°C but not at 425°C.

6.4 COPPER ALLOYS.. 219

6.4.1 EFFECT OF FISSION NEUTRON IRRADIATION ON THE TENSILE AND ELECTRICAL PROPERTIES OF COPPER AND COPPER ALLOYS – S. A. Fabritsiev (D.V. Efremov Institute, St. Petersburg, Russia), A. S. Pokrovsky (SRIAR, Dimitrovgrad, Russia), S. J. Zinkle (Oak Ridge National Laboratory), and D. J. Edwards (Pacific Northwest Laboratory)... 221

The tensile and electrical properties of several different copper alloys have been measured following fission neutron irradiation to ~1 and 5 dpa at temperatures between ~90 and 200°C in the SM-2 reactor. These low temperature irradiations caused significant radiation hardening and a dramatic decrease in the work hardening ability of copper and copper alloys. The uniform elongation was higher at 200°C compared to 100°C, but still remained below 1% for most of the copper alloys. As expected, specimens shielded from the thermal neutrons (which produced fusion-relevant solid transmutation rates) exhibited a lower increase in their electrical resistivity compared to unshielded specimens. A somewhat surprising observation was that the radiation hardening was significantly higher in unshielded copper specimens compared to spectrally-shielded specimens.

6.5 ENVIRONMENTAL EFFECTS IN STRUCTURAL MATERIALS........ 229

6.5.1 FABRICATION AND PERFORMANCE TESTING OF CaO INSULATOR COATINGS ON V-5%Cr-5%Ti IN LIQUID LITHIUM – J.-H. Park and G. Dragel (Argonne National Laboratory)... 231

The electrical resistance of CaO coatings produced on V-5%Cr-5%Ti by exposure of the alloy to liquid Li that contained 0.5-85 wt.% dissolved Ca was measured as a function of time at temperatures between 250 and 600°C. The solute element, Ca in liquid Li, reacted with the alloy substrate at 400-420°C to produce a CaO coating. Resistance of the coating layer measured in-situ in liquid Li was ≈0.4 and 6.4 x 10^6 Ω at 267 and 400°C, respectively. Thermal cycling between 300 and 700°C changed the resistance of the coating layer, which followed insulator behavior. Examination of the specimen after cooling to room temperature revealed cracks in the CaO coating; therefore preliminary tests were conducted to investigate in-situ self-healing behavior. At ≥360°C, relatively fast healing was indicated. These results suggest that thin homogeneous coatings can be produced on variously shaped surfaces by controlling the exposure time, temperature, and composition of the liquid metal. This coating method is applicable to reactor components. The liquid metal can be used over and over because only the solutes are consumed, not the liquid metal itself. The technique can be applied to various shapes (e.g., inside/outside of tubes, complex geometrical shapes) because the coating is formed by liquid-phase reaction.

6.5.2 FABRICATION OF ALUMINUM NITRIDE AND ITS STABILITY IN LIQUID ALKALI METALS – K. Natesan and D. L. Rink (Argonne National Laboratory)............ 245

AlN has been selected as a prime candidate to electrically insulate the V-alloy first wall in the self-cooled concept for ITER application. Several methods are being evaluated for fabrication of AlN coatings with adequate thickness and the desirable physical, electrical, chemical, and mechanical properties. Coatings developed thus far are being evaluated by exposure to liquid Li at temperatures of 300 to 400°C.

6.5.3 CHEMICAL COMPATIBILITY OF STRUCTURAL MATERIALS IN ALKALI METALS – K. Natesan, D. L. Rink, R. Haglund, and R. W. Clark (Argonne National Laboratory)... 249

Candidate structural materials are being evaluated with regard to their compatibility, interstitial element transfer, and corrosion in liquid alkali metal systems such as lithium and NaK. Type 316 stainless steel and V-5Cr-5Ti coupon specimens with and without prealuminizing treatment have been exposed to a lithium environment of commercial purity for 3200 h at 350°C. Weight change data showed negligible corrosion of these materials at this temperature.

7.0 SOLID BREEDING MATERIALS AND BERYLLIUM 253

7.1 AN INVESTIGATION OF THE DESORPTION OF HYDROGEN FROM LITHIUM OXIDE USING TEMPERATURE PROGRAMMED DESORPTION AND DIFFUSE REFLECTANCE INFRARED SPECTROSCOPY – J. P. Kopasz and C. E. Johnson (Argonne National Laboratory) and J. Ortiz-Villafuerte (Escuela Superior de Fisica y Matematicas, Mexico). 255

A combination of Temperature Programmed Desorption (TPD) and Diffuse Reflectance Infrared Fourier Transform Spectroscopy (DRIFTS) is being used to investigate the desorption of hydrogen from lithium oxide. Initial studies have indicated that there are four different types of hydroxyl groups which can be observed on a lithium oxide surface. The particular species present vary depending on the temperature and hydrogen pressure of the system. Under some conditions where hydrogen is present in the purge gas surface hydride species have been observed. This suggests heterolytic adsorption of hydrogen has occurred.

8.0 CERAMICS 265

8.1 FATIGUE CRACK GROWTH RATE (FCGR) BEHAVIOR OF NICALON/SiC COMPOSITES – N. Miriyala, P. K. Liaw, N. Yu, and C. J. McHargue (University of Tennessee), L. L. Snead (Oak Ridge National Laboratory), and D. K. Hsu (Iowa State University). 267

Ultrasonic measurements were continued on the Nicalon/SiC composite specimens to correlate elastic moduli with percentage porosity in the in-plane as well as through-thickness directions. A micromechanics model based on periodic microstructure was developed to predict the elastic stiffness constants of the Nicalon/SiC composites. The predicted values were in good agreement with the experimental results.

8.2 ADVANCED SIC COMPOSITES FOR FUSION APPLICATIONS – L. L. Snead and O. J. Schwarz (Oak Ridge National Laboratory). 274

Chemically vapor infiltrated silicon carbide (SiC) composites have been fabricated from continuous fibers of either SiC or graphite and tested for strength and thermal conductivity. Of significance is that the Hi-Nicalon^{TM} SiC based fiber composite has superior unirradiated properties as compared to the standard Nicalon grade. Based on previous results on the stability of the Hi-Nicalon fiber, this system should prove more resistant to neutron irradiation. A graphite fiber composite has been fabricated with very good mechanical properties and thermal conductivity an order of magnitude higher than typical SiC/SiC composites.

8.3 THERMAL CONDUCTIVITY DEGRADATION OF GRAPHITES IRRADIATED AT LOW TEMPERATURE – L. L. Snead and T. D. Burchell (Oak Ridge National Laboratory). 289

Several graphites and graphite composites (C/C's) have been irradiated near150°C and at fluences up to a displacement level of 0.24 dpa. The materials ranged in unirradiated room temperature thermal conductivity varied from 114 W/m-K for H-451 isotropic graphite, to 670 W/m-K for unidirectional FMI-1D C/C composite.. At the irradiation temperature a saturation reduction in thermal conductivity was seen to occur at displacement levels of approximately 0.1 dpa. All materials were seen to degrade to approximately 10 to 14% of their original thermal conductivity after irradiation. The effect of postirradiation annealing on the thermal conductivity was also studied.

The effects of fiber thermal creep on the relaxation of crack bridging tractions in SiC-SiC ceramic matrix composites (CMCs) is considered in the present work, with the objective of studying the time-to propagation of sub-critical matrix cracks in this material at high temperatures. Under the condition of fiber stress relaxation in the bridging zone, it is found that the crack opening and the stress intensity factor increase with time for sub-critical matrix cracks. The time elapsed before the stress intensity reaches the critical value for crack propagation is calculated as a function of the initial crack length, applied stress and temperature. Stability domains for matrix cracks are defined, which provide guidelines for conducting high-temperature crack propagation experiments.

In the past six months, we have conducted studies of subcritical crack growth on SiC/SiC composite materials in a corrosive (O_2) as well as an inert (Ar) atmosphere for temperatures ranging from 800 to 1100°C. Two materials, one with ~1 µm carbon (C) interface and the other with ~0.5 µm boron nitride (BN), were investigated. Apparent activation energies (E_{act}) were determined from both the crack velocity and thermogravimetric analysis. In pure Ar, it was found that the apparent activation energy gradually increased with time, consistent with the development of steady-state bridging zone. The asymptotic value for E_{act} from crack growth data was found to be ~205 kJ/mol and ~234 kJ/mol for BN- and C-interface materials, respectively, in good agreement with published data (~200 kJ/mol) for creep of Nicalon fibers. In the presence of oxygen, E_{act} decreased to ~40-50 kJ/mol for C-interface and ~50-68 kJ/mol for BN-interface. Microstructural characterization of the oxidized samples indicated that the growth rate of the reaction front for BN-interface materials is an order of magnitude lower than for C-interface ones. At higher temperatures, a glassy phase was observed to seal off the BN-interface, whereas the C-interface remained open during all tests.

The dimensional stability and some mechanical properties of two similar 2D 0-90° weave SiC_f/SiC composite made with Nicalon^{TM} ceramic-grade (CG) fiber were characterized and compared after neutron irradiation to those properties for β-SiC. The major difference between these two composites was that one had a thin (150 nm) and the other a thick (1000 nm) graphite interface layer. The irradiation conditions consisted of relatively high doses (4.3 to 26 dpa-SiC) at high temperatures (430 to 1200°C).

Up to about 900°C, swelling of the irradiated SiC_f/SiC composites (<0.5%) was slightly less than for irradiated monolithic SiC and was relatively independent of dose. The strengths and the modulus of these SiC_f/SiC composites were reduced by about 50% by the irradiation. During irradiation, the Nicalon CG fibers tended to densify and shrink, thus partially decoupling the fibers from the matrix. The decoupling of the fibers from the matrix led to loss of load transfer capability and effectively increased the porosity of the material. Considerable microcracking of the matrix also resulted due to the residual stresses between the shrinking fibers and the expanding matrix.

Synthesis of irradiation resistant SiC_f/SiC composites in the future will require fabrication using improved SiC fibers with better irradiation damage stability. Only then can the fiber/matrix interface thickness and perhaps type be optimized for better performance.

Cross section transmission electron microscopy has been used to investigate the microstructure of $MgAl_2O_4$ (spinel) and Al_2O_3 (alumina) following irradiation with ions of varying mass and energy at room temperature and 650°C. Dislocation loop formation was suppressed in specimens irradiated with light ions, particularly in the case of spinel. An evaluation of the data showed that dislocation loop formation during irradiation at 650°C was suppressed when the ratio of the electronic- to nuclear-stopping power was greater than ~10 and ~1000 for spinel and alumina, respectively. The effect of uniform background levels of ionizing radiation on the microstructural evolution in spinel was investigated by performing simultaneous dual-beam (He^+ and heavy ion) irradiations. The uniform ionizing radiation source did not affect the microstructural evolution of spinel unless the ionization was very intense (average electronic- to nuclear-stopping power ratio >100). These results clearly indicate that light ion and electron irradiations produce microstructures which are not representative of the microstructure that would form in these ceramics during fission or fusion neutron irradiation.

It has been observed that some oxide ceramics which have an electric field applied to them while simultaneously being irradiated may undergo a degradation of their insulating properties under certain conditions. An *in-situ* DC conductivity capsule has been constructed to study the effect of neutron irradiation on the electrical conductivity of alumina with an applied electric field at the HFBR. The current capsule differs from a previous design in that the current measurements are performed on the low voltage side of the circuit.

The data acquisition system to be described here has been built and will be used to perform the electrical conductivity measurements in an experiment scheduled to begin in October 1994.

The crystal structures of $MgAl_2O_4$ spinel single crystals irradiated to high neutron fluences [$5 \cdot 10^{26}$ n/m^2 (E_n>0.1 MeV)] were examined by neutron diffraction. Crystal structure refinement of the highest dose sample indicated that the average scattering strength of the tetrahedral crystal sites decreased by ~20% while increasing by ~8% on octahedral sites. Since the neutron scattering length for Mg is considerably larger than for Al, this result is consistent with site exchange between Mg^{2+} ions on tetrahedral sites and al^{3+} ions on octahedral sites. Least-squares refinements also indicated that, in all irradiated samples, at least 35% of Mg^{2+} and Al^{3+} ions in the crystal experienced disordering replacements. This retained dpa on the cation sublattices is the largest retained damage ever measured in an irradiated spinel material.

Elastic constants (C_{11}, C_{12}, and C_{44}) of spinel ($MgAl_2O_4$) single crystals irradiated to very high neutron fluences have been measured by an ultrasonic technique. Although results of a neutron diffraction study show that cation occupation sites are significantly changed in the irradiated samples, no measurable differences occurred in their elastic properties. In order to understand such behavior, the elastic properties of a variety of materials with either normal or inverse spinel structures were studied. The cation valence and cation distribution appear to have little influence on the elastic properties of spinel materials.

ITER plasma performance will be monitored by fiber optics cables capable of transmitting light of various wavelengths in the ultraviolet, visible, and near infrared regime. The fibers must retain their optical integrity under extreme conditions of elevated temperature and mixed neutron and γ-ray exposure. Previous research has shown that fibers composed of pure silica cores and fluorine-doped cladding might be appropriate candidates for this application. Optical absorption and emission on commercially-available silica fibers containing both low (<1 ppm) and high (600-800 ppm) OH concentrations, that had been irradiated at the Los Alamos Spallation Radiation Effects Facility (LASREF) to a fluence of 10^{23} n-m^2, were measured in the wavelength interval 200-800 nm. Generally the low-OH fiber performance was superior, although neither fiber exhibited the optimum optical integrity required for ITER diagnostic applications. Both unirradiated fibers showed good transmissivity in the region of 400-800 nm; however, following irradiation each exhibited strong absorption over the entire wavelength region except for a small interval around 400 to 500 nm. Attempts to thermally anneal or photobleach the radiation-induced damage were only partially successful. In addition to the poor transmission properties of the irradiated fibers in the 200-800 nm region, there was intrinsic luminescence near 460 nm that occurred during exposure to *continuous* x irradiation at room temperature. This emission, if induced by neutrons and γ-rays of the ITER environment, would interfere with optical diagnostic measurements.

1.0 IRRADIATION FACILITIES, TEST MATRICES, AND EXPERIMENTAL METHODS

STATUS OF U.S./JAPAN COLLABORATIVE PROGRAM PHASE II HFIR TARGET AND RB* CAPSULES – J. E. Pawel, K. E. Lenox, A. W. Longest, R. L. Senn, (Oak Ridge National Laboratory), and K. Shiba (Japan Atomic Energy Research Institute)

OBJECTIVE

The objective of the HFIR irradiations is to determine the response of various U.S. and Japanese austenitic and ferritic steels with different pretreatments and alloy compositions to the combined effects of displacement damage and helium generation. Specimen temperatures during irradiation range from 60 to 600°C and fluences range up to 60 dpa. The RB* experiments are a continuation of the ORR spectrally tailored experiments in which the spectrum is modified with a hafnium shield to simulate the expected fusion helium to damage (He/dpa) ratio. In the HFIR target capsules, many specimens have been isotopically tailored in order to achieve fusion helium generation rates.

SUMMARY

Capsules HFIR-MFE-JP9 through 16 were installed in the High Flux Isotope Reactor (HFIR) target July 20, 1990 for irradiation beginning with HFIR fuel cycle 289. Of these eight target capsules, JP10, 11, 13, and 16 accumulated 18 dpa and were removed from the reactor in September 1991. JP14 was removed from the reactor at the end of cycle 310 (September 1992) after achieving a peak of 34 dpa. Capsules JP9, 12, and 15 completed 35 cycles on April 1, 1994 and were removed from the target region. Each capsule had accumulated a peak of approximately 57 dpa.

Three additional capsules, HFIR-MFE-JP20, 21, and 22, have been designed to complete the original experiment matrix of the JP9 through JP16 series capsules. Irradiation began in December 1993 with the start of cycle 322. Capsule JP20 was removed from the reactor on June 3, 1994, after accumulating a peak of 8 dpa. As of September 16, 1994 (end of cycle 329), each of the other two capsules had achieved approximately 9.5 dpa.

The RB* experiments are the continuation of the ORR spectrally tailored experiments. In this stage, a hafnium liner is used to modify the spectrum to simulate the fusion helium to displacements per atom (He/dpa) ratio in the austenitic steel specimens. Of the four capsules in this set, two (60J-1 and 330J-1) have been disassembled and testing is in progress. Two capsules (200J-1 and 400J-1) are in the reactor and have accumulated 8 dpa.

PROGRESS AND STATUS

Target Capsules JP9 through JP16

Capsules HFIR-MFE-JP9 through 16 were installed in the High Flux Isotope Reactor (HFIR) target July 20, 1990 for irradiation beginning with HFIR fuel cycle 289. A complete description and details of the design, construction, and installation of capsules JP9 through JP16 have been previously reported [1,2,3]. The as-built specimen matrix can be found in a previous report [3]. These capsules contain primarily transmission electron microscopy disks (TEM) and SS-3 flat tensile specimens. A wide variety of alloys and thermomechanical conditions are included. Many of the TEM disks were made from isotopically tailored alloys to produce a range of He/dpa ratios (<0.1, 10, 20, 70 appm/dpa). Details of the irradiation history of these capsules are shown in Table 1. Capsules JP10, 11, 13, and 16 were removed at the end of Cycle 300 (September 1991) after achieving a total of 18 dpa. Capsule JP14 was removed at the end of Cycle 310 (September 1992), after accumulating 34 dpa. Capsules JP9, 12, and 15 completed 35 cycles and achieved a peak fluence of 57 dpa on April 1, 1994 and were removed from the reactor target region. These three capsules were disassembled in September 1994 and specimen testing is scheduled to begin during the next reporting period.

Table 1. Irradiation History of HFIR Target Capsules JP-9, -12, and -15

HFIR Operation				**JP-9, -12, -15†**	
Cycle No.	Start Date	End Date	MWd/Cycle	MWd	dpa*
289	7/20/90	9/7/90	1879	1879	1.64
290	9/19/90	10/11/90	1852	3731	3.26
291	10/17/90	11/13/90	1838	5569	4.86
292	11/25/90	12/10/90	1847	7416	6.47
293	12/27/90	1/23/91	1965	REMOVED FOR 1 CYCLE	
294	2/1/91	2/25/91	1906	9322	8.14
295	3/1/91	3/24/91	1908	11230	9.80
296	4/6/91	4/28/91	1874	13104	11.44
297	5/19/91	6/15/91	1845	14949	13.05
298	6/20/91	7/11/91	1747	16696	14.58
299	7/25/91	8/15/91	1741	18437	16.10
300	8/28/91	9/17/91	1724	20161	17.60
301	9/27/91	10/19/91	1851	22012	19.22
302	10/27/91	11/21/91	1829	23841	20.81
303	12/1/91	12/22/91	1821	25662	22.40
304	12/31/91	1/24/92	1826	27488	24.00
305	1/30/92	2/27/92	1876	29364	25.63
306	3/31/92	4/27/92	1845	31209	27.25
307	5/1/92	5/28/92	1842	33051	28.85
308	6/2/92	6/30/92	1938	34989	30.55
309	7/3/92	8/1/92	1949	36938	32.25
310	8/27/92	9/18/92	1848	38786	33.86
311	9/25/92	10/12/92	1856	40642	35.48
312	10/22/92	11/14/92	1834	42476	37.08
313	11/21/92	12/15/92	1858	44334	38.70
314	12/20/92	1/12/93	1867	46201	40.33
315	1/19/93	2/11/93	1861	48062	41.96
316	2/17/93	4/3/93	1807	49869	43.54
317	4/23/93	5/14/93	1841	51710	45.14
318	5/20/93	6/13/93	1878	53588	46.78
319	6/18/93	7/10/93	1863	55451	48.41
320	7/15/93	8/7/93	1934	57385	50.10
321	8/12/93	9/4/93	1884	59269	51.74
322	12/16/93	1/7/93	1854	61123	53.36
323	1/23/94	2/14/93	1874	62997	55.00
324	3/5/94	4/1/94	1907	64904	56.66
				REMOVED EOC 324	

†JP-10, -11, -13, and -16 removed at End of Cycle 300; JP-14 removed at End of Cycle 310

*dpa levels based on 0.000873 dpa/MWd in the target capsules

Target Capsules JP20 through 22

Three additional capsules, HFIR-MFE-JP20, 21, and 22, were designed to complete the original experiment matrix of the JP9 through JP16 series capsules [4]. Specimen temperatures in each capsule are 300, 400, 500, or 600°C. The complete test matrix is described in Reference 5. Irradiation began December 16, 1993 with the start of cycle 322. Capsule JP20 was removed from the reactor on June 3, 1994, after accumulating a peak dose of 8 dpa, and was disassembled in September 1994. As of September 16, 1994 (end of cycle 329), each of the other two capsules had achieved approximately 9.5 dpa (see Table 2).

Table 2. Irradiation History of HFIR Target Capsules JP-20, 021, and -22

	HFIR Operation			**JP-20, -21, -22†**	
Cycle No.	Start Date	End Date	MWd/Cycle	MWd	dpa*
322	12/16/93	1/7/94	1854	1854	1.62
323	1/23/94	2/14/94	1874	3728	3.25
324	3/5/94	4/1/94	1907	5635	4.92
325	4/10/94	5/3/94	1907	7542	6.58
326	5/8/94	6/3/94	1825	9367	8.18
327	6/26/94	7/18/94	1903	REMOVED FOR	
328	7/31/94	8/21/94	1922	2 CYCLES	
329	8/27/94	9/16/94	1513‡	10880	9.50

†JP-20 removed at End of Cycle 326

*dpa levels based on 0.000873 dpa/MWd in the target capsules

‡Due to power variations over this cycle, this number is not exact

RB* Capsules HFIR-MFE-60J-1, 200J-1, 330J-1 and 400J-1

The RB* capsules are irradiated in the removable beryllium positions of the HFIR. These experiments are a continuation of the ORR spectrally tailored experiments ORR-MFE-6J and 7J. At this stage in the experiment, a hafnium liner surrounds the capsules in order to harden the spectrum and achieve the expected fusion helium generation rate in the austenitic steel specimens. Capsule design, assembly and details of specimen loading have been previously described [6-9]. Capsules 60J-1 and 330J-1 were removed from the reactor in November 1992 after accumulating approximately 11 dpa in the HFIR. Details concerning the performance of these capsules can be found in Reference 10. Most of the specimens had also been irradiated to approximately 7 dpa in the ORR (for a total of 18 dpa in these specimens). These capsules were disassembled in February 1994. Capsules 200J-1 and 400J-1 have completed 17 of the scheduled 20 irradiation cycles, as shown in Table 3. The capsules are performing as designed, with the temperatures holding within the expected ranges. Details of the capsule performances have been described [11].

Gamma counting was conducted on four of the 24 flux monitors from each of 60J-1 and 330J-1. These data have been analyzed and are reported in Reference 12. In addition to the flux analysis, helium analysis was performed on one TEM disk, irradiated in both the 7J and 330J-1 experiments. The results indicate that these experiments were successful in producing fusion relevant helium/dpa levels. The maximum helium (appm)/dpa ratio is 10.2 for 60J-1 and 11.8 for 330J-1.

Tensile testing of J316 alloy specimens, in either the solution annealed or cold-worked condition, was conducted during this reporting period. Details of these tests and the results are described elsewhere [13].

Table 3. Irradiation History of HFIR-MFE-200J-1 and 400J-1

HFIR Operation				**200J-1 and 400J-1**	
Cycle No.	Start Date	End Date	MWd/Cycle	MWd	dpa*
313	11/21/92	12/15/92	1858	1858	0.46
314	12/20/92	1/12/93	1867	3725	0.91
315	1/19/93	2/11/93	1861	5586	1.37
316	2/17/93	4/3/93	1807	7393	1.81
317	4/23/93	5/14/93	1841	9234	2.26
318	5/20/93	6/13/93	1878	11112	2.72
319	6/18/93	7/10/93	1863	12975	3.18
320	7/15/93	8/7/93	1934	14909	3.65
321	8/12/93	9/4/93	1884	16793	4.11
322	12/16/93	1/7/94	1854	18647	4.57
323	1/23/94	2/14/94	1874	20521	5.03
324	3/5/94	4/1/94	1907	22428	5.49
325	4/10/94	5/3/94	1907	24335	5.96
326	5/8/94	6/3/94	1825	26160	6.41
327	6/26/94	7/18/94	1903	28063	6.88
328	7/31/94	8/21/94	1922	29985	7.35
329	8/27/94	9/16/94	1513‡	31498	7.72

*dpa levels based on 0.000245 dpa/MWd

‡Due to power variations over this cycle, this number is not exact

REFERENCES

1. R. L. Senn, "Status of U.S./Japan Collaborative Program Phase II HFIR Target Capsules," Fusion Reactor Materials Semiannual Progress Report for the Period Ending September 30, 1987, DOE/ER-0313/3, U.S. DOE Office of Fusion Energy, 1988, p. 8.

2. R. L. Senn, "Status of U.S./Japan Collaborative Program Phase II HFIR Target Capsules," Fusion Reactor Materials Semiannual Progress Report for the Period Ending March 31, 1988, DOE/ER-0313/4, U.S. DOE Office of Fusion Energy, 1988, p. 7.

3. R. L. Senn, "Status of U.S./Japan Collaborative Program Phase II HFIR Target Capsules," Fusion Reactor Materials Semiannual Progress Report for the Period Ending September 30, 1988, DOE/ER-0313/5, U.S. DOE Office of Fusion Energy, 1989, p. 6.

4. J. E. Pawel and R. L. Senn, "Status of U.S./Japan Collaborative Program Phase II HFIR Target Capsules," Fusion Reactor Materials Semiannual Progress Report for Period Ending March 31, 1992, DOE/ER-0313/12, U.S. DOE Office of Fusion Energy, 1992, p. 15.

5. J. E. Pawel, A. W. Longest, R. L. Senn, K. Shiba, D. W. Heatherly, and R. G. Sitterson, "Status of U.S./Japan Collaborative Program Phase II HFIR Target and RB* Capsules," Fusion Reactor Materials Semiannual Progress Report for Period Ending September 30, 1993, DOE/ER-0313/15, U.S. DOE Office of Fusion Energy, 1994, p. 3.

6. A. W. Longest, J. E. Corum, D. W. Heatherly, and K. R. Thoms, "Design and Fabrication of HFIR-MFE RB* Spectrally Tailored Irradiation Capsules," Fusion Reactor Materials Semiannual Progress Report for Period Ending September 30, 1987, DOE/ER-0313/3, U.S. DOE Office of Fusion Energy, 1988, p. 2.

7. A. W. Longest, J. E. Corum, and D. W. Heatherly, "Design and Fabrication of HFIR-MFE RB* Spectrally Tailored Irradiation Capsules," Fusion Reactor Materials Semiannual Progress Report for Period Ending March 31, 1988, DOE/ER-0313/4, U.S. DOE Office of Fusion Energy, 1988, p. 2.

8. A. W. Longest, J. E. Corum, and D. W. Heatherly, "Design and Fabrication of HFIR-MFE RB* Spectrally Tailored Irradiation Capsules," Fusion Reactor Materials Semiannual Progress Report for Period Ending September 30, 1988, DOE/ER-0313/5, U.S. DOE Office of Fusion Energy, 1989, p. 2.

9. A. W. Longest, J. E. Pawel, D. W. Heatherly, R. G. Sitterson, and R. L. Wallace, "Fabrication and Operation of HFIR-MFE RB* Spectrally Tailored Irradiation Capsules," Fusion Reactor Materials Semiannual Progress Report for Period Ending March 30, 1993, DOE/ER-0313/14, U.S. DOE Office of Fusion Energy, 1993, p. 14.

10. A. W. Longest, D. W. Heatherly, E. D. Clemmer, and J. E. Corum, "Fabrication and Operation of HFIR-MFE RB* Spectrally Tailored Irradiation Capsules," Fusion Reactor Materials Semiannual Progress Report for Period Ending September 30, 1991, DOE/ER-0313/11, U.S. DOE Office of Fusion Energy, 1992, p. 17.

11. A. W. Longest, J. E. Pawel, D. W. Heatherly, R. G. Sitterson, and R. L. Wallace, "Fabrication and Operation of HFIR-MFE RB* Spectrally Tailored Irradiation Capsules," Fusion Reactor Materials Semiannual Progress Report for Period Ending September 30, 1993, DOE/ER-0313/15, U.S. DOE Office of Fusion Energy, 1992, p. 23.

12. L. R. Greenwood, C. A. Baldwin, and B. M. Oliver, "Neutron Dosimetry, Damage Calculations, and Helium Measurements for the HFIR-MFE-60J-1 and MFE-330J-1 Spectral Tailoring Experiments," this report.

13. J. E. Pawel, M. L. Grossbeck, A. F. Rowcliffe, and K. Shiba, "Initial Tensile Test Results from J316 Stainless Steel Irradiated in the HFIR Spectrally Tailored Experiment," this report.

VANADIUM ALLOY IRRADIATION EXPERIMENT X530 IN EBR-II*

H. Tsai, R. V. Strain, A. G. Hins, H. M. Chung, L. J. Nowicki, and D. L. Smith
(Argonne National Laboratory)

OBJECTIVE

The objective of the X530 experiment in EBR-II was to obtain early irradiation performance data, particularly the fracture properties, on the new 500-kg production heat of V-4Cr-4Ti material before the scheduled reactor shutdown at the end of September 1994.

SUMMARY

To obtain early irradiation performance data on the new 500-kg production heat of the V-4Cr-4Ti material before the scheduled EBR-II shutdown, an experiment, X530, was expeditiously designed and assembled. Charpy, compact tension, tensile and TEM specimens with different thermal mechanical treatments (TMTs), were enclosed in two capsules and irradiated in the last run of EBR-II, Run 170, from August 9 through September 27. For comparison, specimens from some of the previous heats were also included in the test. The accrued exposure was 35 effective full power days, yielding a peak damage of ≈4 dpa in the specimens. The irradiation is now complete and the vehicle is awaiting to be discharged from EBR-II for postirradiation disassembly.

PROGRESS AND STATUS

Introduction

V-4 wt.%Cr-4 wt.%Ti has been identified as the most promising vanadium-based alloy for application in fusion reactor first wall and blanket structures. A 500-kg production heat of the V-4Cr-4Ti alloy was recently produced (see accompanying article in this report) as part of the developmental effort. It is important to confirm at an early date the performance of this new heat with irradiation in a fast flux environment. A decision was made in June 1994 to test this material in an irradiation experiment in EBR-II before the scheduled reactor shutdown at the end of September 1994.

In addition to the production heat V-4Cr-4Ti material, several earlier heats of ternary and binary vanadium alloys, and a Russian heat of V-4Cr-4Ti, were included in the experiment for comparison. A ^{10}B-doped V-4Cr-4Ti material was included to study the effect of helium generation on mechanical properties. The irradiation temperature for the test was ≈375-400°C, the lowest attainable in EBR-II, because of the importance of low-temperature data for ITER.

Thermal mechanical treatments are known to have significant effects on the mechanical properties of body-center-cubic metals, e.g., the vanadium alloys. One of the objectives of the experiment was to investigate these effects. The production heat and a V-5Cr-5Ti material were given different heat treatments before irradiation for this study.

Experiment Description

Hardware

The irradiation consisted of two Mark B7 (0.807-in. diameter) capsules with six subcapsules in each capsule. Near the top and bottom end of the capsules, holes were drilled through the capsule walls so that

---

* This work has been supported by the U.S. Department of Energy, Office of Fusion Energy Research, under Contract W-31-109-Eng-38.

reactor coolant sodium could flow between the capsule and the subcapsules to provide heat transfer. Lithium was used as a heat transfer medium for the specimens in the sealed subcapsules. All capsule and subcapsule components were fabricated from Type 316 stainless steel.

The specimens were machined from either sheets or plates of the specified heats of material. The as-machined specimens were polished and then given a heat treatment in a vacuum to remove any hydrogen that may have been adsorbed during these procedures.

An important aspect of the fabrication of the subcapsules was the handling, purification, and loading of the lithium. Primary operations were performed in an ultra-high-purity helium glovebox (oxygen level ≈30 ppb). Prior to introducing lithium into the helium glovebox, an initial purification step was removal of the outer rind from the lithium ingots that were stored in oil. This operation was performed in a small argon-atmosphere glovebox. The interstitial content of the lithium was reduced by heating it with SAES getter pellets at 650°C for about 22 h. During this process, the nitrogen content was reduced from ≈400 ppm to ≈10 ppm. After the purification, the lithium was poured into tantalum trays at a temperature of 250°C. The lithium was prepared for loading into the subcapsules by cutting 0.625-in.-diameter pellets from the 0.5-in.-thick sheets in the tantalum trays with a "cork borer." The Li pellets were cut to length and loaded into the bottom of the subcapsules. The specimens were then placed on top of the Li-pellet (a typical loading is shown in Fig. 1). The subcapsules were capped with a tight-fitting lid and transferred to another He-atmosphere glovebox for welding.

Lithium Loading

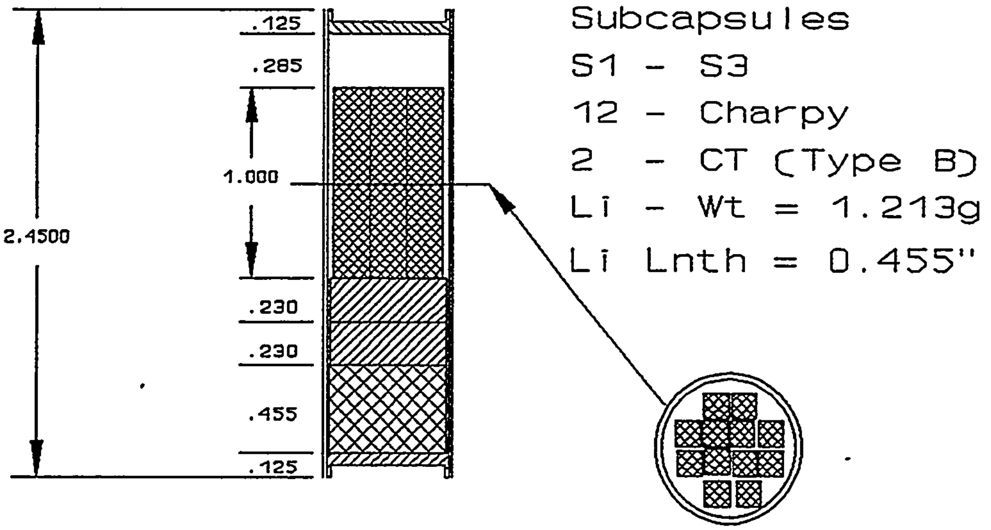

Fig. 1. Typical Subcapsule Loading for the X530 Irradiation.

The subcapsules and appropriate spacers and shields were then loaded into the capsules as shown in Figs. 2 and 3. These two capsules, four dummy rods, and a capsule containing samples of yttria (for the National Institute of Standards and Technology) were assembled in a Mark B7A subassembly and placed in Row 2 of EBR-II. The surface temperatures for the subcapsules were calculated using the HECTIC heat transfer code. Heat transfer from the adjacent subassemblies was important in this low-power, low-flow subassembly. The temperature calculations indicated that specimen temperatures differed with their axial positions in the subassembly (Fig. 4) and were between 370 and 410°C.

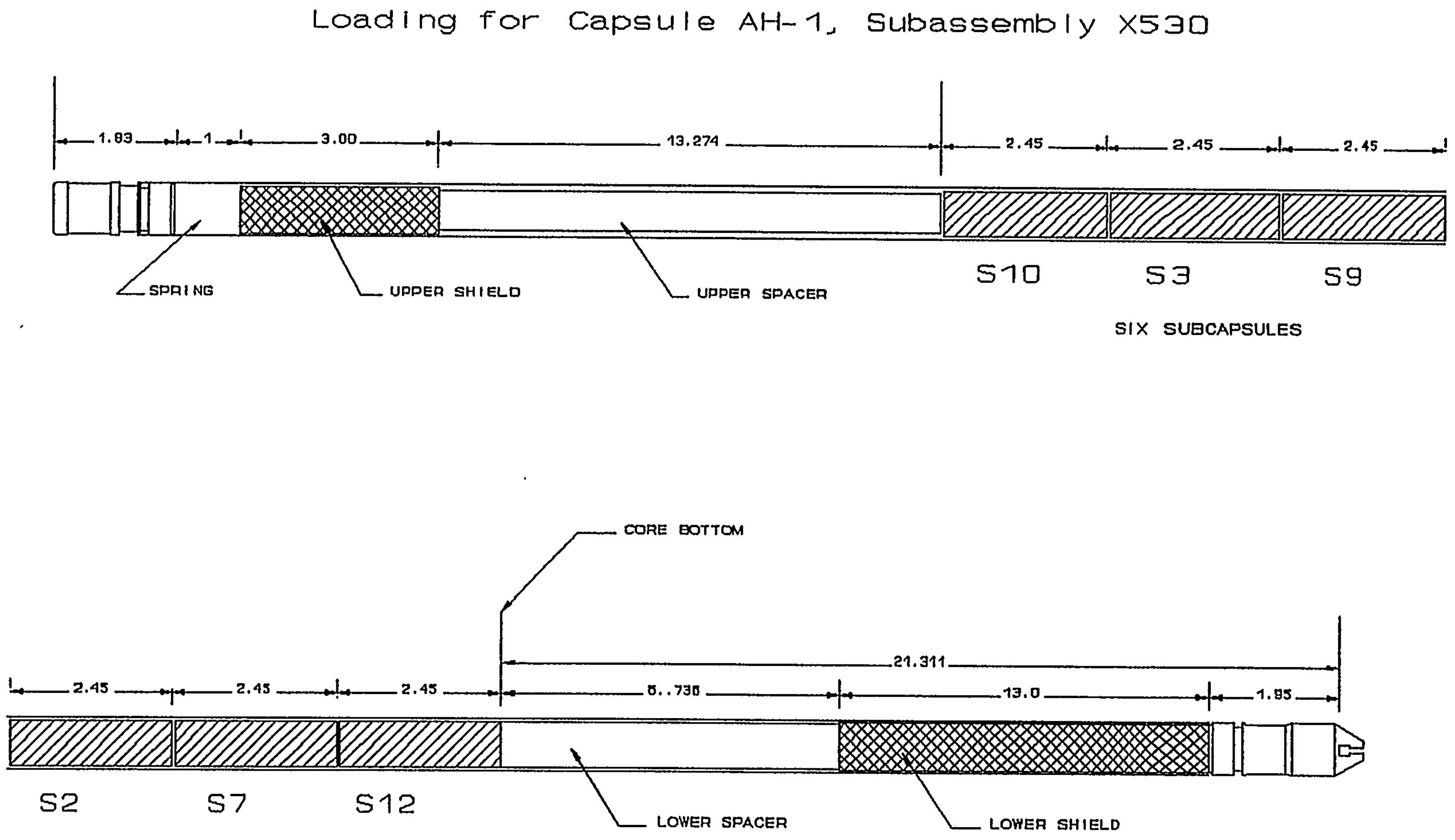

Fig. 2. Loading of Capsule AH-1 for X530.

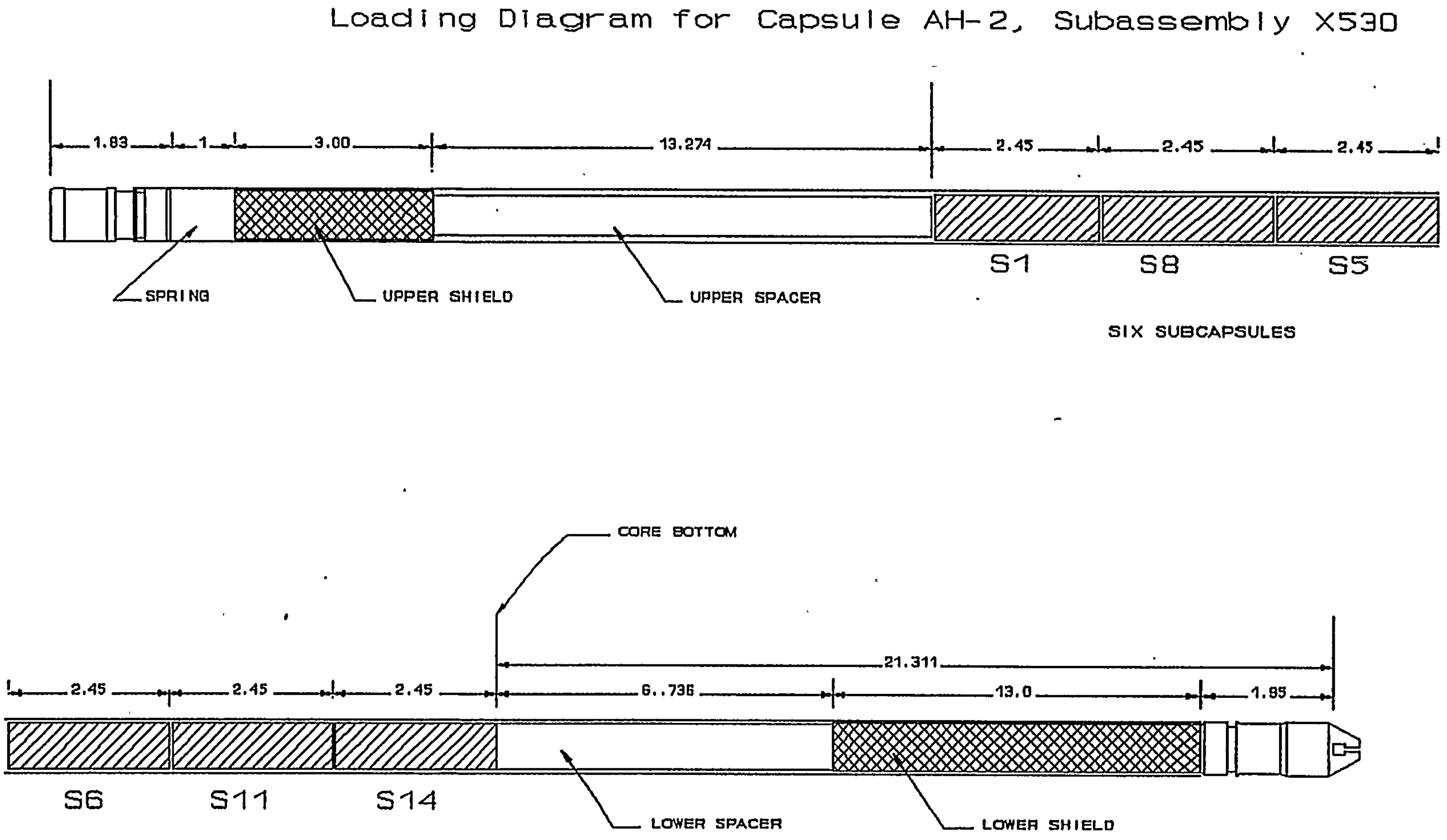

Fig. 3. Loading of Capsule AH-2 for X530.

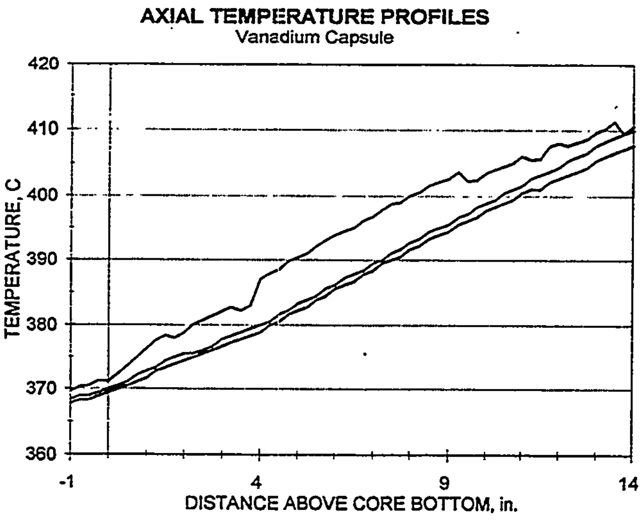

Fig. 4. Calculated Axial Temperature Profile for Capsule AH–1.

Test Matrix

The list of specimens included in the X530 experiment is shown in Table 1, and specimen loadings in the subcapsules are summarized in Table 2.

The most important, and hence most extensively tested, material in the X530 experiment was the 500-kg production heat V-4Cr-4Ti material (Heat No. 832665, also designated BL-71). The test specimens consisted of disk compact tension, 1/3-size Charpy, SS-3 tensile, and transmission electron microscopy disks. These specimens were prepared from sheets/plates that were hot rolled at ≈400°C, followed by a vacuum annealing at 950, 1050, or 1125°C. The purpose of the different annealing temperatures was to yield data on the effects of TMT on mechanical properties.

The other materials included in the X530 test were

- A 250 ppm-^{10}B-doped V-4Cr-4Ti material (BL-70) to study the effect of helium generation,
- A Russian Federation heat of V-4Cr-4Ti material (BL-69),
- A V-5Cr-5Ti material (BL-63) whose original fracture properties were marginal and that was modified for this test by additional TMTs, i.e., either cold rolling or warm rolling at 400°C, then annealing at 950 or 1050°C, and
- Several other earlier heats of materials with different binary or ternary compositions.

Depending on emphasis and material availability, as shown in Table 1, not all forms of specimens were prepared for all materials.

Irradiation History

Subassembly X530 was loaded into EBR-II core position 2F1 (with a fast flux of 2.4 x 10^{15} $n\cdot cm^{-2}\cdot s^{-1}$, E>0.11 MeV) and irradiated for the entire 170A run from August 19 until the final reactor shutdown on September 27. The accrued exposure was 35 effective full power days, yielding a peak damage of ≈4 dpa in the vanadium specimens.

For Run 170A, the reactor inlet temperature was lowered from the nominal 371 to 366°C. The flow rate for the subassembly was 13.3 gpm, within the requested range.

Table 1. Types and Numbers of Specimens Irradiated in the X530 Experiment

Composition, wt.%	ANL ID Number	DCT-A, 0.140 in.	DCT-B, 0.230 in.	1/3-size Charpy	SS-3 Tensile	TEM
V-3Ti-1Si	BL-45	-	-	5	2	-
V-5Ti	BL-46	3	-	5	2	5
V-4Cr-4Ti	BL-74	-	4	6	-	-
V-7Cr-5Ti	BL-49	3	-	5	2	5
V-5Cr-3Ti	BL-54	-	-	5	-	-
V-3Ti	BL-62	3	-	5	2	4
V-5Cr-5Ti	BL-63	-	2	5	2	-
V-5Cr-5Ti	BL-63-CR950	1	-	5	2	3
V-5Cr-5Ti	BL-63-CR1050	1	-	5	2	3
V-5Cr-5Ti	BL-63-WR950	1	-	5	2	3
V-5Cr-5Ti	BL-63-WR1050	1	-	5	2	3
V-4Cr-4Ti-RF	BL-69	-	-	-	5	5
V-4Cr-4Ti-B	BL-70	4	4	6	5	5
V-4Cr-4Ti	BL-71-WR950	4	-	6	5	5
V-4Cr-4Ti	BL-71-WR1050	4	-	6	5	5
V-4Cr-4Ti	BL-71-WR1125	3	-	6	5	5
SUBTOTAL		28	10	80	43	51

B = Boron doped (250 appm ^{10}B)
RF = Russian Federation
CR950 = Cold roll and final anneal at 950°C
CR1050 = Cold roll and final anneal at 1050°C
WR950 = Warm roll and final anneal at 950°C
WR1050 = Warm roll and final anneal at 1050°C
WR1125 = Warm roll and final anneal at 1125°C

FUTURE ACTIVITIES

X530 has successfully completed the planned irradiation in EBR-II Run 170. Instructions have been given to EBR-II personnel to discharge and disassemble the test vehicle. Nondestructive examination, including neutron radiography, is scheduled for the two capsules before their return to ANL-East for disassembly and specimen retrieval. Initial results on specimen examination and testing are expected to be available in the next reporting period.

Table 2. Subcapsule Specimen Loading for X530

Capsule	Specimen Type	Material Composition	Quantity	Capsule	Specimen Type	Material Composition	Quantity
S1	DCT-B	V-4Cr-4Ti (BL-74)	2	S8	Tensile	V-3Ti (BL-62)	2
	Charpy	V-3Ti-1Si (BL-45)	5		Tensile	V-5Ti (BL-46)	2
	Charpy	V-5Ti (BL-46)	5		Tensile	V-7Cr-5Ti (BL-49)	2
	Charpy	V-7Cr-5Ti (BL-49)	2		Tensile	V-3Ti (BL-62)	2
					Tensile	V-5Cr-5Ti (BL-63	2
S2	DCT-B	V-4Cr-4Ti (BL-74)	2		Tensile	V-5Cr-5Ti (BL-63)	2
	Charpy	V-4Cr-4Ti (BL-74)	6		Tensile	V-5Cr-5Ti (BL-63)	2
	Charpy	V-7Cr-5Ti (BL-49)	1		Tensile	V-5Cr-5Ti (BL-63)	2
	Charpy	V-5Cr-3Ti (BL-54)	5		Tensile	V-5Cr-5Ti (BL-63)	2
					Tensile	V-4Cr-4Ti (RF)	3
S3	DCT-B	V-5Cr-5Ti (BL-63)	2		TE	V-5Ti (BL-46)	5
	Charpy	V-7Cr-5Ti (BL-49)	2		TE	V-7Cr-5Ti (BL-49)	5
	Charpy	V-3Ti (BL-62)	5		TE	V-3Ti (BL-62)	4
	Charpy	V-5Cr-5Ti (BL-63)	5		TE	V-5Cr-5Ti (BL-63)	3
					TE	V-5Cr-5Ti (BL-63)	3
S14	DCT-B	V-4Cr-4Ti-B (BL-70)	2		TE	V-5Cr-5Ti (BL-63)	3
	Charpy	V-5Cr-5Ti (BL-63)	5		TE	V-5Cr-5Ti (BL-63)	3
	Charpy	V-4Cr-4Ti-B (BL-70)	6				
				S9	Tensile	V-4Cr-4Ti (RF)	2
S4	DCT-B	V-4Cr-4Ti-B (BL-70)	2		Tensile	V-4Cr-4Ti-B (BL-70)	5
	Charpy	V-5Cr-5Ti (BL-63)	5		Tensile	V-4Cr-4Ti (BL-71)	5
	Charpy	V-4Cr-4Ti (BL-71)	6		Tensile	V-4Cr-4Ti (BL-71)	5
					Tensile	V-4Cr-4Ti (BL-71)	5
S6	DCT-A	V-5Ti (BL-46)	2		TE	V-4Cr-4Ti (RF)	5
	Charpy	V-5Cr-5Ti (BL-63)	5		TE	V-4Cr-4Ti-B (BL-70)	5
	Charpy	V-4Cr-4Ti (BL-71)	6		TE	V-4Cr-4Ti (BL-71)	5
					TE	V-4Cr-4Ti (BL-71)	5
S7	DCT-A	V-5Ti (BL-46)	1		TE	V-4Cr-4Ti (BL-71)	5
	DCT-A	V-7Cr-5Ti (BL-49)	1				
	Charpy	V-5Cr-5Ti (BL-63)	5	S10	DCT-A	V-7Cr-5Ti (BL-49)	2
	Charpy	V-4Cr-4Ti (BL-71)	6		DCT-A	V-3Ti (BL-62)	3
					DCT-A	V-4Cr-4Ti (BL-71)	3
				S11	DCT-A	V-5Cr-5Ti (BL-63)	1
					DCT-A	V-5Cr-5Ti (BL-63)	1
					DCT-A	V-5Cr-5Ti (BL-63)	1
					DCT-A	V-5Cr-5Ti (BL-63)	1
					DCT-A	V-4Cr-4Ti-B (BL-70)	4
				S12	DCT-A	V-4Cr-4Ti (BL-71)	4
					DCT-A	V-4Cr-4Ti (BL-71)	4

2.0 DOSIMETRY, DAMAGE PARAMETERS, AND ACTIVATION CALCULATIONS

Vanadium Irradiation at ATR - Neutronics Aspects - Itacil C. Gomes and Dale L. Smith (Argonne National Laboratory)

SUMMARY

Calculations were performed to estimate damage and transmutation rates in vanadium irradiated in the ATR (Advanced Test Reactor) located in Idaho. The main focuses of the study are to evaluate the transmutation of vanadium to chromium and to explore ways to design the irradiation experiment to avoid excessive transmutation. It was found that the A-hole of ATR produces damage rate of ~ 15-30 dpa/full power year with a transmutation rate of ~ 0.2%/dpa of vanadium to chromium. A thermal neutron filter can be incorporated into the design to reduce the vanadium-to-chromium transmutation rate to low levels. A filter 1-2 mm thick of gadolinium or hafnium can be used.

ATR Reactor

The Idaho National Engineering Laboratory's Advanced Test Reactor has a nominal full power output of 250 MW [1]. The reactor is composed basically of five nearly independent lobes which can operate at different power levels from each other during the same cycle. The nominal power of each lobe is 50 MW but power shifting allows a maximum lobe power of 60 MW - a minimum lobe power of 17 MW and the other lobes in between, producing a total power of 250 MW. Several irradiation holes are provided, with a variety of dimensions and neutron energy spectra. The vertical neutron flux distribution is relatively flat over a large portion of the height of the core (~70-80 cm of the ~120 cm core) which allows a larger active length of the irradiation capsule compared to other test reactors. This study focuses primarily on the A-10 hole position of the reactor; however, the numbers derived here can also be applied to holes which have a similar neutron energy spectrum to this particular hole.

Damage and Transmutation Rates

Despite having a nominal power level of 250 MW the ATR reactor has typically been operating at 125 MW [2]. The lobe in which the A-10 hole is located, in this operating scenario, has a power of 30 MW. Figure 1 shows the neutron energy spectrum at the A-10 hole. Table 1 presents the breakdown between fast and thermal neutron flux at this position compared with the HFIR (High Flux Irradiation Reactor) RB* position with and without hafnium cover (3mm thick).

Table 1. Breakdown of the neutron flux between fast and thermal components.

	ATR A-10	HFIR/RB*	HFIR/RB* with Hf
Fast (E>0.1MeV)	5.4×10^{14}	4.5×10^{14}	4.5×10^{14}
Thermal (E<1eV)	2.6×10^{14}	8.5×10^{14}	1.0×10^{14}

As one can notice from Table 1, the fast-to-thermal ratio in the A-10 hole is larger than the HFIR/RB* without using any thermal neutron filter. In terms of fusion materials irradiation testing, this ratio must be large to better simulate a fusion environment. The fast-to-thermal ratio in a first wall of a fusion device is typically larger than 30 and may even higher for some blanket concepts.

The calculated damage rate for the A-10 hole is 15 dpa/year for vanadium at a lobe power level of 30 MW. (It would be 30 dpa/fpy if one considers 60 MW). This damage rate can be compared with the HFIR/RB* position which produces a damage rate of 9 dpa/fpy for vanadium.

Figure 2 displays the variation of the chromium concentration in the V4Cr4Ti alloy as a function of the damage rate (dpa) for several reactors. These calculations indicate that the transmutation rate for ATR without any thermal neutron filter is considerably less than the RB* position of HFIR. Similar calculations for vanadium transmutations in the core-edge region of the SM-3 reactor (Russian reactor) are based on two different sources of information. The high value (0.3%/dpa) is based on the Russian calculation for the transmutation rate, whereas the lower rate (0.11%/dpa) is based on U.S. calculations using a neutron energy spectrum provided by the Russians. There remain high uncertainties in the actual values for the SM-3 reactor.

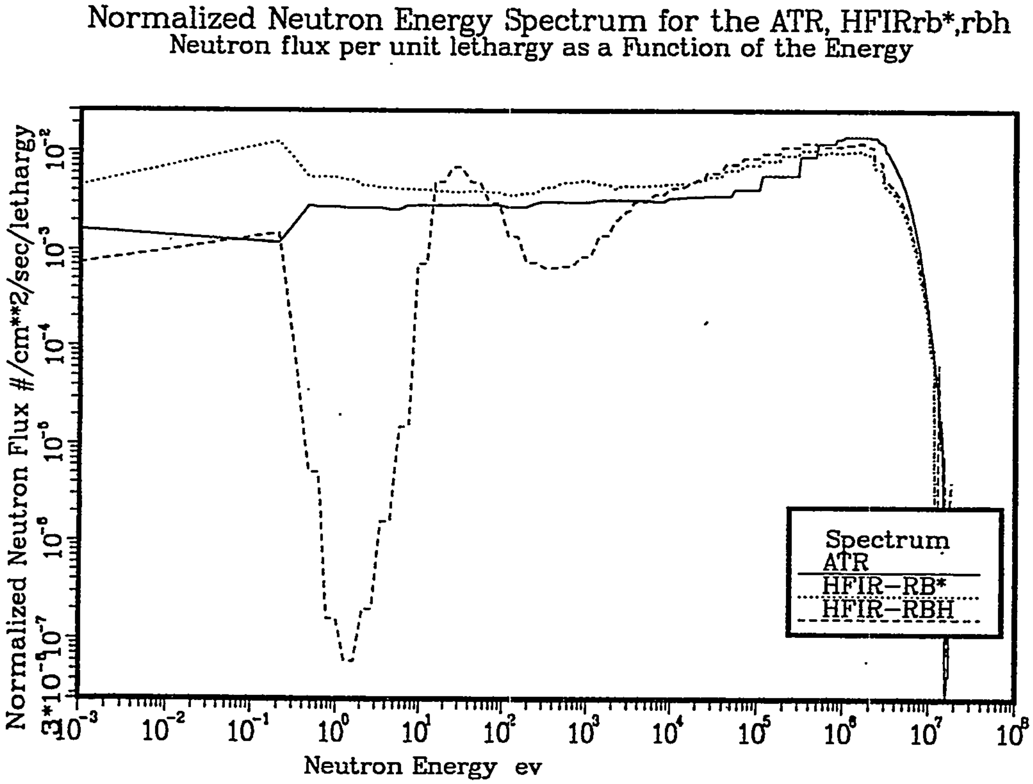

Figure 1. *Normalized neutron energy spectrum for the A-10 hole of the ATR reactor.*

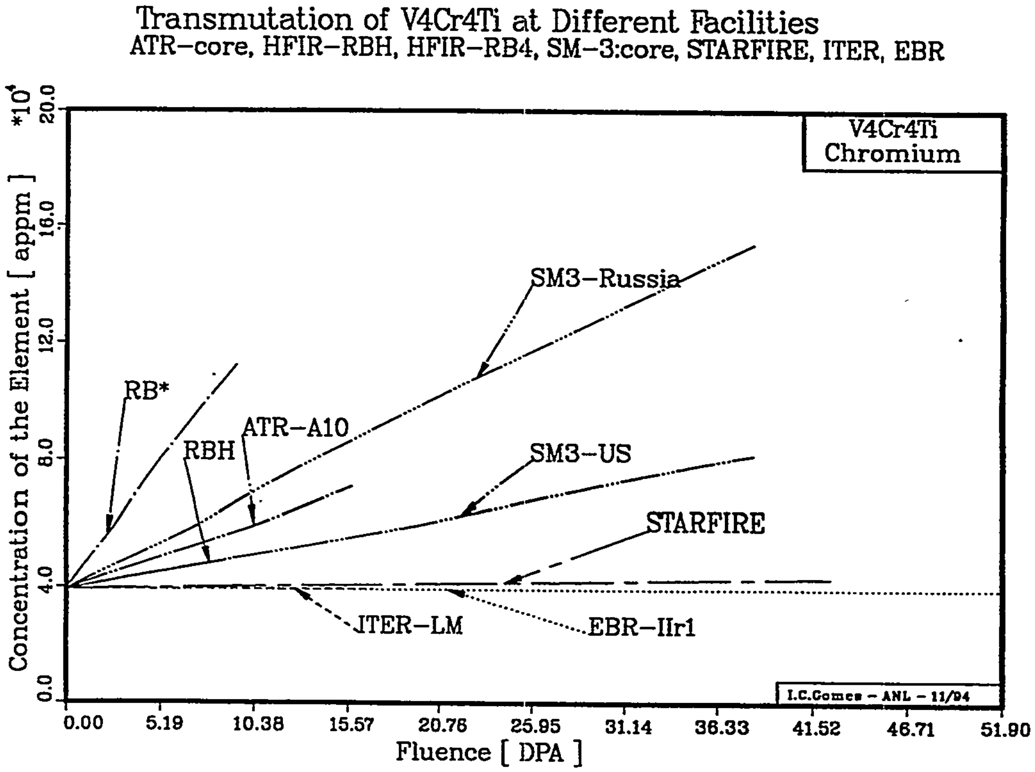

Figure 2. *Variation of the chromium concentration in the V4Cr4Ti alloy for different neutron environments as a function of the fluence (dpa).*

Thermal Neutron Filter

The transmutation of the elements in an alloy during irradiation testing should be compatible with that expected in the proposed operating environment, otherwise the post-irradiation test would be performed on a material with different compositional characteristics than that for the projected application. Vanadium has a significant transmutation cross-section (5 barns) at the thermal neutron energy region $[^{51}V(n,\gamma)\,^{52}V \rightarrow T\ 1/2 = 3.7\ \text{min.} \rightarrow {}^{52}Cr]$. Under high thermal neutron flux irradiation, transmutation rates up to 1%/dpa increase in the chromium content can be expected. For a typical fusion reactor first wall-spectrum, this transmutation rate is very low. This is also the case for fast fission reactor irradiations. To avoid significant changes in the composition of the vanadium alloys during irradiation in water cooled fission test reactors, the use of thermal neutron absorbers (or filters) is recommended in most of the cases.

In this section we analyze a few possible thermal neutron filters, including Hf, Cd, Gd and B_4C. Figure 3 displays a comparison of the performance of these filters without accounting for the burnup of the absorber atoms (assuming that the filter layer is thick enough to survive the full irradiation time represented). As one can see, Gd, Cd, and B_4C present a very good performance in absorbing the thermal neutrons and reducing the transmutation rate of vanadium. Hafnium reduces the transmutation rate by more than 50%, which may be acceptable for low fluence tests. Other issues associated with the use of the various thermal neutron filters are summarized below.

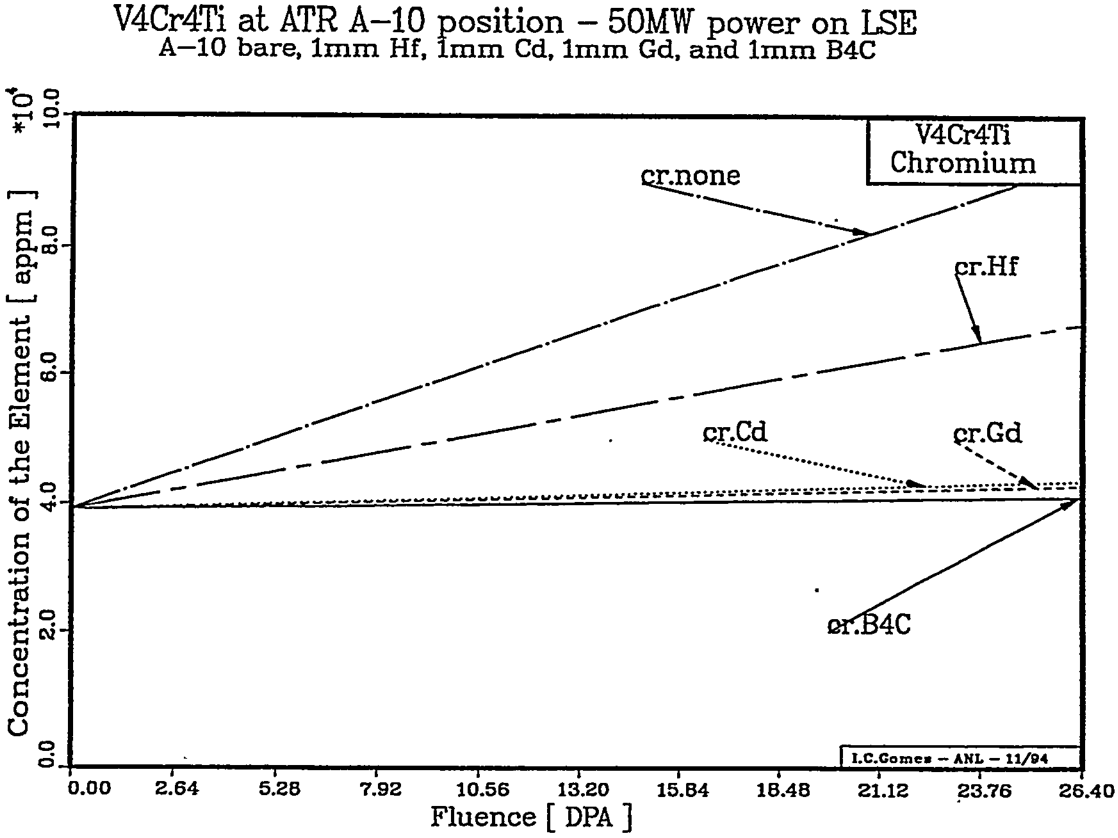

Figure 3. Influence of the different thermal neutron filters (1 mm thick) chromium in the A-10 hole of ATR.

- **Gadolinium:** The principal isotopes in the natural occurring gadolinium for thermal neutron absorption are the 155 and 157, which together account for 30.45% of the natural occurring gadolinium atoms. Burn-out of these isotopes will limit the lifetime of a gadolinium filter. In ATR with the lobe of the A-10 hole operating at 30 MW, a 1.7 mm layer of gadolinium is adequate for a fluence of 5 dpa. The increase in the chromium concentration under this scenario would be only ~ 0.007%. The additional gamma heating from the neutron absorption reaction was estimated to be 3 W/g in stainless steel.

- **B_4C:** Boron-10 is the isotope which absorbs the neutrons. In the ATR, under the conditions of this study, 1 mm of B_4C would last roughly 135 days or about 6 dpa in vanadium. But, the problem with B_4C is that for each neutron absorbed, one lithium-7 and one Helium-4 atoms are created. If the B_4C layer is confined, the pressure created by the helium gas would be unacceptable. On the other hand, if some space is left to allow the gas to flow to some kind of plenum, the lithium-7 production (about 20% of the boron atoms after 135 days of irradiation) would probably have a significant effect on the B_4C layer. Further studies are required to evaluate this solution.

- **Cadmium:** Cd-113 is the isotope which has a high absorption cross-section and its natural abundance is 12.22%. In the case studied, 1 mm-Cd cover would last about 50 days (~ 2 dpa) as an effective absorber.

- **Hafnium:** None of the hafnium isotopes have a very high cross-section in the thermal region. The highest cross-section for hafnium is in the epithermal region. The most important isotope in terms of reducing the neutron flux is Hf-177 and it has a natural abundance of 18.6%. A hafnium cover 1.1 mm thick would allow a fluence of 5 dpa with roughly a 0.5% increase in the chromium concentration.

CONCLUSION

To perform irradiation of vanadium in ATR is feasible and the transmutation from vanadium to chromium can be controlled using a thin filter cover of 1.7 mm of gadolinium or 1.1 of hafnium to reach fluences of 5 dpa with low transmutation rates.

REFERENCES

1. J.W. Rogers, R.A. Anderl, and M.H. Putnam, "Neutron Spectrum Studies in the ATR", Seventh ASTM-EURATOM Symposium on Reactor Dosemetry, Strasbourg, France, Agust 1990.

2. John Brasier, personal communication.

NEUTRON FLUX SPECTRA AND RADIATION DAMAGE PARAMETERS FOR THE RUSSIAN BOR-60 AND SM-2 REACTORS - A. V. Karasiov (D. V. Efremov Scientific Research Institute of Electrophysical Apparatus, St. Petersburg, Russia) and L. R. Greenwood (Pacific Northwest Laboratory)[a]

OBJECTIVE

To compare neutron irradiation conditions in Russian reactors and similar US facilities.

SUMMARY

Neutron fluence and spectral information and calculated radiation damage parameters are presented for the BOR-60 (Fast Experimental Reactor - 60 MW) and SM-2 reactors in Russia. Their neutron exposure characteristics are comparable with those of the Experimental Breeder Reactor (EBR-II), the Fast Flux Test Facility (FFTF), and the High Flux Isotope Reactor (HFIR) in the United States.

PROGRESS AND STATUS

Andrei Karasiov recently visited the Pacific Northwest Laboratory (PNL) as part of the Young Scientist's Exchange agreement between Russia and the U. S. Department of Energy, Office of Fusion Energy. The purpose of the visit was to perform radiation damage calculations for the BOR-60 (fast reactor) and SM-2 (mixed-spectrum reactor) facilities in Russia; the calculations were based on neutron flux and spectral information provided by the reactor facility operations.[1,2] The reactors are at Dimitrovgrad, Russia, and are operated by the Scientific Research Institute of Investigation of Atomic Reactors (SRIIAR).

Since the closure of the FFTF and EBR-II fast research reactors in the United States, reactors in other countries have been evaluated as potential sites for fusion materials irradiation research programs.

The SM-2 reactor, which began operation in 1961, has a high-flux trap in the center to produce tranuranic elements and other radioisotopes, as shown in figures 1 and 2.[1] The reactor core is 42-cm square by 35-cm high, and has a total volume of 50 L. The light-water cooled reactor has a beryllium reflector, similar to that of HFIR, and operates on 90% enriched uranium oxide fuel. Experiments may be placed in channels with either water or gas cooling, and operating temperatures are in the range of 100 to 800°C. The reactor normally operates on a 40-to-45 day cycle with 5 to 6 days for refueling. The facility thus is available on about 240 full-power days per year. The central flux trap has a maximum thermal neutron flux of about 5×10^{15} n/cm^2-s; the fast flux (>0.1 MeV) is about 2×10^{15} n/cm^2-s. However, other positions are of interest for fusion materials experiments (see figure 2). Experimental samples may be placed in special fuel assemblies, 20 channels in the beryllium, or 5 channels in the reflector. Some of these channels have temperature control and are instrumented for materials testing. Neutron flux and spectral data were available from recent experiments in the active zone (AZ) of the reactor core (SM-2 AZ) and in channel 2 (SM-2 C2). Sample capsules for irradiation in the AZ position are 8 to 9 mm in diameter, and those in the C2 position are 52 mm.

The BOR-60 facility is a fast, sodium-cooled reactor operating on either 90% enriched uranium oxide or mixtures of up to 40% plutonium oxide. The facility started operation in 1969 and was designed to test

---

[a] Pacific Northwest Laboratory is operated for the U.S. Department of Energy by Battelle Memorial Institute under Contract DE-AC06-76RLO 1830.

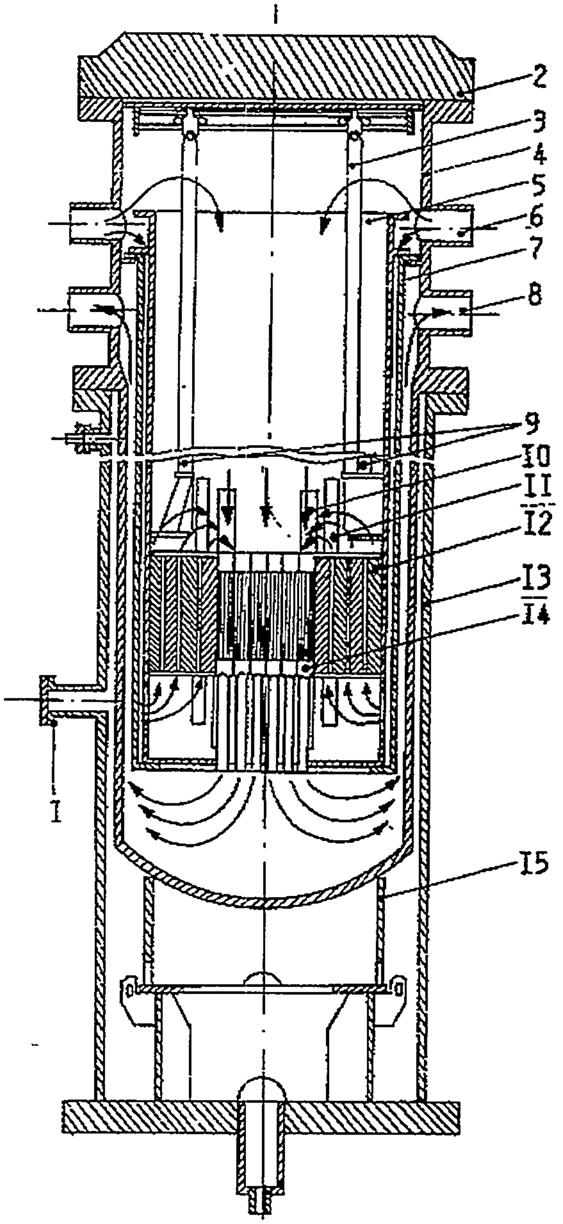

Figure 1 The SM-2 reactor. 1-horizontal channel; 2-cover; 3-fuel loader; 4-reactor vessel; 5-separator; 6,8-input and output tubes; 7-shield; 9-fuel savers; 10,11-compensator tubes; 12-Be shield; 13-pressure vessel; 14-core (fuel); 15-bottom.

fuel elements, structural materials, and fast-reactor safety issues. The cylindrical core, which measures 40.4 cm in diameter by 40 cm high, is surrounded by a stainless steel reflector and a depleted uranium-oxide breeder region, as shown in figures 3 and 4. The hexagonal assemblies have a minimum width of 4.4 cm. Nominal operating temperatures are in the range from 340 to 1000°C, and radiation heating is about 4 W/g. Experimental assemblies can be placed in most of the positions shown in figure 4. Some positions are temperature controled and are instrumented for materials experiments. Horizontal and vertical experimental channels are also located in the bulk of the biological radial blanket. The maximum

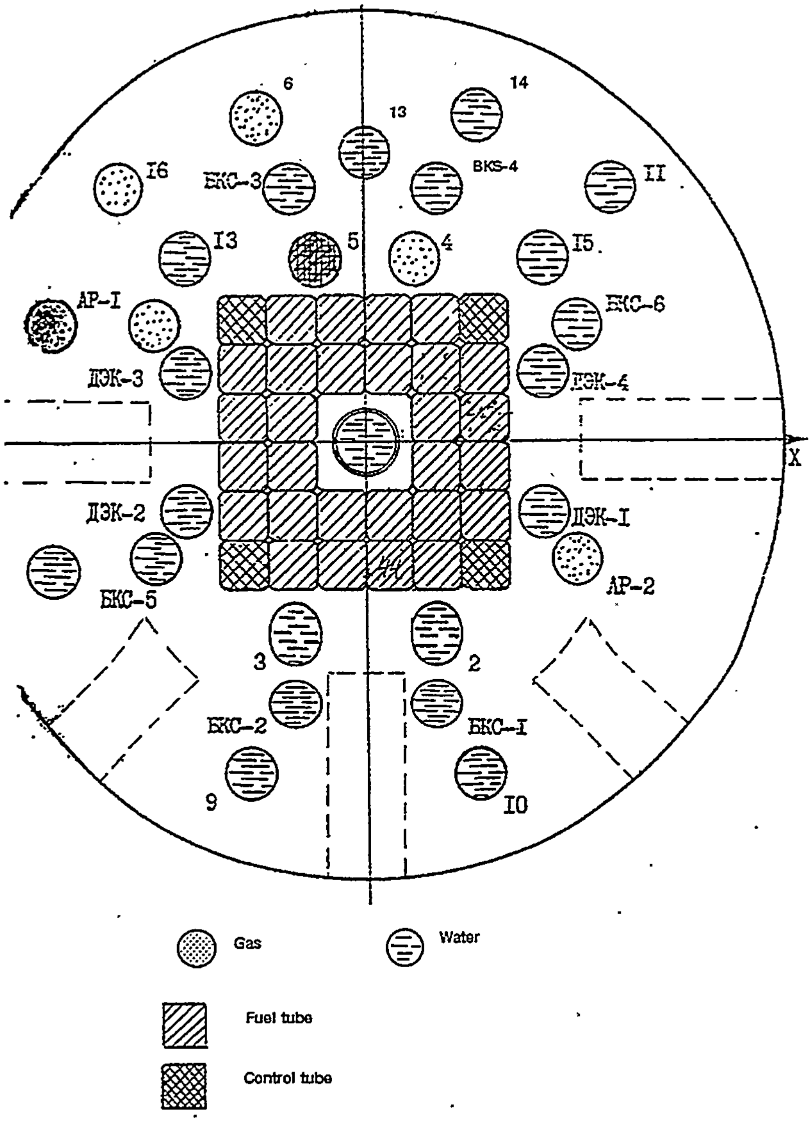

Figure 2 Core diagram of the SM-2 reactor. Fuel elements are shown by diagonal lines and compensators (CO) by cross hatching. Horizontal channels are filled either with water (dashes) or gas (dots).

neutron flux in the horizontal channels is 1.2 x 10^{14}n/cm^2-s and in the vertical channels is 3.8 x 10^{13} n/cm^2-s.

Characteristics of the various reactors are compared in Table 1. Quoted neutron flux levels are for the reactor centerline positions. Flux values for the U. S. reactors were taken from recent neutron dosimetry experiments.[3,4,5] Figures 5 and 6, respectively, compare the neutron flux spectra for fast reactors and mixed spectrum reactors. The two Russian reactors are quite comparable to the corresponding U. S. facilities. The HFIR reactor can operate at 100 MW; however, operations are currently restricted to 85 MW to limit radiation damage to reactor components. The FFTF facility originally operated at 400 MW; however, in its last years before closure it operated at only 295 MW to save operating costs. BOR-60 can

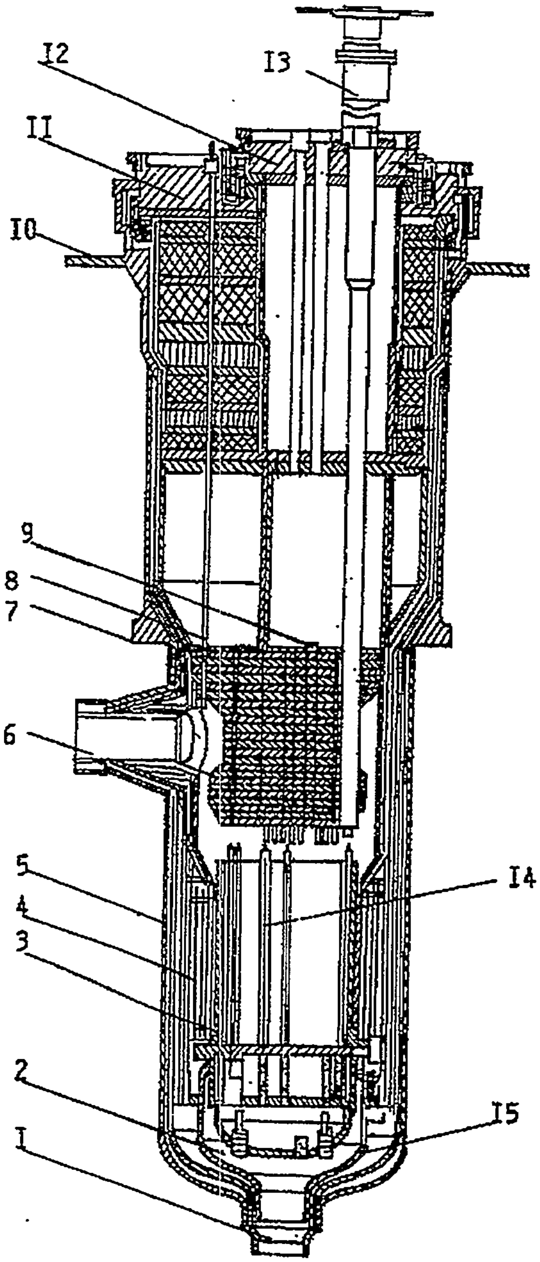

Figure 3 The BOR-60 reactor. 1,6-input and output tubes; 2-input camera; 3-basket; 4-thermal neutron shields; 5-pressure vessel; 7,10-flanges; 8-thermocouples; 9-control rod; 11,12-shields; 13-loading channel; 14-fuel elements; 15-bottom vessel.

operate at 60 MW but normally operates at 40 to 55 MW.

Radiation damage calculations for all of the reactors were performed with the SPECTER computer code.[6] Displacement damage and helium production rates for pure iron are also listed on Table 1. The high thermal neutron flux in SM-2 and HFIR mean that multi-stage reactions in nickel and copper will produce much higher levels of hydrogen and helium as well as some additional displacements per atom (dpa) damage at high neutron fluences.

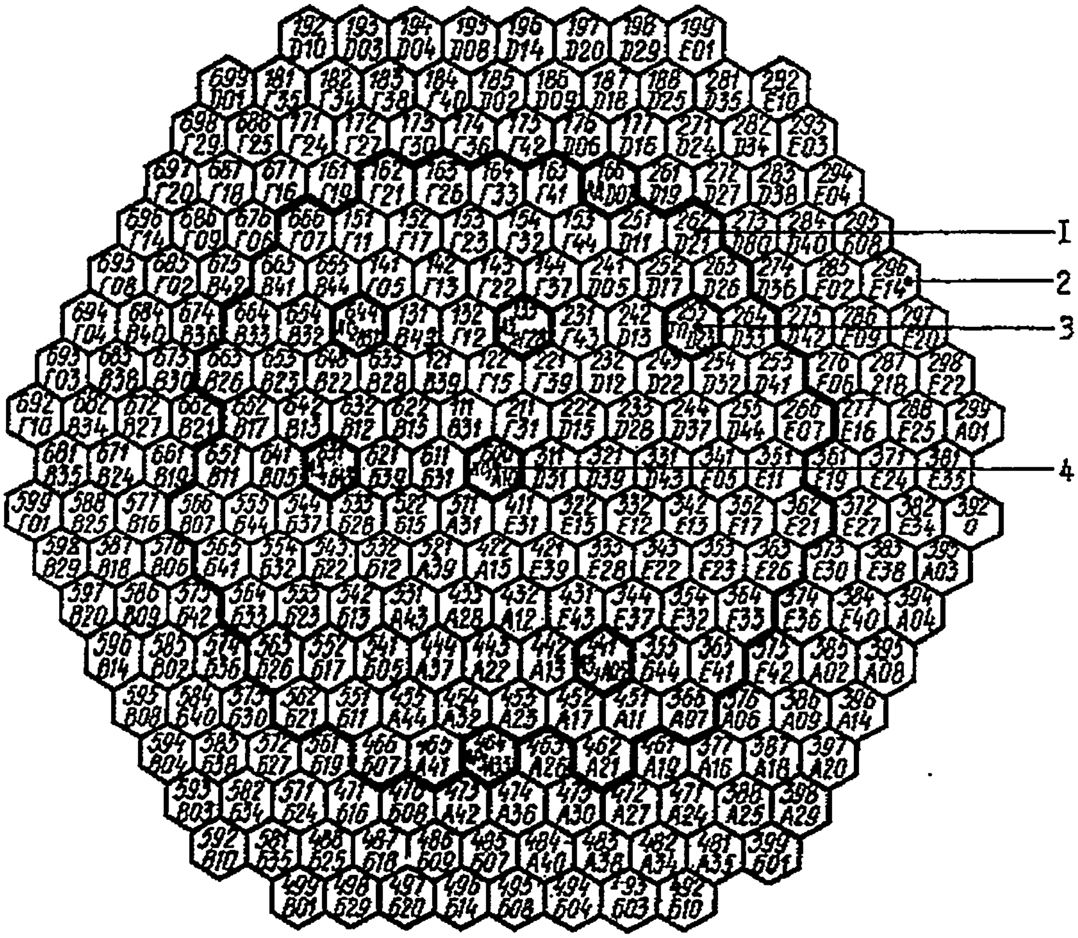

Figure 4 Core diagram of the BOR-60 reactor. 1 - fuel assembly, 2 - radial blanket assembly, 3 - thermometric channel, and 4 - control rod.

CONCLUSIONS

The Russian reactors are comparable to the American reactors in terms of neutron flux and radiation damage. The BOR-60 and SM-2 facilities are available for suitable radiation damage experiments.

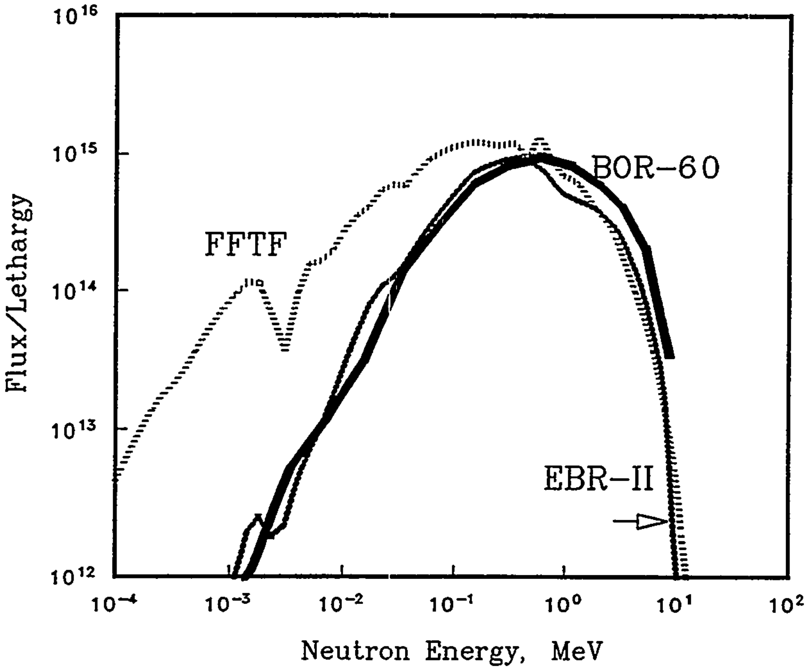

Figure 5 Comparison of centerline neutron spectra for the fast reactors BOR-60, EBR-II, and FFTF.

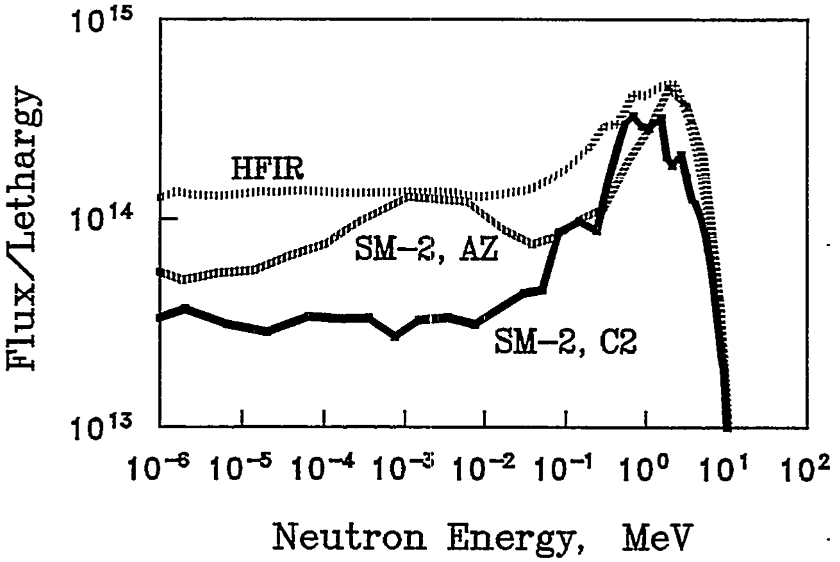

Figure 6 Comparison of midplane neutron spectra for the mixed-spectrum reactors SM-2, at the AZ and channel 2 positions, and HFIR.

Table 1 - Comparison of Russian and U. S. Reactors

	SM-2 AZ	HFIR	BOR-60	EBR-II	FFTF
Thermal Power	100	85[a]	55	62.5	295[b]
Neutron Flux, x10^{15} n/cm^2-s:					
Total	3.5	4.0	2.0	2.6	5.6
Thermal (<0.5 eV)	1.5	1.6	-	-	-
0.5 eV to 0.1 MeV	1.0	1.3	0.22	0.45	1.9
> 0.1 MeV	1.0	1.1	1.8	2.3	3.1
> 1 MeV	0.6	0.6	0.5	0.6	0.6
dpa/y (Fe)	27	26	24	33	34
He,appm/y (Fe)	15	9.3	12	3.5	3.5

[a] HFIR is capable of operation at 100 MW.
[b] FFTF is capable of operation at 400 MW.

REFERENCES

1. G. I. Gadzhiev, A. F. Grachov, V. A. Gremyachkin, V. N. Efimov, V. V. Kalygin, A. V. Klinov, R. I. Korotkov, N. V. Markina, V. Sh. Sulaberidze, Yu. G. Toporov, and V. A. Tzykanov, Research Reactors of SRIIAR and Their Experimental Possibilities, Research Institute of Atomic Reactors, 1993.

2. N. R. Nigmatullin and G. I. Gadzhiev, Measurements of Neutron Spectrum in BOR-60, Dimitrovgrad, 1973.

3. L. R. Greenwood and D. V. Steidl, Dosimetry for the HFIR-CTR-53/54 Experiments, Fusion Reactor Materials Semiannual Progress Report, DOE/ER-0313/8, pp. 40-42, March 1990.

4. L. R. Greenwood and L. S. Kellogg, Neutron Dosimetry for the MOTA-1G Experiment in FFTF, Fusion Reactor Materials Semiannual Progress Report, DOE/ER-0313/14, pp. 51-54, March 1993.

5. L. R. Greenwood, Dosimetry for the EBR-II-X287 Irradiation, Alloy Development for Irradiation Performance Semiannual Progress Report, DOE/ER-0045/8, pp. 74-79, March 1982.

6. L. R. Greenwood and R. K. Smither, SPECTER: Neutron Damage Calculations for Materials Irradiations, ANL/FPP-TM-197, January 1985.

NEUTRON DOSIMETRY, DAMAGE CALCULATIONS, AND HELIUM MEASUREMENTS FOR THE HFIR-MFE-60J-1 AND MFE-330J-1 SPECTRAL TAILORING EXPERIMENTS - L. R. Greenwood (Pacific Northwest Laboratory[a]), C. A. Baldwin (Oak Ridge National Laboratory), B. M. Oliver (Rockwell International)

OBJECTIVE

To provide dosimetry and damage analysis for fusion materials irradiation experiments.

SUMMARY

Neutron fluence measurements and radiation damage calculations are reported for the joint U.S.-Japanese MFE-60J-1 and MFE-330J-1 experiments in the hafnium-lined removable beryllium (RB*) position of the High Flux Isotope Reactor (HFIR) at Oak Ridge National Laboratory (ORNL). These experiments were continuations of the ORR-6J and 7J irradiations performed in the Oak Ridge Research Reactor (ORR). The combination of irradiations was designed to tailor the neutron spectrum in order to achieve fusion reactor helium/dpa levels in stainless steel. These experiments produced maximum helium (appm)/dpa (displacement per atom) levels of 10.2 at 18.5 dpa for the ORR-6J and HFIR-MFE-60J-1 combination and 11.8 at 19.0 dpa for the ORR-7J and HFIR-MFE-330J-1 combination. A helium measurement in one JPCA sample was in good agreement with helium calculations.

PROGRESS AND STATUS

The design of these spectral tailoring experiments has been published,[1,2] as were neutron dosimetry and damage calculations for the ORR-6J and -7J irradiations.[3,4] The ORR irradiations were conducted from June 28, 1983, to March 26, 1987, for a total exposure of 475 effective full power days (EFPD) at 30 MW. The 6J capsules were irradiated in position C7 at 60°C and 200°C. The 7J capsules were in position C3 at 330°C to 400°C. Materials effects specimens were then repackaged for insertion in HFIR. The materials from the 60°C irradiation in ORR-6J were subsequently irradiated in HFIR-MFE-60J-1 and those from ORR-7J were irradiated in HFIR-MFE-330J-1.[1] The 60J-1 and 330J-1 irradiations were conducted from July 20, 1990, to November 14, 1992, for a total of 522.7 EFPD at 85 MW. Both experiments were positioned in hafnium-lined removable beryllium (RB*) positions of HFIR.

The goal of these extended irradiations was to achieve fusion reactor levels of helium(appm)/dpa in stainless steel of about 10/1. Helium production is enhanced by the two-step nickel reactions $^{58}\mathrm{Ni}(n,\gamma)^{59}\mathrm{Ni}(n,\alpha)^{56}\mathrm{Fe}$. The ORR portion of the irradiation produced about 1.5 at% ^{59}Ni in nickel. Further irradiation required a thermal neutron shield (hafnium) to prevent excessive helium accumulation.[1]

Dosimetry for the HFIR-60J-1 and 330J-1 experiments consisted of 24 aluminum capsules, four at each of six vertical levels, about 0.05 in OD by 0.25 in. long. Each capsule contained small wire segments of Fe, Ni, Nb, Ti, 0.1% Co-Al alloy, and 80.2% Mn-Cu alloy. After irradiation, eight capsules (four from each experiment) were opened in hot cells and gamma counted at ORNL.

---

[a] Pacific Northwest Laboratory is operated for the U.S. Department of Energy by Battelle Memorial Institute under Contract DE-AC06-76RLO 1830.

The gamma-counting results were forwarded to Pacific Northwest Laboratory (PNL) for analysis. The measured activities were converted to activation rates as listed in Table 1 by correcting for burnup, gamma self-absorption, decay during irradiation, isotopic abundance and atomic weight. Burnup corrections are based on an iterative procedure for the thermal/epithermal monitor reactions. The resultant estimates of the thermal/epithermal neutron fluences were then used to calculate burnup corrections for the threshold fast neutron monitor reactions. Burnup corrections averaged 10-15% for the thermal/epithermal reactions and only a few percent for the threshold reaction rates. The activation rates listed in Table 1 are normalized to full reactor power of 85 MW and have a net absolute uncertainty of about 5%.

The two irradiations were nearly identical, the largest difference being for the ^{59}Co(n,γ)^{60}Co reaction where the midplane 60J results are about 8.5% higher than the 330J results. The absence of this difference in the ^{93}Nb(n,γ)^{94}Nb reaction suggests that the difference may be due to epithermal neutrons near the Co resonance rather than to remnant thermal neutrons.

The two runs were averaged to determine the best fit to the activation rates. The values in Table 1 were fit to a polynomial function of form $f(x) = f(0)\,[\,1 + a\,x^2\,]$, where x is the vertical height from reactor centerline in cm. All of the data are reasonably well fit by the average polynomial (coefficient a = -1.276 x 10^{-3}). Midplane activation rates were then used in the STAY'SL computer code to adjust the neutron flux spectrum determined in spectral measurements at the RB* position in HFIR.[5] STAY'SL performs a generalized least-squares adjustment of all measured and calculated values including the measured activities, calculated spectra, and neutron cross sections.[6] Neutron cross sections and their uncertainties were generally taken from ENDF/B-V. The resultant neutron fluence values are listed in Table 2, and the neutron energy spectrum is shown in Figure 1. The activation rates and the derived neutron spectra and fluences are in excellent agreement with previous measurements in the RB* position of HFIR.[5]

Neutron damage calculations with the SPECTER computer code[7] were performed for the midplane position. Midplane dpa and helium (appm) values are also listed in Table 2. The fluence and damage values at other experimental positions can be calculated by the gradient equation given above. Damage parameters for other elements or compounds have been calculated and are readily available on request.

Helium production in nickel and nickel alloys requires a more complicated non-linear calculation.[8] Values for the ORR-6J and -7J irradiations were published.[3,4] A further calculation was required to determine the net production of ^{59}Ni. The result predicts maximum ^{59}Ni content in pure nickel of 1.33 at% and 1.52 at% for ORR-6J and -7J, respectively. These values were then assumed as the starting conditions for the HFIR-MFE-60J-1 and -330J-1 irradiations. The growth of ^{59}Ni and helium production in pure nickel for the combined irradiations is illustrated in Figure 2 which illustrates the maximum helium production in both irradiations. The growth of helium in ORR rises sharply with the production of ^{59}Ni; however, helium grows at a much slower rate in HFIR because of the hafnium thermal neutron shield. Helium production in stainless steel is detailed for the MFE-60J-1 and -330J-1 irradiations in Table 3. Table 4 lists the maximum net helium production in stainless steel for the ORR and HFIR irradiation sequences. Because the growth of helium in nickel is non-linear, detailed helium calculations must be performed for each material specimen, depending on the relative location in each reactor assembly.

The helium content in one JPCA sample was measured at Rockwell International. JPCA has the following nominal composition in wt%: C, 0.06; Si, 0.50; Mn, 1.77; P, 0.027; S, 0.005; Ni, 15.6; Cr, 14.22; Mo, 2.28; Ti, 0.24; B, 0.0031; N, 0.0039; Co, 0.002; and Fe, balance. The JPCA sample, identified as ONO5, was irradiated in TEM holder J2 in Level 1 of the 330°C section of ORR-7J at about 0.62" below the reactor centerline and then at 2.6" above the reactor centerline in the HFIR-RB*-330J-1 assembly.

Before helium measurement, the JPCA sample was acid etched to remove surface material that might affect helium recoil into or out of the sample during irradiation. Two pieces were cut from the sample

Table 1. Activation Rates (at/at-s) - MFE-60J/330J

Pos.	Ht,cm	^{54}Fe(n,p)^{54}Mn (E-11)	^{46}Ti(n,p)^{46}Sc (E-12)	^{55}Mn(n,2n)^{54}Mn (E-14)	^{59}Co(n,γ)^{60}Co (E-9)	^{93}Nb(n,γ)^{94}Nb (E-10)
60-1	15.08	0.83	1.18	2.70	3.44	3.06
60-5	9.05	1.04	1.49	3.39	3.85	3.84
60-9	3.02	1.11	1.59	3.60	4.26	4.25
330-11	3.02	[a]	1.72	3.82	3.94	4.33
330-14	-3.02	1.31	1.74	4.01	4.02	4.37
60-16	-3.02	1.23	1.65	3.82	4.38	4.29
330-18	-9.05	1.23	1.57	3.65	3.58	3.92
330-22	-15.08	[a]	1.24	2.95	[a]	3.09

[a] Wire not recovered in hot cell.

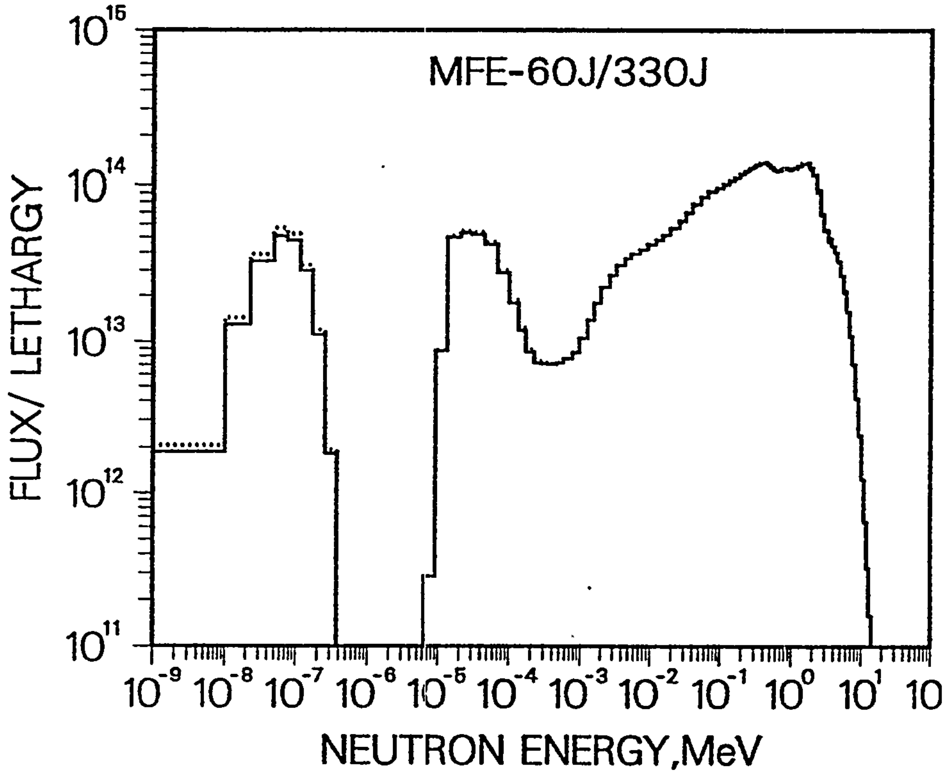

Fig. 1. The STAY'SL adjusted neutron flux spectrum is shown for the hafnium-lined RB* position in HFIR. The structure at low energies results from the thermal neutron absorption and epithermal neutron resonances in hafnium.

Table 2. Midplane Fluence and Damage Values for MFE-60J/330J Only

Neutron Fluence,n/cm^2		Element	dpa	He,appm
Total	3.95E+22	C	14.1	13.9
Thermal (<.5 eV)	4.71E+21	Al	22.5	5.4
0.5 eV - 0.1 MeV	1.54E+22	V	14.6	0.18
> 0.1 MeV	1.94E+22	Cr	12.4	1.3
> 1 MeV	7.04E+21	Fe	11.1	2.4
		Ni Fast	12.3	34.2
		59-Ni	0.5	276.0
		Total	12.8	310.2
		Cu	14.7	2.0

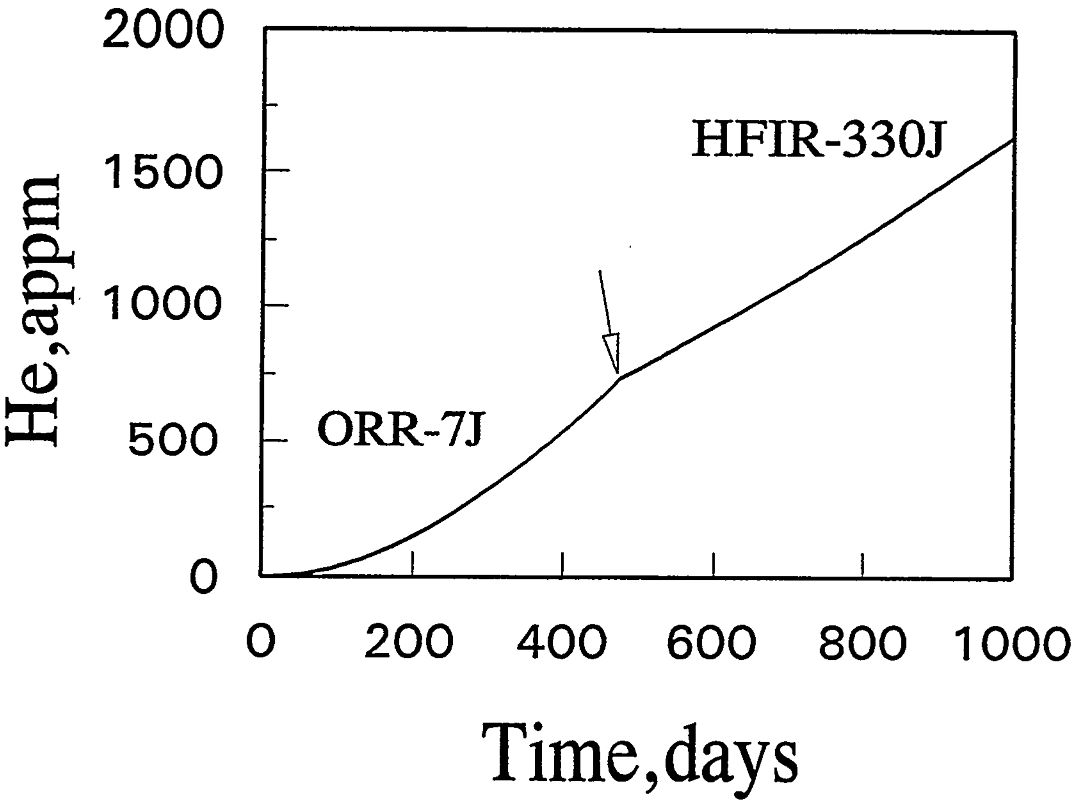

Fig. 2. Helium production in nickel is shown for the ORR-7J and HFIR-330J-1 irradiation sequence as a function of full power days. The arrow indicates the start of the HFIR irradiation.

Table 3. DPA and He Values for 316 SS in MFE-60J/330J only (Includes ^{59}Ni effect)

Ht,cm	dpa	He,appm
0	11.5	42.0
3	11.4	41.3
6	11.0	38.9
9	10.4	35.0
12	9.5	29.9
15	8.4	23.8
18	7.0	17.2

316SS = Fe(0.645), Ni(0.13), Cr(0.18), Mn(0.019), Mo(0.026) wt%

Table 4. Maximum DPA and Helium Production in ORR/HFIR Irradiations (Calculations for 316 Stainless Steel)

	dpa	He,appm		dpa	He,appm
ORR-6J	6.9	75.3	ORR-7J	7.4	102.0
HFIR-60J-1	11.6	112.5	HFIR-330J-1	11.6	122.5
Total	18.5	187.8	Total	19.0	224.5

for duplicate analysis. The helium content in each piece was determined by isotope-dilution gas mass spectrometry after vaporization in a resistance-heated graphite crucible in one of the mass spectrometer system's high-temperature vacuum furnaces.[9] The absolute amount of helium released was measured relative to a known quantity of added ^{3}He spike. The helium spikes were obtained by expanding and partitioning a known quantity of gas through a succession of calibrated volumes.[10] The mass spectrometer was calibrated for mass sensitivity during each series of runs by analyzing known mixtures of ^{3}He and ^{4}He.

The average measured helium content was 250±1 appm. To calculate the helium content, it is necessary to consider both irradiations in ORR and HFIR, as illustrated in Table 4 and Figure 2 for 316 stainless steel. A computer program was written to follow the growth of helium through both irradiations for any given combination of sample positions. This net helium calculation yields a value of 286 appm, about 14% higher than the measurement. One uncertainty in the calculation is the boron content of the JPCA specimen. Given the nominal content of 31 wppm (160 appm) and assuming total burnout of the ^{10}B, then this boron impurity adds about 32 appm helium. Previous measurements by Rockwell International of other stainless steels suggests a much lower boron content, about 1-3 appm, which would provide excellent agreement between the measurement and calculation of helium. Additional helium or boron measurements are needed to resolve this question. Nevertheless, the agreement between measurements and calculations provides some confidence that we can predict helium levels in other materials irradiated in these spectral tailoring experiments.

FUTURE WORK

Detailed helium and damage calculations are being performed for each material specimen package in the joint irradiation sequences. Additional experiments still in progress in HFIR include MFE-200J-1 and MFE-400-J1 as well as JP9-16 and JP20-22. Dosimeters from the JP-10, 11, 13, and 16 irradiations are awaiting analysis at PNL. Dosimeters are being fabricated at PNL for the JP-24-25 irradiations.

REFERENCES

1. A. W. Longest, J. E. Pawel, D. W. Heatherly, R. G. Sitterson, and R. L. Wallace, Fabrication and Operation of the HFIR-MFE RB* Spectrally Tailored Irradiation Capsules, Fusion Reactor Materials Semiannual Progress Report, DOE-ER-0313/14, pp. 14-40, March 1993.

2. J. L. Scott, L. K. Mansur, M. L. Grossbeck, E. H. Lee, K. Farrell, L. L. Horton, A. F. Rowcliffe, M. P. Tanaka, and H. Hishinuma, Alloy Development for Irradiation Performance Semiannual Progress Report, DOE/ER-0045/15, pp. 22-40, September 1985.

3. L. R. Greenwood, Neutron Dosimetry and Damage Calculations for the ORR-MFE-7J Experiment, Fusion Reactor Materials Semiannual Progress Report, DOE-ER-0313/6, pp. 23-25, March 1989.

4. L. R. Greenwood and D. V. Steidl, Neutron Dosimetry and Damage Calculations for the ORR-MFE-6J Experiment, DOE-ER-0313/8, pp. 34-39, March 1990.

5. L. R. Greenwood, Neutron Dosimetry and Damage Calculations, Alloy Development for Irradiation Performance Semiannual Progress Report, DOE/ER-0045/16, pp. 17-24, March 1986.

6. F. G. Perey, Least Squares Dosimetry Unfolding: The Program STAY'SL, ORNL/TM-6062 (1977).

7. L. R. Greenwood and R. K. Smither, SPECTER: Neutron Damage Calculations for Materials Irradiations, ANL/FPP-TM-197, January 1985.

8. L. R. Greenwood, A New Calculation of Thermal Neutron Damage and Helium Production in Nickel, Journal of Nuclear Materials 116, pp. 137-142 (1983).

9. H. Farrar and B. M. Oliver, J. Vac. Sci. Technol. A4, 1740 (1986).

10. B. M. Oliver, J. G. Bradley, and H. Farrar, Geochim. Cosmochim. Acta 48, 1759 (1984).

PRELIMINARY REPORT ON THE IRRADIATION CONDITIONS OF THE HFIR JP-23 EXPERIMENT - A. M. Ermi (Westinghouse Hanford Company) and D. S. Gelles (Pacific Northwest Laboratory)[a]

OBJECTIVE

The objective of this effort was to irradiate a series of alloys over the temperature range 300 to 600°C to approximately 10 dpa in the High Flux Isotope Reactor (HFIR). The alloys covered a wide range of materials and treatments.

SUMMARY

The JP-23 test capsule was irradiated in the HFIR during Cycles 322 through 326. The capsule contained eight transmission electron microscopy (TEM) specimen holders, two each at irradiation temperatures of 300, 400, 500, and 600°C. The test capsule was irradiated for a total of 110 effective full power days (EFPD), achieving estimated peak doses of 1.1×10^{22} n/cm^2 (E>0.1 MeV) and 8.8 dpa (in stainless steel).

PROGRESS AND STATUS

Introduction

The HFIR JP-23 test was a collaborative experiment co-sponsored by the U.S. Neutron Interactive Materials (NIMs) program and the Japanese Monbusho program. The goal of the experiment was to irradiate metallic TEM specimens to a dose on the order of 8 dpa (in stainless steel) at four temperatures (300, 400, 500, and 600°C) in a HFIR inner target position.

This preliminary report characterizes the irradiation conditions for the JP-23 TEM specimens. Estimated fluences and dpa values are based on previous experiments in HFIR. Once the analysis of the JP-23 dosimetry has been completed, a final report can be issued.

Specimen Information

The JP-23 capsule contained eight TEM specimen holders, all gas-gapped in order to obtain irradiation temperatures of 300, 400, 500, and 600°C. The eight TEM specimen holders were divided between the two program sponsors. A cross-sectional view of a typical TEM specimen holder assembly is shown in Figure 1.

The Japanese specimen matrix consisted of ferritic steels, vanadium alloys, copper alloys, molybdenum alloys, and titanium-aluminum compounds. The major purposes of the Monbusho experiment were to study solid transmutation and helium effects.

The U.S. specimen matrix consisted of vanadium alloys, 316 stainless steels, and isotopically tailored ferritic and austenitic alloys. Isotopic tailoring consists of adding natural nickel, Ni^{59} and/or Ni^{60} (without

---

[a] Operated for the U.S. Department of Energy by Battelle Memorial Institute under Contract DE-AC06-76RLO 1830.

any other parameter changes) to alter the helium generation response. The major purposes of the NIMs experiment were to study the effects of irradiation in vanadium and 316 stainless steel and to study the effects of helium generation in ferritic and austenitic alloys.

The loading summary for the HFIR JP-23 capsule is given in Table 1. The TEM discs are nominally 3 mm (0.118 in.) in diameter and 0.25 mm (0.010 in.) thick. Exceptions are noted in Table 2. The alloy compositions for the Monbusho specimens are given in Tables 3 through 5, and the compositions for the U.S. specimens are given in Table 6.

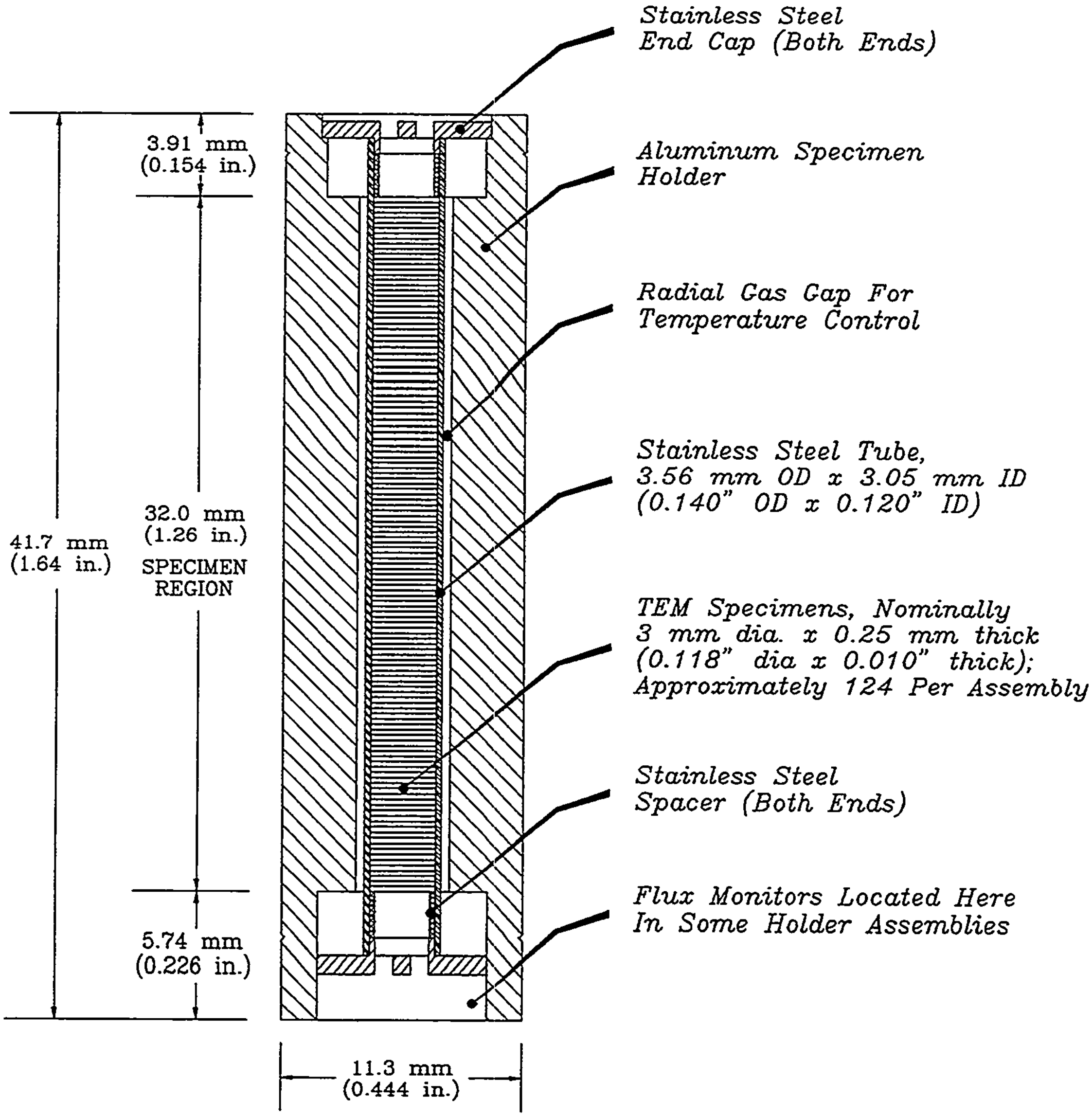

Figure 1. Cross-section of Typical TEM Specimen Holder Assembly

Table 1. Loading Summary for HFIR Capsule JP-23

Position Number	Program Sponsor	Design Temperature	Specimen Type	Specimen Material and No. of Specimens	
3	Japanese Monbusho	300°C	TEM	Ferritics Vanadium Alloys Copper Alloys	25 26 25 76
4	Japanese Monbusho	400°C	TEM	Ferritics (JPN) Vanadium Alloys Copper Alloys Ti-Al Alloys Ferritics (US)	25 36 25 15 36 137
5	Japanese Monbusho	500°C	TEM	Ferritics Vanadium Alloys Ti-Al Alloys Mo Alloys	25 35 15 24 99
6	Japanese Monbusho	600°C	TEM	Vanadium Alloys Ti-Al Alloys Mo Alloys	40 15 24 79
7	U.S. NIMs	600°C	TEM	Ferritics Austenitics Vanadium Alloys Titanium getters	47 43 27 2 119
8	U.S. NIMs	500°C	TEM	Ferritics Austenitics Vanadium Alloys Titanium getters	50 44 27 2 123
9	U.S. NIMs	400°C	TEM	Ferritics Austenitics Vanadium Alloys Titanium getters	49 44 27 2 122
10	U.S. NIMs	300°C	TEM	Ferritics Austenitics Vanadium Alloys Titanium getters	50 44 27 2 123

Table 2. Dimensions of Non-Standard TEM Discs

Program Sponsor	Material Description	TEM Disc Thickness (If Different From 0.25 mm [0.010 in.])	TEM Disc Diameter (If Different From 3.0 mm [0.118 in.])
Japanese Monbusho	Vanadium Alloys	---	2.5 mm (0.098 in.)
Japanese Monbusho	Copper Alloys	0.20 mm (0.008 in.)	---
Japanese Monbusho	Molybdenum Alloys	0.082 to 0.192 mm (0.003 to 0.008 in.) Average: 0.15 mm (0.006 in.)	---
Japanese Monbusho	Titanium-Aluminum Alloys	0.25 to 0.39 mm (0.010 to 0.015 in.) Average: 0.31 mm (0.012 in.)	---
U.S. NIMs	316L and 316Ti 20% CW Austenitics	0.20 mm (0.008 in.)	---
U.S. NIMs	Titanium Getter Discs	0.18 mm (0.007 in.)	---

Table 3. Alloy Compositions for Japanese Low Activation Ferritic Steels[a]

Material	Fe	Cr	Ni	Mn	Ti	Si	W	V	Ta	C	B	N
JLF-1 / UTY/JLF-1	Bal.	9.0	--	0.5	--	0.05	2.0	0.2	0.07	0.1	--	0.05
NSL21 / NS/L21	Bal.	9.0	0.1	0.3	--	0.1	2.0	0.2	0.1	0.06	--	0.05
F82H / JRI/JTKW-H	Bal.	7.7	--	--	--	--	2.0	0.2	0.04	0.09	--	--
NLF-0 / TU3A	Bal.	9.0	--	0.5	0.1	--	2.0	0.25	--	0.1	--	--
NLF-1 / TU2A	Bal.	9.0	--	0.5	0.1	--	2.0	0.25	--	0.1	0.003	--

[a] All values in weight percents

Table 4. Alloy Compositions for Japanese Vanadium Specimens[a]

Material	V	Ti	Cr	Si	Y	Al	B
Pure V / 88-50	99.9	--	--	--	--	--	--
V-5Ti / 88-54	Bal.	5 a/o	--	--	--	--	--
V-5Cr / 88-55	Bal.	--	5 a/o	--	--	--	--
V-1Cr / 93-71	Bal.	--	1 a/o	--	--	--	--
V-10Cr / 93-72	Bal.	--	10 a/o	--	--	--	--
V-5Ti-1Cr / 93-73	Bal.	5 a/o	1 a/o	--	--	--	--
V-5Ti-5Cr / 93-74	Bal.	5 a/o	5 a/o	--	--	--	--
V-5Ti-5Cr / 90-11	Bal.	5.0	5.0	0.9	0.8	1.0	--
V-100B / 93-002	Bal.	--	--	--	--	--	100 appm
V-500B / 93-003	Bal.	--	--	--	--	--	500 appm
V-2500B / 93-004	Bal.	--	--	--	--	--	2500 appm
V-5Cr-B / 93-005	Bal.	--	5 a/o	--	--	--	100 appm

[a] All values in weight percents except as noted:
a/o = atomic percent
appm = atomic parts per million

Summary of HFIR Operations

The JP-23 test capsule was inserted into HFIR target position G6 (marked on Figure 2) on December 13, 1993. The HFIR was started on December 16th, commencing Cycle 322. The reactor is typically run for 22 day cycles (@ 85 MW) followed by 7 to 10 day outages. The actual reactor operation during the irradiation of the JP-23 test capsule is shown in Table 7. The JP-23 irradiation was concluded at the end of Cycle 326 on June 3, 1994. The test capsule was removed from the core shortly thereafter and stored in the reactor pool area. The test capsule was scheduled to processed at Oak Ridge National Laboratory (ORNL) during August-September 1994. At that time, it is to be transferred to a hot cell for disassembly, removal of the specimen holders, and preparation of the specimen holder tubes for shipment to Hanford. Specimen examination at Hanford will start in 1995.

Summary of Reactor Conditions for HFIR JP-23

Temperatures

The eight gas-gapped specimen holders were designed to operate at temperatures of 300, 400, 500 and 600°C. Results from the thermal analysis and design work for JP-23 were summarized in Reference 1. Since there were no temperature monitoring devices in JP-23, the temperatures assigned to the specimens are the design temperatures. These temperatures are to be considered final since more precise temperature values cannot be assigned to the specimens.

An uncertainty analysis of the design temperatures has never been performed by ORNL for this specific type of experiment. However, a wealth of information does exist from other fusion experiments that have corroborated expected temperatures. Therefore, based on long experience in irradiating many capsules of similar design, ORNL states that it is reasonable to assume that calculated temperatures are accurate within ±25°C.

Table 5. Alloy Compositions for Japanese Cu, Mo, and Ti/Al Specimens[a]

Material	Cu	Ni	Zn	Mn	Mo	Re	Zr	Ti	Al	C
Copper	Bal.	--	--	--	--	--	--	--	--	--
Cu - Cold Worked	Bal.	--	--	--	--	--	--	--	--	--
Cu-5Ni	Bal.	5.0	--	--	--	--	--	--	--	--
Cu-3.5Zn	Bal.	--	3.5	--	--	--	--	--	--	--
Cu-5Ni-2Zn	Bal.	5.0	2.0	--	--	--	--	--	--	--
Cu-0.5Mn	Bal.	--	--	0.5	--	--	--	--	--	--
Cu-2Mn	Bal.	--	--	2.0	--	--	--	--	--	--
Cu-2Mn - Cold Worked	Bal.	--	--	2.0	--	--	--	--	--	--
Mo-2Re / R or SR	--	--	--	--	Bal.	2.0	--	--	--	--
Mo-5Re / R or SR	--	--	--	--	Bal.	5.0	--	--	--	--
Mo-10Re / R or SR	--	--	--	--	Bal.	10.0	--	--	--	--
Mo-41Re / R or SR	--	--	--	--	Bal.	41.0	--	--	--	--
TZM / R or SR	--	--	--	--	Bal.	--	0.10	0.48	--	0.013
Mo / R or SR	--	--	--	--	Bal.	--	--	--	--	--
TiAl	--	--	--	--	--	--	--	50 a/o	50 a/o	--

[a] All values in weight percents except as noted; a/o = atomic percent

Table 6. Alloy Compositions for U.S. Materials[a]

Material	I.D. Code	Final Condition	Fe	Cr	Ni (total)	Ni (Nat.)	Ni-59	Ni-60	Mn	Ti	Si	W	V	Mo	Co	C	N	O
E62R	6A	1040°C/1 h/AC +760°C/1 h/AC	Bal.	12.0	--	--	--	--	--	--	--	--	--	--	--	--	--	--
R168	71	1040°C/1 h/AC +760°C/1 h/AC	Bal.	11.7	1.32	--	--	1.32	--	--	--	--	--	--	--	0.004	--	--
R169[d]	73	1040°C/1 h/AC +760°C/1 h/AC	Bal.	12.0	1.5	--	1.5	--	--	--	--	--	--	--	--	--	--	--
R170	74	1040°C/1 h/AC +760°C/1 h/AC	Bal.	11.5	1.54	1.54	--	--	--	--	--	--	--	--	--	0.004	--	--
R178[d]	7P	20% CW	Bal.	17.5	13.69[c]	--	2.06[c]	11.63[c]	1.7	--	0.53	--	--	2.3	--	0.05	--	--
R178[d]	7R	20% CW +1050°C/1 h/AC	Bal.	17.5	13.69[c]	--	2.06[c]	11.63[c]	1.7	--	0.53	--	--	2.3	--	0.05	--	--
R179	7T	20% CW	Bal.	18.4	12.7[b]	2.06[c]	--	11.63[c]	1.57	--	0.56	--	--	2.39	--	0.027	--	--
R179	7U	20% CW +1050°C/1 h/AC	Bal.	18.4	12.7[b]	2.06[c]	--	11.63[c]	1.57	--	0.56	--	--	2.39	--	0.027	--	--
R180a,b[d]	7V	1050°C/½ h/AC +760°C/5 h/AC	Bal.	12.0	2.0	--	2.0	--	0.5	--	0.18	0.5	0.3	1.0	--	0.2	--	--
R181a,b	7X	1050°C/½ h/AC +760°C/5 h/AC	Bal.	12.1	2.39	2.39	--	--	0.54	--	0.18	0.43	0.2	0.91	--	0.15	--	--
BL-47	47	1125°C/1 h/FC	--	4.1	--	--	--	--	--	4.3	0.087	--	Bal.	--	--	0.02	0.022	0.035
BL-62	62	1125°C/1 h/FC	--	--	--	--	--	--	--	3.1	0.066	--	Bal.	--	--	0.0109	0.0086	0.032
BL-63	63	1125°C/1 h/FC	--	4.6	--	--	--	--	--	5.1	0.031	--	Bal.	--	--	0.0073	0.0028	0.044
316L	EA	Solid Solution	Bal.	17.22	14.14	14.14	--	--	1.41	--	0.29	--	--	2.25	--	0.025	--	--
316L	EB	20%CW	Bal.	17.22	14.14	14.14	--	--	1.41	--	029	--	--	2.25	--	0.025	--	--
316Ti	EE	Solid Solution	Bal.	18.0	13.47	13.47	--	--	1.79	0.319	0.80	--	--	2.64	0.033	0.055	--	--
316Ti	EF	20%CW	Bal.	18.0	13.47	13.47	--	--	1.79	0.319	0.80	--	--	2.64	0.033	0.055	--	--
Ti (getter)	--	--	--	--	--	--	--	--	--	99.9	--	--	--	--	--	--	--	--

[a] All value in weight percent
[b] Measured value
[c] Intended Value
[d] Mildly radioactive

Table 7. Summary of HFIR Operation During the JP-23 Irradiation

HFIR Operation							JP-23 Capsule		
Cycle No.	Start Date	End Date	Outage Lengths	MWd	EFPD[a]	dpa[b]	Total MWd	Total EFPD[a]	Total dpa[b]
322	Dec. 16, 1993	Jan. 7, 1994	16 days	1854	21.8	1.75	1854	21.8	1.75
323	Jan. 23, 1994	Feb. 14, 1994	19 days	1874	22.0	1.77	3728	43.8	3.52
324[c]	Mar. 5, 1994	Mar. 15, 1994	4 days	1907	22.4	1.80	5635	66.3	5.33
	Mar. 19, 1994	Apr. 1, 1994	9 days						
325	Apr. 10, 1994	May 3, 1994	5 days	1907	22.4	1.80	7542	88.7	7.13
326[d]	May 8, 1994	May 20, 1994	4 days	1825	21.5	1.72	9367	110.2	8.85
	May 24, 1994	June 3, 1994	---						

[a] Based on 85 MW full power

[b] Peak dpa based on 0.000945 dpa/MWd for stainless steel (from ORNL)

[c] Mid-cycle shutdown for maintenance

[d] Mid-cycle shutdown due to a pressurizer pump trip

Damage Parameters

Six dosimetry sets were included in the JP-23 capsule. The dosimeter tubes were fabricated from high purity aluminum (99.5%) with nominal dimensions of 9.6 mm (0.38 in.) in length, 1.5 mm (0.058 in.) in diameter and a wall thickness of 0.15 mm (0.006 in.). The dosimeter wires each measured approximately 1.0 to 1.5 mm (0.04 to 0.06 in.) in diameter by 2 mm (0.08 in.) in length, and consisted of milligram quantities of Fe, Ti, Ni, Nb, 0.1% Co-Al, and 80.2% Mn-Cu. The tubes containing the wires were welded in a helium-argon environment. The monitors were placed in holes drilled horizontally through the bottom endcaps of six of the specimen holder assemblies:

JP-23 Position Number	Flux Monitor Number
3	114
4	118
6	120
7	121
8	125
10	129

However, since the dosimetry will not be analyzed for several more months, damage parameters were estimated from results of previous experiments in HFIR. Using a peak fast flux value of 1.10×10^{15}n/cm^2-s (derived from Reference 2), a peak dpa value of 8.85 (from ORNL), and the estimated normalized flux profile illustrated in Figure 3 (also derived from Reference 2), fast flux, fast fluence, and dpa profiles were generated (Figures 4, 5, and 6 and Table 8). These values could then be used to assign damage parameters to the JP-23 specimens (Table 9). Also included in Table 9 are the temperatures and other pertinent information for each specimen holder.

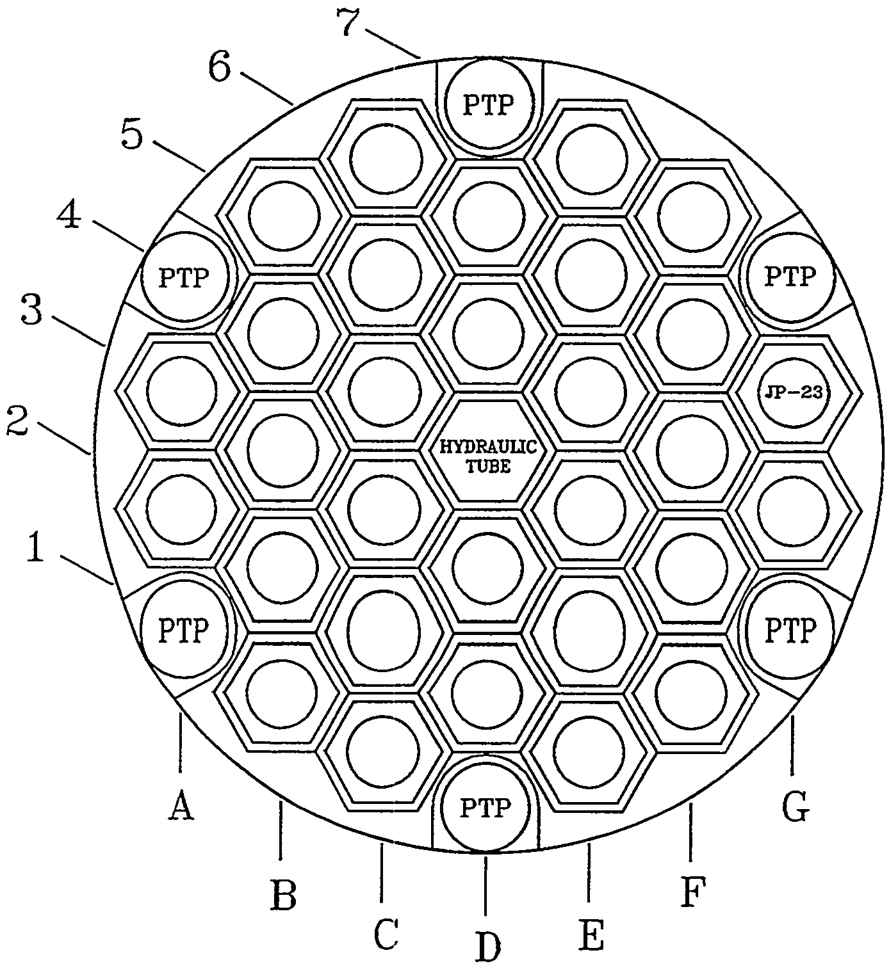

PTP — Peripheral Target Position
JP-23 — Test Located In Position G6

Position Designation	Radial Distance From Center
C3, C4, D3, D5, E4, E5	1.689 cm
B3, C2, C5, E3, E6, F5	2.926 cm
B2, B4, D2, D6, F4, F6	3.378 cm
A2, A3, B1, B5, C1, C6, E2, E7, F3, F7, G5, G6	4.465 cm
A1, A4, D1, D7, G4, G7 (PTPs)	5.067 cm

Figure 2. HFIR Target Position Designations, Showing the JP-23 Test.

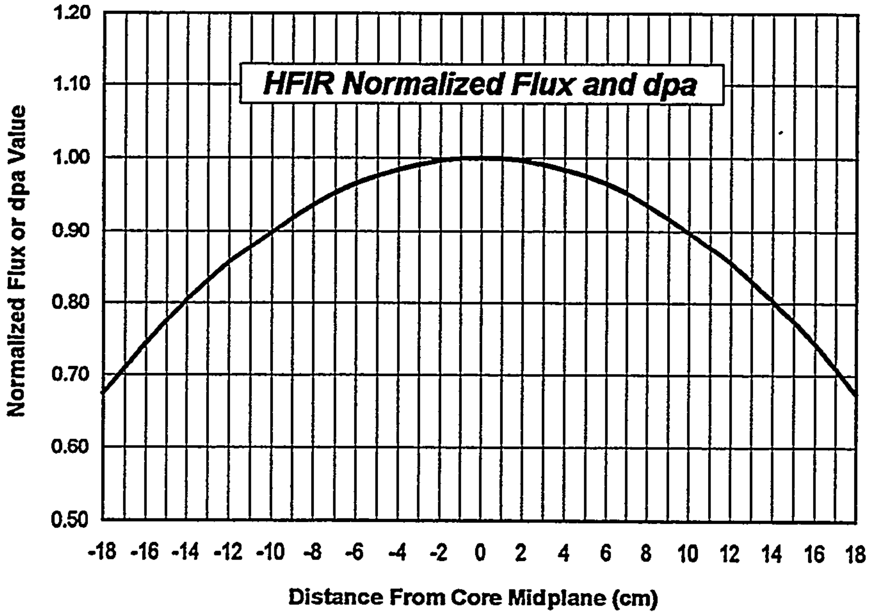

Figure 3. Estimated Normalized Flux and dpa Profile for HFIR

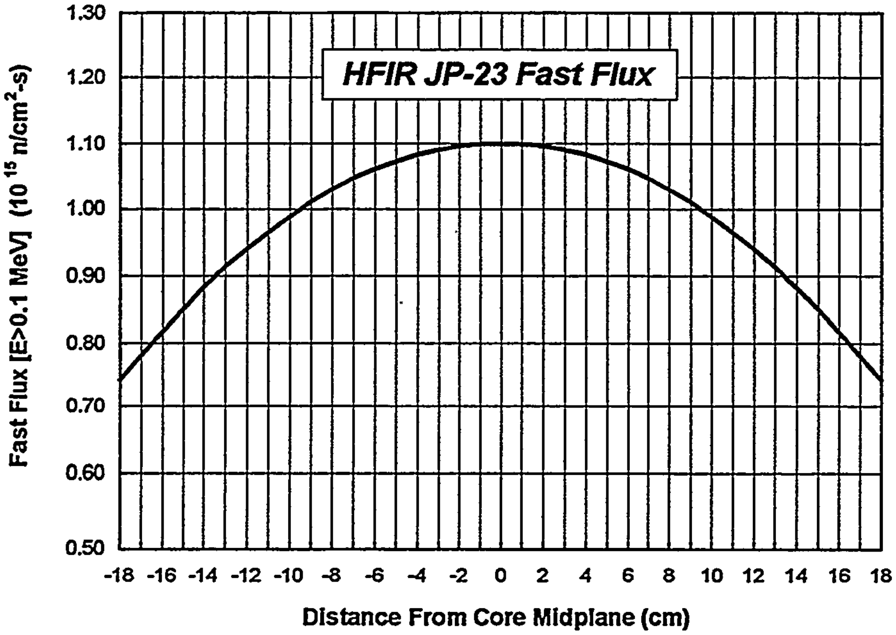

Figure 4. Estimated Fast Flux Profile for the JP-23 Test

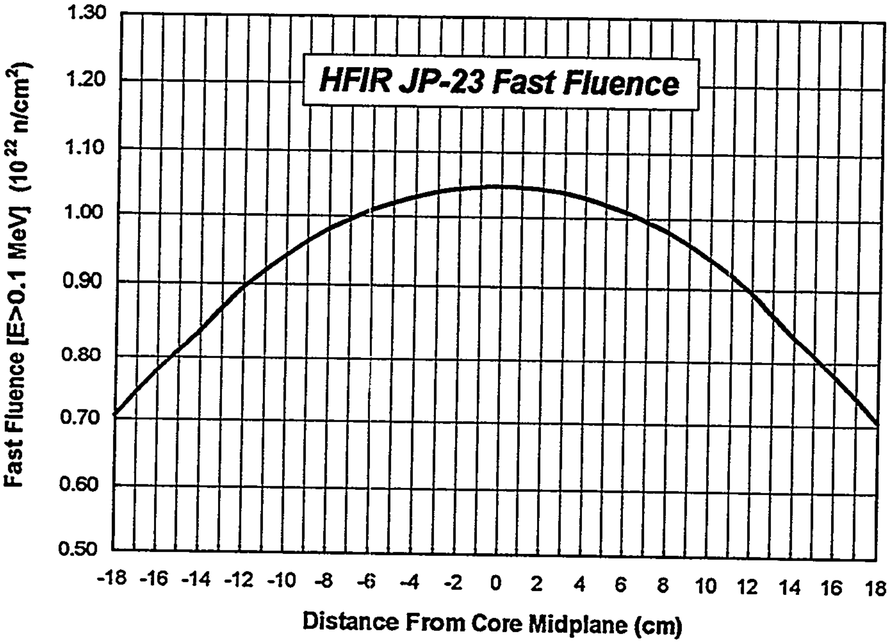

Figure 5. Estimated Fast Fluence Profile for the JP-23 Test

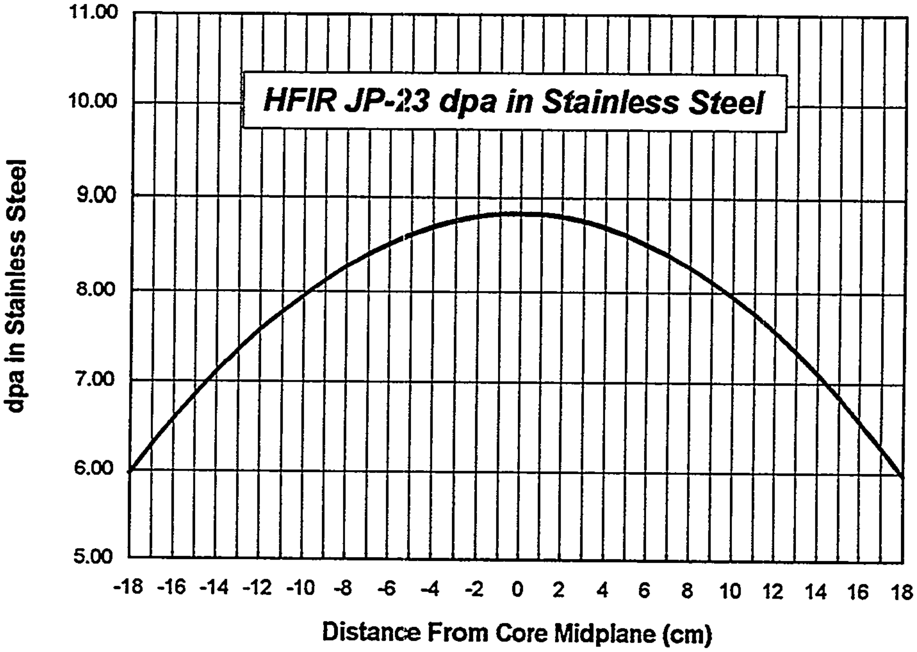

Figure 6. Estimated dpa (in stainless steel) Profile for the JP-23 Test

Table 8. Estimated Flux, Fluence, and dpa Data for the HFIR JP-23 Test
Based on 9367 MWd for HFIR Cycles 322-326

Distance From Horizontal Midplane (cm)	Normalized Flux or dpa Profile Value	Fast Flux, E>0.1 MeV (10^{15} n/cm^2-s)	Fast Fluence, E>0.1 MeV (10^{22} n/cm^2)	dpa in Stainless Steel
+18	0.674	0.741	0.706	5.97
+17	0.710	0.781	0.744	6.28
+16	0.743	0.817	0.778	6.58
+15	0.774	0.851	0.811	6.85
+14	0.803	0.883	0.841	7.11
+13	0.830	0.913	0.869	7.35
+12	0.855	0.941	0.895	7.57
+11	0.877	0.965	0.919	7.76
+10	0.898	0.988	0.941	7.95
+9	0.918	1.010	0.961	8.13
+8	0.936	1.030	0.980	8.29
+7	0.951	1.046	0.996	8.42
+6	0.964	1.060	1.010	8.53
+5	0.975	1.073	1.021	8.63
+4	0.984	1.082	1.031	8.71
+3	0.991	1.090	1.038	8.77
+2	0.996	1.096	1.043	8.82
+1	0.999	1.099	1.046	8.84
0	1.000	1.100	1.047	8.85
-1	0.999	1.099	1.046	8.84
-2	0.996	1.096	1.043	8.82
-3	0.991	1.090	1.038	8.77
-4	0.984	1.082	1.031	8.71
-5	0.975	1.073	1.021	8.63
-6	0.964	1.060	1.010	8.53
-7	0.951	1.046	0.996	8.42
-8	0.936	1.030	0.980	8.29
-9	0.918	1.010	0.961	8.13
-10	0.898	0.988	0.941	7.95
-11	0.877	0.965	0.919	7.76
-12	0.855	0.941	0.895	7.57
-13	0.830	0.913	0.869	7.35
-14	0.803	0.883	0.841	7.11
-15	0.774	0.851	0.811	6.85
-16	0.743	0.817	0.778	6.58
-17	0.710	0.781	0.744	6.28
-18	0.674	0.741	0.706	5.97

- Based on 85 MW full power
- Profile from Reference 2
- Peak flux based on 85% of 100 MW values from Reference 2
- Peak dpa based on 0.000945 dpa/MWd for stainless steel (from ORNL)

Table 9. Summary of Estimated HFIR JP-23 Irradiation Parameters

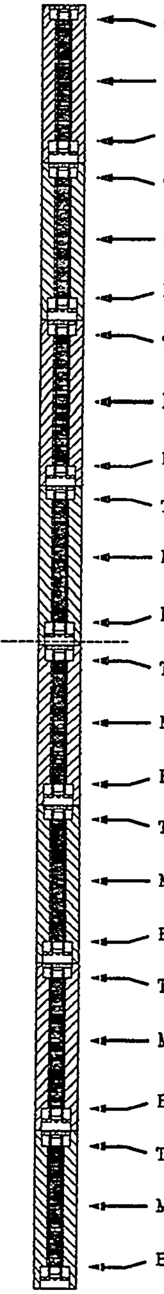

JP-23 Position Number	Program Sponsor	Irrad. Temp.		Distance From Reactor Midplane, cm (inches)	Fast Fluence [E>0.1 MeV] n/cm^2	dpa in SS
3	Japanese Monbusho	300 °C	Top:	+16.2 (+6.37)	0.77×10^{22}	6.5
			Mid:	+14.6 (+5.74)	0.82×10^{22}	6.9
			Bot:	+13.0 (+5.11)	0.87×10^{22}	7.3
4	Japanese Monbusho	400 °C	Top:	+12.0 (+4.73)	0.90×10^{22}	7.6
			Mid:	+10.4 (+4.10)	0.93×10^{22}	7.9
			Bot:	+8.8 (+3.47)	0.96×10^{22}	8.2
5	Japanese Monbusho	500 °C	Top:	+7.8 (+3.09)	0.98×10^{22}	8.3
			Mid:	+6.2 (+2.46)	1.01×10^{22}	8.5
			Bot:	+4.6 (+1.83)	1.02×10^{22}	8.7
6	Japanese Monbusho	600 °C	Top:	+3.7 (+1.45)	1.03×10^{22}	8.7
			Mid:	+2.1 (+0.82)	1.04×10^{22}	8.8
			Bot:	+0.5 (+0.19)	1.05×10^{22}	8.8
	---- Reactor Core C_L ----					
7	U.S. NIMs	600 °C	Top:	−0.5 (−0.19)	1.05×10^{22}	8.8
			Mid:	−2.1 (−0.82)	1.04×10^{22}	8.8
			Bot:	−3.7 (−1.45)	1.03×10^{22}	8.7
8	U.S. NIMs	500 °C	Top:	−4.6 (−1.83)	1.02×10^{22}	8.7
			Mid:	−6.2 (−2.46)	1.01×10^{22}	8.5
			Bot:	−7.8 (−3.09)	0.98×10^{22}	8.3
9	U.S. NIMs	400 °C	Top:	−8.8 (−3.47)	0.96×10^{22}	8.2
			Mid:	−10.4 (−4.10)	0.93×10^{22}	7.9
			Bot:	−12.0 (−4.73)	0.90×10^{22}	7.6
10	U.S. NIMs	300 °C	Top:	−13.0 (−5.11)	0.87×10^{22}	7.3
			Mid:	−14.6 (−5.74)	0.82×10^{22}	6.9
			Bot:	−16.2 (−6.37)	0.77×10^{22}	6.5

AME / August 25, 1994

CONCLUSIONS

The JP-23 test capsule has been irradiated in the HFIR during Cycles 322 through 326. The capsule contained eight transmission electron microscopy (TEM) specimen holders, two each at irradiation temperatures of 300, 400, 500 and 600°C. The test was irradiated for a total of 110 Effective Full Power Days (EFPD), achieving estimated peak doses of 1.1 x 10^{22} n/cm^2 (E>0.1 MeV) and 8.8 dpa (in stainless steel).

FUTURE WORK

Specimens from the JP-23 experiment will be distributed to experimenters.

REFERENCES

1. R. L. Senn, "Experimental Plan for the US/Japan Irradiation Program HFIR Target Capsule JP-23," ORNL Document No. MET-MIE-EP-092, Rev. 0, August 25, 1993.

2. L. R. Greenwood and C. A. Seils, "Dosimetry and Damage Calculations for the JP4, JP5 and JP8 US/Japanese Experiments in HFIR," Fusion Reactor Materials Semiannual Progress Report for the Period Ending September 30, 1987, DOE/ER-0313/3 (March 1988) pp. 30-32.

3.0 MATERIALS ENGINEERING AND DESIGN REQUIREMENTS

No contributions.

4.0 FUNDAMENTAL MECHANICAL BEHAVIOR

CORRELATION BETWEEN SHEAR PUNCH AND TENSILE DATA FOR NEUTRON-IRRADIATED ALUMINUM ALLOYS

- M. L. Hamilton and D. J. Edwards (Pacific Northwest Laboratory)[(a)], M. B. Toloczko and G. E. Lucas (University of California-Santa Barbara), W. F. Sommer and M. J. Borden (Los Alamos National Laboratory), and J. F. Dunlap and J. F. Stubbins (University of Illinois)[a]

OBJECTIVE

This work was performed to determine whether shear punch and tensile data obtained on neutron irradiated aluminum alloys exhibited the same type of relationship as had been seen in other work and to assess the validity of extrapolating the results to proton-irradiated alloys. This work was also meant to be the first of a series of similar test matrices designed to determine whether the shear punch/tensile relationship varied or was the same for different alloy classes.

SUMMARY

Tensile specimens and TEM disks of two aluminum alloys in two tempers were irradiated at 90-120°C with neutrons from spallation reactions in the Los Alamos Spallation Radiation Effects Facility (LASREF) at the Los Alamos Meson Physics Facility (LAMPF). The materials were exposed to a fluence of 3.4-4 x 10^{20} n/cm^2. This work was part of a study to determine the potential for using aluminum alloys as structural components in accelerators used to produce tritium. Shear punch tests and tensile tests were performed at room temperature and at 100°C, a temperature characteristic of the operating temperature in the application of interest. Shear punch and tensile data from unirradiated specimens were used to develop a correlation between shear punch and tensile strengths. Using the shear punch data from the neutron irradiated TEM disks, the correlation predicted the tensile strength of the neutron irradiated condition reasonably well. Shear punch data on similar 760 MeV proton-irradiated specimens were used with the correlation in an attempt to predict uniaxial strength in the proton irradiated condition.

PROGRESS AND STATUS

Introduction

Aluminum alloys are being considered for blanket and target structural applications in the Accelerator Production of Tritium (APT) Program at Los Alamos National Laboratory (LANL). The irradiation environment will consist of both high energy protons and neutrons as well as a large number of neutrons over a range of energies below the initial spallation neutron energy spectrum. Aluminum alloys were selected because of their low absorption of thermal neutrons, their high thermal conductivity, their fabricability and joinability, their performance under prototypic and other irradiation conditions, and their low activation under such conditions.

Irradiation performance data for materials in such an environment are extremely limited. Miniature tensile specimens and transmission electron microscopy (TEM) disks that were previously irradiated with neutrons or protons were available for the alloys of interest, however, which eliminated the time typically required for materials irradiation prior to testing. Both tensile specimens and TEM disks were available for the

---

[a] Pacific Northwest Laboratory is operated for the U.S. Department of Energy by Battelle Memorial Institute under Contract DE-AC06-76RLO 1830.

neutron irradiated condition, while only TEM disks were available for the proton irradiated condition. The alloys available were 6061, in both an annealed (O) and precipitation strengthened (T6) condition, and a German version of 5052, also in an annealed (O) and in a strengthened (similar to H38) condition. While this material is slightly different in composition than that specified in Reference 1, it is referred to in this work as alloy 5052 for simplicity.

The specimens were irradiated in LASREF at the Los Alamos Meson Physics Facility (LAMPF), exposing the materials of interest to either medium energy protons or spallation neutrons. Irradiation in the neutron flux proceeded at temperatures ranging from 90 to 120°C. The neutron dose achieved was 3.4-4 x 10^{20} n/cm^2 with about 1% of the neutrons having E > 1 MeV. The proton irradiation was conducted at temperatures estimated by calculation to be 200-300°C. The proton dose on these samples reached 2-3 x 10^{20} p/cm^2 with a proton energy of about 760 MeV.

Mechanical properties data for irradiations under these types of irradiation conditions are extremely limited. The most cost effective use of irradiated test specimens allows the extraction of as much data as possible from the fewest number of specimens. This becomes particularly significant when materials irradiations are performed in small volumes. Miniature tensile specimens have been used for many years, but the use of even smaller specimens to generate tensile data has been considered by many researchers. The shear punch test is one such test that was developed a number of years ago as a technique for extracting strength and ductility information from TEM disks.(2) It utilizes a cylindrical punch with a flat end to deform a lightly clamped disk to failure. The disk material is forced to deform primarily in a small region corresponding roughly to the region below the clearance between the punch and die. It has been found empirically that the yield and maximum loads can be correlated with the uniaxial yield and ultimate stresses, respectively, and that the displacement at failure can be related to uniaxial reduction in area.

Since both neutron irradiated tensile specimens and neutron irradiated TEM disks were available, the current test program was seen as an opportunity to further develop the relationship between tensile and shear punch behavior, and to use this relationship to try to predict the tensile behavior of proton irradiated material from the shear punch behavior of proton irradiated disks. A sufficient number of unirradiated specimens existed to establish a correlation between shear punch and tensile strength for the unirradiated condition. The tensile strength predicted by the correlation for the neutron irradiated condition on the basis of the shear punch data obtained on neutron irradiated TEM disks was compared to the actual tensile properties obtained on neutron irradiated tensile specimens. Assuming that the neutron irradiated data would be consistent with the correlation developed on unirradiated material, then the correlation would be used to predict the tensile properties of the proton irradiated conditions from the shear punch data obtained in the same conditions.

While the specific alloys considered in this particular project were of interest to LANL, and while partial financial support for this work was provided by LANL, the shear punch/tensile correlation work itself is being investigated due its potential for application within the fusion materials program. The development of miniature specimens will be of particular importance to the fusion materials program when an advanced neutron source is built for the simulation of fusion neutrons. Such a device will have only a very limited volume for the irradiation of materials specimens, and existing tensile specimens are quite large relative to the TEM disk used for the shear punch test. Thus the data obtained in this effort will be used in the evaluation of the shear punch test as a viable means of extracting tensile data from TEM disks.

Experimental Procedure

Shear Punch Testing. Shear punch tests were performed at both room temperature and 100°C (±2°C). Room temperature tests were performed to facilitate comparison to data available on these alloys after irradiation in mixed spectrum fission reactors. Tests at 100°C were selected as being representative of the expected operating temperature in APT structural elements as well as being representative of the irradiation temperature. Punch tests were performed in a screw-driven Instron test machine at a crosshead speed of 0.127 mm/min (0.005 in./min). Room temperature tests were performed in air. Elevated temperature was achieved by resistance heating in an argon-filled, insulated test chamber. Heat-up time was ~30 minutes. Specimen displacement during a test was assumed to be equal to crosshead travel.

Shear punch tests were performed on both unirradiated control specimens and a set of LAMPF-irradiated specimens. Ten tests were done for each of the four unirradiated alloy conditions at both room temperature and 100°C. One or two tests were done for each of the four neutron irradiated alloy conditions at both room temperature and 100°C. One test was done at room temperature for each of the four proton irradiated alloy conditions. The specimens were fabricated by punching, and nominally measured 0.25 mm (0.010 inches) thick and 2.79 mm (0.110 inches) in diameter. All irradiated specimens were flattened prior to shear punch testing in a device that applied a small load to the specimens while they were located in a recessed die. The specimens were flattened to facilitate testing, and no change in dislocation structure was anticipated as a result of the flattening operation. The unirradiated specimens were not flattened.

Specimen thicknesses were measured using a calibrated dial micrometer with a rounded contact, attached to a flat anvil. Specimen thickness was measured at least six times in different places on each specimen to verify that the three measurements recorded were representative. Shims of the appropriate thickness were placed between the two fixture halves to control the spacing between the two to be a fraction of a mil less than the specimen thickness. The specimen was placed over the blanking hole in the lower fixture with the deburred (i.e., cupped) side of the specimen facing up to ensure good specimen/die and specimen/punch contact. The upper fixture was placed on top of the assembly and the bolts holding it in place were tightened while the upper and lower fixture alignment was maintained. A push pin 1.00 mm (0.0395 inches) in diameter was used to punch the specimens. The guide hole for the push pin consisted of a bushing with a 1.02 mm (0.0400 inch) inner diameter in the upper half of the fixture. A bushing with a 1.04 mm (0.0410 inch) inner diameter formed the die hole in the lower half of the fixture.

Uniaxial Tensile Testing. Uniaxial tensile tests were performed on both unirradiated control specimens and a set of LAMPF-irradiated specimens. Ten tests were done for each of the four unirradiated alloy conditions at both room temperature and 100°C. Two tests were done for each of the four neutron irradiated alloy conditions at both room temperature and 100°C. The specimens were sheet specimens measuring nominally 0.25 mm (0.010 in.) in thickness, 18 mm (0.710 in.) in gauge length, and 3 mm (0.120 in.) in gauge width. Tensile properties were measured using a standard hydraulic tensile frame with an extension rate of 0.1 mm/m. The elevated temperature tests were carried out in a heated air furnace chamber where the specimen was brought to uniform temperature in ~10 minutes. Displacement was controlled by an LVDT attached to a hydraulic piston, and load was monitored with a standard load cell. Other details of the tensile tests and a discussion of the results are described elsewhere in this proceedings.(3)

Results and Discussion

Shear Punch Data. The average strengths determined from the tensile and shear punch tests are given in Table 1. The tensile data are described in more detail in Reference 3. The shear punch strengths were determined for both yield and maximum conditions according to $\tau = \frac{P}{2\pi rt}$, where τ is the shear stress,

Table 1. Average shear punch and tensile data

MATERIAL	YIELD STRENGTH (MPa)			MAXIMUM STRENGTH (MPa)		
	UNIRR[a]	N IRR[b]	P IRR[b]	UNIRR[a]	N IRR[b]	P IRR[b]
Shear punch, room temperature						
6061-O	44 ± 4[c]	-[d]	35	91 ± 2	-	89
6061-T6	131 ± 5	140	29	188 ± 3	193	88
5052-O	71 ± 6	62	73	142 ± 3	139	145
5052-H38	136 ± 4	119	45	180 ± 3	182	141
Shear punch, 100°C						
6061-O	45 ± 3	-	-	90 ± 2	-	-
6061-T6	122 ± 6	135 ± 0	-	182 ± 3	187 ± 2	-
5052-O	83 ± 3	70 ± 6	-	146 ± 2	148 ± 3	-
5052-H38	137 ± 7	127 ± 5	-	178 ± 3	179 ± 0	-
Tensile, room temperature(3)						
6061-O	49	54	-	128	147	-
6061-T6	233	244	-	311	305	-
5052-O	96	101	-	208	213	-
5052-H38	301	264	-	335	320	-
Tensile, 100°C(3)						
6061-O	62	63	-	129	137	-
6061-T6	259	221	-	305	287	-
5052-O	104	113	-	215	221	-
5052-H38	285	259	-	315	318	-

[a] 8-10 tests per condition
[b] One test per condition
[c] Standard deviation
[d] Indicates no test performed or test data invalid

P is the load, t is the average specimen thickness, and r is an effective radius defined as the average of the punch and blanking radii, or 20.16 mils for the push pin used for these tests. The load value for the yield condition was determined at the point where the load-displacement trace deviated from linearity. Standard deviations are given only for those conditions where two or more specimens were tested. Note that the shear punch test produces a stress state that is not pure shear, and the shear punch strengths cannot truly be considered to be shear yield and shear maximum strengths.(2) This terminology will be used, however, for the sake of simplicity.

The average shear punch data are shown in Figures 1 and 2 versus the average tensile data that are given in Table 1. The data clustered in the lower left quadrant of these two figures were obtained on the annealed alloys, while the data clustered in the upper right quadrant were obtained on the strengthened alloys. The data appear to cluster fairly linearly, consistent with earlier work on shear punch testing.(2) The difference between properties observed at room temperature and at 100°C was slight, indicating that the microstructure is reasonably stable at 100°C, at least for short periods of time. Only minor changes in shear punch or tensile strength were observed following neutron irradiation.

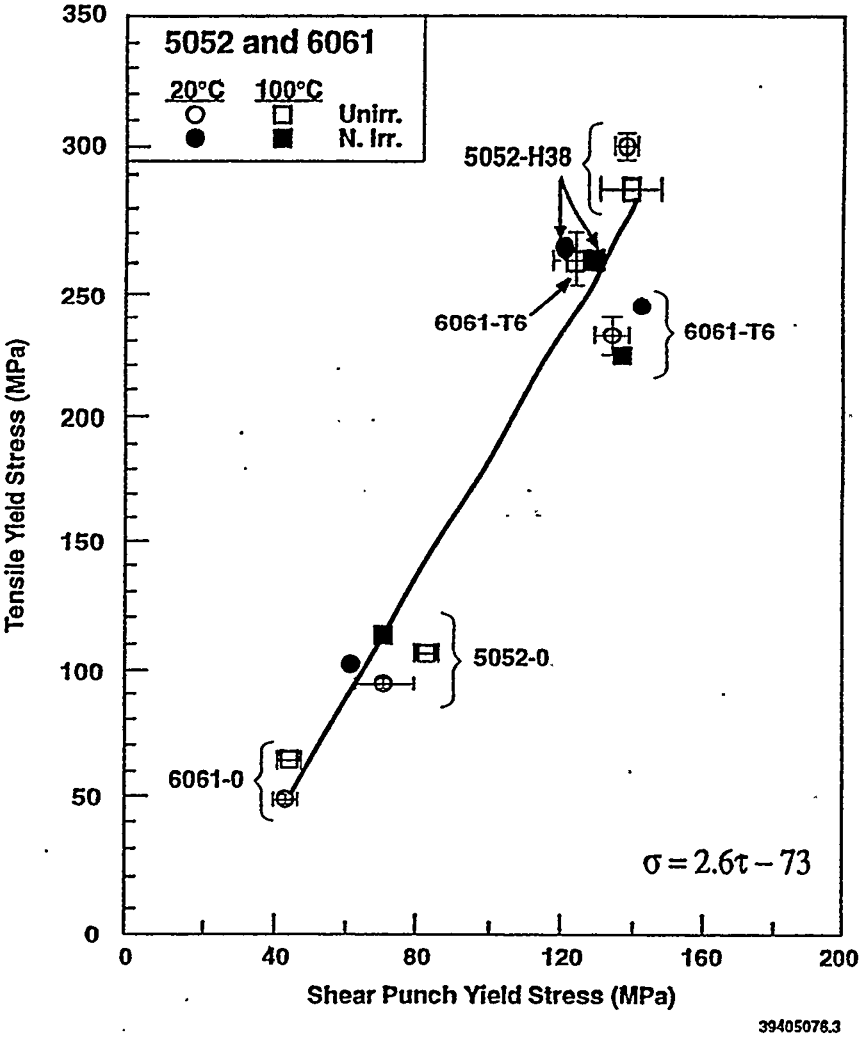

Figure 1. Average tensile yield versus shear yield strength for unirradiated and neutron irradiated alloys 5052 and 6061, with the regression line for the data from unirradiated specimens.

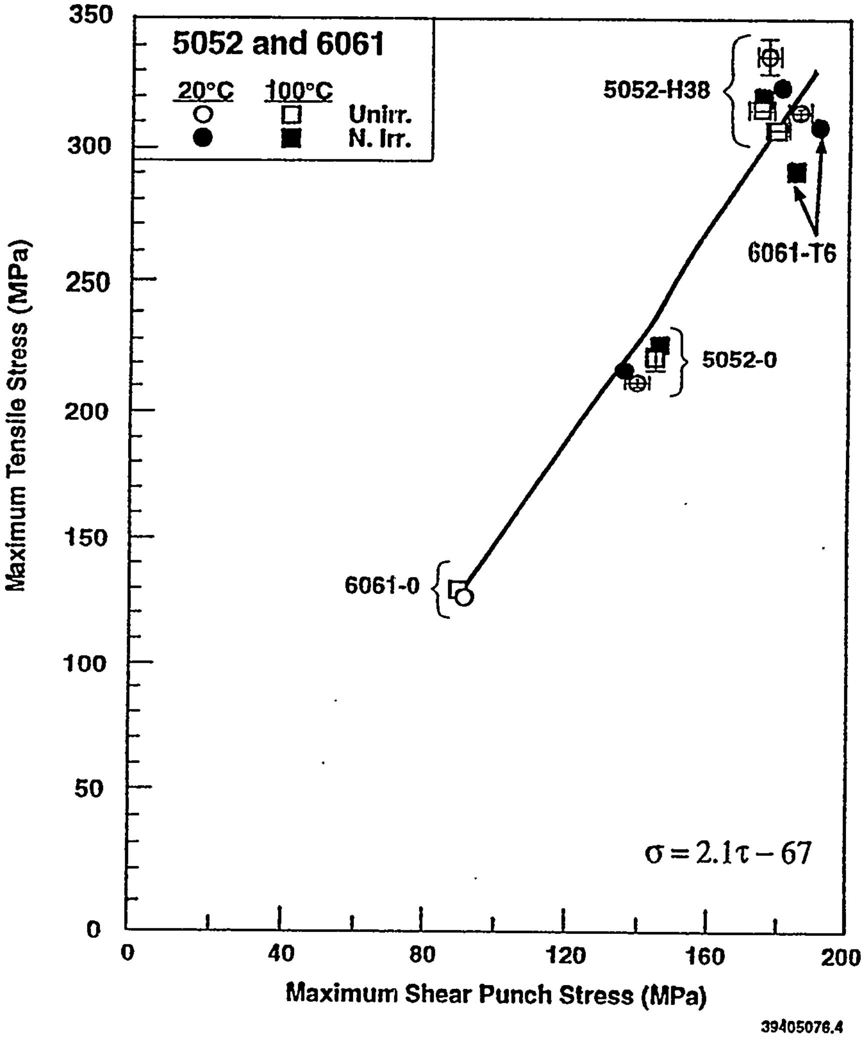

Figure 2. Average tensile maximum versus shear maximum strength for unirradiated and neutron irradiated alloys 5052 and 6061, with the regression line for the data from unirradiated specimens.

Inspection of the data in Table 1 reveals that there are some anomalies in both the tensile and shear data. First is the fact that the strength observed at 100°C is sometimes greater than that observed at room temperature. This is evident in both the tensile and the shear data for several different test conditions. While Reference 4 indicates that the yield and maximum strengths of these alloys typically decrease slightly as the temperature is increased from 20 to 100°C, other researchers have also observed an increase in strength over this temperature range.(5) Only the 5052 load-displacement traces, however, exhibited the serrations typical of dynamic strain aging.

While very little change in strength was observed following neutron irradiation (the largest shift was by 38 MPa; the majority of alloy conditions shifted by less than 20 MPa), significant strength changes were observed in the strengthened alloys following proton irradiation. The strength of the annealed alloys remained essentially the same after proton irradiation, but the hardened alloys softened significantly. The yield and maximum strength of the precipitation strengthened 6061 decreased down to values effectively the same as those exhibited in the annealed condition. These results are consistent with a loss of strengthening due to the dissolution of the Mg_2Si precipitates during the exposure to 760 MeV protons.

While the maximum strength of the strengthened 5052 also decreased to that of the annealed material, the yield strength decreased much more, to a value well below that observed in the annealed condition. This softening is most likely due to the recovery of the cold work dislocation structure at elevated temperature, accelerated by radiation enhanced diffusion. More discussion of these phenomena is given in Reference 1.

Correlation Development. The data given in Table 1 were used to develop a correlation relating the shear punch to the tensile data. The averaged shear data were weighted in the correlations according to the number of data points used to calculate the shear strength averages. Regression lines are of the form $\sigma = C\tau + K$ were fit to the data, where σ is the uniaxial tensile stress and τ is the shear stress. The constant K was allowed to vary since the data do not appear in Figures 1 and 2 to lie on a line that goes through the origin.

Since there is no apparent distinction between the data obtained at room temperature and 100°C, all the data obtained in the unirradiated condition was used to generate the following equations for the yield and maximum load conditions, respectively:

$$\sigma_y = 2.6\tau_y - 73 \qquad \text{and} \qquad \sigma_m = 2.1\tau_m - 67$$

where both σ and τ are in MPa. The r^2 values for both of these regressions was 0.98.

The correlations determined by G. E. Lucas were of the form $\tau = m\sigma$, with m = 0:54 and 0.62 for the yield and ultimate conditions, respectively. Thus the values from Lucas' work that are comparable to C are actually 1/m, or 1/0.54 = 1.85 and 1/0.62 = 1.61 for the yield and ultimate conditions, respectively. There is no constant K in Lucas' correlations because the offset from the axis was considered to be a frictional component of the shear stress and was incorporated into the original calculation of shear stress according to $\tau = \frac{P-F}{2\pi r t}$. Lucas' values of C are somewhat different from the values obtained in the current study. This is most likely due to either the way the offset was incorporated or to the fact that, since the original correlations were determined for a combination of data obtained on copper, brass, steel, aluminum and stainless steel alloys, they represent an average of the behavior of all the alloys considered.

Data in Reference 4 suggest that the relationship between shear and tensile strength varies between alloy systems. Figures 3 and 4 show maximum shear and tensile strength data obtained on full size specimens of a variety of aluminum alloys (Figure 3) and copper-zinc alloys (Figure 4). The aluminum alloys for which data on full size specimens are shown in Figure 3 range from the 1000 to the 7000 series and include alloys strengthened by a number of mechanisms. All the alloys appear to obey the same relationship between shear and tensile strength. The data obtained in the current study on miniature specimens are shown in the same plot. The data on the full size and miniature specimens appear to obey the same relationship despite the fact that the miniature specimens were subjected to the shear punch test and the full size specimens were probably tested in torsion. The data shown in Figure 4 are for copper-zinc alloys ranging from 5 to 40 weight percent zinc. All the data appear to obey the same relationship between shear and tensile strength except for the Cu-40Zn alloy, which is the only alloy in the group for which the zinc level exceeds the limit of solid solubility in Cu. It is worth noting that, while the maximum tensile and shear strengths of many different types of aluminum alloys obey the same relationship, the same is not true for the copper-zinc alloys. It is also worth noting that, counter to what one might expect intuitively, the regression lines fit to the data in Figures 3 and 4 do not intersect the origin.

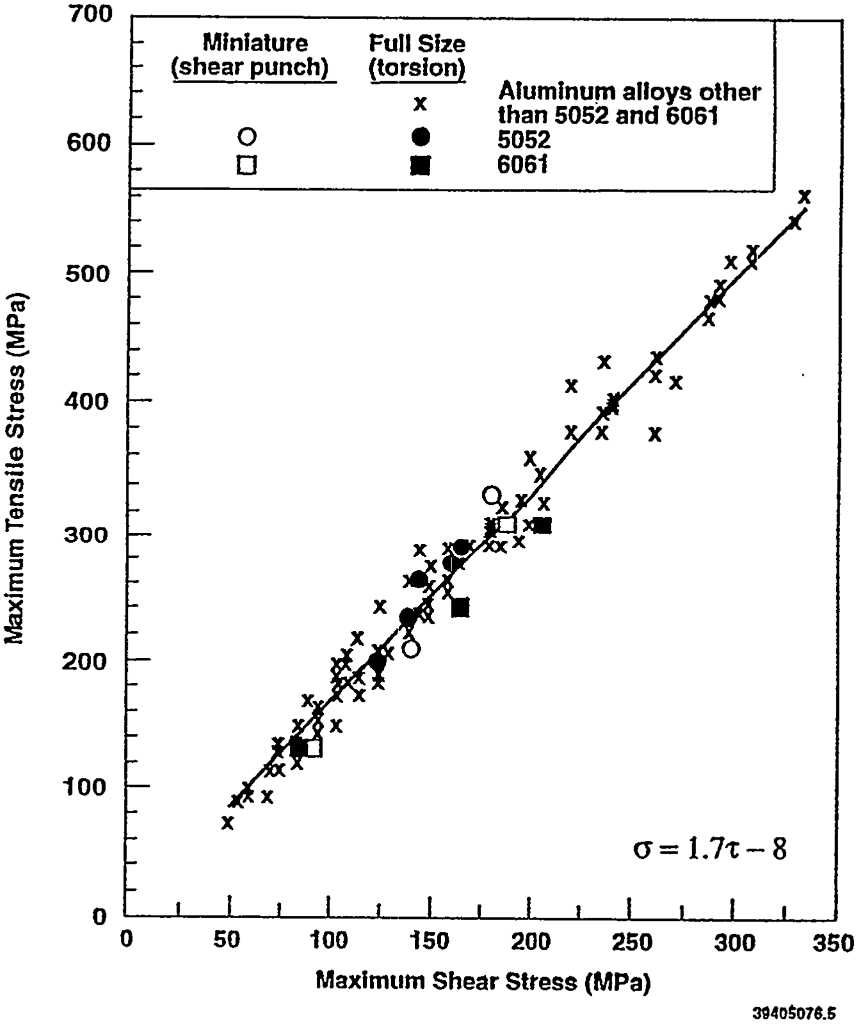

Figure 3. Maximum tensile and maximum shear strength data obtained on full size specimens of a number of aluminum alloys (Reference 4).

The constants C and K are compared in Table 2 for the data sets discussed above. The data are ordered by increasing slope (i.e., increasing value of C). There is a range of values observed for both C and K. It is not known at this time if the range of values is related to the differences between alloy classes, to the number of data points used to generate the correlations, to a difference in the results obtained in tests on full size and miniature specimens, or the degree of shear to which specimens in the shear punch test are subjected (it is assumed that the handbook data on standard specimens was obtained in torsion, or pure shear). It is somewhat counter-intuitive that the value of K is not zero for at least the yield condition; this implies that either the relationship between shear and tensile strengths is nonlinear at the lower values of strength, or that there is some threshold below which the relationship between the two is simply not valid. Clearly a large negative value of the intercept K will dominate any prediction of tensile strength when a low shear strength is obtained.

Table 2. Regression constants for $\sigma_m = C\tau_m + K$, where σ_m and τ_m denote the maximum strengths.

Alloy	Test temp. (°C)	Specimen size	Test type	No. of data points	C	K
Steel, aluminum, copper, stainless steel, brass	RT[a]	Miniature	Shear punch	24	1.6	-
Various aluminum	RT	Full	Torsion[b]	126	1.7	-8
6061 + 5052 aluminum	RT, 100	Miniature	Shear punch	8	2.1	-67
Various copper-zinc (up through 35% zinc)	RT	Full	Torsion[b]	72	2.9	-335

[a] RT = room temperature

[b] It is assumed that the data from Reference 4 were obtained on standard, full size specimens in torsion; this information was not specified.

Proton irradiated condition. Since the correlation that was developed on the basis of the data from unirradiated specimens seemed to make reasonable predictions of the tensile strength observed in the neutron irradiated specimens, the correlation was applied to the shear punch data on proton irradiated specimens to predict the tensile strength of the proton irradiated condition. The tensile values calculated for the proton irradiated condition are shown in Table 4. Since no tensile data are available for comparison, no firm conclusions can be drawn on the basis of these results about the applicability of any of the correlations to the proton irradiated aluminum alloys. Several observations related to the predictions are pertinent, however.

The good agreement observed in the neutron irradiated condition between the ultimate tensile strength and the predicted values suggests that the predicted values of ultimate tensile strength for the proton irradiated condition could be considered quantitatively. The yield strength predictions, however, seem suspect, particularly since two out of the four values are quite low. The shear yield strength in all alloy conditions following proton irradiation is generally the same as or lower than the shear yield strength of the corresponding alloy in the unirradiated annealed condition. Thus it is reasonable that the predicted tensile strengths follow a similar trend. The stress ranges observed in the shear punch tests on proton irradiated specimens were either well below or only marginally overlapped the values obtained in tests on specimens in the other conditions. The validity of extrapolating the correlations to these stress ranges is therefore somewhat questionable.

CONCLUSIONS

Neutron irradiation at 90-120°C caused only minor changes in the strength of annealed and strengthened aluminum alloys 6061 and 5052 at a fluence of ~3 x 10^{20} n/cm^2. Irradiation with 760 MeV protons at 200-300°C to ~3 x 10^{20} p/cm^2, however, produced a significant decrease in strength in the strengthened alloy conditions. A correlation was developed using the data from unirradiated specimens that describes the relationship between the shear and uniaxial yield and maximum strengths. The uniaxial data obtained

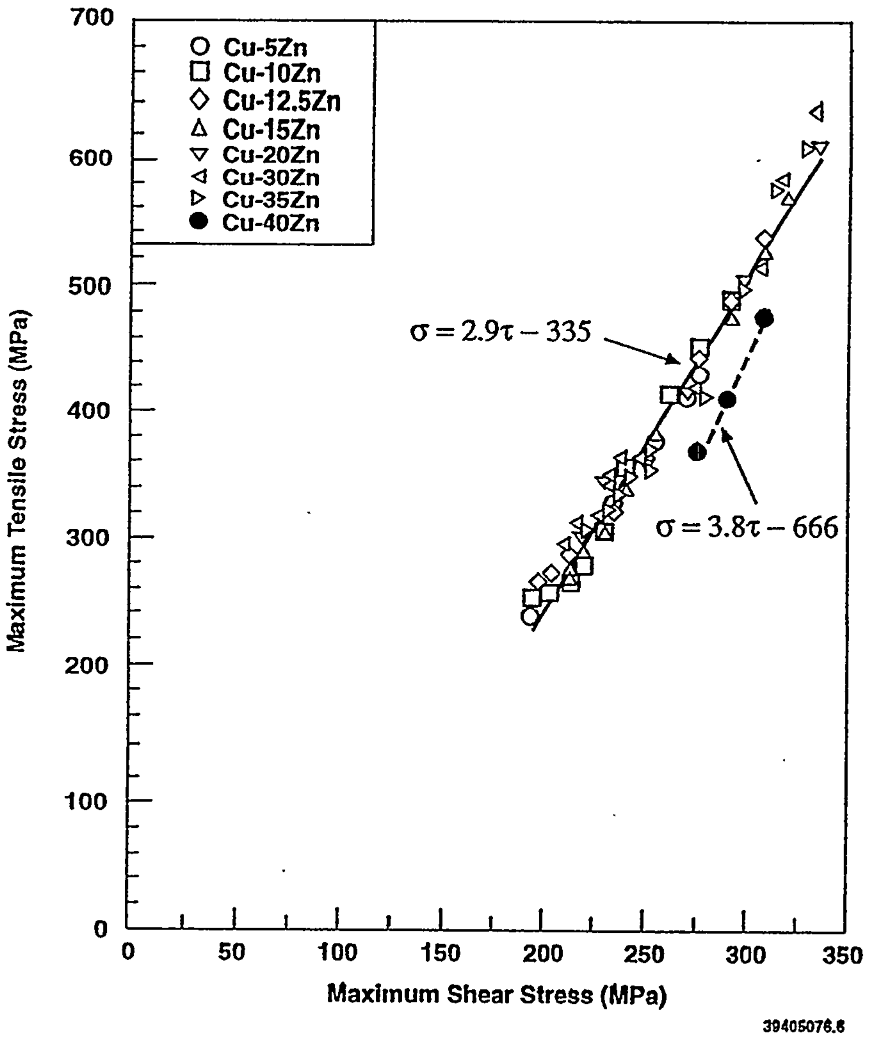

Figure 4. Maximum tensile and maximum shear strength data obtained on full size specimens of a number of copper alloys (Reference 4).

Correction Predictions.

Neutron irradiated condition. The tensile values calculated on the basis of the neutron irradiated shear punch data, using the correlations determined from the unirradiated shear punch data, are shown in Table 3 along with the tensile data obtained on neutron irradiated tensile specimens. The predictions of the correlation developed for the unirradiated data from Reference 4 on full size specimens (Table 2) are included since the miniature specimen data appeared to overlap the full size specimen data quite well. The ultimate strength (UTS) predictions are typically within about 10% of the actual tensile values obtained regardless of which correlation was used. The yield strength (YS) predictions were slightly less accurate. The implication is that the data on miniature specimens of the two aluminum alloys can be considered part of a larger group that includes data on full size specimens of many aluminum alloys.

Table 3. Correlation predictions of tensile properties for neutron irradiated aluminum alloys

SPECIMEN DESCRIPTION		TENSILE VALUES (MPa)			
		PREDICTED*		ACTUAL	
ALLOY	TEST TEMP (°C)	YS (% error)	UTS (% error)	YS	UTS
6061-T6	20	291 (19)	333 (9) 320 (5)	244	305
	100	278 (26)	320 (11) 310 (8)	221	287
5052-O	20	88 (-13)	221 (4) 228 (7)	101	213
	100	109 (-4)	240 (9) 244 (10)	113	221
5052-H38	20	236 (-10)	310 (-3) 301 (-6)	264	320
	100	257 (-1)	304 (-4) 296 (-7)	259	318

*The first line in each row represents the prediction of the correlation developed on the basis of the unirradiated shear punch data. The second line in the UTS column represents the prediction of the correlation developed on the basis of the data from Reference 4 on full size specimens.

on the neutron irradiated specimens was in reasonable agreement with the predictions of the correlation calculated using the shear punch data for the neutron irradiated condition. While the correlation predictions for the maximum uniaxial strength in the proton irradiated condition appear to be valid, the uniaxial yield strength predictions are somewhat suspect.

FUTURE WORK

Shear punch and tensile tests will be done on alloys in several different materials classes to determine whether a linear relationship exists between shear and tensile strengths for these classes of alloys, and whether such a relationship varies with alloy class. The materials for which tests are currently planned include a variety of steels as well as copper and vanadium alloys. In addition, similar tests will be performed on irradiated specimens if it is determined that such a relationship exists for unirradiated materials, to ascertain whether the same relationship holds for irradiated materials behavior.

Table 4. Shear strength changes and predicted tensile strength changes at room temperature with proton irradiation.

ALLOY	SHEAR PUNCH TEST		TENSILE TEST	
	UNIRR	P IRR	UNIRR	PREDICTED FOR PROTON IRRADIATION
YIELD STRENGTH (MPa)				
6061-O	44 ± 4	35	49	18
6061-T6	131 ± 5	29	233	2
5052-O	71 ± 6	73	96	117
5052-H38	136 ± 4	45	301	44
MAXIMUM STRENGTH (MPa)				
6061-O	91 ± 2	89	128	120
6061-T6	188 ± 3	88	311	118
5052-O	142 ± 3	145	208	238
5052-H38	180 ± 3	141	335	229

REFERENCES

1. APT Materials Safety Experiments Technical Report, LA-UR-93-2850, September 1993.

2. G. E. Lucas, J. W. Sheckherd, G. R. Odette, "Shear Punch and Microhardness Tests for Strength and Ductility Measurements," ASTM STP 888, American Society for Testing and Materials (1986) pp. 112-140.

3. J. F. Dunlap, J. F. Stubbins, M. J. Borden and W. F. Sommer, "Room and Elevated Temperature Tensile Properties of Aluminum Alloys 6061 and 5052 Following Irradiation with Spallation-Produced Neutrons, this proceedings.

4. Metals Handbook, volume 2, (1990), American Society for Testing Materials.

5. K. Farrell and R. T. King, "Tensile Properties of Neutron-Irradiated 6061 Aluminum Alloy in Annealed and Precipitation-Hardened Conditions," ASTM STP 633, (1979) pp. 440-449.

5.0 RADIATION EFFECTS, MECHANISTIC STUDIES, THEORY AND MODELING

COMPARISON OF DEFECT CLUSTER ACCUMULATION AND PATTERN FORMATION IN IRRADIATED COPPER AND NICKEL

– S.J. Zinkle and L.L. Snead (Oak Ridge National Laboratory), B.N. Singh (Risø National Laboratory), and D.J. Edwards (Pacific Northwest Laboratory)

OBJECTIVE

The objective of this study is to compare the contrasting behavior of defect cluster formation in neutron-irradiated copper and nickel specimens.

SUMMARY

Transmission electron microscopy was used to examine the density and spatial distribution of defect clusters produced in copper and nickel as the result of fission neutron irradiation to damage levels of 0.01 to 0.25 displacements per atom (dpa) at irradiation temperatures between 50 and 230°C (0.24 to 0.37 T_M in Cu). A high density of small stacking fault tetrahedra (SFT) and dislocation loops was observed in both materials, and a moderate density of small voids was observed in the copper specimens irradiated at 230°C. The visible defect cluster density in both materials approached a saturation value at doses >0.1 dpa. The visible defect cluster density in nickel was a factor of 5 to 10 lower than that in copper at all damage levels. The defect clusters in Ni organized into{001} walls at damage levels >0.1 dpa, whereas defect cluster alignment was not observed in copper. A comparison with published results in the literature indicates that defect cluster wall formation occurs in nickel irradiated at 0.2 to 0.4 T_M in a wide variety of irradiation spectra. Defect cluster wall formation apparently only occurs in copper during low temperature irradiation with electrons and light ions. These results are discussed in terms of the thermal spike model for energetic displacement cascades.

PROGRESS AND STATUS

1. Introduction

The effect of energetic displacement cascades on the microstructural evolution in metals is an interesting phenomenon for both fundamental and technological reasons. As reviewed elsewhere [1,2], the fraction of surviving defects (relative to the Kinchin-Pease calculated displacements) decreases with increasing primary knock-on atom (PKA) energy due to in-cascade recombination. On the other hand, in-cascade clustering produces a higher fraction of clustered defects under energetic displacement cascade conditions compared to low PKA energy irradiations. Due to the small size (~10 nm) and short lifetime ($\sim 10^{-11}$ s) of displacement cascades in metals, direct experimental investigation of individual cascades cannot be performed. Molecular dynamics (MD) simulations have been increasingly employed in recent years to provide some information on the evolution of the displacement cascade, including the distribution of clustered and isolated point defects [2-5]. Most of these MD studies have focused on copper due to the availability of realistic atomic potentials.

Copper and nickel are commonly used as model face-centered cubic metals in radiation effects studies. One useful approach for investigating radiation effects is to examine the fine-scale defect cluster formation in irradiated metals with transmission electron microscopy. Unfortunately, there is a lack of published information on the microstructure of copper and nickel irradiated to "moderate" doses (>0.01 dpa) at 50 to 300°C [44]. This temperature range corresponds to the transitional regime between recovery Stages III and V, which according to the one-interstitial model is associated with the initiation of vacancy migration and the thermal breakup of vacancy clusters, respectively.

Several experimental studies have noted that the small defect clusters produced in irradiated face-centered-cubic (FCC) metals such as Ni [6-15] and Cu [13,14] have a tendency to become aligned along {001} planes under certain conditions. The defect cluster alignment in Ni becomes noticeable at damage levels of ~0.1 displacements per atom (dpa), and remains stable up to damage levels in excess of 20 dpa. This alignment has been modeled on the basis of nonlinear diffusion-controlled coupling of point defects with the defect structure [16,17]. These models have shown that defect cluster patterning ("self-organization") is expected when vacancy clusters are the dominant point defect sink [16,17]. In addition, the presence of specific orientation relationships between the defect cluster pattern and the host lattice was concluded to be due to anisotropic elastic strain fields around the defect clusters [16]. However, there has not yet been an attempt to systematically examine the effect of irradiation spectrum or material on defect cluster pattern formation.

The present study focuses on a comparison of the dose-dependent defect cluster density in neutron irradiated Cu and Ni (and their propensity to form aligned defect cluster patterns). Due to their similar mass and FCC crystal structure, Ni and Cu are attractive for studying fundamental aspects of irradiation, such as defect clustering processes associated with displacement cascades. Low energy ion irradiations [18-24] have demonstrated that a significantly higher density of visible vacancy clusters are produced in Cu compared to Ni over a wide range of irradiation temperatures. On the other hand, the amount of ion beam mixing [25] and the total surviving defect fraction (clustered and isolated point defects) associated with ion and neutron irradiation [26-29] have been found to be lower in Cu compared to Ni following irradiation near 4 K. These seemingly contradictory results have been interpreted as evidence for the presence of thermal spikes in displacement cascades . According to the thermal spike model, the lower melting point and weaker electron-phonon coupling in Cu compared to Ni both act to increase the duration and affected volume of the liquid-like region associated with a displacement cascade [3, 21-25]. The relatively large volume and slow cooling rate for the thermal spike in Cu promotes point defect recombination and leads to more pronounced clustering of the surviving defects. One criticism of the low energy ion irradiation studies is that the cascades are produced close to the specimen surface, and therefore the surface may be exerting some influence over the visible cluster formation. In addition, it is possible that the implanted ions in these low-energy irradiations may influence the details of the cluster formation process. One of the objectives of the present study was to examine the defect cluster formation process in neutron-irradiated specimens to determine if the trends observed in the ion irradiation studies are also observed under bulk irradiation conditions.

Further support for the thermal spike model was obtained in some limited MD studies that compared the response of Cu and Ni to low energy (<5 keV) PKA irradiations [3-5]. The calculated fraction of defects that survived the cascade quench was lower in copper, and the relative proportion of defects contained in clusters for a given PKA energy was higher in copper compared to nickel, in agreement with the ion beam mixing, surviving defect fraction, and vacancy loop production exper-imental measurements. Similar results were also obtained with a heat equation model that used an initial displacement cascade energy distribution obtained from binary collision calculations [30,31].

2. Experimental Procedure

The materials used in this investigation were 99.99% (VP grade) nickel obtained from Materials Research Corporation and oxygen free high-conductivity copper. The major impurities in the nickel were 37 ppm C, 18 ppm O, 25 ppm Fe, 25 ppm Si, 10 ppm Cu and 10 ppm Mn. Transmission electron microscope (TEM) disks with a diameter of 3 mm were punched from nickel and copper sheets of thickness 200 μm and 100 μm, respectively. The TEM disks were recrystallized by vacuum annealing at 750°C and 550°C for 2 h for the nickel and copper disks, respectively.

Two different fission reactors were used for the irradiations. The High Flux Isotope Reactor (HFIR) irradiations were performed in the HT-3 hydraulic rabbit tube facility with a fast neutron flux of 7.8×10^{18} n/m^2-s (E>0.1 MeV) and a thermal neutron flux of 2.2×10^{18} n/m^2-s, which produced a calculated [32] damage rate of 7.2×10^{-7} dpa/s in copper, assuming a threshold displacement energy of 30 eV. Specimens were irradiated at a temperature of 230°C in separate capsules for time periods of 4.6, 46 and 115 hours. Further details of the HFIR irradiations are given elsewhere [15]. The DR-3 irradiations were performed at a temperature of 50°C at approximately an order of magnitude lower damage rate (5×10^{-8} dpa/s) compared to the HFIR irradiations. The HFIR and DR-3 irradiation conditions are summarized in Table 1. The displacement damage levels ranged from 0.01 to 0.25 dpa.

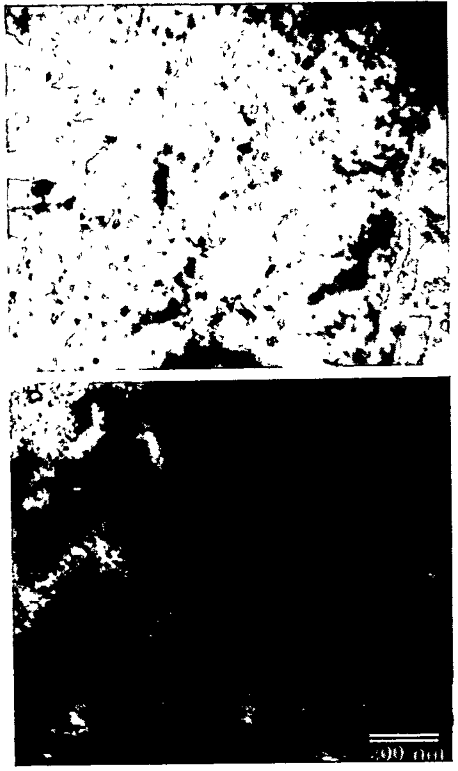

ORNL Photo 3885-94

Fig. 1. Comparison of the general microstructure of copper following neutron irradiation at 230°C to a damage level of 0.012 dpa (top) and 0.12 dpa (bottom). The beam direction is near <110> in both micrographs.

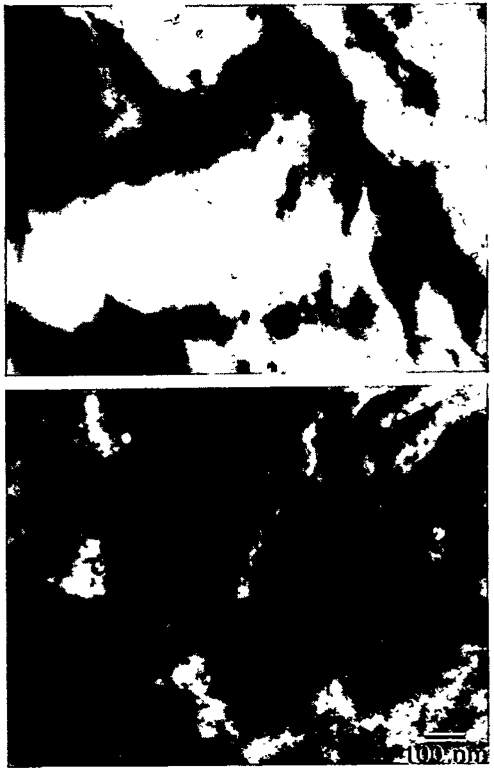

ORNL Photo 3887-94

Fig. 2. Cavity formation observed in copper following neutron irradiation at 230°C to a damage level of 0.012 dpa (top) and 0.12 dpa (bottom).

Table 1. Summary of Neutron Irradiation Conditions

Material	Reactor	Temperature (°C)	Damage Levels (dpa)
Cu	HFIR	230	0.01, 0.1
Cu	DR-3	50	0.01, 0.1, 0.2
Ni	HFIR	230	0.1, 0.25

The TEM disks were jet-electropolished following irradiation, and examined in JEOL 2000FX electron microscopes located at Risø and Oak Ridge National Laboratories. A combination of con-ventional bright field and weak beam dark field (WBDF) techniques were used to examine the defect microstructure. The general microstructural features, including void formation, network dislocation density and the presence or absence of defect cluster patterning, was performed in regions with a typical thickness of 100 to 150 nm. The density and size of the small "black spot" defect clusters was obtained from WBDF (g,4g or g,5g diffraction conditions) micrographs taken in regions with a typical foil thickness of <40 nm. The foil thickness was determined from the number of weak beam fringes.

3. Results

The unirradiated microstructure of both the copper and nickel specimens was typical of annealed single-phase metals, with a grain size of ~100 μm and a dislocation density of ~$10^{12}/m^2$. Irradiation introduced fine defect structures. Figure 1 shows the general microstructure of the two copper specimens irradiated in HFIR to damage levels of 0.01 and 0.1 dpa. A heterogeneous network dislocation density of ~$6x10^{12}/m^2$ was present in both specimens. There was no evidence of aligned defect clusters or defect cluster wall formation in either of the irradiated copper specimens. A low density (<$1x10^{20}/m^3$) of dislocation loops with diameters >5 nm is also visible at both doses in Fig. 1. A similar low network dislocation density was also observed in the copper specimens irradiated in DR-3 at 50°C.

The major radiation-induced microstructural feature of the copper specimens irradiated in DR-3 at 50°C was a high density of small defect clusters. The network dislocation density was ~10^{12}/m^2 at all three doses of 0.01, 0.1, and 0.2 dpa. The measured density of small defect clusters was 5.3x10^{23}/m^3 after 0.01 dpa, 6.7x10^{23}/m^3 after 0.1 dpa, and 6.6x10^{23}/m^3 after 0.2 dpa. Greater than 60% of the defect clusters were resolvable as SFTs at both doses. The mean defect cluster size was ~2.5 nm. There was no evidence for defect cluster alignment at any dose in the DR-3 specimens.

A moderate density of small voids was observed in both of the copper specimens irradiated in HFIR at 230°C. Figure 2 compares the void microstructures in copper irradiated at 230°C to 0.01 and 0.1 dpa. The void distribution appeared to coarsen with increasing dose. The measured void density decreased from 3x10^{20}/m^3 at 0.01 dpa to 1x10^{20}/m^3 at 0.1 dpa, and the corresponding average void diameter increased from 10 nm to 27 nm. The volumetric swelling calculated from the void measurements was ~0.01% at 0.01 dpa and ~0.1% at 0.1 dpa. The measured void densities at 0.01 and 0.1 dpa are similar to densities previously reported for copper irradiated with neutrons near 250°C at higher doses of 0.1 to 1 dpa [44], indicating that void nucleation in copper is completed at temperatures of 230 to 250°C after damage levels of ~0.01 dpa.

Figure 3 shows an example of the high density of small defect clusters observed in copper following HFIR irradiation at 230°C to 0.01 and 0.1 dpa. The measured defect cluster density was ~1.6x10^{23}/m^3 at both irradiation doses, which suggests that the cluster density had reached a saturation level already at 0.01 dpa. The fraction of the total defect cluster density identified as stacking fault tetrahedra was between 90 and 95% for both irradiation doses. The mean defect cluster size (predominantly SFTs) was about 2.5 nm at both damage levels, in agreement with previous studies on neutron-irradiated copper [35,53-56].

A high density of small defect clusters was observed in nickel following irradiation. The measured defect cluster density was 1.9x10^{23}/m^3 after 0.1 dpa, and 2.0x10^{23}/m^3 after 0.25 dpa. Typical microstructures for the two damage levels are shown in Fig. 4. About 33% of the defect clusters were resolvable as SFTs in the 0.1 dpa specimen, and this fraction decreased to about 28% in the 0.25 dpa specimen. In addition, the fraction of defect clusters that were resolvable as dislocation loops on {111} habit planes increased slightly from 50% to 60% as the dose increased from 0.1 to 0.25 dpa. The remaining 12 to 17% of the defect clusters at the two damage levels could not be unambiguously identified due to their small size. The average size of the visible SFTs was about 2 nm at both doses, whereas the average diameter of the resolvable {111} loops increased from 5.4 nm to 6.6 nm as the dose increased from 0.1 to 0.25 dpa. This caused the total defect cluster mean size to increase from 3.5 to 4.3 nm with increasing dose. Previous studies have reported similar average SFT sizes of ~2 nm in nickel irradiated with neutrons at a comparable temperature of 200°C [57]. Average interstitial loop sizes as large as ~60 nm have been reported for Ni irradiated with neutrons at 200°C to a dose of ~0.01 dpa at a low damage rate [58].

In contrast to the pure copper results, the dislocation density in nickel increased considerably after neutron irradiation. The measured network dislocation density in Ni varied from ~1x10^{14}/m^2 for the 0.1 dpa specimen to ~5x10^{13}/m^2 for the 0.25 dpa specimen. Figure 5 shows the general microstructure of nickel following irradiation to a damage level of 0.1 dpa. There was some alignment of the small defect clusters into a {100} planar wall configuration in the 0.1 dpa specimen. The defect cluster alignment became more pronounced after irradiation to a damage level of 0.25 dpa, as indicated in Fig. 6. The average spacing between the {100} walls of defect clusters was about 45 nm. The network dislocations did not show any tendency toward alignment at either irradiation dose. Cavity formation was not observed in either of the irradiated nickel specimens.

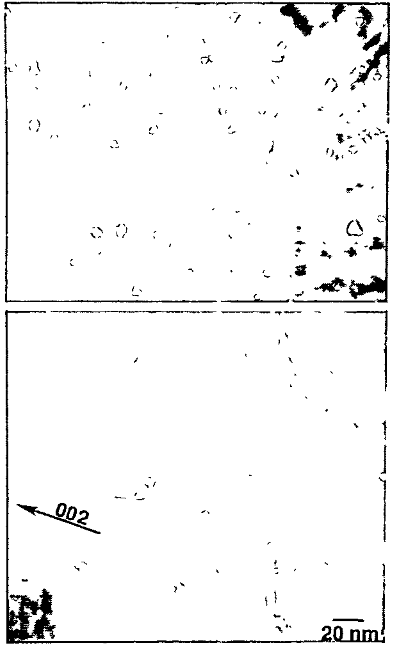

Fig. 3. Weak beam (g,4g) g=002 micrograph of small defect clusters produced in copper during irradiation at 230°C to a damage level of 0.012 dpa (top) and 0.12 dpa (bottom). The beam direction is near <110> in both micro-graphs, and the direction of the diffraction vector is indicated on the bottom micrograph.

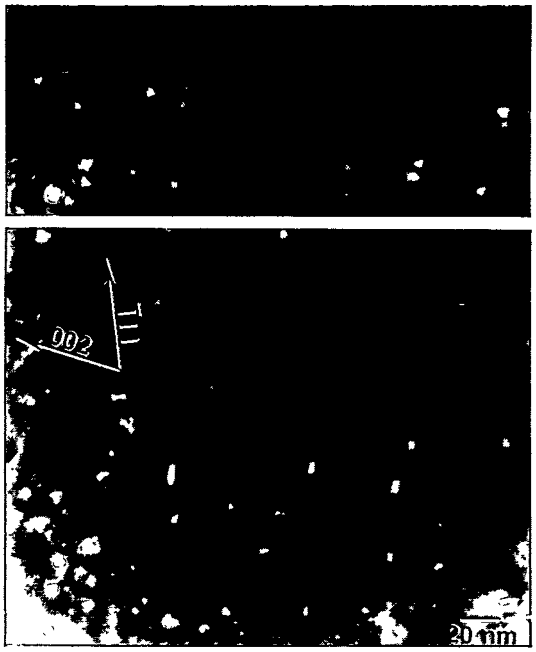

Fig. 4. Weak beam (g,4g) g=002 micrograph of small defect clusters produced in nickel during irradiation at 230°C to a damage level of 0.1 dpa (top) and 0.25 dpa (bottom). The beam direction is near <110> in both micrographs.

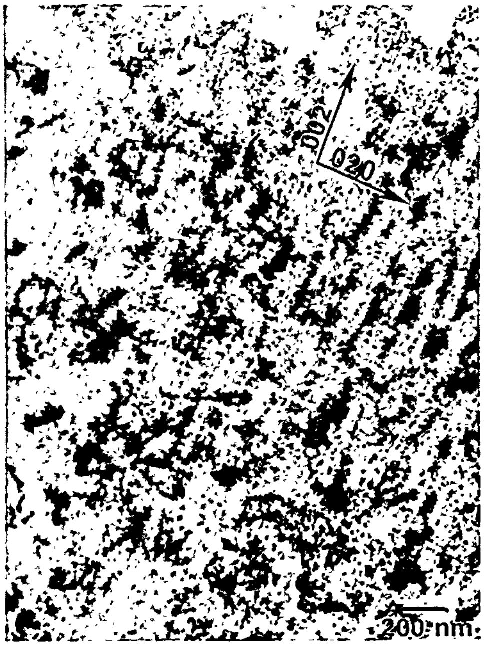

Fig. 5. Dislocations and defect clusters in nickel following neutron irradiation at 230°C to a damage level of 0.1 dpa. The beam direction is near <100>.

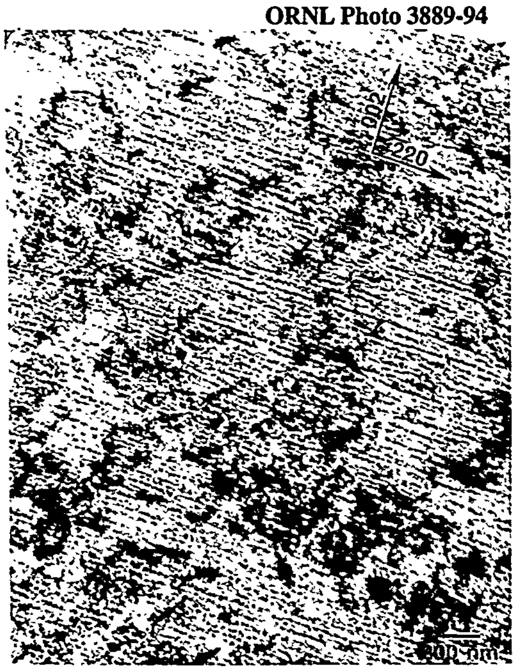

Fig. 6. Network dislocations and aligned defect clusters in nickel following irradiation to a damage level of 0.25 dpa. The beam direction is near <110>.

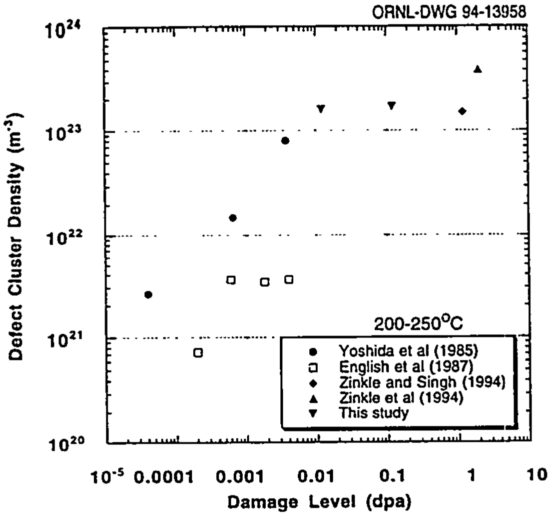

Fig. 7. Dose-dependent defect cluster formation in copper following irradiation at 200 to 250°C [33,59-61].

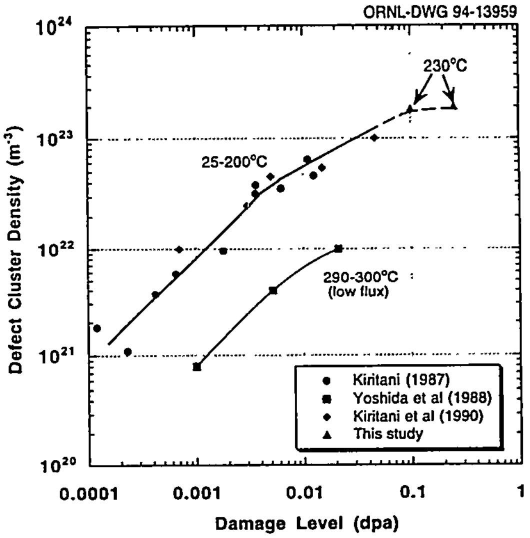

Fig. 8. Dose-dependent defect cluster formation in nickel following neutron irradiation at 25 to 300°C [64-66].

4. Discussion

Figure 7 compares the defect cluster densities measured in copper in this study with previously reported data [33,59-61] in the same irradiation temperature range of 200 to 250°C. These results suggest that the defect cluster density approaches a saturation value of ~$2x10^{23}/m^3$ after an irradiation dose of only 0.01 dpa at ~230°C. High dose studies performed on copper at other temperatures have found that the defect cluster density approaches a saturation value near $1x10^{24}/m^3$ after irradiation to damage levels >0.1 dpa near room temperature, and this saturation defect cluster density decreases rapidly with increasing neutron irradiation temperature above ~150°C [33,44]. The decrease in the saturation defect cluster density in Cu at neutron irradiation temperatures above ~150°C (0.31 T_M) may be attributed to thermal evaporation of SFTs. The detailed quantitative behavior of the SFT density at elevated temperatures depends on the balance between their production in displacement cascades and their subsequent shrinkage. At very high damage rates typically encountered in ion irradiation experiments (~10^{-3} dpa/s), the vacancy cluster lifetime is controlled by interstitial annihilation events [62]. At damage rates typical for neutron irradiations (<10^{-6} dpa/s), the vacancy cluster lifetime is controlled by thermal evaporation. In both cases, however, the quantitative value of the defect cluster density at elevated temperatures depends on the damage rate [62].

One striking feature associated with copper is that the defect cluster size and geometry at temperatures up to ~200°C is remarkably insensitive to irradiation dose. Previous irradiation studies performed at damage rates near 10^{-8} to 10^{-7} dpa/s have found that the SFT fraction is 60 to 65% of the total defect cluster density in copper irradiated at ~200°C to damage levels between $5x10^{-5}$ dpa and 2 dpa [33,59-61]. The SFT fraction approaches 100% of the defect cluster density at higher irradiation temperatures [61,63]. In the present study, the measured SFT fraction was approximately 90% of the total defect cluster density following irradiation at 230°C at both 0.01 and 0.1 dpa. The average size of SFTs in Cu has been found to be 2 to 3 nm over a very wide range of damage levels (10^{-5} to 10 dpa) and temperatures (20 to 300°C) density in nickel irradiated at "low" temperatures (<0.3 T_M) is five to ten times lower than that in copper at all damage levels from 10^{-4} dpa to ~1 dpa (see Fig. 12). For example, the defect cluster density in Cu reaches an apparent saturation value of ~$1.0x10^{24}/m^3$ for damage levels >0.1 dpa at homologous neutron irradiation temperatures <0.31 T_M [44], whereas the measured defect cluster density in Ni irradiated at 0.29 T_M to damage levels of 0.1 and 0.25 dpa in the present study was only ~$2.0x10^{23}/m^3$ (Fig. 8).

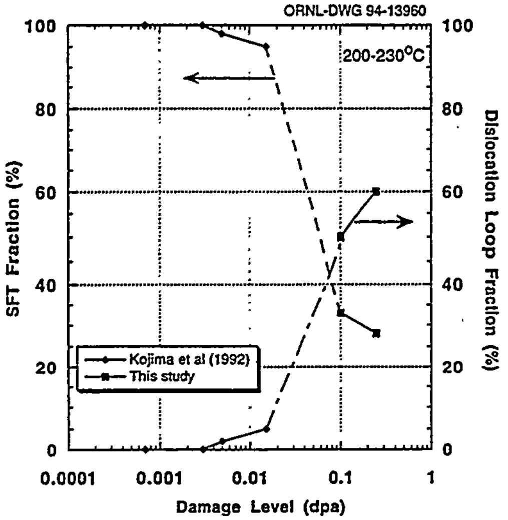

Fig. 9. Evolution of the defect cluster morphology in irradiated nickel at 200 to 230°C [58].

In contrast to the behavior of copper, the morphology of the defect clusters in nickel exhibits an apparent strong dependence on irradiation dose. Figure 9 shows the effect of irradiation dose on the dislocation loop and SFT fractions in nickel irradiated at 200 to 230°C [58]. Although only a limited amount of data are available, the results indicate that there is a gradual change from a SFT-dominant microstructure at low doses to an interstitial dislocation loop-dominant microstructure at high doses. The microstructural evolution following heavy ion, 600 to 750 MeV proton, or fission or fusion neutron irradiation [33,34,35,53-56,59-61]. The insensitivity of SFT size in Cu to irradiation temperature and dose may be attributed to their direct formation in energetic displacement cascades, as opposed to a classical monovacancy nucleation and growth process.

Figure 8 summarizes the dose dependence of the defect cluster density in nickel following irradiation at temperatures between room temperature and 300°C [64-66]. The data indicate that the defect cluster density accumulation is independent of irradiation temperature up to at least 200°C (0.27 T_M). Furthermore, the data suggest that the defect cluster density in nickel reaches an apparent saturation value of ~$2x10^{23}/m^3$ after irradiation to doses above 0.1 dpa at low temperatures (<0.30 T_M). A significantly lower defect cluster accumulation rate occurred during low flux (~10^{-8} dpa/s) irradiation at temperatures near 300°C (0.33 T_M). The defect cluster densities measured in the two specimens irradiated to 0.1 and 0.25 dpa at 230°C in the present study are the highest defect cluster densities reported to date for neutron irradiated nickel. Since the irradiation temperature of 230°C (0.29 T_M) is close to the temperature where SFTs would be expected to be thermally unstable in nickel, it is uncertain if a defect cluster density somewhat higher than $2x10^{23}/m^3$ would be produced by high dose irradiation at lower temperatures. It is interesting to note that the visible defect cluster appears to be most pronounced at damage levels between 0.01 and 0.1 dpa. Further study is needed to confirm this apparent pronounced evolution from an SFT-dominant microstructure to a dislocation loop-dominant microstructure.

When the present results are considered along with previously reported data on irradiated copper and nickel, several material-dependent differences are evident. First, the total defect cluster density observed in copper at homologous temperatures below 0.3 T_M is a factor of five to ten higher than that observed in irradiated nickel (Fig. 12). Second, the density of dislocation loops and network dislocations in copper is very low at all irradiation conditions [33,35,61,63]. The loop and network dislocation density in copper is at least an order of magnitude lower than that observed in nickel at comparable irradiation conditions for doses >0.1 dpa. The low density of loops and network dislocations in copper appears to be related to difficulties in interstitial loop nucleation. This is reflected in the insensitivity of the copper SFT and loop fractions to the displacement damage level. It is possible that the high sink density in copper associated with the SFTs produced in displacement cascades may inhibit interstitial loop nucleation and growth at temperatures up to ~0.3 T_M. However, studies perfomed on copper irradiated at higher temperatures have shown that the interstitial loop density is also very low at 0.3 to 0.5 T_M (where the sink density associated with SFTs is low) [35,61,63].

It is interesting to note that a well-developed network dislocation density is not needed to achieve high void swelling rates (>0.5%/dpa) in copper. According to standard rate theory models, the highest void swelling rates in metals such as copper and nickel would be expected to occur in the presence of moderate dislocation densities of ~$10^{14}/m^2$ [67]. These moderate dislocation densities produce a point defect sink density that is comparable to the sink density at voids, and the preferential absorption of interstitials at

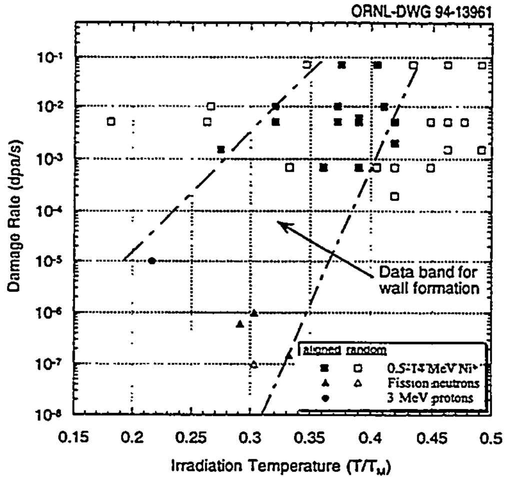

Fig. 10. Data compilation showing the temperature and dose rates where {001} defect cluster wall formation has been observed in irradiated nickel. The data include Ni^+ ion [6,7,10-12], fission neutron [8,9,15, this study], and proton [13,14] irradiations. The filled symbols denote conditions where defect cluster wall formation was observed.

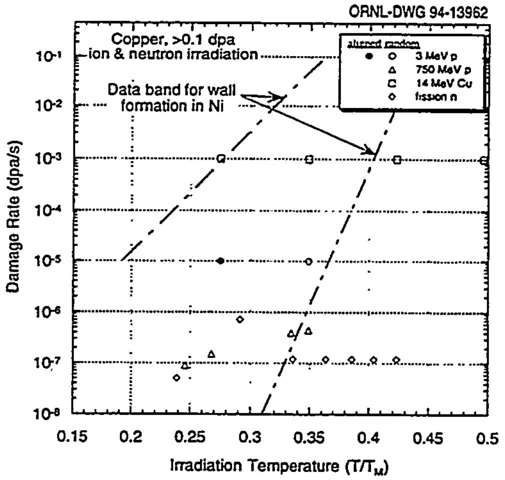

Fig. 11. Microstructural observations of the absence (open symbols) or presence (filled symbol) of aligned defect cluster walls in irradiated copper. The dashed lines outline the data band for observations of wall formation in irradiated nickel (Fig. 5). The Cu data include 3-MeV protons [13,14], 750-MeV protons [33], Cu^+ ions [34] and fission neutrons [15, 35,this study].

dislocations (dislocation bias) provides a vacancy supersaturation that is sufficient to sustain high levels of void swelling. Significant amounts of void swelling (~0.5%/dpa) have been observed in copper irradiated at 220 to 400°C despite network dislocation densities $<10^{13}/m^2$ [35,61,68,69]. On the other hand, nickel apparently exhibits a very low steady-state swelling rate (~0.1%/dpa) in the presence of a network dislocation density of $\sim 2x10^{13}/m^2$ after an initial high-swelling transient [70]. The high amount of swelling in the presence of a low dislocation density in neutron-irradiated copper can be reconciled by invoking the recently developed "production bias" model [71,72]. This model recognizes that a sufficiently high vacancy supersaturation to support significant void swelling can be achieved even in metals with low dislocation densities, due to the preferential loss of small interstitial clusters that are formed in displacement cascades by one-dimensional glide to dislocations and permanent sinks such as grain boundaries.

4. 1 Defect cluster wall formation

The formation of periodic walls of defect clusters in irradiated metals has been reviewed elsewhere [16], and is part of a more general self organization process that occurs under certain irradiation conditions [17]. In the present study, defect cluster alignment into {001} planar walls began to occur in the neutron irradiated Ni specimens at an irradiation dose of 0.1 dpa, and was easily visible (but not completely developed) by 0.25 dpa. The observed 45 nm spacing between the {001} walls in the present study agrees well with previous results obtained in nickel following neutron and ion irradiation [16].

In order to make a better assessment of the similarities and differences between irradiated nickel and copper regarding their propensity to form aligned defect cluster walls during irradiation, we have compiled the pertinent studies into plots showing the temperature and dose rates where {001} defect cluster walls have been observed in irradiated nickel and copper. As shown in Fig. 10, defect cluster patterning occurs in nickel at homologous irradiation temperatures between 0.2 and 0.42 T_M (depending on the dose rate) [6-15]. These studies have found that wall formation in Ni becomes observable at damage levels >0.1 dpa, and is fully developed by 0.5 to 1 dpa [15,16]. One important feature is that the defect clusters contained in the {001} walls are vacancy in nature [16]. From a theoretical viewpoint, self-organization of defect clusters into aligned patterns is expected only when the vacancy clusters are the dominant sink for interstitials and vacancies [16,17]. Defect cluster alignment is generally not observed at high irradiation temperatures due to thermal dissolution of vacancy clusters (recovery Stage V) [16]. The physical mechanism responsible for the apparent lack of defect cluster patterning at low temperatures (Fig. 10) is not as clear. It has been proposed [16] that defect cluster ordering is suppressed at low temperatures and high damage rates because point defect matrix recombination becomes the dominant annihilation mechanism (as opposed to annihilation at defect clusters). However, according to the microstructural observations in the present study, the sink strength associated with defect clusters in neutron or ion irradiated nickel should be $>10^{15}/m^2$ at these low temperatures (since the defect clusters are produced directly in the displacement cascade, the cluster density is only weakly dependent on irradiation temperature [20,22]). It is difficult to imagine that annihilation could occur predominantly via point defect matrix recombination in the presence of such a high sink strength.

Figure 11 shows the corresponding dose rate-temperature plot for defect cluster patterning in irradiated copper [13-15,33-35]. The most striking feature in this plot is the lack of defect cluster wall formation in copper at irradiation conditions which caused significant {001} wall formation in nickel. Neglecting electron irradiation studies which will be discussed later, defect cluster wall formation has only been observed in copper irradiated with 3-MeV protons [13,14]. In some cases such as the present study, the accumulated dose (0.1 dpa) may have been too low to allow the full development of defect cluster patterning. However, some evidence of pattern formation should have been detectable, since evidence for wall formation was observable in Ni already at damage levels of 0.1 dpa (Fig. 5).

Several different studies have observed the presence of aligned defect clusters in copper [36-40] and nickel [40] following electron irradiation. Regular arrays of SFTs along <001> have been observed in copper during electron irradiation at temperatures between 170 and 350 K (0.12 to 0.26 T_M) and in nickel at temperatures between 380 and 540 K (0.22 to 0.31 T_M) [40]. In summary, it appears that defect cluster patterning occurs readily in nickel in irradiation spectra ranging from high PKA energies (Ni^+ ion and neutron) to low PKA energies (3 MeV protons and 1 MeV electrons). On the other hand, copper apparently only forms defect cluster patterns in irradiation spectra that produce low PKA energies.

One possible explanation for the contrasting behavior of copper and nickel regarding defect cluster patterning is associated with their contrasting displacement cascade (thermal spike) behavior. As mentioned in the introduction, experimental and MD studies have demonstrated that considerable differences exist in the defect production and in-cascade clustering for energetic cascades in Cu versus Ni. Table 2 summarizes experimental measurements on the surviving defect fraction and the fraction of visible vacancy clusters per cascade (defect cluster yield) in copper and nickel irradiated with ions or neutrons [18-24,26-29]. The surviving defect fraction (fraction of the modified Kinchin-Pease displacements) was determined from in-situ electrical resistivity measurements during fission or 14-MeV neutron irradiation at temperatures near 4 K [26-29]. Since defect migration in Cu or Ni is not possible at this low temperature, these measurements include all defects (clustered or isolated point defects) that remain following the cascade quench. The data summarized in Table 2 have in some cases been modified from the originally published values in order to consistently use the recommended [41] threshold displacement energies of 30 eV for Cu and 40 eV for Ni and Frenkel pair electrical resistivities [27] of 2.0 and 6.0 μΩ-m for Cu and Ni, respectively. The surviving defect fraction measurements indicate that the total number of defects remaining after the cascade quench is equal or slightly higher in nickel compared to copper. The defect cluster yield measurements summarized in Table 2 were obtained from in-situ TEM analysis of thin specimens that were irradiated at 30 K or room temperature with either 50 keV Kr^+ ions, 50 keV Ni^+ ions or 30 keV Cu^+ ions [18-20,22,24], and is a measure of the fraction of defects that survive the cascade quench in the form of vacancy clusters. The ion irradiation conditions selected for Table 2 produce displacement cascades that equal or exceed the threshold PKA energy for subcascade formation [42]. The absolute values for the defect yield measured by different workers have an uncertainty of about ±0.1 due to differences in the counting procedure [23], but the general trend for higher in-cascade production of vacancy clusters in copper compared to nickel at all temperatures is unmistakable.

Due to the close proximity of the surface to the displacement cascades created by the 30 to 50 keV ion irradiations, the defect yield measurements summarized in Table 2 only contain information on vacancy clusters [21,23, 43]. Some information about interstitial clustering can be obtained from TEM studies on neutron-irradiated bulk specimens [43], although it must be recognized that many of the interstitial clusters

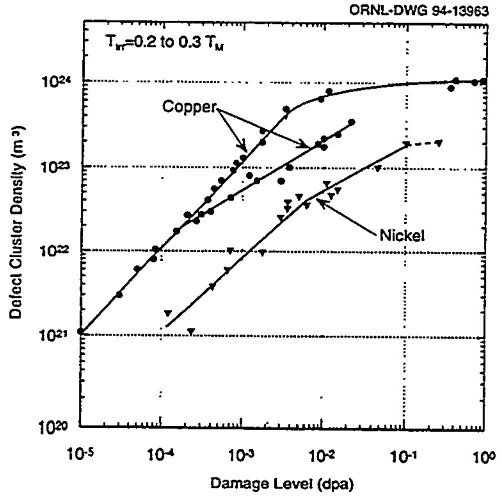

Fig. 12. Comparison of the dose-dependent defect cluster density in nickel and copper irradiated at low temperatures. Details about the original references are given elsewhere [15,44].

observed in these studies may have been formed by diffusion of interstitials following the cascade quench. Figure 12 compares the dose-dependent defect cluster density in copper and nickel irradiated at homologous temperatures between 0.2 and 0.3 T_M [15,44]. The rate of defect cluster accumulation is proportional to the damage level in both copper and nickel at low doses. However, the observed defect cluster density in nickel at a given dose is an order of magnitude smaller in nickel compared to copper. Both materials approach a saturation level in defect cluster density at doses >0.1dpa. The saturation defect cluster density is apparently a factor of five lower in nickel at low doses. However, However, the observed defect cluster density in nickel at a given dose is an order of magnitude smaller in nickel compared to copper. Both materials approach a saturation level in defect cluster density at doses >0.1 dpa.

The saturation defect cluster density is apparently a factor of 5 lower in nickel compared to copper ($2x10^{23}/m^3$ vs. $1x10^{24}/m^3$). The fraction of defects resolvable of SFTs (vacancy clusters) in Cu and Ni ranges between 50 and 90%, depending on dose. Therefore, the neutron irradiation measurements are consistent with the ion irradiation defect yield studies (Table 2) that vacancy cluster production is higher in copper compared to nickel.

Table 2. Comparison of the total [26-29] and visible (clustered) [18-20,22,24] defect fractions. The surviving defect fraction was obtained from electrical resistivity measurements on neutron irradiated specimens, and the defect cluster yield was obtained from in-situ TEM measurements on specimens irradiated with 30 to 50 keV self- or Kr^+-ions.

	Total Surviving Defect Fraction at 4 K (NRT dpa fraction)	Visible Defect Cluster Yield (Observed # of Clusters per Cascade)	
		30 K	300 K
Cu	0.32	0.20	0.44
Ni	0.34	0.10	0.22

A further difference between the microstructure of neutron irradiated copper and nickel is apparent at damage levels of ~0.1 dpa. The interstitial dislocation loop size and density in nickel irradiated at homologous temperatures between 0.2 and 0.3 T_M increase steadily with increasing dose, and the loop density exceeds the SFT density ($1x10^{23}/m^3$) at damage levels greater than about 0.1 dpa [15]. On the other hand, the resolvable (>5 nm diameter) interstitial loop density in copper irradiated in this temperature range remains below $1x10^{21}/m^3$ at least up to damage levels of ~1 dpa [33]. According to conventional chemical rate theory predictions, the homogeneous interstitial loop nucleation and growth rates should be similar in Cu and Ni because the interstitial atomic volumes are similar. This suggests that there may be some difference in the initial disposition of interstitials (clustered vs. isolated fraction) produced in displacement cascades in copper compared to nickel. A similar conclusion was reached by Watanabe et al. [45] during their evaluation of in-cascade defect cluster formation in 14-MeV neutron irradiated copper and nickel.

As mentioned in the introduction, molecular dynamics simulations indicate that significant differences exist between the cascade quench behavior of Cu and Ni [3-5]. The MD studies suggest that the duration and affected volume of the "thermal spike" is larger in copper compared to nickel, which results in increased clustering and a lower surviving defect fraction in Cu for a given PKA energy. According to the thermal spike model, the longer thermal spike lifetime in Cu is due to the lower T_M and less efficient electron-phonon coupling in Cu [3-5,46-49]. Another parameter of interest is the size distribution of defect clusters produced in displacement cascades in copper versus nickel. The size and duration of the thermal spike in copper should result in a larger average cluster size for both vacancies and interstitials. Recent MD studies suggest that small defect clusters containing up to 6 interstitials are highly glissile along <110> directions [1,50]. Therefore, it seems conceivable that the relative proportioning of interstitial clusters produced in displacement cascades between small, glissile and large, sessile clusters could have a strong influence on the microstructural evolution in metals.

One possible mechanism for the formation of aligned {001} defect cluster patterns in irradiated Cu and Ni is based on the propagation of glissile interstitial clusters along <110> directions. A similar mechanism (based on dynamic crowdion migration) was proposed by Seeger and coworkers [40] to explain the presence of SFT ordered arrays in electron-irradiated FCC metals. However, it seems unlikely that dynamic crowdions could account for the wall formation observed for example in Ni at temperatures between 0.2 and 0.4 T_M since crowdions would not be thermally stable in this temperature regime. From geometric considerations, preferential one-dimensional migration of small interstitial clusters along <110> directions would lead to the formation of {001} walls of vacancy clusters [40]. This potential mechanism for defect cluster patterning suggests that the resistance of copper to form defect cluster walls under energetic displacement cascade conditions could be due to the formation of oversized (sessile) interstitial clusters during the thermal spike. On the other hand, the relatively less efficient interstitial clustering process in nickel during the thermal spike could preferentially produce a larger fraction of small (glissile) interstitial clusters in the displacement cascade. The decreased efficiency of defect clustering in copper irradiated at lower average PKA energies (e.g., 3-MeV protons) could result in a higher fraction of small glissile interstitial clusters, thereby promoting wall formation. Finally, homogeneous nucleation of small interstitial clusters under the high damage rate conditions associated with electron irradiation could also produce a sufficient density of glissile interstitial clusters to induce wall formation.

The low temperature limit in Cu for defect cluster pattern formation during electron irradiation of 0.12 T_M [40] is consistent with the onset of recovery Stage II [51]. Recovery Stage II has generally been attributed to rearrangement of interstitial clusters that either nucleated homogeneously or else directly in the displacement cascade [51]. Diffuse X-ray scattering measurements performed on irradiated FCC metals [51,52] indicate that small interstitial clusters become mobile and coarsen during recovery Stage II.

An alternative explanation for the lack of defect cluster patterning in copper under energetic displacement cascade conditions is associated with the high density of defect clusters produced directly in the displacement cascade. The relatively low fraction of mobile defects (point defects and small defect clusters) and the high sink strength of sessile clusters produced directly in energetic displacement cascades in copper could effectively inhibit the formation of defect cluster patterns. On the other hand, the relatively high fraction of mobile defects and low fraction of sessile defect clusters produced in energetic displacement cascades in nickel could produce conditions favorable for defect cluster patterning. The present study has demonstrated that patterning does not occur in neutron irradiated copper at 50°C at low doses of ~0.01 dpa (where defect cluster density is only $\sim 1\times10^{21}/m^3$). This suggests that the relative partitioning between mobile and sessile clusters may be a key parameter for wall formation. The in-cascade production of interstitial defect clusters in Cu should shift from predominantly sessile to predominantly glissile clusters with decreasing PKA energy, which may allow the patterns to form during proton irradiation. One useful test of this hypothesis would be to perform a sequential irradiation of copper involving energetic displacement cascade damage (e.g. neutron irradiation) to introduce a high defect cluster sink density, followed by low-PKA irradiation (e.g., 3-MeV protons).

5. Summary and Conclusions

Despite their similarities in mass, copper and nickel exhibit significantly different responses to energetic particle irradiation. In agreement with previous molecular dynamics and ion irradiation studies, the present study indicates that the magnitude of in-cascade point defect clustering at a given homologous irradiation temperature is lower in neutron irradiated nickel compared to copper. The apparent maximum visible defect cluster densities in neutron irradiated copper and nickel are $1x10^{24}/m^3$ and $2x10^{23}/m^3$, respectively. The high cluster density in copper is due to a high density of SFTs and unidentified small defect clusters (presumably interstitial dislocation loops) produced directly in the displacement cascade. The nucleation and growth of visible interstitial dislocation loops is also much more pronounced in nickel compared to copper. The density of easily resolvable (>5 nm diameter) dislocation loops is two orders of magnitude lower in copper compared to nickel ($1x10^{23}/m^3$ vs. $1x10^{21}/m^3$) at damage levels above 0.1 dpa. These dramatic differences in the nature and total density of defect clusters in copper compared to nickel can be rationalized on the basis of a more rapid quenching of the thermal spike phase for energetic displacement cascades in nickel.

The formation of {001} planar arrays of defect clusters at damage levels above 0.1 dpa is a typical feature in Ni irradiated with a wide variety of particles at homologous temperatures between 0.2 and 0.4 T_M, but only occurs in copper for irradiation spectra that produce low-energy PKAs. The sensitivity of Cu to irradiation spectrum is attributed to changes in the fraction of glissile interstitial clusters created at different PKA energies, although the overall lower defect cluster density in Ni may also be playing a role.

The present study provides additional support that significant void swelling (>0.5%/dpa) can occur in copper without the presence of a well-developed dislocation network, in agreement with the production bias void swelling model. Literature data suggest that the steady-state swelling rate in neutron-irradiated Ni is very low (~0.1%/dpa) compared to Cu, despite the presence of a higher network dislocation density that is theoretically more favorable for dislocation bias-driven void swelling.

Acknowledgements

The pure annealed nickel specimens used in this study were supplied by K. Farrell. The irradiated specimens were thinned by L.T. Gibson, W.S. Eatherly and J. Lindbo. This work was supported in part by Risø National Laboratory and by the Office of Fusion Energy, US Department of Energy, under contract DE-AC05-84OR21400 with Martin Marietta Energy Systems, Inc. and contract DE-AC06-76RLO1830 with Battelle Memorial Institute.

References

[1] S.J. Zinkle and B.N. Singh, J. Nucl. Mater. 199 (1993) 173.
[2] W.J. Phythian, R.E. Stoller, A.J.E. Foreman, A.F. Calder and D.J. Bacon, submitted to J. Nucl. Mater.
[3] T. Diaz de la Rubia, R.S. Averback, H. Hsieh and R. Benedek, J. Mater. Res. 4 (1989) 579.
[4] T. Diaz de la Rubia, R.S. Averback, R. Benedek and I.M. Robertson, Rad. Eff. Def. Solids 113 (1990) 39.
[5] M.W. Finnis, P. Agnew and A.J.E. Foreman, Phys. Rev. B 44 (1991) 567.
[6] G.L. Kulcinski and J.L. Brimhall, in Effects of Radiation on Substructure and Mechanical Properties in Metals and Alloys, ASTM STP 529, J. Moteff, ed. (Amer. Soc. for Testing and Materials, Philadelphia, 1973) p. 258
[7] J.L. Brimhall, Battelle Pacific Northwest Laboratory report BNWL-1839 (1974).
[8] J.O. Stiegler and K. Farrell, Scripta Met. 8 (1974) 651.
[9] A. Silvent and C. Regnard, 16eme Colloque de Metallurgie INSTN Paris, CEA-CONF-2437 (1974) p. 209.
[10] J.E. Westmoreland, J.A. Sprague, F.A. Smidt and P.R. Malmberg, Rad. Eff. 26 (1975) 1
[11] P. Regnier and L.D. Glowinski, J. Nucl. Mater. 57 (1975) 243.
[12] J.B. Whitley, Ph.D. Thesis, University of Wisconsin-Madison (1978)
[13] W. Jäger, P. Ehrhart, W. Schilling, F. Dworschak, A.A. Gadalla and N. Tsukuda, Mater. Sci. Forum 15-18 (1987) 881.
[14] W. Jäger, P. Ehrhart and W. Schilling, Sol. State Phenom. 3&4 (1988) 279.
[15] S.J. Zinkle and L.L. Snead, in Proc. 17th Int. Conf. on Effects of Radiation on Materials, J. Nucl. Mater., in press.
[16] W. Jäger and H. Trinkaus, J. Nucl. Mater. 205 (1993) 394.
[17] C. Abromeit, Intern. J. Mod. Phys. B 3 (1989) 1301.

[18] A.Y. Stathopoulos, Philos. Mag. A 44 (1981) 285.; also A.Y. Stathopoulos , C.A. English, B.L. Eyre and P.B. Hirsch, ibid. 309.
[19] M.A. Kirk, I.M. Robertson, M.L. Jenkins, C.A. English, T.J. Black and J.S. Vetrano, J. Nucl. Mater. 149 (1987) 21.
[20] J.S. Vetrano, I.M. Robertson and M.A. Kirk, Scripta Met. 24 (1990) 157.
[21] C.A. English, Rad. Eff. Def. Solids 113 (1990) 15.
[22] I.M. Robertson, J.S. Vetrano, M.A. Kirk and M.L. Jenkins, Philos. Mag. A 63 (1991) 299.
[23] M.L. Jenkins, M.A. Kirk and W.J. Phythian, J. Nucl. Mater. 205 (1993) 16.
[24] I.M. Robertson, D.K. Tappin and M.A. Kirk, Philos. Mag. A 68 (1993) 843.
[25] S-J Kim, M-A Nicolet, R.S. Averback and D. Peak, Phys. Rev. B 37 (1988) 38.
[26] P. Jung, Phys. Rev. B 23 (1981) 664.
[27] C.E. Klabunde and R.R. Coltman, Jr., J. Nucl. Mater. 108&109 (1982) 183.
[28] M.W. Guinan, J.H. Kinney and R.A. Van Konynenburg, J. Nucl. Mater. 133&134 (1985) 357.
[29] G. Wallner, M.S. Anand, L.R. Greenwood, M.A. Kirk, W. Mansel and W. Waschkowski, J. Nucl. Mater. 152 (1988) 146.
[30] M. Caro, A. Ardelea and A. Caro, J. Mater. Res. 5 (1990) 2652.
[31] M. Alurralde, A. Caro and M. Victoria, J. Nucl. Mater. 183 (1991) 33.
[32] L.R. Greenwood, Damage Analysis and Fundamental Studies quarterly progress report DOE/ER-0046/24 (Feb. 1986) p. 5 (the Cu dpa calculations in this report assumed a nonstandard threshold displacement energy of 40 eV).
[33] S.J. Zinkle, A. Horsewell, B.N. Singh and W.F. Sommer, J. Nucl. Mater., 212-215 (1994) 132.
[34] S.J. Zinkle, G.L. Kulcinski and R.W. Knoll, J. Nucl. Mater. 138 (1986) 46.
[35] S.J. Zinkle and K. Farrell, J. Nucl. Mater. 168 (1989) 262.
[36] N. Yoshida and M. Kiritani, J. Phys. Soc. Jap. 38 (1975) 1220.
[37] W. Jäger and K. Urban, in Proc. 4th Int. Conf. on High Voltage Electron Microscopy, B. Jouffrey and P. Favard, eds. (SFME, Paris, 1976) p. 175.
[38] H. Fujita, T. Sakata and H. Fukuyo, Jap. J. Appl. Phys. 21 (1982) L235.
[39] N.Y. Yin, F. Phillipp and A. Seeger, Phys. Stat. Sol. (a) 116 (1989) 91.
[40] A. Seeger, N.Y. Jin, F. Phillipp and M. Zaiser, Ultramicroscopy 39 (1991) 342.
[41] ASTM Standard Practice for Neutron Radiation Damage Simulation by Charged-Particle Irradiation, E521-89, Annual Book of ASTM Standards, Vol. 12.02 (ASTM, Philadelphia).
[42] H.L. Heinisch and B.N. Singh, Philos. Mag. A 67 (1993) 407.
[43] H. Fukushima, Y. Shimomura and H. Yoshida, J. Nucl. Mater. 179-181 (1991) 939.
[44] B.N. Singh and S.J. Zinkle, J. Nucl. Mater. 206 (1993) 212.
[45] N. Watanabe, R. Nishiguchi and Y. Shimomura, J. Nucl. Mater. 179-181 (1991) 905.
[46] C.P. Flynn and R.S. Averback, Phys. Rev. B 38 (1988) 7118.
[47] A. Caro and M. Victoria, Phys Rev. A 40 (1989) 2287.
[48] S. Prönnecke, A. Caro, M. Victoria, T. Diaz de la Rubia and M.W. Guinan, J. Mater. Res. 6 (1991) 483.
[49] I. Koponen, Phys. Rev. B 47 (1993) 14011.
[50] A.J.E. Foreman, C.A. English and W.J. Phythian, Philos. Mag. A 66 (1992) 655.
[51] W. Schilling and K. Sonnenberg, J. Phys. F: Metal Phys. 3 (1973) 322.
[52] R. Rauch, J. Peisl, A. Schmalzbauer and G. Wallner, J. Phys. Condens. Matter 2 (1990) 9009.
[53] S.J. Zinkle, J. Nucl. Mater. 150 (1987) 140.
[[54] A. Horsewell, B.N. Singh, S. Prönnecke, W.F. Sommer and H.L. Heinisch, J. Nucl. Mater. 179-181 (1991) 924.
[55] T. Muroga, H.L. Heinisch, W.F. Sommer and P.D. Ferguson, J. Nucl. Mater. 191-194 (1992) 1150.
[56] Y. Satoh, I. Ishida, T. Yoshiie and M. Kiritani, J. Nucl. Mater. 179-181 (1988) 443.
[57] S. Kojima, T. Yoshiie and M. Kiritani, J. Nucl. Mater. 179-181 (1988) 1249.
[58] S. Kojima, T. Yoshiie, K. Hamada, K. Satori and M. Kiritani, J. Nucl. Mater. 191-194 (1992) 1155.
[59] N. Yoshida, Y. Akashi, K. Kitajima and M. Kiritani, J. Nucl. Mater. 133-134 (1985) 405.
[60] C.A. English, B.L. Eyre and J.W. Muncie, Philos. Mag. A 56 (1987) 453.
[61] S.J. Zinkle and B.N. Singh, manuscript in preparation
[62] S. Ishino, J. Nucl. Mater. 206 (1993) 139.
[63] S.J. Zinkle, K. Farrell and H. Kanazawa, J. Nucl. Mater. 179-181 (1991) 994.
[64] M. Kiritani, Mater. Sci. Forum, 15-18 (1987) 1023.

[65] N. Yoshida, T. Muroga, H. Watanabe, K. Araki and U. Miyamoto, J. Nucl. Mater. 155-157 (1988) 1222.
[66] M. Kiritani, T. Yoshiie, S. Kojima, Y. Satoh and K. Hamada, J. Nucl. Mater. 174 (1990) 327.
[67] F.A. Garner and W.G. Wolfer, J. Nucl. Mater. 122&123 (1984) 201.
[68] H.R. Brager, J. Nucl. Mater. 141-143 (1986) 79.
[69] F.A. Garner, M.L. Hamilton, T. Shikama, D.J. Edwards and J.W. Newkirk, J. Nucl. Mater. 191-194 (1992) 386.
[70] J.F. Stubbins and F.A. Garner, J. Nucl. Mater. 191-194 (1992) 1295; also J.F. Stubbins, in 17th ASTM Symposium on Effects of Radiation on Materials, D.S. Gelles et al., eds., in press
[71] B.N. Singh, C.H. Woo and A.J.E. Foreman, Mater. Sci. Forum 97-99 (1992) 75.
[72] H. Trinkaus, B.N. Singh and A.J.E. Foreman, J. Nucl. Mater. 206 (1993) 200.

6.0 DEVELOPMENT OF STRUCTURAL ALLOYS

6.1 Ferritic Martensitic and Bainitic Steels

EFFECT OF INTERNAL HYDROGEN ON THE MIXED-MODE I/III FRACTURE TOUGHNESS OF A FERRITIC/MARTENSITIC STAINLESS STEEL - H. Li (Associated Western Universities—Northwest Division), R. H. Jones (Pacific Northwest Laboratory[a]), J. P. Hirth (Washington State University) and D. S. Gelles (Pacific Northwest Laboratory[a]).

OBJECTIVE

To investigate the effect of hydrogen on mode I and mixed mode I/III fracture toughness at room temperature for a low activation ferritic/martensitic stainless steel (F82-H).

SUMMARY

The effects of H on the mixed-mode I/III critical *J*-integrals (J_{TQ}) and tearing moduli (*dJ/da*) were examined for a ferritic/martensitic stainless steel at ambient temperature. A H content of 4 ppm(wt) was attained after charging in a H_2 gas chamber (138 MPa) at 300°C for 2 weeks. Results showed that H decreased J_{TQ} and *dJ/da* values compared to steel tested without H. However, the presence of H did not change the dependence of J_{TQ} and *dJ/da* values on crack angle. Both J_{IQ} and dJ_I/da exhibited the highest relative values. The minimum values of both J_{TQ} and *dJ/da* occurred at a crack angle between 35 and 55° [$P_{iii}/(P_{iii}+P_i) = 0.4$ and 0.6]. A mechanism of the combined effect of H and mixed-mode on J_{TQ} and *dJ/da* is discussed.

INTRODUCTION

Traditionally, mode I fracture has been used to study elastic-plastic fracture mechanics. However, in recent years, mixed-mode fracture has become a focus of many studies, in particular for the mixed-mode I/III case [1-9]. In tough materials [such as a high-purity rotor steel (HPRS) [5,6], which fail primarily by a microvoid nucleation and growth mechanism], the presence of a mode III loading component lowers the J_{TQ} values considerably from their mode I values. The J_{TQ} values pass through a minimum at a position between mode I and mode III on a plot of J_{TQ} vs crack inclination angle. More generally, materials can be divided into three categories according to their process zone size as presented by J_{TQ}/σ_Y and the ratio of J_{TQ} (at crack angle of 45°) to J_{IQ}, as shown in Fig. 1 [10]. The materials in Region I are brittle and sensitive to mode I loading and, consequently, mode I fracture toughness is the lowest as compared with mixed-mode I/III fracture toughness. Therefore, for such materials, mode I fracture toughness is properly used for design. Those materials in Region II are tough and sensitive to mixed-mode I/III loading, mode I fracture toughness is no longer the largest, and the minimum mixed-mode J_{TQ} is recommended as a design criterion. For the materials in Region III, mode I and mixed-mode fracture toughness are similar and the mode I value can be used for design with small uncertainty. Our results [11,12] on the fracture toughness of a F-82H steel showed that the steel is a tough material which falls in Region II in Fig. 1. The presence of a mode III stress component lowers its fracture toughness significantly. However, the minimum upper shelf fracture toughness is still higher than the J_{IQ} values for most tough materials that have been tested.

Structural materials in fusion energy systems will be exposed to hydrogen (H) from the plasma and (n, σ) reactions. For a tough rotor steel, the introduction of H was found to decrease the overall mixed-mode I/III fracture toughness [6,13]. Hence, an investigation of the combined effects of mixed-mode loading and H on the fracture toughness of F-82H steel was undertaken to determine its suitability for fusion power reactor applications. The other purpose was to further study the mechanism by which H affects the mixed-mode I/III fracture toughness.

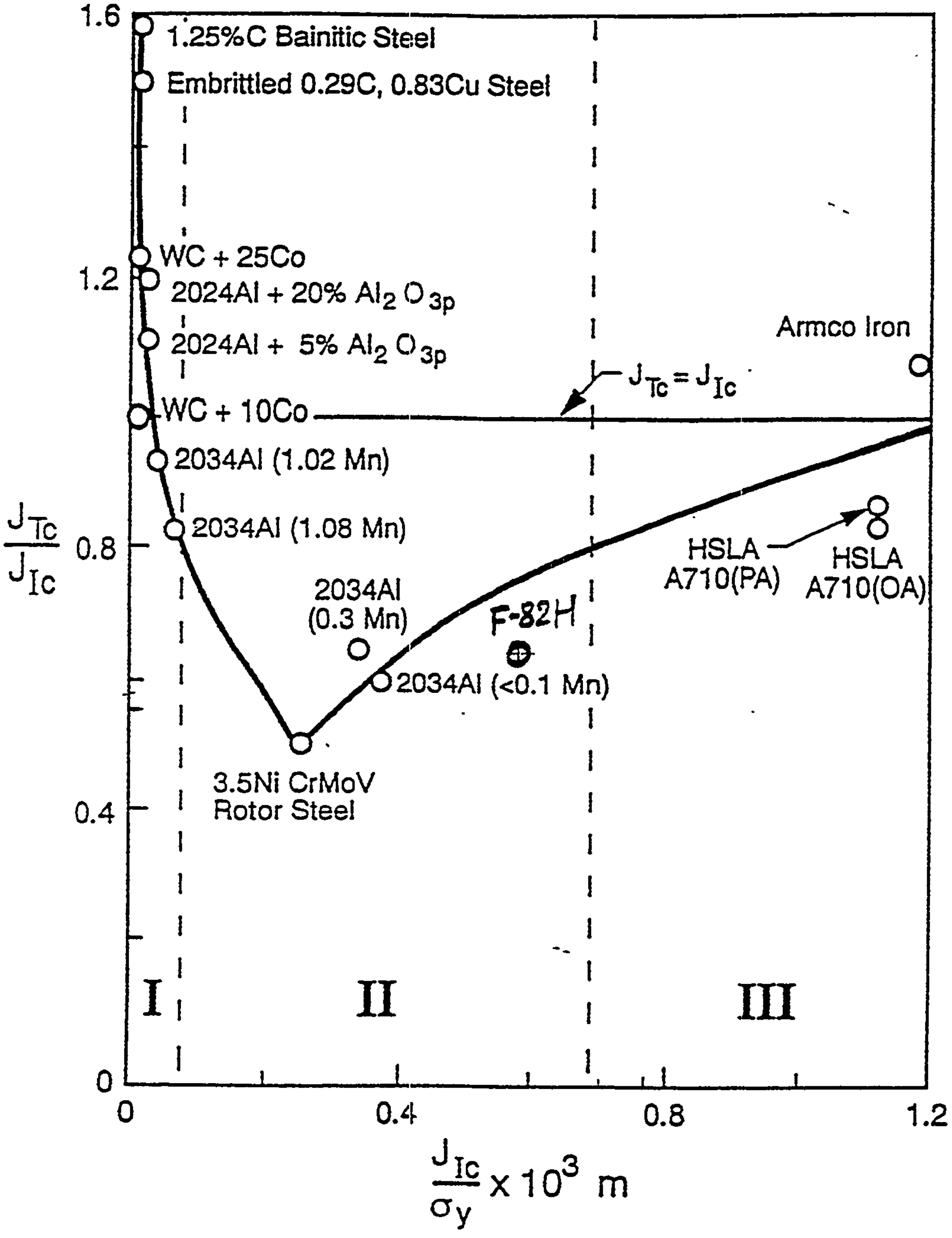

Fig. 1. J_{TC}/J_{IC} versus J_{Ic}/σ_y for different materials; where J_{TC} is the mixed-mode I/III J-integral at σ_{iii}/σ_i = 1, and σ_y is yield strength. The materials in Region I, II, and III are low toughness, tough, and ductile/tough materials, respectively.

MATERIAL AND EXPERIMENTAL METHODS

1. Material and Hydrogen-Charging

The F-82H steel plate used in this study was supplied by the Nippon Kokan Steel Company (NKK) in Japan. The chemical composition of the plate (as provided by NKK) is (by wt%): 0.096C-7.71Cr-2.1W-0.18V-0.04Ta-0.003P-0.003S. Specimens used in this study were cut in the T-L orientation as specified in ASTM E399-90 and were given a heat-treatment of 1000°C/20h/air cooling (AC), 1100°C/7min/AC, and 700°C/2h/AC. The resulting microstructure was tempered martensite. The mean intercept grain size was 25 μm. The heat-treatment resulted in a yield strength (σ_y) of 648 MPa, an ultimate tensile strength (σ_{uts}) of 735 MPa, an elongation of 16.7%, and a reduction in area of 70%.

H-charging was performed at Sandia National Laboratories, Livermore, CA. The specimens were charged with H at a H_2 gas pressure of 138 MPa at 300°C for two weeks, which resulted in a H content of 4 ppm(wt). H contents were measured with the inert gas fusion technique. A Cu coating was applied immediately after H-charging. The specimens with Cu coating were stored at -60°C. Before *J*-integral testing commenced, a specimen was warmed up to 24°C. *J* testing took about 60 minutes. H loss during *J* testing was minimized because of a low H diffusivity in ferritic/martensitic stainless steel at 24°C [14] and the added barrier of the Cu coating.

2. Experimental Methods

The geometry of the modified compact-tension specimens used for mixed-mode I/III testing is schematically shown in Fig. 2. The magnitude of the mode III loading components (P_{iii}) can be varied by changing the crack slant angle Φ since $P_{iii} = P_{appl} \sin \Phi$, where P_{appl} is the applied load. An angle of 0° represents mode I loading and the geometry of a 0° specimen becomes the standard compact-tension specimen as specified in ASTM standard E813-89. As Φ increases, the contribution of the mode III loading components increases. The crack-inclination angles used in this study were 0, 15, 25, 35, 45, and 55°. Side grooves of 20% reduction of total thickness were incorporated in all specimens. These side grooves increase the stress triaxiality at the edges of a growing crack and serve to constrain the advancing crack in the original crack plane. The calculation of the *J*-integrals in mixed-mode I/III requires a measurement of both vertical displacement (δ_v) and horizontal displacement (δ_h) of the load points. A pair of knife edges was secured to the front face of a specimen. A standard crack opening distance clip gage was positioned on the knife edges. The load-line δ_v values were calculated from the front face δ_v values with the method proposed by Saxena and Hudak, Jr. [15]. We found that δ_h increased with δ_v in a linear manner [1,3]. Hence, δ_h values were calculated approximately from the relation $\delta_h = \alpha\delta_v$, where $\alpha = \delta_{hmax}/\delta_{vmax}$.

An electric discharge machine (EDM) was used to make thin cuts with a small radius (radius = 0.051 mm) and approximately 1.3 mm long. The cuts were used as a substitute for a fatigue pre-crack (FPC) because an FPC tends to grow out of the original crack plane in mixed-mode specimens. The EDM cuts were made after final heat-treatment. The single-specimen technique was used in this study, which allows a *J-R* curve (*J* vs crack extension Δa) to be generated with one specimen. During testing, the specimen was frequently and partially unloaded, and the partial unloading compliances were used to calculate the corresponding crack lengths following the procedure described in ASTM E813-89 and by Li et al [15]. *J* values matching those crack lengths were also calculated by means of Eq. (1) in the next section. At least 20 pairs of *J*-Δa data were used to construct a *J-R* curve.

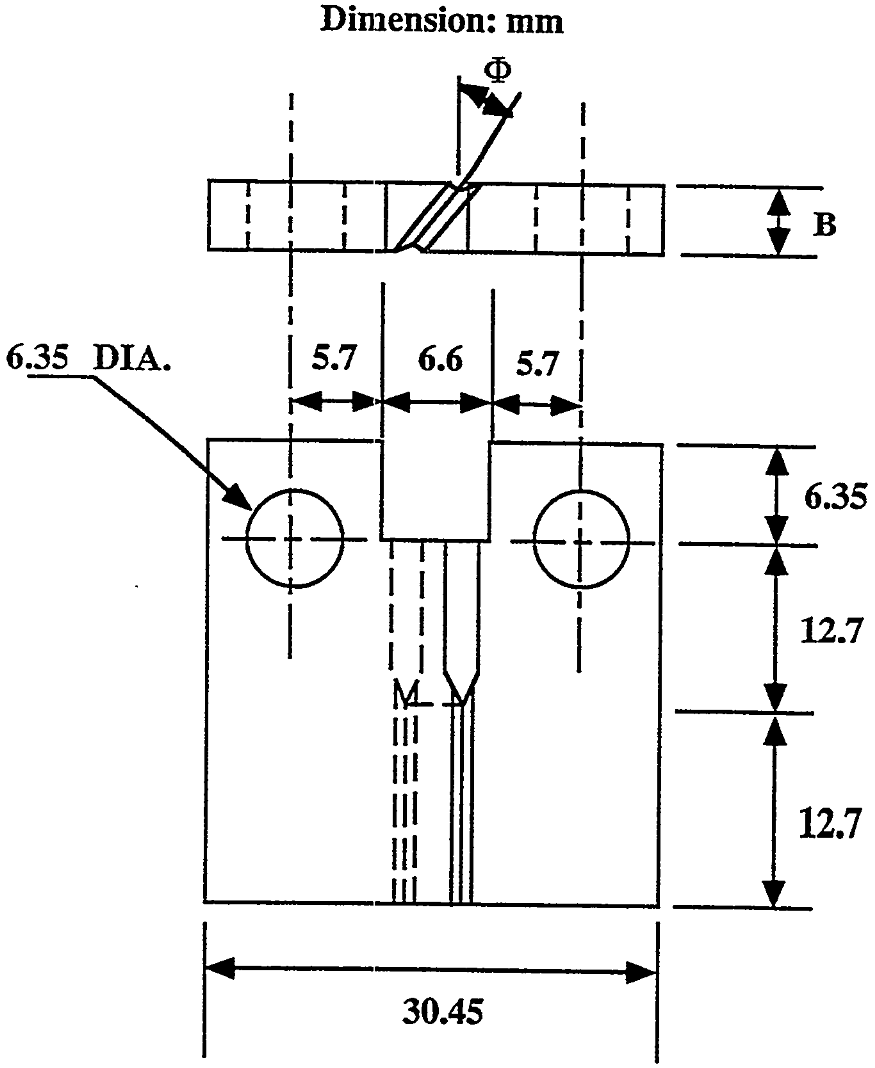

Fig. 2. The geometry of a modified compact tension specimen.

All of the fracture surfaces were examined by means of a scanning electron microscope (SEM) with an attached energy-dispersive X-ray spectroscope. A stereo microscopy technique [16] was used to study asperities on fracture surfaces.

DATA ANALYSIS

The mode I J_I and mixed mode I/III J_T were calculated from the area under the load vs load-line-displacement curve by means of Eq. (1) [17]:

$$J = \frac{2}{B_{net}\, b_o} \int_0^{\delta_v} P \, d\delta_v \qquad (1)$$

where

B_{net} = 0.8B/cosΦ (the net crack front width excluding the 10% side grooves on each side)

B = the overall specimen thickness

Φ = the crack-inclination angle

b_o = W - a_o

W = the specimen width

a_o = the initial physical crack length.

To construct *J-R* curves and determine critical *J* values (J_{IQ} and J_{TQ}), the ASTM E813-89 procedure was used. The subscript "Q" was used because F82-H steel was so tough that the specimen thickness did not meet the plane strain requirement. Since there is no standard for constructing a mixed-mode I/III blunting line, the analogy to the case of pure mode I was used. The slope of the blunting line for mixed mode I/III was calculated from Eq. (2):

$$m_{i/iii} = \frac{m_i \cos\Phi + m_{iii} \sin\Phi}{\sin\Phi + \cos\Phi} \qquad (2)$$

where $m_i = (\sigma_y + \sigma_{uts})$ and $m_{iii} = (\sigma_y + \sigma_{uts})/2$, which are the blunting line slopes for pure mode I and mode III loading, respectively. When Φ equals 0 or 90°, $m_{i/iii}$ is equal to m_i or m_{iii}, respectively. A best-fit straight line was also constructed from the J-Δa data between the upper and lower exclusion lines, and the slope of the straight line was taken as the unnormalized tearing modulus (dJ_I/da or dJ_T/da) for each specimen. The critical mode I and mode III *J* components (J_{ic} and J_{iiic}) in mixed-mode specimens also could be calculated in terms of the corresponding resolved loads and displacements. The methods of calculation of the resolved mode I and mode III load components (P_i and P_{iii}) and displacement components (δ_i and δ_{iii}), and the determinations of J_{ic} and J_{iiic} have been reported in detail in Refs. 6, 7, and 12.

RESULTS

1. The Critical *J* Values and the Tearing Moduli (*dJ/da*)

The effect of H on J_{TQ} is shown in Fig. 3. In the limit of Φ = 0°, J_{TQ} is equal to J_{IQ}; for $0 < \Phi < 90°$, J_{TQ} represents the total critical *J* value under mixed-mode loading. The J_{TQ} values for specimens without H are also included for comparison. From Fig. 3, one can see that the introduction of H into the F-82H steel decreases its overall fracture toughness considerably, to a degree which is independent of crack angle. However, the presence of H did not change the trend of the J-$[P_{iii}/(P_{iii} + P_i)]$ curve; J_{IQ} is still the highest *J* value. As $[P_{iii}/(P_{iii} + P_i)]$ increases, J_{TQ} decreases until it reaches a minimum at a $[P_{iii}/(P_{iii} + P_i)]$ ratio between 0.4 and 0.6, corresponding to a crack angle range of 35 to 55°. The change of J_{TQ} with $[P_{iii}/(P_{iii} + P_i)]$ is similar to that for a steel without H, and follows a second-order polynomial function. The effect of H on J_{TQ} of the F-82H steel is similar to that for another tough steel, HPRS [6,13], in which the addition of H also lowered the overall J_{TQ}. However, the minimum J_{TQ} for H-charged F-82H steel is around 100 kJ/m^2, higher than the value of 64 kJ/m^2 reported for the HPRS [6,13].

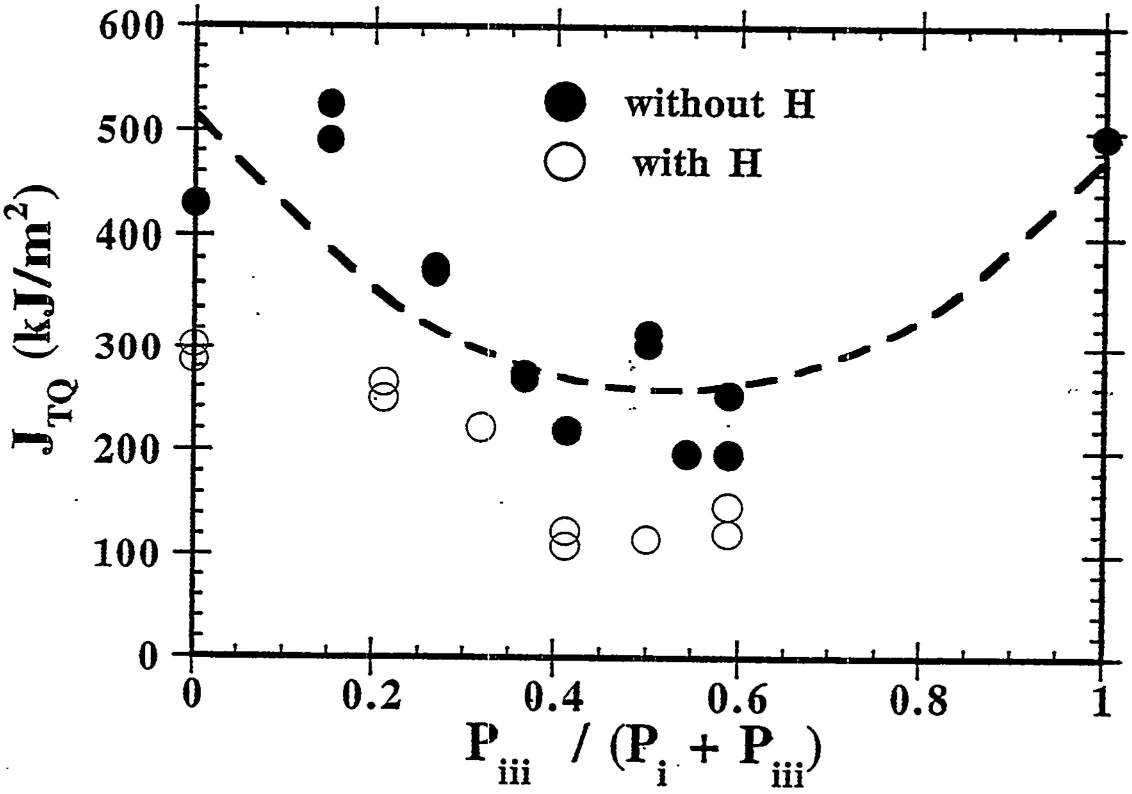

Fig. 3 The dependence of J_{TQ} on mode III loading component.

The introduction of H also reduced the resistance to crack growth, i.e. lowered the overall mixed-mode *dJ/da* relative to the steel without H. The unnormalized *dJ/da* corresponding to different $[P_{iii}/(P_{iii}+P_i)]$ values are shown in Fig. 4. From Fig. 4, one can see that H does not change the dependence of *dJ/da* on $[P_{iii}/(P_{iii}+P_i)]$. The variation of *dJ/da* with $[P_{iii}/(P_{iii}+P_i)]$ is also found to obey a second-order polynomial, similar to the curve without H.

2. Fractography

The crack fronts of all specimens remained in their initial orientation during *J* testing. Investigation of fracture surfaces with SEM showed that internal H in the F-82H steel did not induce intergranular or cleavage facets. All of the specimens exhibited a microvoid coalescence type of fracture, as shown in Fig. 5. Most of the larger voids initiated from sulfide particles and the spacing of the finer voids is consistent with nucleation at tempered carbide particles. But, H appeared to affect the processes of void initiation and coalescence. Fig. 6 shows two pairs of low magnification (about 4 X) fracture surfaces, mode I specimens ($\Phi = 0°$) and mixed-mode I/III specimens ($\Phi = 35°$), respectively. Fig. 6 indicates that a specimen with H has less thickness reduction (%TR) at the crack tip and critical crack tip opening (COD)

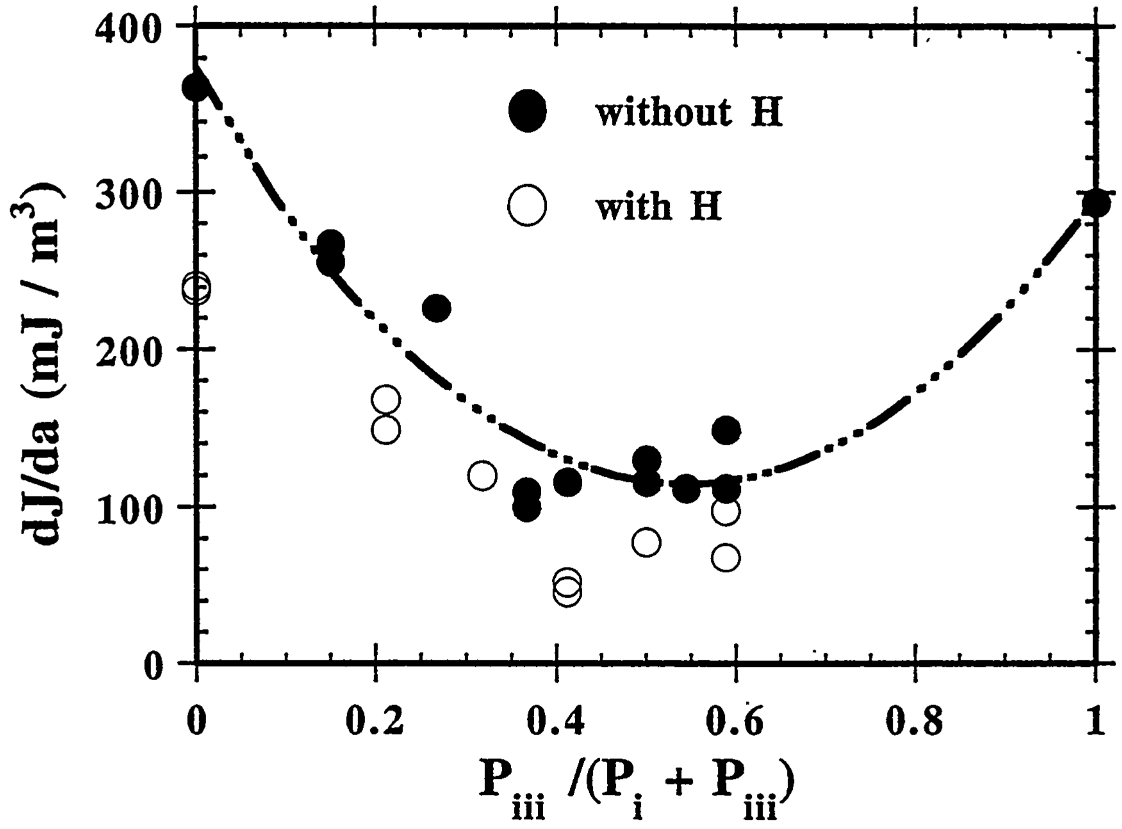

Fig. 4. The dependence of *dJ/da* on mode III loading component.

than those without H. The data of the %TR and COD values for these specimens are listed in Table 1 along with the corresponding J_{TQ} values. Evidently, the effect of H on J_{TQ}, COD and the %TR values of the F-82H steel is consistent in that the cases with lower J_{TQ} values with H present corresponded to the cases of little lateral necking and crack tip plastic deformation prior to final fracture. Furthermore, H decreased the roughness of fracture surfaces in all specimens (Fig. 6). While the difference on the 0° specimens is not as evident as that on the 35° specimens at low magnification, it is manifested at higher magnification (Figs. 7a and 7b). Overall, the crack has very high tortuosity. Stereo pair SEM views of regions such as that in Fig. 7a show that reentrant regions on one surface match salient features on the other and vice-versa, with slopes of up to about ±45°. Thus, at the coarsest size scale, the crack is locally a mixed-mode I-II-III crack with large roughness. At the next level, the larger dimples reflect voids at the 3-10 μm scale and usually contain sulfide particles. Those can be seen in Fig. 8a and 8b. At the finest scale, there are more fine voids, 0.5-1 μm, in the presence of H and these voids tend to be flatter. The smaller microvoid size in the H-charged specimens indicated that H facilitated void initiation and coalescence. The overall flatter and more well defined tear ridges in the H-charged case showed that H avored cracking along the trajectories of intense shear flow, resulting in lower J_{TQ} and *dJ/da* values.

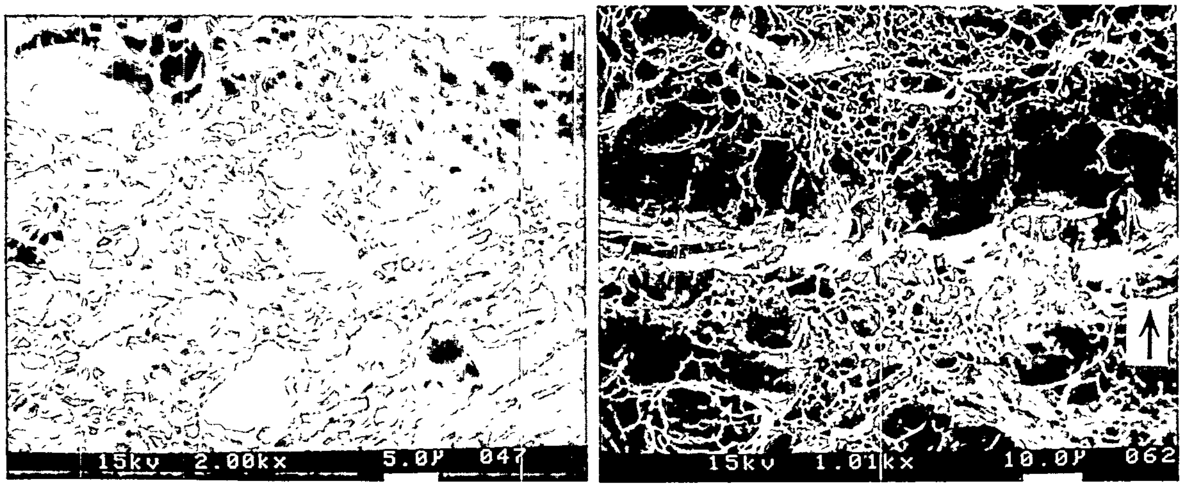

(a) (b)

Fig. 5. SEM fractographs showing the microvoid coalescence nature fracture surfaces. (a) Mode I specimen; (b) 35° specimen. The arrow indicates shear direction.

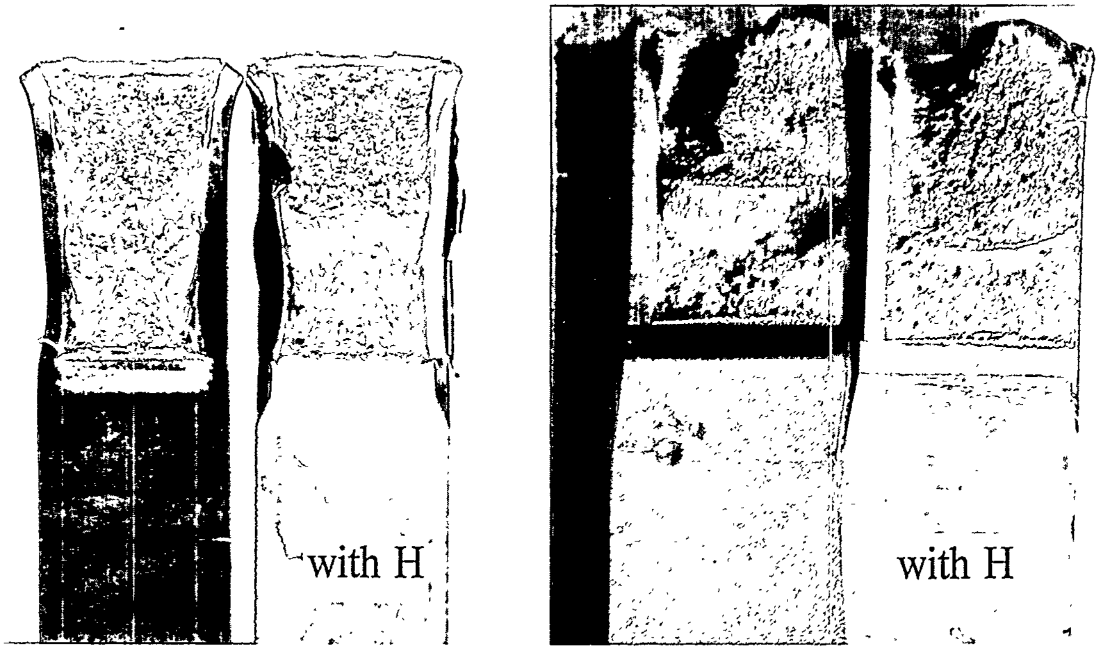

(a) (b)

Fig. 6. Optical microscope photos showing the effects of H on thickness reduction at the crack tips and roughness of fracture surfaces. a. Mode I specimen; b. 35° specimen.

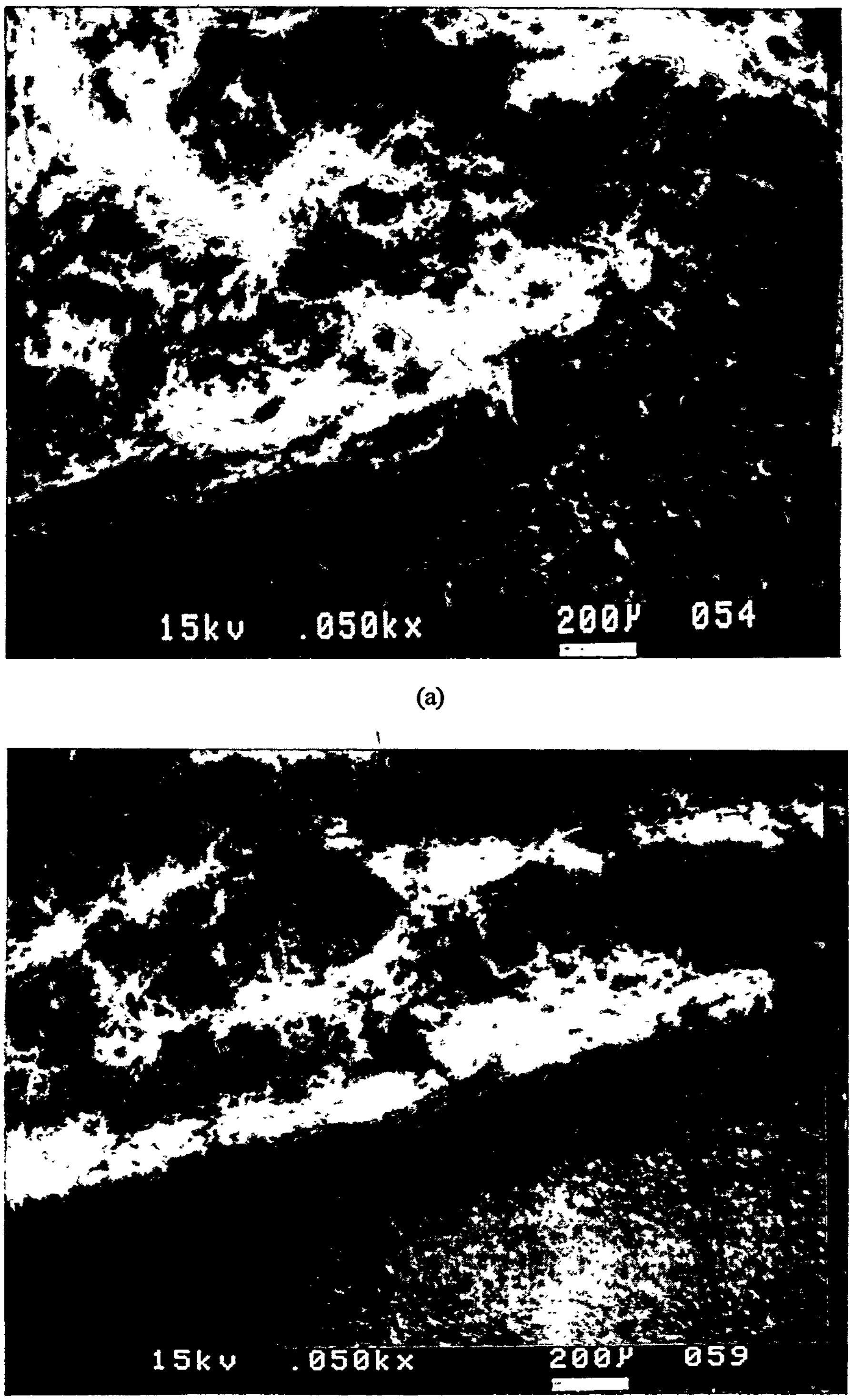

(a)

(b)

Fig. 7. SEM fractographs of mode I specimens showing the effect of H on void size. a. Without H; b. with H.

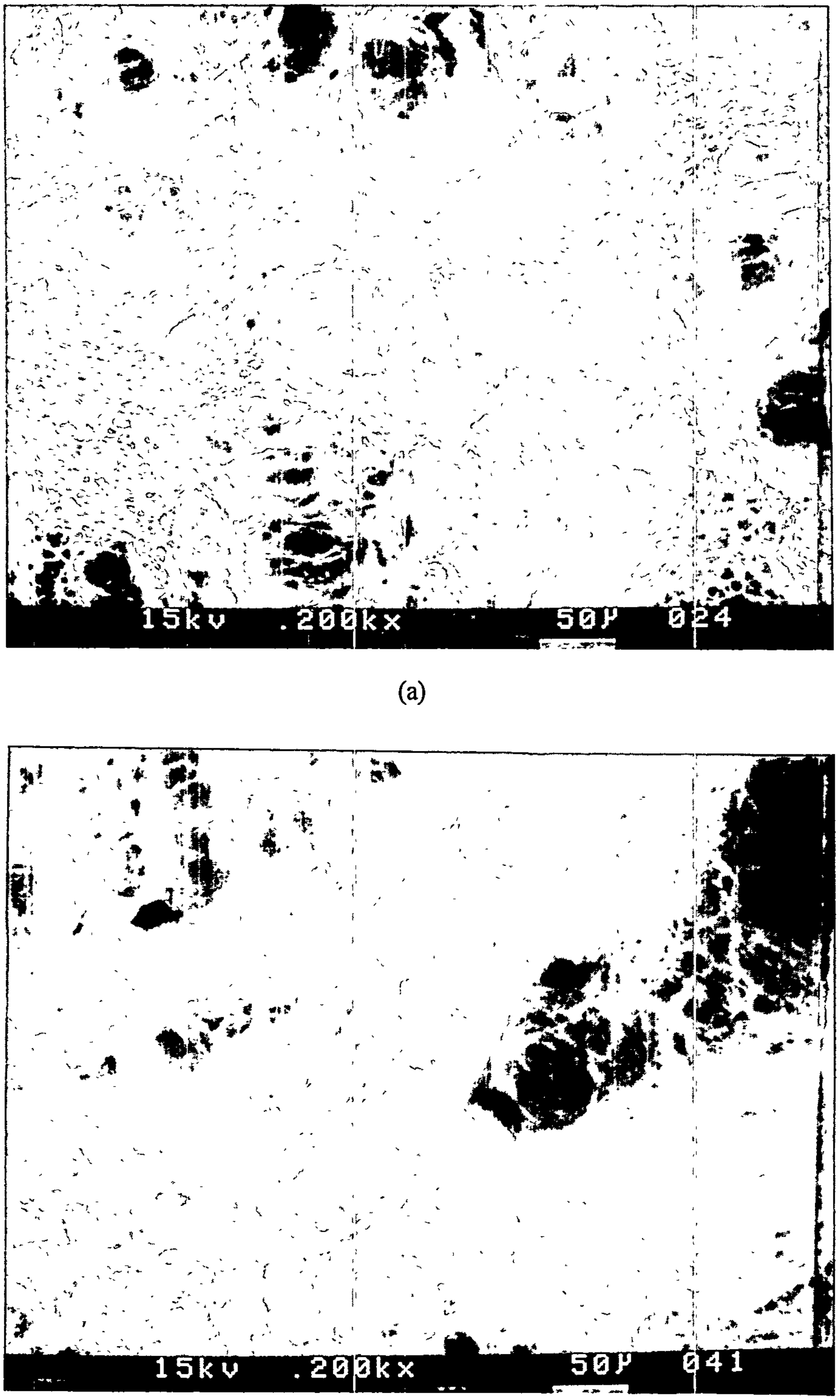

(a)

(b)

Fig. 8. SEM micrographs of mode I specimens at higher magnification showing the effect of H on void size. a. Without H; b. with H.

Table 1. Effect of H on J_{TQ}, thickness reduction (%TR) & COD (δ)

Crack angle	0°		35°	
	with H	no H	with H	no H
J_{TQ} (kJ/m^2)	303	429	110	219
%TR	11	16	≈ 0	≈ 3
δ_{meas}^{*} (mm)	.37	.58	.24	.36
δ_{cal} (mm)	.41	.60	.16	.31

* Subscript "meas" and "cal" mean measured and calculated values.

DISCUSSION

The addition of a mode III loading component to mode I loading has been found to increase, decrease, or have little or no effect on the J_{TQ}, depending on the toughness of the materials. For brittle materials, such as glass [18], 0.29C-0.83Cu, steel and 1.25C bainitic steels [4,8-10], in which fracture was controlled by tensile stress and the local crack-opening displacements, the addition of mode III loading components had little or no effect on the values of J_{ic}, but tended to increase J_{TQ}. For tough steels, such as HPRS [6], which failed primarily by microvoid coalecense, the presence of shear strain in the crack plane associated with mode III loading produced incompatibility stresses at the particle interfaces in the trajectory of the crack, causing decohesion or particle fracture (shear damage). This process led to enhanced void formation that limited the mode I plastic flow field and caused premature separation of voids by the mode I normal stress. Accordingly, tough materials exhibited a lower fracture toughness for a mixed-mode crack than for a mode I crack. For those materials with intermediate toughness, such as AISI 1090 steel, the addition of a mode III loading component decreased J_{ic} moderately, and had little effect on J_{TQ}.

As seen from Fig. 3, the F-82H steel is very tough and very sensitive to incompatibility stresses at particle interfaces caused by the mode III loading component. Under mixed-mode loading, J_{TQ} decreased as the mode III load component increased, reaching a minimum at a crack angle between 40 and 50°.

The issue remains regarding the mechanism for the degrading effect of H in the F82-H steel, in which H degrades the properties but leaves the ductile fracture mechanism unchanged. A variety of studies of such steels in plane strain tension [17-28] have shown that H promotes the onset of plastic instability in the form of shear localization. In relatively pure, single phase materials, this may be the consequence of a lowered flow stress for dislocation glide [29-31] or a tendency for increased coplanarity of slip [32]. In multiphase engineering materials, the effect instead is associated with localized damage in the form of enhanced void formation by particle decohesion and cracking [31-36] and of enhanced void growth and agglomeration [33-35]. Voids also enhance shear localization [36-38]. Thus, the H enhances void formation, which enhances shear localization, which in turn enhances further void formation because of incompatibility effects. This autocatalytic phenomenon leads to failure at lower strains in the presence of H.

Fractographic analysis indicates that H plays a similar role in reducing J_{TQ} in H-charged F-82H steel. The out-plane shear strain induced by a mode III loading component caused shear damage in the form of void initiation at sulfides and carbides. The presence of H further enhances void formation, growth and agglomeration, consistent with the tensile test results [31-38] and thereby enhances the degradation of toughness. Hence, the combined effect of H and mode III shear stress made crack initiation and growth easier, resulting in lower J_{TQ} and *dJ/da* in H-charged F-82H steel at all crack angles.

CONCLUSION

The presence of H reduced both J_{TQ} and *dJ/da* for a ferritic/martensitic stainless steel, independent of crack slant angles. However, H did not change the dependence of J_{TQ} and *dJ/da* on crack angles. Both J_{IQ} and dJ_I/da exhibited the highest values, the minimum J_{TQ} and *dJ/da* were attained at a crack angle between 35 and 55°, where the ratio of $P_{iii}/(P_{iii} + P_i)$ is between 0.4 and 0.6. However, the minimum J_{TQ} remained high, at about 100 kJ/m^2.

ACKNOWLEDGEMENTS

We are grateful to Dr. N. R. Moody of Sandia National Laboratories, Livermore, CA for H-charging. The assistance of Mr. J. L. Humason at Pacific Northwest Laboratory in developing the test methods is gratefully acknowledged. This research was supported by the Office of Fusion Energy of the U. S. Department of Energy under Contract DE-AC06-76RLO 1830 with Battelle Memorial Institute.

REFERENCES

1. M. T. Miglin, I.-H. Lin, J. P. Hirth, and A. R. Rosenfield, in Fracture Mechanics: 14th Symp. — Vol. II: Testing and Applications, ASTM STP 791, J. C. Lewis and G. Sines, Eds., ASTM, Philadelphia, 1983, pp. II-353-II-369.

2. M. T. Miglin, J. P. Hirth, and A. R. Rosenfield, Res. Mech., 11 (1984), pp. 85-95.

3. J. G. Schroth, J. P. Hirth, R. G. Hoagland, and A. R. Rosenfield, Met. Trans. A, 18A (1987), pp. 1061-1072.

4. M. Manoharan, J. P. Hirth, and A. R. Rosenfield, J. of Test. and Eval., 18 (1990), No.2, pp. 106-114.

5. S. Raghavachary, A. R. Rosenfield, and J. P. Hirth, Met. Trans. A, 21A (1990), pp. 2539-45.

6. J. A. Gordon, J. P. Hirth, A. M. Kumar, and N. R. Moody, Jr., Met. Trans. A, 23A (1991), pp. 1013-1020.

7. M. Manoharan, S. Raghavachary, J. P. Hirth, and A. R. Rosenfield, J. Eng. Mater. Technol., 111 (1989), pp. 440-442.

8. A. M. Kumar and J. P. Hirth, Scripta Metall. Mater., 25 (1991), pp. 985-90.

9. M. Manoharan, J. P. Hirth, and A. R. Rosenfield, Scripta Metall. Mater., 23 (1989), pp. 763-766 and pp. 1647-1648.

10. S. V. Kamat and J. P. Hirth, Scripta Metall. Mater., 30 (1994), pp. 145-48.

11. Huaxin Li, R. H. Jones, J. P. Hirth, and D. S. Gelles, J. of Nuclear Materials, 1994, in press.

12. Huaxin Li, R. H. Jones, J. P. Hirth, and D. S. Gelles, Metall. and Mater. Trans. A, 1994, submitted.

13. A. M. Kumar, N. R. Moody, Jr., J. P. Hirth, and J. A. Gordon, Met. Trans. A, 24A (1993), pp. 1450-1451.

14. J. Xu, X. Z. Yuan, X. K. Sun and B. M. Wei, Scripta Metall. Mater., 29 (1993), pp. 925-30.

15. Ashok Saxena and S. J. Hudak, Jr, Int. J. Fract., 14 (1978), pp. 453-468.

16. D. S. Gelles and F. H. Huang, in Alloy Development for Irradiation Performance, Semiannual Progress Report, DOE/ER-0045/8, Oak Ridge National Lab., Oak Ridge, TN (March 31, 1982), pp. 442-459.

17. J. R. Rice, P. C. Paris, and J. G. Merkle, in ASTM STP 536, ASTM, Philadelphia, 1973, pp. 231-235.

18. A. R. Rosenfield and W. H. Duckworth, Int. J. Fract., 32, (1987), p. R59.

19. A. W. Thompson and I. M. Bernstein, in Proc. Hydrogen in Metal Congress, Paris, France, Pergamon Press, Oxford, 1977, vol. 3, pp. 1-8.

20. T. D. Lee, T. Goldenberg, and J. P. Hirth, Metall. Trans. A, 10A (1979), pp. 199-208.

21. T. D. Lee, T. Goldenberg, and J. P. Hirth, Metall. Trans. A, 10A (1979), pp. 439-48.

22. O. A. Onyewuenyi and J. P. Hirth, Metall. Trans. A, 14A (1983), pp. 259-69.

23. S. C. Chang and J. P. Hirth, Metall. Trans. A, 17A (1986), pp. 1485-7.

24. A. Chatterjee, R. G. Hoagland, and J. P. Hirth, Mater. Sci. and Engin., A142 (1991), pp. 235-43.

25. I. G. Park and A. W. Thompson, Metall. Trans. A, 21A (1990), pp. 465-77.

26. I. G. Park and A. W. Thompson, Metall. Trans. A, 22A (1991), pp. 1615-26.

27. C. Hwang and I. M. Berstein, Acta Metall., 34 (1986), pp. 1001-10, pp. 1011-20.

28. T. D. Lee, I. M. Bernstein, and S. Mahajan, Acta Metall. Mater., 41 (1993), pp. 3363-80.

29. C. D. Beachem, Met. Trans. 3 (1972), pp. 437-451.

30. T. Tabata and H. K. Birnbaum, Scripta Metall. 17 (1983), pp. 947-950.

31. I. M. Robertson and H. K. Birnbaum, Acta Metall. 34 (1986), pp. 353-366.

32. H. Matsui, A. Kimura, and H. Kimura: in Strength of Metals and Alloys, P. Haasen, V. Gerold and G. Kostorz, eds., vol. 2, MP 977-87, Pergamon, Oxford, 1979.

33. R. Garber, I. M. Bernstein, and A. W. Thompson, Metall. Trans. A, 12A (1981), pp. 225-34.

34. H. Cialone and R. J. Asaro, Metall. Trans. A, 10A (1979), pp. 376-75.

35. R. A. Oriani and P. H. Josephic, Acta Metall. 22 (1974), pp. 1065-1074.

36. J. W. Hutchinson and V. Tvergaard, Int. J. Mech. Sci., 22 (1980), pp. 339-54.

37. J. W. Hutchinson and V. Tvergaard, Int. J. Solids Structures, 17 (1981), pp. 451-70.

38. L. Anand and W. A. Spitzig, J. Mech. Phys. Solids, 28 (1980), pp. 113-28.

DEPENDENCE OF MODE I AND MIXED MODE I/III FRACTURE TOUGHNESS ON TEMPERATURE FOR A FERRITIC/MARTENSITIC STAINLESS STEEL - H. Li (Associated Western Universities--Northwest Div.), R. H. Jones (Pacific Northwest Laboratory), J. P. Hirth (Washington State University), and D. S. Gelles (Pacific Northwest Laboratory)

OBJECTIVE

To investigate the dependence of mode I and mixed mode I/III fracture toughness on temperature in the range of -95°C to 25°C for a low activation ferritic/martensitic stainless steel (F82-H).

SUMMARY

Mode I and mixed mode I/III fracture toughnesses were investigated in the range of -95°C to 25°C for a F82-H steel heat-treated in the following way; 1000°C/20 h/air-cooled (AC), 1100°C/7 min/AC, and 700°C/2 h/AC. Mode I fracture toughness (J_{IC}) was determined with standard compact tension (CT) specimens, and mixed-mode I/III fracture toughness (J_{MC}) was determined with modified CT specimens, which resulted in 0.41 ratio of $P_{iii}/(P_{iii} + P_i)$. The F82-H was very tough at room temperature (RT), giving a J_{IC} value of about 284 kJ/m^2. Mixed-mode I/III loading dramatically lowered fracture toughness. The J_{MC} value was only 150 kJ/m^2 at RT. J_{IC} values exhibited a strong temperature dependence and decreased rapidly with decrease of temperature. J_{IC} at -90°C was only 30 kJ/m^2. On the other hand, J_{MC} values depended much more weakly on temperature. J_{MC} at -95°C was 50 kJ/m^2, about 70% higher than J_{IC} value at -90°C. At RT the mode I specimens fractured by microvoid coalescence. Mixed mode specimens also fractured by microvoid coalescence, but tortuosity and void size on fracture surfaces were significantly less than those in mode I specimens. Interestingly, at -90°C, a crack in a mode I specimen initiated and grew by quasi-cleavage fracture; but a crack in mixed mode specimen initiated and propagated a short distance (0.5 mm) by a mixture of intergranular fracture and ductile tearing. Then the crack turned to mode I and fractured by quasi-cleavage failure. Our results indicate that crack tip plasticity was increased by mixed mode loading, and suggest that at low temperature, mode I fracture toughness is the critical design parameter, but at temperatures above RT, especially concerning fatigue and creep-fatigue crack growth rate, a mixed mode loading may be more harmful than a mode I loading for this steel because a mixed mode loading results in lower fracture toughness and higher crack tip plasticity (or dislocation activity).

PROGRESS AND STATUS

Introduction

In tough materials, which fail primarily by a microvoid nucleation and growth mechanism, the presence of a mode III loading component lowers the J_{MC} (total J-integral from mode I and mode III components) values considerably from their mode I values. The J_{MC} values pass through a minimum at a position between mode I and mode III on a plot of J_{MC} vs crack inclination angle. J_{IC} (mode I J-integral) turned out to be the highest fracture toughness value. For brittle materials such as ceramics and brittle steels, on the other hand, J_{IC} values are the lowest fracture toughnesses. The introduction of a mode III loading component increased J_{MC} values in brittle materials. More generally, materials can be divided into three categories according to their process zone size as presented by J_{IC}/σ_Y and the ratio of J_{MC} (at crack angle of 45°) to J_{IC}, as shown in Fig. 1 [1]. The materials in Region I are brittle and sensitive to mode I loading and, consequently, mode I fracture toughness is the lowest as compared with mixed-mode I/III

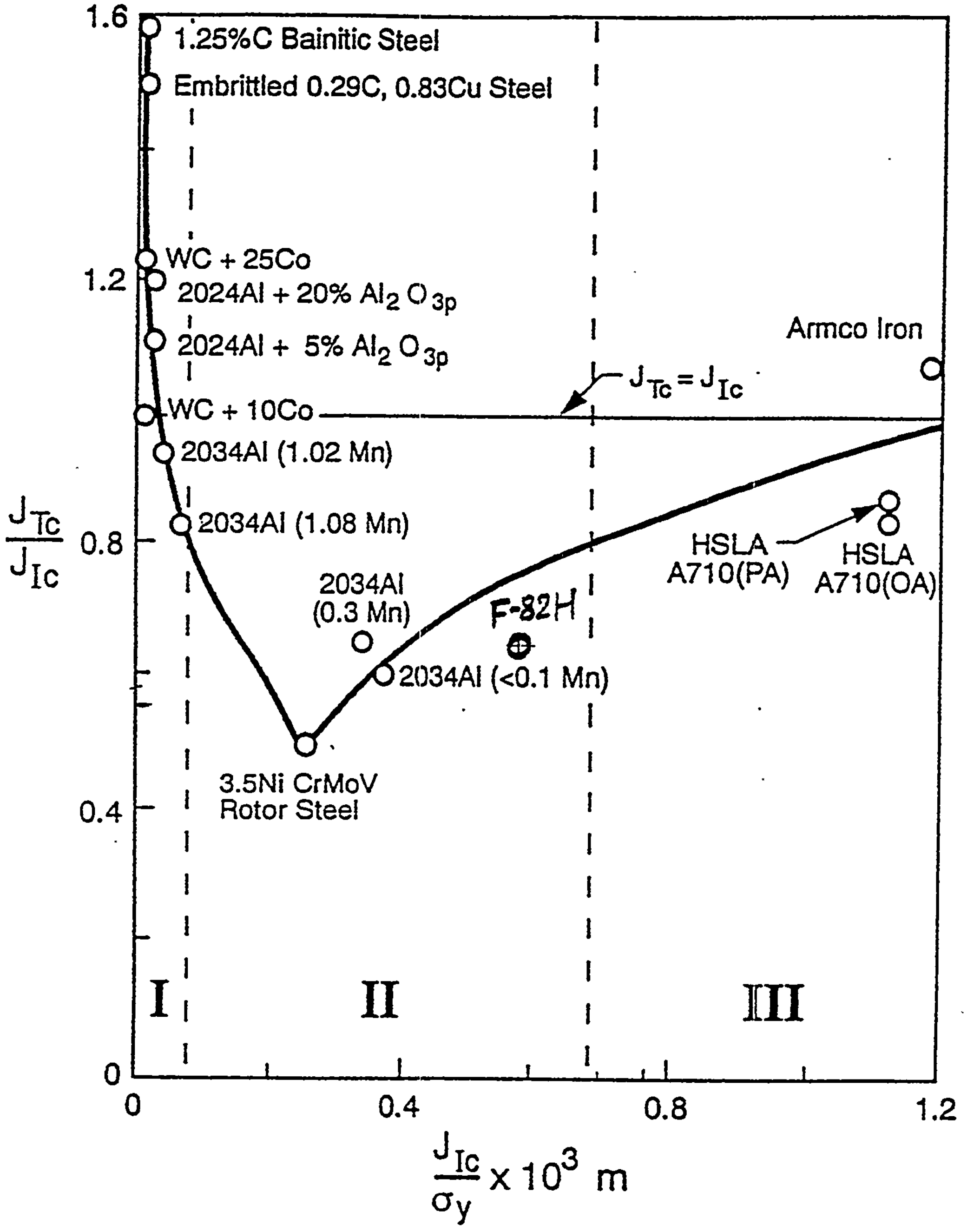

Fig. 1. J_{TC}/J_{IC} vs J_{IC}/σ_y for different materials; where J_{TC} is mixed-mode I/III J-integral at $\sigma_{iii}/\sigma_i = 1$, and σ_y is yield strength. The materials in Region I, II, and III are low toughness, tough, and ductile/tough materials, respectively.

fracture toughnesses. Therefore, for such materials, mode I fracture toughness is properly used for design. Materials in Region II are tough and sensitive to mixed-mode I/III loading, mode I fracture toughness is no longer the lowest, and the minimum mixed-mode J_{MC} is recommended as a design criterion. For the materials in Region III, mode I and mixed-mode fracture toughness levels are similar and the mode I value can be used for design with small uncertainty. We have reported [2,3] that F-82H steel is a tough material which falls in Region II in Fig. 1. The presence of mode III stress component lowers its fracture toughness significantly. It is well known that a ferritic/martensitic steel will experience a ductile to brittle transition as temperature is lowered. However, the dependence of J_{MC} on temperature has not been reported. In this study, the dependence of J_{IC} and J_{MC} values was investigated in a temperature range of -95°C to 25°C.

Material

The F-82H steel plate used in this study was supplied by the Nippon Kokan Steel Company (NKK) in Japan. The chemical composition of the plate (as provided by NKK) is (by wt%): 0.096C-7.71Cr-2.1W-0.18V-0.04Ta-0.003P-0.003S. Specimens used in this study were cut in the T-L orientation as specified in ASTM E399-90 and were given a heat-treatment of 1000°C/20 h/AC, 1100°C/7 min/AC, and 700°C/2 h/AC. This heat treatment produced smaller grain size and higher strength than those produced by 1050°C/0.5 h/AC and 760°C/5 h/AC. The resulting microstructure was tempered martensite. The mean intercept grain size was 25 μm. The heat-treatment resulted in a yield strength (σ_y) of 648 MPa, an ultimate tensile strength (σ_{uts}) of 735 MPa, an elongation of 16.7%, and a reduction in area of 70%.

Experimental Methods

The geometries of a standard compact tension (CT) specimen and a modified CT specimen are shown in Fig. 2. The specimen shown in Fig. 2a was used for determination of mode I stress intensity (K_{IC}) at temperatures below -40°C. K_{IC} values then were converted to critical *J*-integrals (J_{IC}) by means of Eq. 1. Modified CT specimens were used for mixed-mode I/III testing. The magnitude of a mode III loading component can be varied by changing the crack slant angle Φ. As Φ increases, the mode III component increases owing to $P_{iii} = P_{appl} \sin\Phi$, where P_{appl} is the applied load. The crack-inclination angles used in this study were 0 and 35°, respectively. A 0° specimen represents mode I loading and the geometry of a 0° specimen becomes the standard CT specimen with side grooves as specified in ASTM standard E813-89, which was used for mode I *J*-integral testing at RT. A 35° specimen gives a ratio of mode III loading component to the total load $[P_{iii} /(P_{iii} + P_i)]$ 0.41. This specimen was used for both mixed mode *J*- and *K*-tests. Side grooves of 20% reduction of total thickness were used to increase the stress triaxiality at the specimen surfaces and constrain the advancing crack on the original crack plane. Calculating mixed-mode I/III *J*-integral (J_M) requires measuring both the vertical displacement (δ_v) and horizontal displacement (δ_h) of the load points. A standard crack opening displacement (COD) gage was positioned on the knife edges. We found that the δ_h increased with δ_v in a linear manner. Hence δ_hs were calculated approximately using a relation of $\delta_h = \alpha \times \delta_v$, where $\alpha = \delta_{hmax} / \delta_{vmax}$.

ASTM E813-89 was used to determine critical *J*-integrals and ASTM E399-90 was used to determine the critical stress intensity factor. The single-specimen technique was used in this study, which allows a J-R curve (J vs crack extension Δa) to be generated with one specimen. At least 40 pairs of J-Δa data were used to construct a J-R curve. J_{MC} values at -95°C were calculated from mode I K_{ic} and mode III K_{iiic} components by means of Eq. 2. Subzero temperatures were achieved by means of a refrigerator and controlled to within ±5°C during testing.

$$J_{IC} = \frac{K_{IC}^2\,(1 - \nu^2)}{E} \qquad (1)$$

where E is Young's modulus and ν is Poisson ratio.

$$J_{ic} = \frac{K_{ic}^2\,(1 - \nu^2)}{E} \qquad (2a)$$

$$J_{iiic} = \frac{K_{iiic}^2\,(1 + \nu)}{E} \qquad (2b)$$

$$J_{MC} = J_{ic} + J_{iiic} \qquad (2c)$$

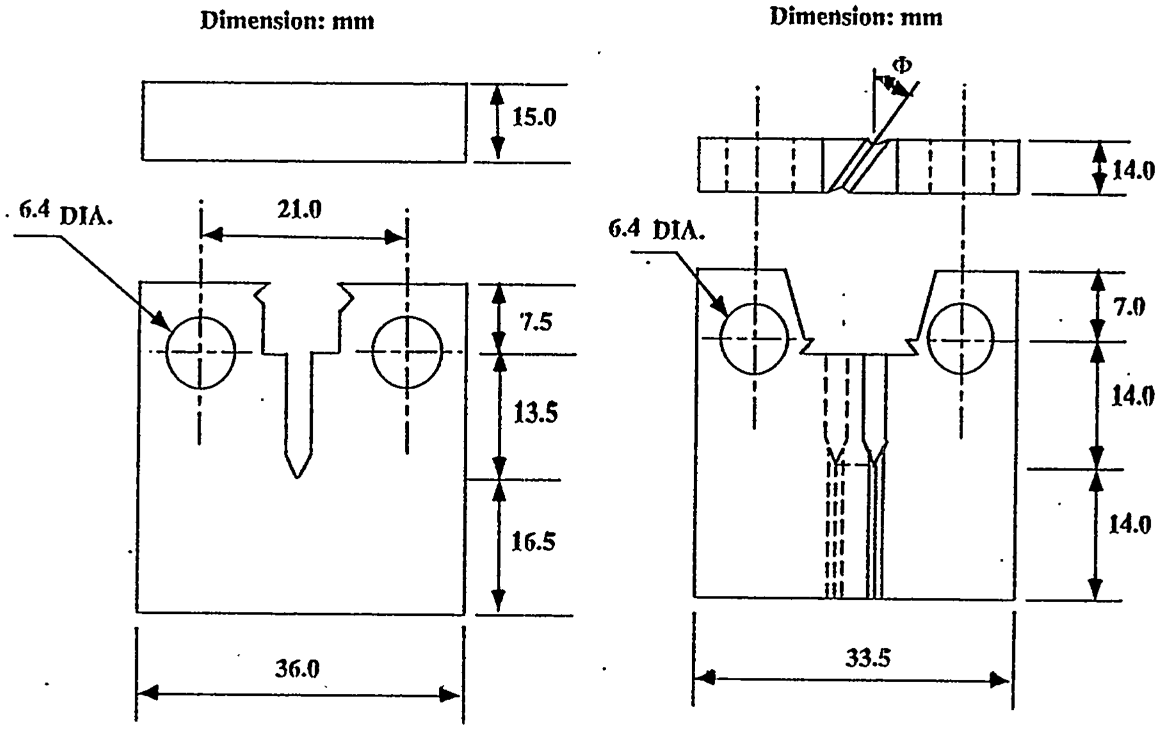

Fig. 2. The geometry of a compact tension specimen (2a) and a modified compact tension specimen (2b).

Results

At RT, the F-82H steel is very tough, J_{IC} is 284 kJ/m^2. The addition of a mode III loading component reduced J_{MC} dramatically, from 284 for mode I to 150 kJ/m^2 for mixed mode. Both mode I and mixed mode specimens fractured by microvoid coalescence, as shown in Fig. 3. However, the introduction of a mode III loading component reduced the tortuosity of the fracture surface and void size greatly, indicating lower energy dissipation during crack initiation and propagation. Consequently, mixed mode loading resulted in significantly lower critical J-integral.

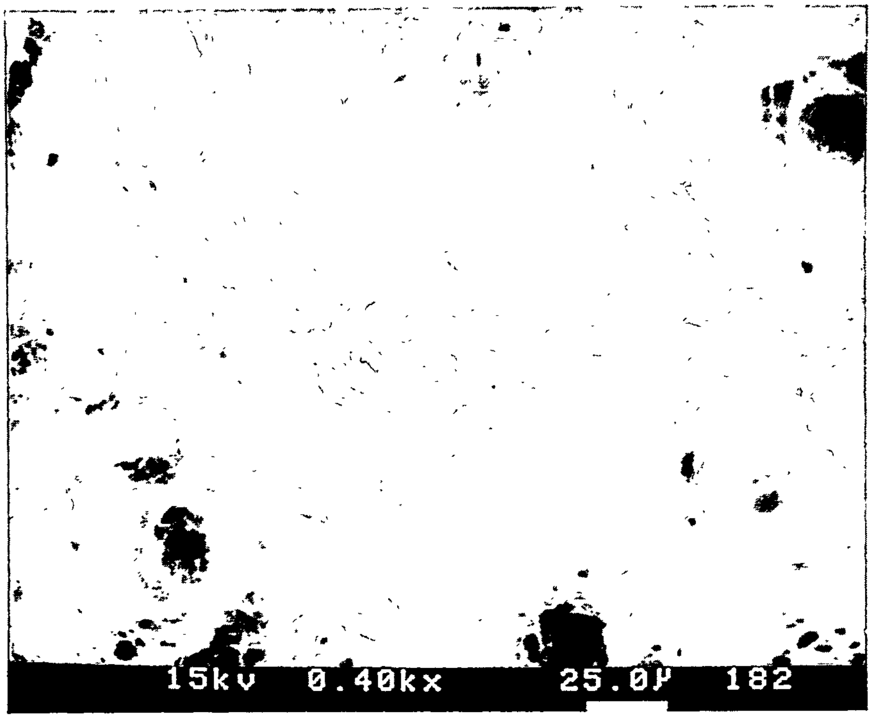

Fig. 3. SEM fractograph showing the microvoid coalescence nature fracture surfaces of a mode I specimen tested at room temperature.

The effect of temperature on fracture toughness (J_{IC} and J_{MC} values) and fractography is summarized in Table 1, and also shown in Fig. 4. It is evident that temperature has a much stronger effect on J_{IC} values than on J_{MC} values. At -90°C, J_{IC} is only 30 kJ/m^2, but J_{MC} is 50 kJ/m^2, about 70% higher. Fractographic investigation with SEM revealed that at -90°C, a mode I crack initiated and propagated by quasi-cleavage fracture (Fig. 5), indicating brittle characteristics consistent with a low J_{IC} value. On the other hand, a mixed mode crack tested at -95°C initiated and grew a short distance (0.5 mm) along the original crack plane, then changed to a mode I crack, as shown in Fig. 6. SEM investigation showed that the mixed mode crack propagated by a mixture of intergranular fracture and ductile tearing (Fig. 7). However, when the crack changed to mode I, it propagated by quasi-cleavage (Fig. 8). The information from the fracture surface of the mixed mode specimen suggests that mixed mode I/III loading increase crack tip plasticity, resulting in a higher fracture toughness.

Table 1. The dependence of fracture toughness and fracture surface appearance on temperature

	Mode I		Mixed Mode	
Temp. (°C)	J_{IC} (kJ/m^2)	Frac. surface	J_{MC} (kJ/m^2)	Frac. surface
25	284	dimple	150	dimple
-55	60	quasi-cleavage		
-90	30	quasi-cleavage	50	dimple & I.G.*

* I.G.: intergranular fracture.

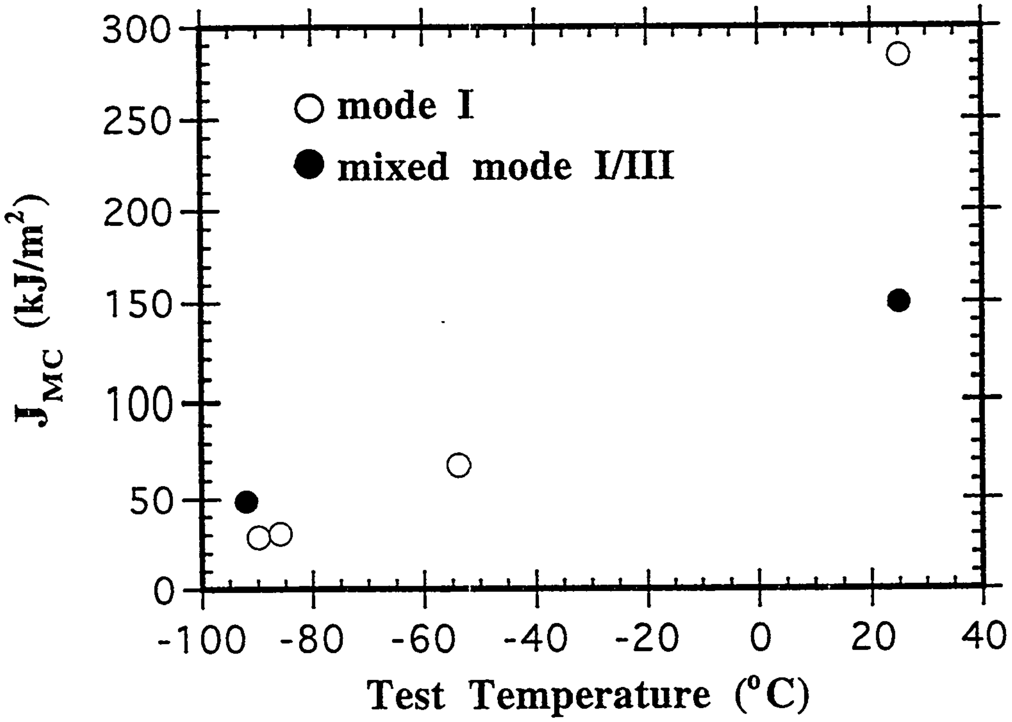

Fig. 4. The dependence of J_{IC} and J_{MC} values on testing temperature.

Discussion

The addition of a mode III loading component to mode I loading could increase, decrease, or have little or no effect on the J_{MC}, depending on the material toughness, as shown schematically in Fig. 9. For brittle materials (class A), such as glass [4], 0.29C-0.83Cu and 1.25C bainitic steels [5-7], where fracture was controlled by tensile stress and local crack-opening displacements, the addition of mode III loading components had little or no effect on the J_{ic} value (mode I J component of J_{MC}), but tended to increase the J_{MC} value. For those materials with intermediate toughness (class B), such as AISI 1090 steel [8], the introduction of a mode III loading component decreased J_{ic} values moderately, and had little effect on J_{MC}. For tough steels (class C), such as a high purity rotor steel [9] and the F82-H steel [2,3], which failed primarily by microvoid coalescence, the addition of a shear stress resulted in plastic shear localization

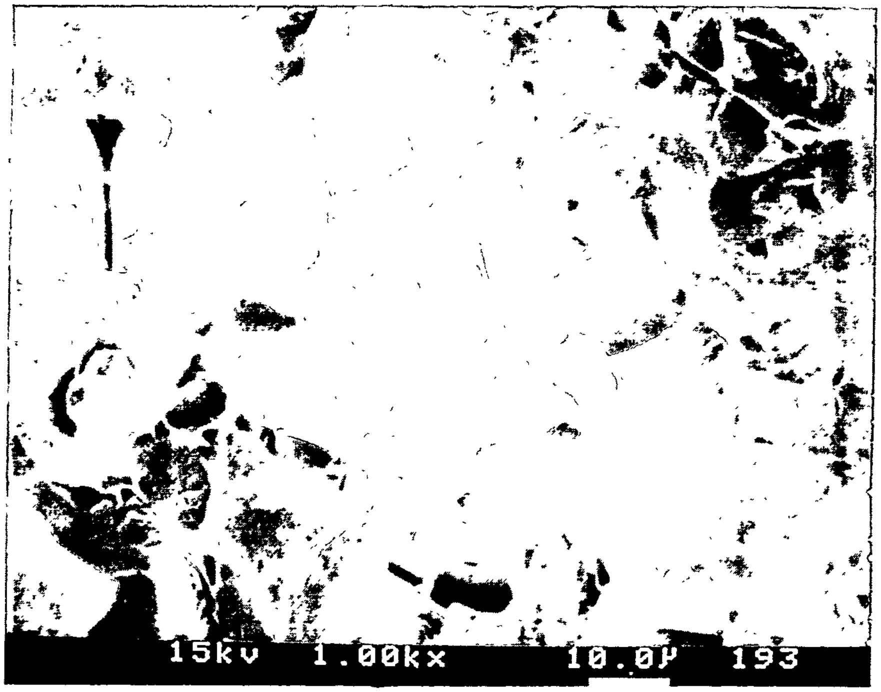

Fig. 5. SEM fractograph showing the quas-icleavage nature fracture surfaces of a mode I specimen tested at -90°C.

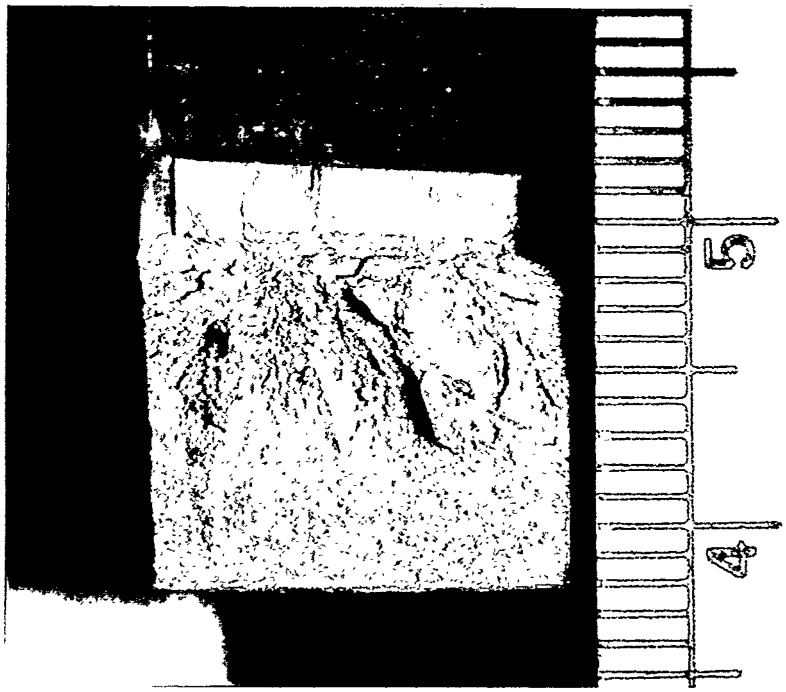

Fig. 6. An overview of a mixed mode I/III specimen tested at -95°C, showing the crack grows in mixed mode for about 0.5 mm and then switched to mode I.

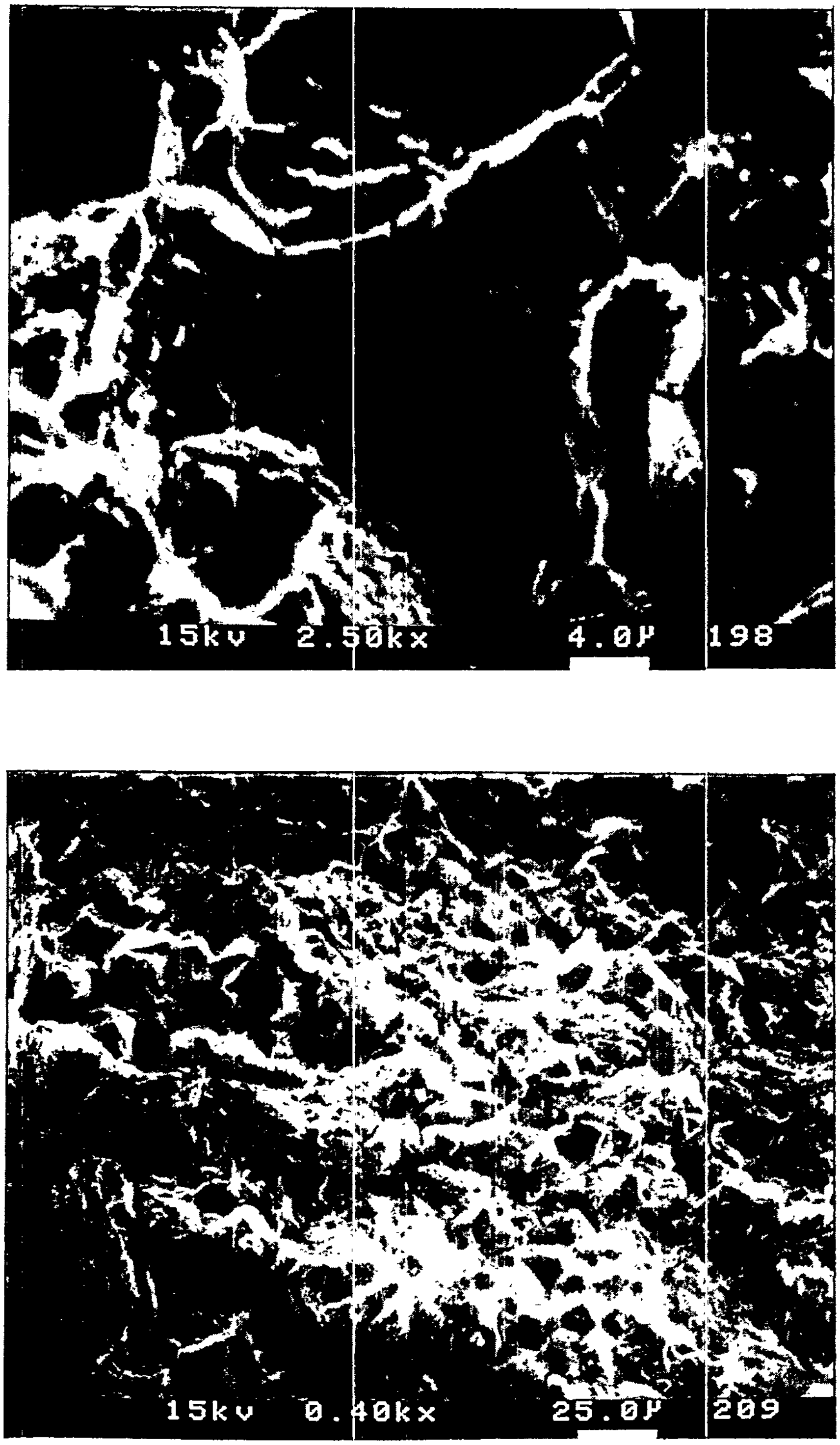

Fig. 7. SEM fractographs of intergranular facets and plastic tearing on the fracture surface within 0.5 mm from original crack tip where the crack is in mixed mode in a mixed mode specimen tested at -95°C. a. lower magnification; b. higher magnification.

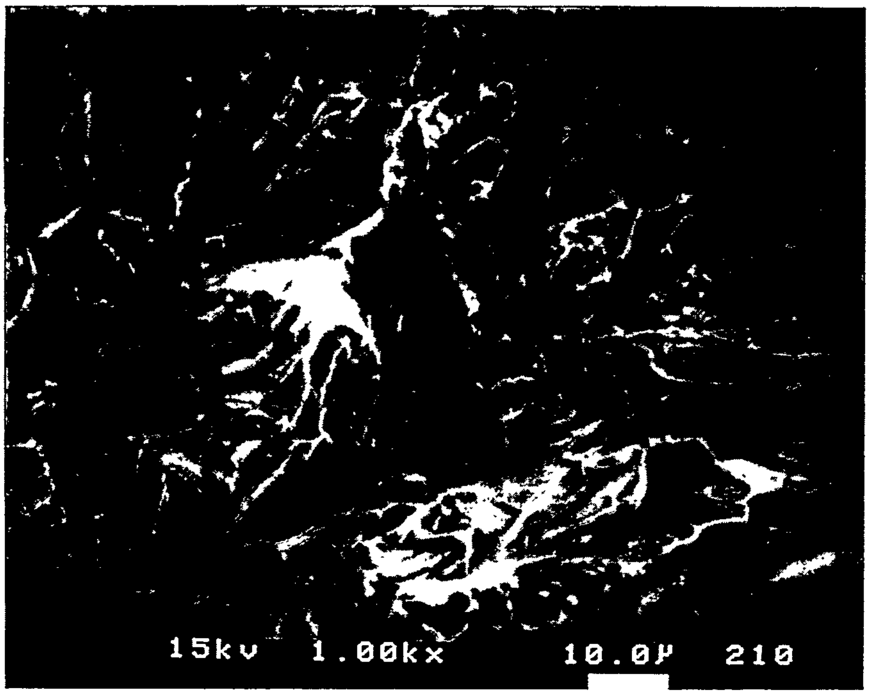

Fig. 8. SEM fractograph of cleavage surface in a mixed mode specimen tested at -95°C after the crack mode becomes mode I.

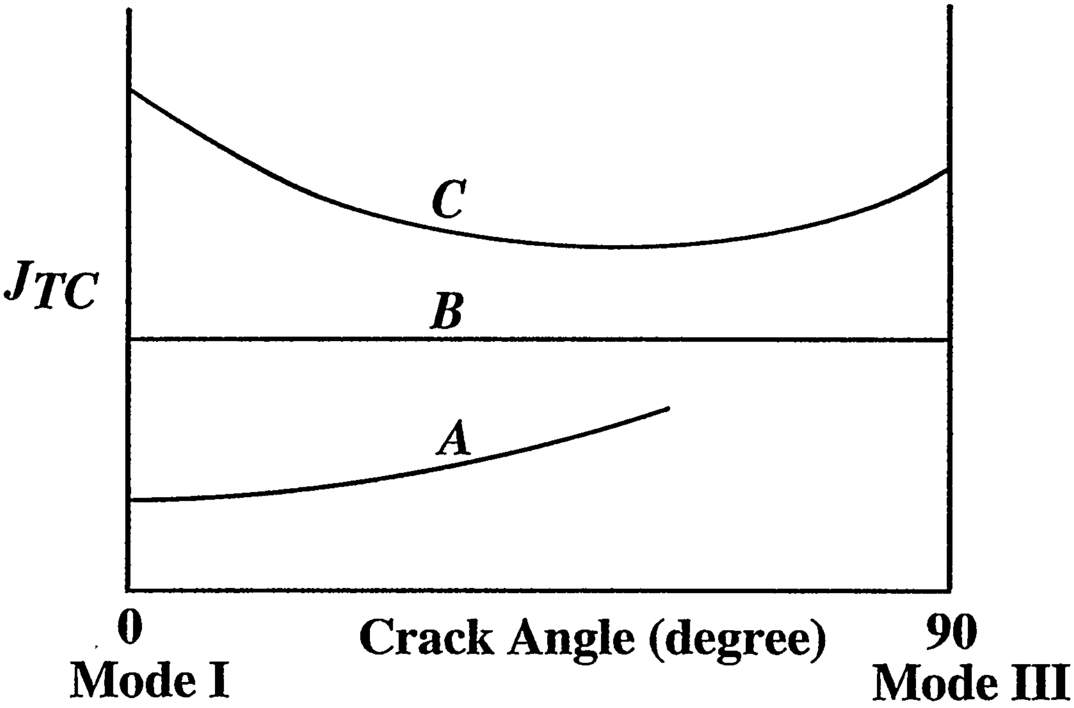

Fig. 9. Dependence of mixed I/III *J*-integral toughness for various structural materials on crack inclination angles. Brittle materials, intermediate tough materials,and tough materials follow curve **A**, curve **B**, and curve **C**, respectively.

ahead of the crack tip in the trajectory of the crack plane. Large stress concentrations emerge at hard particles in the path of such a sheared region because of strain incompatibility [10], which promotes either the decohesion of particles from the matrix or particle fracture (shear damage), and, therefore, void initiation. Continuum mechanics models [11,12] show that the presence of voids further promotes shear localization. Thus, an autocatalytic process of voids promoting shear localization and shear localization promoting voids follows. This process leads to void formation that limits the mode I plastic flow field and causes premature cracking by the coalescence of closely spaced voids under the action of the mode I stress. Accordingly, tough materials exhibit lower fracture toughness for a mixed-mode crack than that for a mode I crack.

The F-82H steel is a very tough steel at RT, and very sensitive to incompatibility stresses at the particle/matrix interface caused by the mode III component. Introducing a mode III loading component (shear stress on the crack plane) dramatically decreased toughness, from J_{IC} (284 kJ/m^2) to J_{MC} (150 kJ/m^2). As temperature decreased, the F82-H steel became brittle and sensitive to mode I loading, resulting a lower J_{IC} value. The result is consistent with the prediction of the mixed mode I/III fracture mechanics theory. However, that mixed mode loading contributes to both enhanced crack tip plasticity and intergranular fracture in the steel at low temperature has not been reported, and the mechanism is not clear yet.

The present results indicate that crack tip plasticity was increased by mixed mode loading, and suggest that at low temperature, mode I fracture toughness controls the performance of the steel, but at temperatures above RT, especially concerning fatigue and creep-fatigue life, the mixed mode loading should be addressed because it lowers fracture toughness and increases crack tip plasticity.

CONCLUSIONS

1. At RT, F-82H steel is a very tough steel. J_{IC} is about 284 kJ/m^2. Mixed-mode I/III loading dramatically lowered the fracture toughness. With a crack angle of 35°, where the ratio of $P_{iii}/(P_{iii} + P_i)$ is 0.41, the J_{MC} is only 150 kJ/m^2.

2. At RT, loading modes did not change the fracture mode (microvoid coalescence). However, the mode III loading component reduced fracture surface roughness and void size significantly.

3. At about -90°C, J_{MC} (50 kJ/m^2) was greater than J_{IC} (30 kJ/m^2).

4. At -90°C, mode I crack initiated and grew by quasi-cleavage fracture; but at -95°C the mixed mode I/III crack initiated and propagated a short distance (0,5 mm) by a mixture of intergranular fracture and ductile tearing. When the mixed mode crack switched to mode I, it fractured by quasi-cleavage.

FUTURE WORK

To complete the tests and investigate the effects of loading modes on fracture behavior at low temperatures.

ACKNOWLEDGEMENTS

The assistance of Mr. J. L. Humason at Pacific Northwest Laboratory in developing the test methods is gratefully acknowledged. This research was supported by the Office of Fusion Energy of the U. S. Department of Energy under Contract DE-AC06-76RLO 1830 with Battelle Memorial Institute.

REFERENCES

1. S. V. Kamat and J. P. Hirth, Scripta Metall. Mater., 30 (1994), pp. 145-48.
2. Huaxin Li, R. H. Jones, J. P. Hirth, and D. S. Gelles, J. of Nuclear Materials, 1994, in press.
3. Huaxin Li, R. H. Jones, J. P. Hirth, and D. S. Gelles, Metall. and Mater. Trans. A, 1994, submitted.
4. A. R. Rosenfield and W. H. Duckworth: *Int. J. Fract.*, 1987, vol. 32, p. R59.
5. M. Manoharan, J. P. Hirth, and A. R. Rosenfield: *J. of Testing and Evaluation*, 1990, vol. 18, no. 2, p. 106.
6. M. Manoharan: *Scripta Metall. Mater.*, 1992, vol. 26, p. 1187.
7. M. Manoharan, J. P. Hirth, and A. R. Rosenfield: *Scripta Metall. Mater.*, 1989, vol. 23, p. 763 and p. 1647.
8. M. Manoharan, S. Raghavachary, J. P. Hirth, and A. R. Rosenfield: *J. of Eng. Materials and Technology*, 1989, vol. 111, October, p. 440.
9. S. Raghavachary, A. R. Rosenfield, and J. P. Hirth: *Met. Trans. A*, 1990, vol. 21A, p. 2539.
10. T. D. Lee, T. Goldenberg, and J. P. Hirth: *Met. Trans. A*, 1979, vol. 10A, p. 199.
11. R. J. Asaro and J. R. Rice: *J. Mech. Phys. Solids*, 1977, vol. 23, p. 309.
12. V. Tvergaard, A. Needleman, and K. K. Lo: *J. Mech. Phys. Solids*, 1981, vol. 29, p. 115.

EMBRITTLEMENT OF Cr-Mo STEELS AFTER LOW FLUENCE IRRADIATION IN HFIR – R. L. Klueh and D. J. Alexander

OBJECTIVE

The goal of this work is the determination of the possible effect of the simultaneous formation of helium and displacement damage during irradiation on the Charpy impact behavior.

SUMMARY

Subsize Charpy impact specimens of 9Cr-1MoVNb (modified 9Cr-1Mo) and 12Cr-1MoVW (Sandvik HT9) steels and 12Cr-1MoVW with 2% Ni (12Cr-1MoVW-2Ni) were irradiated in the High Flux Isotope Reactor (HFIR) at 300 and 400°C to damage levels up to 2.5 dpa. The objective was to study the effect of the simultaneous formation of displacement damage and transmutation helium on impact toughness. Displacement damage was produced by fast neutrons, and helium was formed by the reaction of 58Ni with thermal neutrons in the mixed-neutron spectrum of HFIR. Despite the low fluence relative to previous irradiations of these steels, significant increases in the ductile-brittle transition temperature (DBTT) occurred. The 12Cr-1MoVW-2Ni steel irradiated at 400°C had the largest increase in DBTT and displayed indications of intergranular fracture. A mechanism is proposed to explain how helium can affect the fracture behavior of this latter steel in the present tests, and how it affected all three steels in previous experiments, where the steels were irradiated to higher fluences.

PROGRESS AND STATUS

Introduction

In addition to the displacement damage formed in a fusion power plant first wall by high-energy neutrons from the fusion reaction, helium will be formed by transmutation. About 110 appm He will form in a martensitic steel in one year of operation at a wall loading of 1 MW/m2. This contrasts with <6 appm He formed in the steel irradiated for one year in a fast reactor, even though the displacement damage is similar. Irradiation of ferritic steels in a fast reactor below ≈450°C can cause an increase in strength. This increase in strength is accompanied by an increase in the ductile-brittle transition temperature (DBTT), and a decrease in the upper-shelf energy (USE), as measured in a Charpy test [1-7]. DBTT values can be raised to well above room temperature.

Because no operating fusion reactors are available, simulation techniques are used to study the simultaneous effects of displacement damage and transmutation helium. One simulation technique involves adding nickel to the ferritic/martensitic steels and irradiating them in a mixed-spectrum reactor, such as the High Flux Isotope Reactor (HFIR) [8]. Displacement damage is produced by the fast neutrons in the spectrum, and helium is generated from 58Ni by a two-step transmutation reaction with the thermal neutrons in the spectrum. For a ferritic steel containing 2% Ni, the He/dpa ratio produced during irradiation in HFIR approximates that of a tokamak reactor. This technique has been used to examine the effect of helium on swelling at 300 to 600°C [9-11], on tensile properties after irradiation at 50, 300, 400, and 500°C [12-14], and on impact properties of subsize Charpy specimens irradiated at 50, 300, and 400°C [3,7,15].

Data have been published for the 9Cr-1MoVNb (modified 9Cr-1Mo) and 12Cr-1MoVW (the Sandvik HT9 composition) steels and these steels with up to 2% Ni irradiated to ≈27 and 40 dpa at 300 and 400°C, respectively, in the HFIR [15]. The shifts in DBTT observed after irradiation at 400°C were the largest ever observed for these steels. Steels with 2% Ni showed a larger effect than steels without the nickel additions. Furthermore, the steels that contained helium developed much larger shifts than those irradiated in a fast reactor, where little helium formed during irradiation.

For this paper, Charpy impact specimens of 9Cr-1MoVNb and 12Cr-1MoVW steels and the 12Cr-1MoVW steel with 2% Ni (12Cr-1MoVW-2Ni) were irradiated in the HFIR at 300 and 400°C to 2.5 dpa or less. The results were compared with results from doped and undoped steels irradiated to higher fluences in the HFIR [3,15] and in fast reactors [2,4,6]. Note that fluences of 2.5 dpa and less are designated "low" fluences in this paper. By low, it is meant that they are low relative to previous HFIR and fast reactor experiments, to which they will be compared. It is recognized that even these "low" fluences are high (by several orders of magnitude) relative to fluences under which some pressure vessel steels are embrittled when irradiated in a light water reactor.

Experimental Procedure

The 9Cr-1MoVNb (heat XA 3590), 12Cr-1MoVW (heat XAA 3587), and 12Cr- 1MoVW-2Ni (heat XAA 3589) steels were 25-kg electroslag-remelted (ESR) heats prepared by Combustion Engineering, Inc., Chattanooga, Tennessee. These heats were irradiated previously in the HFIR [3,7,12-15] and the EBR-II [4]. Chemical compositions are given in Table 1.

Table 1. Composition of 9Cr-1MoVNb and 12Cr-1MoVW Heats of Steel

	Concentration (wt%)		
Element	9Cr-1MoVNb (XA 3590)	12Cr-1MoVW (XAA 3587)	12Cr-1MoVW-2Ni (XAA 3589)
C	0.09	0.21	0.20
Mn	0.36	0.50	0.49
P	0.008	0.011	0.011
S	0.004	0.004	0.004
Si	0.08	0.18	0.14
Ni	0.11	0.43	2.27
Cr	8.62	11.99	11.71
Mo	0.98	0.93	1.02
V	0.21	0.27	0.31
Nb	0.063	0.018	0.015
Ti	0.002	0.003	0.003
Co	0.013	0.017	0.021
Cu	0.03	0.05	0.05
Al	0.013	0.030	0.028
B	<0.001	<0.001	<0.001
W	0.01	0.54	0.54
As	<0.001	<0.001	<0.001
Sn	0.003	0.002	0.002
Zr	<0.001	<0.001	<0.001
N	0.050	0.020	0.017
O	0.007	0.005	0.007
Fe	Bal	Bal	Bal

Charpy impact specimens were machined from 63.5-mm-thick hot-rolled plate in the normalized-and-tempered condition. The austenitizing treatment for the 9Cr-1MoVNb steel was 0.5 h at 1040°C and for the 12Cr-1MoVW and 12Cr-1MoVW-2Ni steels was 0.5 h at 1050°C, after which they were air cooled. Tempering was for 1 h at 760°C for 9Cr-1MoVNb, for 2.5 h at 780°C for 12Cr-1MoVW, and for 5 h at 700°C for 12Cr-1MoVW-2Ni. Tempered martensite microstructures were obtained by such heat treatments. Details on heat treatment and microstructure have been published [8].

Miniature Charpy specimens were machined from the heat-treated plate in the longitudinal (L-T) orientation. The subsize specimens were one-half the standard size: 5 by 5 by 25.4 mm with a 0.76-mm-deep 30° V-notch with a 0.05- to 0.08-mm-root radius. Such miniature specimens show a transition from ductile to brittle fracture similar to that found in full-sized Charpy specimens, although over a different temperature range [16,17].

Two capsules, each containing 16 specimens of the three steels, were irradiated in the HFIR at nominal temperatures of 300 and 400°C. For irradiation, specimens were enclosed in stainless steel holders, and the holders were placed inside aluminum sleeves. Nuclear heating was used to achieve the desired temperature. To control the temperature, the gas gap between the outer diameter of the steel specimen holder and the aluminum sleeve was adjusted to compensate for the variation in nuclear heating rate along the length of the capsule. (Instrumented capsules have been used previously to verify nuclear heating rates.) A thermal gradient exists from the interior to the exterior surface of the specimens; this has been calculated to be less than 45°C. Three flux monitors were loaded into each capsule, and they were analyzed to determine the fluences achieved. Displacement damage and helium concentrations were calculated based on these fluences.

The specimens were intended to be irradiated to 10 dpa. Unfortunately, they were inserted into the HFIR just prior to the unforeseen suspension of operation of the reactor. Because of the reduction in operating power from 100 to 85 MW when HFIR was restarted, it was decided not to irradiate the specimens beyond the one 22-day cycle they obtained when originally inserted.

The capsules were irradiated in a peripheral target position of the HFIR to a maximum total fluence of $\approx 8.4 \times 10^{25} n/m^2$, a maximum fast fluence of $\approx 2.3 \times 10^{25} n/m^2$ ($E > 0.11$ MeV), and a thermal fluence of $\approx 3.4 \times 10^{25} n/m^2$. At the capsule midplane, a displacement-damage level of ≈2.5 dpa was obtained. The fluence decreased symmetrically with distance from the midplane, and the displacement-damage levels at the ends of the capsules were ≈1.1 dpa. Displacement-damage levels for specimens between the midplane and the ends varied systematically between these limits. Similarly, helium levels varied, depending on the position of the specimens in the capsule and the amount of nickel in the alloys. Specimens irradiated at 300°C were near the ends of the capsules, which meant they were irradiated to the lowest dpa and contained the least helium. Because of space limitations, a limited number of specimens were irradiated (six each for the 9Cr-1MoVNb and 12Cr-1MoVW steels, but only four specimens for the 12Cr-1MoVW-2Ni steel).

Charpy tests were conducted in a pendulum-type, instrumented impact machine modified for subsize specimens [17,18]. To obtain the DBTT and USE, impact energy-temperature curves were generated by fitting the data with a hyperbolic tangent function. The primary objective was the determination of the shift in DBTT. The DBTT was determined for the energy corresponding to half of the USE and at fixed energy levels of 5.5 and 9.2 J (analogous to the 41 and 68 J often used for full-size Charpy specimens) [17].

Results

Table 2 shows the results for the Charpy impact tests. The DBTT and USE are given, along with the shift in DBTT (ΔDBTT) calculated using the DBTT determined at one-half the USE. Displacement-damage levels and helium concentrations for each set of specimens are given. Specimens irradiated at 400°C had damage levels of 2.1 to 2.5 dpa, and those irradiated at 300°C were 1.1 to 2 dpa.

Helium concentrations were small and varied, depending on the nickel concentration of the steel and the fluence achieved. Because the 9Cr-1MoVNb steel contained only 0.1% Ni, compared to 0.4% in the 12Cr-1MoVW steel (Table 1), it contained <1 appm He at both 300 and 400°C. The maximum helium concentration in the 12Cr-1MoVW steel was slightly more than 1 appm. The most helium was ≈3.5 appm in the 12Cr-1MoVW-2Ni irradiated at 400°C. At 300°C, this steel contained less than half this amount, because the specimens were at the ends of the capsule, where they received 1.5 dpa or less.

Despite the low fluences, large shifts in DBTT occurred. The steels without a nickel addition--the 9Cr-1MoVNb and 12Cr-1MoVW steels--developed a larger ΔDBTT at 300°C than at 400°C. For 12Cr-1MoVW-2Ni steel, however, the ΔDBTT at 400°C was larger than at 300°C.

Table 2. Impact Properties of Cr-Mo Steels Irradiated in HFIR

Conditions			Transition Temperature (°C)			ΔDBTT[a]	Use
Temp. (°C)	Displ. (dpa)	He (appm)	5.5J	9.2J	1/2 USE	(°C)	(J)
			12Cr-1MoVW (Heat XAA 3587)				
Control	0	0	-58	-35	-18	26	
300	1.1-2.0	0.4-1.0	150	123	148	166	17
400	2.2-2.5	1.0-1.3	106	141	128	146	16
			12-Cr-1MoVW-2Ni (Heat XAA 3589)				
Control	0	0	-57	-25	-32		17
300	1.2-1.5	1.1-1.6	98	120	109	141	15
400	2.2-2.4	3.1-3.5	162	–	148	180	9
			9Cr-1MoVNb				
Control	0	0	-49	-37	-29		25
300	1.1-1.9	0.3-0.6	41	43	45	74	26
400	2.1-2.3	0.7-0.8	12	19	27	56	28

Selected fractured surfaces were examined by scanning electron microscopy (SEM). Fracture surfaces of the irradiated 9Cr-1MoVNb and 12Cr-1MoVW steels appeared similar to those of the steels in the unirradiated condition: ductile shear on the upper shelf and cleavage or quasi-cleavage on the lower shelf, with a combination of these in the transition region. Most observations on 12Cr-1MoVW-2Ni were similar to the steels without nickel additions. However, as seen in Fig. 1, isolated areas of a 12Cr-1MoVW-2Ni specimen irradiated at 400°C and tested in the transition region showed indications of intergranular separation.

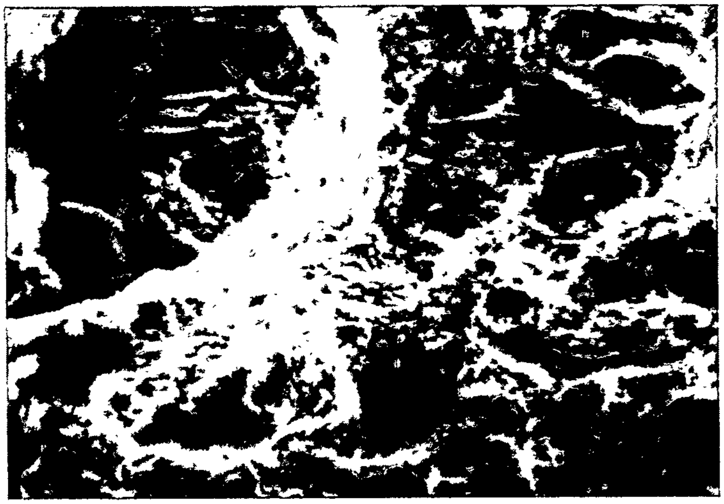

Fig. 1. Scanning electron micrograph of fracture surface of 12Cr-1MoVW-2Ni steel Charpy specimen irradiated at 400°C that shows indications of intergranular fracture.

Discussion

The observations will first be compared with previous results, followed by a discussion of possible mechanisms to explain these and other observations.

Comparison With Previous Work

Hu and Gelles [6] irradiated 9Cr-1MoVNb and 12Cr-1MoVW steels to 13 and 26 dpa at 390°C in the Experimental Breeder Reactor (EBR-II), a fast reactor where little helium forms. The ΔDBTT saturated with fluence after 13 dpa at values of 54 and 124-144°C, respectively [6]. Irradiation of the 12Cr-1MoVW heat (XAA 3787) used in this experiment had a ΔDBTT of 122°C when irradiated to 12 dpa at 390°C in EBR-II [4]. Other studies of 12Cr-1MoVW steel irradiated in EBR-II and the Fast Flux Test Facility (FFTF) at 390-420°C indicated that saturation occurred by 10 dpa [4,19,20].

Even for the low fluences of this experiment, embrittlement, as evidenced by the shift in DBTT, was observed at both 300 and 400°C. Examination of the ΔDBTT data in Table 2 after irradiation in HFIR at 400°C indicates that the ΔDBTT for the 9Cr-1MoVNb (56°C) and 12Cr-1MoVW (146°C) steels approached the saturation values in a fast reactor (54 and 124-144°C, respectively) [6]. Saturation in a fast reactor occurred by 10 dpa, the lowest fluences used [4,6,19,20]. Because little helium formed in 9Cr-1MoVNb (<1 appm He) and 12Cr-1MoVW (<1.5 appm He) specimens irradiated to 2.2-2.5 dpa at 400°C in HFIR in the present tests and the ΔDBTT of the steels approached those for irradiation in a fast reactor at 400°C, it is concluded that the saturation ΔDBTT due to displacement damage (in the absence of a helium effect) must be reached in as little as 2 dpa.

The results for 9Cr-1MoVNb and 12Cr-1MoVW steels (Table 2) show that the ΔDBTT was larger at 300°C than at 400°C, even though the fluence at 300°C was slightly less than at 400°C. Such a decrease in ΔDBTT with an increase in temperature agrees with results from fast reactor irradiations at 365 to 550°C [2,4,6,19]. Fast reactor irradiation temperatures below ≈365°C cannot be achieved, so it is not known if the 300°C values in Table 2 are saturation values.

Although the ΔDBTT for 9Cr-1MoVNb (56°C) and 12Cr-1MoVW (146°C) after irradiation to 2.2-2.5 dpa at 400°C are similar to saturation values observed in fast reactors (54 and 124-144°C for 9Cr-1MoVNb and 12Cr-1MoVW, respectively), they are less than after 40 dpa in HFIR (202 and 242°C, respectively). The larger ΔDBTTs after 40 dpa were attributed to the simultaneous production of helium and displacement damage in HFIR, compared to just displacement damage in a fast reactor [3,15]. Because of the small amounts of helium in the 9Cr-1MoVNb and 12Cr-1MoVW steels in the present experiment (1-1.3 appm), it is not unexpected that the steels behave as they do in a fast reactor. In both cases, helium levels were too small to affect the ΔDBTT.

A similarity in saturation behavior between a fast-spectrum and a mixed-spectrum reactor was also observed for 1/3-size Charpy specimens of 12Cr-1MoVW irradiated in EBR-II [6] and in the mixed-spectrum Oak Ridge Research Reactor (ORR) [19]. Because of the low thermal flux in the ORR, irradiation of 12Cr-1MoVW steel to ≈7 dpa at 330 and 400°C produced <3 appm He. The ΔDBTT results for 7 dpa at 400°C were similar to those after irradiation to 13 and 26 dpa in EBR-II at 390°C, where similar small amounts of helium were generated [6]. Interpolation of the ORR results at 330 and 400°C to 365°C indicated good agreement between 12Cr-1MoVW irradiated to 7 dpa in ORR and irradiated to saturation (10 dpa) at 365°C in FFTF [19]. The ΔDBTT at 330°C exceeded that at 400°C, similar to observations on temperature effects in EBR-II and the present experiment.

The 12Cr-1MoVW-2Ni steel behaved differently from the 9Cr-1MoVNb and 12Cr-1MoVW steels (Table 2) in that the ΔDBTT for 12Cr-1MoVW-2Ni at 400°C exceeded that at 300°C and was greater than that for 12Cr-1MoVW at 300 and 400°C. Furthermore, the ΔDBTT at 400°C was double the shift observed for 12Cr-1MoVW-2Ni irradiated in EBR-II to 12 dpa at 390°C [4]. Qualitatively, these observations on 12Cr-1MoVW-2Ni agree with those in the high-fluence HFIR irradiations [15], except that the shifts were not as great as for the previous tests. Also, in the higher fluence experiments in HFIR [15], the ΔDBTT values at 400°C for 9Cr-1MoVNb and 12Cr-1MoVW steels were larger than those at 300°C [15], just as they were for 12Cr-1MoVW-2Ni in the present experiments and for 12Cr-1MoVW in an earlier high-fluence experiment [3].

In previous HFIR irradiations [3,7,15], higher fluences were used, which produced higher helium concentrations, even without nickel additions. The "reverse temperature effect" (i.e., a higher ΔDBTT at 400 than 300°C) was observed for 9Cr-1MoVNb, 9Cr-1MoVNb-2Ni, 12Cr-1MoVW, and 12Cr-1MoVW-2Ni after high-fluence HFIR irradiations [3,15], but not after fast reactor irradiations [4,7]. Also, after HFIR irradiation, a larger ΔDBTT was observed for the 9Cr-1MoVNb-2Ni and 12Cr-1MoVW-2Ni steels than for these steels without nickel. These observations were attributed to helium and indicated that as little as 30 appm helium significantly affected embrittlement at 400°C [3,15].

The most helium in the present tests formed in the 12Cr-1MoVW-2Ni irradiated at 400°C. Intuitively, this small amount of helium (3-3.5 appm) would not be expected to affect the impact toughness; however, the observations are consistent with the previous high-helium results [3,15].

Since a larger ΔDBTT than the saturation for fast reactors and a reverse temperature effect were observed in previous HFIR experiments for both nickel-doped and undoped steels [3,15], the effects are not related to the nickel additions made to the standard compositions. In one experiment [3], 12Cr-1MoVW steel irradiated in HFIR at 400°C to ≈7 dpa and ≈18 appm He developed a ΔDBTT of 195°C, compared to the saturation value of 124-144°C after 13 dpa in EBR-II at 390°C. After irradiation of 12Cr-1MoVW in HFIR at 400°C to ≈40 dpa and ≈100 appm He, a still larger ΔDBTT of 242°C was observed. The 9Cr-1MoVNb irradiated to ≈40 dpa and 32 appm He at 400°C had a ΔDBTT of 204°C, compared to a saturation at 13 dpa in EBR-II at 390°C of 56°C. All experiments contained specimens at 300°C, and a reverse temperature effect occurred in each case.

Graphical comparison of the ΔDBTTs from HFIR and EBR-II for 9Cr-1MoVNb (Fig. 2) and 12Cr-1MoVW (Fig. 3) indicates the dichotomy of the irradiation effects in the two reactors. Figures 2 and 3 contain data from all HFIR experiments [3,5,7,15], including those at 50°C [5,7]. Data are labeled with dpa and helium concentration (in appm). The only EBR-II data shown are those of Hu and Gelles [6], because these are the only data from a single heat of steel over a range of temperatures. Fast reactor data for other heats of steel irradiated around 400°C agree with the trends in the figures [1,4].

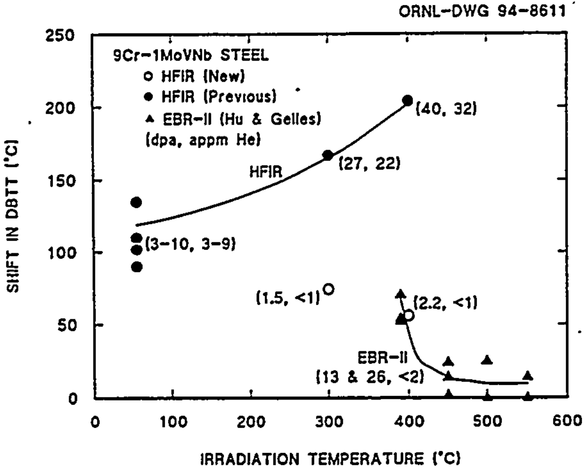

Fig. 2. A plot of the shift in DBTT against irradiation temperature for 9Cr-1MoVNb steel irradiated in HFIR and EBR-II. Numbers in parentheses adjacent to the data show the displacement damage in dpa and helium concentration in appm.

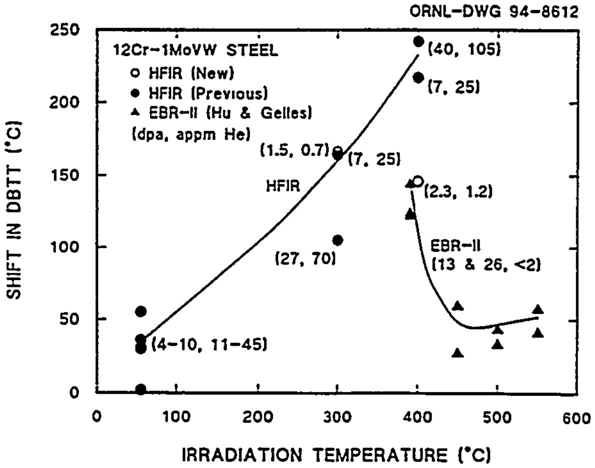

Fig. 3. A plot of the shift in DBTT against irradiation temperature for 9Cr-1MoVNb steel irradiated in HFIR and EBR-II. Numbers in parentheses adjacent to the data show the displacement damage in dpa and helium concentration in appm.

The 300 and 400°C data from the present study are comparable to the fast-reactor data; therefore, these data were not used to draw the trend curves for the HFIR data. For 9Cr-1MoVNb, the ΔDBTT for the 300°C irradiation from the present experiment falls significantly below data from HFIR after 27 dpa (Fig. 2). However, the ΔDBTT for 12Cr-1MoVW irradiated at 300°C agrees with one point (7 dpa) from a previous HFIR experiment [3], but not with the other (27 dpa) [15], which had a much smaller ΔDBTT. No explanation for this discrepancy for the 27 dpa irradiation exists, other than the high degree of scatter in the five specimens available for the 27 dpa tests [15] and less scatter for the eight specimens for the 7 dpa test [3].

Proposed Mechanism for Helium-Affected Fracture

Transmutation helium can affect the behavior of an irradiated alloy in three ways [21,22]. First, helium stabilizes vacancy clusters, which, in turn, cause an increase in the number of interstitial clusters (i.e., helium ties up vacancies and reduces interstitial-vacancy recombination). Interstitial clusters can then grow into dislocation loops and increase the strength [21,22]. Secondly, helium stabilizes the clusters to a higher temperature than in the absence of helium [21,22]. The third effect involves the migration of helium to grain boundaries during irradiation, which can then affect mechanical properties [21,22].

One clue to how helium affected fracture in the present experiments through the third helium effect is the observation that the 12Cr-1MoVW-2Ni steel irradiated to 2.2-2.4 dpa at 400°C showed indications of intergranular fracture that were not observed on the 9Cr-1MoVNb and 12Cr-1MoVW steels (Fig. 1). Previous observations on the 9Cr-1MoVNb, 9Cr-1MoVNb-2Ni, 12Cr-1MoVW, and 12Cr-1MoVW-2Ni steels irradiated to higher fluences in HFIR also showed indications of intergranular fracture [15]. Intergranular fracture was not observed after irradiation in fast reactors or in the unirradiated condition [2,6,15].

Figure 4 is a schematic diagram from Hawthorne [23] illustrating how the increase in flow stress due to irradiation hardening can cause a shift in DBTT. Hardening can be caused by radiation-produced point defects, which collect into dislocation loops to form barriers to dislocation motion, and by irradiation-induced precipitates. These two effects contribute to the hardening of steels irradiated in HFIR or a fast reactor, such as EBR-II.

Tensile studies on the nickel-doped and undoped steels irradiated in HFIR indicated that helium provided an increment of hardening above that due to radiation-produced defects and precipitates [14]. This hardening by helium, presumably through the first and second mechanisms discussed above, was concluded to saturate at around 80 appm He [14]. However, a recent reanalysis of all 400°C data [13,14] suggests that data scatter makes a definite conclusion concerning saturation at 80 appm He somewhat uncertain. What can be stated is that there is probably a slight increment of hardening at 400°C due to helium, presumably caused by the first two mechanisms discussed above. Low-temperature data indicate that the magnitude of the hardening due to helium is larger at 50°C than at 400°C [12]. Therefore, hardening by dislocation loops, precipitates, and helium could all contribute to the increase in flow stress for HFIR irradiation (Fig. 4).

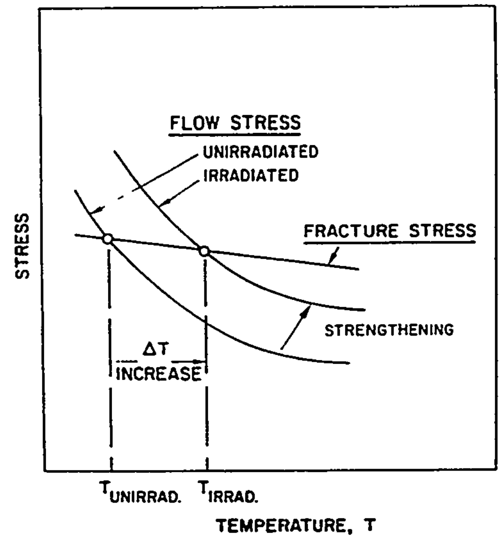

Fig. 4. Schematic diagram of mechanism by which strength increase due to irradiation causes an upward shift in the ductile-brittle transition temperature

The ΔDBTT after HFIR irradiation at 400°C exceeded the saturation value after fast reactor irradiation and did not appear to saturate with helium concentration [15]. Thus, this shift was not caused by the increase in flow stress alone (illustrated in Fig. 4). Rather, the larger shift in the presence of helium was attributed to a lower fracture stress caused by a change in fracture mode [15,24].

An increase in DBTT can be caused by: (1) more or larger flaws, (2) less resistance to the initiation of a flaw, and (3) less resistance to the propagation of a flaw. Inclusions or carbides are likely sources of microcracks that initiate fracture in steels [25,26]. The larger ΔDBTT for 12Cr-1MoVW than 9Cr-1MoVNb in FFTF (little helium) was attributed to the larger amounts of large precipitate particles in 12Cr-1MoVW steel [20]. The 12Cr-1MoVW contains twice as much precipitate as 9Cr-1MoVNb because it contains twice as much carbon [27].

It is now proposed that when the steels contain sufficient helium, the microcrack source could be a helium-containing bubble or bubbles on a prior-austenite grain boundary or a lath boundary. Helium is envisioned to collect into small cavities that under stress become nuclei for fracture and/or enhance crack propagation, explaining why fracture surfaces of HFIR-irradiated, helium-containing steels contain intergranular facets.

This hypothesis can be used to explain the reverse temperature effect. Formation of helium bubbles at grain boundaries will require helium diffusion to prior-austenite grain boundaries or lath boundaries. More rapid diffusion at 400°C than at 300°C means that at 400°C more helium reaches boundaries to produce larger bubbles and a larger ΔDBTT. At 300°C, helium takes longer to reach the boundary and bubbles take longer to form. Until enough helium is available at the boundary, helium will not affect fracture.

As helium generation at 300°C is increased by higher fluences (longer diffusion times) or higher helium generation rates, the larger helium concentration will produce larger bubbles with an increase in the ΔDBTT. This was observed for the 9Cr-1MoVNb-2Ni and 12Cr-1MoVW-2Ni irradiated to 27 dpa at 300°C, where these steels developed a larger ΔDBTT than the steels without any nickel additions [15]. The hypothesis also explains why the ΔDBTT for 9Cr-1MoVNb after 27 dpa in HFIR at 300°C was much larger than after 1-2 dpa at 300°C (Fig. 2), but was not as large as after the 400°C irradiation. A possible problem with this explanation is that the ΔDBTT for 12Cr-1MoVW after 7 dpa [3] at 300°C is similar to that expected without helium in EBR-II (determined by extrapolation from 400°C) and after 1-2 dpa in HFIR (the abnormally low 27 dpa point in HFIR was ignored for this discussion). This could be explained by the ΔDBTT in this case being determined by the larger amount of precipitate formed in 12Cr-1MoVW [20,27]. That is, even in the presence of helium, the fracture process at 300°C in 12Cr-1MoVW is controlled by the precipitates, just as it is in the absence of helium. This will be discussed further below.

Fracture Behavior

From the above discussion, it follows that the fracture mechanism will depend on various factors, including chemical composition, irradiation temperature, and helium concentration. A comparison of Figs. 2 and 3 indicates that the ΔDBTT for 12Cr-1MoVW irradiated in HFIR at 50°C is less than half that for 9Cr-1MoVNb [7]. The opposite is true after EBR-II irradiation at 390°C [6], where the ΔDBTT for 12Cr-1MoVW is over twice that for 9Cr-1MoVNb. On the other hand, for irradiation in HFIR at 300 and 400°C to a high dpa, the ΔDBTT of 12Cr-1MoVW is just slightly greater than that for 9Cr-1MoVNb.

It was previously suggested that the observations for HFIR irradiation at 50 and 300-400°C mean 9Cr-1MoVNb is more susceptible to helium [7]. As pointed out above, the results for HFIR irradiation at 300°C may mean that helium has relatively less effect on 12Cr-1MoVW because its properties are already adversely affected by the greater amount of precipitate in its microstructure. The helium effect at 300 and 400°C was assumed to cause helium-assisted intergranular fracture. At 50°C, helium diffusion will not be sufficient to affect fracture. Furthermore, 9Cr-1MoVNb (0.1% Ni) contains less helium after irradiation than 12Cr-1MoVW (0.4% Ni) [7,13]. Finally, SEM showed no change in fracture mode after irradiation at 50°C [31]. Thus, helium cannot explain why 9Cr-1MoVNb has a higher ΔDBTT than 12Cr-1MoVW after irradiation at 50°C in HFIR [7], but has a lower ΔDBTT after irradiation in EBR-II at 390°C.

The most logical explanation is that the change in irradiation temperature caused a change in fracture behavior for one of the steels. Support for this is found in work by Gelles et al. [28], who observed δ-ferrite stringers on the cleavage fracture surface of 12Cr-1MoVW steel irradiated in EBR-II at 390°C [2], but not at 50°C in HFIR [28]. They concluded that the large ΔDBTT for 12Cr-1MoVW at 390°C was due to "precipitation at δ-ferrite stringers" in the 12Cr-1MoVW [2]. However, Gelles et al. [28] concluded that the reason for the difference between 9Cr-1MoVNb and 12Cr-1MoVW at 50°C was due to an irradiation effect on the 9Cr-1MoVNb. Carbide crystal structure alteration due to recoil dissolution was suggested as a possibility. It is now suggested that neutron irradiation at 50°C has an inherently greater relative hardening effect on 9Cr-1MoVNb than 12Cr-1MoVW, and then the magnitude of the effect reverses at higher temperatures because of the change in fracture mode of the 12Cr-1MoVW caused by precipitation.

Because of the irradiation-enhanced diffusion at 390°C in EBR-II, precipitates can form at δ-ferrite/martensite interfaces of the 12Cr-1MoVW steel during irradiation, and these precipitates cause a change in fracture behavior. No such diffusion-assisted precipitates would be expected to form after <10 dpa at 50°C. Thus, although the ΔDBTT of 12Cr-1MoVW at 50°C is about half as large as the ΔDBTT of 9Cr-1MoVNb, the change in fracture process for the 12Cr-1MoVW makes the ΔDBTT greater at the higher temperatures.

This explanation for the different relative behavior of 9Cr-1MoVNb and 12Cr-1MoVW at 50 and 390°C is supported by Anderko et al. [29], who showed that the δ-ferrite in 12Cr steels did not by itself cause early cleavage, as suggested by other investigators. Rather, they concluded that fracture was initiated at precipitates (carbides) on the δ-ferrite/martensite interface [2]. Therefore, the fact that δ-ferrite stringers were not observed by Hu and Gelles on the 12Cr-1MoVW fracture surface after the 50°C irradiation [28] suggests that the absence of interface precipitation at 50°C was probably responsible for the inherently better behavior of 12Cr-1MoVW than 9Cr-1MoVNb at 50°C. At higher temperatures where precipitation occurs, the carbides on the δ-ferrite/martensite interface cause a larger ΔDBTT for 12Cr-1MoVW than 9Cr-1MoVNb in the absence of helium because 9Cr-1MoVNb does not contain δ-ferrite and does not show a change in the fracture behavior with increasing temperature. This explanation implies that when helium is present, it does not necessarily have a greater effect on 9Cr-1MoVNb than 12Cr-1MoVW. Rather, the negative effect of precipitates in causing a large ΔDBTT for 12Cr-1MoVW in the absence of helium means there will be a relatively smaller effect of helium on this steel.

It should be pointed out that no δ-ferrite was detected in the heat of 12Cr-1MoVW (XAA 3587) used in this and other experiments [10,11], compared to a few percent found by Hu and Gelles [2]. This may mean that there was a very small amount present, but not detected, or that the more extensive radiation-induced precipitation in 12Cr-1MoVW (and not 9Cr-1MoVNb) in the temperature range 300-500°C [11,33] is responsible for the relative change in fracture behavior of 9Cr-1MoVNb and 12Cr-1MoVW between 50 and 400°C.

Figure 5 is a reproduction of the ΔDBTT-temperature relationship of Fig. 2 for the 9Cr-1MoVNb steel with a schematic representation of how the various irradiation effects are postulated to affect fracture behavior between 50 and 400°C. Although no data are available for irradiation in fast reactors below ≈365°C, a postulated curve for EBR-II irradiation down to 50°C has been added to the figure. Irradiation-produced defects and precipitation account for the DBTT shift in EBR-II. The relative contribution of the two processes is temperature dependent, with precipitation becoming more important with increasing temperature, but with the effect of both processes becoming negligible above ≈450°C.

Irradiation in HFIR was postulated to lead to a further increment of hardening caused by helium [12-14,21,22], which the tensile behavior indicated also decreases to zero above 425-450°C [13]. As discussed above, the extent of hardening due to helium has not been adequately assessed, and the extent of this region is uncertain. It could be wider or narrower than indicated. In this helium-affected region and the region where hardening is dominated by defects and precipitates, the brittle region of the Charpy curve is determined by cleavage and/or quasi-cleavage.

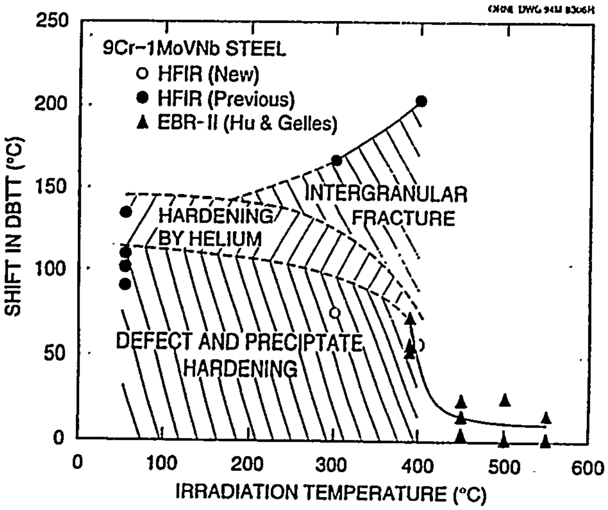

Fig. 5. The plot in Fig. 2 of the shift in DBTT against irradiation temperature for 9Cr-1MoVNb steel modified to indicate the postulated hardening and fracture mechanisms.

The third region in Fig. 5 designates where intergranular fracture occurs. Around 300°C and above, the change in fracture stress that causes intergranular fracture in the presence of helium becomes important. The shape of the intergranular portion of the diagram will depend on the helium concentration, temperature, and fluence.

Similar reasoning applies for the 12Cr-1MoVW steel, although a diagram for this steel will be complicated by the increase in the ΔDBTT with increasing temperature because of the change in fracture mode caused by precipitation. It should be noted that the 50°C tests for both steels were for relatively low-fluence irradiations (<10 dpa), and therefore, saturation may or may not have been achieved. The low-temperature irradiations also showed a slightly higher ΔDBTT for the nickel-doped steels [7], which agrees with the hardening effect of helium observed in tensile tests of the steels irradiated at 50°C [13,14].

Other Considerations

Alternate explanations for the HFIR observations that do not involve helium were considered in a previous paper [15]. Those considered included the effect of other transmutation reactions with thermal neutrons in HFIR, thermal aging effects, and nickel involvement in hardening effects. None of these provided a satisfactory explanation for the observations [15].

Since the previous publication [15], a mechanism for intergranular fracture of irradiated ferritic steels was proposed by Faulkner and co-workers [30, 31]. This involves irradiation-induced segregation of impurities to prior austenite grain boundaries or lath boundaries. They demonstrated that silicon and phosphorus segregate to lath boundaries in the martensitic steel FV448 (Fe-10.7Cr-0.64Mo-0.16V-1.0Mn-0.65Ni-0.3Nb-0.38Si-0.1C) when irradiated to 46 dpa in a fast reactor at 465°C. A segregation model was developed where a linkage exists between impurities (Si, P, etc.) and irradiation-produced point defects to drive the transfer of impurities to grain boundaries [30]. Kimura et al. observed intergranular fracture in 9Cr-2Mn-1W and 12Cr-6Mn-1W steels irradiated to 10 and 25 dpa at 365°C in FFTF [32]. Based on Auger spectroscopy of fracture surfaces, they attributed the fracture behavior to radiation-induced segregation of manganese and silicon to grain boundaries. However, for segregation to explain the present observations, helium would have to enhance segregation, since no similar effect occurs when these materials are irradiated in a fast reactor.

Faulkner and co-workers also found indications of irradiation-induced segregation of nickel to lath boundaries [30] in FV448. Segregation of nickel would amplify the helium produced at a boundary in nickel-containing steels over that involving helium diffusion alone. This could enhance the effect of helium, especially on steels with 2% Ni, irradiated to both the high displacement rates of previous experiments [15] and to the low displacement rates of the present experiments. However, it should not affect the relevance of the observations for fusion, since the concentration of helium on grain boundaries in the undoped steels irradiated to high doses and in the 12Cr-1MoVW-2Ni steel irradiated to low doses should still be well below concentrations relevant for boundaries in a fusion reactor first wall.

Implications for a Fusion Reactor

Considerable speculation is inherent in this discussion. However, if helium plays the role postulated, then impact toughness could be affected in a fusion reactor, where large amounts of helium would be generated in the first wall. With enough helium generated during irradiation, the ΔDBTT below 400°C could become as large or larger than at 400°C. It is unclear what might happen above 400°C, since no HFIR experiments on Ni-doped Charpy specimens have been conducted at these temperatures. The diffusion rate increases with temperature, thus increasing the rate at which helium can migrate to boundaries. On the other hand, irradiation hardening decreases rapidly above 400°C and disappears above ≈450°C [13]. Therefore, even if helium is present on boundaries, the reduced yield stress may preclude a larger ΔDBTT than observed for fast reactor irradiation.

It needs to be pointed out that the use of Charpy tests to evaluate embrittlement has limited applicability. A critical need exists for fracture toughness data, and an understanding of how the Charpy data are related to fracture toughness needs to be developed. Only with such data can the implications of the helium effects observed in these studies be evaluated in the context of fusion reactor design.

SUMMARY AND CONCLUSIONS

Charpy tests were made on 9Cr-1MoVNb, 12Cr-1MoVW, and 12Cr-1MoVW-2Ni steels irradiated in HFIR at 300 and 400°C to ≈2.5 dpa. Irradiation of the nickel-containing steels in the mixed-neutron spectrum of HFIR produced helium, but only small amounts because of the low fluence. The most helium was produced in the 12Cr-1MoVW-2Ni (≈3.5 appm at 400°C and 1.6 appm at 300°C). Less than 1.5 appm He was produced in the 12Cr-1MoVW and <1 appm He in the 9Cr-1MoVNb at either 300 or 400°C.

Charpy impact behavior of the 9Cr-1MoVNb and 12Cr-1MoVW steels irradiated to the low fluences at 400°C was comparable to these steels irradiated to 13-26 dpa in a fast reactor, such as EBR-II, and was unlike the behavior after irradiation to high fluences in HFIR. That similarity between HFIR and EBR-II was attributed to the small amount of helium produced, since the difference in behavior between the steels irradiated in EBR-II and HFIR at high fluences had been previously attributed to the helium produced in HFIR. The 12Cr-1MoVW-2Ni steel after the low-fluence irradiation showed similarities with the high-fluence irradiations. An indication of intergranular fracture was observed for 12Cr-1MoVW-2Ni but not for the steels to which no nickel was added. The difference between the 9Cr-1MoVNb and 12Cr-1MoVW steels and the 12Cr-1MoVW-2Ni steel was attributed to a larger helium concentration in 12Cr-1MoVW-2Ni, even though there was only 3.5 appm He in 12Cr-1MoVW-2Ni, compared to 1 appm in the 12Cr-1MoVW.

It was postulated that when enough helium is present at 400°C (and probably 300°C), grain boundary voids can nucleate intergranular cracks that exacerbate the shift in DBTT over that in the absence of helium.

Finally, a word of caution is required. Conclusions that helium affect the impact toughness have been based on tests in different reactors and sometimes on different heats of steel. A problem with all irradiation experiments is the limited amount of reactor space available per experiment. This is especially critical for Charpy tests, where the accuracy of the curve can depend on the number of specimens tested. For some of the earlier experiments, it was necessary to generate a curve with as few as three specimens. In addition to this, the fluence each specimen receives in a capsule in HFIR depends on its position in the capsule relative to the reactor centerline. Given these conditions, it is not unreasonable to sometimes find considerable scatter in the data, as pointed out for both the tensile and Charpy data. In the near future, we intend to complete a HFIR experiment where some of these uncertainties are minimized.

ACKNOWLEDGMENTS

Experimental work was carried out by N. H. Rouse, J. J. Henry, Jr., and E. T. Manneschmidt. Dr. L. R. Greenwood of the Battelle Pacific Northwest Laboratories evaluated the flux monitors from the capsules. Helpful discussions on the work and manuscript were held with Drs. K. Farrell, J. M. Vitek, R. K. Nanstad, J. J. Kai, A. F. Rowcliffe, and E. E. Bloom.

REFERENCES

1. F. A. Smidt, Jr., J. R. Hawthorne, and V. Provenzano, in: Effects of Radiation on Materials: Tenth Conference, STP 725, Eds. D. Kramer, H. R. Brager, and J. S. Perrin (American Society for Testing and Materials, Philadelphia, 1981) p. 269.
2. W. L. Hu and D. S. Gelles, in: Ferritic Alloys for Use in Nuclear Energy Technologies, J. W. Davis and D. J. Michel, Eds. (Metallurgical Society of AIME, Warrendale, PA, 1984) p. 631.
3. J. M. Vitek, W. R. Corwin, R. L. Klueh, and J. R. Hawthorne, J. Nucl. Mater. 141-143 (1986) 948.
4. W. R. Corwin, J. M. Vitek, and R. L. Klueh, J. Nucl. Mater. 149 (1987) 312.
5. D. S. Gelles, J. Nucl. Mater. 149 (1987) 192.
6. W. L. Hu and D. S. Gelles, in: Influence of Radiation on Material Properties: 13th International Symposium (Part II), ASTM STP 956, F. A. Garner, C. H. Henager, Jr., and N. Igata, Eds. (American Society for Testing Materials, Philadelphia, 1987) p. 83.
7. R. L. Klueh, J. M. Vitek, W. R. Corwin, and D. J. Alexander, J. Nucl. Mater. 155-157 (1988) 973.
8. R. L. Klueh, J. M. Vitek, and M. L. Grossbeck, in: Effects of Irradiation on Materials: Eleventh Conference, ASTM STP 782, H. R. Brager and J. S. Perrin, Eds. (American Society for Testing Materials, Philadelphia, 1982) p. 648.
9. J. M. Vitek and R. L. Klueh, in: Ferritic Alloys for use in Nuclear Energy Technologies, J. W. Davis and D. J. Michel, Eds. (The Metallurgical Society, Warrendale, Pennsylvania, 1984) p. 551.
10. J. M. Vitek and R. L. Klueh, J. Nucl. Mater. 122 & 123 (1984) 254.
11. P. J. Maziasz, R. L. Klueh, and J. M. Vitek, J. Nucl. Mater. 141-143 (1986) 929.
12. R. L. Klueh and J. M. Vitek, J. Nucl. Mater. 161 (1989) 13.
13. R. L. Klueh and J. M. Vitek, J. Nucl. Mater. 150 (1987) 272.
14. R. L. Klueh and P. J. Maziasz, J. Nucl. Mater. 187 (1992) 43.
15. R. L. Klueh and D. J. Alexander, J. Nucl. Mater. 187 (1992) 60.
16. W. R. Corwin, R. L. Klueh, and J. M. Vitek, J. Nucl. Mater. 122 & 123 (1984) 343.
17. W. R. Corwin and A. M. Hougland, in: The Use of Small-Scale Specimens for Testing Irradiated Material, ASTM STP 888, W. R. Corwin and G. E. Lucas, Eds. (American Society for Testing and Materials, Philadelphia, 1986) p. 325.

18. D. J. Alexander, R. K. Nanstad, W. R. Corwin, and J. T. Hutton, Applications of Automation Technology to Fatigue and Fracture Testing, ASTM STP 1092, A. A. Braun, N. E. Ashbaugh, and F. M. Smith, Eds. (American Society for Testing and Materials, Philadelphia, 1990) p. 83.

19. R. L. Klueh and D. J. Alexander, in: Effects of Radiation on Materials: Fifteenth International Symposium, ASTM STP 1125, R. E. Stoller, A. S. Kumar, and D. S. Gelles, Eds. (American Society for Testing Materials, Philadelphia, 1992) p. 1256.

20. R. L. Klueh and D. J. Alexander, J. Nucl. Mater. 191-194 (1992) 896.

21. K. Farrell, Radiation Effects 53 (1980) 175.

22. K. Farrell, P. J. Maziasz, E. H. Lee, and L. K. Mansur, Radiation Effects 78 (1983) 277.

23. J. R. Hawthorne, in: Treatise on Materials Science and Technology, Vol. 25 (Academic Press, Inc., New York, 1983) p. 461.

24. G. E. Lucas and D. S. Gelles, J. Nucl. Mater. 155-157 (1988) 164.

25. R. W. Hertzberg, Deformation and Fracture Mechanics of Engineering Materials, 3rd Edition (John Wiley & Sons, New York, 1989) p. 253.

26. C. J. McMahon, Jr., Fundamental Phenomena in the Materials Sciences, Vol. 4, L. J. Bonis, J. J. Duga, and J. J. Gilman, Eds. (Plenum Press, New York, 1967) p. 247.

27. J. M. Vitek and R. L. Klueh, Met. Trans.A, 14A (1983) 1047.

28. D. S. Gelles, W. L. Hu, F. H. Huang, and G. D. Johnson, Alloy Development for Irradiation Performance, Semiannual Progress Report for Period Ending September 30, 1983, U. S. Department of Energy, Office of Fusion Energy, DOE/ER-0045/11 (March 1984) p. 115.

29. K. Anderko, L. Schafer, and E. Materna-Morris, J. Nucl. Mater. 179-181 (1991) 492.

30. R. G. Faulkner, E. A. Little, and T. S. Morgan, J. Nucl. Mater. 191-194 (1992) 858.

31. R. G. Faulkner, S. Song, and P. J. Flewitt, J. Nucl. Mater. to be published.

32. A. Kimura, L. A. Charlot, D. S. Gelles, D. R. Baer, and R. H. Jones, J. Nucl. Mater. 191-194 (1992) 885.

6.2 Austenitic Stainless Steels

INITIAL TENSILE TEST RESULTS FROM J316 STAINLESS STEEL IRRADIATED IN THE HFIR SPECTRALLY TAILORED EXPERIMENT – J. E. Pawel, M. L. Grossbeck, A. F. Rowcliffe (Oak Ridge National Laboratory) and K. Shiba (Japan Atomic Energy Research Institute)

OBJECTIVE

The objective of this work is to determine the effects of neutron irradiation on the mechanical properties of austenitic stainless steel alloys. In this experiment, the spectrum has been tailored to reduce the thermal neutron flux and achieve a He/dpa level near that expected in a fusion reactor.

SUMMARY

The HFIR-MFE-RB* experiments are designed for irradiation in the removable beryllium (RB*) positions of the High Flux Isotope Reactor. A hafnium shield surrounds the capsules in order to reduce the thermal neutron flux and achieve a He/dpa level near that expected in a fusion reactor. The J316 austenitic alloy specimens irradiated in this experiment were in the solution annealed (SA) and 20% cold-worked (CW) condition. The specimens were irradiated at 60 and 330°C to a total of 19 dpa (11 appm He/dpa). For both irradiation temperatures, there was no significant difference between the strength properties of the CW J316 following irradiation to 7 dpa or 19 dpa. The strength properties saturate at a fluence less than 7 dpa. The same is true for the SA J316 irradiated at 60°C. However, at 330°C, there is a small but significant further increase in yield stress between 7 and 19 dpa. There is a marked difference in deformation behavior seen after irradiation at 60°C and 330°C. After irradiation to 19 dpa at 60°C, J316 maintains a uniform elongation greater than 20% while the uniform elongation of the 330°C material is less than 0.5%. The yield strength of the cold-worked material remains higher than that of the solution annealed material at both 7 and 19 dpa. The severe reduction in uniform elongation seen at 330°C is a synergistic effect of both the irradiation temperature and the test temperature.

PROGRESS AND STATUS

Introduction

An austenitic stainless steel with the 316 LN composition has been chosen for the first wall/shield (FW/S) structure for the International Thermonuclear Experimental Reactor (ITER). Austenitic stainless steel was selected because, in addition to favorable strength, toughness, and fabrication properties, there is an enormous reservoir of experience in fabricating and operating code qualified austenitic stainless steel components in nuclear systems. Also, the austenitics do not suffer from the ductile-to-brittle transition that is characteristic of body-centered-cubic alloy systems. However, a drastic loss of uniform elongation and work hardening capacity is often observed in tensile tests after irradiation at temperatures between 200 and 350°C [1-3]. Definition of the irradiation regimes in which this phenomenon occurs are essential to the establishment of design rules to protect against various modes of failure.

The HFIR-MFE-RB* experiments are designed for irradiation in the removable beryllium (RB*) positions of the High Flux Isotope Reactor (HFIR). A hafnium shield surrounds the capsules in order to reduce the thermal neutron flux and achieve a He/dpa level near that expected in a fusion reactor. The J316 austenitic alloy specimens irradiated in this experiment were in the solution annealed and 20% cold-worked conditions. They had been previously irradiated to about 7 dpa in the Oak Ridge Research Reactor (ORR) in dual-temperature capsules designated ORR-MFE-6J (which operated at 60 and 200°C) and ORR-MFE-7J (which operated at 330 and 400°C). The operating temperature of the HFIR-MFE-RB*-60J-1 capsule was 60°C, with the specimens in direct contact with the reactor cooling water. The HFIR-MFE-RB*-200J-1, 330J-1, and 400J-1 capsules operate at 200, 330, and 400°C, respectively, with the temperature actively controlled by changing the gas mixture around the specimen holder in response to 21 thermocouples located inside the holder. The 60J-1 and 330J-1 capsules were irradiated from July 1990 to November 1992 and accumulated approximately 12 dpa in the HFIR (in addition to 7 dpa in the ORR). The irradiation of the 200J-1 and 400J-1 capsules is in progress. Initial results obtained during this reporting period concerning tensile properties of J316 solution annealed and cold worked alloys irradiated to about 19 dpa at 60 and 330°C are discussed in this report.

Experimental Procedure

The composition of J316 is given in Table 1. Solution annealed (SA) and 20% cold-worked (CW) specimens were irradiated. The specimens were in the form of SS-1 flat tensile specimens with an overall length of 44.45 mm. The gage section of this type of specimen is 20.32 mm long by 1.52 mm wide by 0.76 mm thick.

The irradiation in the ORR produced approximately 75-100 appm He in the steel, giving a fusion-relevant He/dpa ratio of about 11 appm/dpa. The details of this irradiation are described elsewhere [4-6]. Some of these specimens were then re-encapsulated into irradiation vehicles designed to operate in the HFIR RB* positions with a hafnium shield to reduce the thermal neutron flux and continue the irradiation at a He/dpa level near that expected in a fusion reactor. Two of the four capsules in this set have achieved the goal fluence in the HFIR of 11.6 dpa (1.94×10^{22} n/cm^2, $E > 0.1$ MeV) [7]. Preliminary dosimetry results also indicate that the 316 stainless steel specimens accumulated approximately 188 appm He in 60J-1 and 225 appm He in 330J-1 [7]. The helium content calculation was confirmed by isotope-dilution gas mass spectrometry [7]. This irradiation, combined with the ORR irradiation, resulted in a helium to displacement ratio of 10.2 appm He/dpa in 60J-1 and 11.8 appm He/dpa in 330J-1. Details of the irradiation can be found in Table 2 and elsewhere [7-9].

An Instron universal testing machine was used for the tensile testing. The specimens irradiated at 60°C (from the 60J-1 capsule) were tested at room temperature (25°C) in air. The specimens irradiated at 330°C (from 330J-1) were tested at 330°C under vacuum. In each case, the strain rate was 0.0004/s. The 0.2% offset yield strength (YS), ultimate tensile strength (UTS), uniform elongation (E_u), and total elongation (E_t) were calculated from the engineering load-elongation curves.

Results and Discussion

The results of these tensile tests were compared with data from control specimens as well as with data taken from sibling specimens irradiated to 7 dpa in the ORR. These data, as well as the previously obtained results, are given in Tables 3 and 4. This report will focus primarily on the new, 19 dpa, data as the 7 dpa (60, 200, 330, and 400°C) data have been discussed previously [1, 3].

Table 1. Composition of the J316 (Japanese Atomic Energy Research Institute) Alloy

	Composition, weight percent											
Alloy	C	Mn	P	S	Si	Ni	Cr	Mo	Nb	Ti	Co	Fe
J316	0.058	1.8	0.028	0.003	0.61	13.52	16.75	2.46	<0.1	0.05	<0.1	bal.

Table 2. Maximum dpa and Helium Production (Reactor Centerline) in ORR and HFIR Irradiations

Experiment	dpa	He, appm	appm He/dpa
ORR-MFE-6J	6.9	75.3	
HFIR-MFE-RB*-60J-1	12	113	
Total	19	188	10
ORR-MFE-7J	7.4	102	
HFIR-MFE-RB*-330J-1	12	123	
Total	19	225	12

Table 3. Tensile Data From Solution Annealed J316.

Specimen	Dose, dpa (peak)	He, appm (peak)	He/dpa	Irradiation Temp., °C	Test Temp., °C	YS, MPa	UTS, MPa	E_u, %	E_t, %
EL-61	0	0	...	...	25	327	602	50	57
EL-26	0	0	...	...	25	283	552	50	54
EL-30	0	0	...	...	200	254	492	32	36
EL-62	0	0	...	...	200	263	503	31	35
EL-31	0	0	...	...	330	230	484	29	31
EL-63	0	0	...	...	330	262	508	28	35
EL-32	0	0	...	...	400	252	476	26	28
EL-64	0	0	...	...	400	222	476	33	35
EL-33	6.9	75	11	60	25	703	752	25	30
EL-34	6.9	75	11	60	25	690	745	28	33
EL-43	6.9	75	11	200	200	745	745	0.2	4.0
EL-44	6.9	75	11	200	200	758	765	0.2	16
EL-46	6.9	75	11	200	200	733	737	12	15
EL-1	7.4	100	14	330	330	848	855	0.3	3.1
EL-2	7.4	100	14	330	330	869	869	0.3	2.9
EL-14	7.4	100	14	400	400	595	677	4.6	7.0
EL-15	7.4	100	14	400	400	650	717	4.3	6.8
EL-16	7.4	100	14	400	25	725	850	17	21
EL-36	19	190	10	60	25	716	743	20	25
EL-37	19	190	10	60	25	747	765	20	26
EL-38	19	190	10	60	330	596	614	10	13
EL-4	19	220	12	330	330	903	913	0.4	3.1
EL-5	19	220	12	330	330	909	921	0.4	3.1

Table 4. Tensile data from 20% cold-worked J316.

Specimen	Dose, dpa (peak)	He, appm (peak)	He/dpa	Irradiation Temp., °C	Test Temp., °C	YS, MPa	UTS, MPa	E_u, %	E_t, %
FL-63	0	0	...	...	25	743	808	6.8	12
FL-26	0	0	...	...	25	672	723	14	21
FL-28	0	0	...	...	200	516	592	3.7	7.1
FL-64	0	0	...	...	200	685	724	1.0	4.3
FL-56	0	0	...	...	330	630	668	1.0	3.4
FL-65	0	0	...	...	330	632	674	1.0	3.7
FL-57	0	0	...	...	400	545	601	1.2	3.1
FL-58	0	0	...	...	400	403	487	1.3	3.4
FL-31	6.9	75	11	60	25	834	869	0.6	8.5
FL-32	6.9	75	11	60	25	855	883	0.6	7.5
FL-39	6.9	75	11	200	200	793	821	0.6	4.4
FL-42	6.9	75	11	200	200	843	870	0.5	3.3
FL-47	6.9	75	11	200	200	821	862	0.6	3.4
FL-13	7.4	100	14	330	330	862	876	0.4	2.3
FL-14	7.4	100	14	330	330	993	1007	0.3	2.0
FL-15	7.4	100	14	330	330	972	993	0.4	2.4
FL-3	7.4	100	14	400	400	800	848	1.6	3.4
FL-2	7.4	100	14	400	400	811	876	1.3	3.4
FL-37	19	190	10	60	25	840	852	0.6	10
FL-36	19	190	10	60	25	869	884	0.6	9.1
FL-16	19	220	12	330	330	988	1008	0.4	2.4
FL-17	19	220	12	330	330	1000	1011	0.4	2.9

Typical engineering stress-strain curves for the solution annealed material are shown in Figures 1 and 2. Zero strain is set where the modulus line extrapolates to the x-axis. However, this is not a true modulus line since it includes machine load train deflection. Irradiation at 60°C results in an approximately threefold increase in yield stress. Following an initial yield drop, the material work hardens at a rate similar to that of the unirradiated material and elongates ~20% before necking and failure occur. At both 6.9 and 19 dpa, the material work hardens after the yield point but the UTS is less than 10% higher than the YS. After irradiation and testing at 330°C (Figure 2), deformation behavior is significantly different. The increase in yield stress is greater than that at 60°C by ~200 MPa. After yielding, the material does not exhibit any work hardening capability. The applied load falls rapidly and failure occurs after only ~3% total elongation. The uniform elongation is less than 0.5%.

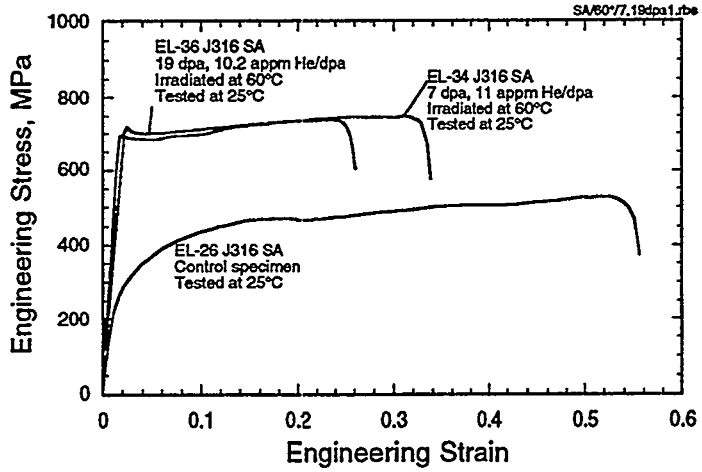

Figure 1. Engineering stress-strain curves for solution annealed material irradiated at 60°C and tested at 25°C. A control specimen curve is shown for comparison.

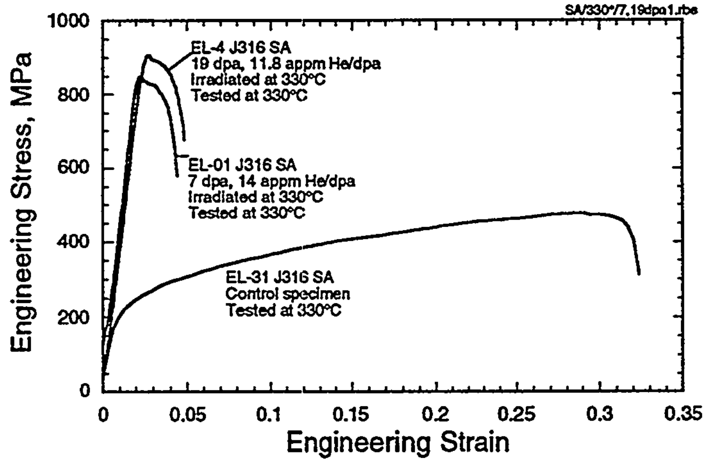

Figure 2. Engineering stress-strain curves for solution annealed material irradiated and tested at 330°C. A control specimen curve is shown for comparison.

The solution annealed material irradiated to 7 dpa showed a peak in the radiation-induced hardening curve as a function of temperature at 330°C (Figure 3). The 19 dpa data superimposed on this figure for comparison follow the same trend. This peak in hardening corresponds to a minimum in ductility.

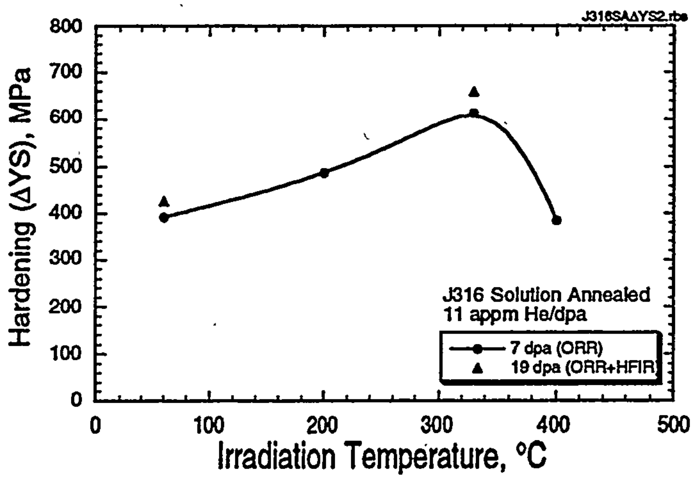

Figure 3. Radiation-induced hardening as a function of irradiation temperature for solution annealed J316. The curve is fit to the 7 dpa data.

The yield strength and the ultimate tensile strength of both the solution annealed and cold-worked specimens irradiated to a total of 19 dpa were only slightly higher than the values obtained after irradiation to 7 dpa (Figures 4 and 5). At both fluences, the yield strength is about equal to the UTS after irradiation and testing at these temperatures. There is some evidence that the strength as a function of fluence curve, as shown in Figures 4 and 5 should be steeper at the lower fluences. Tavassoli [10] reports significant increases in yield and ultimate tensile strength at fluences less than 1 dpa and saturation of these strengths at approximately 3 dpa for 316LN irradiated at temperatures less than 400°C. Kallstrom et al. [11] irradiated 316LN to only 0.3 dpa at 35°C and report a yield strength of 552 MPa after testing at 75°C. Heinisch [12] also reports significant increases in the yield strength of 316 as the result of very low dose irradiations (< 0.01 dpa). The present data are not inconsistent with these observations since displacement levels below 7 dpa were not investigated.

Irradiation to 7 and 19 dpa at either temperature resulted in significant hardening, rather than softening, of the cold-worked material. The yield strength of the cold-worked material remains higher than the that of the solution annealed material at both 7 and 19 dpa, but the difference is less at 330°C than at 60°C (Figures 6 and 7). This observation is consistent with Grossbeck et al. [2, 13], who reported convergence of the SA and CW yield strengths after irradiations to dpa levels between 20 and 30. Elen and Fenici [14] report CW strengths 200 MPa higher than solution annealed strengths for irradiations of 316L up to 11 dpa at 250°C. Garner et al. [15] also reported hardening of CW 316 after irradiation at 427°C in a fast reactor; similar irradiations at 538 and 650°C resulted in softening.

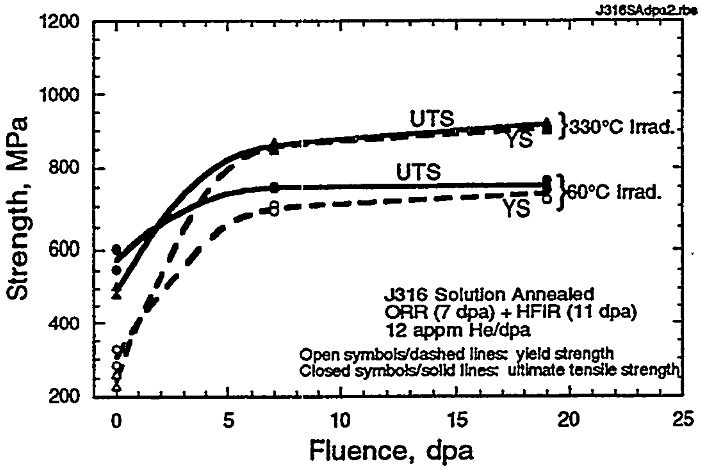

Figure 4. Yield strength and ultimate tensile strength of solution annealed J316 as a function of fluence for 60 and 330°C irradiations.

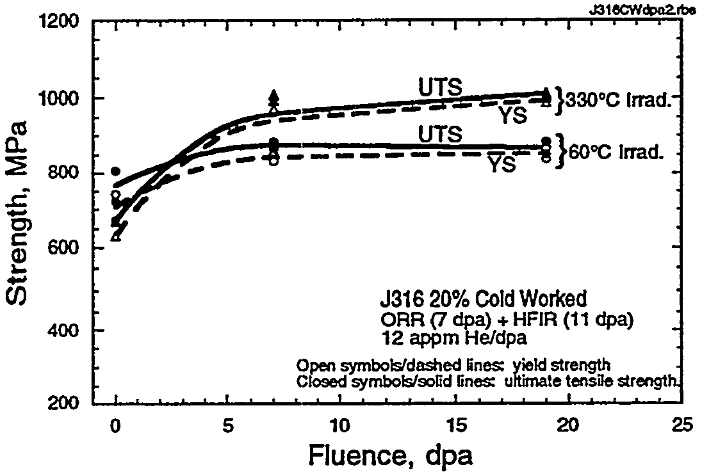

Figure 5. Yield strength and ultimate tensile strength of cold-worked J316 as a function of fluence for 60 and 330°C irradiations.

To further investigate the behavior seen after irradiation at 330°C, one solution annealed specimen irradiated to 19 dpa at 60°C was tested at 330°C. Compared to the specimens irradiated and tested at 330°C, this specimen showed less hardening and larger E_u. Compared to the 60°C specimens, this specimen showed less hardening but also less E_u. This latter comparison is consistent with the unirradiated data, which show a decrease in both YS and E_u with increasing test temperature. The stress-strain curves are shown in Figure 8. This implies that the severe reduction in uniform elongation seen at 330°C is a synergistic effect of both the irradiation temperature and the test temperature.

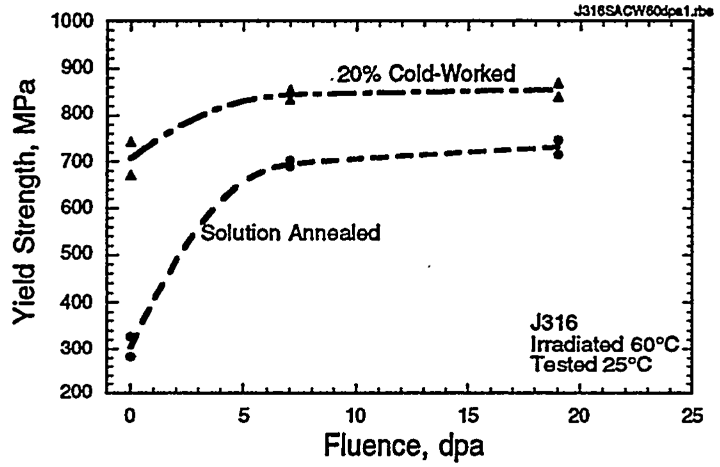

Figure 6. Yield strength as a function of fluence for solution annealed and cold-worked J316 material irradiated at 60°C.

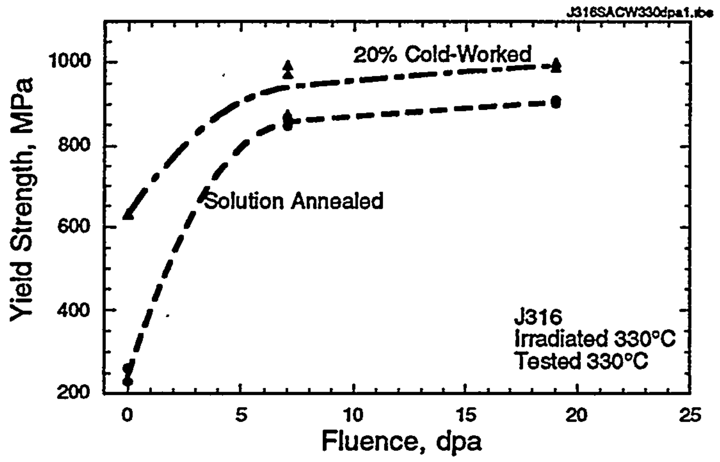

Figure 7. Yield strength as a function of fluence for solution annealed and cold-worked J316 material irradiated at 330°C.

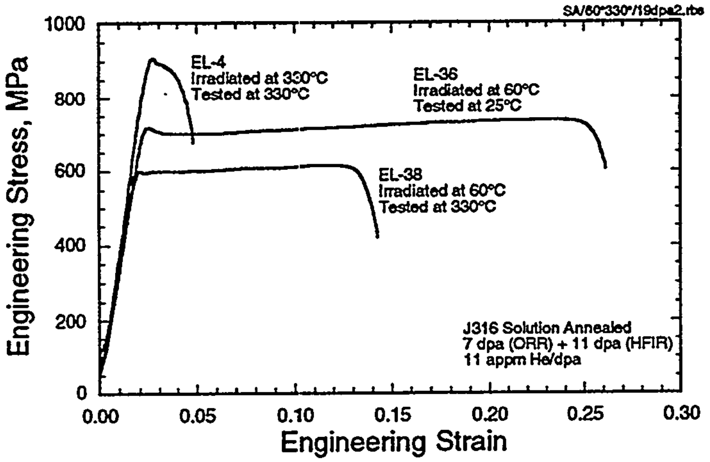

Figure 8. Engineering stress-strain curves of solution annealed J316 irradiated to 19 dpa at 60 and 330°C, and tested at 25 and 330°C.

Conclusions

For both irradiation temperatures, there was no significant difference between the strength properties of the CW J316 following irradiation to 7 dpa or 19 dpa. The strength properties saturate at a fluence less than 7 dpa. The same is true for the SA J316 irradiated at 60°C. However, at 330°C there is a small but significant further increase in yield stress between 7 and 19 dpa. There is a marked difference in ductility behavior seen after irradiation at 60°C and 330°C. Both have high yield strengths compared to the unirradiated values, but the 60°C material maintains a uniform elongation greater than 20% while the uniform elongation of the 330°C material is less than 0.5%. The yield strength of the cold-worked material remains higher than that of the solution annealed material at both 7 and 19 dpa. The severe reduction in uniform elongation seen at 330°C is a synergistic effect of both the irradiation temperature and the test temperature.

FUTURE WORK

Future work includes analyses to better define the low work hardening regime as a function of fluence and temperature and the comparison of these data with other results on the basis of helium content, He/dpa ratio, and dose rate. In particular, similar materials irradiated at 200 and 400°C remain to be tested.

REFERENCES

1. Grossbeck, M.L., T. Sawai, S. Jitsukawa, and L.T. Gibson, Fusion Reactor Materials Semiannual Progress Report, DOE/ER-0313/6, Office of Fusion Energy (1989), p. 259.
2. Grossbeck, M.L., Fusion Reactor Materials Semiannual Progress Report, DOE/ER-0313/6, Office of Fusion Energy (1989), p.243.
3. Jitsukawa, S., P.J. Maziasz, T. Ishiyama, L.T. Gibson, and A. Hishinuma, J. Nucl. Mater. 191-194 (1992) 771.
4. Siman-Tov, I.I., Fusion Reactor Materials Semiannual Progress Report, DOE/ER-0313/3, Office of Fusion Energy (1988), p. 7.
5. Greenwood, L.R., Fusion Reactor Materials Semiannual Progress Report, DOE/ER-0313/6, Office of Fusion Energy (1989), p. 23.
6. Greenwood, L.R., and D.V. Steidl, Fusion Reactor Materials Semiannual Progress Report, DOE/ER-0313/8, Office of Fusion Energy (1990), p. 34.

7. Greenwood, L.R., C.A. Baldwin, and B.M. Oliver, this report.
8. Longest, A.W., J.E. Pawel, D.W. Heatherly, R.G. Sitterson, and R.L. Wallace, Fusion Reactor Materials Semiannual Progress Report, DOE/ER-0313/14, Office of Fusion Energy (1993), p. 14.
9. Longest, A.W., D.W. Heatherly, E.D. Clemmer, and J.E. Corum, Fusion Reactor Materials Semiannual Progress Report, DOE/ER-0313/11, Office of Fusion Energy (1992), p. 17.
10. Tavassoli, A.A., "Assessment of Austenitic Stainless Steels," ITER Task BL-URD3, N.T. SRMA 94-2061, Revision June 1994.
11. Kallstrom, R., Josefsson, B., and Y. Haag, STUDSVIK/M-93/45 (PSM 1-1) Studsvik Material AB, Sweden, 1993.
12. Heinisch, H.L., J. Nucl. Mater. 155-157 (1988) 121.
13. Grossbeck, M.L., K. Ehrlich, and C. Wassilew, J. Nucl. Mater. 174 (1990) 264.
14. Elen, J.D., and P. Fenici, J. Nucl. Mater. 191-194 (1992) 766.
15. Garner, F.A., M.L. Hamilton, N.F. Panayotou, and G.D. Johnson, J. Nucl. Mater. 103 & 104 (1981) 803.

6.3 Refractory Metal Alloys

CHEMICAL AND MECHANICAL INTERACTIONS OF INTERSTITIALS IN V-5%Cr-5%Ti -

J. H. DeVan, J. R. DiStefano, J. W. Hendricks, and C. E. Matos*, Oak Ridge National Laboratory, P.O. Box 2008, Oak Ridge, TN 37831-6156

OBJECTIVE

A vanadium alloy structure with liquid lithium is the favored concept for an advanced breeding blanket for ITER. The objective of this task is to determine the kinetics of reactions of vanadium alloys with hydrogen and oxygen as a function of alloy composition and TMT.

SUMMARY

Gas-metal reaction studies of V-5Cr-5Ti were conducted to determine the kinetics of reactions with H_2 and O_2, respectively, at 450-500°C. Reaction rates were determined through weight change measurements and chemical analyses, and effects on mechanical properties were evaluated by room temperature tensile tests. Exposures to hydrogen at 450°C and 0.1 torr pressure resulted in a significant loss in room temperature ductility in the case of alloys that had been annealed at 1125°C but not in the case of alloys annealed at 1050°C. Adding oxygen at 500°C at concentrations as low as 200 ppm seriously embrittled V-5Cr-5Ti specimens when the specimens were held for 100h in vacuum at 500°C. A subsequent heat treatment in vacuum at 950°C restored the ductility. Exposure to air at 400°C and a subsequent vacuum heat treatment at 500°C caused ductility decreases similar to those observed after the small oxygen additions, and ductility again was restored by a 950°C vacuum anneal. However, similar heat treatments following air exposures at 450 and 500°C, respectively, resulted in ductility losses that were not recovered by the 950°C anneal. The latter exposures also resulted in the formation of thin oxide films.

INTRODUCTION

Materials and Procedures

Interactions of the V-5Cr-5Ti alloy with hydrogen were investigated using an ultra-high vacuum Sievert's apparatus to control the hydrogen pressure and temperature at conditions prototypic of the ITER plasma-first wall interface and the diverter. High purity hydrogen was admitted to the apparatus through a controllable leak valve at the same rate that it was extracted by a turbomolecular pump, and the pressure at the specimen was fixed within the range 10^{-1} to 10^{-2} torr (13-1.3 Pa). Exposure temperatures were 450 and 500°C with times ranging from 24 to 100 hours. A similar apparatus was used to make controlled oxygen additions to the alloy. In this case the alloy was exposed at 500°C for 4 h to pure oxygen at 2×10^{-6} torr (2.6×10^{-4} Pa), and then was heat treated at 500°C under ultra-high vacuum to diffuse the oxygen into the specimen. Some specimens were given a secondary heat treatment in vacuum at 950°C to remove the oxygen from solid solution. Additional exposures were carried out in an air atmosphere at 400, 450, and 500°C, respectively. Subsequent heat treatments were the same as those following the exposures to oxygen at 2×10^{-6} torr. In all tests the reaction rates were determined through weight change measurements and chemical analyses, and effects on mechanical properties were evaluated by room temperature tensile tests.

The V-5Cr-5Ti alloy used for these studies was produced by Teledyne Wah Chang Albany and has been given the designation BL-63. The compositions of major components are listed in Table 1. Small tensile specimens (SS-3), nominally 0.76 mm thick with 1.5 mm x 7.6 mm gage sections, were machined or stamped from 40% warm-reduced sheet stock of the alloys. One set of specimens was vacuum annealed for 1 h at 1125°C and a second set for 1 h at 1050°C. Another set of identically-shaped specimens was stamped

---

* Visiting student

from 0.75 mm sheet that had been autogenously welded using the gas-tungsten arc (GTA) process.[1] The weld bead was positioned laterally at the center of the gage length, and the specimens were not heat treated before testing.

Table 1. Composition of Vanadium Alloy

Heat #	Concentration wt %			Concentration wt ppm			
	Cr	Ti	Fe	O	N	C	Si
WC 832394 (BL63)	4.2	5.4	<0.045	427	52	40	<0.031

RESULTS AND DISCUSSION

To evaluate the effects of prior heat treatment on hydrogen embrittlement, specimens annealed at 1050°C and 1125°C, respectively, were exposed side-by side in 0.1 torr hydrogen at 450°C for times of 24 and 100 hours, respectively. As shown in Table 2, room temperature ductilities of specimens annealed at 1050°C were significantly higher than the corresponding ductilities of specimens annealed at 1125°C. Prior to hydrogen exposure, elongations were on the order of 30% irrespective of the heat treatment temperature. Specimens annealed at 1050°C showed only a slight drop in elongation, while specimens annealed at 1125°C showed elongations of only 2-5%.

The embrittlement of the specimens annealed at 1125°C and exposed to hydrogen at 450°C torr was significantly less when the hydrogen pressure was reduced to 0.01 torr than for exposures at 0.1 torr. Room temperature ductilities after exposures at the respective pressures are compared in Table 3. In contrast to the elongations of 2-5% reported above for exposures at 0.1 torr, elongations after exposure at 0.01 torr were all above 14%. However, the latter elongations were still less than elongations of specimens annealed at 1050°C and exposed at 0.1 torr (Table 2).

The weight gains measured in these tests, shown in Tables 2 and 3, generally exceed those which could have accrued from hydrogen pickup alone. Although hydrogen concentrations in these specimens are still being analyzed, based on analyses of earlier tests in hydrogen[2], the bulk of the weight gains over 50 ppm can be attributed to oxygen pickup. As discussed below, ingress of oxygen at 500°C, even at the relatively low levels indicated by the weight changes in these tests, can significantly degrade the room temperature ductility of the V-5Cr-Ti alloy. In the case of the present tests, which were conducted at 450°C, the diffusion rate of oxygen into the specimens is sufficiently slow that the embrittlement resulting from the 24-hour exposures can be assumed to be due primarily to hydrogen effects; however, the further decrease in ductility resulting from the 100-hour exposures probably reflects oxygen ingress more than hydrogen. As discussed below, the effect of prior annealing treatment on elongation in these tests may be associated more with oxygen contamination than with hydrogen effects. A further investigation of the effect of annealing treatment on hydrogen-induced property changes is being carried out under conditions designed to limit oxygen pickup.

Effects of oxygen contamination on the room temperature properties of the reference V-5Cr-5Ti alloy were evaluated in both the welded and unwelded conditions. Specimens were initially exposed to oxygen at 2×10^{-6} torr for 4 h at 500°C, resulting in a pickup of approximately 200-250 ppm of oxygen. Part of these specimens were then heat treated under ultra-high vacuum for 100 h at 500°C, and a group of the latter specimens were further heat treated for 4 h at 950°C. Table 4 shows results for specimens that had been welded by the GTA process. The addition of 250 ppm oxygen at 500°C produced a measurable reduction in elongation even in 4 h, but with the additional 100 h anneal in vacuum the elongation was reduced to 2%. A further anneal at 950°C completely restored the ductility to its value in the as-welded condition. These results are quite comparable to results for unwelded specimens of the same heat that were annealed at

1125°C prior to oxygen exposure, as reported earlier.[2] However, as shown in Table 5, very different results were obtained for specimens that were annealed at 1050°C prior to oxygen exposure and subsequent annealing. The latter specimens showed only a small reduction in ductility for a comparable oxygen pickup following the 100-h anneal at 500°C, although again the ductility was fully recovered by the 950°C anneal.

It was previously reported that embrittlement by oxygen under the present test conditions depends strongly on the alloy grain size.[2] The ductility differences between specimens annealed at 1050°C and 1125°C can be attributed to this grain size effect. Specimens having an ASTM grain size of 5 or less, as produced by the 1125°C anneal, suffer a greater reduction in ductility for a given amount of oxygen absorbed at 450-500°C than specimens with ASTM grain size 6-7, as produced by the 1050°C anneal. Since autogenous welding induces even greater grain coarsening, it is not surprising that the welded specimens showed even greater susceptibility to oxygen embrittlement than the specimens annealed at 1125°C. Consistent with these findings is the observation that fractures of the lower ductility specimens tend to be predominantly intergranular, while those of the higher ductility specimens are transgranular. These results all indicate that oxygen ingress in V-5Cr-5Ti at 450-500°C is occurring mainly along grain boundaries.

Table 2. Effect of Annealing Temperature on V-5Cr-5Ti Exposed to H_2 at 450 C
(Specimens exposed at a pressure of 0.1 torr)

Specimen	Annealing Temp. (C)	Exposure Time (h)	Weight Change (ppm)	Yield Strength (MPa)	Ultimate Strength (MPa)	Elong. (%)	Cooling Rate
VN 13	1050	24	38	404	494	21.3	fast
VN 10	1125	24	348	441	476	5.6	fast
VN14	1050	100	423	414	499	19.2	fast
VN11	1125	100	231	451	451	1.6	fast
VN 18	1050	100	270	430	515	16.7	slow
VN 09	1125	100	232	441	462	1.8	slow

Table 3. Room Temperature Properties of V-5Cr-5Ti after Exposure to H_2 at 450 C

Specimen*	Hydrogen Pressure (torr)	Exposure Time (h)	Weight Change (ppm)	Yield Strength (MPa)	Ultimate Strength (MPa)	Elong. (%)	Cooling Rate
VR30	0.01	24	59	396	469	20.7	fast
VN 07	0.1	24	308	430	494	10.0	fast
VR20	0.01	100	58	395	474	21.3	fast
VN11	0.1	100	231	451	451	1.6	fast
VN19	0.01	100	75	353	465	14	slow
VN12	0.1	100	329	452	470	3.8	slow

*Specimens annealed at 1125C prior to exposure to H_2

Test results for exposures of the reference V-5Cr-5Ti alloy (annealed at 1125°C) to ambient air at 400, 450, and 500°C are shown in Table 4. Exposure to air for 24 h at 400°C resulted in a pickup of approximately 500 ppm oxygen, and the effects on room temperature ductility were similar to those for the exposures in 2×10^{-6} torr oxygen, discussed above. The ductility, which dropped only slightly following the 24-h air

Table 4. Oxygen Effects on Room Temperature Properties
(Specimens exposed to 1.0E-6 torr O2 at 500C for 4 hours)

Specimen	Weight Change (ppm)	Holding Time (C)	Holding Temp. (h)	Yield Strength (MPa)	Ultimate Strength (MPa)	Elongation (%)
			Weld Specimens			
VO04	Control	100	500	475	578	14.5
VO05	" "	100 4	500 950	335	428	16.8
VO01	250	As-oxidized		467	516	7.2
VO02	250	100	500	494	556	1.9
VO03	242	100 4	500 950	329	436	15.6
			As Annealed - 1050C			
VN04	Control	100	500	376	454	26.6
VN05	" "	100 4	500 950	315	416	27.8
VN01	116	As-oxidized		363	452	26.7
VN02	193	100	500	374	481	23.9
VN03	233	100 4	500 950	312	432	28.5

Table 5. Effect of Air Exposures on Properties of V-5Cr-5Ti*

Specimen	Anneal Time (h)	Conditions Temp. (C)	Weight Change (ppm)	Yield Strength (MPa)	Ultimate Strength (MPa)	Elongation (%)
			Exposed to air for 24 h at 400C			
VR09	As-exposed		441	363	442	26.2
VR08	100	500	500	400	425	4.0
VR04	100 4	500 950	500	327	466	27.2
			Exposed to air for 25 h at 450C			
VB95	As-exposed		1101	375	464	24.7
VB89	100	500	1420	401	447	19.7
VB92	100 4	500 950	956	362	494	19.2
			Exposed to air for 25 h at 500C			
VB94	As-exposed		1855	387	481	21.0
VB85	100	500	1971	401	427	9.4
VB91	100 4	500 950	2290	401	428	7.2

*Annealed at 1125C

exposure, was substantially reduced following a subsequent heat treatment in vacuum for 100h at 500°C but then was fully recovered by a secondary heat treatment in vacuum at 950°C. Exposures to air for 25 h at 450 and 500°C resulted in substantially greater oxygen pickup than at 400°C, and in this case the effects on ductility were different from the exposures to oxygen and to 400°C air. After the 450°C air exposure, the subsequent heat treatment for 100 h at 500°C lowered the ductility less than after the 400°C air exposure, and the subsequent heat treatment at 950°C had no effect on the ductility. After the 500°C air exposure, the subsequent 500°C vacuum heat treatment reduced the ductility to the same order as had occurred for the 400°C air exposure, but, like the 450°C air exposure, the ductility was not recovered by the subsequent 950°C vacuum heat treatment. One important difference in the 450 and 500°C air exposures from other tests conducted to date was a marked darkening of the specimen surfaces, indicative of the presence of an oxide film. How the morphology and chemistry of this film may have affected the oxygen uptake by the vanadium alloy is still under investigation.

REFERENCES

1. G. M. Goodwin and J. F. King, "Welding Development for V-Cr-Ti Alloys" in *Fusion Reactor Materials Semiannual Progress Report for Period Ending March 31, 1994*, DOE/ER-0313/16, Oak Ridge National Laboratory.

2. J. H. DeVan, J. R. DiStefano, and J. W. Hendricks, "Chemical and Mechanical Interactions of Interstitials in V-5%Cr-5%Ti" in *Fusion Reactor Materials Semiannual Progress Report for Period Ending March 31, 1994*, DOE/ER-0313/16, Oak Ridge National Laboratory.

FATIGUE BEHAVIOR OF UNIRRADIATED V-5Cr-5Ti

B. G. Gieseke, C. O. Stevens and M. L. Grossbeck (Oak Ridge National Laboratory)

OBJECTIVE

The objective of this research is to determine the low cycle fatigue behavior of V-5Cr-5Ti alloys for a range of temperatures and the extent of environmental effects at ambient temperatures.

SUMMARY

The results of in-vacuum low cycle fatigue tests are presented for unirradiated V-5Cr-5Ti tested at room temperature (25), 250, and 400°C. A comparison of the fatigue data generated in rough and high vacuums shows that a pronounced environmental degradation of the fatigue properties exists in this alloy at room temperature. Fatigue life was reduced by as much as 84%. Cyclic stress range data and SEM observations suggest that this reduction is due to a combination of increases in rates of crack initiation and subsequent growth. The relative contribution of each difference is dependent upon the strain range.

In high vacuum, the fatigue results also show a trend of increasing cyclic life with increasing temperature between 25 and 400°C. From the limited data available, life at 250°C averages 1.7 times that at 25°C, and at 400°C, life averages 3.2 times that at room temperature. Like the environmental effects at 25°C, the effect of temperature seems to be a function of strain range at each temperature.

The total strain range and cycles to failure were correlated using a power law relationship and compared to 20% cold-worked 316 stainless steel and several vanadium-base alloys. The results suggest that V-5Cr-5Ti has better resistance to fatigue than 316-SS in the temperature range of 25 to 400°C. At 400°C, the data also show that V-5Cr-5Ti out performs Vanstar alloys 7 and 8 over the entire range of strains investigated. Furthermore, the fatigue properties of the V-5Cr-5Ti alloy compare favorably to V-15Cr-5Ti (at 25°C) and Vanstar 9 (at 400°C) at strains greater than 1%. At lower strains, the lower fatigue resistance of V-5Cr-5Ti is attributed to the higher strengths of the V-15Cr-5Ti and Vanstar 9 alloys.

PROGRESS AND STATUS

Introduction

Low cycle fatigue tests were conducted on samples of V-5Cr-5Ti from Teledyne Wah Chang Ht. 832394 (ANL designation BL63) at temperatures of 25, 250, and 400°C and pressures less than 7.3×10^{-6} Pa (5.5×10^{-8} torr). In addition to these data, the effect of environment on fatigue properties at ambient temperatures was examined by conducting additional tests in a rough vacuum of ~ 2.6×10^{3} Pa (20 torr). The results are compiled in the form of tables and plots. Where data permit, comparisons are made between this V-5Cr-5Ti alloy and other vanadium-base alloys and 316 stainless steel.

Materials and Procedures

Specimens were fabricated from a 6.35 mm (0.25 in) thick plate of V-5Cr-5Ti produced by Teledyne Wah Chang (Heat 832394). The chemical composition (wt.%) of the plate was 5.1 Ti, 4.5 Cr, 310 ppm Si, 35 ppm C, 364 ppm O, 52 ppm N, and 1.1 ppm H with the balance being vanadium. The mechanical properties of this heat have been studied extensively at the Argonne National Laboratory (ANL), where this heat of material is referred to as BL63. The plate was received in the annealed condition (1 *h* at 1125°C) and specimens were fabricated with the geometry shown in Fig. 1. Following machining, the specimens were etched using a solution of 60% H_2O - 30% HNO_3 - 10% HF for approximately two minutes, wrapped in Ta foil, and annealed at 1125°C for 1 *h* in a vacuum of less than 1×10^{-5} Pa (10^{-7} torr). The resulting microstructure is shown in Fig. 2. An equiaxed grain structure is present within an average ASTM grain size of 6.

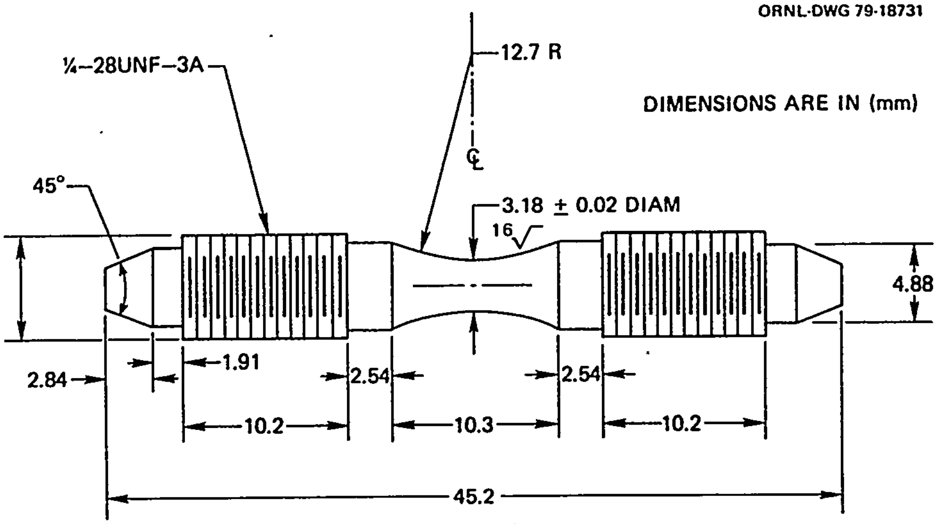

Fig. 1. Miniature hourglass fatigue specimen employed in fatigue testing. Dimensions are in millimeters.

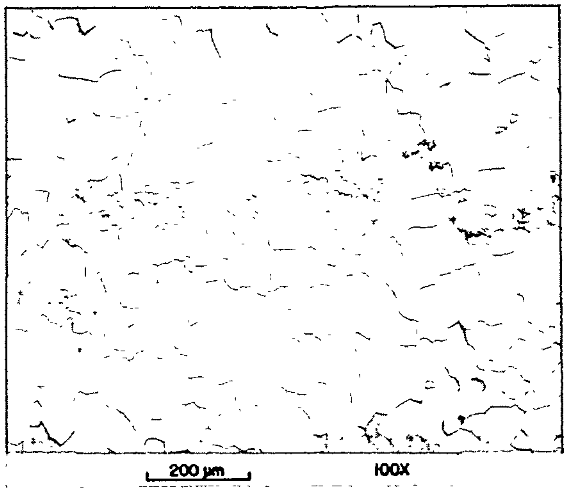

Fig. 2. Photomicrograph of V-5Cr-5Ti alloy (93-0991-1).

Tests were conducted on a servo-hydraulic test frame using a strain computer to convert diametral strain to an equivalent axial strain. The tests were conducted in axial strain control at a constant strain rate of 4×10^{-3}/s. During the course of testing, it was observed that V-5Cr-5Ti exhibits serrated yielding under some combinations of strain and temperature such that the strain range often had to be gradually increased to the desired level during the first 10-25 cycles. The presence of this behavior prevented testing at total strain ranges greater than 1.75% at the elevated temperatures and became more prominent as temperature increased. Typically, serrated yielding occurred at the onset of cycling in tests with a strain range ≥ 0.75% and would disappear within several hundred cycles, only to re-emerge near the end of the tests.

Heating was accomplished using RF induction, and temperatures were maintained within ±2°C of the desired setpoint. Initial tests at room temperature were conducted in a rough vacuum of ~ 2.6×10^{3} Pa (20 torr) that was used to maintain the cleanliness of the test chamber. All other experiments were initiated after a pressure of less than 7.3×10^{-6} Pa (5.5×10^{-8} torr) was obtained while at the desired test temperature. Pressures typically continued to drop to less than 2.0×10^{-6} Pa during cycling.

Experimental Results

The results of the fatigue tests have been listed in Table 1 and plotted in Fig. 3. The data were fitted to a power law expression originally suggested by Manson [1] and given by:

$$\Delta\varepsilon_t = AN_f^{-\alpha} + BN_f^{-\beta}$$

where, $\Delta\varepsilon_t$ = total strain range in %, N_f = number of cycles to failure, and A, B, α and β are material constants. The values of these constants can be found in Table 2. The data for α have values on the same order of magnitude as reported by Liu [2] for V-15Cr-5Ti, but must be viewed with caution since the data used to generate them came from tests in which the cyclic lives are relatively short. The values for ß also compare well with those reported by Liu for V-15Cr-5Ti, but the values of β for both V-15Cr-5Ti and V-5Cr-5Ti differ from the 0.5 to 0.6 often reported in engineering alloys.

Table 1. Summary of Test Conditions and Results for LCF Experiments Conducted on V-5Cr-5Ti (TWC Ht. 832394)

Spec. No.	$\Delta\varepsilon t$ (%)	Temp. (°C)	Nf	$\Delta\varepsilon p$ (%)[a]	$\Delta\varepsilon E$ (%)[b]	$\Delta\sigma$ (MPa)[a]	Pressure (Pa)
VA 05	0.49	25	134,923	≈ 0	0.49	58.8	2.6 x103
VA 04	0.59	25	49,367	0.011	0.579	711.3	2.6 x103
VA 03	0.732	25	22,165	0.018	0.714	882.7	2.6 x103
VA 07	0.98	25	5906	0.121	0.859	1016.6	2.6 x103
VA 02	1.54	25	2240	0.62	0.92	1068.3	2.6 x103
VA 06	2.04	25	1088	1.12	0.92	1116.1	2.6 x103
VA 16	0.77	25	136,829	0.033	0.74	921.5	≤ 7.3 x10-6
VA 14	1.02	25	37,379	0.138	0.882	1007.2	≤ 7.3 x10-6
VA 15	1.52	25	11,613	0.60	0.92	1033	≤ 7.3 x10-6
VA 20	0.78	250	206,642	0.11	0.67	805.4	≤ 7.3 x10-6
VA 18	1.00	250	74,381	0.253	0.747	826.7	≤ 7.3 x10-6
VA 19	1.38	250	30,476[c]	0.74	0.64	843.7	≤ 7.3 x10-6
VA 21	1.54	250	18,550	0.80	0.74	851.4	≤ 7.3 x10-6
VA 17	0.76	400	336,030	0.07	0.69	811.3	≤ 7.3 x10-6
VA 09	1.00	400	164,277	0.286	0.714	869.9	≤ 7.3 x10-6
VA 11	1.23	400	75,052	0.482	0.748	905.0	≤ 7.3 x10-6
VA 13	1.53	400	33,476	0.743	0.787	940.0	≤ 7.3 x10-6
VA 12	1.77	400	25,272	0.98	0.79	921.1	≤ 7.3 x10-6

Notes:
(a) Measured from a loop near midlife. $\Delta\varepsilon_p$ = width of hysteresis loop at zero load.
(b) The quantity $\Delta\varepsilon_E = \Delta\varepsilon_t - \Delta\varepsilon_p$.
(c) Strain range dropped during test, resulting in unusually long cycle life. Datum plotted but not considered in determination of material constants.

Table 2. Material Constants in Coffin-Manson Equation for V-5Cr-5Ti Alloy

Temperature (°C)	Press. (Pa)	A	α	B	β
25	2.6 x 103	2.85	0.1464	50,093	1.493
25	≤7.3 x 10-6	2.384	0.0983	35,143	1.176
250	≤7.3 x 10-6	1.47	0.0646	2611	0.823
400	≤7.3 x 10-6	1.39	0.0552	611	0.638

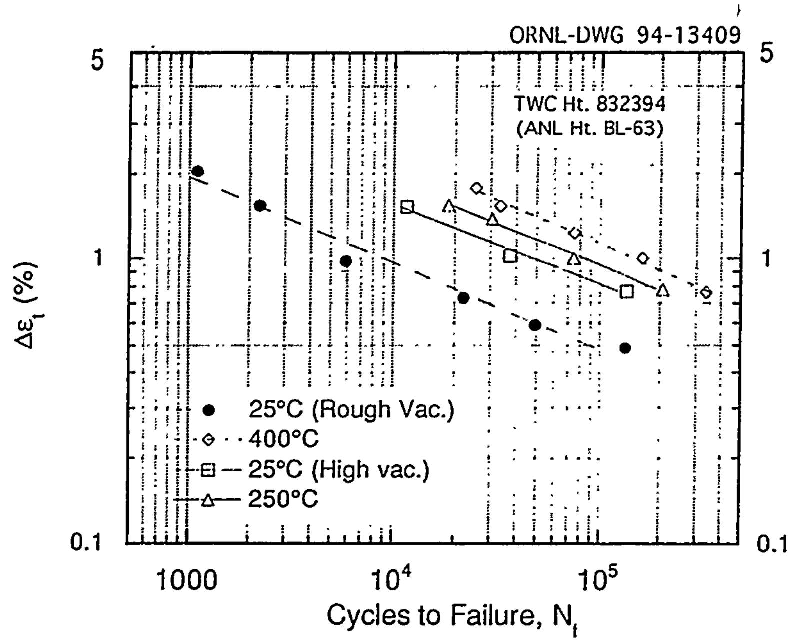

Fig. 3. Cyclic fatigue data for V-5Cr-5Ti tested at 25, 250, and 400°C in rough and high vacuums.

Two observations can be easily drawn from Fig. 3. First, the fatigue lives in high vacuum increase with increasing temperature over the range investigated. This increase in life varies from a factor of 1.5 to 4.4 times that observed at 25°C (refer to Table 3.). Swindeman [3] has reported similar results on niobium alloy D-43 where he observed increasing plastic strain resistance (*ie.*, life) at temperatures up to 871°C. Swindeman also noted that above 871°C, the magnitude of the increase began to decrease and it is likely that similar behavior would be observed in the V-5Cr-5Ti alloy. The second observation is that at room temperature there is a considerable effect of environment on the fatigue life. Between rough and high vacuum, there is an increase in life that ranges from a factor of about 5 to 6 (Refer to table 3.).

Table 3. Comparison of Cyclic Lives Under Various Conditions for Selected Strain Ranges

Nominal Δet (%)	Nhv/Nrv at 25°C	N250/N25	N400/N25
0.75	6.17	1.51	2.46
1.00	6.33	1.99	4.39
1.53	5.18	1.60	2.88

Notes: (a) N_{hv}/N_{rv} is the ratio of observed life at 25°C in high vacuum to that observed in a rough vacuum.

(b) N_{250}/N_{25} is the ratio of fatigue life at 250°C to that at 25°C for tests conducted in a high vacuum.

(c) N_{400}/N_{25} is the ratio of fatigue life at 400°C to that at 25°C for tests conducted in a high vacuum.

In Figs. 4, 5 and 6, plots of the stress range as a function of cycle count (Δσ vs. N) are shown for select fatigue tests at 25°C and all those conducted at 250 and 400°C. In all the tests, the V-5Cr-5Ti alloy cyclically hardens up to the point of crack initiation. At 25°C, in most tests conducted in high vacuum, initiation takes place early and a considerable fraction of life is spent propagating a crack. Conversely, plots of the stress range as a function of cycle count for tests (at 25°C) conducted in rough vacuum suggest that crack initiation dominated and crack propagation was rapid.

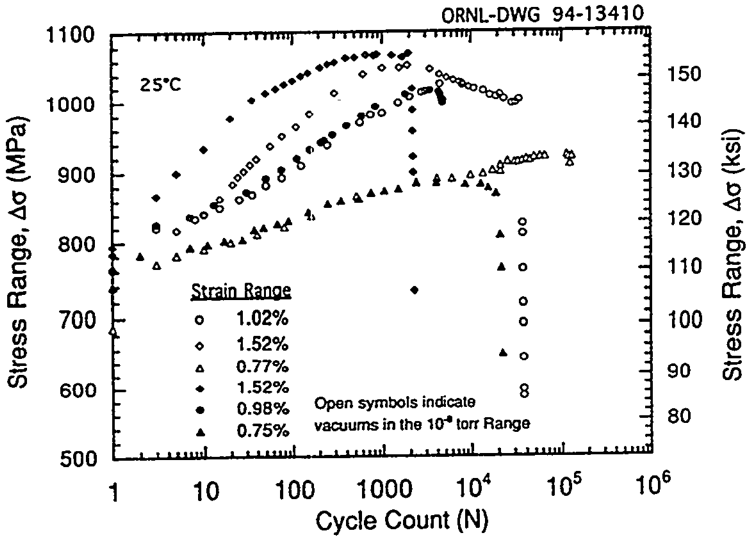

Fig. 4. Comparison of room temperature cyclic stress behavior of V-5Cr-5Ti alloy in rough and high vacuums.

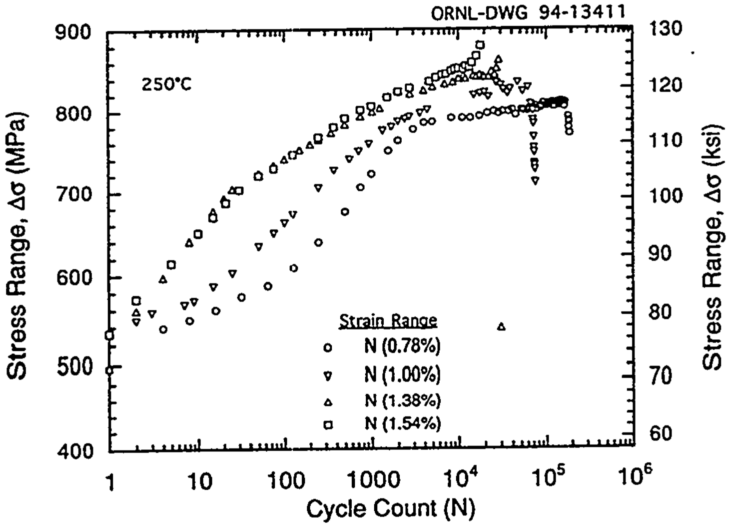

Fig. 5. Cyclic stress ranges vs cycle count for V-5Cr-5Ti alloy at 250°C.

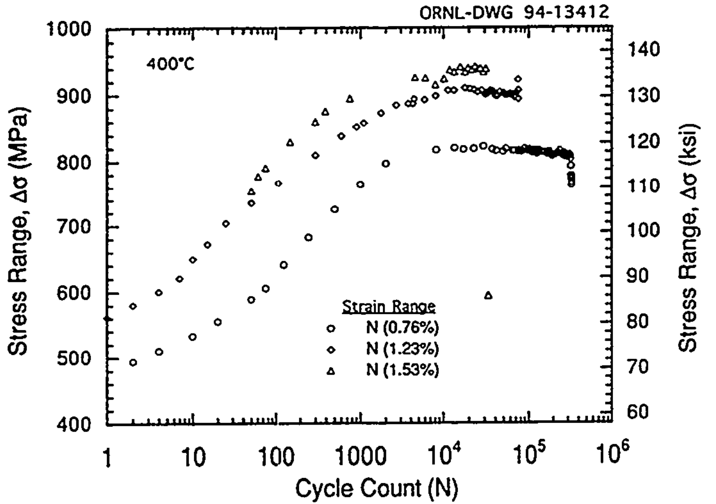

Fig. 6. Cyclic stress ranges vs cycle count for V-5Cr-5Ti alloy at 400°C.

Fatigue fracture surfaces from six specimens were examined using scanning electron microscopy (SEM) to better understand the nature of crack propagation and the effect of environment. In all tests, crack propagation appears to have occurred in a predominantly transgranular fashion with small amounts of intergranular fracture. Intergranular fracture typically occurred when grain boundaries were oriented such as to trap an approaching crack.

In Fig. 7, SEM micrographs are shown for tests conducted in rough and high vacuums at a nominal total strain range of 0.75%. The fracture morphology for the test conducted in rough vacuum (Fig. 7a) shows a courser striation spacing in combination with secondary cracking and a more brittle appearance than that observed for the test conducted in high vacuum (Fig. 7b). When viewed at a higher magnification (refer to Fig. 8a), the area shown in Fig. 7b shows signs of ductility on a microscopic scale, which is not present for the test in rough vacuum (*cf.* Fig. 8b),. This microductility was also observed in tests conducted at elevated temperatures conducted in high vacuum. With increasing temperatures, the amount of ductility appears greater, as one might expect.

The fine dipples creating the appearance of microductility on some of these fracture surfaces are associated with very fine particles. Previous studies have shown that the primary precipitates identified in vanadium alloys are titanium oxycarbonitrides [4] and it is assumed that these are present here. In other areas, the average size of features associated with this phenomena suggest that crack face welding has occurred during the compressive portion of the strain cycle.

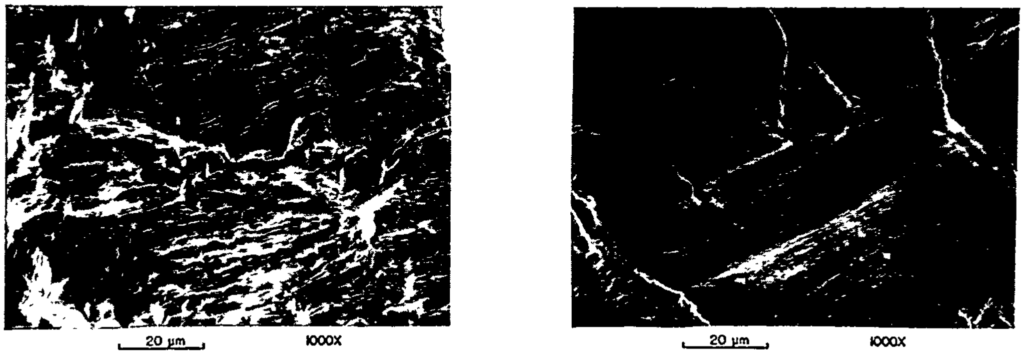

(a) (b)

Fig. 7. Scanning electron microscopy of RT fatigue fracture surfaces indicates differences in the fatigue crack propagation process for a nominal 0.75% strain range. (a) Sample 03 - tested in rough vacuum (U 007477). (b) Sample 16 - tested under high vacuum (U 007479).

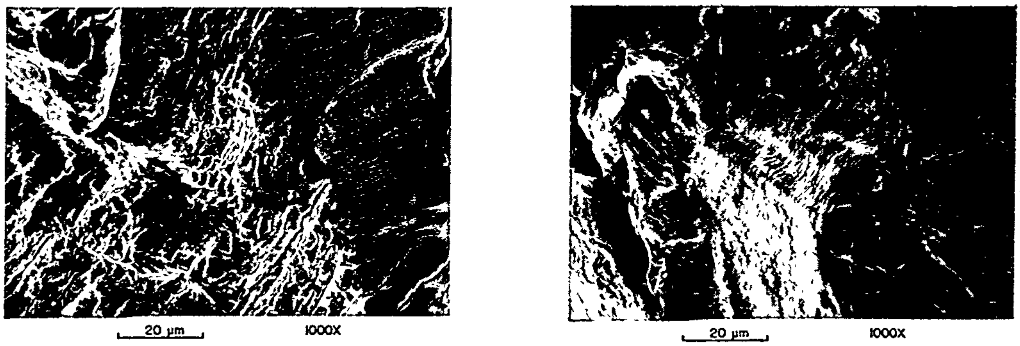

(a) (b)

Fig. 8. Scanning electron microscopy of RT fatigue fracture surfaces from tests conducted at a nominal 0.75% strain range. (a) Sample 16 - tested under high vacuum showing ductility on a microscopic scale (U 007476). (b) Sample 03 - tested in rough vacuum (U 007480).

DISCUSSION OF RESULTS

Environmental Effects

Several possible mechanisms exist which may explain the reduction in life observed in experiments conducted in a rough vacuum, including; (1) pickup of O and N interstitials, (2) changes in the crack initiation and/or growth mechanisms, and (3) hydrogen embrittlement arising from the interaction of moisture with the alloy. Oxygen and nitrogen are potent hardeners, but it is unlikely that diffusion rates of these species are sufficiently high at 25°C to have penetrated into the alloy and embrittled the alloy to any notable extent. Korth and Schmunk [5] conducted tests in air on Vanstar alloys 7, 8, and 9 at 400°C and found no change in oxygen content in post-test analyses of their samples. Hence, negligible oxygen (and nitrogen) diffusion at 25°C can be assumed.

On the other hand, oxygen or moisture present in the vacuum chamber may have formed a brittle oxide layer on any freshly exposed surfaces, such as those created by the rupture of a surface oxide during plastic deformation in each cycle or at persistent slip bands. Oxidation at persistent slip bands would result in earlier initiation and the repeated process oxide formation and rupture at a crack tip would lead to increased rates of crack growth. Furthermore, the formation of an oxide layer on the crack faces may prevent rewelding of these surfaces during the compression portion of the strain cycle, again, leading to increased crack growth rates. From the results shown in Fig. 4, a combination of these mechanisms is likely.

As Fig. 4 indicates, at the two lower strain ranges (nominally 0.75 and 1.0%) the data show little difference between rough and high vacuum up to point of maximum $\Delta\sigma$. At a nominal strain range of 1.5%, there is a notable difference in the hardening behavior for the majority of life. The reason for this is not known. The curves suggest that initiation occurs at approximately the same cycle count in the 1.53% strain range tests and that the difference in life is the result of a difference in crack growth rates. At the 1% strain range, it appears that differences in both the rate of initiation and crack growth are present. At the lowest strain range (0.75%), the curves suggest that both crack initiation and crack growth proceed more slowly in high vacuum. Hence, these curves suggest that the failure processes are complex and dependent upon the strain range. Additional testing would be required to estimate the relative contributions of each mechanism at work.

Surface oxides function as a barrier to hydrogen, but if it is removed by polishing, scratching, or chemical etching, hydrogen may be introduced from an aqueous medium, moisture in air, or an acid [6]. Cycling prior to crack initiation and during crack growth may have created and maintained an avenue for airborne moisture to reach and oxidize the alloy with the release and absorption of free hydrogen.

Comparison to Competing Alloys

An attempt has been made to compare data generated on V-5Cr-5Ti to other alloys under consideration for use in fusion reactors, including Vanstar alloys at 400°C, V-15Cr-5Ti alloy at 25°C, and 316 stainless at 25°C [7] and 430°C [6]. In most cases, test conditions are not identical to those used in the current study and a very limited data base exists making any comparison difficult.

In Fig. 9, a comparison of the room temperature low cycle fatigue properties of the V-5Cr-5Ti alloy is made with both 316 stainless steel [7] and a V-15Cr-5Ti alloy [2]. From the limited data, both the vanadium alloys appear to have better plastic strain resistance than does 316 stainless. The data may suggest that the endurance strain in the 316 SS is 0.25%, whereas estimates for the V-5Cr-5Ti and V-15Cr-5Ti are 0.5% and 0.75%, respectively. At strains greater than 1%, the data for the V-base alloys appear to converge, as would be expected since the ductilities do not differ by more than two percent [8] and strain controls life in this regime. The difference found at longer lives (lower strains) is attributed to increased strength of the V-15Cr-5Ti alloy and the resulting reduction in plastic strain ranges. Loomis et al., [8] report that both the yield and tensile strengths of the 5Cr alloy are 71-72% of those for the 15% alloy (σ_{ys} = 387 vs. 545; σ_{uts} = 454 vs. 634 MPa).

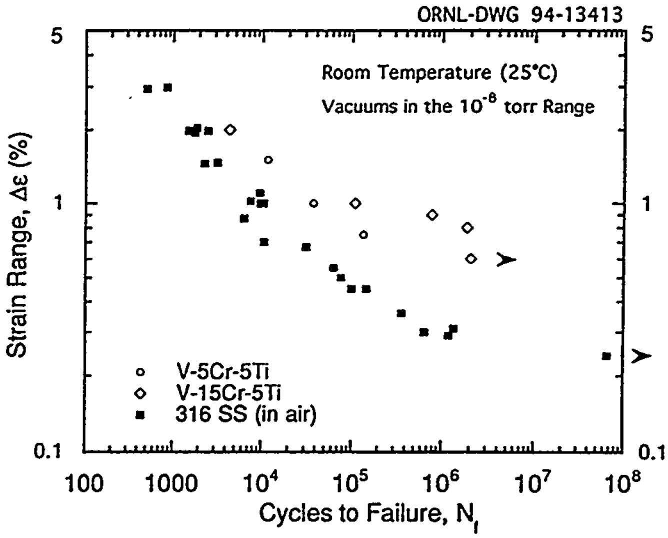

Fig. 9. Comparison of fatigue properties of V-5Cr-5Ti and V-15Cr-5Ti alloys to 316-SS at 25°C. Data for 316 stainless steel were obtained from Ref. 7 and those for V-15Cr-5Ti were obtained from Ref. 2.

Korth and Schmunk [5] tested Vanstar alloys 7, 8 and 9 in air at 400°C using a diametral extensometer and controlling the equivalent axial strain. Their data show little difference between the number of cycles, N_0, at initiation and the number of cycles to failure, N_f ,and they suggested that atmosphere had little effect on test results. In light of the results for V-5Cr-5Ti alloy, it is likely that N_f for tests conducted in vacuum would have been much greater. Notwithstanding this difficulty, the data are plotted in Fig. 10 and several observations can be drawn. First, at strain ranges of 1% or more, the V-5Cr-5Ti alloy shows better resistance to fatigue damage than Vanstar 9. At lower total strain ranges, the opposite is true. The better performance of Vanstar 9 at lower total strain ranges is, again, attributed to its higher yield strength (ie., 360 MPa [5] vs 250 MPa [8]) and the resulting reduction in plastic strains.

A second observation is that the V-5Cr-5Ti out performs alloys Vanstar 7 & 8 at all strain ranges shown. A comparison of the tensile data of Korth and Schmunk [5] on the Vanstar alloys to that of Loomis et al. [8] on V-5Cr-5Ti indicates that the V-5Cr-5Ti has greater strength than the Vanstar alloys 7 & 8 at 400°C. However, the authors believe that the testing of Vanstar alloys 7, 8, and 9 in vacuum would result in higher cyclic lives and probably eliminate much of the observed differences.

In Fig. 10, a comparison of the low cycle fatigue properties of the V-5Cr-5Ti alloy at 400°C is also made with 316 stainless steel [9] tested at 430°C. In this case, Grossbeck and Liu used the same specimen geometry and test method as was used in testing the V-5Cr-5Ti alloy such that the data should be very easily comparable with the exception of temperature. Again, the results suggest that the V-5Cr-5Ti alloy has better low cycle fatigue properties than does the 316 stainless around 400°C. While insufficient data exist to allow an endurance strain to be determined from the V-5Cr-5Ti alloy, it should be in the 0.5-0.6% range in comparison to the 0.3-0.4% value for the 316 stainless.

CONCLUSIONS

In-vacuum low cycle fatigue tests have been conducted on unirradiated V-5Cr-5Ti tested at temperatures of 25, 250, and 400°C. A comparison of the fatigue data generated in rough and high vacuums shows that a pronounced environmental degradation of the fatigue properties exists in this alloy at room temperature. Fatigue life was reduced by as much as 84%. The cyclic stress range data and SEM observations suggest that this difference is due to a combination of differences in rates of crack initiation and subsequent crack growth. The relative contribution of each difference is dependent upon the strain range.

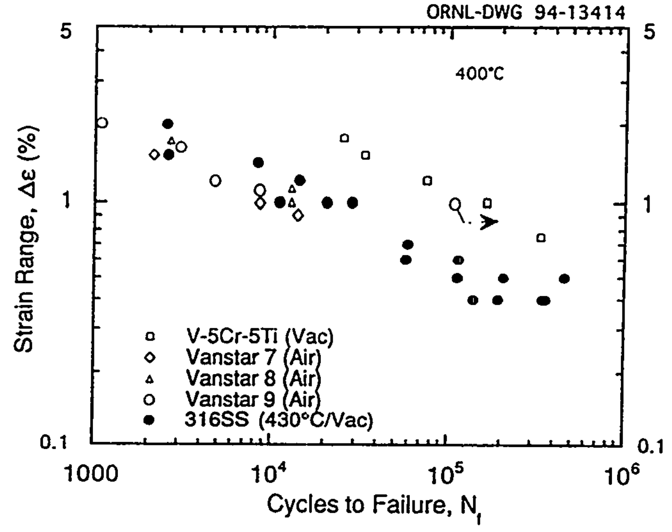

Fig. 10. Comparison of fatigue data for vanadium-base alloys and 316 stainless steel at temperatures 400 to 430°C. Data for 316 stainless were obtained from Ref. 9. Data for Vanstar alloys were obtained from Ref. 5.

In high vacuum, the fatigue results also show a trend of increasing cyclic life with increasing temperature between 25 and 400°C. From the limited data available, life at 250°C averages 1.7 times that at 25°C, and at 400°C, life averages 3.2 times that at 25°C. Like the environmental effects at 25°C, the effect of temperature seems to be a function of strain range at each temperature.

The total strain range and cycles to failure were analyzed using a power law correlation and compared to 20% cold-worked 316 stainless steel and several vanadium-base alloys. The results suggest that V-5Cr-5Ti has better resistance to fatigue than 316-SS in the temperature range of 25 to 400°C. At 400°C, the data also show that V-5Cr-5Ti out performs Vanstar alloys 7, and 8 over the entire range of strains investigated. Furthermore, the fatigue properties of the V-5Cr-5Ti alloy compare favorably to V-15Cr-5Ti (at 25°C) and Vanstar 9 (at 400°C) at strains greater than 1%. Differences seen at higher lives (lower strains) are attributed to the higher strength of the V-15Cr-5Ti and Vanstar 9 alloys.

FUTURE WORK

Low cycle fatigue studies are complete on this heat of V-5Cr-5Ti. Additional LCF tests may be conducted on the new 500 kg heat of this alloy currently being melted by TWC for ANL. The emphasis of future testing will likely shift to fatigue crack propagation measurements on this new heat of material.

REFERENCES

1. S.S. Manson, discussion of ASME paper 61-WA-199 by Tavernelli and Coffin, **J. Basic Eng. (Trans. ASME), 84 (No. 4)**, Dec 1962, 537-541.

2. K.C. Liu, *High Temperature Fatigue Behavior of Unirradiated V-15Cr-5Ti Tested in Vacuum,* **Journal of Nuclear Materials, 103 & 104, (1981) 913-918.**

3. R.W. Swindeman, *Low-Cycle Fatigue Study of Columbium Alloy D-43,* in **Fatigue at High Temperature**, ASTM STP 459, American Society for Testing and Materials, 1969, 31-41.

4. T. Schober and D.N. Braski, *The Microstructure of Selected Annealed Vanadium-Base Alloys,* **Met. Trans., 20A, (1989), 1927.**

5. G.E. Korth and R.E. Schmunk, *Low-Cycle Fatigue of Three Irradiated and Unirradiated Vanstar Alloys*, in **Effects of Radiation on Structural Materials**, ASTM STP 683, J.A. Sprague and D. Krammer, Eds., American Society for Testing and Materials, 1979, 466-476.

6. M.L. Grossbeck, *et al.*, *Fabrication of Vanadium Alloy Product Forms for Specimen Preparation*, in **Fusion Reactor Materials Semiannual Progress Report for Period Ending March 31, 1994**, U.S. Department of Energy, DOE/ER-0313/16 (1994).

7. C.E. Jaske and N.D. Frey, *High Cycle Fatigue of Type 316 Stainless Steel at Temperatures Up to 593°C (1100°F)*, Rockwell International, Report No. ESG-DOE-13307.

8. B.A. Loomis, *et al.*, *Tensile Properties of Vanadium and Vanadium-Base Alloys*, in **Fusion Reactor Materials Semiannual Progress Report for Period Ending March 31, 1991**, U.S. Department of Energy, DOE/ER-0313/10 (1991) 145-155.

9. M.L. Grossbeck and K.C. Liu, *Fatigue Behavior of Type 316 Stainless Steel Irradiated in a Mixed Spectrum Fission Reactor Forming Helium*, **Nuclear Tech**, **58**, Sep. 1982, 538-547.

WELDING DEVELOPMENT FOR V-Cr-Ti ALLOYS - J. F. King, G. M. Goodwin and D. J. Alexander (Oak Ridge National Laboratory)

OBJECTIVE

A vanadium structure, cooled with helium, is a favored concept for an advanced breeding blanket for fusion systems. The objective of this task is to develop the metallurgical and technological base for the welding of thick sections of V-Cr-Ti.

SUMMARY

The subsize Charpy test results for electron beam weld metal from the V-5Cr-5Ti alloy has shown significant improvement in Charpy fracture energy compared to both gas tungsten arc (GTA) weld metal and the base metal itself. These results are preliminary, however, and additional confirmation testing and analysis will be required to explain this improvement in properties.

PROGRESS AND STATUS

Introduction

The weldability and weldment properties of V-Cr-Ti alloys are being characterized. The reactive nature of vanadium alloys causes concerns with welding the potentially large components of the ITER system, and the selection of weld processes and procedures will have strong economic impact on component fabrication. Several welding processes are being evaluated, with the primary consideration being the effect of interstitial pickup on mechanical properties.

Experimental

A previous report[1] described the conditions for producing GTA welds in ~7 mm thick plate of the V-5Cr-5Ti alloy heat no. 832394. Identical welding conditions were used to produce two weldments (GTA 1 and GTA 2) in a glove box atmosphere containing less than 10 appm oxygen. An electron beam (EB) weld was made in the same plate material. Welding parameters were selected to produce a full penetration weld deposit in the vanadium plate. These were 150 kV accelerating voltage and 20.6 mA beam current at a welding speed of 12.7 mm/s.

One third size Charpy V-notch specimens were machined from the two GTA weldments and the EB weldment. Specimens were notched so that the crack propogated in the fusion zone along the welding direction.

Results

The Charpy properties of the GTA welds were significantly worse than those of the base metal annealed at 1125°C, Fig. 1. Although the number of specimens used was insufficient to define a complete impact energy-temperature curve, the CVN transition temperature of the weldments is clearly 100-150°C higher than that of the base metal. A set of specimens from GTA II was vacuum annealed at 400°C to remove any hydrogen that may have been picked up during welding or subsequent handling. As shown in Fig. 1, the 400°C anneal did not significantly affect CVN properties and it is concluded that hydrogen is not responsible for the poor fracture resistance of the GTA weld. On the other hand, annealing in vacuum at 950°C for 1 hour produced a dramatic improvement in impact properties (Fig. 1). Following the 950°C anneal, the impact properties were similar to those of the base metal.

A section of the completed EB weld was removed for metallographic examination. Examination of the weld cross section (Fig. 2) revealed no indication of weld discontinuities and little evidence of grain coarsening (Fig. 3) in the heat affected zone (HAZ). Hardness measurements were made across the weldment at approximately the middle of the plate thickness. The base metal had an average hardness of 177 DPH. The HAZ exhibited a higher average hardness of 198 DPH with measurements ranging from 180 to 229 DPH. The weld metal was very uniform with an average of 194 DPH. The variation in hardness values is relatively small across the weldment.

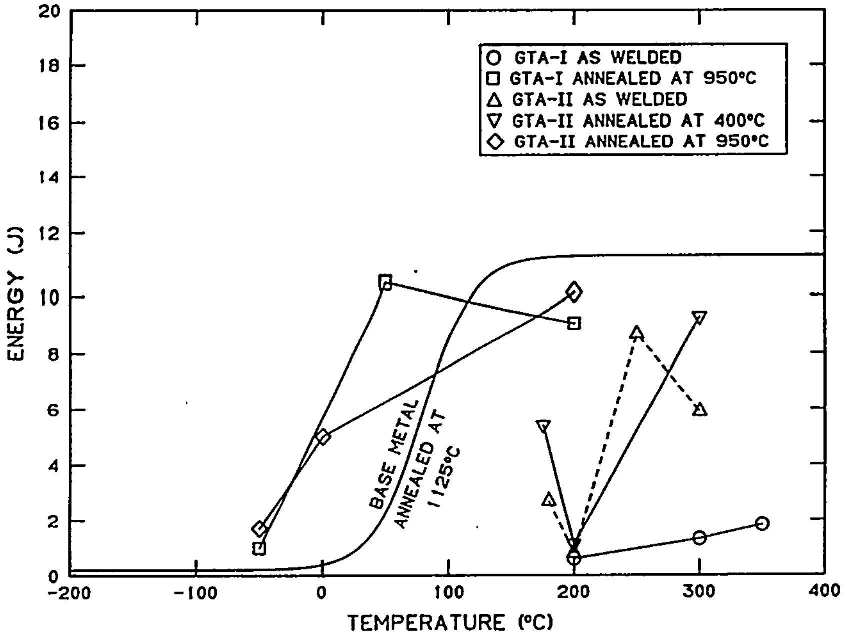

Fig. 1. Subsize Charpy V-notch test result from gas tungsten arc weldments in V-5Cr-5Ti alloy from heat 832394.

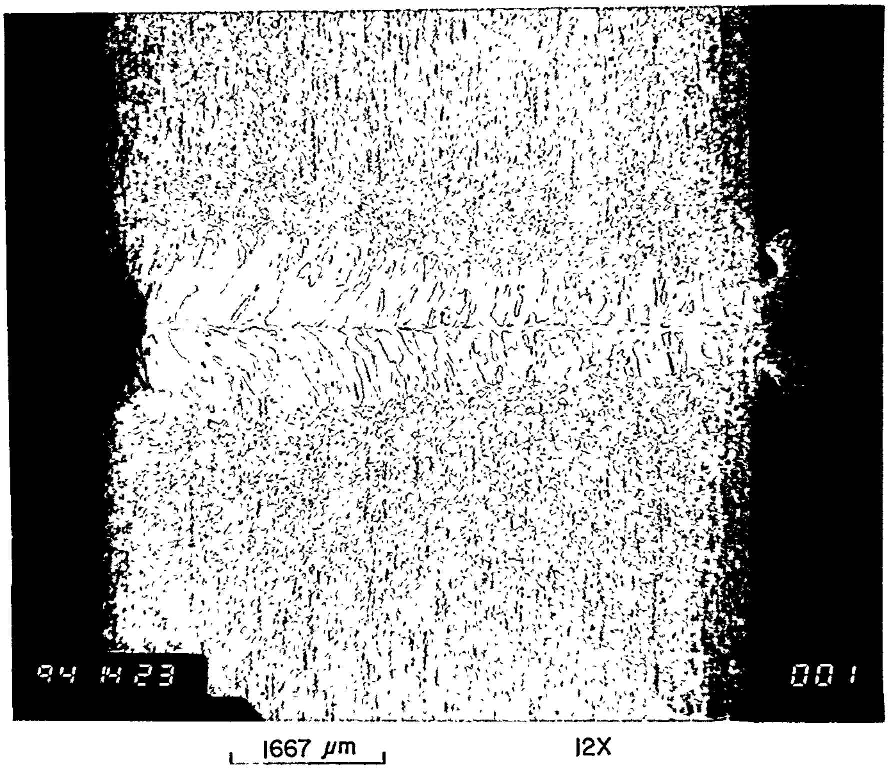

Fig. 2. Transverse cross-section of full penetration electron beam weld in 7 mm thick V-5Cr-5Ti alloy.

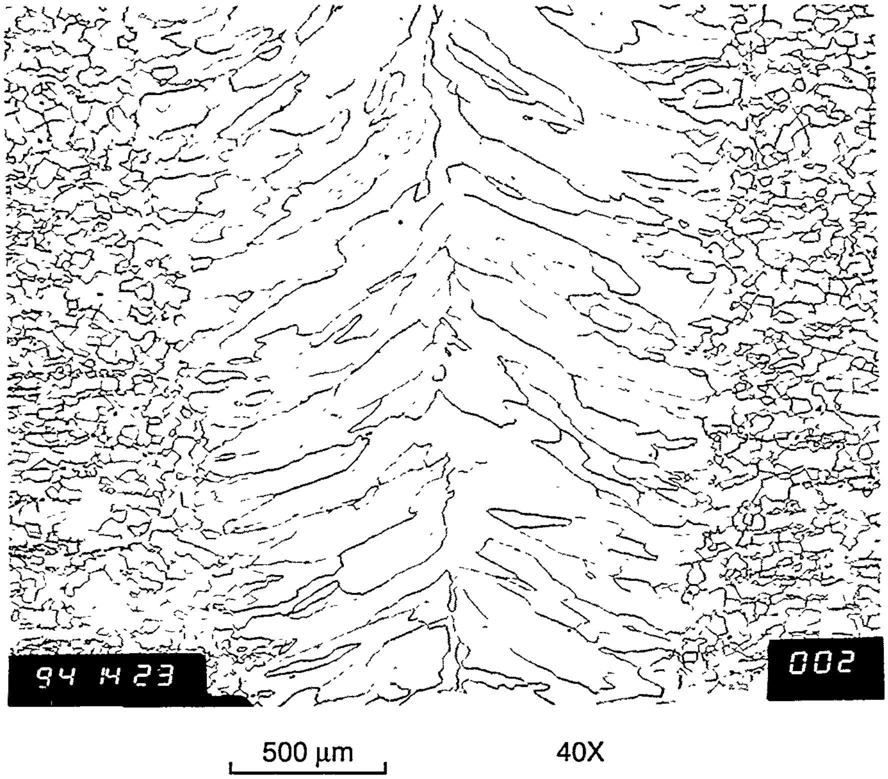

Fig. 3. Transverse cross-section of the HAZ of the electron beam weld in the V-5Cr-5Ti alloy shows little evidence of grain coarsening.

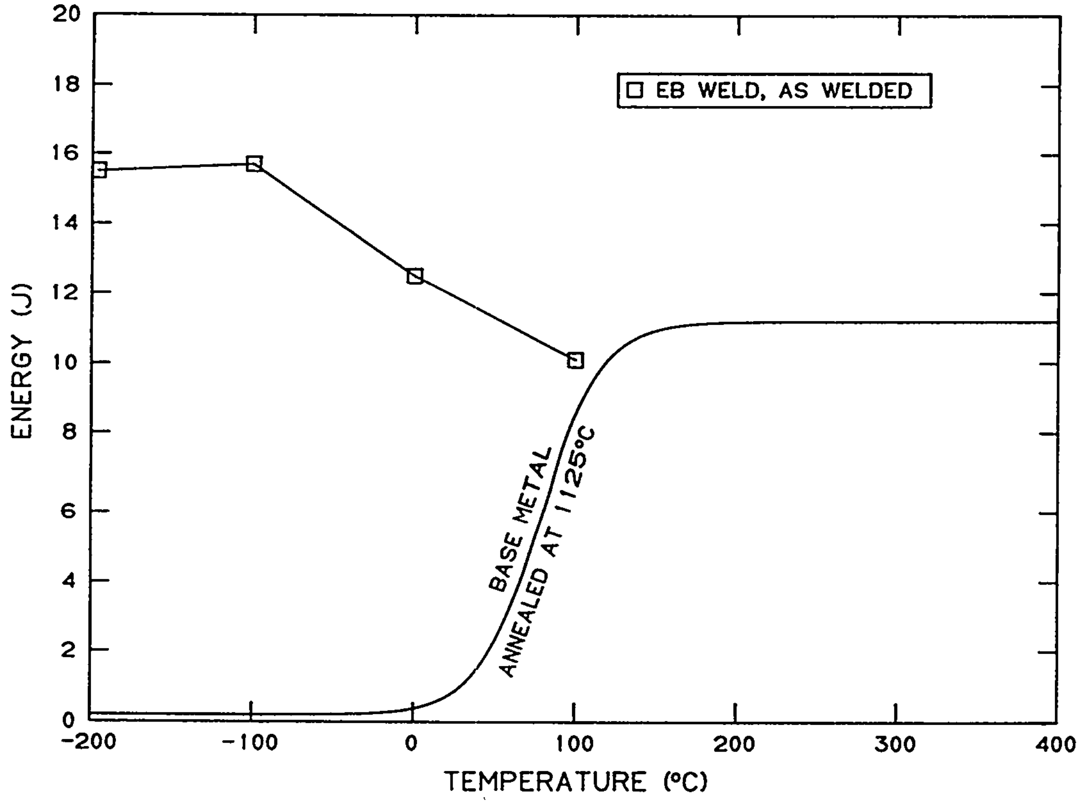

Fig. 4. Subsize Charpy V-notch tests results from earlier electron beam weld (EB-I) and present electron beam (EB-II) in V-5Cr-5Ti alloy from Heat 832394.

Subsize Charpy V-notch specimens were machined from the weldment and notched in the center of the weld fusion zone such that the fracture occurs in the direction of welding. Four of these specimens were tested in the as-welded condition at temperatures ranging from ~100°C down to ~-200°C. At each temperature, specimens failed in a predominantly ductile mode with high values of absorbed energy (Fig. 4). This is a rather surprising result in view of the coarse-grained (~500 μm) microstructure of the fusion zone; and implies that a post weld heat treatment may not be required

FUTURE WORK

SEM, TEM, and Auger measurements are in progress (a) to understand the mechanisms involved in the beneficial effects of the 950°C post-weld heat treatment on the properties of the GTA welds, and (b) to understand the superior properties of the EB weld. Further weld development will focus on the new large heat of V-4Cr-4Ti.

REFERENCES

1. G. M. Goodwin and J. F. King, "Welding Development for V-Cr-Ti Alloys," Fusion Materials Semiannual Progress Report (DOE/ER-0313/16), p. 235.

DISLOCATION DEVELOPMENT IN V-5CR-5TI AND PURE VANADIUM - D. S. Gelles, (Pacific Northwest Laboratory)[a] and M. L. Grossbeck, (Oak Ridge National Laboratory)

OBJECTIVE

The objective of this work is to explain notch sensitivity noted in the candidate alloy V-5Cr-5Ti.

SUMMARY

Microstructural examinations have been performed on deformed tensile specimens of V-5Cr-5Ti and pure vanadium in order to explain notch sensitivity noted in the candidate alloy V-5Cr-5Ti. SS-3 tensile specimens have been prepared, stress relieved and deformed to 5% strain. The resulting deformation structures have been examined by transmission electron microscopy. It is found that 5% deformation in V-5Cr-5Ti produces a higher dislocation density consisting of long straight dislocations, typical of Stage II, and many small loops, whereas in pure vanadium, the dislocation arrangements are more complex, typical of Stage III, and the small loops are at a lower density.

These results are interpreted in light of the tendency for enhanced notch sensitivity found in V-5Cr-5Ti.

PROGRESS AND STATUS

Introduction

A vanadium alloy in the composition range V-5Cr-5Ti is being considered as an alternate structural material for the International Thermonuclear Experimental Reactor (ITER) design.[1] Research and Development task 5.4.1.1 calls for compatibility and irradiation tests for vanadium alloys. Vanadium may provide a major improvement in performance in comparison with other options such as austenitic and ferritic steels because of inherently better high temperature properties and inherently reduced long term radioactivity after neutron irradiation. However, a great deal remains to be learned about the behavior of this alloy class before it can be code qualified for reactor construction.

Recently, efforts have been started to quantify fracture toughness response in V-5Cr-5Ti.[2] Those efforts demonstrated that at 100°C, the fracture toughness remains very high and shows response similar to the very tough Martensitic steel F-82H, whereas at 25°C, toughness is much lower. Also, both preliminary fracture toughness testing and fractographic examination suggested that V-5Cr-5Ti is notch sensitive.[2] Similar indications can be deduced from V-5Cr-5Ti Charpy impact specimens tested with a range of notch root radii, and may indicated that V-5Cr-5Ti has a higher notch sensitivity than ferritic steels.

As a part of the effort to understand the notch sensitivity of V-5Cr-5Ti, the present work was undertaken. The original concept was to examine deformation behavior in V-5Cr-5Ti by deforming single crystals and comparing the response to pure vanadium. The intent was to determine if the number of slip planes was reduced, or if some other details could be identified in the dislocation structure to explain the behavior. However, the work scope was reduced by limiting experiments to polycrystalline material and making use of V-5Cr-5Ti miniature tensile specimens already available. Pure vanadium was tested for comparison.

---

[a] Pacific Northwest Laboratory is operated for the U.S. Department of Energy by Battelle Memorial Institute under Contract DE-AC06-76RLO 1830.

Experimental Procedure

Pure vanadium sheet 1.44 mm in thickness was provided by R. Peterson, Teledyne Wah Chang, Albany, Oregon. V-5Cr-5Ti sheet 1 mm in thickness was from heat BL63 #832394, also produced by Teledyne Wah Chang. Composition information is given in Table 1. Specimens to SS-3 specifications with a gage section 1.52 x 0.76 x 7.62 mm in length were machined from the sheet, etched in 10% hydrofluoric acid and 30% nitric acid in water, and annealed for 1 hour at 1125°C. During heat treatment, they were wrapped in tantalum foil in a vacuum below 10^{-5} Pa.

Table 1. Composition of pure vanadium and V-5Cr-5Ti (Heat BL63 #832394) as supplied by Teledyne Wah Chang.

Alloy	Composition in ppm unless noted, balance Vanadium								
	Al	B	C	Cr	Fe	H	Hf	Mo	Ni
Pure Vanadium	<300	<10	<100	<20	<200	<5	<100	<200	<20
V-5Cr-5Ti	200	<5	73	4.6%	<370	NA	NA	500	NA
	Nb	O	P	S	Si	Ta	Ti	U	Zr
Pure Vanadium	<250	<400	<100	<20	<400	<300	<50	<2	<100
V-5Cr-5Ti	<50	<5	<30	NA	310		5.1%	<1	NA

Tensile specimens were deformed to 5% strain at a strain rate of $1.1 \times 10^{-3}\ s^{-1}$ at room temperature. The gauge section was cut into 3 mm sections. Specimens were prepared for transmission electron microscopy using a Tenupol twin jet electropolishing device with a solution of 5% sulfuric acid in methanol at 40 V and moderate pump speed. Foils with acceptable thin area were possible using a small dimple size. Cleaning was in methanol.

Microstructural examinations used a JEM 1200EX transmission electron microscope equipped with a double tilting goniometer stage. Procedures involved a series of dislocation imaging conditions using $\vec{g} = 200$ as a stereo pair, $01\bar{1}$, $21\bar{1}$, $2\bar{1}1$, $1\bar{2}1$, $12\bar{1}$, and $\bar{1}10$, (or the equivalent) for a foil near an [011] orientation. This notation is defined in Figure 1, and the resultant imaging conditions are defined in Table 2. A review of Table 2 will show that all $\frac{a}{2}<111>$ Burgers vectors are imaged using $\vec{g} = 200$, half are imaged with $\vec{g} = 110$, and for each of the $\vec{g} = 211$ images, one Burgers vector is invisible, and one is in stronger contrast than the remaining two. From the series of imaging conditions used in the present work, shown in bold in Table 2, all Burgers vectors can be uniquely identified. The procedure will be described in greater detail in the results section.

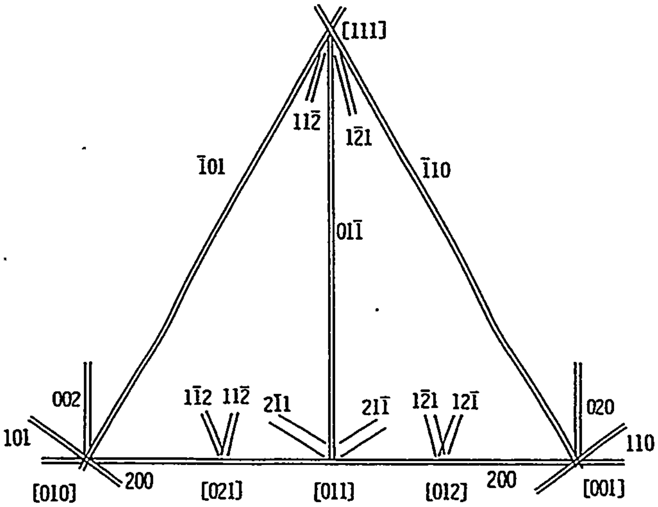

Figure 1. Definition of notation as represented on a Kikuchi map for bcc dislocation imaging conditions.

Table 2. The $\vec{g} \cdot \vec{b}$ imaging criteria for various bcc imaging conditions and Burgers vector combinations.

$\vec{g}$	Burgers vector			
	$\frac{a}{2}[111]$	$\frac{a}{2}[\bar{1}11]$	$\frac{a}{2}[1\bar{1}1]$	$\frac{a}{2}[11\bar{1}]$
200	**1**	**1**	**1**	**1**
020	1	1	1	1
002	1	1	1	1
$01\bar{1}$	**0**	**0**	**1**	**1**
$\bar{1}10$	**0**	**1**	**1**	**0**
$\bar{1}01$	0	1	0	1
101	1	0	1	0
$11\bar{2}$	0	1	1	2
$1\bar{2}1$	**0**	**1**	**2**	**1**
$2\bar{1}1$	**1**	**1**	**2**	**0**
$21\bar{1}$	**1**	**1**	**0**	**2**
$1\bar{1}2$	1	0	2	1
$12\bar{1}$	**1**	**0**	**1**	**2**

Results

Tensile Testing

The tensile test traces for specimens deformed to 5% strain are shown in Figure 2. Figure 2a shows response for pure vanadium strained to 5% and indicates load drop behavior. The upper yield strength was 409.5 MPa (59.4 ksi), and the tensile strength at 5% strain was 435.7 MPa (63.2 ksi). Figure 2b shows similar response for V-5Cr-5Ti with a slightly higher yield strength, but no yield drop and at a lower work hardening rate. The yield strength was 421.3 MPa (61.1 ksi), and the tensile strength at 5% strain was 421.3 MPa (73.6 ksi).

Microstructures

Dislocation development as a result of 5% deformation at room temperature was found to differ as a function of alloying. Pure vanadium developed a complex dislocation structure typical of stage III deformation (forest dislocation development) with large spaces between tangles, whereas V-5Cr-5Ti dislocation structures were less complicated but more uniformly distributed, often containing long straight dislocations typical of stage II. Both materials also showed dislocation loop formation with loop sizes on the order of 10 nm in diameter. Slip band orientations could not be identified based on stereoscopic examination of the dislocation structures.

Examples of these dislocation structures following deformation are shown in Figures 3 and 4. Each figure is arranged to provide a stereo pair using $\vec{g} = 200$ taken near the (011) orientation in Figures 3 a) and b), using $\vec{g} = 01\bar{1}$ near (011) in 3 c), $\vec{g} = \bar{1}10$ near (112) in 3 d), and $\vec{g} = 21\bar{1}$, $2\bar{1}1$, $1\bar{2}1$, and $12\bar{1}$, in 3 e), f), g) and h), respectively.

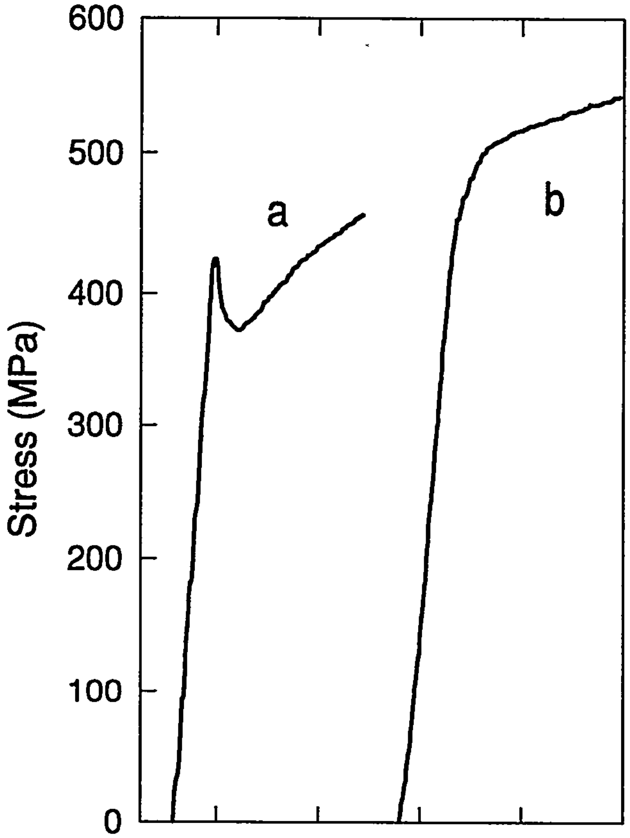

Figure 2. Stress strain curves for a) pure vanadium and b) V-5Cr-5Ti deformed at room temperature to 5% strain.

From Figure 3 for pure vanadium, it is apparent that the dislocation structure in deformed pure vanadium consists of dislocation tangles and isolated loops. Comparing the dislocation images in Figure 3, the following can be demonstrated. Several of the possible Burgers vectors are present, as different imaging conditions show different structures. The Burgers vectors can be determined based on the information in Table 2. For example, the dislocations in Figures 3 c) and 3 d) are different, but all can be found in Figures 3 a) and b). Therefore, the dislocations are indeed of type $\frac{a}{2}$<111>, and the dislocations appearing only in 3 c) have Burgers vector $\frac{a}{2}[11\bar{1}]$, and the dislocations appearing only in 3 d) have Burgers vector $\frac{a}{2}[1\bar{1}1]$. {Those appearing in both 3 c) and d) have Burgers vector $\frac{a}{2}[1\bar{1}1]$, and those appearing in 3 a) and b) but not in 3 c) and d) have Burgers vector $\frac{a}{2}[111]$.} Similarly, the loops are predominantly of Burgers vector $\frac{a}{2}[11\bar{1}]$, but examples of $\frac{a}{2}[1\bar{1}1]$ can be noted at the upper right in Figure 3 d). These conclusions can be verified from Figures 3 e) to h) by noting that $\frac{a}{2}[1\bar{1}1]$ dislocations do not appear, and $\frac{a}{2}[11\bar{1}]$ are in strong contrast in Figure 3 e); $\frac{a}{2}[11\bar{1}]$ dislocations do not appear, and $\frac{a}{2}[1\bar{1}1]$ are in strong contrast in Figure 3 f); $\frac{a}{2}[111]$ dislocations do not appear, and $\frac{a}{2}[1\bar{1}1]$ are in strong contrast in Figure 3 g); and $\frac{a}{2}[\bar{1}11]$ dislocations do not appear, and $\frac{a}{2}[11\bar{1}]$ are in strong contrast in Figure 3 h).

An example of the dislocation structures found in V-5Cr-5Ti are shown in Figure 4. The imaging conditions match those in Figure 3, but the dislocation structures are different. Dislocations appear as straight parallel lines, and many loops are visible. Burgers vector analysis gives similar results, however, with the highest density of Burgers vector type $\frac{a}{2}[11\bar{1}]$, and type $\frac{a}{2}[1\bar{1}1]$ at lower density.

Microstructural Analysis

The dislocation and loop structures were quantified, and the results are provided in Table 3. From Table 3, it can be shown that the dislocations structures of the two conditions examined are similar in many ways, the major difference being a somewhat higher dislocation density, and a factor of three times higher loop density for V-5Cr-5Ti. It can be noted for example, the most prevalent Burgers.vector present is the same in both cases and by a factor of two, that being $\frac{a}{2}[11\bar{1}]$.

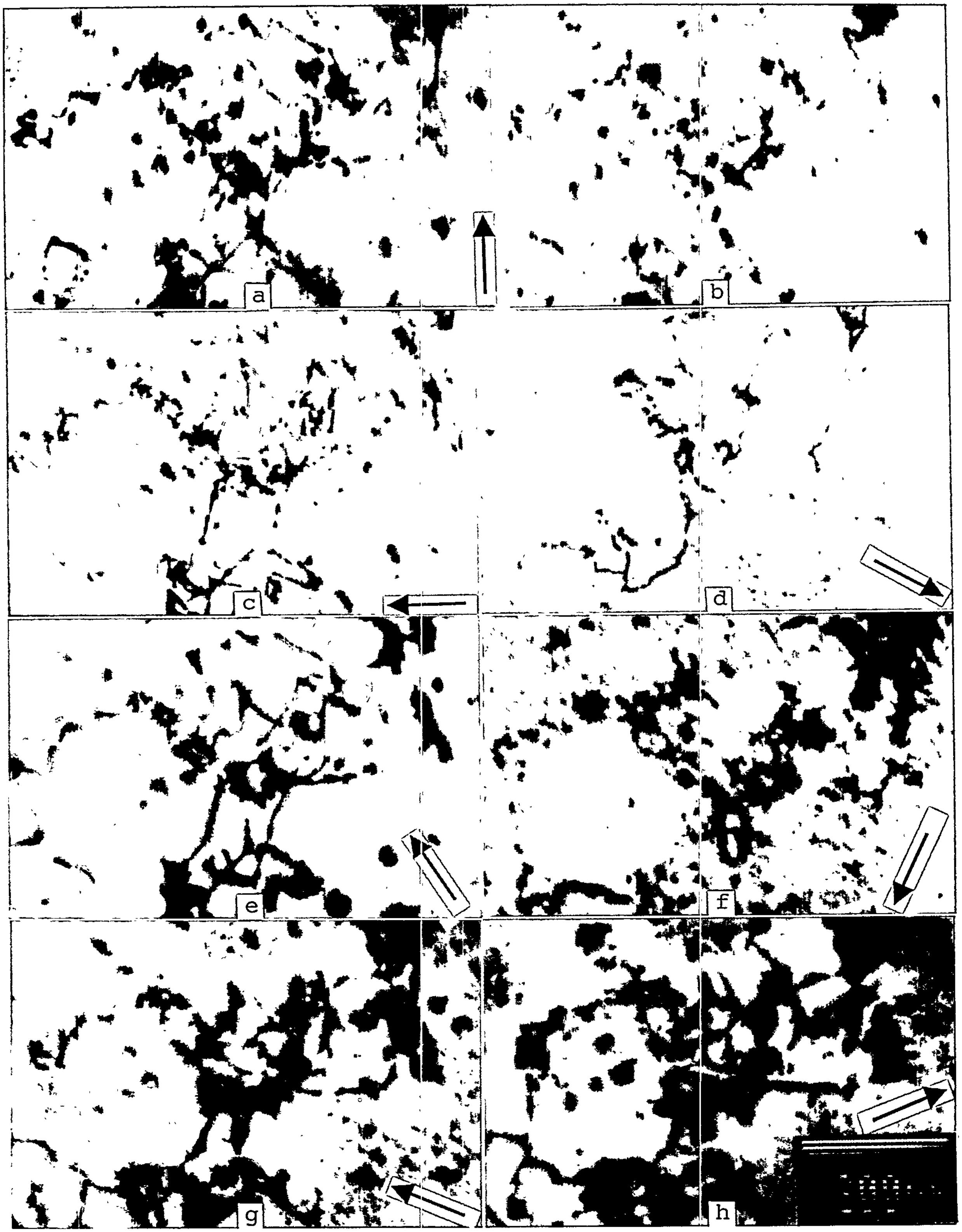

Figure 3. Dislocations in pure vanadium strained 5% at room temperature under the following contrast conditions: a) 200 near (011), b) 200 near (013), c) $01\bar{1}$ near (011), d) $\bar{1}10$ near (112), e) $21\bar{1}$ near (011), f) $2\bar{1}1$ near (011), g) $1\bar{2}1$ near (013), and h) $12\bar{1}$ near (013).

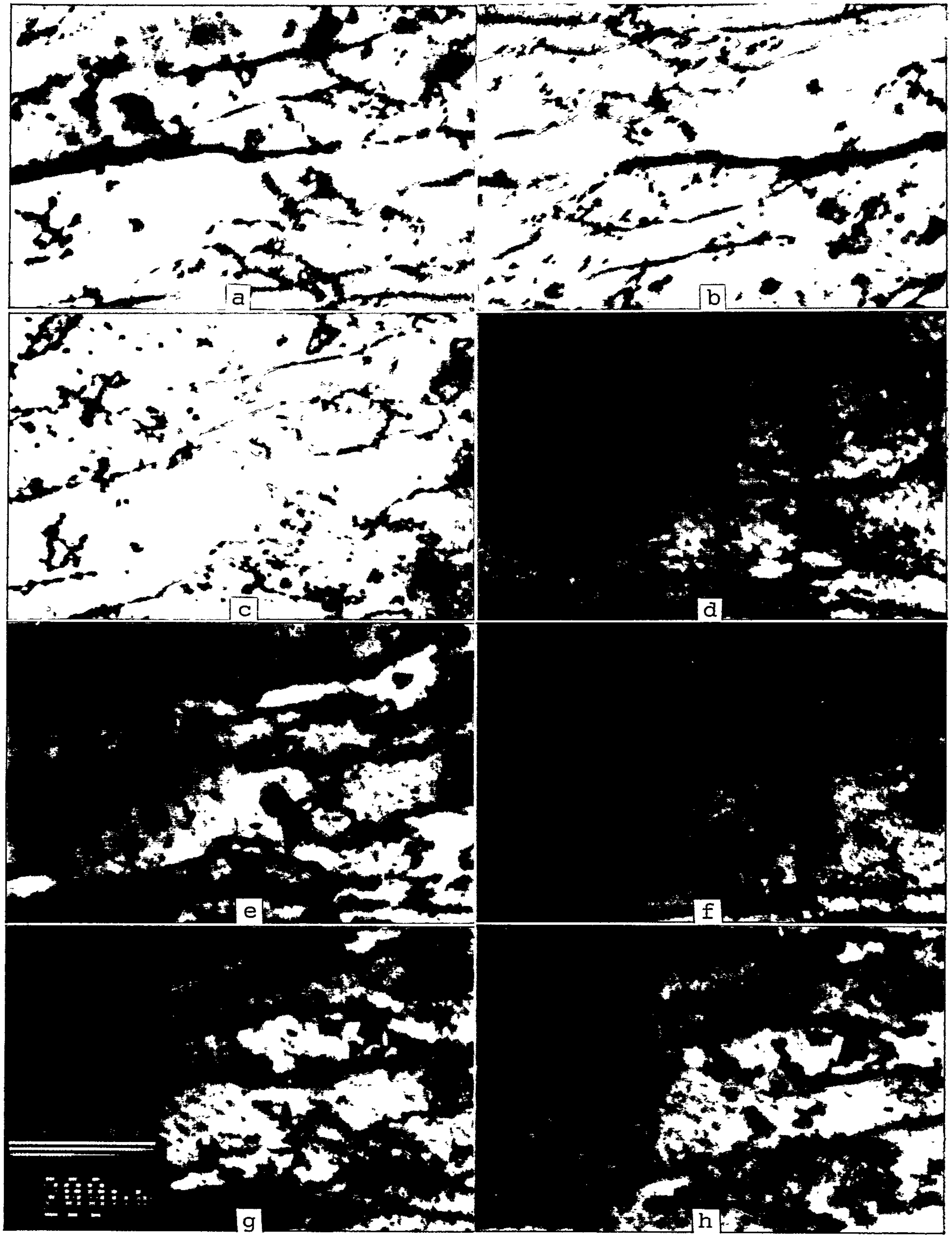

Figure 4. Dislocations in V-5Cr-5Ti strained 5% at room temperature under the following contrast conditions: a) 200 near (011), b) 200 near (013), c) $01\bar{1}$ near (011), d) $\bar{1}10$ near (112), e) $21\bar{1}$ near (011), f) $2\bar{1}1$ near (011), g) $1\bar{2}1$ near (013), and h) $12\bar{1}$ near (013).

Table 3. Results of quantitative dislocation analyses.

Alloy	Dislocations (cm^{-2})					Loops	
	$\frac{a}{2}[111]$	$\frac{a}{2}[\bar{1}11]$	$\frac{a}{2}[1\bar{1}1]$	$\frac{a}{2}[11\bar{1}]$	Total	# Density (cm^{-3})	Mean Diameter (nm)
Pure Vanadium	$1.2x10^8$	$1.4x10^9$	$1.2x10^8$	$2.7x10^9$	$4.3x10^9$	$6.2x10^{14}$	11.9
V-5Cr-5Ti	N.M.	$2.3x10^9$	N.M.	$4.2x10^9$	$6.5x10^9$	$1.8x10^{15}$	8.1

N.M. = not measured, too small to measure given the limited statistics

Discussion

Slip modes in vanadium and its alloys

Dislocation development in vanadium and its alloys has been reported a number of times. Edington and Smallman showed typical microstructures as a function of test temperature in polycrystalline vanadium.[3] The predominant slip response was later documented by private communication[4] as follows: both at room temperature and at low temperature, {110}(T) and {112}(T). Russian work was on slip in single crystals of vanadium for the temperature range 150 to 400K oriented to favor $(112)[\bar{1}\bar{1}1]$ slip in Stage I, with $(\bar{2}11)[111]$ coming into play in Stage II.[5] As a function of temperature, slip began on $(1\bar{1}0)[111]$ at 150K, but on $(112)[\bar{1}\bar{1}1]$ and $(\bar{2}11)[111]$ at higher temperatures. The Stage II dislocation structures were similar to those found in the present study in V-5Cr-5Ti (Figure 4) whereas the Stage III dislocation structures were similar to those for pure vanadium (Figure 3). In contrast, Belgian work on pure vanadium showed that slip in single crystals of vanadium in the temperature range 77 to 298K was on {101} at low temperatures and was noncrystallographic at 298K, deviating towards the $(\bar{1}01)$ plane.[6] Slip on {112}-type planes was rarely observed. The analysis was based on slip trace analysis. Most recently, the Russian results were reviewed,[7] including results for two vanadium alloys: at low temperature, the $(011)[11\bar{1}]$ system operated in the range 77 to 150K for vanadium, in the range 77 to 270K for V-5Ta and in the range 77 to 300K for V-25Ta whereas the $(112)[11\bar{1}]$ system operated in the range 120 to 650K for vanadium, and in the range 250 to 650 for V-5Ta and V-25Ta. The work also assesses the transition temperature to form a cellular dislocation structure and notes that this occurs at 320K in vanadium, but at 350 and 560K in V-5Ta and V-25Ta, respectively.

Explanation for notch sensitivity in V-5Cr-5Ti

The present effort has provided several results that may be relevant to the question of increased notch sensitivity in V-5Cr-5Ti. Those results will be summarized, and then the results will be considered in light of their effect on notch sensitivity.

Tensile tests to 5% deformation show that in comparison to pure vanadium, V-5Cr-5Ti has a higher yield strength and a lower work hardening rate, but no yield drop. A higher yield strength should correspond to a smaller crack tip plastic zone size, and the lower work hardening rate can be expected to provide higher toughness. The lack of a yield drop can also be expected to enhance toughness.

Microstructural examinations demonstrate that Stage II deformation is maintained to 5% strain in V-5Cr-5Ti, whereas in pure vanadium, Stage III behavior is found at 5% strain. Also, the density of loops is found to be higher in V-5Cr-5Ti. The observation of Stage II response in V-5Cr-5Ti is likely a consequence of a lower work hardening rate and may be a measure of a tendency to avoid cross slip, but the increased loop density is expected to be a measure of strain centers arising from the presence of increased titanium levels and the resultant tendency for formation of Ti(C,N,O) complexes.

It can be noted that the tendency for reduced cross slip and delay in the transition to Stage III can be expected to be related to a lower stacking fault energy.[8] Noskova[9] has shown that as a function of increasing tantalum in vanadium, the stacking fault energy is reduced, from 80 to 100 MJ/m^2 for pure vanadium, from 73 to 80 MJ/m^2 for V-5Ta and from 37 to 70MJ/m^2 for V-15Ta. Similar reductions in stacking fault energy can be expected to arise with additions of titanium and chromium, although no measurements are available to support such an assumption. However, it can also be noted that the work hardening rate is generally inversely related to stacking fault energy so that high work hardening rates arise when stacking fault energies are low, in opposition to the present situation. Also, Stage III work hardening rates are lower than Stage II. Therefore, the lower work hardening rate found in V-5Cr-5Ti must be a consequence of some other factor such as reduced interstitial hardening due to the presence of titanium gettering.

Increases in notch sensitivity are likely to arise from three effects: interstitial impurity hardening, grain boundary segregation, and large precipitate particles ahead of the crack tip. The present work only points to an effect due to the interaction of a higher stress field (associated with a sharper crack) with crack nucleation sites ahead of the propagating crack. If sufficient potential nucleation sites for cavity formation exist, then a higher stress state will be more likely to activate cavitation ahead of the propagating crack. Conversely, notch insensitivity can be expected when the crack tip plastic zone size is small compared to the spacing of potential crack nucleation sites. Therefore, key factors affecting notch sensitivity can be expected to be plastic zone size and spacing between potential cavity nucleation sites.

The present work does not provide clear guidance on the effect of alloying on plastic zone size. Strength is increased due to alloying, but stage II is prolonged to higher strains, and work hardening rates are reduced. The relative increase in strength is small due to the avoidance of yield drop behavior. Therefore, it is likely that the plastic zone sizes for pure vanadium and V-5Cr-5Ti are similar.

The most likely reason for increased notch sensitivity in V-5Cr-5Ti can be traced to potential cavity nucleation site density. Alloying is expected to promote the formation of Ti(C,N,O) complexes, and microstructural observation of enhanced loop density following deformation is interpreted as evidence supporting this assertion. However, the sites promoting loop formation are probably too small to be potential cavity nucleation sites. A more reasonable feature for a cavity nucleation site is larger Ti(C,N,O) precipitate particles, approximately 100 nm or larger in diameter, that can easily be found in V-5Cr-5Ti. The distribution of these larger precipitate particles can be expected to be altered by heat treatment in the temperature range 900°C and above. Therefore, it can be tentatively concluded that enhanced notch sensitivity in V-5Cr-5Ti is a consequence of the scavenging effect of titanium additions and the resultant increase in the density of potential cavity nucleation sites. This density of sites can be altered, at least to some degree, by suitable heat treatment.

CONCLUSIONS

Deformation response of V-5Cr-5Ti has been compared with that of pure vanadium. It is found that alloying increases yield strength, reduces work hardening rate, and avoids yield drop response. Following deformation to 5% strain, Stage II response is maintained in the alloy, whereas Stage III is reached without alloying. Alloying also increases the density of dislocation loops formed during deformation. These results are interpreted to conclude that alloying does not significantly alter crack tip plastic zone size, whereas it can significantly increase Ti(C,N,O) precipitation and therefore potential sites for cavity nucleation.

FUTURE WORK

This work will be continued when warranted.

REFERENCES

1. ITER Design and R&D Program, MAC6, Garching Germany, 7-8 July 1994.

2. Huaxin Li, R. H. Jones, and J. P. Hirth, DOE/ER-0313/16, in press.

3. J. W. Edington and R. E. Smallman, Acta Met., 12 (1964) 1313.

4. Table 9-2 "Slip planes in bcc metals" in Theory of Dislocations by J. P. Hirth and J. Lothe (McGraw Hill, NY., 1968) pg. 258.

5. N. I. Noskova and V. I. Dolgopolov, Phys. Met. Metall., 45 (1979) 130.

6. J. Bressers and P. De Meester, J. Less-Common Metals, 84 (1982) 11.

7. N. I. Noskova, A. I. Zhuravleva, N. F. Vil'danova, and I. A. Pereturina, Phys. Met. Metall., 64 (1987) 128.

8. R. E. Smallman, Modern Physical Metallurgy (Buttersworth, London) 349.

9. N. I. Noskova, Phys. Met. Metall., 60 (1985) 165.

EFFECT OF HEAT TREATMENT ON MICROSTRUCTURE AND FRACTURE TOUGHNESS OF A V-5Cr-5Ti ALLOY - H. Li (Associated Western Universities--Northwest Division), M. L. Hamilton and R. H. Jones (Pacific Northwest Laboratory)

OBJECTIVE

The purpose of this research is to investigate the effect of heat treatment on microstructure and fracture toughness in the range of -50 to 100°C for a V-5Cr-5Ti alloy.

SUMMARY

Fracture toughness and impact tests were performed on a V-5Cr-5Ti alloy. Specimens annealed at 1125°C for 1 h and furnace cooled in a vacuum of 1.33 x 10^{-5} Pa were brittle at room temperature (RT) and experienced a mixture of intergranular and cleavage fracture. Fracture toughness (J_{IQ}) at RT was 52 kJ/m^2 and the impact fracture energy (IFE) was 6 J. The IFE at -100°C was only 1 J. While specimens exhibited high fracture toughness at 100°C (J_{IQ} is 485 kJ/m^2), fracture was a mixture of dimple and intergranular failure, with intergranular fracture making up 40% of the total fracture surface. The ductile to brittle transition temperature (DBTT) was estimated to be about 20°C. When some specimens were given an additional annealing at 890°C for 24 h, they became very ductile at RT and fractured by microvoid coalescence. The J_{IQ} value increased from 52 kJ/m^2 to ~1100 kJ/m^2. The impact test failed to fracture specimens at RT due to a large amount of plastic deformation. The IFE at -115°C was 4 J, four times as much as when annealed only at 1125°C. The specimens became brittle at -50°C and fractured by cleavage, giving a J_{IQ} value of 50 kJ/m^2. The DBTT was estimated to be -40°C. Analysis of Auger electron microscopy showed significant sulfur segregation (6 at%) on grain boundaries in the specimens annealed only at 1125°C, but only 0.9 at% on grain boundaries if the additional annealing at 890°C was given. Moreover, significantly more second phase particles were found in the specimens annealed at 1125°C plus 890°C. The possible mechanism by which heat treatment affects fracture toughness is discussed.

PROGRESS AND STATUS

Introduction

We have reported[1] that a V-5Cr-5Ti alloy (ANL Heat BL-63) was brittle at RT and experienced mixed intergranular and cleavage fracture when heat treated at 1125°C for 1h and furnace cooled. While it became ductile at 100°C, it still failed by a mixture of intergranular and microvoid coalescence modes. The mixed mode I/III fracture toughness (J_{TQ}) at a crack angle of 45° (where the mode III loading component is equal to the mode I loading component) was much less than pure mode I fracture toughness, as shown in Fig. 1. The data from a ferritic/martensitic stainless steel (F82-H) is included for comparison. Specimens fractured in an Auger electron microscope (AEM) vacuum chamber at low temperature (estimated about -20°C) consisted of intergranular and cleavage fracture. AEM analysis revealed a significant enrichment of S (6 at%) on the grain boundaries, as comparing to 0.3 at% S on the cleavage facets. On the other hand, a specimen annealed at 1050° for 1h fractured in the AEM by microviod coalescence. To produce an intergranular fracture surface, hydrogen had to be introduced by cathodic charging. The result indicated that the lower annealing temperature improved the ductility of the V-5Cr-

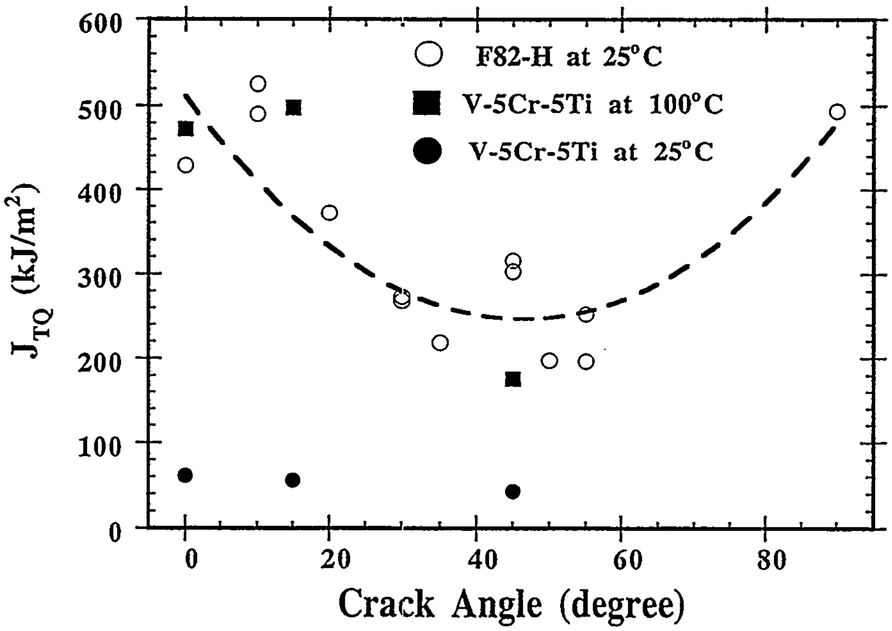

Fig. 1. The dependence of critical total J-integrals of V-5Cr-5Ti on crack inclination angles and temperatures. The results for a reduced activation ferritic/martensitic steel (F-82H) is included for comparison.

5Ti alloy. This research is an ongoing effort to understand the embrittlement observed in the V-5Cr-5Ti alloy at RT following annealing at 1125°C for 1h. The present study considers the effect of heat treatment on fracture toughness and impact fracture energy.

Material and Experimental Methods

A 6.35 mm thick V-5Cr-5Ti alloy plate (ANL Heat No. BL-63) was produced by Teledyne Wah Chang-Albany. The chemical composition of the plate (as provided by the vendor) is listed in Table 1.

Table 1. Chemical Composition of V-5Cr-5Ti (BL-63)

(in wt%)	Cr	Ti	(in wt ppm)	O	C	N	Si	V
	4.6	5.1		440	73	28	310	bal.

In order to gain more information about effect of heat treatment on grain size, precipitates, and grain boundary chemistry, the following heat treatments were investigated.

(1). 1125°C / 1 h/ furnace cooled (FC) (HT1);
(2). HT1 plus 890°C / 24 h/ FC (HT2);
(3). 1050°C / 1 h/ FC (HT3);
(4). HT3 plus 890°C / 24 h/ FC (HT4);
(5). HT3 plus 730°C / 24 h/ FC (HT5).

All of the heat treatments were conducted in a vacuum of 1.33 x 10^{-5} Pa. Grain boundary chemistry was analyzed by means of a scanning Auger electron spectrometer (AES) (PERKIN-ELMER-660). Specimens were cooled down to low temperature by extracting heat with liquid nitrogen and were fractured in-situ in the AES chamber in a vacuum of 1 X 10^{-7} Pa or better. Auger spectra were taken at an accelerating voltage of 5 kV and an incident electron current of about 250 nA. At least 22 intergranular facets and 6 grain interiors were analyzed; sometimes duplicate tests were performed. Microstructure was analyzed using an optical microscope. Investigation using a scanning electron microscope (SEM) equipped with energy dispersive x-ray spectrometry (EDS) and a transmission electron microscope (TEM) is currently under way.

Based on the results from the AES and the optical metallographic analysis, only HT1 and HT2 were used to heat treat the fracture test specimens. The specimens used for fracture toughness and impact tests were cut in the T-L orientation as specified in ASTM E399-90. The geometry of compact tension specimen is shown in Fig. 2. ASTM E813-89 was used to determine critical J-integrals (J_{IQ}) and ASTM E399-90 was used to determine the critical stress intensity factor (K_{IQ}). The subscript "Q" is used because our specimen size did not totally satisfy plane strain conditions. Mechanical properties used for determination of J_{IQ} were provided by Loomis[2], which are listed in Table 2. Charpy V impact specimens of 23.6x3.33x3.33 mm (1/3 scaled) were tested in the range of -115°C to 50°C to estimate DBTT. Fracture toughness was determined at -50, 25, and 100°C. Fracture surfaces of all specimens were investigated by means of a SEM.

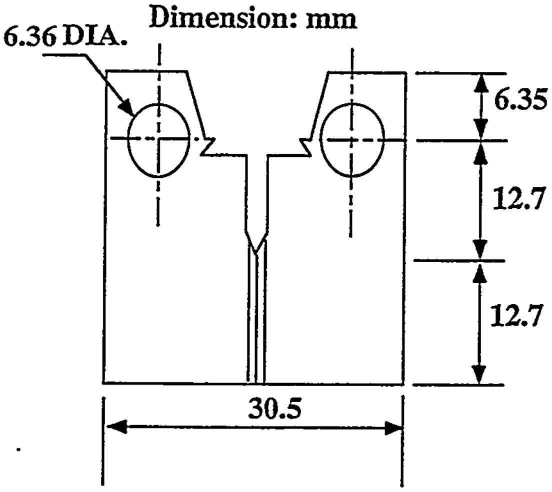

Fig. 2. The geometry of the compact tension specimen used in this study.

Table 2. Mechanical Properties of a V-5Cr-5Ti Alloy (ANL Heat No BL-63)[2]

Temp. (°C)	Yield strength (MPa)	UTS* (MPa)	Elongation (%)
25	387	454	34

* UTS: ultimate tensile strength.

Fracture toughness was determined by the J-test method for an HT1 treated specimen tested at 100°C and an HT2 treated specimen tested at RT. Fracture toughness was measured using the K-test method for an HT1 treated specimen tested at RT and for an HT2 treated specimen tested at -50°C. The K_{IQ} values were then converted to J_{IQ} values by means of Eq. 1. Temperatures were controlled within ±5°C during testing using either a heating tape or a refrigerator, respectively. The single-specimen technique was used in this study, which allows a J-R curve (J vs crack extension Δa) to be generated with one specimen. At least 40 pairs of J-Δa data were used to construct a J-R curve.

$$J_{IQ} = \frac{K_{IQ}^2 \ (1 - v^2)}{E} \tag{1}$$

where E is Young's modulus and ν is Poisson ratio.

Results

Effect of Heat Treatment on Microstructure and Grain Boundary S Concentration

The specimens subjected to HT1 were brittle at RT and fractured with a mixture of intergranular and cleavage modes. The result indicated that the grain boundary strength was low and the interior of grains was brittle. AES analysis of more than 40 intergranular facets in two specimens showed significant enrichment of S (6 at%), as compared to 0.3 at% on the cleavage facets. The specimens treated by HT3 displayed improved ductility and fractured in the AES by microvoid coalescence. To produce intergranular facets, hydrogen had to be introduced by cathodic charging. AES analysis showed that the S concentration on grain boundary facets (more than 20 facets) was only 2 at%, three times less than that in the specimens treated by HT1. Except for the specimens treated using HT1 in order to obtain an intergranular facet, all of the specimens had to be charged with hydrogen before fracture in the AES chamber. The effect of heat treatment on grain size, grain boundary chemistry, and microstructure was summarized in Table 3. The P, O, N, and C concentrations were also investigated with AES, but their concentrations did not vary significantly with heat treatment, so only S was listed in Table 3. The microstructure produced by selected heat treatments is shown in Fig. 3. From Table 3, it is evident that HT2 gives the second lowest grain boundary S concentration, HT1 gives the highest. The HT2 treatment also produced significantly more second phase particle precipitates than HT1, as shown in Fig. 3c and 3d. However, the grain sizes were almost same in the specimens treated using either HT1 or HT2. Therefore, HT1 and HT2 were chosen to investigate the effect of grain boundary S and microstructure on fracture properties of the V-5Cr-5Ti alloy.

Table 3. Effect of Heat Treatment on Grain Boundary S Concentrations and Fracture Toughness/DBTT

Heat treatments	G.S.(μm)*	GB S	PCT	DBTT(°C)	J_{IQ} at RT	Fracture
1125°C/1h	45	6	few	20		IG, CL**
1125°C/1h	48	6	few		52 kJ/m^2	IG, CL
1125°C/890°C/24h	45	.9	many	<-40	~1100 kJ/m^2	Dimple
1050°C/1h	40	2	some			
1050°C/890°C/24h		.5				
1050°C/730°/24h		1.5				
As received	37		some			

* G.S.: grain size; GB S: grain boundary sulfur (at%); PCT: Precipitates.

** Heat treated at Oak Ridge National Lab., the temperature may have been 1150°C as indicated by the plastic bag containing the specimens; IG: intergranular; CL: cleavage.

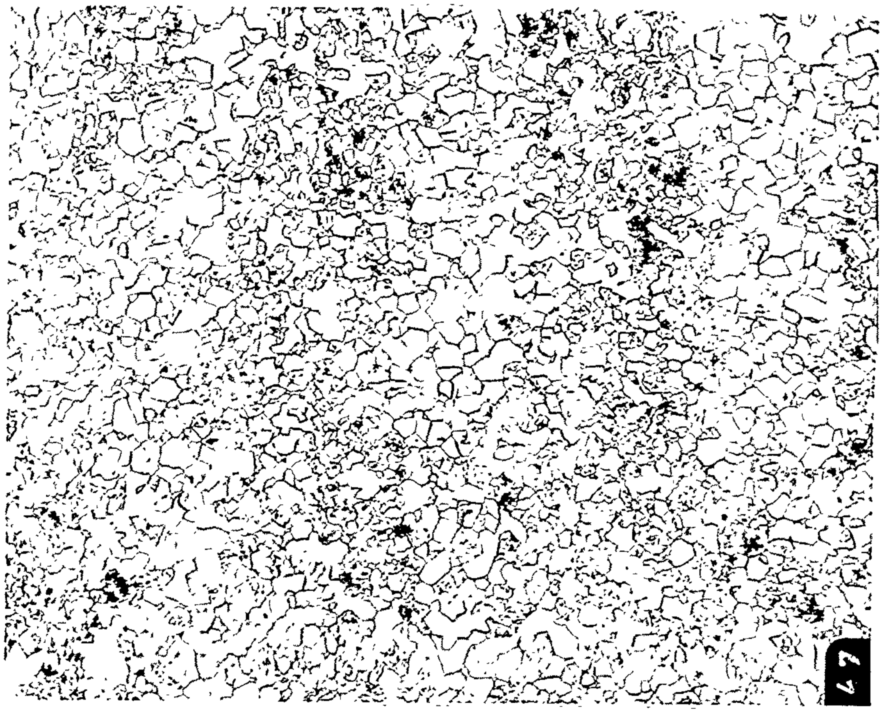

a.

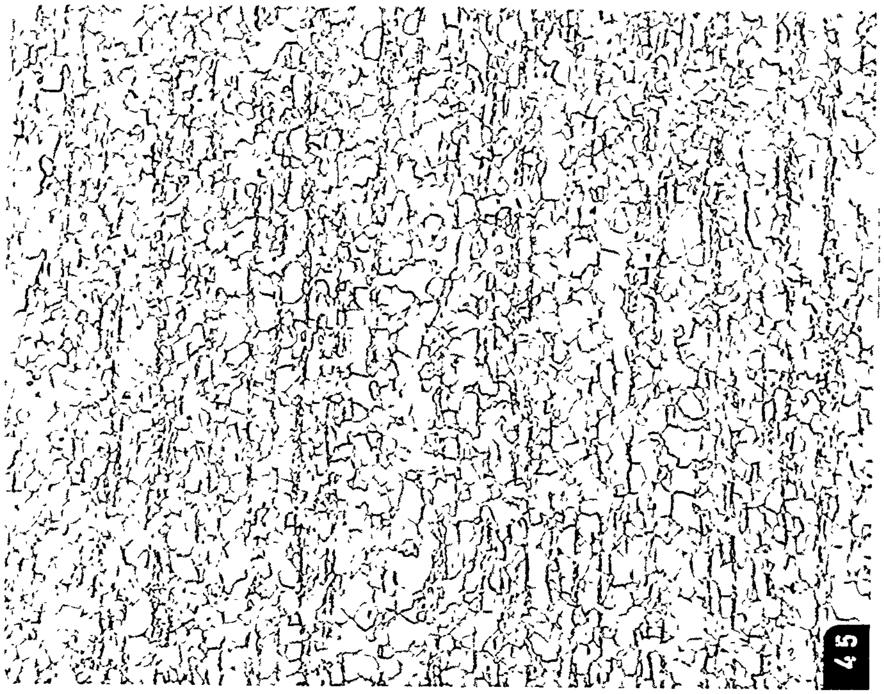

b.

Fig. 3. Overleaf.

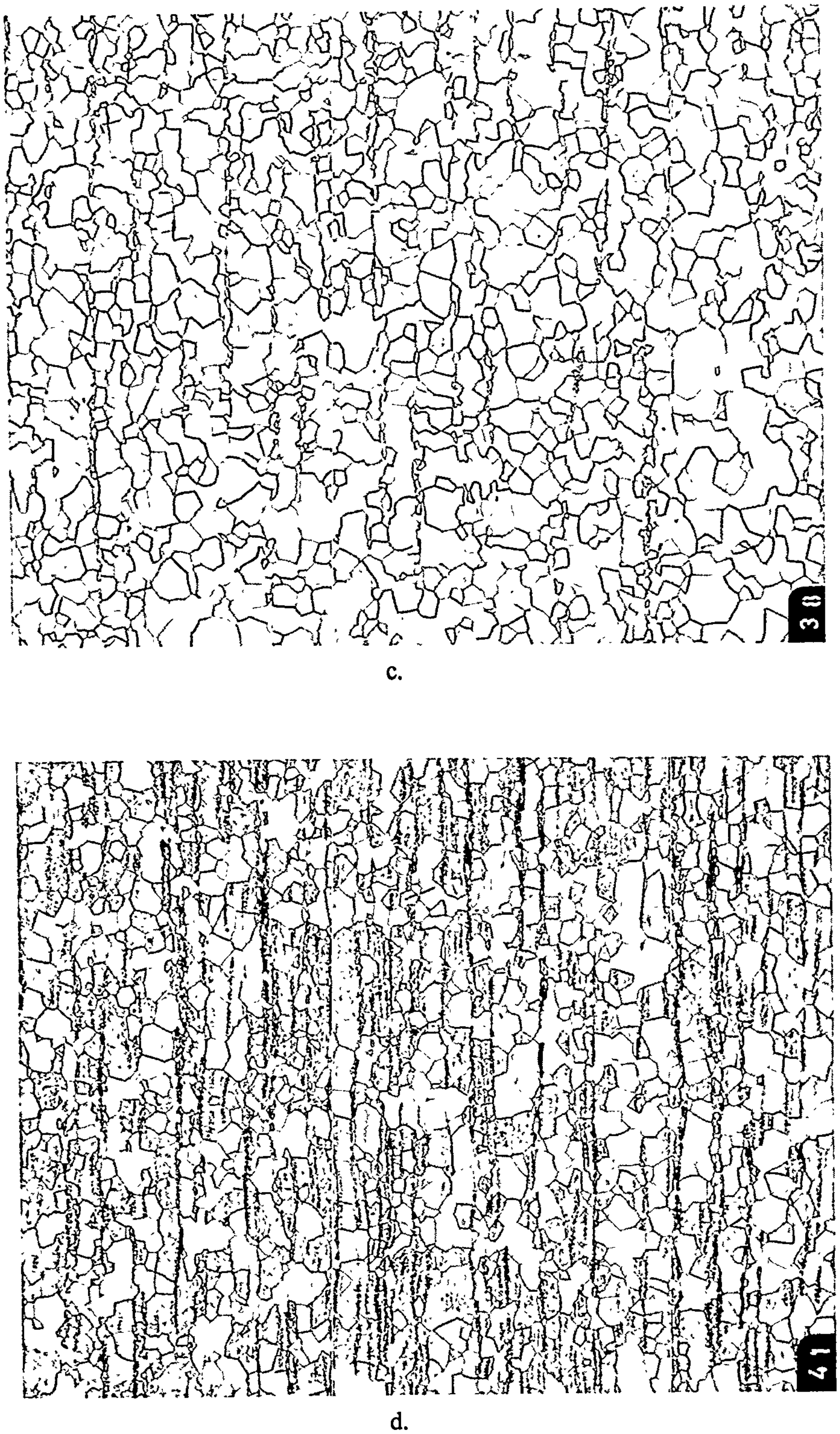

c.

d.

Fig. 3. Optical micrographs (50 X) showing microstructures resulting from: a.) as-received; b.) 1050°C/ 1h/ furnace cooled (FC); c.) 1125°C/ 1h/ FC; and d.) 1125°C/ 1h/ FC plus 890°C/ 24h/ FC.

Mechanical Properties

Specimens Treated Using HT1

The specimens treated using HT1 were brittle at RT and lower. They fractured with a mixture of intergranular and cleavage failure. Fig. 4 shows the fracture surface of a specimen which failed at RT during K-testing. From Fig. 4b, it can be seen that the cleavage facets appear to initiate at the grain boundaries and pass through the whole grain. The dependence of the IFE on temperature is presented in Fig. 5. It can be seen that IFEs at RT and -100°C are 6 J and 1 J, respectively. The DBTT was estimated to be 20°C. J_{IQ} at RT was 52 kJ/m^2. When tested at 100°C, specimens were ductile and exhibited stable crack growth. J_{IQ} was about 485 kJ/m^2 and the tearing modulus was 250 mJ/m^3. Despite the high J_{IQ} value at 100°C, the fracture surface consisted of intergranular and microvoid coalescence features, as shown in Fig. 6. The intergranular portion makes up about 40% of the total fracture surface. However, it is evident from Fig. 6b that the grains experience a large amount of plastic deformation before they fracture along the grain boundaries, giving high fracture toughness.

Specimens Treated Using HT2

The specimens treated using HT2 were very ductile at RT and fractured by microvoid coalescence during J-integral testing, as shown in Fig. 7. Specimens were so ductile that a complete J-R curve could not be constructed with our compact tension specimen (Fig. 2). The J_{IQ} estimated from the partial J-R curve (Fig. 8) is about 1100 kJ/m^2. Charpy testing at RT failed to cause fracture (two specimens) due to a large amount of plastic deformation. The IFE could not be determined. The data point marked by the arrow in Fig. 5 represents mainly plastic deformation energy, not including the energy for crack initiation and

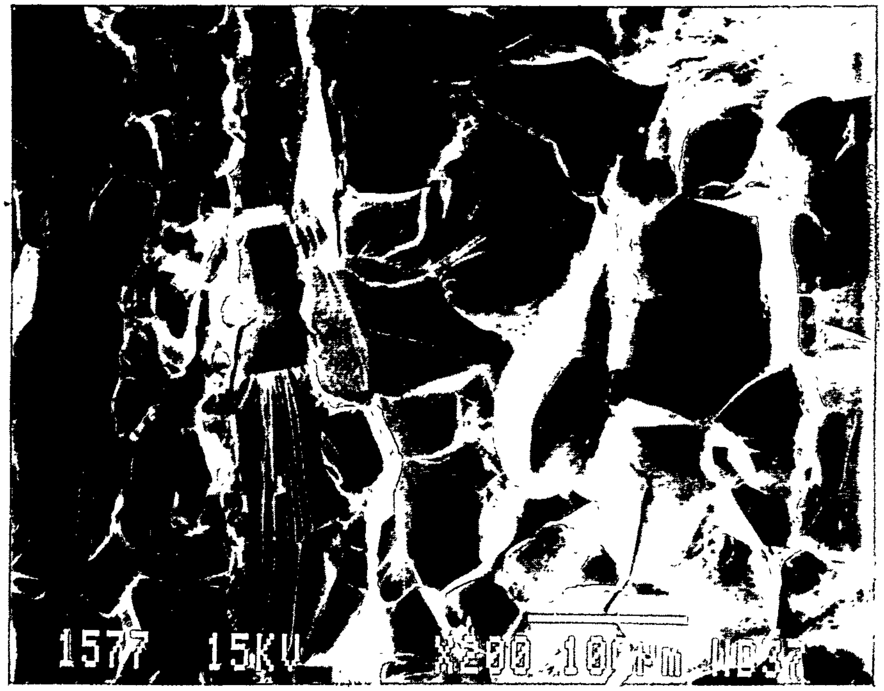

(a)

Fig. 4. Overleaf.

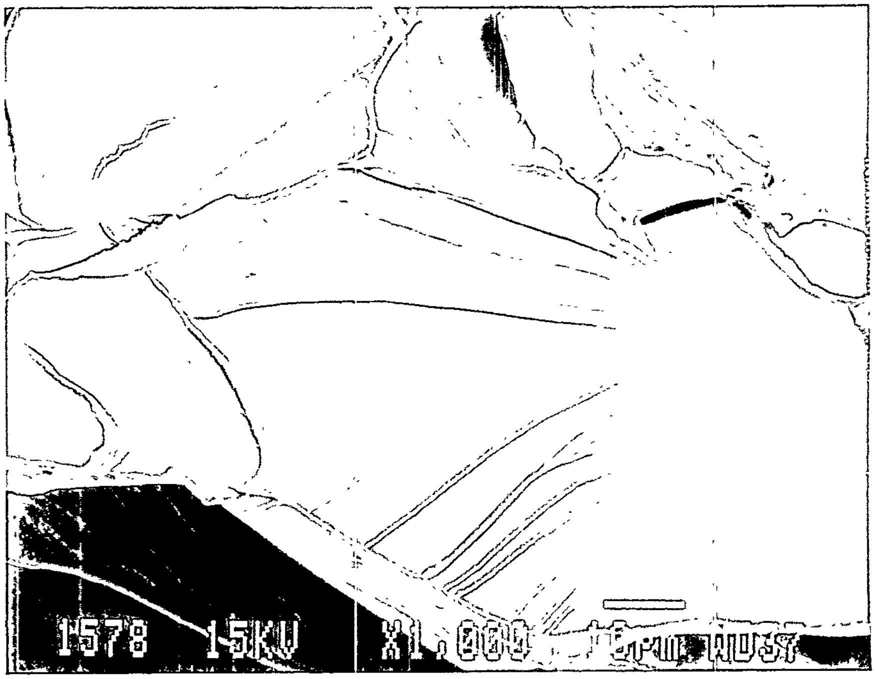

(b)

Fig. 4. Fracture surfaces of specimens annealed at 1125°C for 1h and fractured at room temperature during K testing. a.) a mixture of intergranular, cleavage, and a little dimple failure; b.) a cleavage fracture facet showing the cleavage crack initiates at a grain boundary and passes through the entire grain.

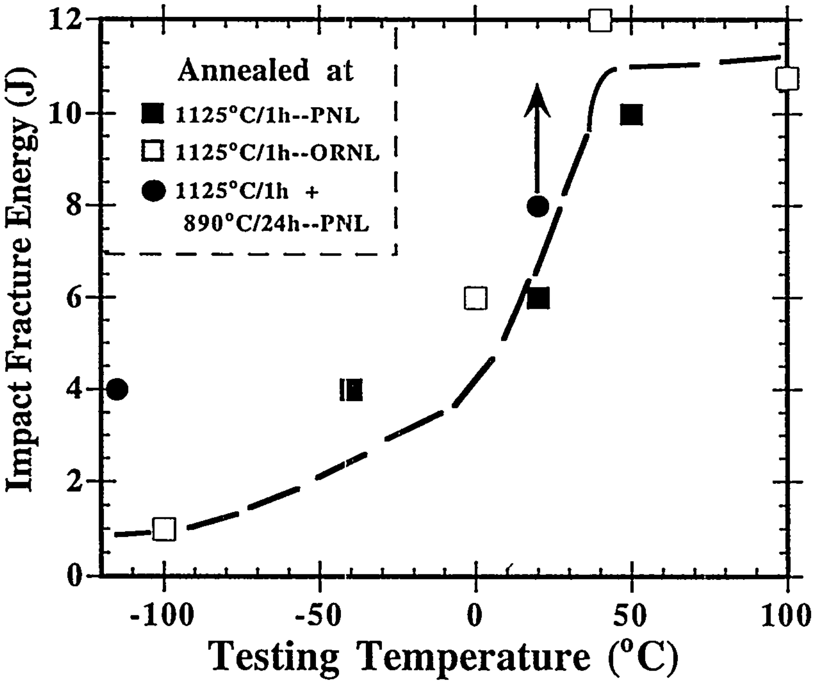

Fig. 5. Impact fracture energy vs testing temperature. PNL and ORNL indicate the tests were performed at Pacific Northwest Laboratory and Oak Ridge National Laboratory, respectively.

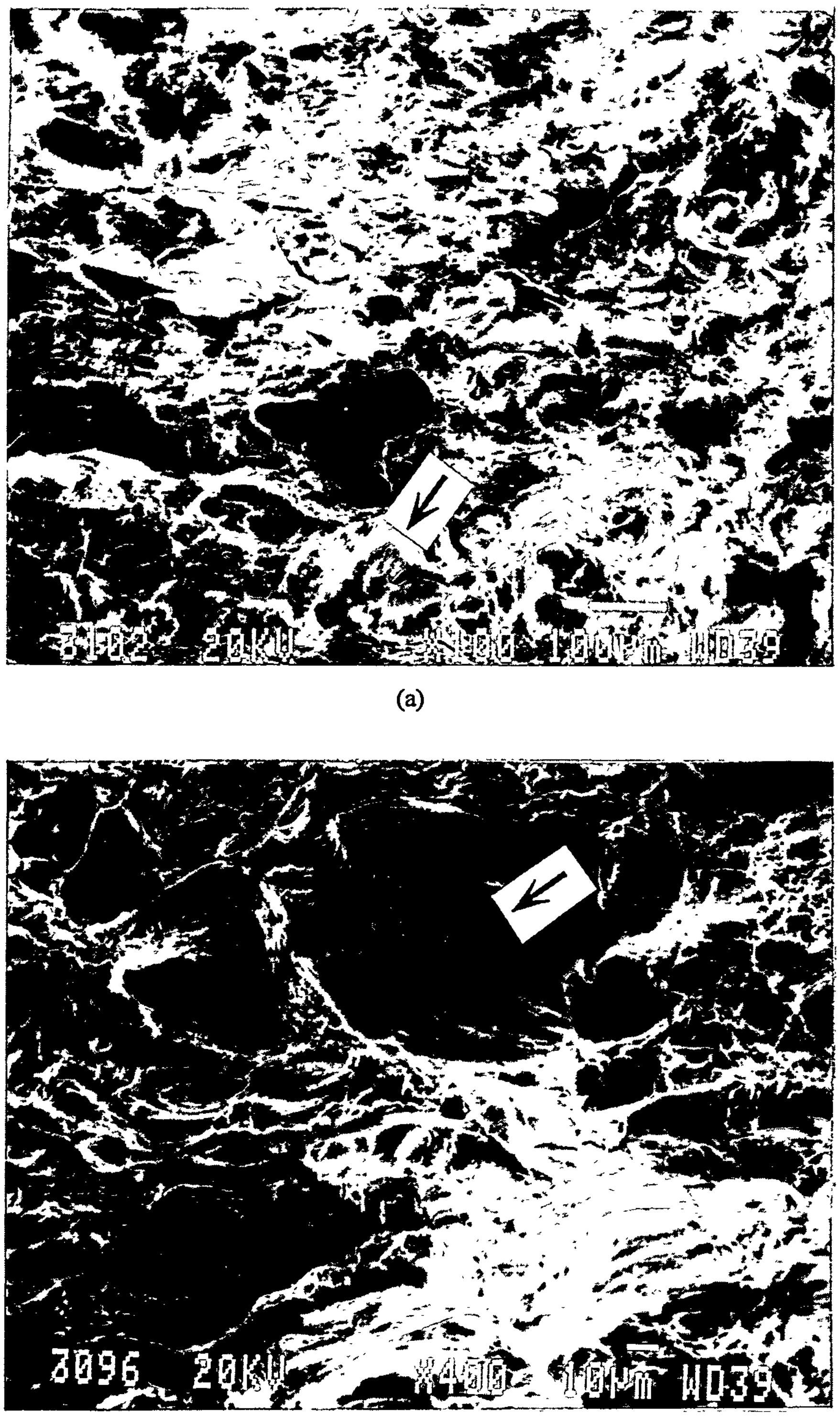

(a)

(b)

Fig. 6. Fracture surfaces of specimens annealed at 1125°C for 1h and fractured at 100°C during J-integral testing. They are a mixture of dimple and intergranular (about 40%) failure. The arrows indicate typical intergranular feature.

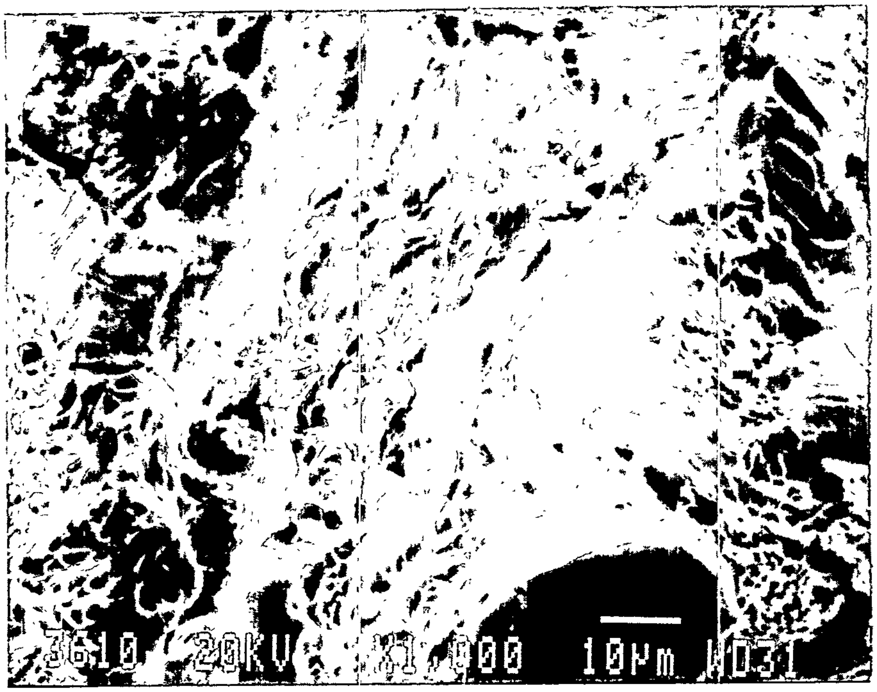

Fig. 7. The dimpled fracture surface of a specimen annealed at 1125°C for 1h plus 890°C for 24h and fractured at RT during J-integral testing.

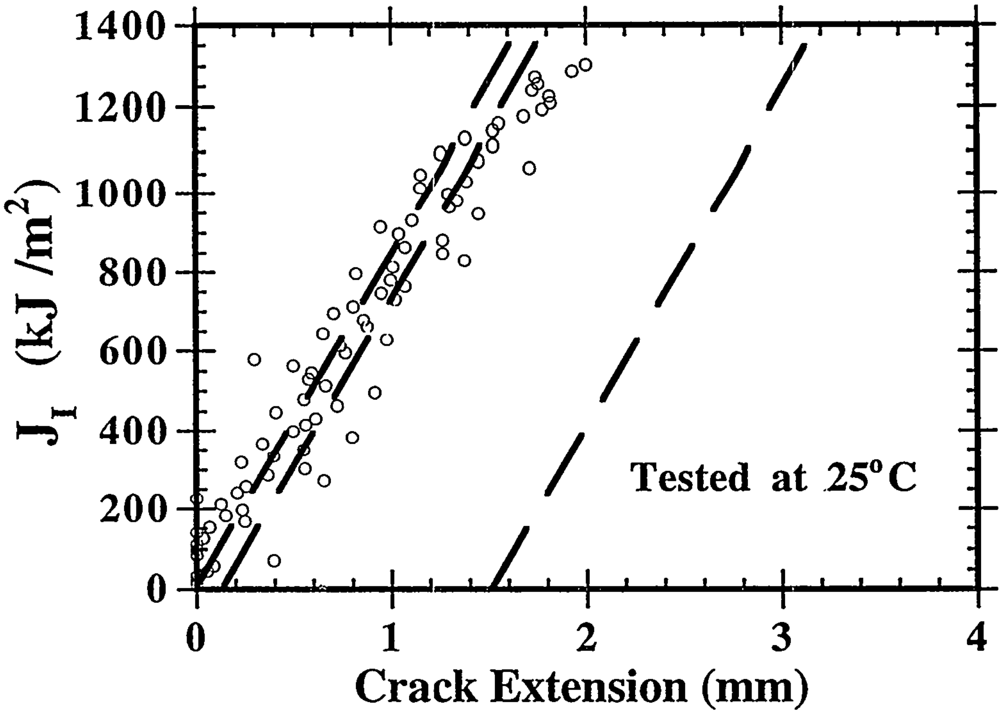

Fig. 8. The J-integral vs crack growth curve generated from a specimen annealed at 1125°C for 1h plus 890°C for 24h during J-integral testing at RT. J_{IQ} is estimated as about 1100 kJ/m^2.

propagation. Therefore, the IFE might be much higher than that in Fig. 5 which is indicated by the arrow. The IFE at -115°C was about 4 J, four times higher than the IFE for HT1 tested at -100°C. The fracture toughness was very sensitive to temperature. J_{IQ} at -50°C was 45 kJ/m^2, only about 1/20 of that at RT. The fracture mode also changed to cleavage fracture, as shown in Fig. 9. The DBTT was estimated to be less than -40°C. The effects of heat treatment and temperature on fracture properties of the V-5Cr-5Ti alloy are summarized in Table 3, Table 4, and in Fig. 10.

Fig. 9. the cleavage fracture surface of a specimen annealed at 1125°C for 1h plus 890°C for 24h and fractured at -50°C during K testing.

Discussion

The brittleness of the V-5Cr-5Ti treated using HT1 seems to stem from the low grain boundary fracture strength and brittleness of the grains themselves. It is known that impurity segregation to grain boundaries in a metallic material can reduce grain boundary strength, and interstitial impurities can enhance cleavage fracture. Because the grain size in the specimens treated using either HT1 or HT2 was almost identical, the increase in fracture strength produced with HT2 probably resulted from two factors. One of them is that HT2 increases grain boundary strength by reducing grain boundary S concentration, and the other is that it improves the ductility of grains by decreasing interstitial impurity concentration via precipitate formation. However, because our experiments are limited and not comprehensive (some data has not beenanalyzed yet), it is highly possible that as our research continues, some new results may surface requiring additional fundamental research. For example, why is this heat of V-5Cr-5Ti alloy sensitive to intergranular fracture, but previous heats of V-5Cr-5Ti and V-4Cr-4Ti alloys are not ?

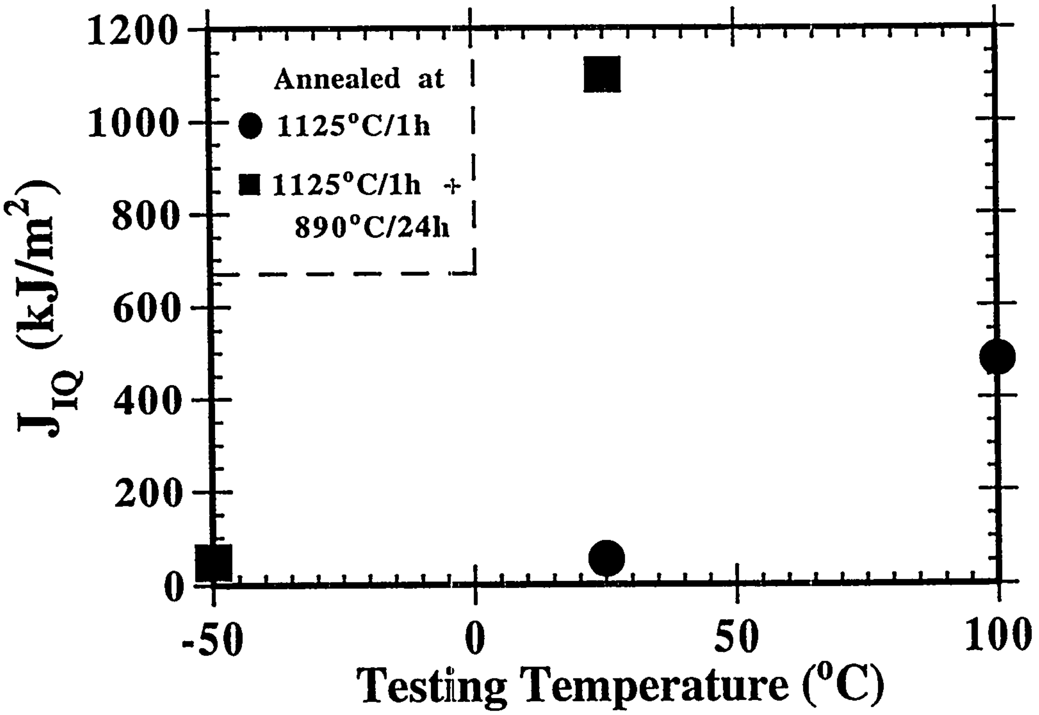

Fig. 10. Fracture toughness vs testing temperature for specimens annealed either at 1125°C for 1h or at 1125°C for 1h plus 890°C for 24h.

Table 4. Effect of Heat Treatment and Temperature on Fracture Toughness

Heat treatment	J_{IQ} (kJ/m^2)@ -50°C	25°C	100°C
HT1		52	485
HT2	45	~1100	

CONCLUSIONS

1. Specimens of V-5Cr-5Ti annealed at 1125°C (HT1) were brittle at room temperature and fractured by intergranular and cleavage modes. The J_{IQ} was about 52 kJ/m^2. The DBTT was about 20°C.

2. At 100°C HT1 treated specimens were ductile, giving a J_{IQ} value of 485 kJ/m^2, but fracture surfaces were composed of both intergranular and dimple fracture.

3. Annealing at 1125 and, then at 890°C (HT2) improved RT fracture toughness dramatically, from 52 to about 1100 kJ/m^2 and changed the mode of fracture to microvoid coalescence. The DBTT was decreased to below -40°C.

4. Specimens treated with HT2 were brittle at -50°C. The J_{IQ} value was 45 kJ/m^2, as compared with about 1100 kJ/m^2 at RT.

5. HT2 reduced grain boundary S concentration (0.9 at%) greatly as compared to HT1 (6 at%) and produced more precipitates.

FUTURE WORK

Further research will be performed with the new heats of V-5Cr-5Ti and V-4Cr-4Ti alloys.

ACKNOWLEDGEMENTS

We are grateful to Dr. M. Grossbeck of ORNL for supplying us with the V-5Cr-5Ti alloy. The assistance of Mr. J. L. Humason at Pacific Northwest Laboratory in developing the test methods is gratefully acknowledged. This research was supported by the Office of Fusion Energy of the U. S. Department of Energy under Contract DE-AC06-76RLO 1830 with Battelle Memorial Institute.

REFERENCES

1. H. Li, R. H. Jones, and P. J. Hirth, Fusion Reactor Materials Semiannual Progress Report DOE/ER-0313/16, Oak Ridge National Lab., Oak Ridge, TN (March, 1994), in press.

2. B. A. Loomis, private letter, April 9, 1994.

FABRICATION OF 500–kg HEAT OF V–4Cr–4Ti* H. M. Chung, H.–C. Tsai, and D. L. Smith (Argonne National Laboratory) and R. Peterson, C. Curtis, C. Wojcik, and R. Kinney (Teledyne Wah Chang Albany)

OBJECTIVE

On the basis of excellent properties that were determined for a laboratory–scale heat, V–4Cr–4Ti has been identified previously as the primary vanadium–based candidate alloy for application in fusion reactor structural components. The objective of this work is to produce a large–scale (500–kg) ingot and fabricate various plates and sheets from the ingot, thereby demonstrating a reliable method of fabricating an industrial–scale heat of V–4Cr–4Ti that exhibits excellent properties.

SUMMARY

A 500-kg heat of V-4Cr-4Ti, an alloy identified previously as the primary vanadium–based candidate alloy for application in fusion reactor structural components, has been produced. The ingot was produced by electron–beam melting using screened high–quality raw materials of vanadium and titanium. Several ≈63.5–mm–thick bars were extruded from the ingot, and plates and sheets of various thicknesses ranging from 0.51 to 12.7 mm were fabricated successfully from the extruded bars. The chemical composition of the ingot and the secondary fabrication procedures, specified on the basis of experience and knowledge gained from fabrication, testing, and microstructural examination of a laboratory–scale heat, were found to be satisfactory. Charpy–impact tests showed that mechanical properties of the large–scale heat are as good as those of the laboratory–scale heat. This demonstrates a method of reliable fabrication of industrial–scale heats of V–4Cr–4Ti that exhibit excellent properties.

INTRODUCTION

Vanadium-base alloys have significant advantages over other candidate alloys (such as austenitic and ferritic steels) for use as structural materials in fusion devices. In the past, extensive investigations have been conducted on the swelling behavior, tensile properties, impact toughness, and microstructural evolution of V, V-Ti, V-Cr, V-Cr-Ti, and V-Ti-Si alloys after irradiation by fast neutrons at 420°C–600°C. These investigations revealed that V-Cr-Ti alloys containing ≈4 wt.% Cr, ≈4 wt.% Ti, 400-1000 wt. ppm Si, and <1000 wt. ppm O+N+C were most desirable because they exhibit superior physical and mechanical properties.[1–6] These results were obtained, however, on small (<30–kg) laboratory–scale heats, including a small heat (ANL ID BL–47) of V-4Cr-4Ti that exhibited excellent resistance to irradiation–induced embrittlement, swelling, and helium embrittlement.[7–9] In the meantime, a relatively larger heat of V–5Cr–5Ti (ANL ID BL–63) and a small heat of V–5Cr–3Ti (ANL ID BL–54), fabricated subsequently under procedures significantly different from those of the small laboratory heat of V–4Cr–4Ti, were found to exhibit less–desirable mechanical properties despite the small differences in alloying element contents.[10] Based on these backgrounds, a joint campaign was initiated at Argonne National Laboratory and Teledyne Wah Chang (Albany, Oregon) to identify an optimal fabrication procedure of the V–(4–5)Cr–(3–5)Ti alloys and to demonstrate of a reliable method of producing an industrial–scale heat of V–4Cr–4Ti that exhibits the excellent properties reported in previous investigations.

SPECIFICATIONS AND PROCEDURES

The production campaign consisted of a large–scale (500–kg) melting of a V–4Cr–4Ti ingot; extruding the ingot into rectangular bars; and subsequent rolling and heat–treatments to manufacture final

---

* Work supported by the U.S. Department of Energy, Office of Fusion Energy, under Contract W-31-109-Eng-38.

products in the form of plates and sheets of various thickness; analyses of chemical composition and phase structure; and Charpy–impact testing to determine the ductile–brittle transition temperatutre (DBTT). The latter information is described in a separate article in this report.[11]

1. Specification of Chemical Composition

The specification of chemical composition was carefully evaluated to reflect the valuable experience and knowledge gained from fabrication, testing, and microstructural examination of the laboratory–scale heats of of V–Ti and V–Cr–Ti alloys, in particular, V–4Cr–4Ti (BL–47), V–5Cr–3Ti (BL–54), and the relatively larger heat of V–5Cr–5Ti (BL–63).[3,5,10] Particular attention was given to control of the following impurities: Nb and Mo (minimize to ensure low neutron activation); Cu (minimize to suppress Cu–rich vanadium oxycarbochlorides);[10] Si (optimize to 400–1000 wppm to suppress swelling);[5] O, N, and C (limit the combined concentration to <1000 wppm); S, P (minimize to avoid segregation to grain boundary and precipitation);[10] and Cl, Ca, K, Na, and B (minimize to avoid formation of the vanadium–based precipitates oxycarbochlorides, vanadates, and borides).[10] The final specification of ingot chemistry is listed in the following:

1.1 Ingot Chemical Specifications

Element	Composition	Element	Composition
Cr	4.0 ± 0.5 wt.%	Ti	4.0±0.5 wt.%
Si	400 - 1000[a]	O	<400[a]
N	<200	C	<200
Al	<200	Fe	<200
Cu	<10	Mo	<10
Nb	<10	Cl	<2
P	<10	S	<10

[a]Concentrations in wt. ppm.

Use only low–chlorine (<5 wppm) double– or triple–melted titanium feedstock in making the ingot.

1.2 Alloying Component Inhomogeneity

Local inhomogeneity of Cr and Ti shall not exceed ±0.3 wt.%.

2. Screening of Raw Materials

The source of the last group of impurities , except for Ca and B (i.e., Cl, K, and Na), is known to be primarily low–quality Ti, which is normally produced by the Kroll process. Therefore, only double– or triple–melted Ti was used in ingot melting. This is in contrast to the use of sponge titanium in melting the ingots of the V–5Cr–5Ti (BL–63) and V–5Cr–3Ti (BL–54), the two heats reported to exhibit inferior mechanical properties.[10]

Chemical composition of the raw vanadium designated for melting of the ingot was also checked (Table 1). At the same time, a piece of the raw vanadium was set aside and machined into 1/3–size Charpy–impact specimens. Normally, unalloyed vanadium of good quality (e.g., iodide[12] or electrorefined[13] vanadium containing low O, N, Ca, and B) should exhibit a DBTT lower than –200°C. However, unusually higher DBTTs have been observed occasionally in the past, in particular for some of the unalloyed vanadium produced by the calcium–reduction process.[13,14] Specimens from one of the unalloyed vanadium (BL–51) that were impact–tested in a previous investigation exhibited a DBTT as high as –150°C.[2] From a subsequent microstructural characterization by analytical electron microscopy, the unusually high DBTT of the heat (BL–51) has been attributed to dense precipitation of very fine (<60 nm diameter) calcium vanadates.[10] In view of these observations, impact tests were conducted on the 1/3–size Charpy specimens of the raw vanadium, and it was verified that the DBTT of the raw material is lower than –196°C.

3. Specification of Secondary Fabrication and Conversion

The procedures for extrusion, secondary fabrication, and conversion to plates and sheets were specified as follows to closely reproduce the procedures used in fabricating the excellent laboratory heat of V–4Cr–4Ti (ANL ID BL–47):

1. Extrude ingot in stainless steel jacket at 1150°C into 63–mm–thick slab.
2. Subsequent warm rolling at 400°C to desired final dimensions.
3. No more than 15 and 50% thickness reduction, respectively, per roll and between anneals.
4. Annealing at 1050°C for 1 h in high–vacuum furnace before each rolling.
5. Annealing at 1050°C for 2 h in high–vacuum furnace for all final products (thicker than ≈3 mm).

FINAL PRODUCTS

The ≈500-kg ingot was produced by electron–beam melting for constituent homogeneity. This is in contrast to small laboratory heats (including Heat BL–47 and a new 13–kg heat of V–5Cr–5Ti, BL–72) that were produced by vacuum–arc melting. The results of chemical analyses, averaged over three measurements on 63–mm–thick extruded bars, are given in Table 1. For comparison, the chemical composition of the excellent laboratory heat of V–4Cr–4Ti (ANL ID BL–47) is also given in the table. The machined cast ingot was encased in a stainless jacket and extruded at 1150°C into bar with a nominal thickness of 63.5 mm (2.5 in.). Three pieces of the ≈63.5–mm–thick extruded bars are shown in Fig. 1.

Table 1. Chemical composition (impurities in wppm) of the industrial–scale (500 kg) heat of V–4Cr–4Ti and the V raw stock used to melt the ingot.

Heat ID	Material	Cr	Ti	Cu	Si	O	N	C	S	P	Ca	Cl	B
820630	V raw stock	<100	<50	<50	780	200	62	75	10	<30	–	<2	<5
832665	V–4Cr–4Ti	3.8 wt.%	3.9 wt.%	<50	783	310	85	80	<10	<30	<10	<2	<5

Following extrusion, ≈72 kg (or 17%) of the extruded bar (≈430 kg recovered) has been used to produce plates and sheets of nominal thicknesses of 12.7, 6.35, 3.81, and 1.02 mm. Plates with a thickness of 3.81 mm and greater were produced by multiple-pass cross–rolling at ≈400°C; the thinner, 1.02-mm-thick sheets were produced by further rolling at room temperature. The thickness reduction was limited to <15% per pass. Annealing treatments of the plates were conducted at 1050°C-1070°C for 2 h in a vacuum better than ≈1.33 x 10^{-3} Pa.

The chemical composition of the heat, similar to that of the excellent laboratory heat (BL–47), conforms with the specification. As expected, results of impact tests of 1/3–sizes Charpy specimens machined from the 3.81–mm plate showed also that mechanical properties of the large–scale heat are as good as those of the laboratory–scale heat.[11]

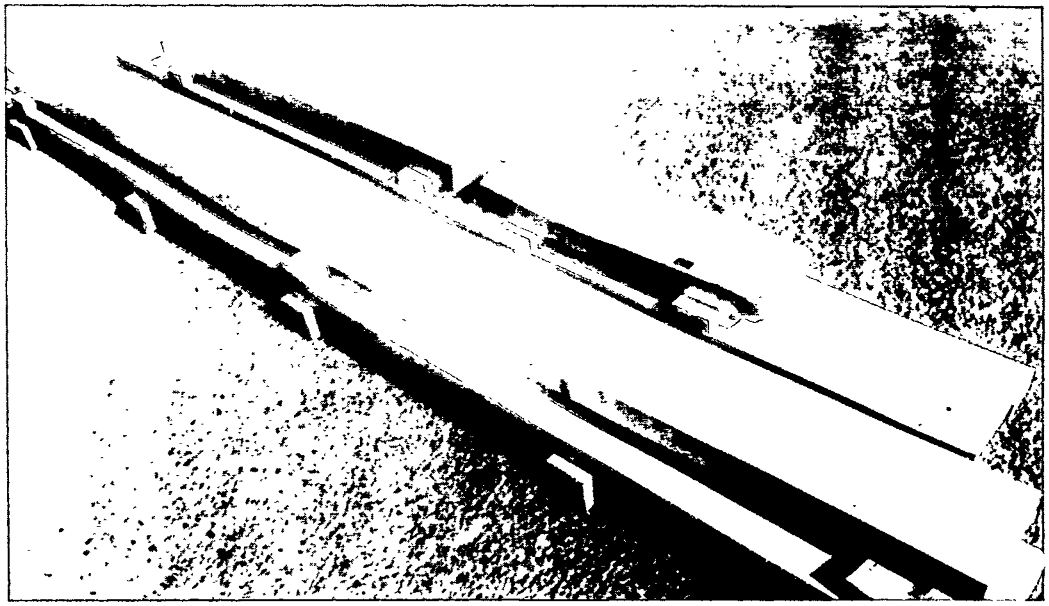

Fig. 1. Three pieces of ≈63–mm–thick bars extruded from 500–kg industrial–scale heats (ID 832665) of V–4Cr–4Ti.

CONCLUSION

A scale–up (500-kg) heat of V-4Cr-4Ti, an alloy identified previously as the primary vanadium–based candidate alloy for application in fusion reactor structural components, has been produced successfully by electron–beam melting of screened high–quality raw materials of vanadium and titanium. Several ≈63.5–mm–thick bars were extruded from the ingot, and plates and sheets of various thicknesses ranging from 0.51 to 12.7 mm were fabricated successfully from the extruded bar. The chemical composition of the ingot and the secondary fabrication procedures, specified on the basis of experience and knowledge gained from fabrication, testing, and microstructural examination of a laboratory–scale heat, were found to be satisfactory. Results of Charpy–impact tests showed that mechanical properties of the large–scale heat are as good as those of the laboratory–scale heat. This demonstrates a method of reliable fabrication of industrial–scale heats of V–4Cr–4Ti of excellent properties.

REFERENCES

[1] B. A. Loomis, L. Nowicki, and D. L. Smith, "Effect of Neutron Irradiation on Tensile Properties of V–Cr–Ti Alloys," in Fusion Reactor Materials, Semiannual. Prog. Report, DOE/ER-0313/15, Oak Ridge National Laboratory, Oak Ridge, TN (1994), pp. 219–222.

[2] B. A. Loomis, H. M. Chung, L. Nowicki, and D. L. Smith, "Effects of Neutron Irradiation and Hydrogen on Ductile-Brittle Transition Temperatures of V–Cr–Ti Alloys," ibid., pp. 253–257.

[3] H. M. Chung, B. A. Loomis, L. Nowicki, J. Gazda, and D. L. Smith, "Irradiation-Induced Density Change and Microstructural Evolution of Vanadium-Base Alloys," ibid., pp. 223–231.

[4] H. M. Chung, B. A. Loomis, and D. L. Smith, "Thermal Creep Behavior of V–5Cr–5Ti and V–10Cr–5Ti Alloys," in Fusion Reactor Materials, Semiannual. Prog. Report, DOE/ER-0313/14, Oak Ridge National Laboratory, Oak Ridge, TN (1993), pp. 309-317.

[5] H. M. Chung, B. A. Loomis, and D. L. Smith, in Effects of Radiation on Materials, ASTM-STP 1175, A. S. Kumar, D. S. Gelles, R. K. Nanstad, and T. A. Little, eds., American Society for Testing and Materials, Philadelphia, 1993, pp. 1185–1200.

[6] H. M. Chung, B. A. Loomis, and D. L. Smith, "Properties of V-4Cr-4Ti for Application as Fusion Reactor Structural Components," Proc. 3rd Intl. Symp. on Fusion Nuclear Technology, June 27-July 1, 1994, Los Angeles, CA, in press.

[7] H. M. Chung, B. A. Loomis, L. Nowicki, and D. L. Smith, "Effect of Dynamically Charged Helium on Tensile Properties of V–4Cr–4Ti," in this report.

[8] H. M. Chung, L. J. Nowicki, D. E. Busch, and D. L. Smith, "Ductile–Brittle Transition Behavior of V–4Cr–4Ti Irradiated in the Dynamic Helium Charging Experiment," in this report.

[9] H. M. Chung, L. Nowicki, J. Gazda, and D. L. Smith, "Void Structure and Density Change of Vanadium-Base Alloys Irradiated in the Dynamic Helium Charging Experiment," in this report.

[10] H. M. Chung, J. Gazda, L. Nowicki, J. E. Sanecki, and D. L. Smith, "Effects of Fabrication Variables on Impact Properties and Microstructure of V–Cr–Ti Alloys," in Fusion Reactor Materials, Semiannual. Prog. Report, DOE/ER-0313/15, Oak Ridge National Laboratory, Oak Ridge, TN (1994), pp. 207–218.

[11] H. M. Chung, L. Nowicki, J. Gazda, and D. L. Smith, "Impact Properties of 500–kg Heat of V–4Cr–4Ti," in this report.

[12] R. W. Thompson and O. N. Carlson, J. Less–Common Met., 9 (1965), 354.

[13] D. R. Mathews, G. H. Keith, and E. A. Loria, Bureau of Mines Report 6637 (1965,), U.S. Dept. of Interior, Washington, DC.

[14] W. R. Clough and A. S. Pavlovic, Trans. ASM 52 (1960) 948.

IMPACT PROPERTIES OF 500-kg HEAT OF V–4Cr–4Ti* H. M. Chung, L. Nowicki, J. Gazda, and D. L. Smith, (Argonne National Laboratory)

OBJECTIVE

Following previous reports of excellent properties of a laboratory heat of V–4Cr–4Ti, the alloy identified as the primary vanadium–based candidate for application as fusion reactor structural components, a large industrial–scale (500–kg) heat of the alloy was fabricated successfully. The objective of this work is to determine the impact properties of the industrial–scale heat.

SUMMARY

A 500-kg heat of V-4Cr-4Ti, an alloy identified previously as the primary vanadium–based candidate alloy for application as fusion reactor structural components, has been produced successfully. Impact tests were conducted at –196°C to 150°C on 1/3–size Charpy specimens of the scale–up heat after final annealing for 1 h at 950, 1000, and 1050°C. The material remained ductile at all test temperatures, and the ductile–brittle transition temperature (DBTT) was lower than –200°C. The upper–shelf energy of the production–scale heat was similar to that of the laboratory–scale (≈15–kg) heat. Effect of annealing temperature was not significant; however, annealing at 1000°C for 1 h produced impact properties slightly better than those from other annealing treatments. Effect of notch geometry was also investigated on the heat. Under otherwise similar conditions, DBTT increased ≈30°C when the notch angle was reduced from 45° (root radius 0.25 mm) to 30° (root radius 0.08 mm).

INTRODUCTION

To develop and identify an optimal vanadium–base alloy for application in fusion reactor first wall/blanket structures, extensive investigations were conducted earlier on the swelling behavior, tensile properties, creep strength, impact toughness, and microstructural stability of V-Ti, V-Cr-Ti, and V-Ti-Si alloys before and after irradiation by fast neutrons at 420°C–600°C. These investigations revealed that V-Cr-Ti alloys containing ≈4 wt.% Cr, ≈4 wt.% Ti, 400-1000 wt. ppm Si, and <1000 wt. ppm O+N+C were most desirable because they exhibit superior physical and mechanical properties.[1–6] These results were obtained, however, on laboratory–scale (<30–kg) heats, including a small heat (ANL ID BL–47) of V-4Cr-4Ti that exhibited excellent resistance to thermal creep,[4] irradiation–induced embrittlement,[1,2] swelling,[3,5] and helium embrittlement.[7–9] In this reporting period, a large (≈500–kg) industrial–scale heat of V–4Cr–4Ti (Heat ID 832665) was fabricated successfully in a joint effort between Argonne National Laboratory and Teledyne Wah Chang (Albany, Oregon) with the objective of demonstrating reliable industrial production of good–quality V–4Cr–4Ti.[10] This report describes results of metallographic examination and Charpy–impact testing of the 500–kg heat. The Charpy–impact test (at –196°C to 150°C) was chosen because it has been shown to be most sensitive to the quality of vanadium–base alloys.

EXPERIMENTAL PROCEDURE

Chemical composition of the 500–kg heat is given in Table 1. Also in the table is the chemical composition of the laboratory–scale heat of V–4Cr–4Ti (ANL ID BL–47) that was shown earlier to exhibit excellent properties.[1–9]

---

* Work supported by the U.S. Department of Energy, Office of Fusion Energy, under Contract W-31-109-Eng-38.

One–third–size Charpy specimens (3.33 x 3.33 x 25.4 mm) were machined from 3.81–mm–thick plates of the material, some of which had been annealed for 2 h at a nominal temperature of ≈1050°C and some of which had been received in as–rolled (at 400°C) condition. The Charpy specimens were machined so that the plane of crack propagation was perpendicular to rolling direction. To investigate the effect of notch geometry, two types of V–notch geometry were investigated; one with a 45° notch angle and 0.25–mm root radius and the other with a 30° angle and 0.08–mm root radius. Notch depth in both types of specimens was kept constant at 0.61 mm. The specimens machined from as–annealed plates were heat–treated at 400°C for 1 h in a vacuum of ≈6 x 10^{-4} Pa prior to impact testing, a customary procedure used to expel hydrogen that could be picked up during specimen machining and preparation. To identify the optimal annealing condition, specimens machined from as–rolled (cross–rolled at 400°C)[10] plates were annealed at 950°C and 1000°C for 1 h in a vacuum of ≈6 x 10^{-6} Pa prior to testing. Details of the drop–weight–type impact test have been described elsewhere.[2]

Table 1. Chemical composition (impurities in wppm) of industrial– (500 kg) and laboratory–scale heats of V–4Cr–4Ti.

Heat ID	ANL ID	Heat Type	Cr	Ti	Cu	Si	O	N	C	S	P	Ca	Cl	Na	K	B
–	BL–47	laboratory, 15 kg	4.1 wt.%	4.3 wt.%	6	870	350	220	200	20	<40	1	1	0.1	0.1	15
832665	BL–71	production, 500 kg	3.8 wt.%	3.9 wt.%	<50	783	310	85	80	<10	<30	<10	<2	–	–	<5

RESULTS AND DISCUSSION

Charpy energies, measured on the production–scale heat of V–4Cr–4Ti after annealing for 1 h at 950, 1000 and 1050°C, are shown in Fig. 1 as a function of impact temperature. All specimens in the figure had a notch angle of 45° and a root radius of 0.25 mm, the same geometry used in previous investigations.[2] From the results in the figure, the optimal annealing temperature appears to be ≈1000°C, the same as that found to produce minimum hardness in ≈85% cold–worked V–4Cr–4Ti (i.e., the smaller laboratory heat BL–47, Table 1).[11] Results in Fig. 1 show that the impact properties of the production–scale heat are as good as those of the smaller laboratory heat, which was vacuum–arc melted. The DBTT of the production heat is no higher than ≈–200°C, similar to that of the laboratory heat. To show a direct comparison, Charpy energies of the two heats are plotted in Fig. 2.

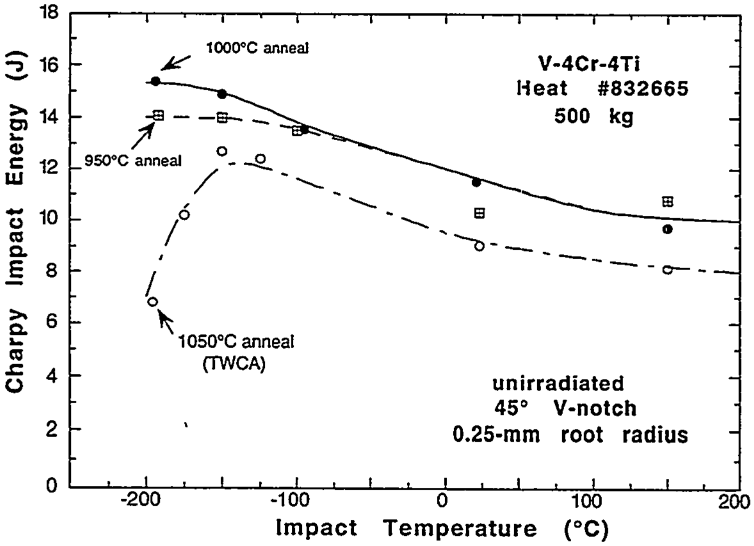

Figure 1. Charpy energy as function of impact temperature of production–scale V–4Cr–4Ti heat after annealing for 1 h at 950, 1000, and 1050°C. Optimal annealing temperature is ≈1000°C.

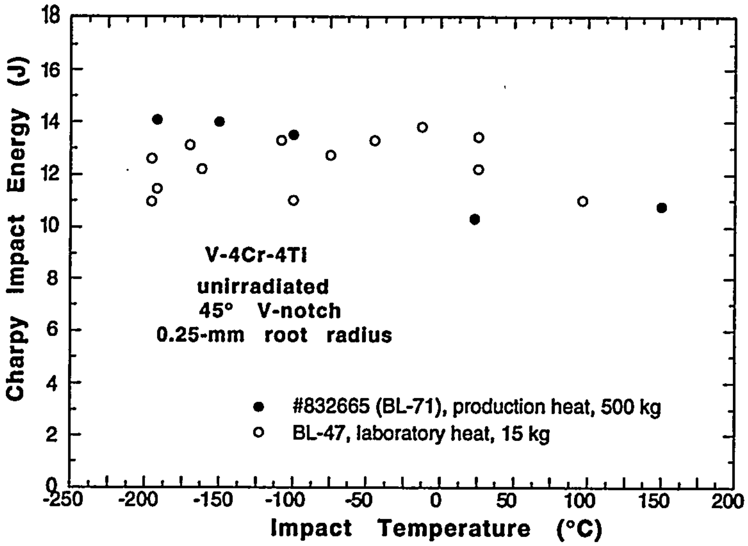

Figure 2.
Comparison of impact properties of the production– and laboratory–scale heats of V–4Cr–4Ti.

Grain structures of the specimens annealed at 950, 1000, and 1050°C are shown in Fig. 3. After annealing at ≈1050°C (for 2 h at Teledyne Wah Chang), most of the material seems to have been fully recrystallized, exhibiting an average grain size of ≈28 µm (Fig. 3C). The material was hardly recrystallized after annealing either at 950°C or 1000°C. When examined under polarized light, etched specimens of the alloy annealed at 950°C revealed what appears to be a lath-shaped, gold–colored secondary phase (the light–contrasted feature denoted by arrows in Fig. 3A). Volume fraction of the phase was negligible, however, when annealed at 1000°C (Fig. 3B). Although the nature of the phase could not be identified at this time, precipitation of the secondary phase does not appear to influence the impact properties significantly.

Effect of notch geometry is shown in Fig. 4. Specimens (average grain size ≈28 µm) in the figure were annealed at a nominal temperature of 1050°C for 2 h at Teledyne Wah Chang. When notch angle and root radius were decreased from 45° to 30° and 0.25 to 0.08 mm, respectively, DBTT increased from ≈–200°C to ≈–170°C, whereas maximum energy decreased from ≈13 to ≈10.5 J. Similar tests of the effect of notch geometry are being conducted on specimens annealed at the optimal temperature of 1000°C.

CONCLUSIONS

(1) Impact tests were conducted on production–scale (≈500-kg) heat of V-4Cr-4Ti at –196°C to 150°C. Results showed that the material remained ductile at –196°C and that the ductile–brittle transition temperature (DBTT) was no higher than –200°C. Upper–shelf energies of the production–scale heat were similar to those of the laboratory–scale heat.

(2) Effect of annealing temperature (950, 1000, and 1050°C) on impact properties of the production–scale heat was not significant, a finding similar to that of the laboratory–scale heat. This is in contrast to the very significant effect of annealing temperature on the impact properties of one heat of V–5Cr–5Ti produced by an incorrect process and found to exhibit inferior mechanical properties. Annealing at 1000°C for 1 h produced optimal impact properties in the production–scale heat of V–4Cr–4Ti that are slightly better than those from other annealing treatments.

(3) When the V–notch angle and root radius were decreased from 45° to 30° and from 0.25 to 0.08 mm, respectively, DBTT increased from ≈–200°C to ≈–170°C, whereas maximum energy decreased from ≈13 to ≈10.5 J.

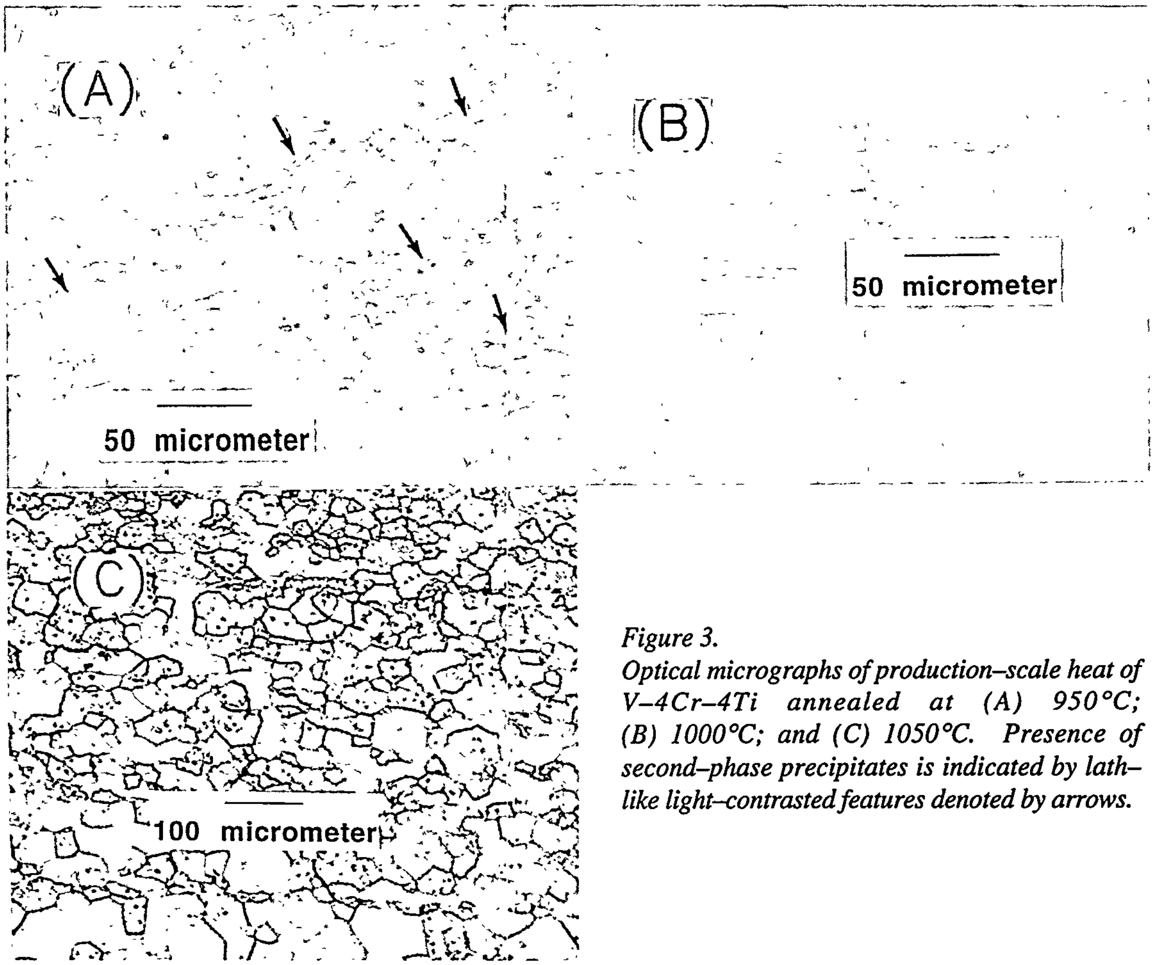

Figure 3.
Optical micrographs of production–scale heat of V–4Cr–4Ti annealed at (A) 950°C; (B) 1000°C; and (C) 1050°C. Presence of second–phase precipitates is indicated by lath–like light–contrasted features denoted by arrows.

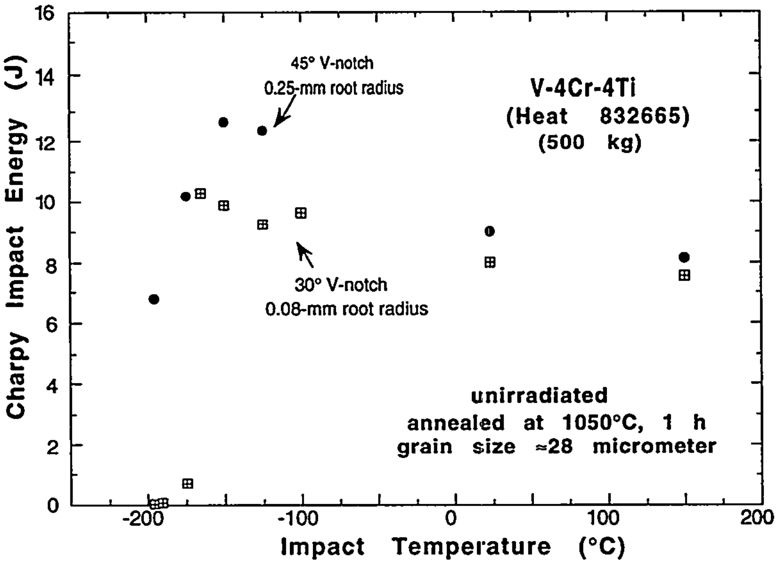

Figure 4.
Effect of notch geometry on impact properties of the production–scale heats of V–4Cr–4Ti.

ACKNOWLEDGMENT

The authors thank W. F. Burke for his contributions to specimen machining and inspection.

REFERENCES

[1] B. A. Loomis, L. Nowicki, and D. L. Smith, "Effect of Neutron Irradiation on Tensile Properties of V–Cr–Ti Alloys," in Fusion Reactor Materials, Semiannual. Prog. Report, DOE/ER-0313/15, Oak Ridge National Laboratory, Oak Ridge, TN (1994), pp. 219–222.

[2] B. A. Loomis, H. M. Chung, L. Nowicki, and D. L. Smith, "Effects of Neutron Irradiation and Hydrogen on Ductile-Brittle Transition Temperatures of V–Cr–Ti Alloys," ibid., pp. 253–257.

[3] H. M. Chung, B. A. Loomis, L. Nowicki, J. Gazda, and D. L. Smith, "Irradiation-Induced Density Change and Microstructural Evolution of Vanadium-Base Alloys," ibid., pp. 223–231.

[4] H. M. Chung, B. A. Loomis, and D. L. Smith, "Thermal Creep Behavior of V–5Cr–5Ti and V–10Cr–5Ti Alloys," in Fusion Reactor Materials, Semiannual. Prog. Report, DOE/ER-0313/14, Oak Ridge National Laboratory, Oak Ridge, TN (1993), pp. 309-317.

[5] H. M. Chung, B. A. Loomis, and D. L. Smith, in Effects of Radiation on Materials, ASTM-STP 1175, A. S. Kumar, D. S. Gelles, R. K. Nanstad, and T. A. Little, Eds., American Society for Testing and Materials, Philadelphia, 1993, pp. 1185–1200.

[6] H. M. Chung, B. A. Loomis, and D. L. Smith, "Properties of V-4Cr-4Ti for Application as Fusion Reactor Structural Components," Proc. 3rd International Symposium on Fusion Nuclear Technology, June 27-July 1, 1994, Los Angeles, CA, in press.

[7] H. M. Chung, B. A. Loomis, L. Nowicki, and D. L. Smith, "Effect of Dynamically Charged Helium on Tensile Properties of V–4Cr–4Ti," in this report.

[8] H. M. Chung, L. J. Nowicki, D. E. Busch, and D. L. Smith, "Ductile–Brittle Transition Behavior of V–4Cr–4Ti Irradiated in the Dynamic Helium Charging Experiment," in this report.

[9] H. M. Chung, L. Nowicki, J. Gazda, and D. L. Smith, "Void Structure and Density Change of Vanadium-Base Alloys Irradiated in the Dynamic Helium Charging Experiment," in this report.

[10] H. M. Chung, H.–C. Tsai, D. L. Smith, R. Peterson, C. Curtis, C . Wojcik, and R. Kinney, "Fabrication of 500–kg Heat of V–4Cr–4Ti," in this report.

[11] B. A. Loomis, "Hardness Recovery of 85% Cold–Worked V–Ti and V–Cr–Ti Alloys on Annealing at 180°C to 1200°C," in this report.

HARDNESS RECOVERY OF 85% COLD-WORKED V-Ti AND V-Cr-Ti ALLOYS UPON ANNEALING AT 180°C TO 1200°C* - B. A. Loomis, L. J. Nowicki, and D. L. Smith (Argonne National Laboratory)

OBJECTIVE

The objective of this research is to determine the effect of heat treatment of cold-worked V-Ti and V-Cr-Ti alloys on their resulting microstructures and to correlate the results with the physical and mechanical properties of these alloys.

SUMMARY

Annealing of 85% cold-worked unalloyed V and V-(1-18)Ti alloys for 1 hr at 180°C to 1200°C results in hardness maxima at 180-250°C, 420-600°C, and 1050-1200°C and in hardness minima at 280-360°C and, depending on Ti concentration in the alloy, at 840-1050°C. Annealing of 85% cold-worked V-(4-15)Cr-(3-6)Ti alloys for 1 hr at 180°C to 1200°C results in hardness maxima at 180-250°C, 420-800°C, and 1050-1200°C, and in hardness minima at 280-360°C and 920-1050°C. Tentative interpretations are presented for the hardness maxima and minima. Annealing of specimens at 1200°C results in significant increase of VHNs upon removal of a 0.05-mm-thickness surface layer from the specimens.

INTRODUCTION

Vanadium-base alloys have been identified as leading candidates for fusion first-wall/blanket applications. The performance advantages of vanadium-base alloys, in addition to their excellent safety and environmental features, have been evaluated in several design studies [1-5]. The current focus of experimental effort on the mechanical and physical properties of vanadium-base alloys is on alloys with 3-5% Cr and 3-5% Ti [6-9]. However, most of the experimental data reported for these alloys have been obtained on materials in the fully recrystallized condition [6-16]. The purpose of the research presented in this report is to comprehensively evaluate the effect of heat treatment of cold-worked V-Ti and V-Cr-Ti alloys on their resulting microstructure and to correlate the results with the physical and mechanical properties of these alloys. Recovery of the microhardness of cold-worked alloys with annealing temperature is utilized for the initial definition of the principal thermodynamic processes that these cold-worked alloys undergo during heat treatment.

MATERIALS AND PROCEDURES

Specimens of unalloyed V, V-Ti alloys, and V-Cr-Ti alloys with the compositions listed in Table 1 were obtained from recrystallized stock containing <30 appm H (Charpy-impact specimens, 0.33-cm thickness, 20-40 μm average grain size) by rolling of this stock to 0.05-cm thickness (85% thickness reduction at 25°C) without an intermediate annealing. One surface of the rolled specimens was polished to a surface finish of 1 μm for hardness measurement. The unalloyed V and V-Ti binary alloy specimens were polished simultaneously. The V-Cr-Ti alloy specimens were also polished simultaneously, but separate from the V-Ti alloys. Hence, the concentration of hydrogen introduced into the V-Ti and V-Cr-Ti alloy specimens during polishing was nearly equivalent. Specimens were also obtained with no alteration of the rolled surface, in order to evaluate the effect on hardness measurement of hydrogen introduced during polishing of the specimens [11]. In addition, hardness measurements were made on specimens annealed at 1200°C after removal of a 0.05-mm-thickness layer for evaluation of the effects of environmental contamination of the specimens and/or thermal evaporation of alloy constituents.

The cold-worked (CW) specimens were annealed in an ion-pumped system capable of maintaining a pressure of $< 2 \times 10^{-5}$ torr during annealing of specimens at 1200°C. The specimens were wrapped in tantalum sheet with an enclosed thermocouple and were heated by a resistance furnace. The specimens were heated at a rate of 10

---

*Work supported by the Office of Fusion Energy, U.S. Department of Energy, under Contract W-31-109-Eng-38.

-15°C/min to the annealing temperature, maintained at the selected temperature (±5°C) for 60 min, and subsequently cooled to <100°C at 50-100°C/min.

Microhardness measurements were conducted on the CW and annealed specimens at 25°C with a Leitz Durimet Hardness Tester equipped with a Vickers indenter. The Vickers Hardness Number (VHN) was obtained from the average of two dimensions of each of two or three indentations on a specimen resulting from application of a 50-g load to the indenter for 0.3 min.

Table 1. Compositions of V, V-Ti alloys, and V-Cr-Ti Alloys. *,**

Material	ANL No.	Cr	Ti	Other	O	N	C	Si
V	BL 51	<100	130	0.03% Mo	570	49	56	370
V-1Ti	BL 50	<100	1.0%	0.08% Al	230	130	235	1050
V-3Ti	BL 62	<100	3.1%	0.07% Al	320	86	109	660
V-5Ti	BL 46	<100	4.6%	0.04% Al	305	53	85	160
V-10Ti	BL 12	<100	9.8%	0.63% Fe	1670	390	450	245
V-18Ti	BL 15	150	17.7%	0.04% Fe	830	160	380	480
V-5Cr-3Ti	BL 54	5.1%	3.0%	0.07% Al	480	82	133	655
V-4Cr-4Ti	BL 47	4.1%	4.3%	0.03% Al	350	220	200	870
V-5Cr-5Ti	BL 63	4.6%	5.1%	0.02% Al	440	28	73	310
V-8Cr-6Ti	BL 49	7.9%	5.7%	0.02% Al	400	150	127	36
V-9Cr-5Ti	BL 43	9.2%	4.9%	0.02% Fe	230	31	100	340
V-14Cr-5Ti	BL 24	13.5%	5.2%	0.05% Fe	1190	360	500	390
V-15Cr-5Ti	BL 41	14.5%	5.0%	0.02% Fe	330	96	120	400

* All compositions in wt. ppm or wt. percent (%).

** Analyses performed by the Analytical Laboratory, Teledyne Wah Chang Albany, Albany, Oregon.

EXPERIMENTAL RESULTS

V and V - (1-18)Ti Alloys

The VHNs for unalloyed V and several V-Ti alloys after annealing of the 85% CW specimens for 1 hr at temperatures ranging from 180°C to 1200°C are shown in Fig. 1. Annealing of 85% CW specimens at 180°C to 1200°C results in hardness maxima at 180-250°C, 420-600°C, and 1050-1200°C and in hardness minima at 280-360°C and 840-1050°C. It can be noted in Fig. 1 that the 840-1050°C hardness minima are strongly dependent on the Ti concentration, with the temperature of the VHN minimum increasing with decreasing Ti concentration in the material. The VHN data (Fig. 1) for unalloyed V and V-Ti alloys after heat treatments at >900°C show that the maxima are ≈1130°C. The VHNs of specimens with polished surfaces were not significantly different from the VHNs of specimens without polished surfaces (data not shown in Fig. 1 for clarity). These results show that the amount of hydrogen (<50 appm) introduced into the specimens during polishing had no significant effect on the recovery behavior of these V and V-Ti alloys.

The dependence of the VHNs for V-Ti alloys on Ti concentration is shown in Fig. 2. The VHNs for V-Ti alloys increase significantly with addition of 1% Ti to vanadium. The VHNs of these V-Ti alloys can increase or decrease when the Ti concentration is increased from 3% up to 5%. Otherwise, the VHNs for the specimens are nearly linearly

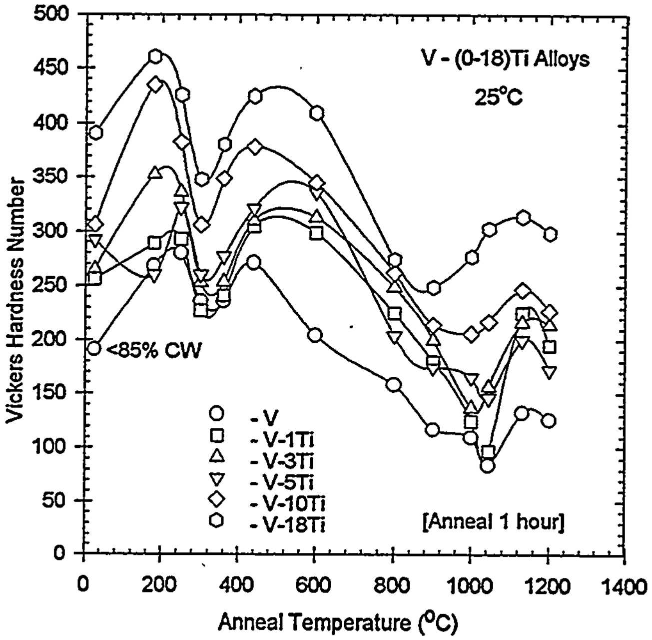

Fig. 1. Recovery of VHN of unalloyed V and V-Ti alloys with 85% CW upon annealing at 180°C to 1200°C.

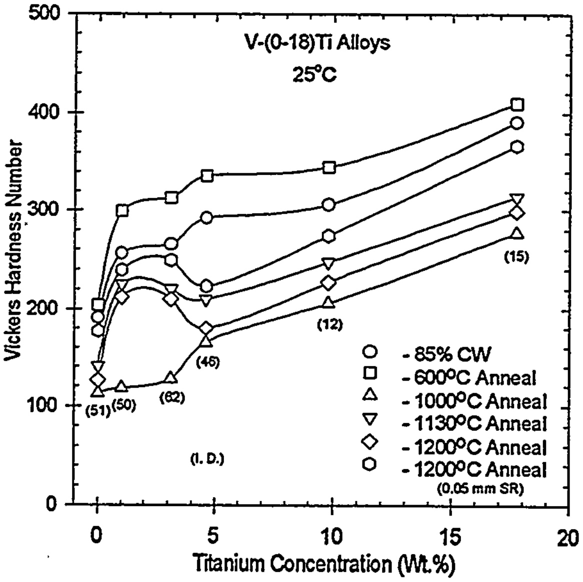

Fig. 2. Dependence of recovery of VHN of V and V-Ti alloys with 85% CW on Ti concentration.

dependent on Ti concentration in the range of 5 to 18% Ti. It can be observed in Fig. 2 that the VHNs of specimens after annealing at 1200°C and removal of a 0.05-mm-thickness surface layer (SR) from the specimens are significantly higher than the VHNs of specimens in the as-annealed condition (1200°C). The difference in VHNs for the specimens with/without SR increased with increasing Ti concentration in the alloy. The surfaces of specimens annealed at 1200°C exhibited significant thermal-induced relief of precipitates and grain boundaries.

V - Cr - (3-6)Ti Alloys

The VHNs of V-Cr-(3-5)Ti alloys after annealing of the 85% CW specimens for 1 hr at temperatures ranging from 180°C to 1200°C are shown in Fig. 3. Annealing of 85% CW specimens at 180°C to 1200°C results in hardness maxima at 180-250°C, 420-800°C, and 1050-1200°C, and in hardness minima at 280-360°C and 920-1050°C. Examination of the data in Fig. 3 for heat treatments of alloys at < 800°C shows that the maxima and minima for the V-4Cr-4Ti alloy (BL 47) are much higher and lower, respectively, than for the V-5Cr-3Ti (BL 54) and V-5Cr-5Ti (BL 63) alloys. In addition, the VHNs for the V-5Cr-3Ti (BL54), V-4Cr-4Ti (BL 47), V-5Cr-5Ti (BL 63), V-9Cr-5Ti (BL 43), and V-14Cr-5Ti (BL 24) alloys heat treated at >1000°C suggest that the VHN maxima are ≈1130°C. As in the case of the V-Ti alloys, the amount of hydrogen (<50 appm) introduced into the V-Cr-Ti specimens during polishing was not sufficient to affect the recovery behavior of these alloys.

The dependence of VHNs for V-Cr-(3-6)Ti alloys on Cr concentration is shown in Fig. 4. These data generally show minimum VHNs for alloys containing 5-8% Cr. It can also be observed in Fig. 4 that the VHNs for the V-14Cr-5Ti alloy (BL 24) are comparable to the VHNs for the V-15Cr-5Ti alloy (BL 41), even though the V-14Cr-5Ti alloy contains substantially higher oxygen, nitrogen, and carbon concentration. The VHNs of specimens annealed at 1200°C (Fig. 4) after removal of a 0.05-mm-thickness surface layer (SR) from the specimens were significantly higher than the VHNs of specimens in the as-annealed condition (1200°C). The difference in VHNs for the specimens with/without SR increased significantly for alloys with increasing Cr concentration in the alloy. The surfaces of specimens annealed at 1200°C exhibited significant thermal-induced relief of precipitates and grain boundaries.

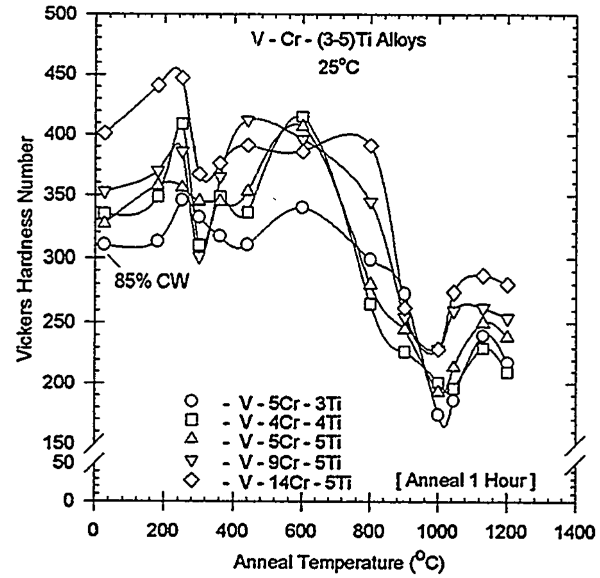

Fig. 3. Recovery of VHN of V-Cr-(3-5)Ti alloys with 85% CW upon annealing at 180°C to 1200°C.

Comparison of Recovery for V-(4-5)Cr-(3-5)Ti Alloys

The dependence of recovery of 85% CW specimens of V-5Cr-3Ti (BL 54), V-4Cr-4Ti (BL 47), and V-5Cr-5Ti (BL 63) alloys upon annealing temperature is shown in Fig. 5. The VHNs for the V-5Cr-3Ti alloy for annealing temperatures < 800°C are, in general, significantly less than the VHNs for the V-4Cr-4Ti and V-5Cr-5Ti alloys. The

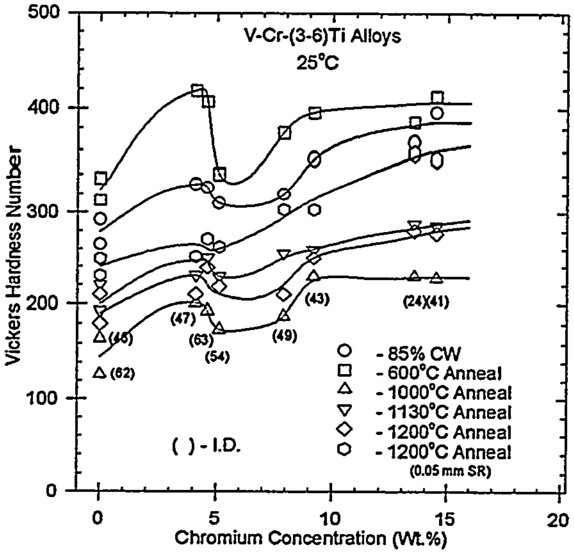

Fig. 4. Dependence of recovery of V-Cr-(3-6)Ti alloys with 85% CW on Cr concentration.

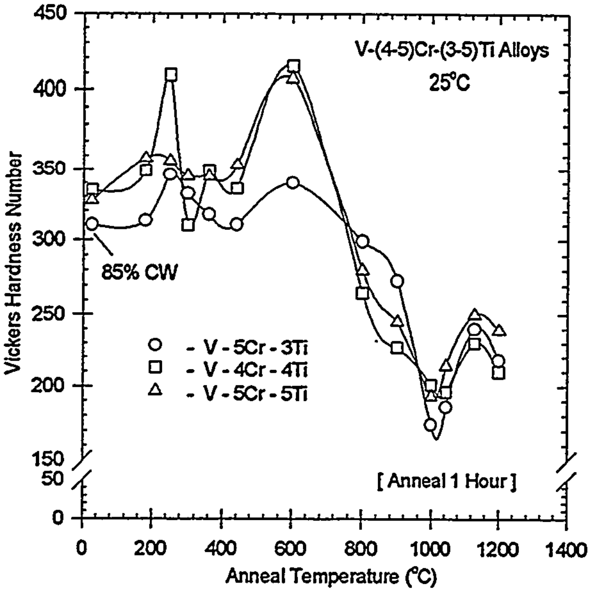

Fig. 5. Recovery of V-5Cr-3Ti, V-4Cr-4Ti, and V-5Cr-5Ti alloys with 85% CW upon annealing.

VHN maximum for the V-4Cr-4Ti alloy after annealing at 250°C is substantially higher than the maximum for the V-5Cr-3Ti and V-5Cr-5Ti alloys; and the VHN minimum for the V-4Cr-4Ti alloy after annealing at 300°C is substantially lower than the minimum for the V-5Cr-3Ti and V-5Cr-5Ti alloys.

DISCUSSION OF RESULTS

The recovery behavior of 85% CW unalloyed V, V-Ti alloys, and V-Cr-Ti alloys upon annealing at temperatures from 180°C to 1200°C (which is evidenced by the VHNs) suggests that similar thermodynamic processes occur in these materials upon heat treatment. However, critical examination of the data in Figs. 1-5 shows that processes are occurring in these materials that require further investigation, e.g., (1) VHN maxima at 840-1050°C in V-Ti alloys that increase with decrease of Ti concentration in the alloys; (2) heat treatment of V-Cr-Ti alloys at < 800°C resulting in VHN maxima and minima for the V-4Cr-4Ti alloy that are significantly higher and lower, respectively, than for the V-5Cr-3Ti and V-5Cr-5Ti alloys; (3) the significant increase of VHN for the materials upon heat treatment at >1050°C; and (4) the increase of VHN of the specimens at 0.05-mm-depth below the surface of specimens after annealing.

Interpretation of the recovery and the maxima and minima of VHNs for the unalloyed V, V-Ti alloys, and V-Cr-Ti alloys upon heat treatment would be supposititious in the absence of a comprehensive series of microstructural observations by optical and transmission electron microscopy. However, it is tentatively suggested that the following processes may be involved in the recovery of the 85% CW microstructure upon annealing of these unalloyed V and V alloys. The maxima at 180-250°C may be due to the diffusion of H, O, N, and C to the CW dislocation structure [11, 17]. The relative contributions to the 180-250°C maxima would seem to favor an effect due to the O, N, and C impurities, since the hydrogen concentration in the specimens was < 50 appm. Moreover, the VHNs for the V-10Ti and V-18Ti alloys (Fig. 1) and V-4Cr-4Ti and V-14Cr-5Ti alloys (Fig. 3) after annealing at 180-250°C are the highest of the alloys, which is in agreement with the highest O, N, and C concentration in the alloys (Table 1). The minima at 300-360°C may be attributed to the evolution of H from the specimens and/or removal of O, N, and C from solid solution by interaction with V atoms (unalloyed V) and Ti solute in the alloys. The maxima at 420-800°C may be attributed to the formation of precipitates, e.g., Ti(C, N, O), $Ti(C_{1-x-y}N_xO_Y)$, V_6O_{13}, VS_4 and V_4C_3[15]. The minima at 840-1050°C may be attributed to a combination of annihilation and rearrangement of CW dislocation structure, recrystallization, grain growth, formation of additional precipitates, e.g., Ti_5Si_3, [8,9] and redistribution of impurities, e.g., S and P. The maxima at 1050-1200°C may be attributed to formation of additional precipitates, e.g., Ti_5Si_3, redistribution of impurities, and thermal evaporation of alloy constituents.

The significant increase of VHNs of 1200°C-annealed specimens upon removal of a 0.05-mm-thickness surface layer (Figs. 2 and 4) is not understood, since it is expected that O, N, and C impurities should equilibrate rapidly throughout the specimen thickness upon annealing at temperatures of >700°C [18]. It may be that evaporation of alloy constituents contributed to the lower VHNs in the near-surface region.

FUTURE EFFORT

(1). The microstructures of the unalloyed V, V-Ti alloys, and V-Cr-Ti alloys will be observed by optical and transmission electron microscopy (TEM) for determination of the significance of the maxima and minima VHNs after heat treatment of the 85% CW material.
(2). The number density and average diameter of precipitates in the 85% CW and heat-treated materials will be determined, and these results will be compared with previously reported data on these parameters for 50% CW and heat-treated material [15].
(3). The dependence of the dislocation density and average grain size in the materials on heat treatment will be determined from optical and TEM observations.
(4). These effects of heat treatment on the recovery and microstructure will be correlated with previously reported experimental data on the physical and mechanical properties of vanadium alloys with different heat treatments [6-16].
(5). The viability of utilizing the temperature-dependent recovery of VHN of CW vanadium alloys for selection of

an alloy with the optimum physical and mechanical properties for use in fusion first-wall/blanket applications will be evaluated.

REFERENCES

[1]. D. L. Smith, et al., Fusion Technology, 8, 10 (1985).
[2]. D. Ehst, et al., Tokamak Power Systerm Studies, Argonne National Laboratory, ANL/FPP/86-1 (1986).
[3]. The ARIES Team, The ARIES-II Tokamak Reactor Study, University of California at Los Angeles, Report UCLA-PPG-1461 (to be published 1994).
[4]. J. Holdren, et al., Report of the Senior Committee on Environmental, Safety, and Economic Aspects of Magnetic Fusion Energy, Lawrence Livermore National Laboratory, Report UCRL-53776 (1989).
[5]. H. K. Birnbaum, et al., Technical Evaluation of the Technology of Vanadium Alloys for Use as Blanket Structural Materials in Fusion Power Systems, Aug. 4, 1993, Report DOE/ER-0313/100.
[6]. B. A. Loomis, L. J. Nowicki, and D. L. Smith, 6th Intl. Conf. on Fusion Reactor Materials (ICFRM-6), Sept. 27-Oct. 1, 1993, Stresa, Italy, to be published in the J. of Nucl. Mater.
[7]. B. A. Loomis, H. M. Chung, L. J. Nowicki, and D. L. Smith, 6th Intl. Conf. on Fusion Reactor Materials (ICFRM-6) Sept. 27-Oct. 1, 1993, Stresa, Italy, to be published in the J. of Nucl. Mater.
[8]. H. M. Chung, B. A. Loomis, and D. L. Smith, 6th Intl. Conf. on Fusion Reactor Materials (ICFRM-6), Sept. 27-Oct. 1, 1993, Stresa, Italy, to be published in the J. of Nucl. Mater.
[9]. H. M. Chung, B. A. Loomis, and D. L. Smith, 6th Intl. Conf. on Fusion Reactor Materials (ICFRM-6), Sept. 27-Oct. 1, 1993, Stresa, Italy, to be published in the J. of Nucl. Mater.
[10]. B. A. Loomis, B. J. Kestel, and D. R. Diercks, J. Nucl. Mater. 141-143 (1986) 523.
[11]. B. A. Loomis, R. H. Lee, D. L. Smith, and J. R. Peterson, J. Nucl. Mater. 155-157 (1988) 631.
[12]. B. A. Loomis, A. B. Hull, and D. L. Smith, J. Nucl. Mater. 179-181 (1991) 148.
[13]. B. A. Loomis and D. L. Smith, J. Nucl. Mater. 179-181 (1991) 783.
[14]. B. A. Loomis and D. L. Smith, J. Nucl. Mater. 191-194 (1992) 84.
[15]. J. Gazda, B. A. Loomis, L. J. Nowicki, D. L. Smith, and S. Danyluk, Fusion Reactor Materials Semiannual Progress Report for Period Ending September 30, 1993, Report DOE/ER-0313/15, pp. 232-239.
[16]. M. L. Grossbeck, A. F. Rowcliffe, and D. J. Alexander, Fusion Reactor Materials Semiannual Progress Report for Period Ending March 31, 1994, Report DOE/ER-0313/16.
[17]. R. W. Powers and Margaret V. Doyle, Acta Met. 6 (1958) 643.
[18]. R. W. Powers and Margaret V. Doyle, J. Appl. Phys. 30 (1959) 514.

EFFECT OF OXIDATION ON TENSILE BEHAVIOR OF V-5Cr-5Ti ALLOY*

K. Natesan and W. K. Soppet (Argonne National Laboratory)

OBJECTIVE

The objectives of this task are to (a) evaluate the oxygen uptake behavior of V-5Cr-5Ti alloy as a function of temperature and oxygen partial pressure in the exposure environment, (b) examine the microstructural characteristics of oxide scales and oxygen entrapped at the grain boundaries in the substrate alloy, (c) evaluate the influence of oxygen uptake on the tensile properties of the alloy at room and elevated temperatures, (d) evaluate oxidation kinetics of the alloy with aluminum-enriched surface layers, and (e) determine the effect of oxygen uptake on tensile behavior of the alloy.

SUMMARY

Oxidation studies were conducted on V-5Cr-5Ti alloy specimens at 500°C in an air environment. The oxidation rates calculated from measurements of thermogravimetric testing are 10, 17, and 25 µm/y at 400, 450 and 500°C, respectively. Uniaxial tensile specimens were oxidized for several time periods in air at 500°C and subsequently tensile-tested at 500°C in air. The hardened layer in each of these oxidized specimens was confined to 75 µm after 1000 h exposure at 500°C. The influence of 1000 h oxidation is to increase the ultimate tensile strength of the alloy by ≈10% while decreasing the tensile rupture strain from 0.23 to 0.14.

INTRODUCTION

Refractory alloys in general and V-alloys in particular are susceptible to pickup of interstitials such as oxygen, carbon, and nitrogen, which can affect the short- and long-term mechanical properties of the materials. The vanadium alloy with a composition of V-5Cr-5Ti contains 5 wt.% Ti (much more stable oxide-former than V and Cr), which can have an even stronger effect on mechanical properties, especially tensile and creep ductility. The degree of influence of interstitials such as oxygen on the alloy's properties will be dictated by alloy grain size (the amount of grain-boundary areas), amount and distribution of oxygen in the alloy, amount and size of second-phase oxide precipitates (such as Ti oxide), and service temperature and time. The purpose of this study is to examine the role of oxygen and oxidation on the tensile properties of the material.

EXPERIMENTAL PROGRAM

The heat of vanadium alloy selected for the study had a composition of V-5 wt.%Cr -5wt.% Ti and had the designation BL-63. Sheet material of the alloy was annealed for 1 h at 1050°C prior to its use in oxidation and tensile testing. Coupon specimens measuring ≈15 x 7.5 x 1 mm were used for the oxidation studies. Oxidation experiments were conducted in air in a thermogravimetric test apparatus. The test temperatures ranged between 300 and 750°C.

Uniaxial tensile tests were conducted at 500°C in air with an Instron machine. The tensile specimens were fabricated according to ASTM specifications and had a gauge length of ≈19 mm and a gauge width of ≈4.5 mm. The specimens were preoxidized in air at 500°C for 24, 250, 600 and 1000 h prior to tensile testing in air at 500°C. Vickers hardness measurements were made on the tested specimens.

RESULTS AND DISCUSSION

Figure 1 shows weight change data for the alloy oxidized in air at several temperatures. The oxidation kinetics followed a parabolic relationship with time. Detailed scanning electron microscopy analysis of the oxidized samples showed the outer layer to be predominantly vanadium-rich oxide and the inner layer to be

---

*This work has been supported by the U.S. Department of Energy, Office of Fusion Energy Research, under Contract W-31-109-Eng-38.

(V,Ti) oxide. Parabolic rate equations were used to calculate oxide scale thicknesses in the specimens, which were in agreement with the values determined by metallography. Figure 2 shows the oxidation rate (based on parabolic kinetics) as a function of temperature in the range 300-575°C. The results show that the oxide will grow at rates of 10, 17, and 25 µm/y at 400, 450, and 500°C, respectively. Even though the oxide thickness values are low at these temperatures, the alloy also exhibits an oxygen-enriched region ahead of the oxide scale, which can lead to hardening of the material and may also embrittle the alloy.

To evaluate the effect of oxidation and oxide penetration into the substrate alloy, several tests are in progress to examine the tensile behavior of the alloy as a function of oxygen ingress and oxide scale

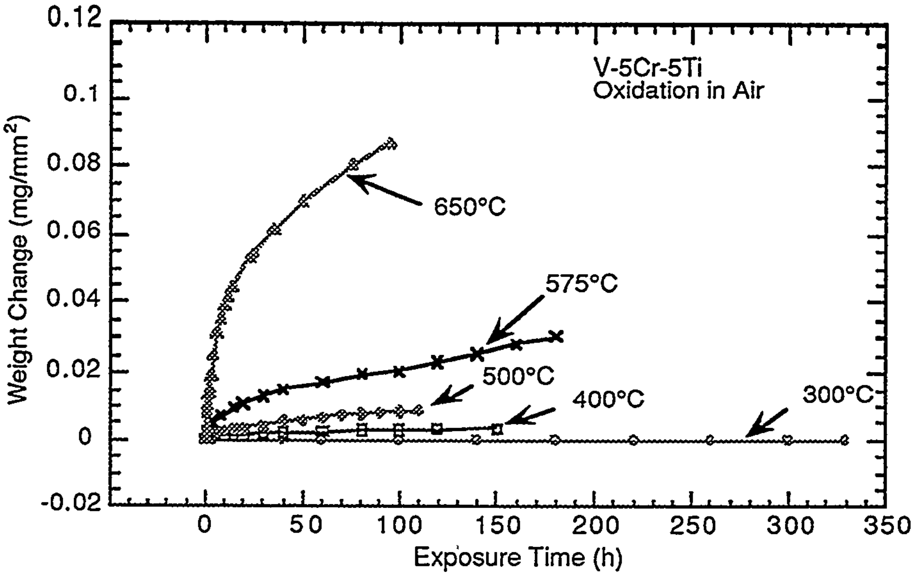

Figure 1. Weight change data for oxidation of V-5Cr-5Ti alloy in air at several test temperatures.

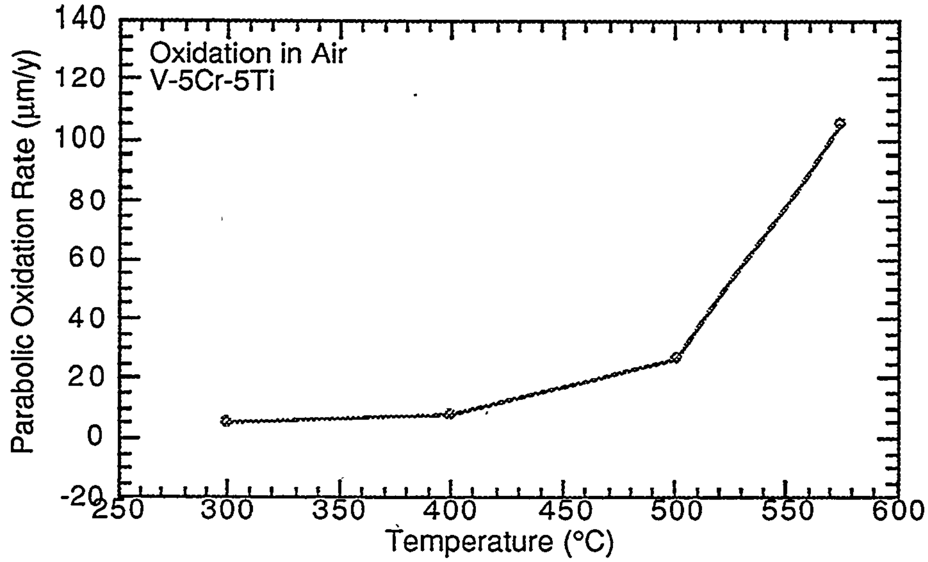

Figure 2. Parabolic rate (for first year) for oxidation of V-5Cr-5Ti alloy in air as a function of exposure temperature.

formation. In the first series of tests, tensile specimens were exposed to air for 24 to 1000 h in air at 500°C and then tensile-tested in air at the same temperature. Most of the tests were conducted at a strain rate of 1.75×10^{-4} s^{-1}, while a few specimens were tested at lower strain rates to evaluate the strain rate effect on tensile properties. Figure 3 shows the Vickers hardness profile of the specimens exposed to air for different times at 500°C. Oxide scale thickness is ≈10 µm but the hardness increase is noted to a depth of 50-70 µm, indicating an oxygen-enriched zone ahead of the oxide scale. Detailed analysis of this oxygen-enriched zone is in progress.

Figure 4 shows the engineering stress/engineering strain curves for specimens in oxidized condition and

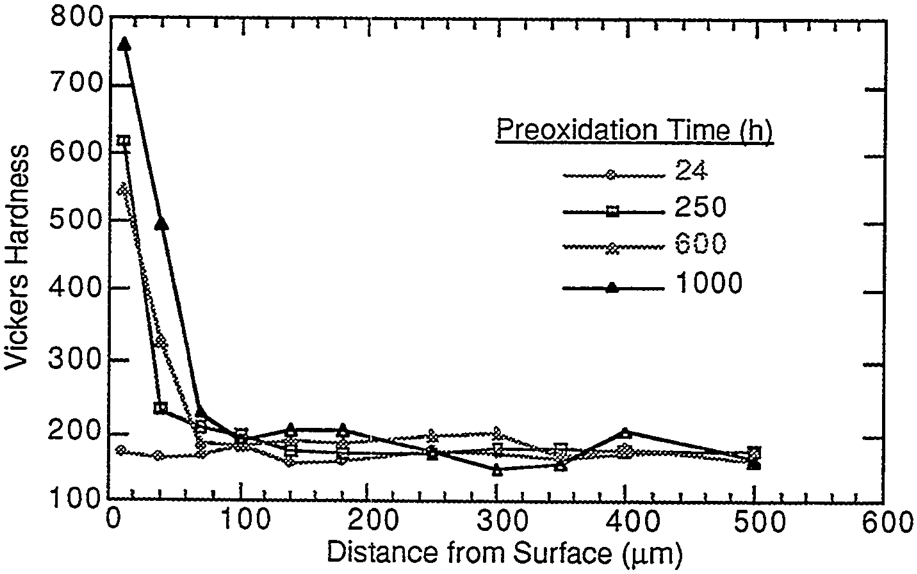

Figure 3. Vickers hardness data for specimens of V-5Cr-5Ti alloy oxidized at 500°C in air for different times.

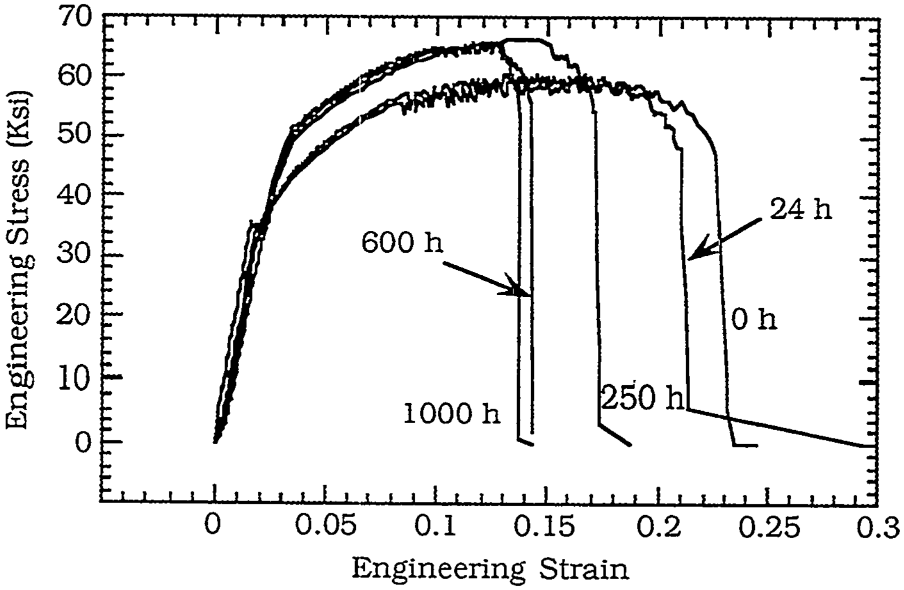

Figure 4. Effect of preoxidation at 500°C on stress-strain behavior of V-5Cr-5Ti alloy tested at 500°C in air at a strain rate of 1.75×10^{-4} s^{-1}.

after preoxidation for 24, 250, 600, and 1000 h in air at 500°C. The results show that air exposure for 24 h at 500°C has a negligible effect on tensile properties. The ultimate tensile strength value was ≈60 ksi for the specimens with and without 24 h exposure. Tensile strain decreased from 0.23 to 0.21 as a result of the 24h oxidation treatment. Air exposures of 250, 600, and 1000 h resulted in some increase in ultimate tensile strength of the material, but strength seemed to saturate at 67 ksi after 1000 h. Tensile strain decreased to 0.175, 0.145, and 0.14 after 250, 600, and 1000 h, respectively. Results to date indicate that the material is not subject to catastrophic embrittlement due to oxygen ingress into the material. Additional exposures as a function of oxygen partial pressure in the exposure environment, as well as tensile tests at lower temperatures, are in progress to establish the performance envelope for the alloy in an oxygenated environment.

EFFECT OF DYNAMICALLY CHARGED HELIUM ON TENSILE PROPERTIES OF V–4Cr–4Ti[*]

H. M. Chung, B. A. Loomis, L. Nowicki, and D. L. Smith (Argonne National Laboratory)

OBJECTIVE

The objective of this work is to determine the effect of displacement damage and dynamically charged helium on tensile properties of V–4Cr–4Ti alloy irradiated to 18–31 dpa at 425–600°C in the Dynamic Helium Charging Experiment (DHCE).

SUMMARY

One property of vanadium-base alloys that is not well understood in terms of their potential use as fusion reactor structural materials is the effect of simultaneous generation of helium and neutron damage under conditions relevant to fusion reactor operation. In the present Dynamic Helium Charging Experiment (DHCE), helium was produced uniformly in the specimen at linear rates of ≈0.4 to 4.2 appm helium/dpa by the decay of tritium during irradiation to 18–31 dpa at 425–600°C in the Li-filled DHCE capsules in the Fast Flux Test Facility. This report presents results of postirradiation tests of tensile properties of V-4Cr-4Ti, an alloy identified as the most promising vanadium–base alloy for fusion reactors on the basis of its superior baseline and irradiation properties. Effects of helium on tensile strength and ductility were insignificant after irradiation and testing at >420°C. Contrary to initial expectation, room–temperature ductilities of DHCE specimens were higher than those of non–DHCE specimens (in which there was negligible helium generation), whereas strengths were lower, indicating that different types of hardening centers are produced during DHCE and non–DHCE irradiation. In strong contrast to tritium–trick experiments in which dense coalescence of helium bubbles is produced on grain boundaries in the absence of displacement damage, no intergranular fracture was observed in any tensile specimens irradiated in the DHCE.

INTRODUCTION

Vanadium-base alloys have significant advantages over other candidate alloys (such as austenitic and ferritic steels) for use as structural materials in fusion devices, e.g., the International Thermonuclear Experimental Reactor (ITER) and magnetic fusion reactors. These advantages include intrinsically lower levels of long-term activation, irradiation afterheat, neutron-induced helium- and hydrogen-transmutation rates, biological hazard potential, and thermal stress factor. Recent attention has focused on V-4Cr-4Ti for fusion reactor structural components because of its excellent combination of mechanical and physical properties before and after irradiation.[1–6] One property of vanadium–base alloys that is not well understood is the effect of helium; no tensile data have been reported on effects of simultaneous generation of helium and neutron displacement damage under fusion–relevant conditions (i.e., ≈5 appm He/dpa ratio), although helium effects on other vanadium alloys have been investigated by less–than–prototypical simulation techniques such as tritium-trick,[7–11] cyclotron-injection,[12–16] and boron-doping.[16–19] In the DHCE,[20–22] the fusion–relevant helium–to–dpa damage ratio is closely simulated by utilizing slow transmutation of controlled amounts of ^{6}Li and a tritium–doped mother alloy immersed in ^{6}Li + ^{7}Li. This report presents results of postirradiation examination of mechanical properties of V-4Cr-4Ti alloy, which has been identified as the most promising candidate alloy on the basis of its superior baseline and irradiation properties.

---

[*] Work supported by the U.S. Department of Energy, Office of Fusion Energy, under Contract W-31-109-Eng-38.

MATERIALS AND PROCEDURES

The elemental composition of the V–4Cr–4Ti alloy, determined prior to irradiation, is given in Table 1. An alloy ingot, melted from low–chlorine titanium and high–purity vanadium, was extruded at 1150°C and annealed at 1050°C several times after 8–10 passes of warm (400°C) rolling between the annealings. Final forms of the product were annealed plates and sheets 3.8–, 1.0–, and 0.3–mm in thickness. SS–3 tensile specimens with a gauge length of 7.62 mm and a gauge width of 1.52 mm were machined from 1.0–mm–thick annealed (1050°C) sheets. The specimens were ≈95% recrystallized and exhibited an average grain size of ≈14 µm. The only secondary phase in the as–annealed specimen was Ti(O,N,C), which is normally observed in titanium–containing vanadium alloys with O+N+C >400 wppm. Tensile properties were measured at 23°C and at irradiation temperatures in flowing argon at a strain rate of 0.0011 s^{-1}. The thickness and gauge width of each specimen were measured individually after irradiation and before each tensile test.

Table 1. Chemical composition of V–4Cr–4Ti

ANL ID	Nominal Composition (wt.%)	O	N	Impurity Composition (wppm) C	Si	S	P	Nb	Mo
BL-47	V–4.1Cr–4.3Ti	350	220	200	870	20	<40	<100	<100

The alloy specimens were irradiated in the Fast Flux Test Facility (FFTF), a fast reactor located near Richland, Washington, at 420, 520, and 600°C to neutron fluences (E > 0.1 MeV) ranging from 3.7 x 10^{22} n/cm^2 (≈18 displacements per atom, or dpa) to 6.4 x 10^{23} n/cm^2 (≈31 dpa). Helium in the alloy specimens was produced by utilizing transmutation of controlled amounts of ^{6}Li and predetermined amounts of tritium–doped vanadium mother alloy immersed in ^{6}Li + ^{7}Li.[20–22] Table 2 summarizes the irradiation temperature, weight of the mother alloy, fraction of ^{6}Li, and tritium and lithium inventory charged in each of the seven DHCE capsules before irradiation.

Table 2. Summary of capsule–loading parameters of DHCE.

Capsule ID No.	Irradiation Temp. (°C)	Total Weight (g) Vanadium[a]	Specimen[b]	Lithium	Fraction of ^{6}Li (%)	Initial Tritium Charged[a] (Ci)	(mmol)
4D1	425	1.5468	5.86	0.765	5.0	99	1.70
4D2	425	1.5536	5.38	0.765	4.5	70	1.20
5E2	425	1.5657	5.38	0.670	1.0	26	0.45
5D1	500	1.5727	5.77	0.938	6.5	73.5	1.26
5E1	500	1.5651	5.82	0.952	1.0	57	0.98
5C1	600	1.5656	5.82	0.808	8.0	16.4	0.28
5C2	600	1.5466	5.95	0.955	8.0	18	0.31

[a] Letter from C. E. Johnson to K. Pearce, April 23, 1991; 1 mmol = 58.3 Ci.

[b] Excluding tritium–charged mother alloy.

Table 3 summarizes actual postirradiation parameters determined from tensile and TEM disk specimens of the V–4Cr–4Ti alloy, i.e., dose and helium and tritium contents measured ≈20–25 days after the postirradiation tests.

Table 3. Summary of irradiation parameters of Dynamic Helium Charging Experiment and helium and tritium contents measured in V–4Cr–4Ti specimens

Capsule ID No.	Irradiation Temp. (°C)	Total Damage (dpa)	Calculated Helium (appm) to dpa Ratio[a] at EOI[b] (Assumed k_a or k_w)[c] k_a=0.073 (k_w=0.01)	Measured Helium Content[d] (appm)	Actual Helium to dpa Ratio (appm/dpa)	Measured Tritium Content[e] (appm)
4D1	425	31	3.8	11.2–13.3	0.39	27
4D2	425	31	2.8	22.4–22.7	0.73	39
5E2	425	18	2.1	3.3–3.7	0.11	2
5D1	500	18	4.4	14.8–15.0	0.83	4.5
5E1	500	18	3.1	6.4–6.5	0.36	1.7
5C1	600	18	1.1	8.4–11.0	0.54	20
5C2	600	18	1.1	74.9–75.3	4.17	63

[a] L. R. Greenwood "Revised Calculations for the DHCE," April 30, 1993.

[b] Beginning of irradiation (BOI) May 27, 1991; end of irradiation (EOI) March 19, 1992; 203.3 effective full power days (EFPD), hot standby at ≈220°C until November 1992.

[c] Equilibrium ratio (k_a by atom, k_w by weight) of tritium in V alloy to that in the surrounding liquid lithium.

[d] Measured June 1994.

[e] Measured August 1994.

Helium and tritium contents were determined by mass spectrometry at Rockwell International Inc., Canoga Park, California. Two TEM disk or broken tensile specimens were selected from each capsule after multiple–bending (at –196°C to 50°C) or tensile tests (at room temperature) and analyzed to determine helium and tritium contents. For each specimen, four separate analyses of ^{3}He and ^{4}He were conducted. The tritium contents were determined on the basis of analysis of ^{3}He decay measured on the same specimens ≈50 days apart.

RESULTS

Yield strength, ultimate tensile strength, uniform elongation, and total elongation measured on tensile specimens irradiated at 425°C–600°C to 18–34 dpa in the DHCE are summarized in Fig. 1. For comparison, similar properties measured on irradiated non–DHCE specimens are also plotted as a function of irradiation temperature.

After irradiation to ≈30 dpa in either a DHCE or a non–DHCE, ductility of the alloy remained significantly high, i.e., >8% uniform elongation and >10% total elongation. Tensile properties measured at 425°C, 500°C, and 600°C (the same as the irradiation temperatures) were essentially the same as those measured on non–DHCE specimens, showing that the effect of helium was insignificant. Room–temperature ductilities of the DHCE specimens (irradiated at 425°C, 500°C, and 600°C) were higher than those of the similar non–DHCE specimens, whereas strengths were lower. This was an unexpected finding. Although the mechanisms leading to the higher ductility and lower strength of the DHCE specimens are not understood at this time, the consistent observations indicate that different types of hardening centers are produced during DHCE and non–DHCE irradiation.

The dependence of uniform and total elongation on irradiation and test temperature, shown in Figs. 1C and 1D, respectively, is in sharp contrast to similar results obtained on specimens in which helium atoms were produced by the tritium–trick method. In the latter type of experiments, total elongation measured at room temperature and at 700–800°C was significantly lower than that measured at

500–600°C because of the strong susceptibility to intergranular cracking associated with extensive formation of grain–boundary helium bubbles.[10] However, no intergranular fracture surface morphology was observed in the tensile specimens irradiated in the DHCE and tested at 25–600°C (including the specimen irradiated in Capsule 5C2 at 600°C at a helium generation rate of 4.2 appm He/dpa), and no ductility degradation similar to that in tritium–trick experiments was observed. This is shown in Fig. 2, where the ratio of total strain in specimens with and without helium is plotted as a function of irradiation and test temperature for tritium–trick and dynamic helium charging experiments.

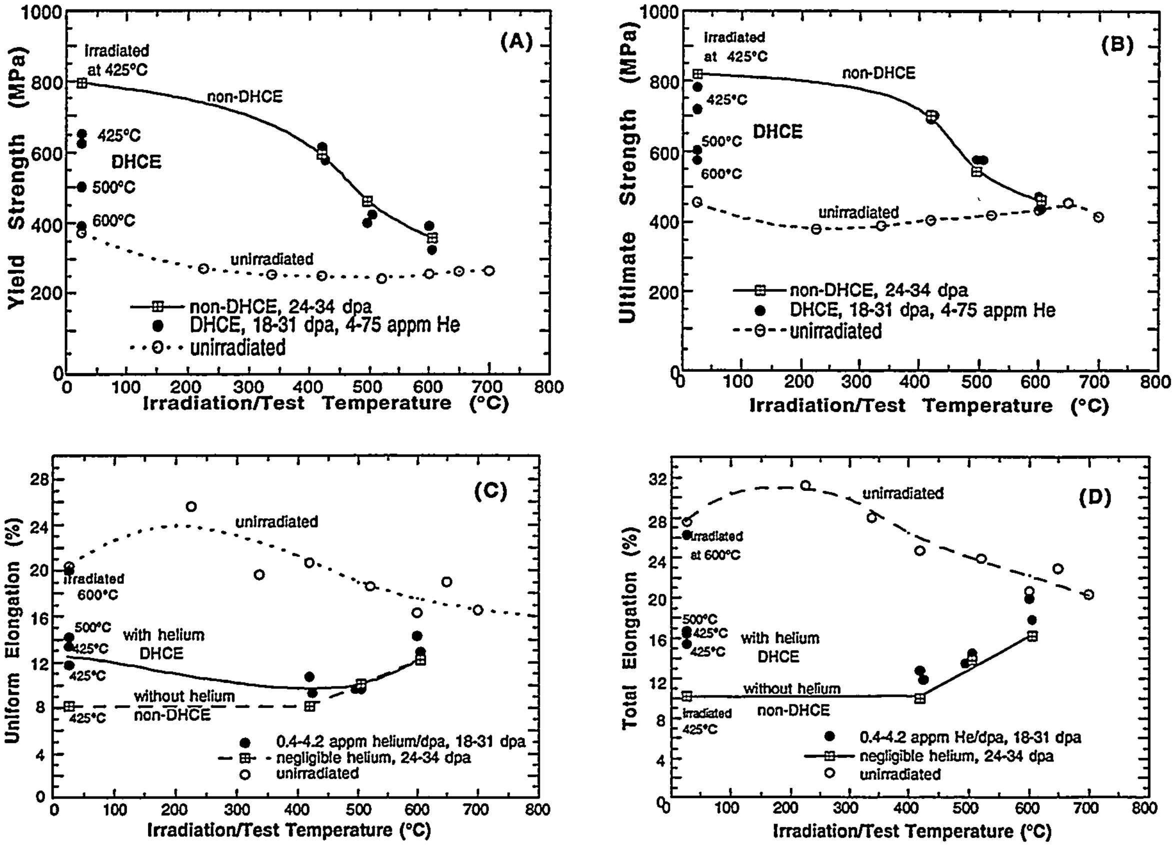

Figure 1. Yield strength (A), ultimate tensile strength (B), uniform elongation (C), and total elongation (D) of V–4Cr–4Ti after irradiation at 420–600°C to 18–34 dpa in DHCE and non–DHCE conventional irradiation (negligible helium generation).

DISCUSSION

An important finding from the DHCE was that the actual (measured) contents of helium and tritium in the V–4Cr–4Ti specimens were significantly lower than those calculated previously (see Table 3) on the basis of assumed equilibrium ratio ($k_W = 0.01$) of tritium in the alloy to that in the liquid lithium (Table 2). Except for specimens iradiated in Capsule 5C1 and 5C2 at 600°C, actual helium/dpa ratios (i.e., 0.36–0.83) were several times lower than those calculated on the basis of an equilibrium ratio of $k_W = 0.01$ (i.e., 2.1–4.4). This indicates that the level of hydrogen and tritium in the Li–cooled V–4Cr–4Ti first wall/blanket structure, and hence the effect of hydrogen and tritium on fracture toughness, will be significantly lower than previously assumed.

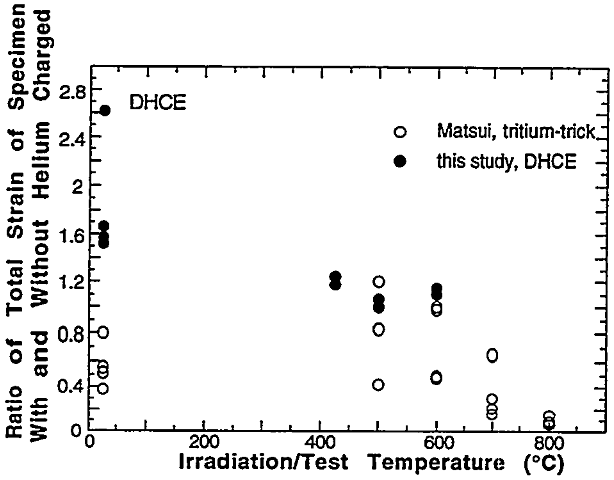

Figure 2.
Ratio of total strain in specimens with and without helium as a function of irradiation and test temperature. Results obtained from tritium-trick experiment and DHCE are shown for comparison.

As described in a separate report,[23] helium microvoids were negligible in all specimens irradiated in DHCE except for those irradiated at 425°C and retrieved from Capsule 4D1 and 4D2; only a few helium bubbles were observed at the interface between the grain matrix and some Ti(O,N,C) precipitates that are normally present in V–Ti and V–Cr–Ti alloys. Even in specimens irradiated at 600°C at the highest helium generation rate of ≈4.2 appm helium/dpa (Capsule 5C2), no microvoids could be detected in either grain matrix or grain boundaries. For specimens irradiated to 31 dpa at 425°C (retrieved from Capsules 4D1, ≈0.4 appm helium/dpa and 4D2, ≈0.73 appm helium/dpa), moderate number densities of diffuse helium bubbles were observed in localized grain matrix and near a limited fraction (≈15%) of grain boundaries.[23] The number density of helium bubbles, observed near the limited region of grain boundaries, was significantly lower than those in other alloys tested in the tritium-trick experiments, where extensive coalescence of helium bubbles occurred on all grain boundaries.[7–11] The absence of intergranular fracture morphology in any of the tensile specimens irradiated in the present DHCE seems to be consistent with the microstructural characteristics described above. However, a more comprehensive data base is needed for irradiation at <400°C to determine the effects of higher helium–dpa ratio (i.e., the fusion-relevant ratio of 4–5 appm helium/dpa) at the lower temperatures.

The uniform and total elongations determined from the room-temperature tensile tests on DHCE specimens were significantly greater than similar room-temperature elongations measured on specimens irradiated in either non-DHCE (Fig. 1) or tritium-trick experiments (Fig. 2). This is also consistent with the absence of continuous aggregation of helium bubbles on grain boundaries in the specimens irradiated in DHCE. In addition, the observation indicates that different types of hardening centers are produced in the alloy during DHCE and non-DHCE irradiation at 425–600°C.

Although the nature of the hardening centers produced during DHCE is not understood at this time, helium atoms are believed to be associated with them. In a series of studies on thermal desorption behavior of helium from unalloyed vanadium and V–5Ti irradiated with helium ions of various energy levels, van Veen et al.[24] and Buitenhuis et al.[25] concluded that helium–oxygen–vacancy and helium–nitrogen–vacancy (and probably helium–vacancy–carbon as well) complexes formed in the irradiated material. These investigators further deduced that the complexes are stable at low temperatures (<230°C) but dissociate into helium atoms and oxygen–vacancy and nitrogen–vacancy complexes at 270–310°C, leading to a prominent helium desorption peak at ≈290°C that was observed consistently in their experiments. Desorption peaks at ≈770°C and ≈1250°C, observed only after irradiation with helium ion to higher doses, were attributed to clusters of helium atoms and helium bubbles, respectively. The clusters and bubbles of helium are believed to be unstable only at the high temperatures. During the degassing treatment in the present study in which DHCE specimens were heated to 400°C at a rate of ≈0.2°C/s, desorption peaks were observed consistently at ≈290°C, although helium desorption was not positively identified by mass spectroscopy, as as done by van Veen et al. and Buitenhuis et al.

Based on these observations, it is likely that stable helium–vacancy–impurity complexes are also present in the specimens irradiated in DHCE during tensile tests at room temperature. In contrast, in specimens irradiated in non–DHCE under similar conditions, vacancies and impurities (such as oxygen, nitrogen, and carbon) are not expected to form complexes in the absence of appreciable helium atoms. Rather, the impurity atoms in solution and vacancies or vacancy clusters will be scattered more or less randomly in interstitial and vacancy sites, respectively. Dislocation motion would then be more difficult, and hence ductility would be lower in the non–DHCE than in the DHCE specimens; this is in accordance with the results shown in Fig. 1.

CONCLUSIONS

1. Tensile ductility of the V–4Cr–4Ti alloy, irradiated to 18–31 dpa at 425°C to 600°C in the Dynamic Helium Charging Experiment (DHCE) at helium generation rates of 0.4–4.2 appm helium/dpa, remained significantly high at 25–600°C, i.e., >8% uniform elongation and >10% total elongation. Tensile properties measured at >400°C were essentially the same as those measured on non–DHCE specimens (negligible helium), showing that effects of helium were insignificant. Room–temperature ductilities of the DHCE specimens (irradiated at 425, 500, and 600°C) were higher than those of the similar non–DHCE specimens, whereas strengths were lower. These observations indicate that different types of hardening centers are present at room temperature in the DHCE specimens (helium–vacancy–impurities complex, impurities being oxygen, nitrogen, and carbon) and in non–DHCE specimens (defects and defect clusters, impurities in interstitial sites).

2. The dependence of uniform and total elongation on irradiation and test temperature and fracture morphology were in sharp contrast to similar results obtained on specimens in which helium atoms were produced by the tritium–trick method. Neither partial nor predominantly intergranular fracture was observed in tensile specimens irradiated in the DHCE and tested at 23 to 600°C.

ACKNOWLEDGMENTS

Successful completion of the Dynamic Helium Charging Experiment, a complex and difficult irradiation test, was possible only through many years of effort and contributions from many investigators in the United States and Japan: F. W. Wiffen, H. Matsui, K. Abe, C. E. Johnson, R. G. Clemmer, J. P. Kopasz, L. R. Greenwood, M. L. Hamilton, K. L. Pearce, R. Ermi, A. Ermi, H.–C. Tsai, R. V. Strain, and D. Donahue. The authors are grateful in particular to L. R. Greenwood and B. M. Oliver for their calculation and measurement, respectively, of helium and tritium contents.

REFERENCES

[1] B. A. Loomis, L. Nowicki, and D. L. Smith, "Effect of Neutron Irradiation on Tensile Properties of V–Cr–Ti Alloys," in Fusion Reactor Materials, Semiannual Prog. Report, DOE/ER-0313/15, Oak Ridge National Laboratory, Oak Ridge, TN (1994), pp. 219–222.

[2] B. A. Loomis, H. M. Chung, L. Nowicki, and D. L. Smith, "Effects of Neutron Irradiation and Hydrogen on Ductile-Brittle Transition Temperatures of V–Cr–Ti Alloys," ibid., pp. 253–257.

[3] H. M. Chung, B. A. Loomis, L. Nowicki, J. Gazda, and D. L. Smith, "Irradiation-Induced Density Change and Microstructural Evolution of Vanadium-Base Alloys," ibid., pp. 223–231.

[4] H. Matsui, M. Tanno, J. Gazda, and H. M. Chung, "Microstructural Stability of V-4Cr-4Ti During Neutron Irradiation," ibid., pp. 240–246.

[5] H. M. Chung, J. Gazda, L. Nowicki, J. E. Sanecki, and D. L. Smith, "Effects of Fabrication Variables on Impact Properties and Microstructure of V–Cr–Ti Alloys," ibid., pp. 207–218.

[6] H. M. Chung, B. A. Loomis, and D. L. Smith, "Thermal Creep Behavior of V–5Cr–5Ti and V–10Cr–5Ti Alloys," in Fusion Reactor Materials, Semiannual Prog. Report, DOE/ER-0313/14, Oak Ridge National Laboratory, Oak Ridge, TN (1993), pp. 309-317.

[7] D. N. Braski, in Influence of Radiation on Material Properties, ASTM-STP 956 (1986), pp. 271-290.

[8] D. N. Braski, J. Nucl. Mater. 141-143 (1986) 1125.

[9] D. N. Braski, in Reduced Activation Materials for Fusion Reactors, ASTM-STP 1047 (1988), pp. 161-178.

[10] H. Matsui, M. Tanaka, M. Yamamoto, and M. Tada, J. Nucl. Mater. 191-194 (1992) 919.

[11] M. Satou, K. Abe, and H. Matsui, J. Nucl. Mater. 191-194 (1992) 938.

[12] W. van Witzenburg, A. Mastenbroek, and J. D. Ellen, J. Nucl. Mater. 103-104 (1981) 1187.

[13] M. P. Tanaka, E. E. Bloom, and J. A. Horak, J. Nucl. Mater. 114 (1981) 895.

[14] M. L. Grossbeck and J. A. Horak, in Influence of Radiation on Material Properties, ASTM-STP 956 (1986), p. 291.

[15] J. M. Vitek, D. N. Braski, and J. A. Horak, J. Nucl. Mater. 141-143 (1986) 982.

[16] W. van Witzenburg and E. de Vries, in Effects of Radiation on Materials, ASTM-STP 1125 (1990).

[17] L. L. Horton and K. Farrell, J. Nucl. Mater. 122-123 (1984) 687.

[18] H. Kawanishi and S. Ishino, in Reduced Activation Materials for Fusion Reactors, ASTM-STP 1047 (1988), pp. 179-189.

[19] H. Kawanishi, Y. Arai, and S. Ishino, J. Nucl. Mater. 191-194 (1992) 933.

[20] D. L. Smith, H. Matsui, L. R. Greenwood, and B. A. Loomis, J. Nucl. Mater. 155-157 (1988) 1359.

[21] D. L. Smith, B. A. Loomis, H. Matsui, M. L. Hamilton, K. L. Pearce, J. P. Kopasz, C. E. Johnson, R. G. Clemmer, and L. R. Greenwood, in Fusion Reactor Materials, Semiannual. Prog. Rep. DOE/ER-0313/10, Oak Ridge National Laboratory, Oak Ridge, TN (1991), p. 159.

[22] H. Tsai, H. M. Chung, B. A. Loomis, and D. L. Smith, "Status of Dynamic Helium Charging Experiment (DHCE)," in Fusion Reactor Materials, Semiannual Prog. Report, DOE/ER-0313/15, Oak Ridge National Laboratory, Oak Ridge, TN (1994), pp. 247–252.

[23] H. M. Chung, B. A. Loomis, L. Nowicki, J. Gazda, and D. L. Smith, "Void Structure and Density Change of Vanadium–Base Alloys Irradiated in the Dynamic Helium Charging Experiment," in this report.

[24] A. van Veen, H. Eleveld, and M. Clement, "Helium Impurity Interactions in Niobium and Vanadium," in Proc. 6th Intl. Conf. on Fusion Reactor Materials, September 27–October 1, 1993, Stresa, Italy, in press.

[25] T. Buitenhuis, A. Fedorov, and A. van Veen, "Thermal Desorption Investigation of V–5Ti Alloy," IRI–131–94–005, Delft University of Technology, The Netherlands, 1994.

DUCTILE–BRITTLE TRANSITION BEHAVIOR OF V–4Cr–4Ti IRRADIATED IN THE DYNAMIC HELIUM CHARGING EXPERIMENT*

H. M. Chung, L. J. Nowicki, D. E. Busch, and D. L. Smith (Argonne National Laboratory)

OBJECTIVE

The objective of this work is to determine the effect of simultaneous displacement damage and dynamically charged helium on the ductile–brittle transition behavior of V–4Cr–4Ti specimens irradiated to 18–31 dpa at 425–600°C in the Dynamic Helium Charging Experiment (DHCE).

SUMMARY

One property of vanadium-base alloys that is not well understood in terms of their potential use as fusion reactor structural materials is the effect of simultaneous generation of helium and neutron damage under conditions relevant to fusion reactor operation. In the present DHCE, helium was produced uniformly in the specimen at linear rates ranging from ≈0.4 to 4.2 appm helium/dpa by the decay of tritium during irradiation to 18–31 dpa at 425–600°C in Li-filled DHCE capsules in the Fast Flux Test Facility. Ductile–brittle transition behavior of V–4Cr–4Ti, recently identified as the most promising vanadium-base alloy for fusion reactor use, was determined from multiple–bending tests (at –196°C to 50°C) and quantitative SEM fractography on TEM disks (0.3–mm thick) and broken tensile specimens (1.0–mm thick). No brittle behavior was observed at temperatures >–150°C, and predominantly brittle–cleavage fracture morphologies were observed only at –196°C in some specimens irradiated to 31 dpa at 425°C during DHCE. Ductile–brittle transition temperatures (DBTTs) were –200°C to –175°C for both types of specimens. In strong contrast to tritium–trick experiments in which dense coalescence of helium bubbles is produced on grain boundaries in the absence of displacement damage, no intergranular fracture was observed in the bend–tested specimens irradiated in the DHCE.

INTRODUCTION

Vanadium-base alloys have significant advantages over other candidate alloys (such as austenitic and ferritic steels) for use as structural materials in fusion devices, e.g., the International Thermonuclear Experimental Reactor (ITER) and DEMO reactor. These advantages include intrinsically low long-term activation, low decay heat, low neutron-induced helium- and hydrogen-transmutation rates, low biological hazard, and high thermal stress factor. Recently, V-4Cr-4Ti has been identified as the most promising vanadium–base alloy for fusion reactor structural components because of its excellent combination of mechanical and physical properties before and after irradiation.[1–6] One property of the alloy that is not well understood is the effect of helium on ductile–brittle transition behavior; no data on impact properties or ductile–brittle transition behavior have been reported on effects of simultaneous generation of helium and neutron displacement damage under fusion–relevant conditions (i.e., ≈5 appm He/dpa ratio), although helium effects on other vanadium alloys have been investigated by less–than–prototypical simulation techniques such as tritium-trick,[7–11] cyclotron-injection,[12–16] and boron-doping.[16–19] In the DHCE,[20–22] the fusion–relevant helium–to–dpa damage ratio is closely simulated by utilizing slow transmutation of controlled amounts of ^{6}Li and a tritium–doped mother alloy immersed in ^{6}Li + ^{7}Li. Effects of the fusion–relevant generation of helium on tensile properties have been investigated on specimens irradiated in the DHCE to 18–31 dpa at 425°C–600°C and are reported elsewhere.[23] However, no Charpy–impact specimens were included in the DHCE capsules because of severe limitations on irradiation space. Therefore, the important information on ductile–brittle transition behavior of the alloy

---

* Work supported by the U.S. Department of Energy, Office of Fusion Energy, under Contract W-31-109-Eng-38.

could be extracted only from miniature specimens such as TEM disks and broken tensile specimens. This paper presents results of multiple-bending tests of V-4Cr-4Ti alloy and quantitative SEM fractography of the fracture surface morphologies conducted subsequently to determine ductile–brittle transition behavior.

MATERIALS AND PROCEDURES

The elemental composition of the V–4Cr–4Ti alloy, determined prior to irradiation, is given in Table 1. Information on fabrication, phase structure, grain size, and other microstructural characteristics of the alloy has been given elsewhere.[4,5,23] The tensile and TEM disk specimens were irradiated in the Fast Flux Test Facility (FFTF) at 420, 520, and 600°C to neutron fluences (E > 0.1 MeV) ranging from 3.7 x 10^{22} n/cm^2 (≈18 displacements per atom, or dpa) to 6.4 x 10^{23} n/cm^2 (≈31 dpa). Helium in the specimens was produced by utilizing transmutation of controlled amounts of ^{6}Li and predetermined amounts of tritium–doped vanadium mother alloy immersed in ^{6}Li + ^{7}Li.[20–22]

Table 1. Chemical composition of V–4Cr–4Ti (ANL ID BL–47)

ANL ID	Nominal Composition (wt.%)	Impurity Composition (wppm)							
		O	N	C	Si	S	P	Nb	Mo
BL–47	V–4.1Cr–4.3Ti	350	220	200	870	20	<40	<100	<100

Table 2 summarizes actual postirradiation parameters determined from tensile and TEM disk specimens of the V–4Cr–4Ti alloy, i.e., fast neutron fluence, dose, and helium and tritium contents measured shortly (≈20–25 days) after the post–irradiation tests. Helium and tritium contents were determined by mass spectrometry at Rockwell International Inc., Canoga Park, California. Two TEM disk or broken tensile specimens were selected from each capsule after multiple–bending (at –196°C to 50°C) or tensile tests (at room–temperature) and analyzed to determine helium and tritium contents. For each disk or broken tensile specimen, four separate analyses of ^{3}He and ^{4}He were conducted. The tritium contents were determined on the basis of analysis of ^{3}He decay measured on the same specimens ≈50 days apart.

Table 2. Summary of irradiation parameters of DHCE and helium and tritium contents measured in V–4Cr–4Ti specimens

Capsule ID No.	Irradiation Temp. (°C)	Total Damage (dpa)	Calculated Helium (appm) to dpa Ratio[a] at EOI[b] (Assumed k_a or k_w)[c] k_a=0.073 (k_w=0.01)	Measured Helium Content[d] (appm)	Actual Helium to dpa Ratio (appm/dpa)	Measured Tritium Content[e] (appm)
4D1	425	31	3.8	11.2–13.3	0.39	27
4D2	425	31	2.8	22.4–22.7	0.73	39
5E2	425	18	2.1	3.3–3.7	0.11	2
5D1	500	18	4.4	14.8–15.0	0.83	4.5
5E1	500	18	3.1	6.4–6.5	0.36	1.7
5C1	600	18	1.1	8.4–11.0	0.54	20
5C2	600	18	1.1	74.9–75.3	4.17	63

[a] L. R. Greenwood "Revised Calculations for the DHCE," April 30, 1993.

[b] Beginning of irradiation (BOI) May 27, 1991; end of irradiation (EOI) March 19, 1992; 203.3 effective full power days (EFPD), hot standby at ≈220°C until November 1992.

[c] Equilibrium ratio (k_a by atom, k_w by weight) of tritium in V alloy to that in the surrounding liquid lithium.

[d] Measured June 1994.

[e] Measured August 1994.

Fracture behavior was determined by repeatedly bending a TEM disk (thickness 0.25–0.3 mm) or a piece of the shoulder region of a fractured tensile (thickness 1.0 mm) specimen[23] in low–temperature baths of liquid nitrogen or mixtures of dry ice and acetone. Tensile specimens fractured in gauge section only at room temperature[23] were selected for this bending tests. The tensile specimens, irradiated at 425°C, 500°C, and 600°C and recovered from four capsules, were not heat treated (at 400°C for 1 h), which has been a customary procedure to expel hydrogen or tritium. Temperature of the surrounding liquid was measured with a calibrated thermocouple. Approximately one–third of each side of a bend specimen was firmly held by two grips in the test bath and the middle portion of the disk was bent repeatedly until fracture. Thus, specimen constraint was similar to that in a four–point bend test. Depending on irradiation conditions and test temperature, 3 to 62 bends were required to produce fracture in the specimens at –196 to 50°C. At a given test temperature, cold–work accumulated in the specimen as the number of bends increased, thereby hardening the material near the bend progressively. After fracture, morphology of the fracture surface was examined quantitatively by SEM. A few dozen SEM fractographs were taken at ≈300 X, and a composite of the whole fracture surface was made. Four types of fracture morphology were observed: cleavage, quasicleavage, ductile-dimple, and fibrous ductile fracture. From the fracture surface composite, the percentage of ductile-fracture morphology was measured for each specimen with a planimeter.

RESULTS AND DISCUSSION

As reported previously,[2,5] brittle fracture of V–4Cr–4Ti (ANL ID BL–47) did not occur at temperatures >–196°C in impact tests on one–third–size Charpy specimens either in the nonirradiated condition or after irradiation to 24–34 dpa at 425–600°C in non–DHCE (i.e., negligible helium/dpa ratio). Consistent with this behavior, only ductile fracture was observed from the present multiple–bend tests in a similar temperature range on disk and broken tensile specimens of the alloy either unirradiated or irradiated in non–DHCE. This is shown in Figs. 1 and 2, respectively.

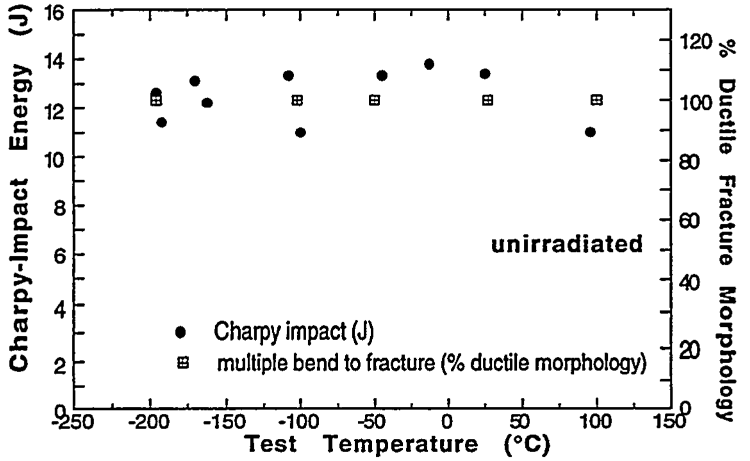

Figure 1. Comparison of Charpy–impact energy and percentage of ductile fracture surface morphology of TEM disks (determined after multiple bend until fracture) of unirradiated V–4Cr–4Ti, plotted as a function of test temperature.

The percentage of fracture surface of disk and broken tensile specimens (irradiated at 425–600°C to 18–31 dpa in the DHCE) with ductile–fracture morphology is plotted as a function of test temperature in Fig. 3. The figure shows combined effects of simultaneous displacement damage (18–31 dpa, Table 2), helium generation (at rates of 0.4–4.2 appm helium/dpa), and tritium (2–63 appm, Table 2) uptake on ductile–brittle transition behavior. For comparison, similar results obtained for nonirradiated and irradiated non–DHCE specimens (containing negligible amounts of helium, tritium, and hydrogen) are also shown in Fig. 3. Despite the thickness difference, ductile–brittle transition behaviors of the disk and broken tensile specimens were similar.

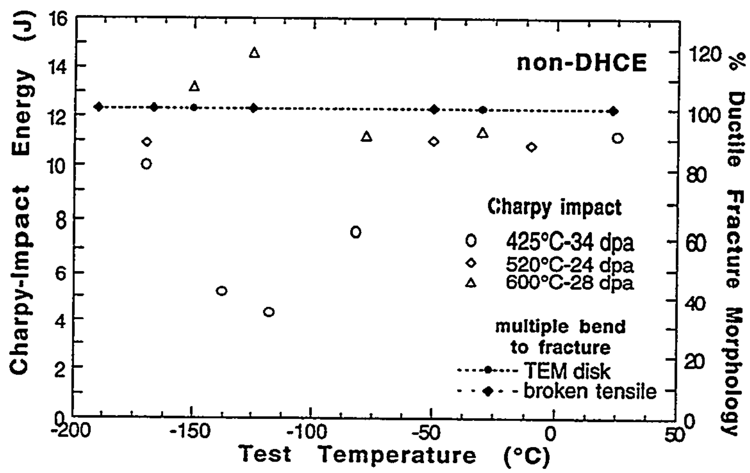

Figure 2. Comparison of Charpy–impact energy and percentage of ductile fracture surface morphology of TEM disks and broken pieces of tensile specimens (determined after multiple bend until fracture) of V–4Cr–4Ti irradiated in non–DHCE, plotted as a function of test temperature.

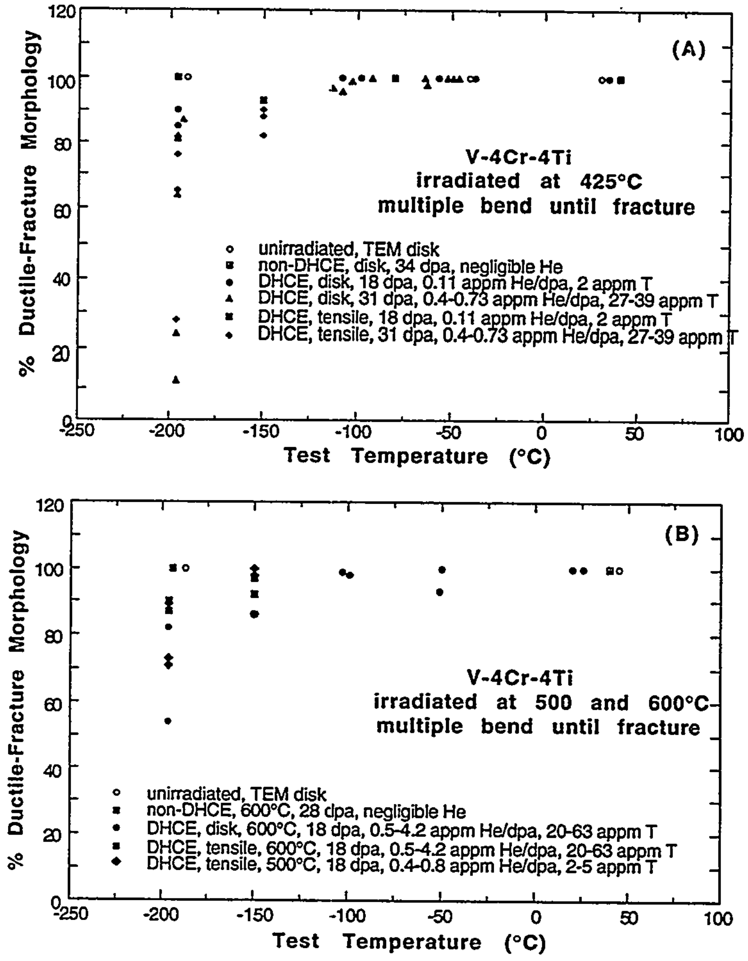

Figure 3. Percent ductile–fracture morphology vs. test temperature of V–4Cr–4Ti disks and tensile specimens irradiated at (A) 425°C and (B) 500 and 600°C and fractured by multiple bending.

The results in Fig. 3 show that the percentage of brittle cleavage measured from fracture surfaces produced near −190°C was more pronounced in specimens irradiated at 425°C and retrieved from high-tritium capsules (e.g., 4D1 and 4D2) than in specimens irradiated at 500–600°C and retrieved from low-tritium capsules (e.g., 5E1 and 5C2). As in non-DHCE irradiation, no brittle behavior was observed at temperatures >−150°C in DHCE specimens in which the helium generation rate was ≈0.4–4.2 appm helium/dpa (Table 2). Predominantly brittle–cleavage fracture morphologies were observed only at −196°C in some specimens irradiated to 31 dpa at 425°C during DHCE. Figure 3 indicates that DBTTs of specimens irradiated at 425°C and 500–600°C are −175°C and −200°C, respectively. As in the tensile tests at 25–600°C,[23] no intergranular fracture was observed in any specimens fractured at −196 to 50°C by multiple bending.

As described in a separate article,[24] helium microvoids were negligible in all specimens irradiated in DHCE except those irradiated at 425°C and retrieved from Capsules 4D1 and 4D2; only a few helium bubbles were observed at the interface between the grain matrix and some Ti(O,N,C) precipitates that are normally present in V–Ti and V–Cr–Ti alloys. Even in specimens irradiated at 600°C at the highest helium generation rate of ≈4.2 appm helium/dpa (Capsule 5C2), no microvoids could be detected in either grain matrix or grain boundaries. In specimens irradiated to 31 dpa at 425°C (retrieved from Capsules 4D1, ≈0.4 appm helium/dpa and 4D2, ≈0.73 appm helium/dpa), moderate number densities of diffuse helium bubbles were observed in localized grain matrix and near a limited fraction (≈15%) of grain boundaries.[24] The number density of helium bubbles, observed near the limited region of grain boundaries, was significantly lower than those in other alloys tested in the tritium–trick experiments, where extensive coalescence of helium bubbles occurred on all grain boundaries.[7–11] The absence of intergranular fracture morphology in any of the present specimens seems consistent with the negligible or insignificant coalescence of helium bubbles on grain boundaries.

CONCLUSIONS

1. Effects of dynamically charged helium, neutron damage, and retained tritium on DBTT of V–4Cr–4Ti alloy were determined after irradiation in the Dynamic Helium Charging Experiment (DHCE). TEM disks and broken pieces of tensile specimens, irradiated at 425–600°C to 18–31 dpa and at helium generation rates of 0.4–4.2 appm helium/dpa, were fractured by repeated bending while submerged in low–temperature baths. Ductile–brittle transition behaviors of both types of specimens were similar. Ductile–brittle transition temperatures, based on quantitative SEM fractography of ductile and brittle fracture surface morphologies, were −175°C and −200°C, respectively, in specimens irradiated at 425°C and 500°C–600°C.

2. Neither partial nor predominantly intergranular fracture was observed in multiple–bending tests at −196 to 50°C. Predominantly brittle–cleavage fracture morphologies were observed only at −196°C in some specimens irradiated to 31 dpa at 425°C in the DHCE. Cleavage fracture was negligible during tests at >−150°C regardless of irradiation temperature, dose, and helium generation rate.

ACKNOWLEDGMENTS

Many investigators in the United States and Japan have contributed over a period of several years to the successful completion of the Dynamic Helium Charging Experiment: F. W. Wiffen, H. Matsui, K. Abe, C. E. Johnson, R. G. Clemmer, J. P. Kopasz, L. R. Greenwood, M. L. Hamilton, K. L. Pearce, R. Ermi, A. Ermi, H.–C. Tsai, R. V. Strain, and D. Donahue. The authors are grateful in particular to L. R. Greenwood and B. M. Oliver for their calculation and measurement, respectively, of helium and tritium contents.

REFERENCES

[1] B. A. Loomis, L. Nowicki, and D. L. Smith, "Effect of Neutron Irradiation on Tensile Properties of V–Cr–Ti Alloys," in Fusion Reactor Materials, Semiannual. Prog. Report, DOE/ER-0313/15, Oak Ridge National Laboratory, Oak Ridge, TN (1994), pp. 219–222.

[2] B. A. Loomis, H. M. Chung, L. Nowicki, and D. L. Smith, "Effects of Neutron Irradiation and Hydrogen on Ductile-Brittle Transition Temperatures of V–Cr–Ti Alloys," ibid., pp. 253–257.

[3] H. M. Chung, B. A. Loomis, L. Nowicki, J. Gazda, and D. L. Smith, "Irradiation-Induced Density Change and Microstructural Evolution of Vanadium-Base Alloys," ibid., pp. 223–231.

[4] H. Matsui, M. Tanno, J. Gazda, and H. M. Chung, "Microstructural Stability of V-4Cr-4Ti During Neutron Irradiation," ibid., pp. 240–246.

[5] H. M. Chung, J. Gazda, L. Nowicki, J. E. Sanecki, and D. L. Smith, "Effects of Fabrication Variables on Impact Properties and Microstructure of V–Cr–Ti Alloys," ibid., pp. 207–218.

[6] H. M. Chung, B. A. Loomis, and D. L. Smith, "Thermal Creep Behavior of V–5Cr–5Ti and V–10Cr–5Ti Alloys," in Fusion Reactor Materials, Semiannual Prog. Report, DOE/ER-0313/14, Oak Ridge National Laboratory, Oak Ridge, TN (1993), pp. 309-317.

[7] D. N. Braski, in Influence of Radiation on Material Properties, ASTM-STP 956 (1986), pp. 271-290.

[8] D. N. Braski, J. Nucl. Mater. 141-143 (1986) 1125.

[9] D. N. Braski, in Reduced Activation Materials for Fusion Reactors, ASTM-STP 1047 (1988), pp. 161-178.

[10] H. Matsui, M. Tanaka, M. Yamamoto, and M. Tada, J. Nucl. Mater. 191-194 (1992) 919.

[11] M. Satou, K. Abe, and H. Matsui, J. Nucl. Mater. 191-194 (1992) 938.

[12] W. van Witzenburg, A. Mastenbroek, and J. D. Ellen, J. Nucl. Mater. 103-104 (1981) 1187.

[13] M. P. Tanaka, E. E. Bloom, and J. A. Horak, J. Nucl. Mater. 114 (1981) 895.

[14] M. L. Grossbeck and J. A. Horak, in Influence of Radiation on Material Properties, ASTM-STP 956 (1986), p. 291.

[15] J. M. Vitek, D. N. Braski, and J. A. Horak, J. Nucl. Mater. 141-143 (1986) 982.

[16] W. van Witzenburg and E. de Vries, in Effects of Radiation on Materials, ASTM-STP 1125 (1990).

[17] L. L. Horton and K. Farrell, J. Nucl. Mater. 122-123 (1984) 687.

[18] H. Kawanishi and S. Ishino, in Reduced Activation Materials for Fusion Reactors, ASTM-STP 1047 (1988), pp. 179-189.

[19] H. Kawanishi, Y. Arai, and S. Ishino, J. Nucl. Mater. 191-194 (1992) 933.

[20] D. L. Smith, H. Matsui, L. R. Greenwood, and B. A. Loomis, J. Nucl. Mater. 155-157 (1988) 1359.

[21] D. L. Smith, B. A. Loomis, H. Matsui, M. L. Hamilton, K. L. Pearce, J. P. Kopasz, C. E. Johnson, R. G. Clemmer, and L. R. Greenwood, in Fusion Reactor Materials, Semiannual Prog. Rep. DOE/ER-0313/10, Oak Ridge National Laboratory, Oak Ridge, TN (1991), p. 159.

[22] H. Tsai, H. M. Chung, B. A. Loomis, and D. L. Smith, "Status of Dynamic Helium Charging Experiment (DHCE)," in Fusion Reactor Materials, Semiannual. Prog. Report, DOE/ER-0313/15, Oak Ridge National Laboratory, Oak Ridge, TN (1994), pp. 247–252.

[23] H. M. Chung, B. A. Loomis, L. J. Nowicki, and D. L. Smith, "Effect of Dynamically Charged Helium on Tensile Properties of V–4Cr–4Ti," in this report.

[24] H. M. Chung, L. J. Nowicki, J. Gazda, and D. L. Smith, "Void Structure and Density Change of Vanadium–Base Alloys Irradiated in the Dynamic Helium Charging Experiment," in this report.

VOID STRUCTURE AND DENSITY CHANGE OF VANADIUM-BASE ALLOYS IRRADIATED IN THE DYNAMIC HELIUM CHARGING EXPERIMENT*

H. M. Chung, L. Nowicki, J. Gazda, and D. L. Smith (Argonne National Laboratory)

OBJECTIVE

The objective of this work is to determine void structure, distribution, and density changes of several promising vanadium–base alloys irradiated in the Dynamic Helium Charging Experiment (DHCE).

SUMMARY

Combined effects of dynamically charged helium and neutron damage on density change, void distribution, and microstructural evolution of V–4Cr–4Ti alloy have been determined after irradiation to 18–31 dpa at 425–600°C in the DHCE, and the results compared with those from a non–DHCE in which helium generation was negligible. For specimens irradiated to ≈18–31 dpa at 500–600°C with a helium generation rate of 0.4–4.2 appm He/dpa, only a few helium bubbles were observed at the interface of grain matrices and some of the Ti(O,N,C) precipitates, and no microvoids or helium bubbles were observed either in grain matrices or near grain boundaries. Under these conditions, dynamically produced helium atoms seem to be trapped in the grain matrix without significant bubble nucleation or growth, and in accordance with this, density changes from DHCE and non–DHCE (negligible helium generation) were similar for comparable fluence and irradiation temperature. Only for specimens irradiated to ≈31 dpa at 425°C, when helium was generated at a rate of 0.4–0.8 appm helium/dpa, were diffuse helium bubbles observed in limited regions of grain matrices and near ≈15% of the grain boundaries in densities significantly lower than those in the extensive coalescences of helium bubbles typical of other alloys irradiated in tritium–trick experiments. Density changes of specimens irradiated at 425°C in the DHCE were somewhat higher than those from non–DHCE irradiation. Microstructural evolution in V–4Cr–4Ti was similar for DHCE and non–DHCE except for helium bubble number density and distribution. As in non–DHCE, the irradiation–induced precipitation of ultrafine Ti_5Si_3 was observed for DHCE at >500°C but not at 425°C.

INTRODUCTION

Recent attention in the development of vanadium–base alloys for application in fusion reactor first wall and blanket structure has focused on V-4Cr-4Ti, an alloy reported to exhibit an excellent combination of mechanical and physical properties before and after irradiation.[1–6] One unresolved issue in the performance of the alloy, however, has been the effect of fusion–relevant simultaneous generation of helium and neutron damage (at a ratio of 4–5 appm helium/displacement per atom [dpa]) on density change and void swelling. Helium effects determined for other vanadium–base alloys by means of less fusion–relevant simulation approaches such as tritium-trick,[7–13] cyclotron-injection,[14–18] and boron-doping[18–21] techniques have been inconsistent with regard to concentration of helium bubbles on grain boundaries and the concomitant propensity for intergranular fracture. In the unique DHCE, the fusion–relevant helium–to–dpa ratio is simulated realistically by utilizing transmutation of controlled amounts of ^{6}Li and a predetermined amount of tritium–doped mother alloy immersed in ^{6}Li + ^{7}Li.[22–24] This report describes results of microstructural characterization and density measurement, primarily of V–4Cr–4Ti alloy specimens irradiated to 18–31 dpa at 425–600°C in the DHCE.

MATERIALS AND PROCEDURES

The elemental composition of the V–4Cr–4Ti alloy (ANL Identification BL–47), determined prior to irradiation, is given in Table 1. Postirradiation examination of other alloys listed in Table 1 (i.e., V–5Ti, V–3Ti–1Si, and V–8Cr–6Ti) was limited; unless pointed out specifically, all results reported in this study refer to V–4Cr–4Ti. Fabrication procedures of the alloy ingots and annealed plates and sheets have been reported

---

* Work supported by the U.S. Department of Energy, Office of Fusion Energy, under Contract W-31-109-Eng-38.

elsewhere.[25] TEM disks, punched from 0.3–mm–thick cold–worked sheets for use in investigating density change, void swelling behavior, and microstructural characteristics, were annealed at 1050°C in an ion–pumped high–vacuum system. The annealed material was ≈95% recrystallized and exhibited an average grain size of ≈14 μm. Phase structures of the alloy, characterized before and after irradiation in a non–DHCE (negligible helium generation), have been described in detail elsewhere.[4] The only secondary phase present in the as–annealed specimens was Ti(O,N,C), which is normally observed in titanium–containing vanadium alloys with O+N+C > 400 wppm.[26]

Table 1. Chemical composition of vanadium–base alloys

ANL ID	Nominal Composition (wt.%)	Impurity Composition (wppm)							
		O	N	C	Si	S	P	Nb	Mo
BL-47	V–4.1Cr–4.3Ti	350	220	200	870	20	<40	<100	<100
BL-46	V–4.6Ti	305	53	85	160	10	<100	<100	–
BL-45	V–2.5Ti–1.0Si	345	125	90	9900	30	–	200	140
BL-49	V–7.9Cr–5.7Ti	400	150	127	360	20	–	<100	170

The alloy specimens were irradiated in the Fast Flux Test Facility (FFTF), at 420, 520, and 600°C to neutron fluences (E > 0.1 MeV) ranging from 3.7 x 10^{22} n/cm^2 (≈18 displacements per atom, or dpa) to 6.4 x 10^{23} n/cm^2 (≈31 dpa). Helium in the alloy specimens was produced by utilizing transmutation of controlled amounts of ^{6}Li and a predetermined amount of tritium–doped vanadium mother alloy immersed in ^{6}Li + ^{7}Li.[22–24] Table 2 summarizes the actual postirradiation parameters determined from tensile and disk specimens of the V–4Cr–4Ti alloy, i.e., dose and helium and tritium content measured shortly after the postirradiation tests. Helium and tritium were determined by mass spectrometry at Rockwell International Inc., Canoga Park, California.

Table 2. Summary of irradiation parameters of dynamic helium charging experiment, and helium and tritium content of V–4Cr–4Ti specimens

Capsule ID No.	Irradiation Temp. (°C)	Total Damage (dpa)	Calculated Helium (appm) to dpa Ratio[a] at EOI[b] (Assumed k_a or k_w)[c] k_a=0.073 (k_w=0.01)	Measured Helium Content[d] (appm)	Actual Helium–to–dpa Ratio (appm/dpa)	Measured Tritium Content[e] (appm)
4D1	425	31	3.8	11.2–13.3	0.39	27
4D2	425	31	2.8	22.4–22.7	0.73	39
5E2	425	18	2.1	3.3–3.7	0.11	2
5D1	500	18	4.4	14.8–15.0	0.83	4.5
5E1	500	18	3.1	6.4–6.5	0.36	1.7
5C1	600	18	1.1	8.4–11.0	0.54	20
5C2	600	18	1.1	74.9–75.3	4.17	63

[a] L. R. Greenwood "Revised Calculations for the DHCE," April 30, 1993.

[b] Beginning of irradiation (BOI) May 27, 1991; end of irradiation (EOI) March 19, 1992; 203.3 effective full power days (EFPD), hot standby at ≈220°C until November 1992.

[c] Equilibrium ratio (k_a by atom, k_w by weight) of tritium in V alloy to that in the surrounding liquid lithium.

[d] Measured June 1994.

[e] Measured August 1994.

The retrieved TEM specimens, which contained helium, tritium, and neutron displacement damage, were cleaned ultrasonically in alcohol prior to density measurement and microstructural analysis. Most of the examined TEM disks were not degassed at 400°C for 1 h, a customary procedure to expel tritium and hydrogen from Charpy–impact and tensile specimens. Several TEM disks were examined after degassing, but none indicated an appreciable difference in void or helium bubble distribution and microstructure from undegassed specimens that should contain tritium and hydrogen in addition to helium. The irradiated specimens were jet-thinned for TEM in a solution of 15% sulfuric acid-72% methanol-13% butyl cellosolve maintained at -5°C. TEM was conducted with a JEOL 100CX-II scanning transmission electron microscope operating at 100 keV, or with a Philips CM-30 analytical electron microscope operating at 200 keV. Density change was determined from specimen weights measured in air and in research-grade CCl_4.

VOID STRUCTURE AND DISTRIBUTION

A summary of microstructural characterization of voids in the DHCE specimens is given in Table 3. Appreciable numbers of voids in the DHCE specimens were absent, except for specimens retrieved from Capsules 4D1 and 4D2, which were irradiated at 425°C. In specimens irradiated at 600°C and retrieved from Capsules 5C1 and 5C2, only a few helium bubbles were observed at interfaces between the grain matrix and a limited number of Ti(O,N,C) precipitates. TEM images of these microstructural characteristics were reported previously.[27]

Table 3. Summary of void distribution in V–4Cr–4Ti irradiated in the DHCE.

Capsule ID No.	Irradiation Temp (°C)	Total Damage (dpa)	Helium–to–dpa Ratio (appm/dpa)	Voids in Grain Matrix	Voids on Boundary of Grain Matrix and Ti(O,N,C)	Voids on Grain Boundaries
non–DHCE	425, 500, 600°C	24–34	–	none	none	none
4D1	425	31	0.39	some	some	some
4D2	425	31	0.73	some	some	some
5E2	425	18	0.11	none	none	none
5D1	500	18	0.83	none	some	none
5E1	500	18	0.36	none	some	none
5C1	600	18	0.54	none	some	none
5C2	600	18	4.17	none	some	none

Specimens irradiated to 18–31 dpa at 425°C–600°C in the other three capsules (Capsule 5E2, helium generation rate of 0.11 appm He/dpa; 5D1, 0.83 appm He/dpa; and 5E1, 0.36 appm He/dpa) exhibited microstructural characteristics essentially similar to those of specimens from Capsule 5C1 and 5C2, i.e., no helium bubbles either in the grain matrix or on grain boundaries, a few helium bubbles on the interface between the grain matrix and a limited number of Ti(O,N,C) precipitates, and ultrafine Ti_5Si_3 precipitates in high density (only in specimens irradiated at 500°C–600°C). In these specimens, virtually all of the dynamically produced helium atoms seem to have been trapped in the grain matrix without significant bubble nucleation or growth.

For DHCE specimens irradiated to 31 dpa at 425°C in high–tritium capsules 4D1 (helium generation rate ≈0.4 He/dpa) and 4D2 (helium generation rate of ≈0.73 He/dpa), helium bubbles (≈5 nm in diameter) were observed in the grain matrix and on ≈15% of the grain boundaries. Helium bubbles observed near grain boundaries in these specimens were characterized by (a) diffuse bubbles in a number density significantly lower than that of the compact coalescences of helium bubbles observed in other alloys irradiated in tritium–trick experiments;[7–12] (b) discontinuous (≈15% of grain boundaries), in contrast to continuous (≈100% of grain boundaries) coalescence observed in tritium–trick experiments;[7–12] and (c) more or less similar bubble distribution in the grain matrix and near grain boundaries, in contrast to virtual concentration of all helium bubbles on grain boundaries in tritium–trick experiments. These observations seem to indicate that most of the helium atoms produced dynamically at 425°C were trapped in the grain matrix, preventing extensive formation of a continuous coalescence of helium bubbles on grain boundaries. Figure 1 shows typical microstructures of the diffuse helium bubbles in the grain matrix and near grain boundaries and helium shells surrounding Ti(O,N,C) precipiates in specimens irradiated at 425°C (helium generation rates 0.4–0.8 appm He/dpa).

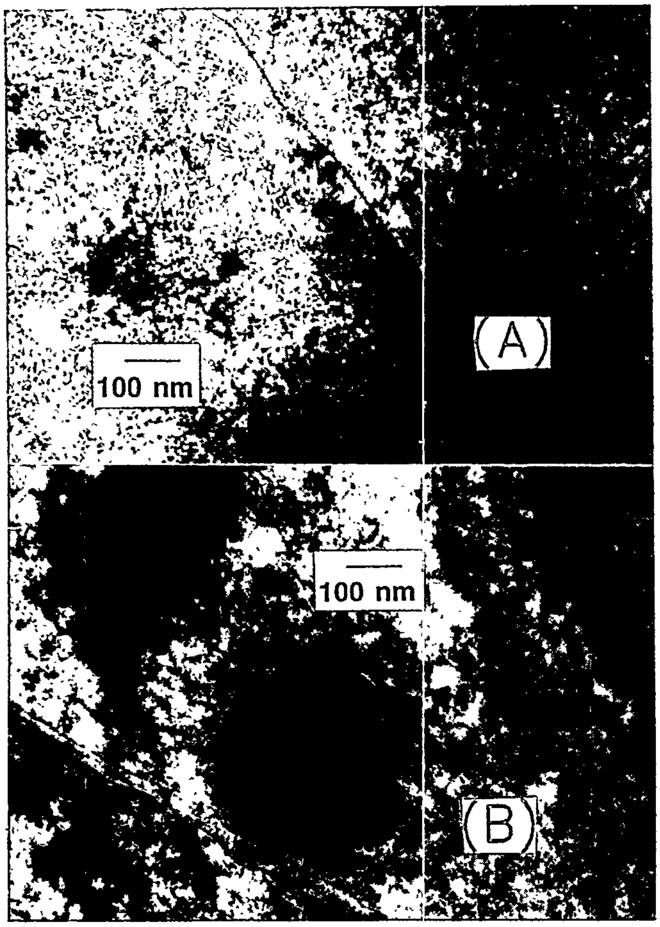

Figure 1.
Void microstructure of V-4Cr-4Ti irradiated at 425°C to ≈31 dpa in DHCE (Capsules 4D2 and 4D1): (A) similar distribution of diffuse voids in grain matrices and near grain boundary; and (B) limited number of voids near grain boundary and void shells surrounding Ti(O, N, C).

As in non–DHCEs,[4] Ti_5Si_3 did not precipitate during irradiation at 425°C in the DHCEs. If Ti_5Si_3 precipitation was indeed significant for 425°C irradiation, void swelling at that temperature would have been suppressed significantly, as in other alloys irradiated at 420°C in non–DHCEs.[28]

DENSITY CHANGE

Results of density measurements for specimens irradiated at 600 (18 dpa in Capsule 5C1) and 425°C (18 dpa in Capsule 5E2, 31 dpa in Capsules 4D1 and 4D2) are given in Figs. 2A and 2B, respectively. The helium generation rates in the DHCE specimens are also given in the figure (see Table 2). For comparison, density changes determined for similar irradiation conditions in non–DHCEs[3] are also shown in the figures.

Density changes in the non–DHCE and DHCE specimens irradiated at 500°C and 600°C were low (<0.6 %). The small density change seems to be consistent with the negligible number density of voids or helium bubbles (Table 3).[27] However, density changes in the DHCE specimens irradiated at 425°C (Capsules 4D1, helium generation rate ≈0.4 He/dpa and 4D2, helium generation rate ≈0.73 He/dpa) were somewhat higher than those of the non–DHCE specimens. The relatively large density changes measured for these specimens seem also to be consistent with the relatively higher number density of helium bubbles (Fig. 1).

Density changes measured in disk specimens of V–5Ti, V–3Ti–1Si, and V–8Cr–6Ti, irradiated to ≈18 dpa at 425°C in a DHCE in Capsule 5E2, are shown in Fig. 3. In the figure, density changes in the DHCE are compared with those obtained on similar specimens irradiated to ≈34 dpa in a non–DHCE. Although the helium content of these alloy specimens was not measured, the actual helium generation rate was expected to be low and similar to that of V–4Cr–4Ti (i.e., 0.11 appm He/dpa). Effects of helium on density changes in these alloy specimens were insignificant.

DISCUSSION

Microvoids or helium bubbles were absent from all of the specimens of V–4Cr–4Ti irradiated in the DHCE at 500–600°C, except for a few helium bubbles at interfaces between the grain matrix and some Ti(O,N,C) precipitates that are normally present in V–Ti and V–Cr–Ti alloys. Preferential formation of voids near blocky precipitates [presumably Ti(O,N,C) precipitates] was also reported by Braski in V–3Ti–1Si specimens that were preimplanted with 82 appm helium by the tritium–trick technique and then irradiated to 40 dpa at 600°C.[8]

Buitenhuis et al. proposed that interfaces between the grain matrix and Ti(O,N,C) precipitates act as preferential sinks for helium.[29] From a series of thermal desorption analyses by mass spectroscopy, these authors have identified a helium desorption peak at the surprisingly low temperature of ≈280°C in V–5Ti specimens that were irradiated and implanted with helium ions. Some of the desorption peaks were sharp and narrow and some were weak and broad below and above ≈280°C. Furthermore, Buitenhuis et al. attributed the former and the latter types of peaks to helium–vacancy–impurity (O, N, and C) complexes that are produced in the grain matrix and near the interfaces between the grain matrix and Ti(O,N,C) precipitates, respectively, and are subsequently dissociated into helium and vacancy–impurity complexes upon heating to ≈280°C or higher. During our degassing treatment in which DHCE specimens were heated to ≈405°C at a linear rate of 0.2°C/s in high vacuum in the present study, desorption peaks were observed consistently at ≈280°C. However, a positive identification of helium desorption was not made from a mass spectroscopic analysis.

One of the important findings from the DHCE was that the actual (measured) helium and tritium content of V–4Cr–4Ti specimens was significantly lower than that calculated on the basis of the assumed equilibrium ratio ($k_w = 0.01$) of tritium in the alloy to that in the liquid lithium (Table 2). This could be interpreted to indicate that k_w is significantly lower than previously thought, in particular for irradiations at 425 and 500°C.

Microvoids or helium bubbles were absent in the grain matrix and on grain boundaries in all of the specimens irradiated at 500–600°C, in which ultrafine Ti_5Si_3 precipitated in high density. Even in specimens irradiated at 600°C at the highest helium generation rate of ≈4.2 appm helium/dpa (Capsule 5C2), no microvoids could be detected either in the grain matrix or on grain boundaries. This correlation between the high–density precipitation of ultrafine Ti_5Si_3 and negligible void swelling seems to be consistent with similar observations reported previously for non–DHCE conditions.[28] Conversely, the relatively higher void swelling and larger density change observed in specimens irradiated at 425°C (in Capsule 4D1 and 4D2) seems to be associated with an absence of precipitation of ultrafine Ti_5Si_3 at the low irradiation temperature.

As pointed out above, the characteristics of grain–boundary helium bubbles observed in the specimens irradiated to 31 dpa at 425°C were in distinct contrast to those observed in specimens from tritium–trick experiments, i.e., diffuse bubbles in significantly lower number density than those of the compact coalescences of helium bubbles in tritium–trick experiments; discontinous (on ≈15% of grain boundaries), in contrast to continuous (≈100% of grain boundaries) coalescences in tritium–trick experiments; and similar bubble distribution in the grain matrix and near grain boundaries, in contrast to virtual concentration of all helium bubbles on grain boundaries in tritium–trick experiments. These characteristics seem to indicate that most of the helium atoms produced at 425°C in DHCEs were trapped by vacancies or vacancy–impurity complexes.

Intergranular fracture morphology was not observed in any of the specimens irradiated in the DHCE and subsequently tested by uniaxial tensile tests at 23 to 600°C and multiple bending tests at –196 to 50°C. Even in specimens irradiated at 425°C and fractured in brittle manner during multiple bending tests at –196°, only cleavage and ductile tearing were observed, i.e., intergranular fracture morphology was absent. These observations, consistent with the characteristics of helium bubble distribution described above, are in distinct contrast to the propensity to intergranular fracture that is commonly observed in tritium–trick experiments.

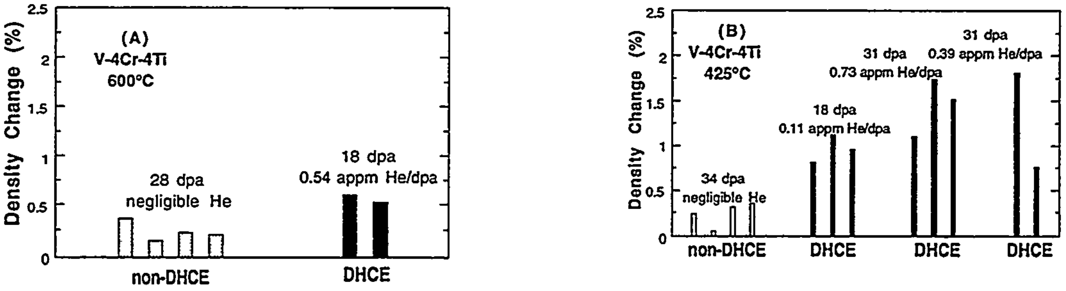

Figure 2. Comparison of density changes of V–4Cr–4Ti from DHCE and non–DHCE experiments: (A) 600°C and (B) 425°C.

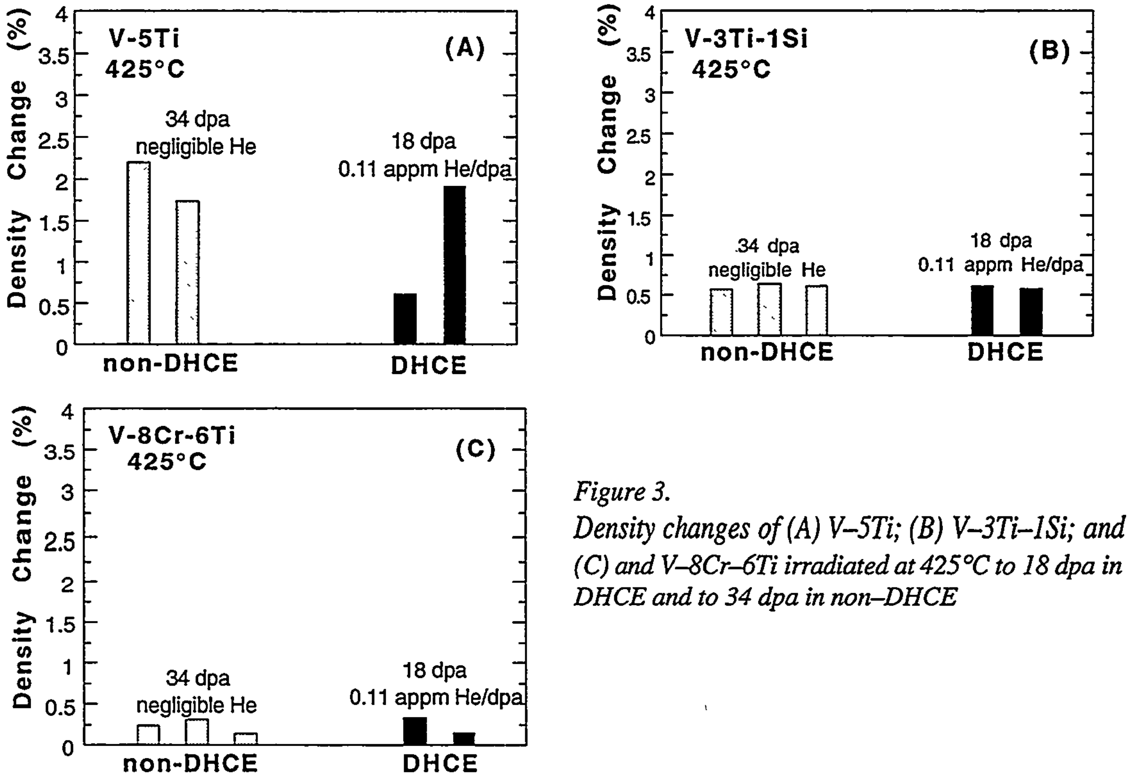

Figure 3.

Density changes of (A) V–5Ti; (B) V–3Ti–1Si; and (C) and V–8Cr–6Ti irradiated at 425°C to 18 dpa in DHCE and to 34 dpa in non–DHCE

CONCLUSIONS

(1) For specimens irradiated to ≈18 dpa at 500–600°C in the Dynamic Helium Charging Experiment (DHCE) with helium generation rates of ≈0.4–4.2 appm He/dpa, void swelling was negligible, and density changes from the DHCE and non–DHCE (negligible helium generation) were similar (<0.6%).

Only limited number of voids or helium bubbles were observed at the interface of the grain matrix and some of the Ti(O,N,C) precipitates. Neither helium bubbles nor voids were observed either in the grain matrix or near grain boundaries. Under irradiation at these temperatures, ultrafine Ti_5Si_3 precipitated in high density and most of the dynamically produced helium atoms seem to be trapped in the grain matrix and at the interface between the matrix and Ti_5Si_3 precipitates, without a significant chance for bubble nucleation or growth.

(2) For DHCE specimens irradiated to 31 dpa at 425°C at helium generation rates of ≈0.4–0.73 appm He/dpa, helium bubbles ≈5 nm in diameter were observed in localized regions of the grain matrix as well as on limited portions (≈15%) of grain boundaries. Grain-boundary helium bubbles in these specimens were diffuse, in contrast to the compact coalescences of helium bubbles observed from tritium–trick experiments; discontinous (near ≈15% of grain boundaries), in contrast to continuous (on ≈100% grain boundaries) coalescence observed in tritium–trick experiments; and more or less evenly distributed in the grain matrix and near grain boundaries, in contrast to virtual concentration of all helium bubbles on grain boundaries in tritium–trick experiments. These observations indicate that most of the helium atoms that were produced dynamically at 425°C were trapped in the grain matrix, preventing formation of continuous coalescence of compact bubbles on grain boundaries. As in non–DHCE, the irradiation-induced precipitation of ultrafine Ti_5Si_3 was not observed after irradiation at 425°C.

(3) Intergranular fracture morphology was not observed in any of the specimens irradiated in DHCEs and subsequently fractured during uniaxial tensile tests at 23 to 600°C and multiple bending tests at −196 to 50°C. This observation, consistent with the characteristic helium bubble distribution, is in distinct contrast to the propensity to intergranular fracture commonly observed in tritium–trick experiments.

(4) The actual measured helium and tritium content of V–4Cr–4Ti was significantly lower than that calculated with an assumed equilibrium ratio (≈0.01 by weight) of tritium in the alloy to that in the liquid lithium. This indicates that the tritium equilibrium ratio is significantly lower than previously assumed, in particular, for irradiations at <500°C. It also indicates that the tritium level in lithium-cooled V–4Cr–4Ti first wall/blanket structures, and hence the effect of tritium on the fracture toughness, will be significantly lower than previously thought.

ACKNOWLEDGMENTS

The successful completion of the complex and difficult Dynamic Helium Charging Experiment was possible through many years of contributions from F. W. Wiffen, H. Matsui, K. Abe, C. E. Johnson, R. G. Clemmer, J. P. Kopasz, L. R. Greenwood, M. L. Hamilton, K. L. Pearce, R. Ermi, A. Ermi, H.–C. Tsai, and R. V. Strain. The authors are grateful to L. R. Greenwood and B. M. Oliver for calculation and measurement, respectively, of helium and tritium contents.

REFERENCES

[1] B. A. Loomis, L. Nowicki, and D. L. Smith, "Effect of Neutron Irradiation on Tensile Properties of V–Cr–Ti Alloys," in Fusion Reactor Materials, Semiannual. Prog. Report, DOE/ER-0313/15, Oak Ridge National Laboratory, Oak Ridge, TN (1994), pp. 219–222.

[2] B. A. Loomis, H. M. Chung, L. Nowicki, and D. L. Smith, "Effects of Neutron Irradiation and Hydrogen on Ductile-Brittle Transition Temperatures of V–Cr–Ti Alloys," ibid., pp. 253–257.

[3] H. M. Chung, B. A. Loomis, L. Nowicki, J. Gazda, and D. L. Smith, "Irradiation-Induced Density Change and Microstructural Evolution of Vanadium-Base Alloys," ibid., pp. 223–231.

[4] H. Matsui, M. Tanno, J. Gazda, and H. M. Chung, "Microstructural Stability of V-4Cr-4Ti During Neutron Irradiation," ibid., pp. 240–246.

[5] H. M. Chung, J. Gazda, L. Nowicki, J. E. Sanecki, and D. L. Smith, "Effects of Fabrication Variables on Impact Properties and Microstructure of V–Cr–Ti Alloys," ibid., pp. 207–218.

[6] H. M. Chung, B. A. Loomis, and D. L. Smith, "Thermal Creep Behavior of V–5Cr–5Ti and V–10Cr–5Ti Alloys," in Fusion Reactor Materials, Semiannual. Prog. Report, DOE/ER-0313/14, Oak Ridge National Laboratory, Oak Ridge, TN (1993), pp. 309-317.

[7] D. N. Braski and D. W. Ramey, in Effects of Radiation on Material Properties, ASTM-STP 870, F. A. Garner and J. S. Perrin, eds., American Society for Testing and Materials, Philadelphia, 1985, pp. 1211–1224.

[8] D. N. Braski, in Influence of Radiation on Material Properties, ASTM-STP 956, F. A. Garner, C. H. Henager, and N. Igata, Eds., American Society for Testing and Materials, Philadelphia, 1987, pp. 271-290.

[9] D. N. Braski, J. Nucl. Mater. 141-143 (1986) 1125.

[10] D. N. Braski, in Reduced Activation Materials for Fusion Reactors, ASTM-STP 1047, Philadelphia (1988), pp. 161-178.

[11] H. Matsui, M. Tanaka, M. Yamamoto, and M. Tada, J. Nucl. Mater. 191-194 (1992) 919.

[12] M. Satou, K. Abe, and H. Matsui, J. Nucl. Mater. 191-194 (1992) 938.

[13] M. Tanaka and H. Matsui, Mater. Trans., JIM, 34 (1993) 1083.

[14] W. van Witzenburg, A. Mastenbroek, and J. D. Ellen, J. Nucl. Mater. 103-104 (1981) 1187.

[15] M. P. Tanaka, E. E. Bloom, and J. A. Horak, J. Nucl. Mater. 114 (1981) 895.

[16] M. L. Grossbeck and J. A. Horak, in Influence of Radiation on Material Properties, ASTM-STP 956, Philadelphia (1986) 291.

[17] J. M. Vitek, D. N. Braski, and J. A. Horak, J. Nucl. Mater. 141-143 (1986) 982.

[18] W. van Witzenburg and E. de Vries, in Effects of Radiation on Materials, ASTM-STP 1125, Philadelphia (1990).

[19] L. L. Horton and K. Farrell, J. Nucl. Mater. 122-123 (1984) 687.

[20] H. Kawanishi and S. Ishino, in Reduced Activation Materials for Fusion Reactors, ASTM-STP 1047, Philadelphia (1988), pp. 179-189.

[21] H. Kawanishi, Y. Arai, and S. Ishino, J. Nucl. Mater. 191-194 (1992) 933.

[22] D. L. Smith, H. Matsui, L. R. Greenwood, and B. A. Loomis, J. Nucl. Mater. 155-157 (1988) 1359.

[23] D. L. Smith, B. A. Loomis, H. Matsui, M. L. Hamilton, K. L. Pearce, J. P. Kopasz, C. E. Johnson, R. G. Clemmer, and L. R. Greenwood, in Fusion Reactor Materials, Semiannual. Prog. Report. DOE/ER-0313/10, Oak Ridge National Laboratory, Oak Ridge, TN (1991), p. 159.

[24] H. Tsai, H. M. Chung, B. A. Loomis, and D. L. Smith, "Status of Dynamic Helium Charging Experiment (DHCE)," in Fusion Reactor Materials, Semiannual. Prog. Report. DOE/ER-0313/15, Oak Ridge National Laboratory, Oak Ridge, TN (1994), p. 247.

[25] H. M. Chung, B. A. Loomis, L. Nowicki, and D. L. Smith, "Effect of Dynamically Charged Helium on Tensile Properties of V–4Cr–4Ti," in this report.

[26] M. Satou and H. M. Chung, in Fusion Reactor Materials, Semiannual Prog. Rep. DOE/ER-0313/13, Oak Ridge National Laboratory, Oak Ridge, TN (1993), p. 227.

[27] H. M. Chung, B. A. Loomis, H. Tsai, L. Nowicki, J. Gazda, and D. L. Smith, "Swelling and Structure of Vanadium Alloys Irradiated in the Dynamic Helium Charging Experiment," in Fusion Reactor Materials, Semiannual. Prog. Report, DOE/ER-0313/16, Oak Ridge National Laboratory, Oak Ridge, TN (1994), in press.

[28] H. M. Chung, B. A. Loomis, and D. L. Smith, in Effects of Radiation on Materials, ASTM-STP 1175, A. S. Kumar, D. S. Gelles, R. K. Nanstad, and T. A. Little, Eds., American Society for Testing and Materials, Philadelphia, 1993, pp. 1185–1200.

[29] T. Buitenhuis, A. Fedorov, and A. van Veen, "Thermal Desorption Investigation of V–5Ti Alloy," IRI–131–94–005, Delft University of Technology Report, The Netherlands, 1994.

6.4 Copper Alloys

EFFECT OF FISSION NEUTRON IRRADIATION ON THE TENSILE AND ELECTRICAL PROPERTIES OF COPPER AND COPPER ALLOYS

– S.A. Fabritsiev (D.V. Efremov Institute, St. Petersburg, Russia), A.S. Pokrovsky (SRIAR, Dimitrovgrad, Russia), S.J. Zinkle and A.F. Rowcliffe (Oak Ridge National Laboratory), B.N. Singh (Risø National Laboratory, Roskilde, Denmark), F.A. Garner and D.J. Edwards (Pacific Northwest Laboratory)

OBJECTIVE

The objective of this study is to evaluate the properties of several copper alloys following fission reactor irradiation at ITER-relevant temperatures of 80 to 200°C. This study provides some of the data needed for the ITER research and development Task T213.

SUMMARY

The tensile and electrical properties of several different copper alloys have been measured following fission neutron irradiation to ~1 and 5 dpa at temperatures between ~90 and 200°C in the SM-2 reactor. These low temperature irradiations caused significant radiation hardening and a dramatic decrease in the work hardening ability of copper and copper alloys. The uniform elongation was higher at 200°C compared to 100°C, but still remained below 1% for most of the copper alloys. As expected, specimens shielded from the thermal neutrons (which produced fusion-relevant solid transmutation rates) exhibited a lower increase in their electrical resistivity compared to unshielded specimens. A somewhat surprising observation was that the radiation hardening was significantly higher in unshielded copper specimens compared to spectrally-shielded specimens.

STATUS AND PROGRESS

1. Introduction

Copper alloys have been proposed for the first wall and divertor structure of the International Thermonuclear Experimental Reactor (ITER). Unfortunately, there is a lack of data on copper and copper alloys irradiated to damage levels greater than 1 dpa at ITER-relevant temperatures of 100 to 350°C [1]. In order to improve the existing data base on radiation effects on copper alloys at ITER-relevant conditions, planning for a collaborative irradiation experiment in the SM-2 reactor in Dimitrovgrad, Russia was initiated in 1992. Sheet tensile specimens and electron microscopy disks were prepared by US and Russian scientists from a wide range of copper and copper alloys [2], and the specimens were irradiated in several capsules between December, 1993 and June, 1994. A total of 74 copper alloys have been irradiated in the SM-2 reactor at temperatures between ~90 and 330°C in the Channel 4 and Core positions of the reactor, resulting in displacement damage levels of ~1 and 5 dpa, respectively [2]. The initial results obtained from postirradiation examination of the specimens are summarized in this report.

2. Experimental Procedure

The list of specimens and design irradiation conditions have been summarized elsewhere [2]. Specimens were irradiated in the form of transmission electron microscope (TEM) disks and sheet tensile specimens designated small tensile specimens (STS, 34 mm long and 0.25 mm thick) and large tensile specimens (LTS, 56 mm long and 1 mm thick). Electrical resistivity measurements were made at room temperature using the 4-point probe technique on the STS and LTS specimens prior to tensile testing. The irradiations were conducted in the Channel 4 and Core positions of the SM-2 reactor. Specimens were irradiated for 42.3 and 49.5 effective full power days in two different capsules in the Channel 4 position at design temperatures of 120 and 240°C (designated SMT-1 and SMT-2, respectively). The Channel 4 capsules consisted of 10 subcapsules in the form of flattened stainless steel tubes 12 to 14 mm in diameter and 170 mm long, with the copper specimens contained therein. The subcapsules were filled with helium at a pressure of 0.1 MPa and sealed. All subcapsules were surrounded by 50 to 60°C reactor coolant water.

Three complete sets of fluence monitors (based on ^{58}Fe, ^{54}Fe, ^{63}Cu, ^{58}Ni, ^{46}Ti, and ^{93}Nb) were used to determine the fast and thermal neutron fluxes as a function of position. Two sets of fluence monitors were positioned at the bottom and horizontal midplane of the reactor in order to determine the axial variation in the neutron flux. Duplicate sets of monitors were positioned at the inner and outer periphery of the capsule at the horizontal midplane in order to examine the radial flux gradient across the capsule. The average fast neutron fluence (E>0.1 MeV) in these capsules was $1.1x10^{25}$ n/m^2, which corresponds to a calculated damage level in copper of ~0.9 displacements per atom (dpa). The fast fluence (E>0.1 MeV) ranged from 0.73 to $2.3x10^{25}$ n/m^2 (~0.56 to 1.8 dpa) depending on specimen position in the capsule. The subcapsules in the bottom half of the Channel 4 capsules (containing all of the US specimens) were enclosed in a 1.5 mm Cd shroud in order to shield the specimens from thermal neutrons. The specimen irradiation temperatures in the Channel 4 capsules were determined from three different chromel-alumel thermocouples installed in the unshielded portion of the capsule. Heat transfer analysis codes were used to calculate the specimen temperatures in the shielded portion of the capsules. The average specimen temperature in the unshielded portion of the SMT-2 capsule was determined to be 160 and 210°C for the TEM specimens and LTS specimens, respectively. The corresponding temperatures in the shielded portion of the capsule were 200 and 220°C, respectively.

Four capsules were used to irradiate specimens in the Core position at design temperatures of 120, 120, 240 and 360°C (designated SMT 3-1, 3-2, 3-3 and 3-4, respectively). All of the Core position capsules were fabricated as a flattened stainless steel tube initially 9 mm in diameter and 350 mm long. The SMT 3-1 and SMT 3-2 capsules utilized Al spacers whereas the SMT 3-3 and SMT 3-4 capsules included strips of Mo and Ta, respectively in order to increase the nuclear heating in the capsule and thereby achieve higher temperatures. All of the capsules were irradiated for a total of 44.5 effective full power days. This produced average fast neutron fluences (E>0.1 MeV) of $5.8x10^{25}$ n/m^2 (~4.5 dpa)in the SMT 3-1 and 3-2 capsules and $7.1x10^{25}$ n/m^2 (~5.5 dpa) in the SMT 3-3 and 3-4 capsules. The corresponding thermal neutron fluences (E<0.67 eV) in these capsules were $6.5x10^{24}$ n/m^2 and $7.9x10^{24}$ n/m^2, respectively. Two sets of fluence monitors were installed in the SMT 3-1 capsule at the top and horizontal midplane of the core. The remaining Core capsules were furnished with one set of fluence monitors, located near the horizontal midplane. The temperature in the Core capsules was determined from postirradiation examination of small packets containing material with different melting temperatures. The SMT 3-1 and 3-2 capsules contained Sn alloy (T_M=156°C) and Pb-Bi alloy (T_M=125°C) packets near the horizontal midplane of the capsule. Melting was not observed in either material, indicating that the temperature in these capsules was <125°C. The SMT 3-3 capsule contained Sn (T_M=232°C) and Bi (T_M=271°C) packets near the top and horizontal midplane of the capsule. Examination of the packets indicated that the irradiation temperature was $\leq$ 270°C at the capsule midplane and $\leq$ 230°C at the top and bottom of the capsule. The SMT 3-4 capsule contained Pb (T_M=327°C) and Zn (T_M=419°C) packets near the midplane and top part of the capsule. The irradiation temperature was determined to be ~410°C at the capsule midplane and ~325°C near the top and bottom of the capsule.

Postirradiation examination of the irradiated specimens is in progress. The present report summarizes some of the measurements which have been made following irradiation near 90 and 200°C. All of the tensile measurements were performed at temperatures of either 100 or 200°C, which is approximately equal to the irradiation temperature.

3. Results and Discussion

3.1 Effect of Cd shielding

One of the important physical properties for copper alloys in high heat flux applications is the thermal conductivity. The effect of irradiation on the thermal conductivity (k_{th}) of copper and copper alloys can be determined from electrical resistivity (ρ_e) measurements (which can be measured more easily and accurately than k_{th}) by utilizing the well-known Wiedemann-Franz relation $k_{th}\,\rho_e$ =L T, where the Lorentz number (L) equals $2.23x10^{-8}$ for copper at 0°C [1]. Table 1 compares the electrical resistivity measured in specimens in the Cd-shielded and unshielded regions of the SMT-1 capsule irradiated in the Channel 4 position to a nominal damage level of ~0.9 dpa at ~90°C. The typical increase in the room temperature electrical resistivity was ~10% for the specimens irradiated in the Cd-shielded positions, whereas the typical resistivity increase was ~30% for the unshielded specimens. The large resistivity increase in the unshielded specimens is due to the high transmutation rate of Cu to Ni and Zn in the presence of thermal neutrons [1]. The transmutation rate for Cu in the Channel 4 position of the SM-2 reactor in the absence of Cd shielding is ~3000 appm Ni/dpa and ~1700 appm Zn/dpa. The transmutation rates in the Cd-shielded regions of the SMT-1 capsule were ~570 appm Ni/dpa and ~320 appm Zn/dpa, which is closer to the fusion first wall transmutation rates [1] of ~190 appm Ni/dpa and ~90 appm Zn/dpa. Table 2 summarizes the corresponding tensile property measurements for Cd-shielded and unshielded specimens in the SMT-1 capsule.

Table 1. Room Temperature Electric Resistivity ρ (μΩ-cm) of Small Tensile Specimens (STS) Irradiated in the SMT-1 Capsule at ~88°C

Alloy	Fluence (10^{25}n/m^2) fast	thermal	$\rho_{nonirr.}$	$\rho_{irr.}$	$\Delta\rho_{nonirr.}$ (%)
Cd shielded					
Cu + B3 cold worked	1.03	0.227	1.942	2.111	8.7
Cu + B1 cold worked	1.21	0.227	1.858	2.046	10.1
Cu + B1 annealed	–	–	1.742	2.099	20.5
Cu + B2 annealed	–	–	1.719	2.085	21.3
Cu pure 1 annealed	1.21	0.227	1.681	1.905	13.3
Cu pure 11 cold worked	1.78	0.292	1.779	1.989	11.8
Cu pure 1 cold worked	1.78	0.292	1.751	1.969	12.5
Cu-Mo-B as wrought	–	–	1.915	2.179	13.8
MAGT-0.2 as wrought	1.53	0.292	2.043	2.282	11.7
Cu + B2 coldworked	–	–	1.801	2.108	17.0
GlidCop Al25 (no B) 20% cold worked	1.27	0.292	1.948	2.266	16.3
GlidCop Al25 (no B) as wrought	–	–	1.981	2.264	14.3
GlidCop Al25 + B as wrought	–	–	1.991	2.144	15.4
Cu 99.999% oxyg. 950°C, 0.5 h	1.21	0.227	1.699	1.918	12.9
Cu 99.999% anneal 400°C, 1 h	1.21	0.227	1.692	1.904	12.5
GlidCop Al15 + B as wrought	0.86	0.227	2.018	2.308	14.4
GlidCop Al15 + B ind. braze	0.86	0.227	2.243	2.435	8.5
GlidCop Al15 + B 70% cold worked	1.27	0.292	1.941	2.218	14.3
Cu 99.999% 80% cold worked	1.27	0.292	1.727	1.943	12.5
GlidCop Al25 (no B) 20% cold worked	1.27	0.292	1.933	2.203	13.9
Cu 99.999% ann. 550°C, 2h	1.21	0.227	1.686	1.880	11.5
without Cd					
Cu + B3 cold worked	1.2	1.24	1.911	2.500	30.8
Cu + B1 cold worked	0.82	0.97	1.819	2.359	29.7
Cu + B1 annealed	1.85	1.4	1.736	2.461	41.8
Cu + B2 annealed	1.42	1.4	1.762	2.455	39.3
Cu pure 1 annealed	1.42	1.4	1.700	2.336	40.0
Cu pure 11 cold worked	–	–	1.776	2.287	28.7
Cu pure 1 cold worked	2.27	1.4	1.750	2.434	39.1
Cu-Mo-B	–	–	2.026	2.579	27.3
MAGT-0.2 as wrought	1.3	0.97	2.048	2.692	31.4
Cu + B2 cold worked	–	–	1.789	2.412	34.8

Table 2. **Mechanical Properties of Copper and Alloys Irradiated in the SMT-1 Capsule at ~88°C and Tested at 100°C (LTS Geometry)**

Alloy	Fluence (10^{25}n/m^2) fast	 thermal	σ_y (MPa)	σ_{UTS} (MPa)	δ_u (%)	δ_{tot} (%)
Cd shielded						
Cu pure 350°C, 1h	0.86	0.227	268	269	0.6	4.4
Cu + B1 350°C, 1h	1.21	0.227	381	394	0.25	0.6
Cu + B2 350°C, 1h	1.78	0.292	411	413	0.16	1.8
MAGT-0.2 as wrought	1.27	0.298	538	544	0.25	0.62
Cu 99.999% as wrought	1.53	0.292	380	388	0.42	1.9
Cu 99.999% 550°C as wrought	1.78	0.292	187	216	12.0	16.4
GlidCop Al15 + B as wrought	1.78	0.292	385	391	0.38	0.5
GlidCop Al15 + B induction brazed	1.27	0.292	322	322	0	0
GlidCop Al25 (no B) as wrought	1.21	0.227	520	538	0.4	2.5
GlidCop Al25 + B as wrought	0.86	0.227	519	519	0.24	0.24
GlidCop Al25 (no B) 20% cold worked	1.03	0.227	458	469	0.41	3.9
GlidCop Al25 + B 20% cold worked	1.21	0.227	420	447	0.5	0.67
without Cd						
Cu pure cold worked	1.85	1.4	444	444	0.2	1.5
Cu pure 350°C, 1h	1.3	0.97	302	319	0.5	3.5
Cu pure 350°C, 1h	1.42	1.4	319	319	0.16	3.8
Cu + B1 350°C, 1 h	1.3	0.97	418	419	0.3	2.4
Cu + B1 350°C, 1 h	2.27	1.4	393	413	0.33	2.7
Cu + B2 350°C, 1h	0.82	0.97	494	497	0.1	1.0
Cu + B1 cold worked	1.9	1.24	506	506	0.16	0.16
Cu-Cr-Zr	2.27	1.4	413	413	0.1	0.1
Cu-Mo as wrought	1.2	1.24	199	206	0.33	1.4
Cu-Be	1.2	1.24	766	894	4.1	6.5
MAGT-0.2 as wrought	1.42	1.4	549	550	0.3	0.6
MAGT-0.2 as wrought	0.82	0.97	519	519	0.1	0.1

Figure 1 shows the measured and calculated electrical resistivity in pure copper as a function of thermal neutron fluence. The measurements were made on copper irradiated in the Core position (capsule SMT 3-1) and in the Cd-shielded and unshielded regions of the SMT-1 capsule irradiated in the Channel 4 position. The calculation assumed that the resistivity increase was mainly due to three contributions: radiation-induced defects (stacking fault tetrahedra and small dislocation loops) and Ni and Zn formed by solid transmutation reactions. The Ni and Zn contributions were calculated from their specific resistivities [1] and their thermal neutron production cross sections. The resistivity increase from radiation defects was taken to be constant (0.13 μΩ-cm) for damage levels greater than 0.1 dpa in accordance with previous studies on copper irradiated near room temperature [e.g., 3,4]. From Fig. 1 it can be seen that the dominant contribution to the resistivity increase at high thermal neutron fluences (> 5×10^{24} n/m^2) is due to Ni produced by transmutation reactions. The resistivity increase at low fluence (< 5×10^{24} n/m^2) is mainly due to defect clusters.

The effect of solid and gaseous (He) transmutations on the strength and electrical resistivity of copper was investigated by comparing the response of pure copper and two Cu-B alloys. High amounts of helium can be produced in boron-doped copper as a result of the thermal neutron ^{10}B(n,α)^{7}Li reaction. Figure 2 shows the electrical resistivity increase in copper as a function of boron content for specimens irradiated in shielded and unshielded regions of the SMT-1 capsule (~0.9 dpa, 90°C). The boron additions had a

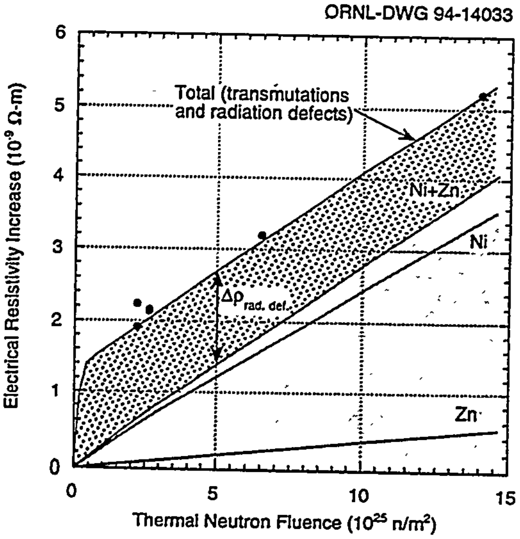

Fig. 1. Comparison of the calculated and experimentally measured effect of solid transmutations and radiation defects on the electrical resistivity of copper irradiated in the SM-2 reactor at 90°C.

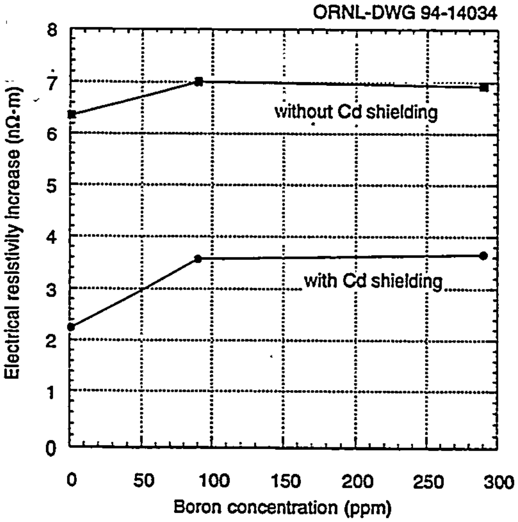

Fig. 2. Electrical resistivity change in copper and Cu-B alloys irradiated in the SMT-1 capsule (~90°C, 1 dpa).

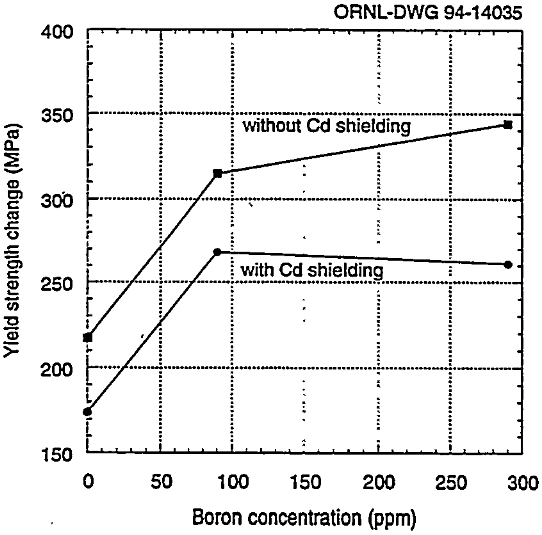

Fig. 3. Effect of Cd shielding and boron concentration on the yield strength of copper irradiated in the SMT-1 capsule (~90°C, 1 dpa).

relatively weak effect on the electrical resistivity increase, particularly in the unshielded specimens. It is obvious from Fig. 2 that the electrical resistivity increase is dominated by solid transmutation effects.

Figure 3 shows the yield strength change in copper as a function of boron content for specimens irradiated in shielded and unshielded regions of the SMT-1 capsule. The irradiated yield strength was relatively insensitive to the boron content. One surprising result was the large difference (>50 MPa) between the yield strength of the Cd-shielded and unshielded specimens. The major transmutation products in the unshielded copper specimens irradiated in SMT-1 capsule to a damage level of ~1 dpa would be ~0.3% Ni and ~0.17% Zn. Both of these elements are soluble in copper, and the resulting solution hardening for these solute concentrations would be expected to be only ~1 MPa [5]. This suggests that the small additions of Ni and Zn are somehow causing the radiation-induced defect structure to become more resistant to dislocation motion, perhaps by modifying the quenching behavior of the displacement cascade [6]. Recent studies have shown that addition of Ni to copper can greatly increase the dislocation loop density that forms during low temperature irradiation [7]. Further work, including TEM analysis, is needed to comprehend this unexpected pronounced dependence of radiation hardening on thermal neutron fluence.

3.2 Tensile Properties of Copper and High Strength Copper Alloys

Irradiation at 90 to 200°C to damage levels of ~0.9 dpa produced significant radiation hardening and an accompanying ductility reduction in all of the irradiated materials. Figure 4 shows the dose-dependent radiation hardening behavior of copper irradiated at temperatures between 20 and 100°C [8-12]. The yield strength in copper approaches an apparent "saturation" value of ~300 MPa after a dose of about 0.1 dpa. Higher dose studies (e.g., the SMT 3-1 capsule specimens that are still awaiting testing) are needed to determine if the yield strength has indeed reached a saturation level. According to the results presented in Fig. 3, it might be anticipated that solid transmutation effects might cause a gradual increase in the irradiated yield strength up high fluences.

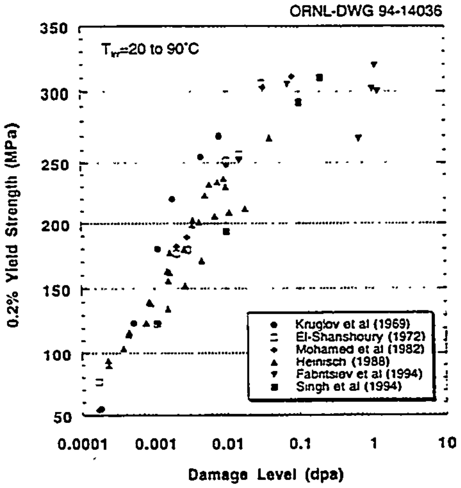

Fig. 4. Dose dependence of the yield strength of copper irradiated at low temperatures [8-12, this study].

Figure 5 shows the effect of irradiation (and test) temperature on the yield strength of GlidCop Al25 oxide dispersion strengthened copper and CuCrZr following irradiation in the Cd-shielded Channel 4 capsules to a damage level of ~1 dpa. The yield strength of all of the alloys was approximately 100 to 200 MPa lower at 200°C compared to 100°C. The two as-wrought GlidCop alloys (with and without ~100 ppm B) had the highest strength following irradiation near 100°C. The 20% cold-worked GlidCop alloy (without B) had the highest strength following irradiation near 200°C. The ultimate tensile strengths of the 5 alloys showed a similar temperature-dependent trend.

Figure 6 compares the temperature-dependent yield strength of as-wrought GlidCop Al-25 (containing ~100 ppm B as a deoxidant) before and after neutron irradiation to ~1 dpa in the Cd-shielded Channel 4 capsules. Irradiation at ~100°C produced ~170 MPa increase in the yield strength compared to the unirradiated material. However, the yield strength of GlidCop irradiated at ~200°C was comparable to the unirradiated material. The strong temperature dependence of radiation hardening in GlidCop is in agreement with previous studies performed on pure copper [13], and may be attributable in large part to thermally activated bypassing of the small defect clusters. At temperatures above 200°C a further rapid drop in the radiation hardening of copper would be expected due to the thermal instability of the radiation-produced defect clusters.

Radiation hardening in the temperature range of ≤200°C produces an increase in the strength of copper and copper alloys, which is generally considered to be a desirable feature. However, this strength increase is accompanied by a dramatic decrease in the work hardening ability of copper and copper alloys. Figure 7 compares the uniform and total elongation of pure copper before and after neutron irradiation at ~100°C to a damage level of ~1 dpa. The uniform elongation decreased from ~29% before irradiation to ~0.6% following irradiation. Similar pronounced decreases in the uniform and total elongation have been observed in all copper alloys examined to date. The smallest elongations occurred in alloys irradiated at 100°C, with significantly higher (although still low) elongations measured after irradiation near 200°C. Figure 8 shows examples of the total elongation in GlidCop oxide dispersion strengthened copper and CuCrZr following irradiation to ~1 dpa at ~100 and 200°C. The total elongation in most of the alloys was approximately doubled as the irradiation temperature increased from 100 to 200°C. A similar improvement in the uniform elongation was observed in all of the alloys as the irradiation temperature increased from 100 to 200°C, although the measured uniform elongation at 200°C was still generally <1%.

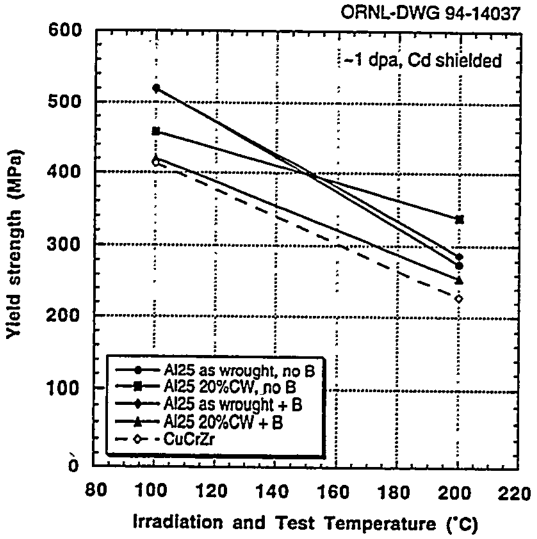

Fig. 5. Effect of temperature on the yield strength of copper alloys irradiated in Cd-shielded capsules to a dose of ~1 dpa.

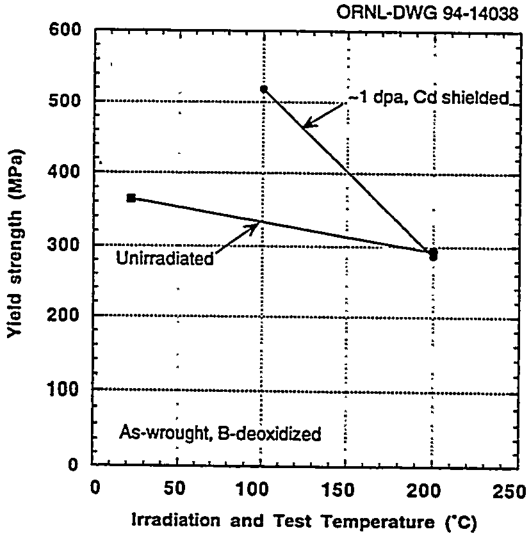

Fig. 6. Comparison of the temperature-dependent yield strength of GlidCop Al-25 before and after neutron irradiation.

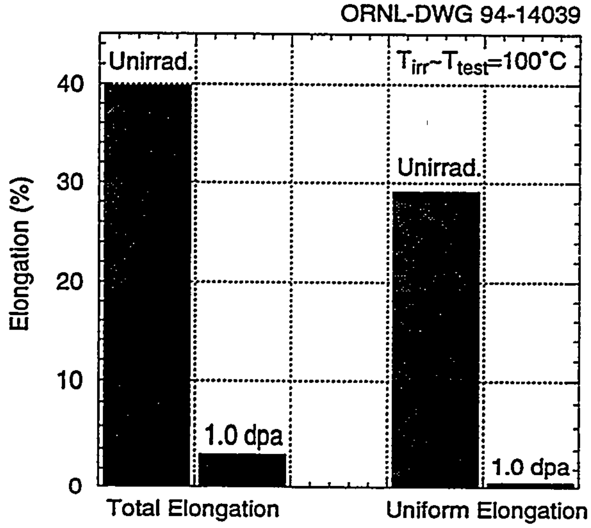

Fig. 7. Low temperature embrittlement of copper irradiated in the SMT-1 capsule. LTS specimens annealed at 350°C before irradiation.

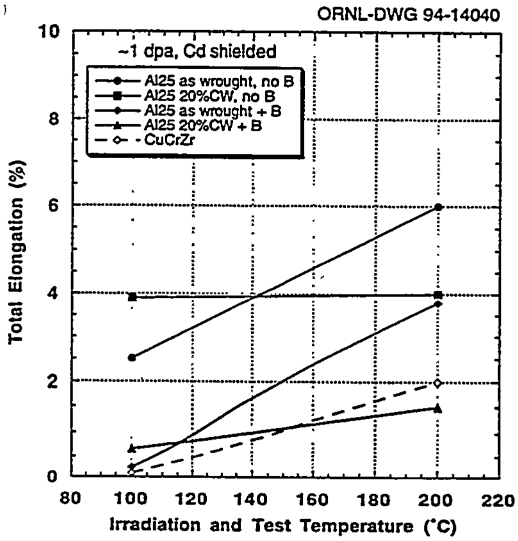

Fig. 8. Effect of temperature on the total elongation of copper alloys irradiated in Cd-shielded capsules to a dose of ~1 dpa.

FUTURE WORK

During the next reporting period, tensile and electrical property measurements will be completed on specimens irradiated in the Channel 4 and Core capsules. Transmission electron microscopy disks of the US specimens will be transported to Risø National Laboratory in Denmark and to PNL and ORNL in the US for immersion density measurements and TEM analysis.

REFERENCES

1. S.J. Zinkle and S.A. Fabritsiev, Fusion Reactor Materials Semiann. Prog. Report for period ending March 31, 1994, DOE/ER-0313/16, p. 314.
2. S.J. Zinkle, F.A. Garner, V.R. Barabash, S.A. Fabritsiev and A.S. Pokrovsky, Fusion Reactor Materials Semiann. Prog. Report for period ending March 31, 1993, DOE/ER-0313/14, p. 347.
3. R.L. Chaplin and R.R. Coltman, J. Nucl. Mater. 108&109 (1982) 175-182.
4. S.J. Zinkle, J. Phys. F: Metal Phys. 18 (1988) 377-391.
5. B. Smola, Czech. J. Phys. B 31 (1981) 447-452.
6. I.M. Robertson, D.K. Tappin and M.A. Kirk, Philos. Mag. A 68 (1993) 843-864.
7. S.J. Zinkle, A. Horsewell, B.N. Singh and W.F. Sommer, J. Nucl. Mater. 212-215 (1984) 132.
8. A.S. Kruglov, V.N. Bykov, I. El-Shanshuri and Kh. Gabor, Sov. Atom. Energy 26 (1969) 582.
9. I.A. El-Shanshoury, J. Nucl. Mater. 45 (1972/1973) 245.
10. H.G. Mohamed, A.M. Hammad and F.H. Hammad, Trans. Ind. Inst. Metals 35 (1982) 258.
11. H.L. Heinisch, J. Nucl. Mater. 155-157 (1988) 121.
12. S.A. Fabritsiev, V.R. Barabash, Y.G. Prokofiev and A.S. Pokrovsky, unpublished data (1994).
13. T.J. Koppenaal and R.J. Arsenault, Metall. Review 16 (1971) 175.

6.5 Environmental Effects in Structural Materials

FABRICATION AND PERFORMANCE TESTING OF CaO INSULATOR COATINGS ON V-5%Cr-5%Ti IN LIQUID LITHIUM* J.-H. Park and G. Dragel (Argonne National Laboratory)

OBJECTIVE

Corrosion resistance of structural materials, and the magnetohydrodynamic (MHD) force and its influence on thermal hydraulics and corrosion, are major concerns in the design of liquid–metal blankets for magnetic fusion reactors (MFRs). The objective of this study is to develop in–situ stable coatings at the liquid-metal/structural-material interface, with emphasis on coatings that can be converted to an electrically insulating film to prevent adverse currents that are generated by the MHD force from passing through the structural walls.[1,2]

SUMMARY

The electrical resistance of CaO coatings produced on V-5%Cr-5%Ti by exposure of the alloy to liquid Li that contained 0.5-85 wt.% dissolved Ca was measured as a function of time at temperatures between 250 and 600°C. The solute element, Ca in liquid Li, reacted with the alloy substrate at 400-420°C to produce a CaO coating. Resistance of the coating layer measured in-situ in liquid Li was ≈0.4 and $6.4 \times 10^6\ \Omega$ at 267 and 400°C, respectively. Thermal cycling between 300 and 700°C changed the resistance of the coating layer, which followed insulator behavior. Examination of the specimen after cooling to room temperature revealed cracks in the CaO coating; therefore preliminary tests were conducted to investigate in-situ self-healing behavior. At ≥360°C, relatively fast healing was indicated. These results suggest that thin homogeneous coatings can be produced on variously shaped surfaces by controlling the exposure time, temperature, and composition of the liquid metal. This coating method is applicable to reactor components. The liquid metal can be used over and over because only the solutes are consumed, not the liquid metal itself. The technique can be applied to various shapes (e.g., inside/outside of tubes, complex geometrical shapes) because the coating is formed by liquid-phase reaction.

INTRODUCTION

Corrosion resistance of structural materials, and the MHD force and its influence on thermal hydraulics, are major concerns in the design of liquid–metal cooling systems for fusion first–wall/blanket applications.[1] Vanadium and V-base alloys (V-Ti or V-Ti-Cr) are leading candidate materials for structural applications in fusion reactors.[3] Previous studies focused on in-situ formation of AlN in liquid Li on an aluminide substrate on V-5Cr-5Ti produced by a chemical vapor deposition method.[4,5] Our recent work has focused on in-situ formation of CaO on V-5Cr-5Ti in liquid Li because the electrical resistivity of CaO is greater than that of AlN by a factor of 10,000 (Fig. 1), and because CaO exhibits a higher thermodynamic stability (Fig. 2) than that of other potential insulator candidates (BeO, MgO, $MgAl_2O_4$, $Y_3Al_2O_{12}$, etc.) in liquid Li.[6,7] The objective of this study is to develop in-situ corrosion–resistant coatings, as well as electrically insulating coatings at the liquid-metal/structural-material interface. These coatings should be capable of forming on various shapes such as the inside of tubes or irregular shapes to prevent adverse currents that are generated by MHD forces from passing through the structural walls. The coatings could also improve general corrosion resistance and act as a diffusion barrier for hydrogen isotopes, viz., deuterium and tritium.

---

*This work has been supported by the U.S. Department of Energy, Office of Fusion Energy Research, under Contract W-31-109-Eng-38.

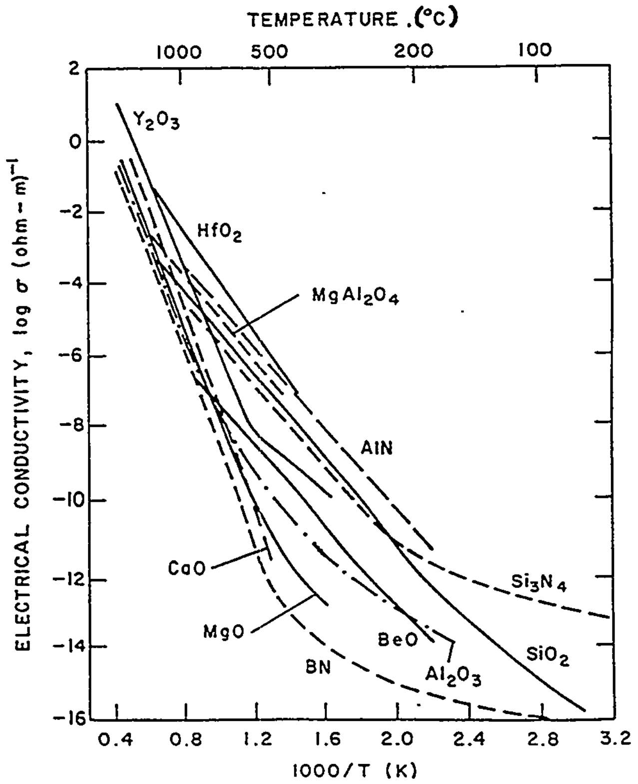

Figure 1. Electrical conductivity of candidate oxide and nitride insulators

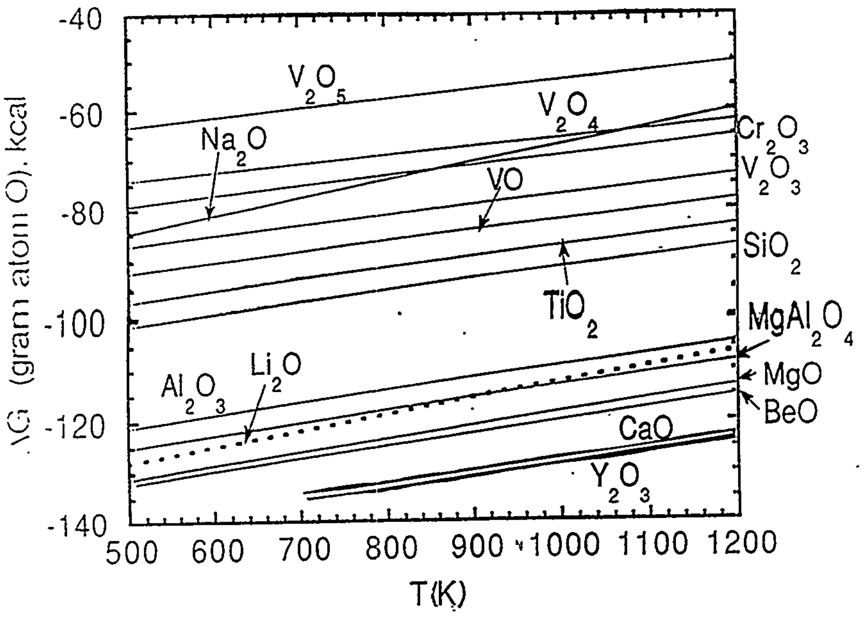

Figure 2. Free energy of formation of various oxides

EXPERIMENTAL PROCEDURE

Various experimental methods have been explored to fabricate and characterize insulator coatings for use in liquid–Li environments: (a) oxygen (O) charging of the near–surface region of V–base alloys in Ar gas and in air, (b) evaluation of liquid-Li compatibility of the O–charged specimens, (c) reaction of the O–enriched V–base alloy with dissolved Ca in Li to form the CaO layer, (d) in-situ electrical resistance measurements of CaO coatings on V-5Cr-5Ti in liquid Li, (e) characterization of the O–charged specimens and insulator coatings by microhardness measurements and scanning electron microscopy (SEM), and (f) optical examination of the coatings for evidence of surface defects such as spallation or cracks. Thermal cycling tests were also conducted to investigate the integrity of coating layers that formed in-situ. Fabrication of coatings at a relatively low temperature (≈400°C) has been emphasized so that the methods can be readily adapted to ITER components.

Oxygen charging of the surface of V-5Cr-5Ti

Metallic solutes dissolved in Li (e.g., Ca, Y, or Mg) do not produce intermetallic phases on V–base alloys, nor do they become incorporated into the material by diffusion interactions at low temperatures. Consequently, another approach was adapted to facilitate formation of an insulating coating (CaO): O was charged into the near–surface region of the alloy under controlled conditions. It is well known that O can be incorporated into the interstitial sublattice in body-centered-cubic (bcc) V and its alloys.[8] Thus, if O or N is present in the alloy (as a reactant), these elements may have a higher affinity for solutes, such as Ca, Y, or Mg dissolved in Li, compared to that of the alloy elements. In the bcc lattice of V-5Cr-5Ti, O can occupy interstitial sites within the lattice up to several atomic percent. Oxygen charging of V-5Cr-5Ti was conducted for up to 48 h at temperatures between 500 and 1030°C in flowing high–purity Ar and N_2 (99.999%) that contained O as an impurity. Specimen weight gain vs. reciprocal temperature is shown in Fig. 3. Diffusion coefficients of O and N in V (Fig. 4) show that diffusion of O in V is 10 to 1800 times faster than that of N. This property is very important for in-situ formation of CaO. Oxygen charging in an N_2 atmosphere lowers the rate (≈5%) because of some participation of N compared with an Ar atmosphere. However, O incorporation into V-5Cr-5Ti predominates even in a 99.999% pure N_2 atmosphere.

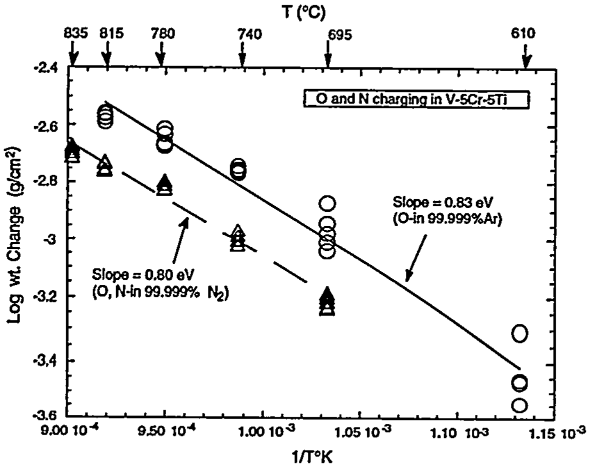

Figure 3. Weight gain of V-5Cr-5Ti vs. reciprocal temperature after exposure to flowing Ar and N_2 for 48 h

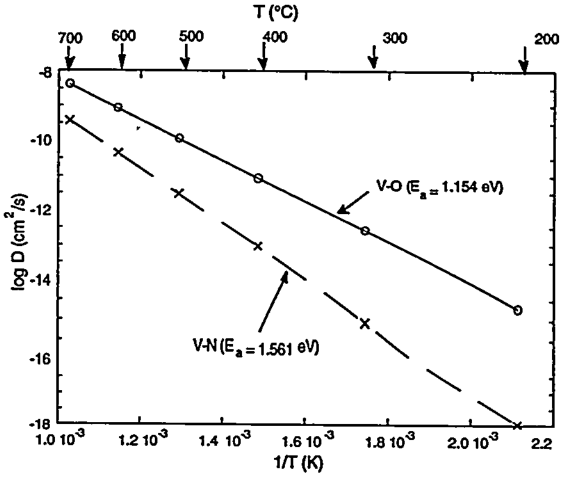

Figure 4. O and N diffusion in V calculated from data in R. Farraro and R. B. McLellan, Mat. Sci. and Eng., 39 (1979) 47-56

Figure 5(a) shows the weight gain per unit area of the alloy at various temperatures after 17 h in N_2, and Fig. 5 (b) shows a cross–sectional view of the specimens. The shiny area at the edge of the specimens depicts the region where O and N are incorporated into the interstitial sublattice of the V-5Cr-5Ti. Based on visual observation and weight gain, we can control the depth of the O–charged layer by exposure temperature and time in a flowing Ar atmosphere. In this study, 99.999% Ar or N_2 was used for O charging. Figure 6 shows SEM photomicrographs of cross sections of V-5Cr-5Ti specimens that were charged with O by exposure to Ar at various temperatures. Oxygen enrichment along grain boundaries is more prevalent at higher temperatures. Oxygen concentration in the near–surface layer was calculated from the weight gain, surface area, and thickness of the hardened region. The O concentration ranged from 250 ppm (as–received) to ≈2–3%, depending on position within the layer and exposure conditions.

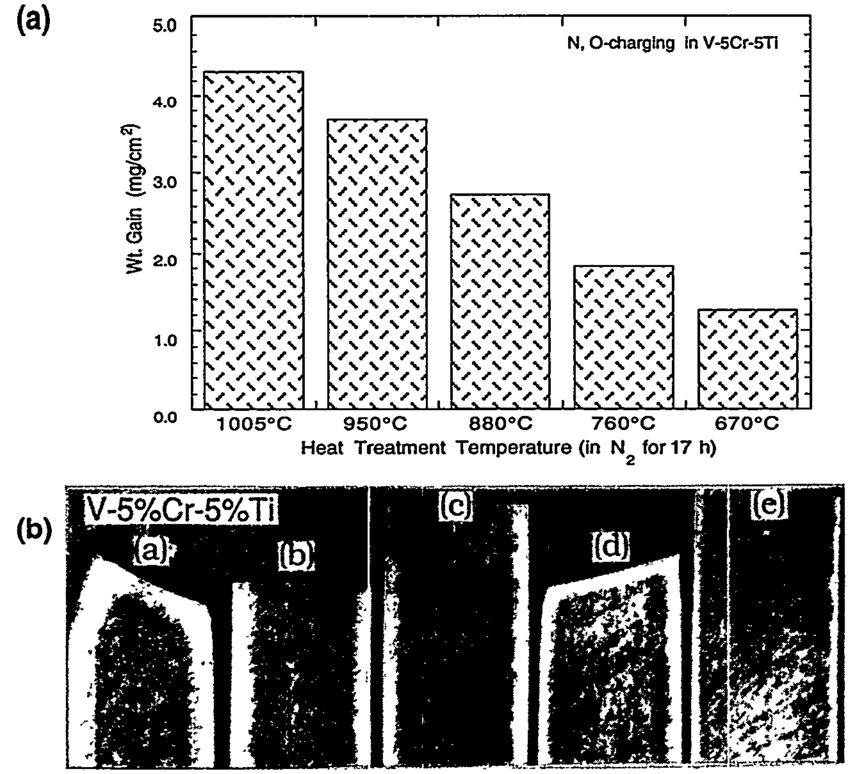

Figure 5. (a) Weight gain of V-5Cr-5Ti specimens after exposure in 99.999% N_2 for 17 h at several temperatures and (b) photomicrographs of specimen cross sections showing O–charged layer

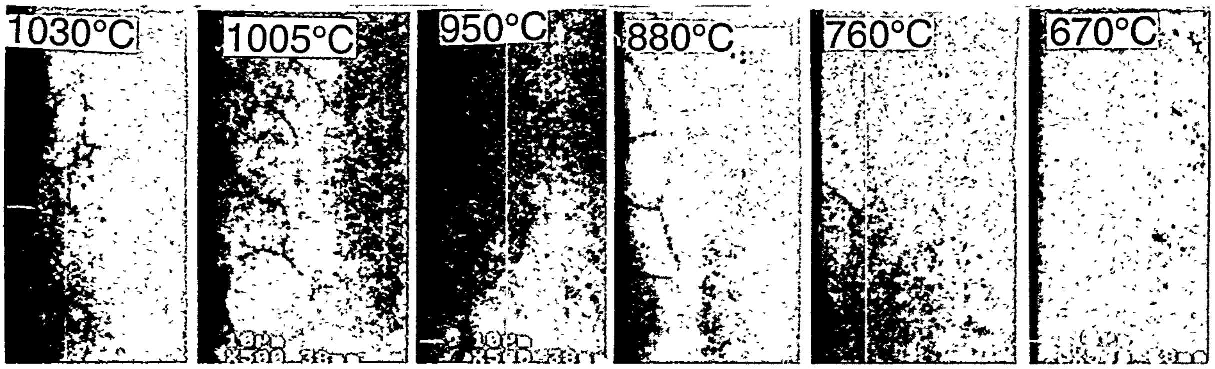

Figure 6. SEM back–scattered electron image from cross sections of V-5Cr-5Ti specimens showing O-charged near–surface region

Oxygen charging was also performed in air at 400°C to avoid melting of V_2O_5 (690°C) during oxidation. Figure 7 shows X-ray diffraction spectra from the surface region of specimens for two heat–treatment conditions. Figure 7(a) corresponds to oxidation in air at 400°C for 20 h, whereupon a blue amorphous layer ($\approx$1 µm) formed at the surface, and Fig. 7(b) represents a similar layer formed by exposure of a V-5Cr-5Ti specimen to high–purity Ar at 650°C for 17 h. Samples charged with O in high–purity Ar or N_2 atmospheres showed the same X-ray spectra before and after O charging. When we measured the ohmic resistance (two–point contact) on the surfaces of heat–treated specimens at room temperature, the specimens charged with O in high–purity Ar or N_2 showed the same ohmic values before and after O charging. The blue oxide that formed in air at 400°C had a resistance of $\approx$5 Ω, not very high in comparison with values for most metal oxides. This oxide is not stable in liquid Li, as shown in Fig. 2.

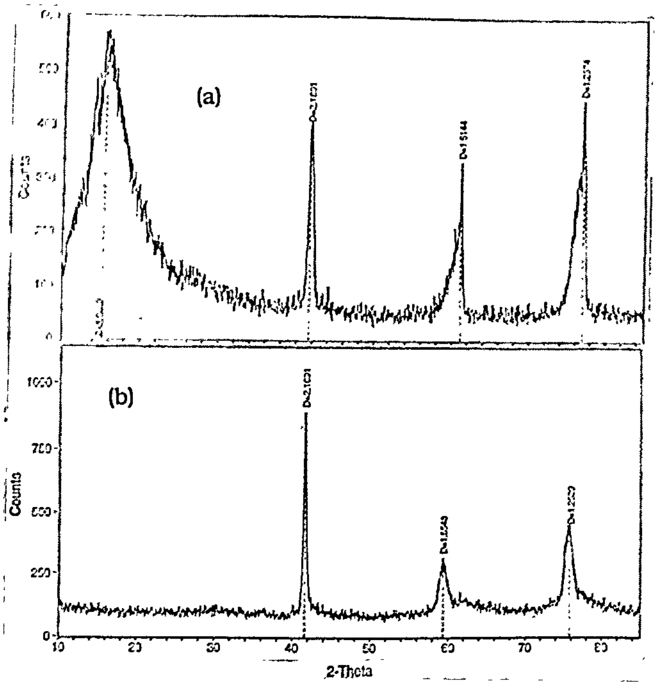

Figure 7.
X-ray diffraction spectra of V-5Cr-5Ti specimens (a) after oxidation in air for 20 h at 400°C, and (b) after O charging in Ar for 17 h at 650°C

Microhardness tests on O-charged V-alloys

Vickers hardness of the O–charged layers and the underlying V-5Cr-5Ti alloy was measured with a 50–g load. Figure 8 shows that the O–charged layers were much harder than the as–received alloys, which can be attributed to interstitial O atoms in the bcc lattice of V. The hardening mechanism appears to be somewhat different than that in most cases where precipitates form in the bulk alloy. Oxygen–charging experiments were performed on pure V, V-10Cr, and V-20Ti specimens in the same atmospheres as for V-5Cr-5Ti to obtain more insight into the hardening phenomenon. Pure V showed the highest hardness values among the different specimens, but the O–charged V-10Cr sample appeared to be more brittle during indentation. Figure 9 shows the dependence of room–temperature Vickers hardness of specimens on temperature of exposure (490 to 890°C) in high–purity Ar for 24 h. Transmission electron microscopy will be performed on several specimens to determine whether the hardening mechanism involves primarily occupation of interstitial sites by O or formation of small particles of V-O.

Compatibility tests on O-charged V-5Cr-5Ti in liquid Li

Figure 10 shows results of compatibility tests on O–charged samples in flowing liquid Li at 443°C for 298 h. Samples charged with O at 1030 and 1005°C showed the highest weight loss during exposure to liquid Li. Results for a similar test at 408°C for 239 h are shown in Fig. 11 for as–received specimens

(250 ppm O) and specimens that were charged with O under different time–temperature conditions. In general, specimens that exhibit the largest weight gain during O charging undergo the largest weight loss during exposure to Li. Presumably, this indicates that an oxide phase (e.g., V_2O_3) that formed during O-charging dissolves in liquid Li. However, weight–loss rates for specimens exposed to Li at 443 and 408°C are virtually the same (i.e., ≈0.0005 g/298 h/cm^2 or 1.68 µg/cm^2-h and ≈0.0002 g/239 h/cm^2 or 0.84 µg/cm^2-h, respectively). In contrast, if weight loss in short–term corrosion tests was controlled primarily by O diffusion in the alloy, the rates would be expected to be relatively independent of the amount of O charged. If O transport to liquid Li was controlled by diffusion in the alloy, diffusion data in Fig. 4 could be used to optimize time–temperature conditions for in-situ formation and self–healing of a CaO coating. This would be applicable to any of the thermodynamically stable oxides in the liquid Li, e.g., BeO, MgO, Y-Al-O garnet, Mg-Al-O spinel, Y_2O_3, and CaO etc., shown in Fig. 2. A similar situation could presumably occur for the formation of nitrides by the reaction of N in the alloy with metallic elements dissolved in Li.

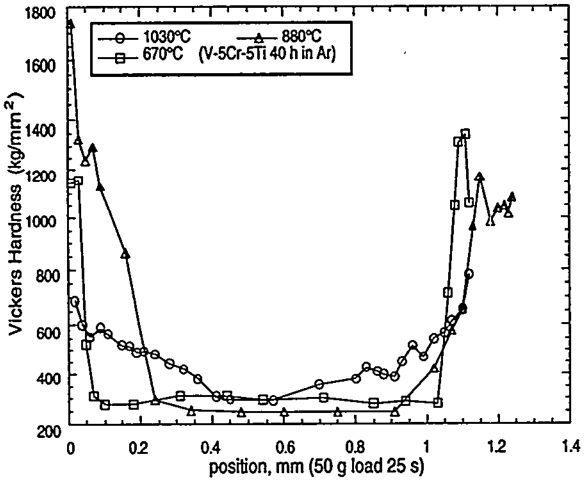

Figure 8. Vickers hardness profiles from cross sections of V-5Cr-5Ti specimens exposed to Ar for 40 h at 670, 880, and 1030°C

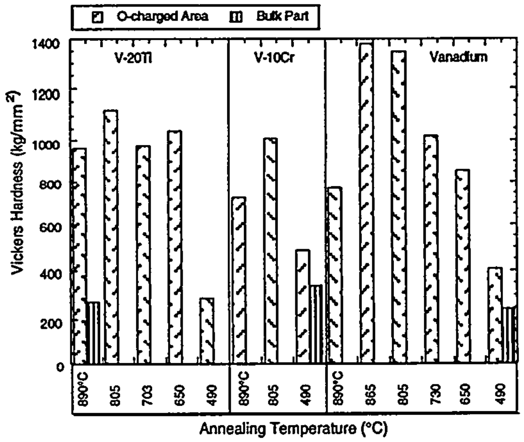

Figure 9. Vickers hardness from cross sections of V-20Ti, V-10Cr, and nonalloyed V specimens in near–surface and center regions after exposure in Ar for 24 h at several temperatures between 490 and 890°C

Nevertheless, it is important to determine the optimum condition for O-charging of V-5Cr-5Ti. Figure 12 shows photomicrographs of the cross sections of O–charged specimens (charging conditions analogous to those in Fig. 10) after exposure in flowing Li for 298 h at 443°C. The dark microstructural features in the near–surface region of the V-5Cr-5Ti specimens charged with O at ≥760°C are not confined to the O–enriched regions or the grain boundaries in the material. They seem to have developed via a phase transformation process during exposure to liquid Li. This phenomenon will be investigated in more detail in the future. Because the specimen charged with O at 670°C did not show these features, further O-charging was conducted at 650°C.

Vickers hardness of liquid–Li exposed specimens was measured with a 50–g load (Fig. 13). When we compare Vickers hardness of the cross section in the near–surface region (≈10 µm) of a specimen charged with O at 1030°C before and after liquid–Li exposure, we find that values were 600-700 and 1400-1600 kg/mm^2, respectively. This suggests that O diffused into the near–surface region. Oxygen charging at lower temperatures typically produces higher near–surface hardness values, as was shown in Fig. 8. Specimens charged with O at 880 and 670°C had relatively high near–surface hardness and hardness decreased after exposure to liquid Li.

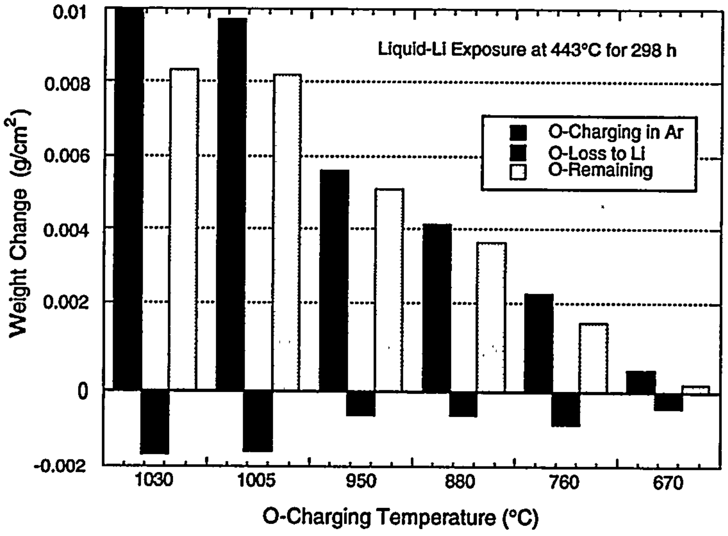

Figure 10.
Weight change of V-5Cr-5Ti specimens after O charging in Ar for 40 h at temperatures between 670 and 1030°C and after exposure of the O-charged specimens to Li at 443°C for 298 h

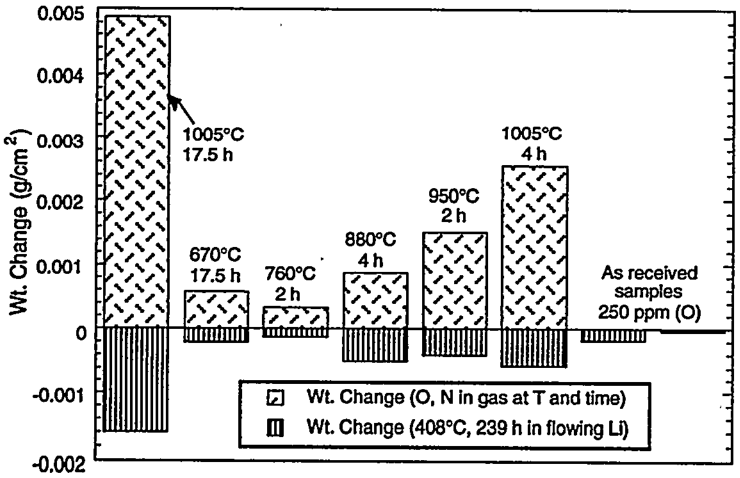

Figure 11.
Weight change of V-5Cr-5Ti specimens after O charging in N_2 at several temperatures between 670 and 1005°C for 2 to 17.5 h and after exposure of as-received and O-charged specimens to Li at 408°C for 239 h

CaO coating on V-5Cr-5Ti

<u>CaO formation on as-received specimens:</u> In-situ formation of CaO on as-received specimens (250 ppm O) has been investigated in liquid Li containing 4 at.% Ca in a Type 304 stainless steel capsule at 700°C during a 7-day exposure. Figure 14 shows an SEM photomicrograph and an EDS spectrum taken from the CaO surface layer. We believe the reaction to form CaO takes place at the interface between O at alloy surface and Ca in the liquid metal. The coating did not completely cover the V-5Cr-5Ti surface, but a high ohmic resistance typical of CaO (two-point contact of >20 MΩ at room temperature) was obtained.

<u>CaO formation on O-charged specimens:</u> To improve the formation of CaO on alloy substrates, O-charged specimens were immersed in Ca-bearing (0.5-85 wt.% Ca) liquid Li for various times and temperatures. This approach was adopted because O in the alloy (as a reactant) may have a higher affinity for a solute such as Ca dissolved in Li compared to that of the alloy elements (i.e., V, Cr, and Ti). Several experiments were performed to test this hypothesis. Specimens of V-5Cr-5Ti were heat-treated in flowing Ar at 650°C to charge the surface of the alloy with O. Because oxides of V are not stable in liquid Li (Fig. 2), conditions were controlled to avoid their formation on the surface during O charging.

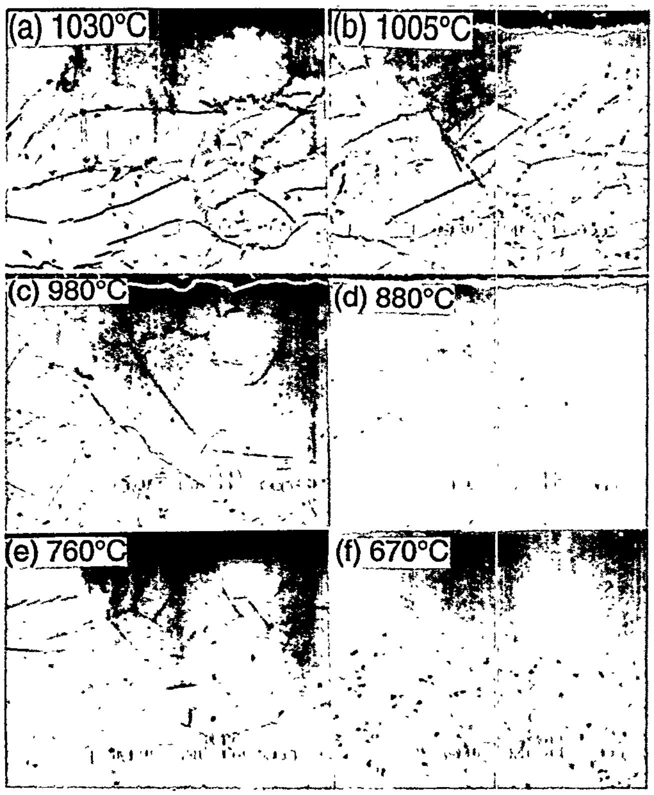

Figure 12.
Photomicrographs of cross sections in the near-surface region of O-charged V-5Cr-5Ti specimens after exposure to Li at 443°C for 239 h. Specimens were charged with O at several temperatures between 670 and 1030°C.

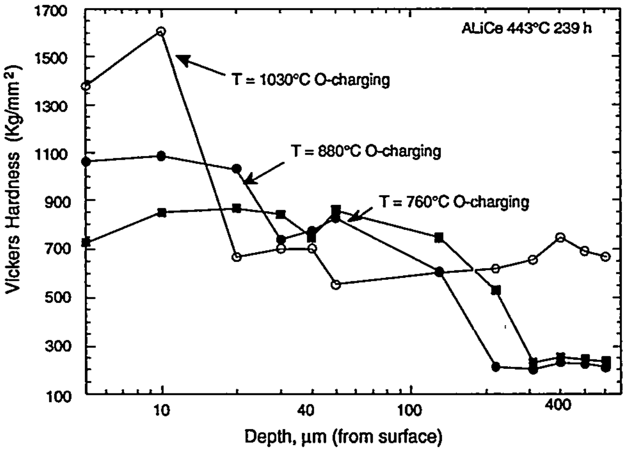

Figure 13.
Vickers hardness vs. depth for O-charged V-5Cr-5Ti specimens after exposure to Li at 443°C for 239 h

Our previous experiments focused on formation of CaO coatings on O-charged V-5Cr-5Ti at 416-750°C. Present results were obtained at 400°C, a temperature that is more consistent with ITER operating conditions. To monitor coating development by electrical resistivity measurements, specimens (1/4" x 1-1/2" x 0.04") were attached to Type 304 stainless steel lead wires (1.2 mm diameter) by electron-beam welding. The specimens were charged with O in an Ar atmosphere at 650°C for 17-20 h, as described previously. Figure 15 shows a set of four specimens after O charging. Two specimens were coupled to form one conductivity measuring unit, as described in a previous report.[4]

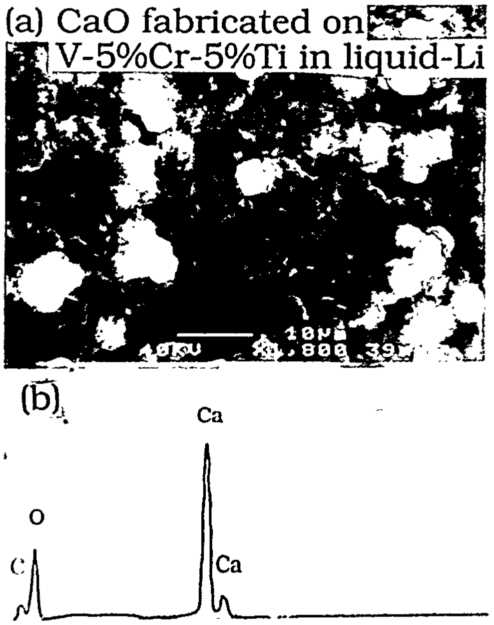

Figure 14.
(a) Photomicrograph of surface of CaO coating formed on as-received V-5Cr-5Ti (250 ppm O) at 700°C and (b) EDS of surface

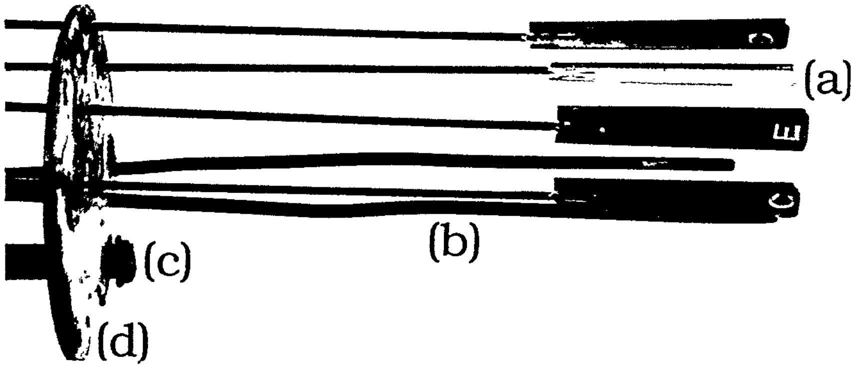

Figure 15. O-charging apparatus consisting of four V-5Cr-5Ti specimens welded to Type 304 stainless steel rods, (b) two K-type thermocouples, (c) Ar injection tube, and (d) spacer

The specimens were immersed for 17 h at 400°C in a solution of Li containing 85 wt.% of Ca, which has a liquidus temperature of ≈380°C. Then the specimens were raised above the liquid level and exposed to an Ar atmosphere at either 400°C or 650°C to oxidize the Ca, similar to the O-charging procedure for the V–base alloy. The specimens were immersed in the liquid Li-Ca alloy again to measure the electrical resistance of CaO films at 400°C. The temperature vs. time history is depicted in Fig. 16. The high resistance values exceeded the 20 MΩ range of the instrument. Only the open–circuit voltage (E_{OC}) of ± 2.336 could be measured with a digital voltmeter (DVM). When the polarity of the input plug in the DVM was switched, the absolute value was the same. Several different sets of conductivity cells were tested in a similar manner.

Figure 17 shows the cell resistance at a current of 100 nA (10^{-7} A) over a ≈30–h period at ≈400°C. An initial iR value was obtained at a current of 1 mA, which was too high and caused polarization of the specimen. At 100 nA, the ohmic value for a 4 cm^2 specimen area was ≈6.4×10^6 Ω, with a fluctuation of ±100 kΩ. At the end of the experiment, the specimens were raised to a position above the liquid metal, the power to the furnace was turned off, and the specimens were cooled to room temperature in flowing Ar gas.

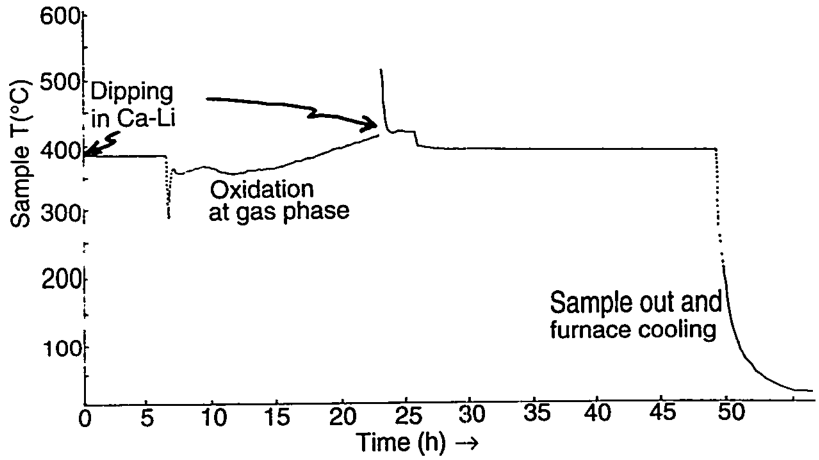

Figure 16.
Specimen temperature vs. time during CaO coating in Li containing dissolved Ca

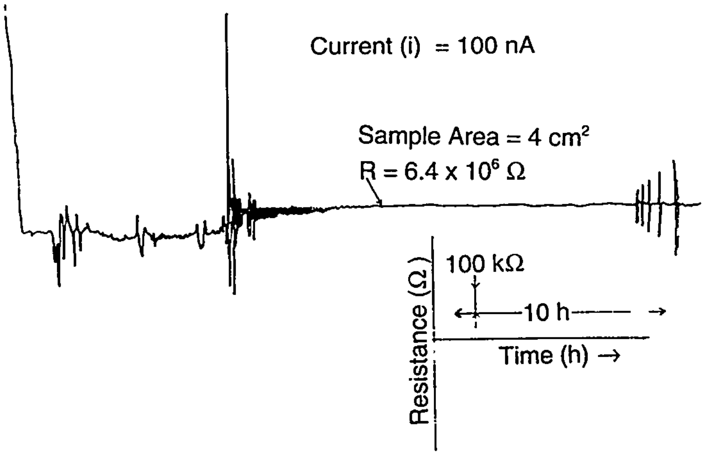

Figure 17.
Voltage (iR drop) vs. time for resistance measurements at 400°C in Li on in-situ formed CaO coating on V-5Cr-5Ti specimens

When the specimens were removed from the chamber, their surfaces were shiny due to the presence of residual liquid metal; however after a few seconds the specimens turned black because of air oxidation. The specimens were immersed in absolute alcohol to dissolve the excess metal and very soon the coating surface was revealed. A specimen was transferred to the SEM/EDS vacuum stage without total drying of the alcohol and a visual investigation of the coating surface was performed. Figure 18 (a) and (b), respectively, show an SEM photomicrograph of the surface and a topographical view that more clearly reveals surface defects. Figure 19 (a) shows another typical region of the coating surface, and 19 (b) shows a region containing microcracking of the CaO surface at high magnification.

To determine coating thickness and compositional depth profiles and to view the microcracks in cross section, the specimens were metallographically mounted using an epoxy resin. Figure 20 shows a cross section of a CaO/V-5Cr-5Ti specimen and a compositional depth profile for the CaO coating layer near the V-5Cr-5Ti interface. The photomicrograph of the CaO layer shows that cracks are perpendicular to the substrate, and that the crack tips reach the base metal. Depth profiles of the alloy elements near the interface show that the composition of Ti and Cr remain constant and that only a small amount (1-2%) of Ca diffused into the V-5Cr-5Ti (1-2 μm depth). From our previous investigation at higher temperatures (≈700°C), elemental diffusion was more significant and ≥10% V was detected in the CaO layer.[9]

Mechanical integrity and self-healing characteristics: With regard to microcracks in the coating layer, CaO has a higher coefficient of thermal expansion than that of V-5Cr-5Ti (12×10^{-6} vs. 9.2×10^{-6}/K), as shown in Fig. 21. Therefore, a CaO layer that forms in-situ on a V-alloy will be subjected to a tensile stress during cooling. Based on the photomicrographs in Figs. 18-20, CaO coatings on V-5Cr-5Ti have the characteristics described below. The crack pattern consists of regions having a diameter of ≈30-40 μm and a crack width of ≤2000 Å over most of the CaO surface, which suggests that the cracks originate by a mismatch of the thermal expansion coefficients during cooling, i.e., "crazing cracks." Adhesion of the CaO film to the V-5Cr-5Ti substrate appears to be quite good. One approach to minimize microcracking would be to decrease the thickness of the CaO film to better match its mechanical strength with that of the V-5Cr-5Ti substrate. For example, a CaO film ≈1 μm in thickness may have a higher fracture strength and also have a resistance of ≥1 MΩ, which is higher than design requirement for ITER by 3-4 orders of magnitude. This is based on the results in Figs. 17 and 20, which indicate that a resistance of ≈6.4 MΩ for a 4 cm^2 area corresponds to a coating thickness of ≈6 μm.

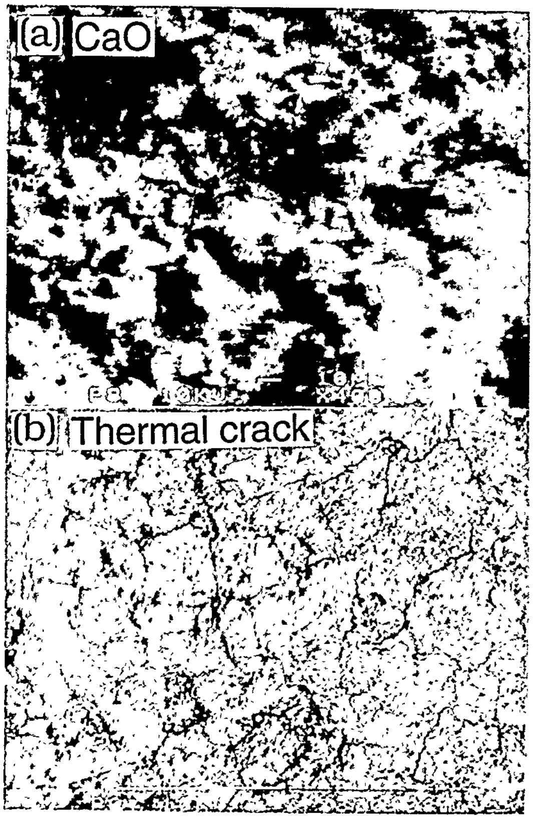

Figure 18.
(a) SEM photomicrograph of surface of CaO coating, and (b) topographical photomicrograph of (a) that reveals surface cracks

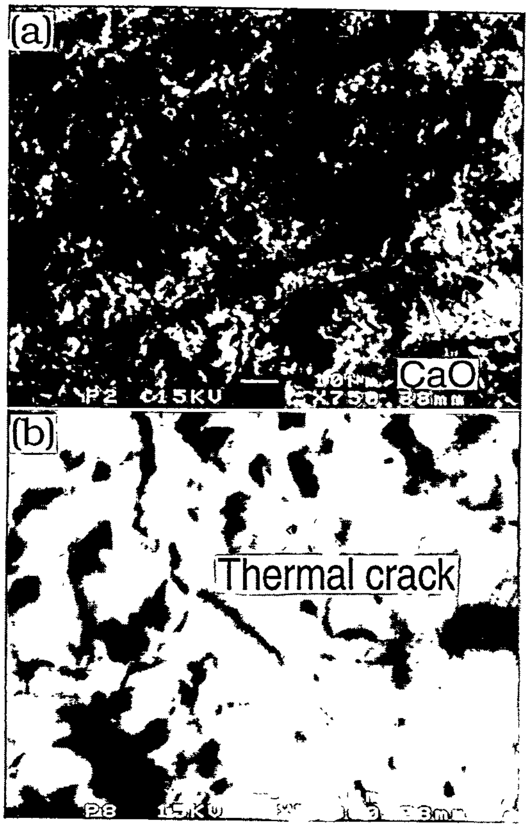

Figure 19.
(a) SEM photomicrograph of surface of CaO coating, and (b) microcracks in coating in (a) at higher magnification

Liu and Smith[10] suggest that no coating may be acceptable because calculated stresses in a coating are greater than the tensile flexural strength for most candidate coatings. Therefore, coatings are subject to cracking in both tension (e.g., CaO) and compression. However, their criterion must be viewed in relationship to the conditions under which the coating is formed (viz., temperature and time), as well as the normal operating temperature. For example, when a CaO film forms at 400°C, no stress develops when the coating operates at 400°C (Fig. 17). However, because the fabrication and operating temperatures may differ and the coating will undergo thermal fluctuation during operation, acceptable temperature ranges must be defined to account for these situations. The surface cracks shown in Figs. 18-20 developed during cooling from 400°C to room temperature. Thermally induced strains are usually calculated by assuming linear thermal expansion, namely

$$
\begin{aligned}
\Delta\varepsilon_{\text{thermal}} &= (\alpha_{\text{CaO}} - \alpha_{\text{V-5Cr-5Ti}}) \times (T_1 - T_2) \qquad (1)\\
&= \Delta\alpha \times \Delta T \approx 3 \times 10^{-6} \times 375\\
&= 1.13 \times 10^{-3}
\end{aligned}
$$

where α_{CaO} and $\alpha_{\text{V-5Cr-5Ti}}$ are the coefficients of thermal expansion of CaO and V-5Cr-5Ti (Fig. 21), respectively, and T_1 and T_2 are the upper and lower values of the temperature change. Stresses in the CaO coating can be relieved by either plastic deformation (including creep), crack formation (microcracking), or spallation. Plastic deformation is possible only when the stress is below the critical stress for the formation of any type of material separation (e.g., cracking).

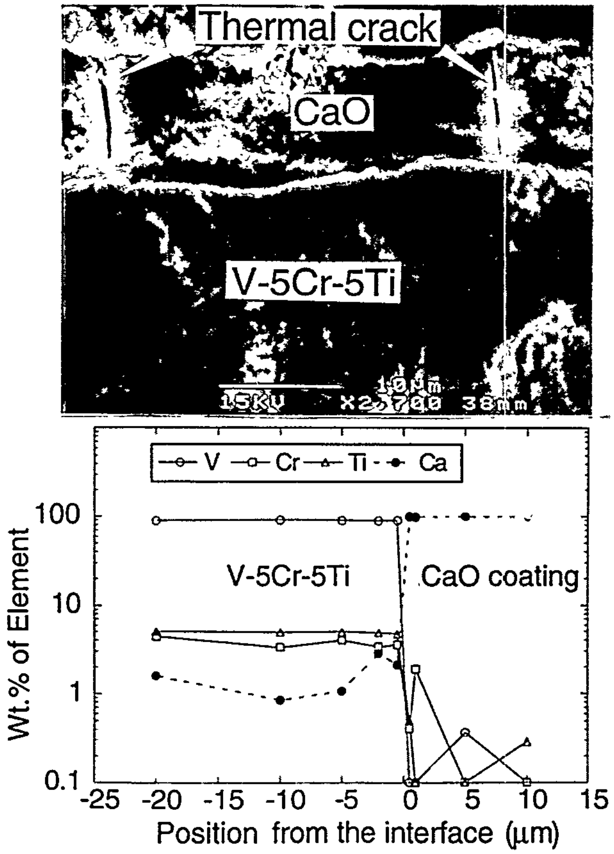

Figure 20.
SEM photomicrograph of cross section and EDS depth profiles of V, Cr, Ti, and Ca at CaO/V-5Cr-5Ti interface of a coating formed at 400°C

The CaO layer is subjected to compressive and tensile stress when the temperature is above and below that at which the film formed. When the temperature is cycled slowly, the coating/substrate interface may undergo relaxation such that cracking or spallation does not occur. In any case, cracking of the CaO layer during cooling is of most concern. Therefore, it is important for the coating to exhibit self–healing characteristics in a liquid–metal environment. Preliminary studies have been conducted to explore the self–healing properties of CaO coatings under temperature cycling. Figure 22 shows the iR response of a CaO layer on V-5Cr-5Ti during stepwise cooling in 20°C increments from 600 to 500°C. For most insulators, the ohmic value increases when temperature decreases, as shown for three increments in Fig. 22. When the temperature was decreased by ≈40°C in the last step, cracks developed and the iR value decreased suddenly but then returned to a high ohmic value indicative of self-healing behavior. This characteristic is as important as the resistivity of a coating in fusion reactor applications.

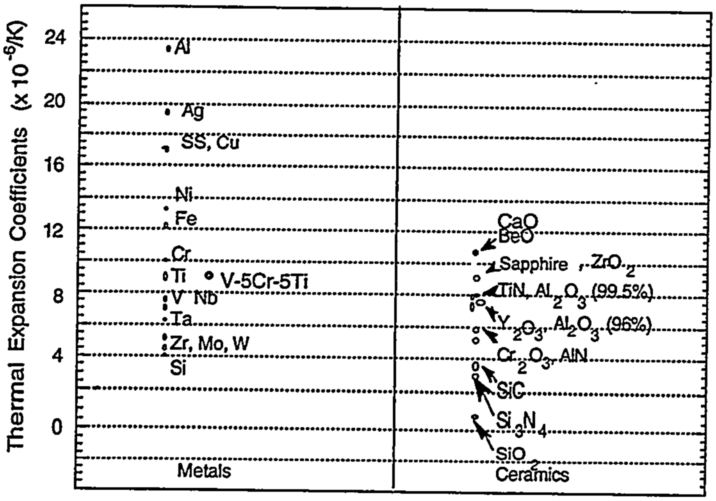

Figure 21.
Thermal expansion coefficients of various metals and ceramics

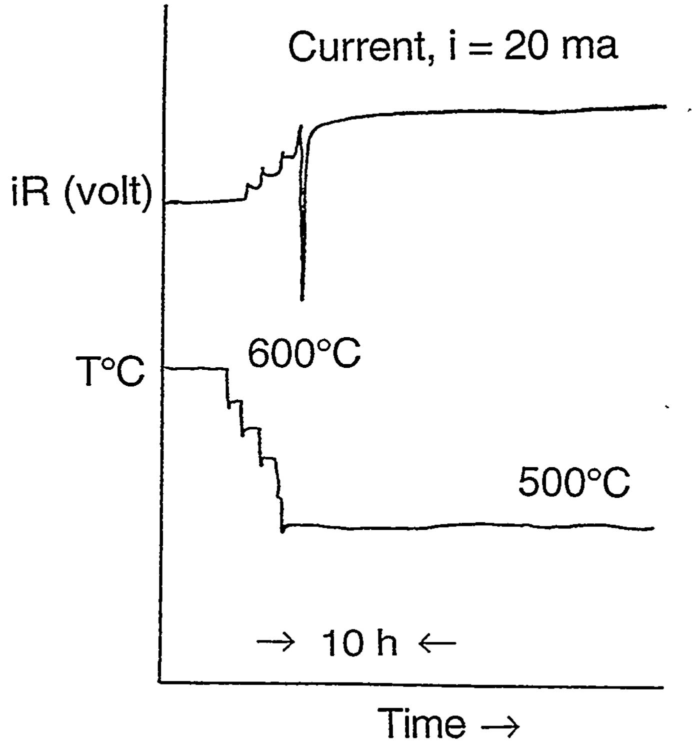

Figure 22.
Voltage (iR drop) and temperature during stepwise cooling from 600 to 500°C vs. time for resistance measurements in Li on in-situ formed CaO coating on V-5Cr-5Ti, showing an increase in resistance during small temperature decreases (20°C) and self-healing of cracks developed after larger temperature decrease (40°C) to 500°C

In other experiments, self-healing of CaO was investigated at temperatures between 300 and 740°C. At 300°C, self-healing did not occur in a 10-h period; at ≥360°C, cracks appeared to heal (e.g., at 450°C, resistivity was restored to its initial value within several hours, and at 500°C in <1 h). When a CaO coating was subjected to compressive stress by increasing the temperature in a similar manner, no appreciable cracking was detected. When temperature was increased to accelerate the healing process, we could not assess whether increases in iR values were caused by closing of cracks or by diffusion-related healing behavior. Nevertheless, when the system temperature was raised, the rapid response resembled healing of the cracks. Further work will be conducted to explore the self-healing process in terms of diffusion and thermal expansion and contraction processes within the CaO layer. With regard to self-healing, reactions that take place at the defect area (i.e., near the Li-Ca/V-5Cr-5Ti (O) interface) are of particular interest in contrast to those that occur at the CaO surface.

CONCLUSIONS AND FUTURE STUDIES

A method was developed for in-situ fabrication of a CaO electrically insulating coating on V–5Cr-5Ti in a liquid–Li environment. The process involves reaction of an O–enriched alloy surface with liquid Li containing Ca at 300–400°C. Self–healing characteristics of cracks produced in the coating by thermal cycling were also investigated. In–situ electrical resistivity measurements indicated that self–healing of defects in the coating occurred at ≥360°C. Additional work will be performed to improve mechanical stability of the coatings during thermal cycling and to establish the mechanisms for self-healing of the coatings.

ACKNOWLEDGMENTS

The author appreciate interactions with Drs. D. L. Smith and R. Mattas regarding the applicability of the work to fusion reactor designs, and with Dr. T. F. Kassner for fruitful discussions and guidance in liquid–Li-related experimental work. B. Tani of Argonne's Analytical Laboratory provided the X-ray diffraction results. R. W. Clark assisted in the liquid-lithium experiments.

REFERENCES

[1]. C. C. Baker et al., *Tokamak Power System Studies FY 1985*, Argonne National Laboratory Report ANL/FPP-85-2 (Dec. 1985).

[2]. T. Kammash, *Fusion Reactor Physics*, Chapter 15, Ann Arbor Science Pub. Inc., Ann Arbor, MI (1975), pp. 405-439.

[3]. R. F. Mattas, B. A. Loomis, and D. L. Smith, *Vanadium Alloys for Fusion Reactor Applications,* JOM, **44**(8), 26 (1992).

[4]. J.-H. Park and G. Dragel, *Development of Electrical-Insulator Coatings: In-situ Electrical Resistance Measurements on V-5%Cr-5%Ti in Liquid Lithium*, Fusion Reactor Materials Semiannual Progress Report for the Period Ending September 30, 1993, DOE/ER–0313/15, pp. 321–325 (1993).

[5]. J.-H. Park and G. Dragel, *Development of Aluminide Coatings on Vanadium–Base Alloys in Liquid Lithium*, Fusion Reactor Materials Semiannual Progress Report for the Period Ending March 31, 1993, DOE/ER–0313/14, pp. 405–410 (1993).

[6]. J.-H. Park, G. Dragel, and R. W. Clark, Development of Electrical Insulator Coatings: In-situ Electrical Resistance Measurements on CaO Coated V-5%Cr-5%Ti in Liquid Lithium, Fusion Reactor Materials Semiannual Progress Report for the Period Ending March 31, 1994, DOE/ER–0313/16, (1994).

[7]. J.-H. Park, T. Domenico, G. Dragel and R. W. Clark, Development of Electrical Insulator Coatings for Fusion Power Applications, paper submitted for 3rd Intl. Symp. on Fusion Nuclear Technology (ISFNT-3), June 27-July 1, 1994, Los Angeles, CA .

[8]. A. U. Seybolt and H. T. Sumsion, Vanadium-Oxygen Solid Solutions, J. Metals Trans. AIME, **292-299** (1953).

[9]. J.-H. Park, Intermetallic and Electrical Insulator Coatings on High-Temperature Alloys in Liquid Lithium Environments, Proc. Symp. on High-Temperature Coatings-I, TMS Fall Meeting, Oct. 2-6, 1994, Rosemont, IL

[10]. Y. Y. Liu and D. L. Smith, Ceramic Electrical Insulators for Liquid Metal Blankets, J. Nucl. Mater., **141-143**, 38 (1986).

FABRICATION OF ALUMINUM NITRIDE AND ITS STABILITY IN LIQUID ALKALI METALS*

K. Natesan and D. L. Rink (Argonne National Laboratory)

OBJECTIVE

The objectives of this task are to (a) evaluate several fabrication procedures for development of aluminum nitride (AlN) coatings on the candidate first–wall structural material V-5wt.%Cr-5wt.%Ti, (b) evaluate the stability of coatings in contact with the structural alloy and liquid Li at temperatures of 200 to 400°C, (c) measure the electrical resistivity of the coated films after exposure to liquid Li, (d) evaluate the effects of coating defects on electrical resistivity, and (e) establish in-situ repair procedures to maintain adequate electrical insulating properties for the coatings.

SUMMARY

AlN has been selected as a prime candidate to electrically insulate the V–alloy first wall in the self-cooled concept for ITER application. Several methods are being evaluated for fabrication of AlN coatings with adequate thickness and the desirable physical, electrical, chemical, and mechanical properties. Coatings developed thus far are being evaluated by exposure to liquid Li at temperatures of 300 to 400°C.

BACKGROUND

Extensive thermodynamic calculations have been made to evaluate potential candidates that are (a) chemically compatible in liquid Li and (b) possess adequate insulating characteristics for use as a coating on the first–wall and blanket structural material. A review of available information on the electrical resistivity values for several oxides, nitrides, and oxynitrides showed that a number of oxides (e.g., CaO, MgO, SiO_2, Al_2O_3, $MgAl_2O_4$) and nitrides (e.g., AlN, Si_3N_4) have resistivities $>10^5$ Ω-m at temperatures below ≈600°C. The requirement is that the product of insulator coating electrical resistivity times thickness should exceed a nominal value of 0.1 Ω m^2 under operating conditions. This translates to a minimum resistivity value of 10^5 Ω-m for a coating thickness of 1 µm, or a resistivity of 10^4 Ω-m for a coating thickness of 10 µm. Based on resistivity values of the materials listed above, a coating layer <1 µm in thickness of any of these materials would be adequate from the insulating standpoint, provided the resistivity is not reduced during operation, i.e., by irradiation. The primary candidate for application in Li is AlN, which, based on thermodynamic stability calculations, will be stable in Li with a wide range of N concentrations [1].

EXPERIMENTAL PROGRAM

Several possible approaches are being examined to develop an AlN coating on the structural material. Some of these are (a) prealuminize the surface of the material by a (pack) diffusion process and subsequently convert it to nitride in an external gas atmosphere, (b) a physical vapor deposition process with and without bond coats, (c) a chemical vapor deposition process at temperatures of 600 to 900°C, (d) a low-temperature method involving sequential reactions, (e) prealuminize the surface of the alloy and convert it to nitride in a high-N Li environment, (f) preexpose the material to liquid Al and convert it to nitride in Li, (g) in-situ formation of coating in Li with high thermodynamic activities for Al and N, and (h) prealuminize specimens of structural material and nitride it by using N_2 cover gas during Li exposure.

---

*This work has been supported by the U.S. Department of Energy, Office of Fusion Energy Research under Contract W-31-109-Eng-38.

RESULTS

Fabrication of Coatings. The pack process is a well-established approach for covering stainless steels and Ni–base alloys with layers of an intermediate phase [2]. The substrate materials are contacted and heated for 4-12 h at ≈900°C with a pack of powders. The composition of such powders (e.g., 65 wt.% Al_2O_3, 33 wt.% Al, 2 wt.% NH_4Cl) provides the packing with metallic Al, alumina as filler material, and NH_4Cl as activator. The amount of Al can be reduced by partial replacement with Ni. The Al deposited on the substrate surface diffuses into the subsurface regions of the material, where it forms intermetallic phases as aluminides of Fe or Ni. Because the substrate materials are heated to temperatures close to the annealing range for times sufficient to cause solution processes in the matrix, the materials need a final treatment in order to optimize the structure. The aluminide layers reach thicknesses of 0.025–0.20 mm, depending on the composition of the substrate materials. Aluminum concentrations as high as 60 wt.% have been obtained at depths of 5-10 µm in the V alloy and decreasing to 30 wt.% at depths of 15-30 µm [3]. The diffusion processes lead to layers of very good adhesion to the substrate. The high temperature of the formation process creates layers that develop compressive stresses at lower temperatures; thus the layers do not contain cracks after preparation is complete.

During this period, aluminum nitride coatings were made by reaction sputtering in low–pressure N_2 atmosphere at a temperature of 400°C. The coating thicknesses after 4 h of deposition were ≈5.2 µm. The coating covered the entire surface of the V–alloy specimen and the layer was found to be of very high resistance, indicating adequate insulating properties. The coated specimens were also given a thermal/chemical treatment at elevated temperature to harden the coating without affecting its insulating characteristics. Aluminum nitride coatings on the V alloy were also prepared by a commercial physical deposition technique. Specimens with ≈10-µm-thick coatings of pure AlN were prepared; they exhibited high resistances similar to those of bulk AlN samples sintered from powder.

Testing of Coatings in Liquid Metals. AlN-coated samples of V-5Cr-5Ti and bulk samples of AlN were exposed at 300°C to a static lithium environment for 120-430 h. Lithium purity was maintained at the levels normally present in commercially available lithium. Another set of specimens were exposed for 430 h to a static lithium environment in which the nitrogen concentration was increased by bubbling 1 vol.% N_2-Argon mixture for 24 h at 300°C. After exposure, lithium from the exposed specimens was dissolved in alcohol and then in water, and the specimens were examined for their insulating characteristics and coating integrity. Figure 1 shows scanning electron micrographs of aluminized V-5Cr-5Ti alloy specimens with sputter-deposited AlN coating after exposure to low- and high-nitrogen lithium environments at 300°C for 430 h. These specimens exhibit multiple layers, the outermost of which is pure AlN. The intermediate layer consists of Al, V, and N. The layer adjacent to the substrate alloy consists predominantly of Al and V and corresponds to that developed during the prealuminizing treatment. Figure 2 shows a scanning electron micrograph of V-5Cr-5Ti alloy specimen with a physical-vapor-deposited layer of AlN after exposure at 300°C to a high-nitrogen lithium environment for 430 h. The thickness of the coating layer initially was ≈12 µm, and after exposure the coating seems to be intact. Resistances of these coated specimens after lithium exposure were high (measurement was not possible with a simple voltmeter) and comparable to those observed in bulk AlN samples. Detailed analysis of these specimens are in progress. Further, long-term exposures of specimens coated by different techniques are in progress in a lithium environment. In addition, coatings with and without deliberately made defects will be exposed to lithium environments.

REFERENCES

1. K. Natesan and D. L. Rink, "Assessment of Alkali Metal Coolants for the ITER Blanket," Presented at 3rd Intl. Symp. on Fusion Nuclear Technology, Los Angeles, CA, June 27-July 1, 1994, and to be published in symposium proceedings.
2. S. R. Levine and R. M. Caves, J Electrochemical Society, 121 [1974] 1051-1064.

3. K. Natesan and D. L. Rink, "Fabrication of Aluminum Nitride and Its Stability in Liquid Alkali Metals," Argonne National Laboratory, Fusion Reactor Materials Semiannual Progress Report for the Period Ending March 31, 1994, Argonne National Laboratory, April 1994.

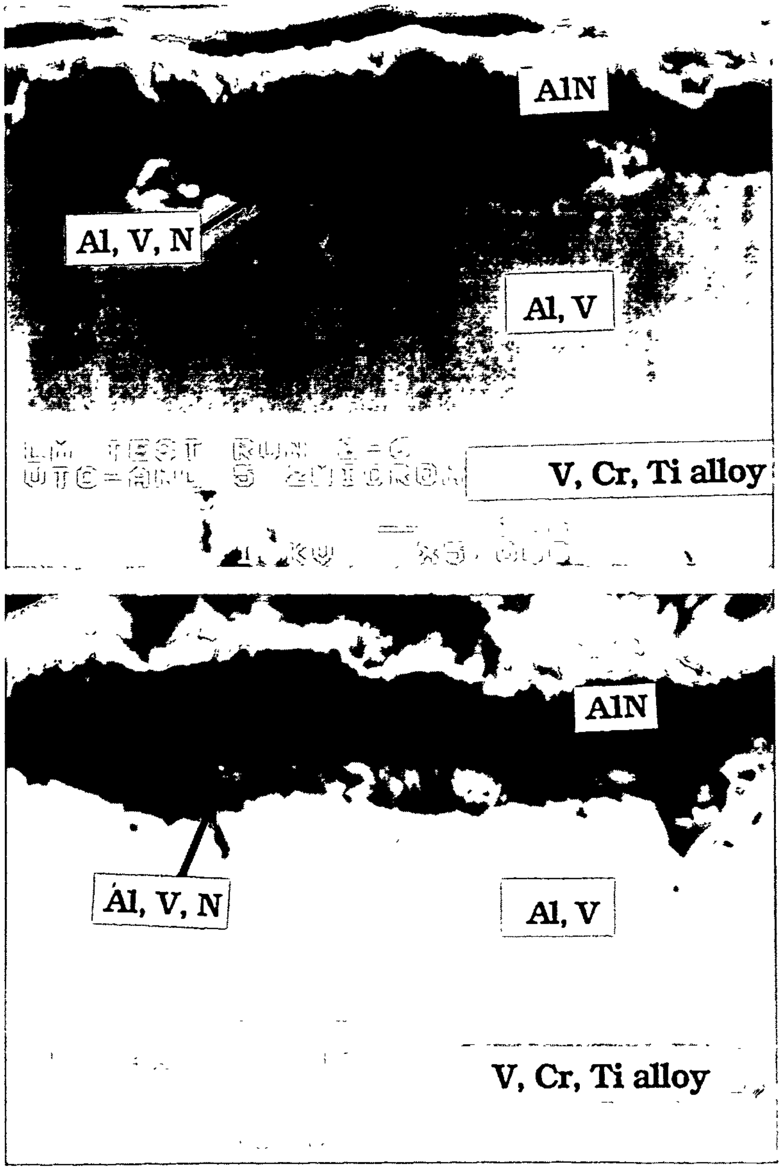

Figure 1. Scanning electron micrographs of aluminized V-5Cr-5Ti alloy specimen with sputter-deposit coating of AlN after exposure at 300°C for 430 h in lithium environment containing (top) low nitrogen and (bottom) high nitrogen.

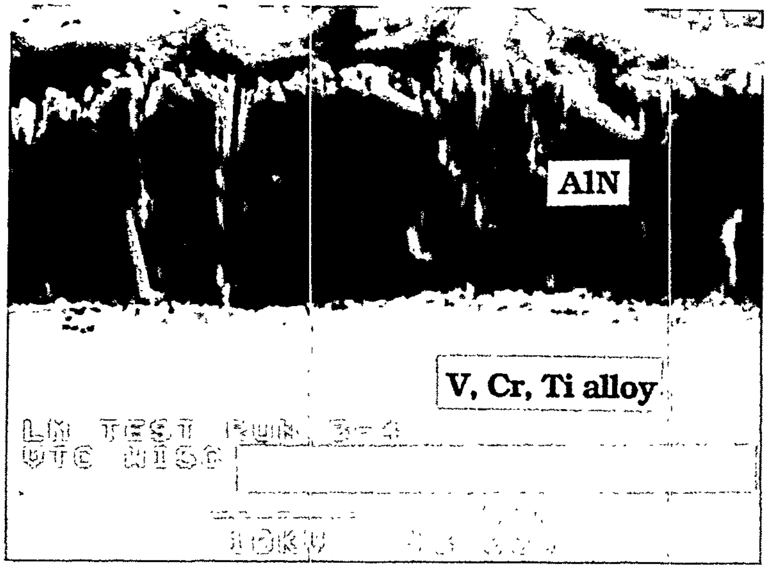

Figure 2. Scanning electron micrograph of V-5Cr-5Ti alloy specimen with physical-vapor-deposited coating of AlN after exposure at 300°C for 430 h in lithium environment containing high nitrogen.

CHEMICAL COMPATIBILITY OF STRUCTURAL MATERIALS IN ALKALI METALS*

K. Natesan, D. L. Rink, R. Haglund, and R. W. Clark
(Argonne National Laboratory)

OBJECTIVE

The objectives of this task are to (a) evaluate the chemical compatibility of structural alloys such as V-5 wt.%Cr-5 wt.%Ti alloy and Type 316 stainless steel for application in liquid alkali metals such as lithium and sodium-78 wt.% potassium (NaK) at temperatures in the range that are of interest for International Thermonuclear Experimental Reactor (ITER); (b) evaluate the transfer of nonmetallic elements such as oxygen, nitrogen, carbon, and hydrogen between structural materials and liquid metals; and (c) evaluate the effects of such transfera on the mechanical and microstructural characteristics of the materials for long-term service in liquid-metal-environments.

SUMMARY

Candidate structural materials are being evaluated with regard to their compatibility, interstitial element transfer, and corrosion in liquid alkali metal systems such as lithium and NaK. Type 316 stainless steel and V-5Cr-5Ti coupon specimens with and without prealuminizing treatment have been exposed to a lithium environment of commercial purity for 3200 h at 350°C. Weight change data showed negligible corrosion of these materials at this temperature.

INTRODUCTION

Liquid metals are being considered for a coolant/tritium-breeding blanket in the ITER. These liquid metals include lithium (Li) and sodium-78wt.% potassium alloy (NaK). The structural materials considered for the first-wall application are Type 316 austenitic stainless steel and V-5 wt.%Cr-5 wt.% Ti alloy. In the fusion application, the structural material of the system must be compatible with the liquid metal and must also maintain structural integrity for long periods during exposure to moderately elevated temperatures, thermal cycling, and possibe intense irradiation; it must also be amenable to low MHD losses during flow in the magnetic field.

In general, structural materials can undergo a variety of interactions upon exposure to liquid metals. The extent of interaction depends upon the conditions of temperature, temperature gradient, liquid-metal velocity and purity, alloy composition, and the materials of construction of the containment system. The peak temperature for the liquid metal in ITER is expected to be ≈400°C, with a maximum temperature gradient of ≈100°C around the loop. Under these conditions, metallic-element mass transfer between the structural materials and the liquid metal occurs predominantly by leaching of the alloy constituents of the materials, which is dictated by the solubility of the alloy constituents in the liquid metal. Nonmetallic elements such as oxygen, carbon, nitrogen, and hydrogen are known to migrate in structural-material/alkali-metal systems as a result of chemical activity differences. The effect of transfer of these elements can affect on the microstructural changes and long-term mechanical properties of the materials. In addition, distribution of hydrogen and hydrogen isotopes between the structural material and liquid metal, as well as permeation of these elements through the structural alloy, must be known in order to control and maintain the desired inventory of tritium in the system.

Some of the key performance variables of importance in the use of liquid metals in first-wall/blankets are:

---

*This work has been supported by the U.S. department of Energy, Office of Fusion Energy Research, under Contract W-31-109-Eng-38.

- (a) Liquid Metal Compatibility
    - Corrosion due to metallic element mass transfer
    - Nonmetallic element (O, C, and N) mass transfer
    - Influence of corrosion on mechanical properties
- (b) Tritium Inventory and Transport
    - Hydrogen/tritium solubility in liquid metal
    - Hydrogen/tritium distribution between liquid metal and structural material
    - Tritium recovery methods
    - Effects on structural materials

EXPERIMENTAL PROCEDURE

Three static liquid-metal systems have been designed and fabricated for studies on compatibility of structural materials in liquid metals. Two of these systems have been filled with ≈5 L of high-purity Li, and the third system was filled with NaK. The two lithium systems are maintained at temperatures of 350 and 400°C, respectively, and the NaK system is operated at 300°C. Figure 1 is a photograph of the experimental systems. Coupon specimens of V-5 wt.%Cr-5 wt.% Ti alloy and Type 316 stainless steel were fabricated for exposure in liquid metals. In addition, specimens of both materials were aluminized by a pack-diffusion process to enrich the near-surface regions of the specimens with aluminum; these specimens were also exposed to liquid metals to evaluate the long-term stability of aluminum-enriched surface layers. Weight change measurements are used to establish the corrosion rates for the structural alloys as a function of temperature, time, and liquid-metal chemistry. After the exposures, the specimens are examined by a scanning electron microscope (SEM) equipped with an energy-dispersive X-ray (EDX) analyzer and by X-ray diffraction.

RESULTS

In the aluminizing pack-diffusion process, the substrate materials are contacted and heated for 4-12 h at temperatures of ≈900°C with a pack of powders. The composition of such powders (e.g., 65 wt.% Al_2O_3, 33 wt.% Al, 2 wt.% NH_4Cl) provides the packing with metallic Al, alumina as filler material, and NH_4Cl as activator. The Al deposited on the substrate surface diffuses into the subsurface regions of the material, where it forms intermetallic phases as aluminides of Fe or Ni in stainless steel and Al-V intermetallic in V alloy. The aluminide layers reach thicknesses of 0.015–0.20 mm, depending on the composition of the substrate materials, length of exposure in the pack, and exposure temperature. Figure 2 shows the elemental concentration profiles of Al, V, Cr, and Ti in a V-5Cr-5Ti alloy sample after an aluminizing treatment.

Figure 3 shows weight-change data for both materials with and without prealuminizing treatment after exposure at 350°C to lithium of commercial purity. The base alloys exhibited very little weight change over a 3200 h period of exposure, indicating virtually no impurity-induced corrosion of the alloys in the lithium environment. The prealuminized specimens exhibit a somewhat greater weight change, especially during the initial 200 h of exposure. This change can be attributed to loss of aluminum oxide particles embedded in the surfaces of the specimens from the aluminizing process. Thermodynamic stability calculations show that aluminum oxide is unstable in a lithium environment and that transfer of oxygen will be from the oxide to lithium. After ≈1500 h exposure, weight losses are negligible for the balance of the exposure period. Because corrosion rates over long periods of time are determined by the slope of the weight change vs. time curves in Fig. 2, it is evident from the data that the rates are negligible for both substrate materials with or without aluminizing treatment at 350°C.

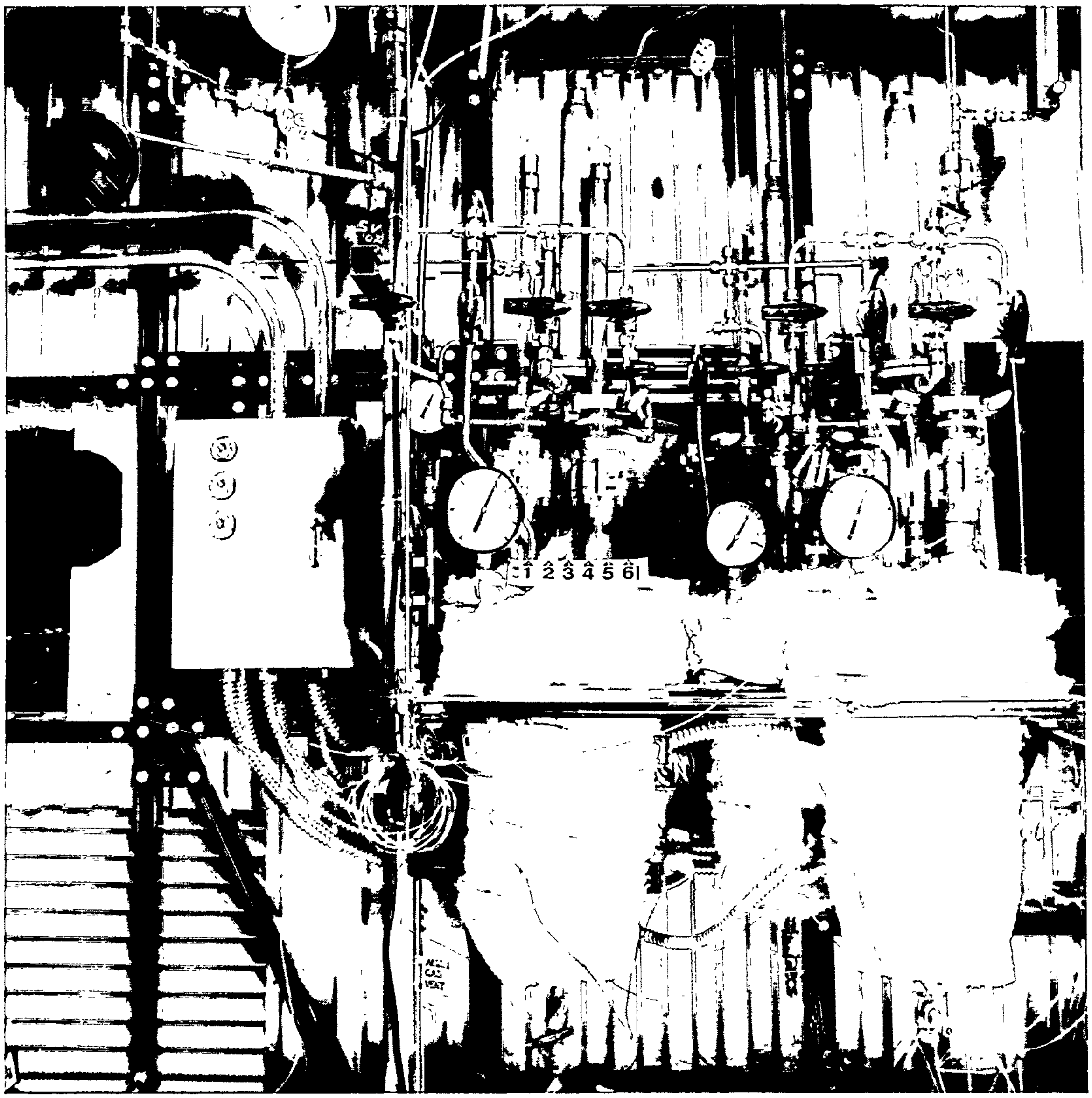

Figure 1. Photograph of alkali metal systems used in the present study.

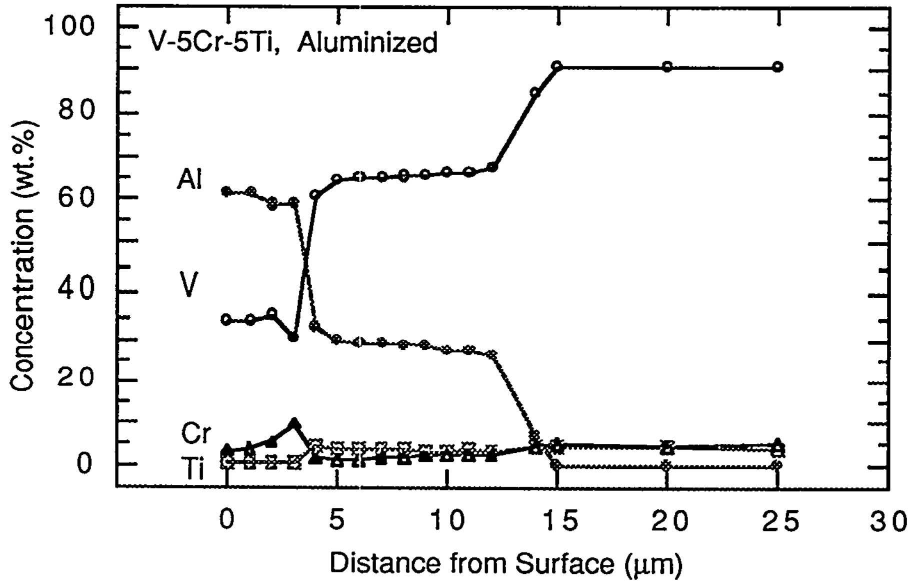

Figure 2. Depth profiles for Al, V, Cr, and Ti for aluminized specimen of V-5Cr-5Ti alloy

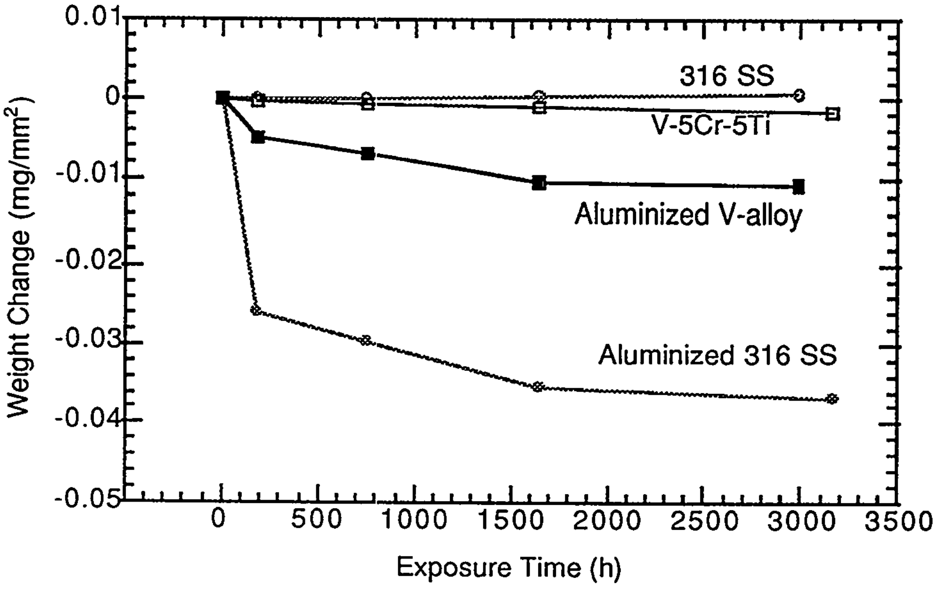

Figure 3. Weight change data for bare and aluminized Type 316 stainless steel, and bare and aluminized V-5Cr-5Ti alloy, after exposure to lithium at 350°C.

7.0 SOLID BREEDING MATERIALS AND BERYLLIUM

An Investigation of the Desorption of Hydrogen from Lithium Oxide using Temperature Programmed Desorption and Diffuse Reflectance Infrared Spectroscopy

J. P. Kopasz and C. E. Johnson (Argonne National Laboratory) and J. Ortiz-Villafuerte (Escuela Superior de Fisica y Matematicas, Mexico)

OBJECTIVE

The addition of hydrogen to the purge stream has been shown to enhance tritium release from ceramic breeder materials; however, this added hydrogen can lead to increased costs in the tritium purification system. The objective of this work is to develop an understanding of the interactions between hydrogen and lithium oxide surfaces so that we can take full advantage of the observed enhancement of tritium release caused by hydrogen addition without incurring high costs in the tritium purification plant.

SUMMARY

A combination of Temperature Programmed Desorption (TPD) and Diffuse Reflectance Infrared Fourier Transform Spectroscopy (DRIFTS) is being used to investigate the desorption of hydrogen from lithium oxide. Initial studies have indicated that there are four different types of hydroxyl groups which can be observed on a lithium oxide surface. The particular species present vary depending on the temperature and hydrogen pressure of the system. Under some conditions where hydrogen is present in the purge gas surface hydride species have been observed. This suggests heterolytic adsorption of hyrdogen has occured.

PROGRESS AND STATUS

Introduction

Lithium oxide is one of the leading candidates for use as a tritium breeding material in a fusion reactor. Many experiments have demonstrated the relative ease of tritium recovery from this material. Tritium release is particularly facile when a purge gas containing hydrogen, typically at levels of about 0.1%, is used. However, addition of hydrogen to the purge has a penalty associated with it when one gets to the tritium purification process. A large amount of hydrogen in the purge will necesitate a larger tritium purification unit, and therefore larger costs. In order to optimize tritium release while minimizing the amount of hydrogen necessary in the purge one must have a better understanding of the tritium desorption step and the interactions of hydrogen with the lithium oxide surface.

One method typically used to study surface desorption processes is Temperature Programmed Desorption (TPD). In this technique a gas is adsorbed on the sample, the sample is then heated at a constant rate and the gas desorbed from the sample detected downstream by a technique such as mass spectrometry. From the shape and position of the desorption peak one can obtain information about the energetics of the desorption process.[1] One shortcoming of this technique is that there is no information on the identity or form of the species that is desorbing as it exists on the surface. For example, if a tritium atom exists on a lithium oxide surface there is the possibility that it exists as a triton (H^+), or as a tritide (H^-). When it desorbs into the gas phase (as HTO or HT) it now can react with hydrogen or water in the gas phase to form an equilibrium mixture of H_2, HT, H_2O, and HTO. At the mass-spectrometer downstream you will only detect the equilibrium mixture, and have no information about whether the desorbed species was T^+ or T^-, or worse whether the species is being desorbed from your sample or from the support structure. When several peaks are observed in a TPD spectra, there is no information other than the energetics to help determine what the different peaks are due to (different surface species, diffusion and desorption of the same species, dsesorption from other surfaces). In addition, when there are several overlapping peaks it is sometimes difficult to determine the number of peaks present.

Diffuse reflectance infrared Fourier Transform Spectroscopy has been used to view hydroxyl groups on the lithium oxide surface [2]. Different infrared absorptions were observed in the OH region, indicating different types of OH groups present on the surface. However, no energetic information was obtained regarding the desorption of these hydroxyl groups. In an effort to gain information about the species present on the surface and how they relate to peaks in the TPD spectra we have turned to a study of hydrogen adsorption and desorption from lithium oxide using a combination of TPD and diffuse reflectance infrared spectroscopy.

Experimental

Temperature Programmed Desorption measurements were performed using an apparatus decribed previously.[3] Hydrogen or deuterium were dried by passing the high purity gas through a commercial deoxygenating unit. Hydrogen (deuterium) was adsorbed on the sample at 250°C for a period from 3 to 24 hours. The purge gas was then changed and the temperature increased linearly while the outlet gas stream was continuosly monitored by mass spectroscopy.

Diffuse reflectance FourierTransform Infrared spectroscopy measurements were performed on a commercial lithium oxide powder (Alfa) using a Bomem spectrometer equipped with a diffuse reflectance attachment (Harrick Scientific DRA-Praying Mantis). The samples were contained in a vaccum chamber equipped for diffuse reflectance (Harrick Scientific) with ZnSe windows and equipped with an internal heater. Experiments were performed by exposing the sample to Ar+0.1%H2 or Ar+0.1%D2 at various temperatures and recording the infrared spectra. Kinetic experiments were performed by switching the purge gas then recording the spectra at specific time intervals.

Psuedo TPD-DRIFTS experiments were performed by exposing the sample , then slowly raising the temperature manually from 200 to 400°Cwhile sampling the purge gas downstream of the sample with the mass spectrometer and recording the infrared spectra at discreet times during the temperature increase. Ar +0.1%D2 was passed over the sample at 115-120°C for 16 h. The purge gas was then switched to Ar+0.1%H2, and the temperature of the sample slowly increased to 400oC. The gas was continuosly sampled by mass spectrometry and diffuse reflectance spectra were recorded at specific temperatures durign the TPD run. Diffuse reflectance spectra were recorded at temperatures of 157, 174, 200, 225, 250, 275, 308, 322, 347, 361, 374, and 395°C.

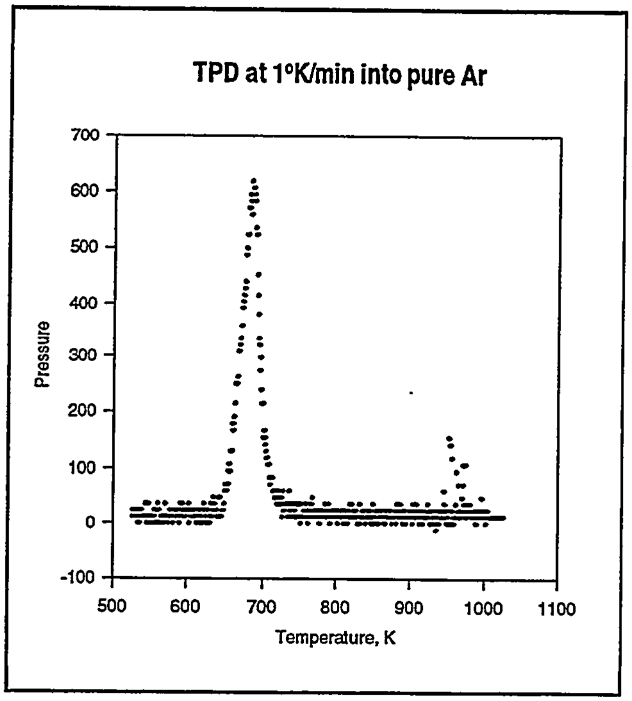

Figure 1

Results and Discussion

TPD

For TPD experiments into a purge gas of pure Ar, one narrow peak was observed for temperature ramps up to 750°C at heating rates of 2, 5 and 10 K/min. For a heating rate of 1K/min one peak with what might be a second small peak near the temperature limit of the experiment was observed. (Fig 1) The main peak is narrow, and attempts to obtain an activation energy for this peak which is self-consistent using line-shape analysis and plots of $\ln(T_m^2/H)$ vs. 1/T have been unsuccessful. The activation energy calculated from the plots of $\ln(T_m^2/H)$ vs. 1/T is 88 kJ/mol while that obtained from line-shape analysis is about a factor of two higher. This suggests desorption into pure Ar is not a simple first-order desorption process.

TPD experiments performed in a purge gas of Ar+0.1% H_2 exhibit more than one peak in the desorption spectra. The main peak occurs at temperatures close to those seen in pure Ar, however additional peaks occur at higher temperatures and at temperatures near the maximum temperature for the experiment. (Fig.2) For the main peak plots of $\ln(T_m^2/H)$ vs 1/T gives an activation energy of 102.5 kj/mol (24.5 kcal/mol); however, line shape analysis again gives a much higher activation energy for this peak. This suggests that the mechanism for desorption of this species is not a simple first-order desorption. For the second peak seen a self-consistent activation energy of 73 kJ/mol is obtained from line shape analysis and plots of $\ln(T_m^2/H)$ vs 1/T. The other peaks were too close to the temperature limit for the experiment to be able to obtain activation energies from these methods.

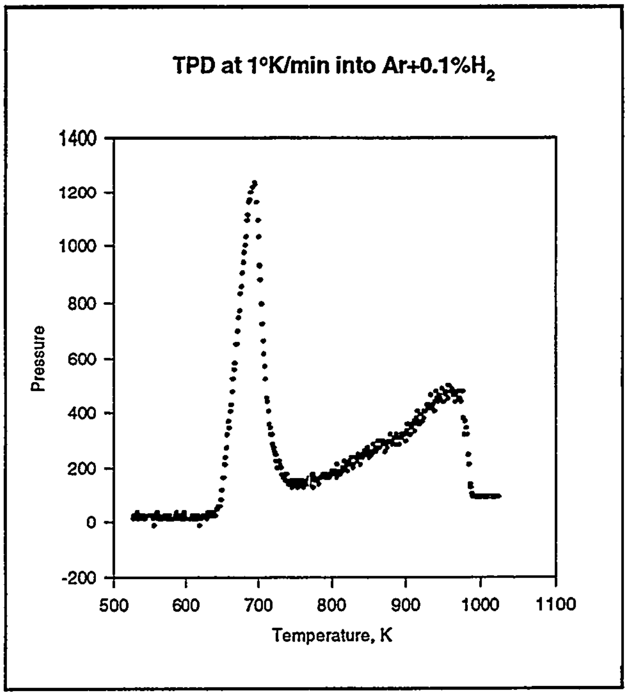

Figure 2

DRIFTS

Diffuse reflectance infrared Fourier transform spectra of a lithium oxide powder after exposure to a purge gas of Ar+0.1%D2 at 365°C is shown in Fig. 3. Several different absorptions are observed for OH and for OD. Under different conditions, other peaks appear more prevalent. From deconvolutions of these curves it appears that there are four different OH absorptions at 3657, 3604, 3480 and 3400 cm^{-1}.

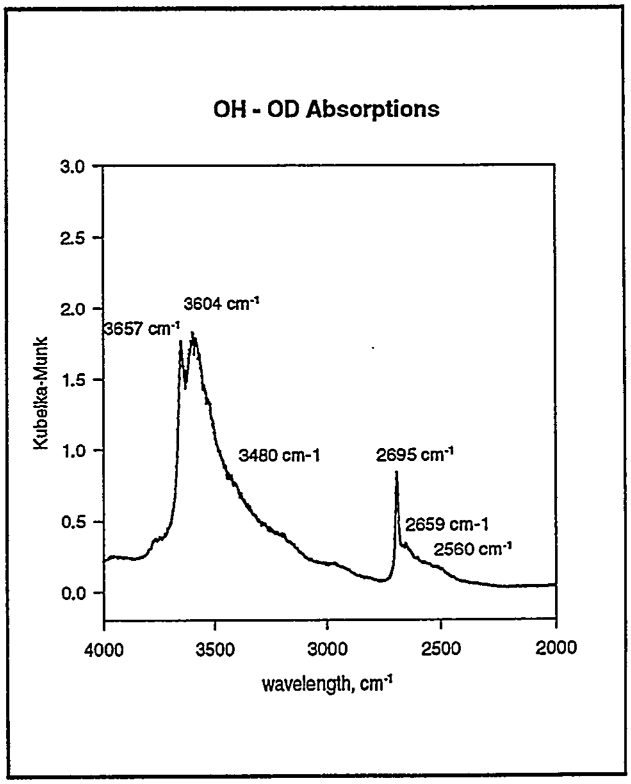

Figure 3

Correponding OD peaks have been observed at 2695, 2659, and 2570 cm^{-1} upon exposure to D_2 (the OD peak corresponding to the OH peak at 3400 cm-1 has not yet been observed, probably due to the very low intensity of this OH peak under the conditions investigated). These absorptions indicate that there are four different OH species on the surface. We propose that these different OH groups are due to OH groups with different coordination numbers, 2, 4, 6 and 8. The strength of the OH bond, and therefore the OH vibration frequency, will depend on the electron density on the oxygen. As the electron density on the oxygen is reduced by coordination to Li atoms in the lattice the O-H bond strength should decrease, decreasing the frequency of the absorption. This is similar to the effect seen for IR absorptions of terminal versus bridging carbonyl groups.

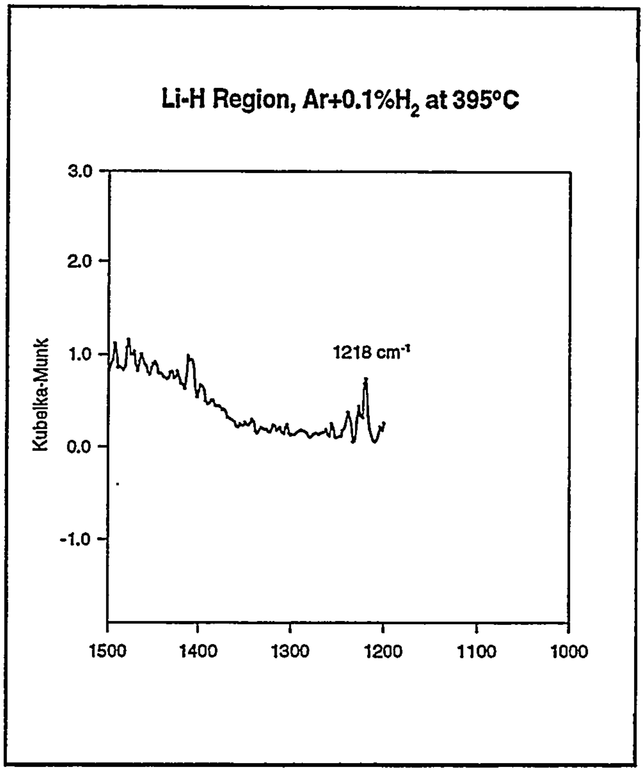

Figure 4

Under certain conditions we have seen infrared absorptions in the region where a Li-H stretch is expected. These infrared absorptions at 1245 to 1212 cm^{-1} are shifted to slightly lower frequencies than that observed for lithium hydride (1280 cm^{-1}). The hydride absorption in the infrared was generally seen at temperatures of about 380°C and higher. Confirmation that this is a Li-H absorption by isotopic substitution with deuterium has not been possible since the deuterium peak would be shifted to a position beyond the absorption edge. However, these absorptions have only been seen in a purge gas containing hydrogen. At 395°C with a purge gas of Ar+0.1% hydrogen an absorption is observed at 1218 cm^{-1}, when the purge gas is changed to pure Ar this peak disappears. (Figs. 4 and 5), giving a strong indication that this absorption is due to the presence of a Li-H species on the surface. The presence of an Li-H species on the surface suggests that hydrogen is adsorbed on the surface heterolytically to form H^+ (OH^-) and H^- (Li-H). Quantum mechanical calculations indicate this type of heterolytic adsorption is expected on some lithium oxide surfaces.[4]

Preliminary kinetic studies have been performed. The decomposition of the hydroxyl species was followed at 400°C by recording the spectra at about 10 minute intervals (see Fig. 6). The preliminary data for the decomposition of the main peak at 3657 cm^{-1} appears consistent with a first order desorption which is an order of magnitude slower than that reported for the decomposition of bulk LiOH, however more data are needed. The decompositions of the secondary peaks do not appear to follow first-order processes. The secondary hydroxyl peaks tend to remain constant until the peak at 3657 cm^{-1} has decayed substantially before they start to decay. This complicated kinetics may be the reason for the difficulty interpreting the sharp peaks seen in the TPD curves and requires more study.

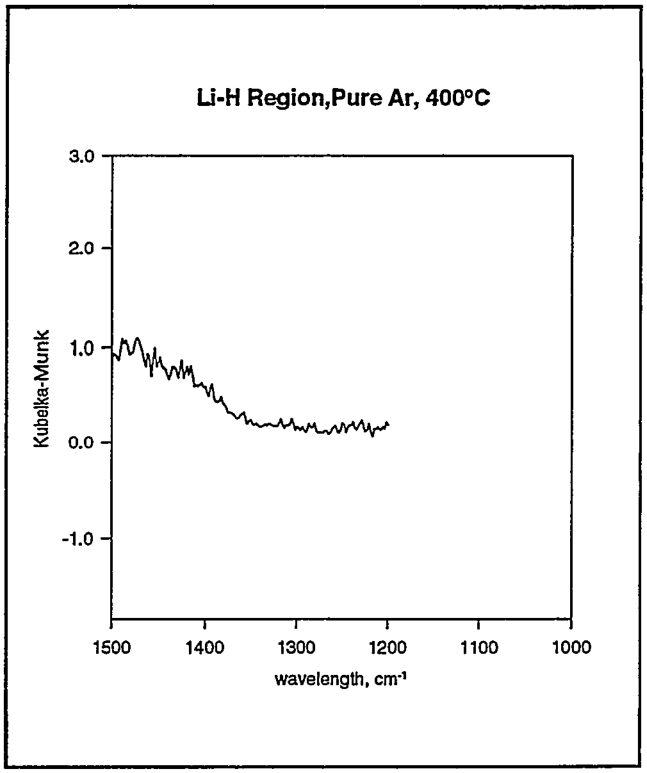

Figure 5

DRIFTS-TPD

As part of a preliminary study to determine the applicability of a combined TPD-DRIFTS experiment a psuedo TPD experiment was performed while recording the diffuse reflectance infrared spectra at discreet times during the temperature increase. Limitations in the apparatus relegated the experiment to a maximum temperature of 400°C and resulted in a heating ramp which was not quite linear so no quantitative information regarding the activation energies could be obtained. However, the results do provide some qualitative answers and indicate that the technique of combined TPD-DRIFTS should be pursued. The pressure-time curve for mass 18 during the temperature ramp is shown in Fig. 7.

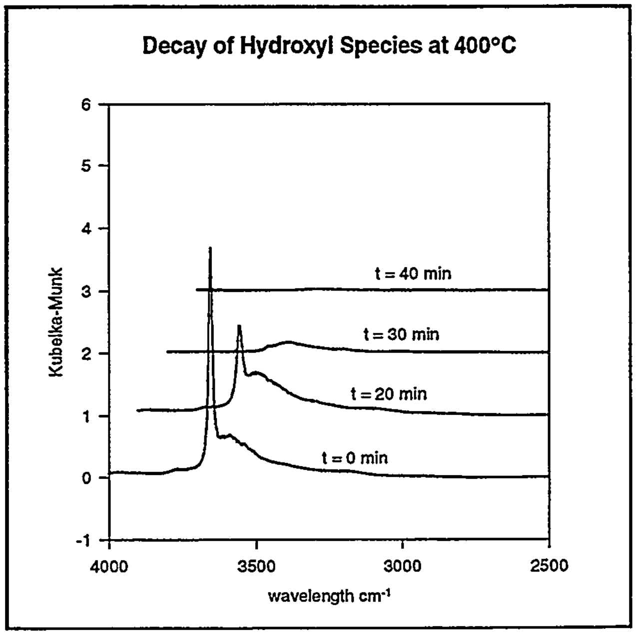

Figure 6

Identical curves were obtained for mass 17 and 19. The infrared spectra show no changes in the spectra until after the desorption peak has started in the TPD. While the desorption peak is rising in the TPD a decrease is seen in the OH absorption intensity at 3657 cm^{-1} . After the TPD peak has reached its maximum, the OH peak at 3657 has disappeared in the infrared spectra (Fig. 8, 395°C curve). At this point, a Li-H peak is seen in the infrared. (Fig. 9, 395°C curve)

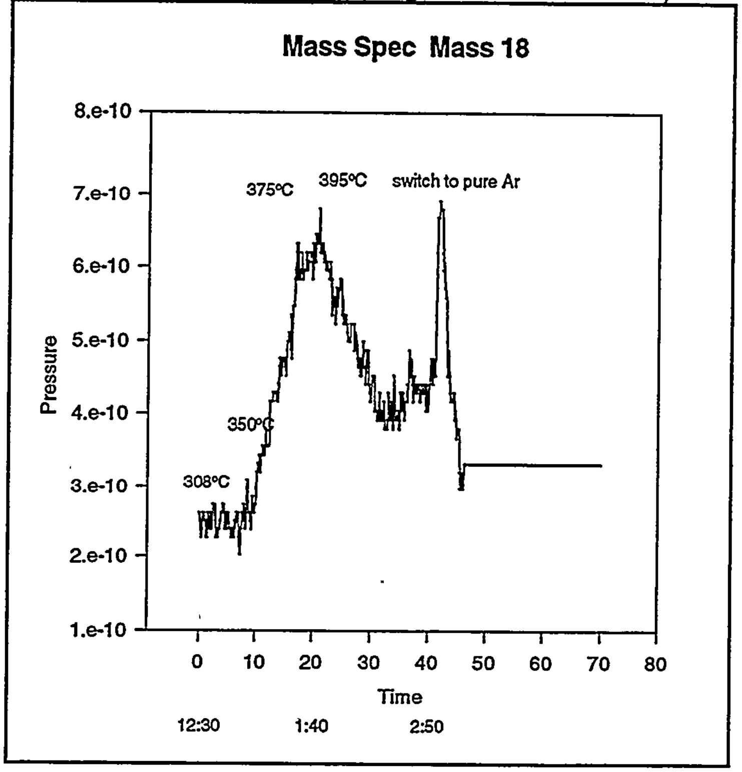

Figure 7

The combination of the TPD curve and the DRIFTS results suggest that the TPD peak observed at about 663K (390°C) is due mainly to removal of the OH species seen in the infrared at 3657 cm^{-1} from the surface. The observation of this species at the surface and the observed change in the concentration of this species with time indicate that the rate controlling mechanism for the disappearance of this peak is not bulk diffusion. If bulk diffusion was the rate controlling process, one would expect the surface concentration to be near zero and for there not to be an appreciable change in the surface concentration of this species during the TPD peak. The combination of the TPD and DRIFTS also indicates that the hydride species is not observed untill the OH species at 3657 cm^{-1} is absent. One possible explanation is that these hydroxide groups occupy the sites at which H^- adsorbs.

Conclusions

Our studies have indicated that there are four different types of hydroxyl groups which can be observed on a lithium oxide surface. The particular species present vary depending on the temperature and hydrogen pressure of the system. Under some conditions where hydrogen is present in the purge gas surface hydride species have been observed. This suggests heterolytic adsorption of hyrdogen has occured.

These studies indicate that the combination of temperature programmed desorption and diffuse reflectance infrared spectroscopy provides a valuable method for studying surface processes. The combination of these methods overcomes the shortcomings of the individual methods, and allows one to determine correlations between species observed on the surface and those detected in the gas phase downstream.

Future Work

The current studies have been limited to temperatures below 400°C. Future work will investigate the surface interactions at temperatures up to about 700°C using the combination of diffuse reflectance infrared spectroscopy and temperatrure programmed desorption.

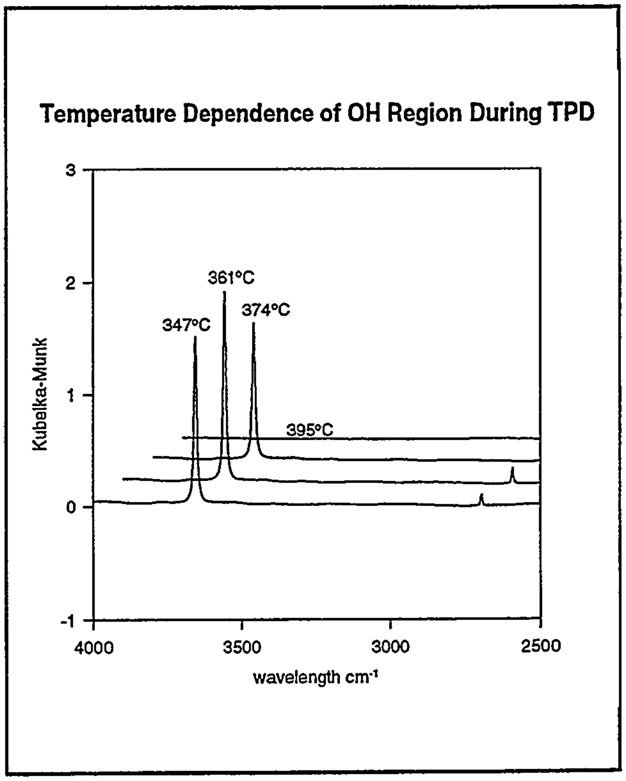

Figure 8

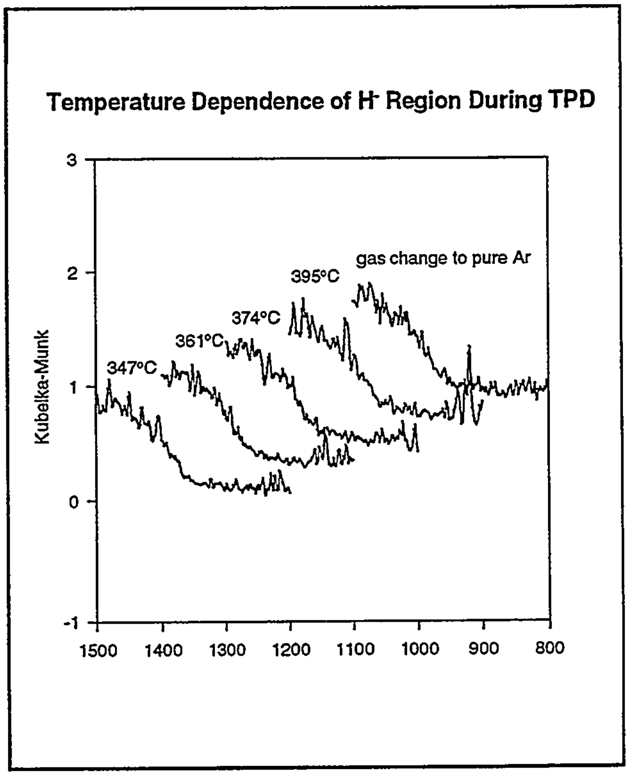

Figure 9

References

[1] J. L. Falconer and J. A. Schwarz, Catal. Rev. -Sci. Eng., 25(2),(1982)141.
[2] S. Tanaka, D. Yamaki, and M. Yamawaki, Proceedings of the International Workshop on Ceramic Breeder Interactions, (Paris , Sept. 22-24, 1993) CE Saclay, Paris, France, 1994 p. 257.
[3] A. K. Fischer and C. E. Johnson, J. Nucl. Mater. 179,812-815,1991.
[4] A. Sutjianto, S. W. Tam, L. A. Curtiss, and C. E. Johnson, Proceedings of the Fourth Symposium on the Fabrication and Properties of Fusion Ceramics, to be published in J. Nucl. mater.

8.0 CERAMICS

FATIGUE CRACK GROWTH RATE (FCGR) BEHAVIOR OF NICALON/SiC COMPOSITES

– N. Miriyala, P. K. Liaw, N. Yu and C. J. McHargue (University of Tennessee), L. L. Snead (Oak Ridge National Laboratory) and D. K. Hsu (Iowa State University).

OBJECTIVE

To develop a fundamental understanding of fatigue crack growth phenomenon in Nicalon/SiC composites.

SUMMARY

Ultrasonic measurements were continued on the Nicalon/SiC composite specimens to correlate elastic moduli with percentage porosity in the in-plane as well as through-thickness directions. A micromechanics model based on periodic microstructure was developed to predict the elastic stiffness constants of the Nicalon/SiC composites. The predicted values were in good agreement with the experimental results.

PROGRESS AND STATUS

Introduction

Ceramic matrix composites (CMCs) are attractive candidate materials for high-temperature structural applications because of their low density and ability to withstand higher temperatures and more aggressive environments than most metals or other conventional engineering materials [1-3]. Although CMCs are now being considered seriously for many potential structural applications, they can be susceptible to degradation under cyclic fatigue loading, even when such loading is fully compressive. However the field of "fatigue in ceramics" is still in its infancy and much work is yet to be done to understand the mechanical behavior of fiber reinforced ceramic matrix composites [4]. In view of the above, it has been decided to study the fatigue crack propagation behavior of Nicalon/SiC composites processed by the Forced Chemical Vapor Infiltration (FCVI) technique, using the ASTM standard E 647-92 for the measurement of fatigue crack growth rate in metallic materials.

Nicalon/SiC composites processed by the FCVI technique have a fabric lay-up of $[0\text{-}30/30\text{-}120/60\text{-}150]_n$. From earlier work [5] it was observed that there are two major types of porosity in the Nicalon/SiC composites, viz.. porosity between the fiber tows and interlaminar porosity . Also, the composite is highly anisotropic and, therefore, it is only to be expected that the mechanical properties of the material will vary significantly along different directions and with different levels of densification. These effects are inherent from the fabrication process used to manufacture the composite material.

Compliance measurements are widely used to measure the crack length as well as characterize the near crack tip field phenomena during monotonic and fatigue crack growth testing. However, the elastic modulus of each sample has to be known to permit the use of the technique. In view of the variation in density values, and consequently moduli values from specimen to specimen, and also to develop an indirect method for measuring the moduli values, ultrasonic measurements were made on the specimens.

Apart from being able to experimentally measure the mechanical properties of the composites, it is also necessary to develop theoretical models to predict the properties of the composite material from the knowledge of the properties of the constituents (fiber and matrix) that we already know. However, there have been only a very few attempts so far to predict the moduli of woven fabric composites [6]. Hence, it was decided to develop a theoretical model to predict the elastic stiffness constants of the Nicalon/SiC composites. A homogenization method was used in the analysis, wherein it is possible to transform a heterogeneous unit cell of the composite material into a homogeneous one comprising of the matrix only, prescribing stress-free (eigen) strains.

Ultrasonic Measurements

Based on acoustic wave theory [7,8] the elastic stiffness constant (C) can be expressed as a function of ultrasonic velocity as

$$C = \rho * V^2 \quad \text{...(1)}$$

Where ρ = density of the material,
V = Ultrasonic Velocity

From longitudinal and shear wave ultrasonic velocity measurements we can estimate the elastic stiffness constants of the material using equation (1). Longitudinal measurements were performed by 'dry coupling' to avoid possible contamination by the couplant. A 'pulse-echo overlap method' was used to measure the wave velocities. A schematic of the experimental setup for longitudinal measurements is shown in Figure 1. The reference signal is obtained by passing ultrasonic waves through a reference test system comprised of a rubber sheet and a fused quartz piece. The test sample is then placed between the transmitting transducer and the rubber sheet reference test system and ultrasonic waves are passed through the setup. The signals are received by the receiving transducer and captured by an oscilloscope. The signal peaks from the reference test system, with and without the presence of sample, are matched as closely as possible, and from the phase shift between the two the time taken by the ultrasonic waves to travel through the sample is measured. The thickness of the sample divided by the time taken for the ultrasonic waves to pass through the sample is taken as the ultrasonic velocity through the sample. Since the two signals are matched as closely as possible (i.e. overlapped), this technique is referred to as the pulse-echo overlap method.

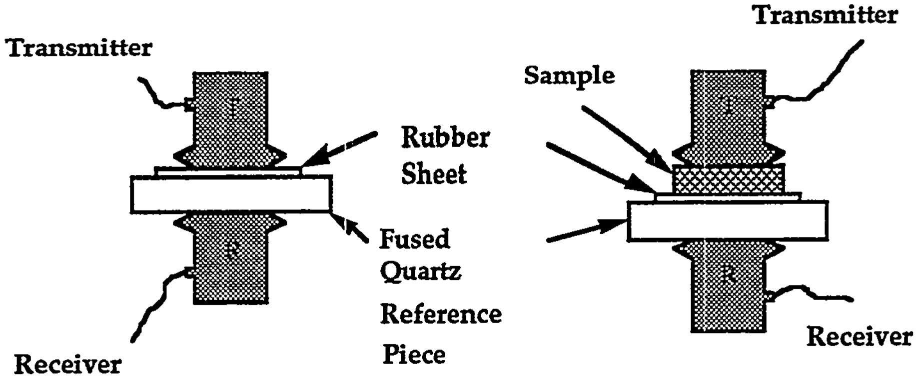

(a) Reference Test System without the Presence of Sample

(b) Test System with the Presence of Sample

Figure 1. Ultrasonic Measurement Setup

Longitudinal wave measurements were made in the in-plane as well as through-thickness orientations. For the shear wave velocity measurements the same setup as in Figure 1 was employed except that the rubber sheet was eliminated and regular contact mode shear wave transducers were coupled with burnt honey. Honey was also used for the coupling between the sample and the reference quartz plate. Because the shear couplant was highly viscous and the area fraction of surface breaking voids on the in-plane surfaces was much less than that on the edges, the effect on velocity due to couplant-filled voids was believed to be small. In this setup the shear wave propagated through the sample in the thickness direction and the polarization direction was in-plane. The polarization vectors of the two transducers were aligned with aligned with each other but not to any particular fiber direction in the plane of the composite laminate.

The density of the samples varied from 2.06 to 2.63 g/cm^3 and the porosity from 11.5 to 30.4%. The longitudinal and shear moduli values are plotted against percent porosity in Figures 2 and 3. It is apparent from Figures 2 and 3 that porosity has a dramatic effect on lowering the moduli values of the composites. From Figure 2 it can also be seen that the longitudinal moduli in the in-plane direction (129 to 248 GPa) were greater than in the through-thickness direction (5.6 to 138.2 GPa), as is to be expected from the fabric lay-up. Shear moduli values of the composites (9.9 to 57.9 GPa) were much lower than the longitudinal moduli values (Figure 3).

Theoretical Modeling

A micromechanics model based on periodic microstructure was developed to estimate the effect of porosity on the elastic properties of the Nicalon/SiC composites. As shown in Figure 4, a representative unit cell, which is repeated in all directions, consists of eight woven fiber tows in the shape of elliptic cylinders and one parallelepiped that is used to model the interlaminar porosity.

When the infinite composite with a periodic microstructure is subjected to a homogeneous strain field, ε^0, due to the existence of periodically distributed fibers and voids, the resulting stress and strain fields are $\sigma^0+\sigma^p(x_1, x_2, x_3)$ and $\varepsilon^0+\varepsilon^p(x_1, x_2, x_3)$, where σ^0 and ε^0 are homogeneous (average) stresses and strains, σ^p and ε^p the periodic disturbance stress and strain fields, respectively. The elastic moduli of the composite are defined by Equation (2).

$$\{\sigma^o\} = [\overline{C}]\{\varepsilon^o\} \quad \text{...}(2)$$

Based on Eshelby's [9] concept of transformation strain, one can replace the porous heterogeneous unit cell by a homogeneous cell comprised of matrix material only and prescribe stress-free strains in the fibers (Ω_1) and voids (Ω_2) such that the average stress and average strain fields remain the same everywhere in the unit cell before and after the homogenization. That is, the following consistency conditions [Equation (3)] must hold:

$$[C^{\Omega_1}]\left\{\varepsilon^o+\langle\varepsilon^p\rangle_{\Omega_1}\right\}=[C^M]\left\{\varepsilon^o+\langle\varepsilon^p\rangle_{\Omega_1}-\varepsilon^{*1}\right\} \quad \text{in } \Omega_1 \text{ ....}3(a)$$

$$[C^{\Omega_2}]\left\{\varepsilon^o+\langle\varepsilon^p\rangle_{\Omega_2}\right\}=[C^M]\left\{\varepsilon^o+\langle\varepsilon^p\rangle_{\Omega_2}-\varepsilon^{*2}\right\} \quad \text{in } \Omega_2 \text{ ....}3(b)$$

where the angle brackets with the subscript Ω_1 (Ω_2) represent the volume average over Ω_1 (Ω_2); C^{Ω_1}, C^{Ω_2}(= 0), and C^M are the stiffness of fibers, voids, and matrix, respectively; ε^{*1} and ε^{*2} are the stress-free homogenization strains prescribed in fibers and voids and are approximated by distinct constants. The average periodic disturbance strains can be related to the stress-free strains [10] by

$$\langle\varepsilon^p\rangle_{\Omega_\alpha}=\left[\hat{\Gamma}\right][C^M]\sum_{n_1,n_2,n_3}^{\pm\infty}\left(f_{\Omega_1}g_1g_\alpha\{\varepsilon^{*1}\}+f_{\Omega_2}g_2g_\alpha\{\varepsilon^{*2}\}\right) \quad \text{for } \alpha=1, 2 \text{ ....}(4)$$

where the term $(n_1, n_2, n_3) = (0,0,0)$ is excluded in the summation, and the components of the fourth-order tensor, Γ, are given by

$$\hat{\Gamma}=\frac{1}{G^M}\left(\xi_\alpha^2-\frac{1}{2(1-\nu^M)}\xi_\alpha^4\right) \quad \text{for } \alpha = 1, 2, 3$$

$$\hat{\Gamma}_{\alpha\beta}=\hat{\Gamma}_{\beta\alpha}=\frac{-1}{2G^M(1-\nu^M)}\xi_\alpha^2\xi_\beta^2 \quad \text{for } (\alpha, \beta) = (1, 2), (2, 3), (3, 1)$$

$$\hat{\Gamma}_{\alpha\alpha} = \frac{1}{G_M}\left(\frac{1}{4}\left(\xi_\beta^2+\xi_\gamma^2\right) - \frac{1}{2(1-\nu^M)}\xi_\beta^2\xi_\gamma^2\right)$$

for (α, β, γ) = (4, 2, 3), (5, 3, 1), (6, 1, 2)

$$\hat{\Gamma}_{\alpha\beta} = 0 \quad \text{otherwise}$$

and

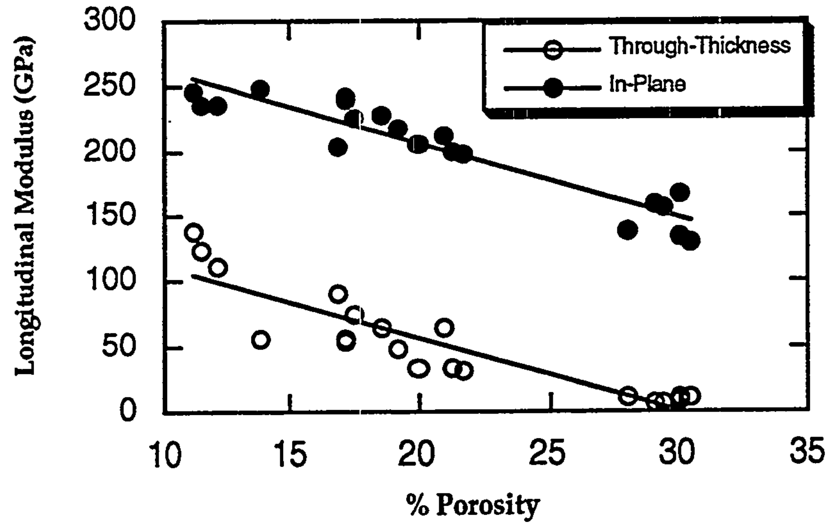

Figure 2. Longitudinal Moduli vs. % Porosity in Nicalon/SiC Composites

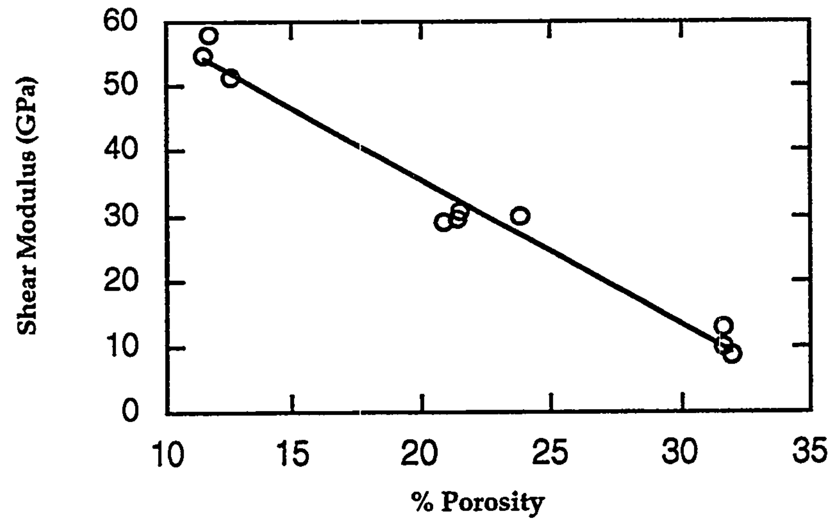

Figure 3. Shear Moduli vs. % Porosity in Nicalon/SiC Composites

$$\xi_i = \frac{n_i}{a_i\sqrt{\left(\frac{n_1}{a_1}\right)^2+\left(\frac{n_2}{a_2}\right)^2+\left(\frac{n_3}{a_3}\right)^2}} \qquad \text{for } i = 1, 2, 3;$$

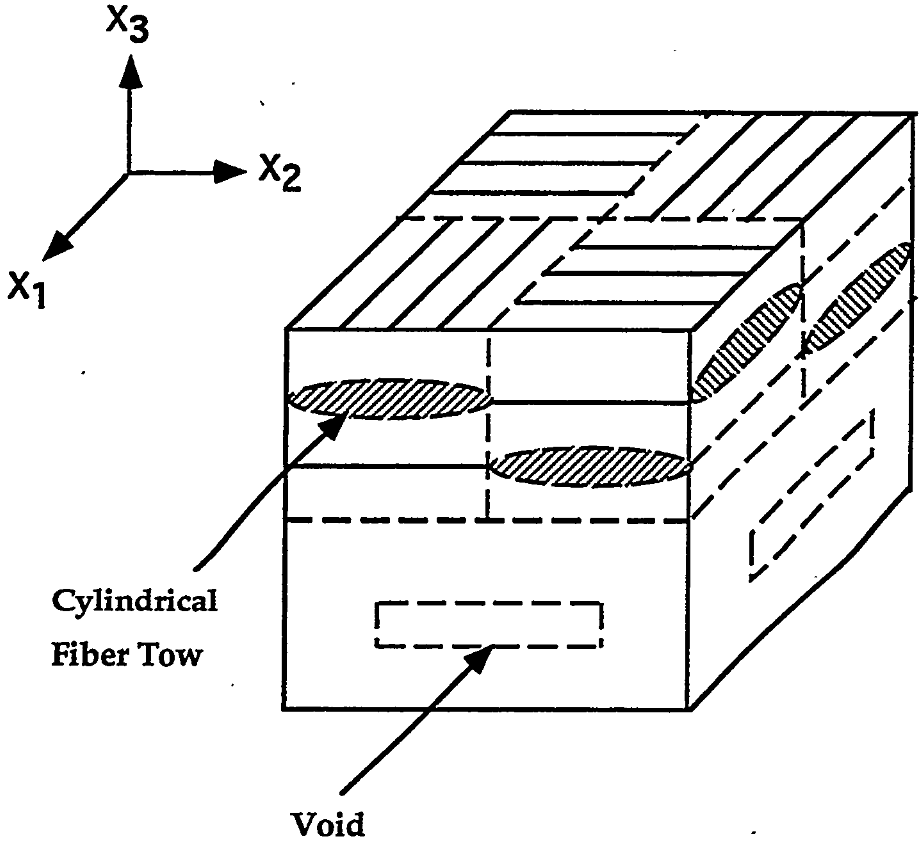

Figure 4. A Model Based on Periodic Microstructure

G^M and ν^M are the shear modulus and Poisson's ratio of the matrix; a_i (i =1, 2, 3) are the dimensions of the unit cell; n_i are integers; f_{Ω_1} and f_{Ω_2} are fiber and void volume fractions, respectively. The shape and size of the fibers and voids are accounted for in g_1 and g_2. For elliptic-cylindrical fiber tows,

$$g_1 = \frac{1}{2}\cos\left(\frac{\pi n_1}{2}\right)\cos\left(\frac{\pi n_2}{2}\right)\cos\left(\frac{\pi n_3}{4}\right)\cos\left(\frac{\pi n_3}{2}\right)(g_A + g_B)$$

where

$$g_A = \frac{2\sin\left(\frac{\pi n_2 c_2}{a_2}\right) J_1\left(\pi\sqrt{\left(\frac{n_1 c_1}{a_1}\right)^2 + \left(\frac{n_3 c_3}{a_3}\right)^2}\right)}{\left(\frac{\pi n_2 c_2}{a_2}\right)\left(\pi\sqrt{\left(\frac{n_1 c_1}{a_1}\right)^2 + \left(\frac{n_3 c_3}{a_3}\right)^2}\right)}$$

$$\text{and } g_B = \frac{2\sin\left(\frac{\pi n_1 c_1}{a_1}\right) J_1\left(\pi\sqrt{\left(\frac{n_2 c_2}{a_2}\right)^2 + \left(\frac{n_3 c_3}{a_3}\right)^2}\right)}{\left(\frac{\pi n_1 c_1}{a_1}\right)\left(\pi\sqrt{\left(\frac{n_2 c_2}{a_2}\right)^2 + \left(\frac{n_3 c_3}{a_3}\right)^2}\right)}$$

with c_1 (or c_2) and c_3 being the principal radii of the elliptic cross-section and c_2 (or c_1) the length of the cylinder; J_1 is the Bessel function of the first kind. For a parallelepiped,

$$g_2 = \cos\left(\frac{n\pi_3}{2}\right)\frac{\sin\left(\frac{\pi n_1 b_1}{a_1}\right)\sin\left(\frac{\pi n_2 b_2}{a_2}\right)\sin\left(\frac{\pi n_3 b_3}{a_3}\right)}{\left(\frac{\pi n_1 b_1}{a_1}\right)\left(\frac{\pi n_2 b_2}{a_2}\right)\left(\frac{\pi n_3 b_3}{a_3}\right)}$$

where b_1, b_2 and b_3 are the dimensions of the parallelepiped.

After solving the consistency conditions for suitable ε^{*1} and ε^{*2}, which preserve the same stress and strain fields before and after homogenization, the elastic moduli of the porous woven-fabric composites are thus determined by Equation (5).

$$[\bar{C}]\{\varepsilon^\circ\} = [C^M]\left(\{\varepsilon^\circ\} - f_{\Omega_1}\{\varepsilon^{*1}\} - f_{\Omega_2}\{\varepsilon^{*2}\}\right) \quad \text{..................................(5)}$$

To calculate the moduli of the composites, the following input data were used [11]; the shear modulus and Poisson's ratio of the Nicalon^{TM} fiber were 80 GPa and 0.12, respectively, and those of the matrix were 146 GPa and 0.2. The predicted values are plotted in Figure 5 along with the experimental results. It can be seen that there is an excellent agreement between the theoretically predicted values and measured elastic moduli.

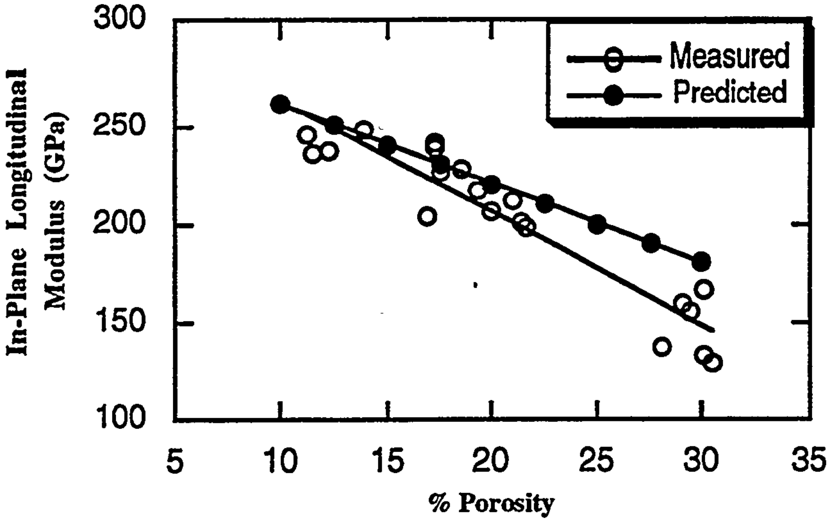

Figure 5. Comparison of Predicted and Measured In-Plane Longitudinal Moduli

FUTURE WORK

(i) Fatigue crack growth testing of the C(T) specimens under different loading conditions at ambient as well as elevated temperatures.

(ii) Fractography of the specimens to assess the various damage and crack shielding mechanisms that govern the fatigue and fracture behavior of the Nicalon/SiC composites.

ACKNOWLEDGMENTS

This work is supported by the Department of Energy under contract No. Martin Marietta 11X-SL261V to the University of Tennessee. We are grateful to Dr. Arthur Rowcliffe and Dr. Everett Bloom of ORNL for their continued encouragement and support in our endeavors.

REFERENCES

[1] K. K. Chawla, Ceramic Matrix Composites (Chapman & Hall, London, 1993) pp. 4-10.
[2] J. A. DiCarlo, Adv. Mater. & Proc., 135 (June 1989) 41.
[3] T. M. Besmann, B. W. Sheldon, R. A. Lowden and D. P. Stinton, Science, 253 (1991) 1104.
[4] R. H. Duaskardt, R. O. Ritchie and B. N. Cox, Advanced Materials and Processes, 144 (August 1993) 30.
[5] P. K. Liaw, D. K. Hsu, N. Yu, N. Miriyala, V. Saini, H. Jeong and K. K. Chawla, Proc. Int. Symp. on High Performance Composites: Commonalty of Phenomena, Rosemont, Illinois, USA, October 2-6, 1994, eds. K. K. Chawla, P. K. Liaw and S. G. Fisherman (TMS, Warrendale, 1994) 377.
[6] N. J. Fang and T. S. Chou, J. Am. Ceram. Soc., 76 (1993) 2539.
[7] H. Jeong, D. K. Hsu, R. E. Shannon and P. K. Liaw, Metallurgical Transactions A, 25 A (1994) 799.
[8] H. Jeong, D. K. Hsu, R. E. Shannon and P. K. Liaw, Metallurgical Transactions A, 25 A (1994) 811.
[9] J. D. Eshelby, Proc. R. Soc. London, A241 (1957) 376.
[10] S. Nemat-Nasser, N. Yu, and M. Hori, Mech. Mater., 15 (1993) 163.
[11] J. L. Bohet, Ph. D Thesis, Bordeaux, France, 1993.

ADVANCED SiC COMPOSITES FOR FUSION APPLICATIONS – Lance L Snead and Otto J Schwarz (Oak Ridge National Laboratory)

OBJECTIVE

This is a short review of the motivation for and progress in the development of ceramic matrix composites for fusion.

SUMMARY

Chemically vapor infiltrated silicon carbide (SiC) composites have been fabricated from continuous fibers of either SiC or graphite and tested for strength and thermal conductivity. Of significance is that the Hi-Nicalon^{TM} SiC based fiber composite has superior unirradiated properties as compared to the standard Nicalon grade. Based on previous results on the stability of the Hi-Nicalon fiber, this system should prove more resistant to neutron irradiation. A graphite fiber composite has been fabricated with very good mechanical properties and thermal conductivity an order of magnitude higher than typical SiC/SiC composites.

PROGRESS AND STATUS

Introduction

The benefit of silicon carbide based materials for fusion reactors has been discussed for many years,[1,2] primarily due to their inherently low induced radioactivities. The application of such a low activation material offers several advantages in the areas of safety, maintenance, and disposal, and is one of the reasons that fusion is considered an attractive future energy source. This was, in fact, the conclusion of the 1988 Department of Energy sponsored report,[3] "Exploring the Competitive Potential of Magnetic Fusion Energy," which compared the future outlook of fossil, fission, and fusion energy.

It is important to note that considerable benefit can be achieved from selective utilization of low activation materials such as SiC composites without completely replacing the higher activity metallic structure, as was proposed in recent reactor studies such as ARIES.[4] In fact, based on our current belief in what a commercial fusion plant will look like, the materials requirements for such a reactor are so diverse and demanding that the exclusive use of low activation materials is very unlikely. However, as the economic and safety benefit of these materials scales with volume of irradiated reactor structure, the goal for the application of low activation materials should be to gain as large a fraction of reactor structural material as possible.

At this time there are no large scale industrial applications of SiC composite materials as load bearing structures and there are only limited data on general engineering properties such as strength and fatigue. It is therefore premature to purport their use in the most extreme environments of a fusion reactor such as the first wall or the divertor plate. In these structures, not only will the static and cyclic loads be extremely high, but they would routinely be subjected to heat loads[5] as high as 15 MW/m^2, and would experience damage levels of tens of displacements per atom (DPA) per year.

There are far less harsh environments in a fusion machine where low activation ceramic composites could be applied in the near-term. Table 1 illustrates the possible regions where ceramic composites could replace metallic structure. This table is based on preliminary design reports for the international thermonuclear experimental reactor (ITER).[5] The ITER fusion core structure is broken down in this table into 5 components and listed in order of decreasingly demanding material requirements (i.e. reduced heat flux and radiation dose). Of significance in this table is that the components which are subjected to the highest heat flux and radiation dose (i.e. areas in which the use of ceramic composites is the most speculative), also correspond to the components with the smallest reactor volume fraction. It is seen that the two reactor components which dominate the volume fraction are the shield and magnet which, due to their reactor location, are also subjected to moderate loads. At least in the near term, utilization of low activation

Table 1. Summary of Major Fusion Reactor Components

			Fusion Core		
Component	Volume* m3 (%)	Dose Activation	Stress MPa	Hermeticity	Development Timescale
First Wall					
Plasma Face	18 (0.2)	**Highest**	High	Not necessary	In-use
Structure	20 (0.2)			Necessary	Very long term
Divertor					
Plasma Face	8 (0.1)		High	Not necessary	In-use
Structure	32 (0.3)			Necessary	Very long term
Blanket					
Breeder	1500				
Structure	300 (3.2)		<200+	Desirable	Near to long term
Shield	1000 (11.0)		<150++	Not necessary	Near term
Magnet					
Conductor	3040				
Structure	8100 (85.5)	**Lowest**	300 (ave.)	Not necessary	Near to long term

materials such as silicon carbide should then focus on replacement of structure in these regions. Also of consideration in reducing the amount of activated structure is that some components are "lifetime" components, such as the vacuum vessel and magnet structure, and some components will require routine change-out, such as the blanket modules. Because of this it is necessary to take the frequency of change-out and the component volume into the overall assessment.

As the stresses expected in fusion reactor structures are substantial, monolithic ceramic components cannot be considered due to their brittle failure mode. For this reason, composite materials, which have a higher degree of toughness and a more uniform statistical distribution of failure (i.e. higher Weibull's modulus), are being considered. While there has been very limited study into the effects of neutrons on SiC composites, the available data show a substantial degradation in mechanical and thermal properties of conventional SiC/SiC at damage levels as low as 1 dpa.[6,7] To this point, all SiC/SiC radiation effects studies have used material processed with Nippon Carbon's Ceramic Grade (Standard) Nicalon fiber. The choice of this fiber is largely due to its excellent mechanical properties and good weavability. The cost and availability of this fiber has also made it attractive to composite manufacturers.

The reason for the significant degradation in mechanical properties seen in Nicalon based SiC/SiC composites is not due to a response in the SiC phase itself, but to the non-SiC phases in the fiber. As discussed in a separate paper,[8] the presence of a substantial siliconoxycarbide phase in the standard grade of Nicalon causes a radiation induced densification and subsequent interfacial debonding leading to reduced composite strength. The composite degradation is demonstrated in Figure 1, which shows flexure curves for both unirradiated and neutron irradiated composite. This plot includes both previously reported data[6] and new data to 20 dpa (displacement energy of carbon assumed). Also given are measured elastic moduli for the matrix (E_m) and the fiber (E_f).

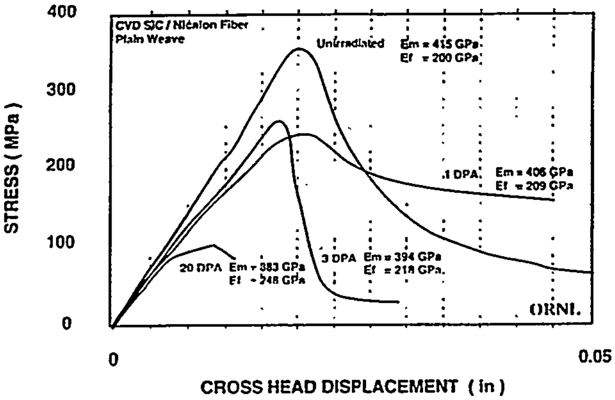

Figure 1: Effect of neutron irradiation on room temperature bend strength of Nicalon composites at temperatures under 500°C.

Table 2. Data on Candidate Fiber Reinforcements

Fiber	Make-up	Structure	σ (GPa)	E (GPa)	ρ (g/cc)	Comment
Nicalon	65% SiC, 23% SiO2, 11% C	3 nm ß-SiC	3	220	2.55	available
Hi-Nicalon	75% SiC, 21% C ~ other	~6 nm ß-SiC	2.8	270	2.74	limited availability
Textron SCS-6	SiC on C core	faulted ß-SiC	3.45	370	3.15	not weavable
Dow Corning SiC	>95% SiC, free C	0.5 µm ß-SiC	2.6	420	~3.1	not available
MER converted	SiC and free C	~0.1 µm ß-SiC	2.0	–	<3.1	developmental
Amoco k1100	Graphite	highly aligned	2.76	900	2.15	limited availability

Based on the significant degradation of these SiC composites, a search for more radiation resistant fibers has been undertaken. Table 2 gives specifics of six candidate fibers including Nicalon for reference. Currently, the most interesting fiber from a radiation damage standpoint is the Hi-Nicalon material, which is processed from the same polymer precursor as standard Nicalon, but has been cured with electrons rather than oxygen.[9] This process reduces the atomic oxygen content from greater than 15% (standard Nicalon) to less than 0.5%.[9] Note from the table that the average SiC crystallite size has been increased for this material while the strength has been slightly reduced and the modulus of the fiber has significantly increased. The density of the Hi-Nicalon is also increased from 2.55 g/cc (standard Nicalon) to 2.74 g/cc, which is approximately 85% of the theoretical density. Recent measurements[8] on Hi-Nicalon following low temperature, low fluence irradiation, showed that the rapid densification seen in standard Nicalon did not occur, and that the irradiated tensile properties behaved as would be expected for a "pure" SiC fiber.

Another popular commercial SiC fiber is processed by chemical vapor deposition of SiC on to a pitch carbon core. This is the process which is used to produce the Textron SCS-6 fiber, for example.[10] The pitch carbon filament used is 33 µm in diameter and the finished CVD SiC fiber is typically 140 µm in diameter. The size of this fiber and consequently its stiffness makes it not possible to weave and fabricate composites with complex geometries. However, if the diameter were decreased substantially, this fiber would have very attractive features from a radiation resistance point of view, as its unirradiated and irradiated properties would be very similar to chemically vapor infiltrated (CVI) SiC matrix.

Also of interest is the MER[11] converted SiC fiber. The process for conversion follows the general reaction:

$$2C(s) + SiO(g) = SiC(s) + CO(g)$$

Graphite tows or fabric are simply reacted in a high temperature furnace (at 1300 to 2000°C) with silicon monoxide gas and converted from the outside of the fiber inward. Fiber strengths greater than 2 GPa have been reported[12] with elastic moduli approaching that of pure silicon carbide. The microstructure of these fibers depends on the grain structure of the starting graphite fiber but are typically microcrystalline with grain sizes varying from 25 nm to 100 nm. Fiber density is in the range of 2.8 to 3.1 g/cc. depending on processing conditions and the final composition being free of excess silicon. Of particular interest for these fibers is the good high temperature strength and excellent creep resistance.

There has recently been progress in both sintered SiC fibers[13] and for advanced polymer precursor fibers.[14] Dow Corning's polymer precursor fiber is melt-spun, cross linked and heated to above 1600°C under argon to drive off oxygen in the form of CO. Such a process would normally result in large-grained, porous material. However, through the incorporation of certain additives, a high density SiC fiber results. The quoted composition[14] of the Dupont fiber is >95% ß-SiC with a crystallite size of ~0.5 µm, along with excess carbon in the form of graphite at the crystallite boundaries. The oxygen and nitrogen content is <0.1 weight percent.

The purpose of this paper is to show the progress made in the fabrication of composites of interest for fusion. Specifically, all composites have been fabricated through the chemical vapor infiltration (CVI) of SiC. Three fiber systems were chosen: Nicalon (standard and the low-oxygen "Hi-Nicalon"), MER converted SiC fiber from Amoco T-300 graphite cloth, and a high conductivity (Amoco K-1100) graphite fiber. The rationale behind studying a CVI SiC/graphite fiber composite system will be discussed later. Two of the SiC-based fibers listed in Table 2 were not fabricated into composites for this study for practical reasons. The Textron AVCO SCS-6 was not considered, primarily due to difficulty in weaving (as mentioned earlier). The Dow Corning polymer precursor material was unavailable, though it would seem an attractive system from a radiation damage standpoint, and should be evaluated when material is released.

Experimental procedure

All materials for this study were processed at the High Temperature Materials Laboratory at the Oak Ridge National Laboratory using the forced chemical vapor infiltration (FCVI) method.[15] The infiltrated silicon carbide matrix was deposited from methyltrichlorosilane. The typical process temperature and time for infiltration was 1200°C and 18 hrs, respectively. The dimensions of the as fabricated disks were 4.45 cm in diameter and 1.25 cm thickness. For each composite a graphitic interface was applied to the composite prior to SiC infiltration by decomposition of propylene gas at 1100°C. Previous work has shown that the structure of interfaces deposited in this manner on Nicalon are partially graphitic with basal planes lying normal to the axis of the fiber.[16]

For the case of SiC/SiC composites, 1k denier (thousand filament yarn) plain weave fabric was laid-up inside a graphite holder with a fiber volume fraction of approximately 40% in the case of the Nicalon fiber and approximately 30% for the MER converted SiC fiber. Due to the highly crystalline nature of the MER converted fiber, it was felt that applying pressure normal to the fabric lay-ups could crack the fibers, thus a reduced fiber volume was chosen. The Nicalon fiber composites were processed with an interfacial graphite thickness of ~0.3 µm, while a range of interfacial thicknesses were chosen for the MER converted SiC fiber. A third composite was fabricated from alternate layers of ceramic grade Nicalon and MER converted SiC fiber onto which an interface of 0.3 µm was applied to the Nicalon. The interface on the MER fabric in this hybrid composite was somewhat thinner.

Both ceramic grade (standard) Nicalon and low-oxygen-content, Hi-Nicalon were used for composite fabrication in this study. The Hi-Nicalon, from lot number NC9302, was obtained in fabric form from the Dow Corning Corporation, presumably manufactured by Nippon Carbon in February of 1993. Sizing of both fiber systems was removed with an acetone wash following fiber lay-up. Materials Electrochemical Research (MER) Corporation supplied their converted fabric as part of a U.S. Department of Energy SBIR Phase 2 contract dealing with the fabrication of SiC/SiC composites for use in fusion systems. This MER fabric was converted from the very high strength, PAN based Amoco T300 graphite fiber which had been converted ~60% such that a graphite core remained.

The graphite fiber preform was composed of a three dimensional, unbalanced weave of Amoco Corporation K1100 and P55 fibers. The P55 fiber was woven in 2-k tows in the x and y directions, while six 2-k tows of K1100 were woven through the orthogonal weave in the z-direction. Due to the high modulus of the K1100 fiber, there was a tendency for the fiber to break as it was looped. For this reason a fugitive nylon yarn was used to maintain preform stability. The preform was then rigidized with polymethylmethacrylate (PMMA). The overall fiber volume fraction was 43.9% of which 7.1% was in the x and y directions and 85.7% was in the z (K1100) direction. The graphite preform was machined into 4.45 cm diameter, 1.27 cm thick disks which were mounted in graphite holders for infiltration. The preform was then heated to 350°C in an argon flow gas to burn out the PMMA binder. Following this a graphite interface was deposited to the fibers followed by FCVI infiltration of SiC.

All materials with the exception of the K1100 composite were cut into bend bars of dimension 0.254 x 0.30 x 3.18 cm and tested in 4-point bending using an upper and lower span width of 0.635 cm and 1.9 cm, respectively. Nine bend bars of each material were tested at a cross head displacement rate of 0.05 cm/sec. Due to the larger unit cell for the K1100 graphite fiber composite material, a larger bend bar and bending fixture was desirable. For this case, bend bars of 0.300 x 0.400 x 5.0 cm were used with an upper and lower span of 1.9 cm and 3.8 cm, respectively.

Sample cubes of 1.27 cm on a side were machined from each composite and room temperature thermal diffusivity was measured using a thermal (xenon) flash technique. An infrared detector was used to measure the back surface temperature rise. The thermal conductivity was calculated as follows using a mass average of specific heats for the graphite fibers and silicon carbide matrix:

$$K = \alpha\rho_{\text{composite}}\,(V_F\,\rho_F\,C_p{}^F + V_M\,\rho_M\,C_p{}^M)/\rho_{\text{composite}}$$

where α is the measured diffusivity, V_F and V_M, ρ_F and ρ_M, C_p^F and C_p^M, are the volume fractions, densities and specific heats of the fiber and matrix respectively and $\rho_{composite}$ is the density of the composite.

Results

Bending Strength

The results of the four point bend tests on all composites fabricated are given in Table 3. For the case of the CVD SiC/Nicalon based fiber composites, a single interfacial coating thickness of 0.3 μm was chosen.

Table 3. Results on Infiltrated Composites

Fiber	Interface (μm)	VF Fiber (%)	σ UTS (MPa)	Std. Dev. (MPa)	Density (g/cc)	Void (%)
Nicalon	~0.3	41	292	26	2.5	~14
Hi-Nicalon	~0.3	42	348	27	2.6	~13
Nicalon-MER	~0.3	34	221	24	2.5	~19
MER-T-300	~0.15	~33	123	6	2.3	~20
MER T-300	~0.3	~34	144	9	2.4	~19
MER T-300	~1.0	~28	123	18	2.1	~30
MER T-300*	~0.3	~32	152	1	2.1	~15
Amoco k1100	~0.3	44	283	30	2.1	~20

*fabric overcoated with CVD SiC prior to graphite interface

This has been shown previously to yield the maximum bend strength for the ceramic grade Nicalon fiber. From the table it is seen that the low-oxygen-content Hi-Nicalon yielded an ultimate bend strength of 348 ±27 MPa versus the 292 ±26 MPa achieved for standard Nicalon. The standard deviation for each was approximately equal, as were the calculated volume fraction of fibers, composite density, and matrix void fraction.

The CVD SiC/MER converted fiber system had a substantially lower bend strength than the Nicalon composite. From Table 3 it can be seen that increasing the interfacial thickness from 0.15 to 0.3 μm increased the measured strength from 123 ±6 to 144 ±9 MPa. In both cases the fiber volume fraction was approximately equivalent at just over 30%. The void fraction for this material was fairly high, calculated at approximately 20%. The thickest interface applied to the MER fabric (1.0 μm) yielded a composite with decreased bend strength from the 0.3 μm interfacial material, and had a significantly higher standard deviation (123 ±18 MPa). Of note is that this material also had a higher void fraction (30%) which would cause the variability in properties.

In order to explore the effect of the fiber surface roughness of the MER fabric composites, a second part was fabricated with the standard 0.3 μm graphitic interface. However, a thin layer of CVD SiC was applied to the converted fiber prior to the deposition of the graphitic interface. This material exhibited the best properties of the MER-only fiber composites with a bend strength of 152 MPa and a low standard deviation (Table 3). A composite was fabricated from alternate layers of the MER converted fabric and ceramic grade Nicalon yielded substantially higher strength (221 ±25 MPa) than the MER-only fabric specimens.

The CVD SiC/K1100 graphite fiber system yielded quite good bend strength considering no process optimization was conducted (due to limited availability of material). The bend strength in this case was found to be 267 ±26 MPa with the major fiber direction parallel to the axis of the bend bar. The estimated void fraction for this composite was approximately 20%, which is reasonable considering the three dimensional orthogonal weave necessarily has large cubic voids that are difficult to completely infiltrate.

The flexure curves for all materials tested are shown in Figure 2. Note that the curves presented in this figure are from representative tests (i.e. one of the nine bend bars tested). It is seen that the lower strength FCVI SiC/MER composites failed in a rather brittle manner while significant fiber pullout and toughness was exhibited by the standard Nicalon composite as well as the Nicalon/MER hybrid composite. Also of interest (Figure 2a) is that none of the curves for the Hi-Nicalon exhibited gradual post-ultimate load drop-

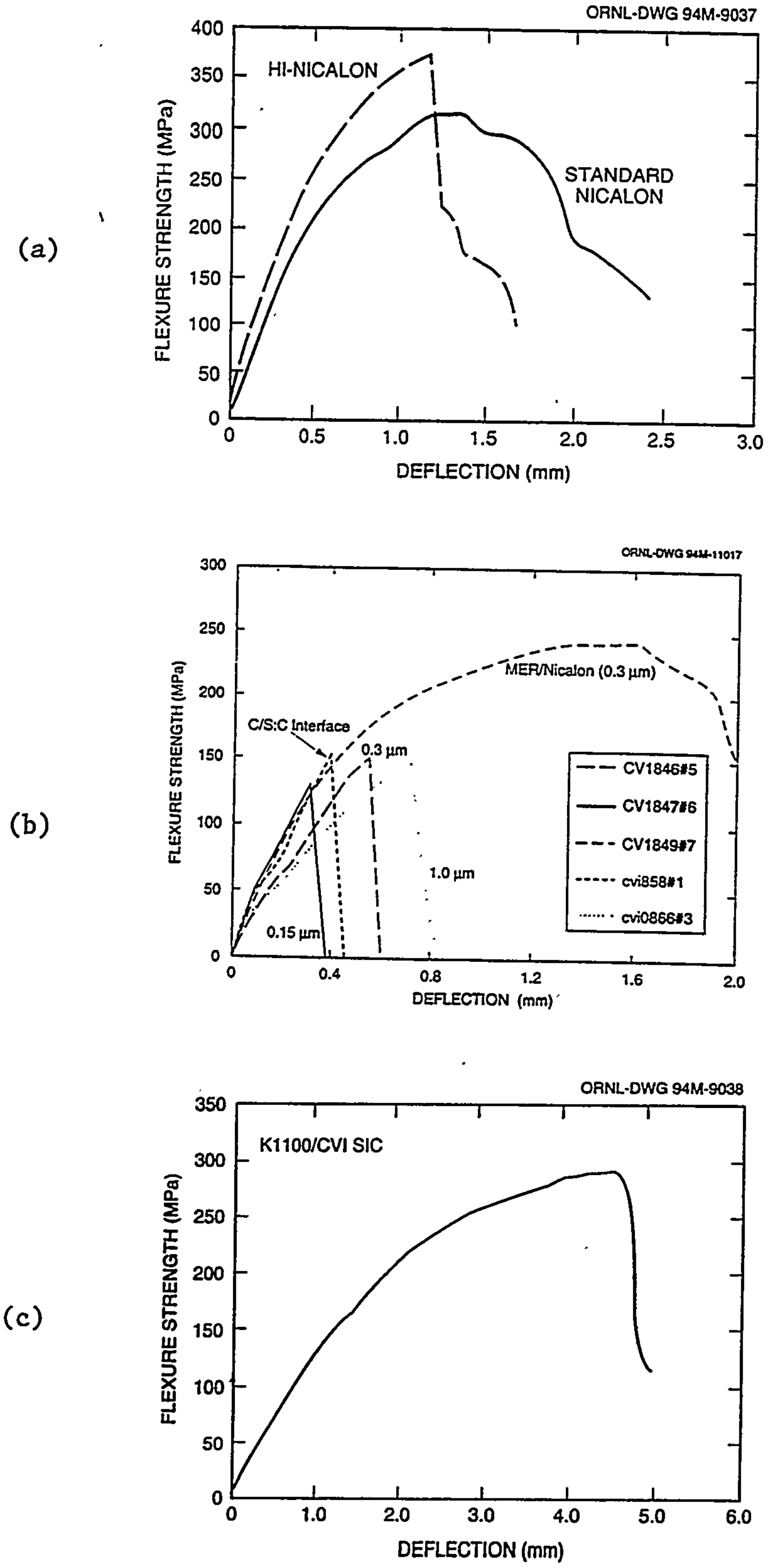

Figure 2: Flexure curves of composite materials: (a) Nicalon fabric composites, (b) MER fabric composites, and (c) K1100 fiber composite

off. A general trend exists for the standard Nicalon composites toward a more "brittle" failure for the materials with higher ultimate bend strength.

Thermal Conductivity

The thermal conductivities for these materials is given in Table 4 for different directions, both parallel (in-plane) and perpendicular (cross ply) to the fabric layers. For the case of the graphite fiber composite, results are given for directions along and perpendicular to the major fiber direction. It is seen that the Nicalon fiber composite has a relatively low thermal conductivity of 20.3 W/m-K in the plane of the fiber lay-ups and 7.4 W/m-K across the plies. The crystalline converted MER fiber shows slightly higher thermal conductivity both in plane (27.8 W/m-K) and cross plane (10.0 W/m-K), which is interesting in light of its greater void fraction. Table 4 also gives data for the SiC fiber composites following a six hour furnace oxidation (in air) at 600°C. This treatment removes the graphitic interface, thus eliminating the fiber contribution to conductivity in the cross ply direction. For the CVD SiC/Nicalon composite the cross ply thermal conductivity has been reduced from 7.4 to 6.8 W/m-K following oxidation. In the case of the MER fiber composites the cross ply conductivity has been somewhat more substantially reduced from 10 to 8.7 W/m-K. The CVD SiC/K1100 graphite fiber composite shows the highest thermal conductivity, yielding 214 W/m-K in the k1100 (major) fiber direction though only 12 W/m-K across the minor fiber direction.

Table 4. Thermal Conductivity of Fabricated Composites

Composite	Diffusivity (cm^2/s)	Calculated Conductivity (W/m-K)
CVI SiC/Nicalon		
cross ply	0.044	7.4
in-plane	0.145	25.3
CVI SiC/Nicalon (Oxidized)		
cross ply	0.039	6.8
in-plane	0.141	24.7
CVI SiC/MER		
cross ply	0.60	10.0
in-plane	0.167	27.8
CVI SiC/MER (Oxidized)		
cross ply	0.052	8.7
in-plane	0.134	22.5
CVI SiC/k1100		
major fiber dir.	1.49	214
across major fiber dir.	0.08	12.0

DISCUSSION

Nicalon Based Composite Material

It has been previously demonstrated[6] (Figure 1) that the Nicalon based SiC composites undergo substantial degradation in strength and toughness following neutron irradiation. At the 20 dpa level shown in Figure 1, the composite has become quite weak and fails in a more brittle manner, and therefore cannot be considered a candidate near the first wall of a fusion machine. In areas such as the shield and magnet, where the lifetime displacement level would not approach 1 dpa and the stress levels are more modest (Table 1), the material may be adequate, however.

The degradation in properties in this composite has been shown to be caused by fiber densification[8] which is attributed to the glassy siliconoxycarbide phase (SiO_xC_y) phase present in the fiber. This phase is a by-product of the oxygen cross-linking step during fiber processing. This production step can be eliminated by the employment of electron beam curing of the fiber which effectively reduces the oxygen content from >10% in the case of standard Nicalon to <0.5% for the electron beam cured Hi-Nicalon. As was mentioned in the introduction, an initial assessment of the radiation response of these fibers indicates that the densification found in standard Nicalon does not occur.[8] For this reason, composites fabricated from Hi-Nicalon fibers appears promising from a radiation-resistance standpoint.

A straightforward comparison of a composite fabricated from standard and Hi-Nicalon, processed at identical conditions, indicates that the unirradiated mechanical properties are superior for the Hi-Nicalon system (Figure 2 and Table 3). It is seen that the ultimate strength in four-point bending is approximately 20% greater for the Hi-Nicalon composite. One possible reason for this increased strength is due to the closer elastic moduli match between the Hi-Nicalon fiber and the matrix. Hi-Nicalon's modulus is quoted as 270 GPa, which is ~23% higher than the standard fiber, and should allow the matrix to take fuller advantage of the fibers strength prior to significant matrix micro cracking.

Of interest is that the load drop-off behavior (Figure 2a) for the Hi-Nicalon composite exhibits a more brittle failure than the ceramic grade Nicalon system. By SEM inspection of the composite fracture surfaces (given in Figure 3), it is apparent that the pull-out length of the fibers was less for the Hi-Nicalon system. The more brittle failure in the Hi-Nicalon composite is most likely an indication that the interfacial coating applied is not optimal. Previous work with standard Nicalon, which yielded a system optimized for high strength (interfacial thickness of ~0.3 μm), demonstrates that the type of failure seen for the Hi-Nicalon system is indicative of an interface that is too thin. Also, inferring from the previous work on standard Nicalon, the effect of increasing the Hi-Nicalon interfacial thickness would be to augment both strength and toughness of this composite. Due to the current high cost of the Hi-Nicalon, optimization of the interfacial layer was not possible in this study. At the time of this writing, Hi-Nicalon was available in only small quantities at a price of $6,900 per kg of fiber tow or about $30,000 per kg in plain weave.

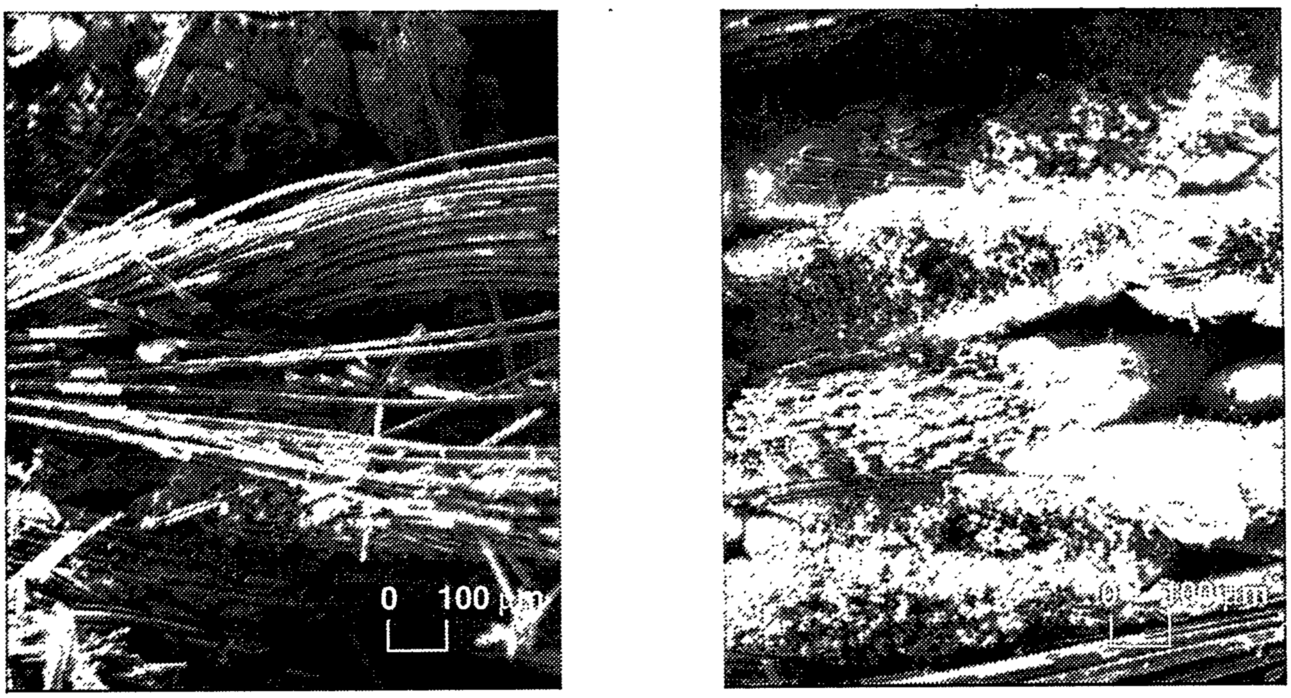

(a)

(b)

Figure 3: Scanning electron micrograph fracture surface comparing: (a) standard Nicalon and (b) Hi-Nicalon.

The measured thermal conductivity of the CVI SiC/Nicalon composite was found to be quite low both along and across the cloth lay-ups. Specifically, the room temperature thermal conductivity across the plies was only 7.4 W/m-K, which is significantly less than the measured value of high quality commercial (Morton, Inc.) CVD SiC of ~250 W/m-K.[17] It is obvious that many factors could act to reduce the thermal conductivity from what would be expected from a simple rule of mixtures assuming ~40% matrix volume fraction of CVD SiC. Firstly, impurity content as well as the crystalline structure of the matrix will affect the thermal conductivity of the material and no attempt has been made to reduce impurity levels in composite materials. Secondly, during processing of the composite, significant micro cracking occurs during cool-down which significantly reduces the matrix thermal conductivity.

The presence of the Nicalon fibers will also reduce the composite thermal conductivity from that of pure CVD SiC, due to the low fiber conductivity (~13 W/m-K).[18] In addition, the phonon scattering at the fiber/matrix interface could also be significant. The small contribution of the fibers to the composite conductivity was demonstrated by removing the graphitic interface through oxidation (Table 4). It was shown that, following oxidation of the graphite interface, the thermal conductivity of the Nicalon composite was reduced by <10%. As the conductivity from matrix to the fiber should have been essentially zero following the oxidation, this implies that the fiber contribution to conductivity is very low.

The low thermal conductivity of SiC/SiC composites is an important issue regarding their use in fusion systems. While some composite materials[19] have been fabricated with room temperature thermal conductivities in the range of 100 W/m-K (through the use of BeO presumably as a sintering aid during hot pressing) the conductivity of typical CVI SiC composite is unacceptably low for thermal management applications such as the first wall of a fusion reactor. It should also be noted that the thermal conductivity will decrease following neutron irradiation. It is well known that the production of point defects in ceramics during irradiation quickly dominates the mean free path of phonons, thus reducing the thermal conductivity. For the case of SiC it has been shown[20] that fission neutron irradiation of pyrolitic ß-SiC caused a reduction in the room temperature thermal conductivity by a factor of 9 following irradiation at 550°C and a factor of 3 following irradiation at 1100°C. For the case of irradiated SiC/Nicalon composite it was observed[7] that the room temperature thermal conductivity was reduced from ~8 to ~3 W/m-K following an irradiation dose of 25 dpa.

MER Converted SiC Fiber Composite Material

Several interfacial coating thicknesses were tried in an effort to optimize both the composite strength and toughness of the MER fabric composite. It is seen by inspection of Table 2 and Figure 2, that for the thinner (0.15 and 0.3 µm) interfacial coatings, the MER fabric composite increased from 123 to 144 MPa in bend strength, though this absolute value is low in comparison with the Nicalon system. For these two coatings the composite still failed in a rather brittle manner. The brittle nature of the failure is seen clearly in the flexure curves (Figure 3) as well as by inspection of the typical fracture surfaces given in Figure 4. This figure shows a scanning electron micrograph of the fracture surface for the MER fiber composite with the ~0.3 µm interface. It is apparent that the amount of pull-out was quite limited,

Figure 4: Scanning electron micrograph fracture surface of MER fiber composite.

generally less than one fiber diameter. The graphite core can be easily distinguished in Figure 4, particularity in some cases where the outer SiC sheath has pulled away from the graphite core.

In an attempt to increase the amount of pull-out in the MER fabric composite system a very thick (~1 μm) interface was applied to the fabric before infiltration with CVD SiC. By increasing the interface thickness a degree of toughness was exhibited by the composite (Figure 3), though after a close inspection of the fracture surface of this material individual fiber pull-out was still not achieved. This material tended to pull out in large tow-sections of fabric (hundreds of fibers). Apparently, the deposited graphite completely encapsulated the fiber bundles, which were then overcoated with SiC and acted as single, large fibers. The associated strength of this composite was also low, 123 MPa, which is identical to the thinnest interface studied. It should be noted that due to very thick interface the void fraction of this material was quite low. Also, after examination of fibers which were properly coated with interface and matrix, pull-out was still very limited, on the order of one fiber diameter.

From these results the reason for the limited pull-out of the T-300 converted MER fabric has been associated with the surface non-uniformity of the fiber. Example of this non-uniformity can be seen in Figure 4. It is seen that the surface of the fiber has axial striations with a peak-to-valley dimension on the order of a tenth of a micron. Also, SEM analysis of bare fiber indicates that small axial undulations are present. These surface nonuniformities negate the effectiveness of the interfacial layer, causing mechanical interlocking of the fiber and matrix leading to the brittle-type failure exhibited in Figure 2b.

Further demonstration of the difference in the behavior of the Nicalon and MER converted fiber pull out is seen by inspection of the fracture surfaces of the hybrid CVI SiC/MER-Nicalon composite. Shown in Figure 5 is a low magnification SEM image of the composite showing one alternating layer of Nicalon (upper) and MER converted T-300 fabric (lower). Pull-out was seen in the case of the larger diameter Nicalon fibers, with the amount of pull-out ranging from several to more than ten times the fiber diameter. The smaller MER fibers, which should have a thinner interfacial layer, showed very limited pull out. A comparison of the interfaces of these fibers is given in Figure 6. Figures 6a and 6b show the thin graphitic interface on the MER fiber and demonstrate that the surface roughness of the fiber causes an correspondingly rough interface. This is to be compared to the smooth interface which has flaked off the Nicalon fiber in Figure 6c. The difference in scale should be noted in these micrographs.

Figure 5: Scanning electron micrograph fracture surface of MER-Nicalon hybrid composite.

ORNL-DWG 94M-9042

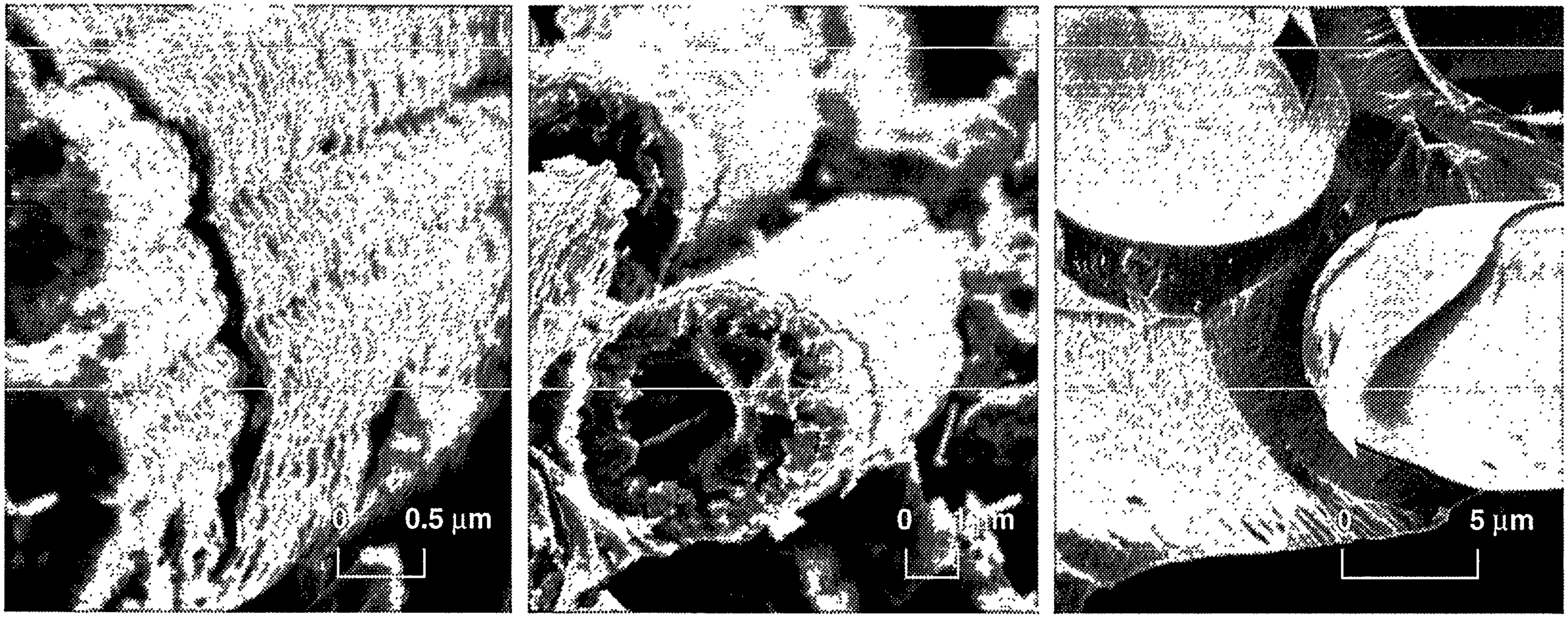

(a) (b) (c)

Figure 6: Scanning electron micrograph comparing interfaces on MER and Nicalon fibers: (a,b) interface on MER fiber (c) interface on Nicalon fiber.

The nonuniformities in the MER converted T-300 fiber has been shown to be an attribute of the original graphite fiber.[21] By starting with a more uniform graphite fiber, the converted fiber will be smoother and should yield superior composite properties. Graphite fibers such as Hercules IM-9 and AS-4, which have a smoother, rounded perimeter are currently being studied.[19]

Graphite Fiber Composite Material

The use of SiC matrix/graphite fiber composites is attractive for use in fusion systems for several reasons. Firstly, though development of this system has been limited, some authors[22-26] have reported these materials to have similar strength to SiC/SiC composites, and in the case of CVI infiltration of very high strength 2-d lay-ups of T-300 graphite fiber,[25] composite bend strength as high as 800 MPa have been reported. Also, it has been shown[22] that for CVI infiltrated graphite composite, the fracture toughness is somewhat higher than for SiC/SiC composites.

The potential for this composite in fusion applications is that it offers a high thermal conductivity composite with significantly lower tritium retention than the advanced carbon/carbon composites (C/C's) currently considered for plasma facing components. The thermal conductivity of the composite system can be engineered to be isotropic or optimized for high conductivity in a single direction, as needed. For the case of the three dimensional composite fabricated in this study, the thermal conductivity was 215 W/m-K in the direction of the high conductivity fibers. This conductivity is approximately one order of magnitude higher than that of SiC/SiC systems. It should be mentioned, by simple rule of mixtures, the calculated thermal conductivity for this SiC/graphite fiber composite should be greater than 400 W/m-K based on manufacturer's quoted fiber conductivity. Due to a processing problem with the early batch from which this fiber was purchased. the thermal conductivity of the composite was significantly reduced from this maximum value. It is reasonable to assume that if the composite were fabricated with a newer batch of fiber, the composite conductivity would be on the order of 400 W/m-k.

Atsumi has demonstrated[27] that the hydrogen retention in graphite is a strong function of the degree of perfection of the graphite crystal. Figure 7 demonstrates that the hydrogen solubility is reduced by more than an order of magnitude as the degree of graphitization (crystalline perfection) in increased from 50 to 80%. This is of particular interest because for typical C/C composites, the degree of graphitization of matrix material is significantly less than that of the highly oriented fibers, indicating that the majority of the tritium resides in the composite matrix. By replacing this (low perfection) graphite matrix with very low hydrogen solubility SiC,[28] the high thermal conductivity of the fibers is still utilized while the significant tritium retention problem associated with the matrix is avoided.

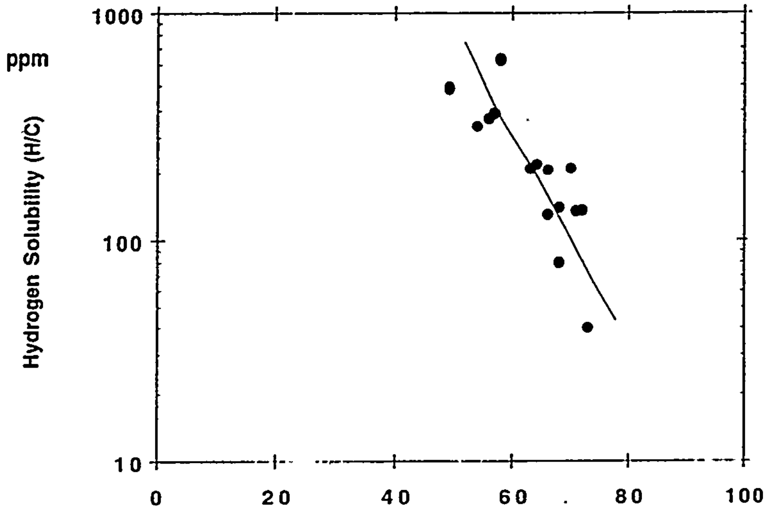

Figure 7: Effect of graphite perfection on hydrogen solubility.[27]

The three dimensional CVD SiC/K1100 composite fabricated for this study yielded reasonably good strength and, from an analysis of the flexure curves and fracture surfaces, possessed a fair amount of toughness. In the major fiber direction, the four point bend strength was 267 ±28 MPa, which was comparable to the Nicalon fabricated material. It should also be noted that the graphite fiber composite was a 3-d composite compared with the 2-d lay-up in the case of the SiC/SiC system. Strength of bend bars across the K1100 major fiber direction would be considerably reduced due to the reduced fraction of (P 55) fibers in this orientation.

Properties such as thermal conductivity and tritium retention, and composite strength will substantially change under irradiation. It has been shown[27] that irradiation can increase the solubility of hydrogen in graphite by a factor of ~17 following fission neutron irradiation to 6×10^{24} n/m^2 (E >1 MeV) at 600°C. Thermal conductivity degradation in graphite and C/C composites has been very well documented[29] and can decrease by over an order of magnitude at low fluence, depending on the irradiation temperature. This decrease in thermal conductivity typically saturates at a neutron fluence level between 0.1 and 1 dpa, depending on irradiation temperature. It could be expected, based on results on relatively high thermal conductivity graphite radiation damage, that at fusion relevant temperatures of 600 to 800°C, a saturation reduction in thermal conductivity of approximately 50% could be expected in the SiC/graphite system presented here. However, even taking this radiation-induced degradation into account, the thermal conductivity of the CVD SiC/graphite fiber system will still be greater than the CVD SiC/SiC composite. It should be mentioned that there is no data to indicate what the mechanical properties of this composite would be like following neutron irradiation. It can be assumed that the CVD SiC would undergo a slight (<0.1%) swelling at temperatures of ~1000°C, while the fibers would exhibit a significant radial expansion and corresponding axial shrinkage. To what extent these radiation induced dimensional changes would effect the mechanical properties needs to be examined.

Concluding Remarks

Several silicon carbide matrix composites have been fabricated with low activation, high strength fiber reinforcements. Of primary interest is that a composite made from Hi-Nicalon with an interfacial coating of 0.3 mm graphite exhibited ~20% higher bending strength than the standard Nicalon composite which possessed an interface optimized for strength. Further increases in strength and toughness can be expected upon further optimization of the interfacial layer for the Hi-Nicalon. Based on recent data regarding the superior radiation stability of the lower oxygen content Hi-Nicalon, a more radiation damage resistant composite compared to standard Nicalon composite is expected.

A high thermal conductivity 3d carbon fiber (K1100), CVD SiC matrix composite has been demonstrated to have high strength (283 MPa) as well as high thermal conductivity (215 W/m-K). The thermal conductivity for this composite is dominated by the fiber contribution and can be substantially increased with little effect on the composite strength by utilizing the current generation of high-conductivity Amoco K1100 fiber. This composite is of interest for thermal management application in fusion reactors not only because of the superior thermal conductivity but also due to the expected reduction in tritium retention in this composite as compared to carbon/carbon materials.

Lastly, a CVD SiC composite has been fabricated from polycrystalline SiC converted from T-300 graphite fibers by the MER Corporation. These fibers are nearly stoichiometric and have shown good strength and excellent creep resistance. The lack of oxygen in these fibers makes them excellent candidate materials for radiation resistance. The composites fabricated from this fiber have to this point yielded somewhat disappointing results. This is mainly due to the fact that the surface roughness intrinsic to the T-300 graphite fiber carries over onto the converted SiC fiber. This surface roughness makes the development of a compliant interface problematic. However, it is likely that this surface roughness problem can be avoided by the choice of a smoother starting graphite fiber, such as the Hercules AS-4 and IM-9.

FUTURE WORK

Low dose HFIR hydraulic tube (in-core) irradiations of Hi-Nicalon fiber composites are planned for both the Hi-Nicalon and Amoco K-1100 fiber composites. Development of improved interfaces for the Hi-Nicalon fiber composite is under way.

for both the Hi-Nicalon and Amoco K-1100 fiber composites. Development of improved interfaces for the Hi-Nicalon fiber composite is under way.

ACKNOWLEDGMENTS

Research sponsored by the Office of Fusion Energy, U.S. Department of Energy under contract DE-AC05-84OR21400 with Martin Marietta Energy Systems, Inc.

REFERENCES

1. G. R. Hopkins, "Silicon Carbide and Graphite Materials for Fusion Reactors," Proc. IAEA Symp. Plasma Physics and Controlled Nuclear Fusion Research, Tokyo, Japan, IAEA-CN-33/s3-3, International Atomic Energy Agency (1974).
2. L. H. Rovner and G. H. Hopkins, "Ceramic Materials for Fusion," Nucl: Technol., [29] (1976) 274.
3. J. P. Holdren, et al., "Exploring the Competitive Potential of Magnetic Fusion Energy: The Interaction of Economics with Safety and Environmental Characteristics," Fusion Tech. [13], Jan. (1988) 7-5.
4. The ARIES-1 Tokamak Reactor Study, Final Report, UCLA-PPG-1323 (1991).
5. International Thermonuclear Experimental Reactor (ITER) Concept Definition. ITER-1, October (1988).
6. L. L. Snead, S. J. Zinkle, and D. Steiner, "Measurement of the Effect of Radiation Damage to Ceramic Composite Interfacial Strength," J. of Nucl. Mat. 191-194 (1992) 566-570.
7. G. W. Hollenberg. et al., "The Effect of Irradiation on the Stability and Properties of Monolithic Silicon Carbide and SiC/SiC Composites up to 25 dpa," submitted to J. Nucl. Mat. (1994).
8. L. L. Snead, M. Osborne and K. L. More, "Effects of Radiation on SiC-Based Nicalon Fibers," submitted J. Mater. Res. 1994.
9. T. Seguchi, N. Kasai, and K. Okamura, "Preparation of Heat-Resistant Silicon Carbide Fiber From Polycarbosilane Fiber Cured by Electron Beam Irradiation," Proc. International Conf. on Evolution in Beam Applications, Takasaki Japan (Nov. 5-8, 1991).
10. AVCO SCS-6 fiber is a tradename of the Textron Corporation, Lowell, Massachusetts.
11. MER Corporation, Tucson, Arizona.
12. "The Development of Silicon Carbide Ceramic Composites for Fusion Reaction (SiC) Applications," Final Report, SBIR Phase 1, Contract No: DEFG02-92ER81271 (May 27, 1993), Materials Electrochemical Research Corporation.
13. F. Frechette, et al., "High Temperature Continuous Sintered SiC Fiber for Composite Applications," Ceram. Eng. Sci. Proc. 12 [7-8] (1991) 992-1006.
14. J. Lipowitz, J. A. Rabe, and G. A. Zank, "Polycrystalline SiC Fibers from Organosilicon Polymers," Ceram. Eng. Proc. 12 [9-10] (1991) 1819-1831.
15. T. M. Besmann et al., "A Method for Rapid Chemical Vapor Infiltration of Ceramic Composites," Proceedings of the Seventh European Conference on Chemical Vapor Deposition, Journal de Physique [50] (Conf-C-5) (1988), 229-239.

16. R. A. Lowden and K. L. More, "The Effect of Fiber Coatings on Interfacial Shear Strength and the Mechanical Behavior of Ceramic Composites," in Interfaces in Composites, Materials Research Society Symposium Proceedings [170], C. G. Pantano and E. J. H. Chen, eds., Materials Research Society, Pittsburgh (1990), 273.
17. Morton International, Woburn, Massachusetts.

18. D. P. H. Hasselman, "Compositional and Structural Effects on the Thermal Diffusivity of Fiber-Reinforced Glass-Ceramic and Ceramic Matrix Composites," Thermal Conductivity **19**, 383-402.

19. J. C. Withers, Personal Communication, MER Corporation, Tucson, Arizona.

20. R. J. Price, "Thermal Conductivity of Neutron-Irradiated Pyrolytic ß-SiC," J. Nucl. Mat. 465, (1973) 268-272.

21. W. Kobel, et al., "Silicon Carbide Fibers from Graphite Precursors for Fusion Energy Applications," submitted 1994, J. Nucl. Mater.

22. L. Heraud and P. Spriet, "High Toughness C-SiC and SiC-SiC Composites in Heat Engines in Whisker and Fiber Toughened Ceramics, Proc. of International Conf, ed. R. A. Bradley, et al., ASM (1988) 217-224.

23. T. Noda, et al., "Carbon Fiber/SiC Composite for Reduced Activation," J. Nucl. Mat 179-181 (1991) 379-382.

24. K. Nakano, et al., "Fabrication and Mechanical Properties of Carbon Fiber Reinforced Silicon Carbide Composites," J. Ceram. Soc. of Japan, 100 [4] (1992) 472-475.

25. E. Tani, K Shobu and T. Watanabe, "Carbon Fiber-Reinforced SiC Composites Produced by Reaction Bonding," J. Ceram. Soc. of Japan, 100 [4] (1992) 596-598.

26. H. Yoshida, et al., "Preparation of Unidirectionally Reinforced Carbon-SiC Composite by Repeated Infiltration of Polycarbosiland," J. Ceram. Soc. of Japan, 100 [4] (1992) 454-458.

27. H. Atsumi, M. Iseki, and T. Shikama, "Trapping and Detrapping of Hydrogen in Graphite Materials Exposed to Hydrogen Gas," submitted to J. Nucl. Mater., 1994.

28. R. A. Causey, et al., "Tritium Migration in Vapor-Deposited ß-Silicon Carbide," J. Nucl. Mater. 203 (1993) 196-205.

29. J. H. W. Simmons, Radiation Damage in Graphite, Pergamon Press (1965).

THERMAL CONDUCTIVITY DEGRADATION OF GRAPHITES IRRADIATED AT LOW TEMPERATURE – L. L. Snead and T. D. Burchell (Oak Ridge National Laboratory)

OBJECTIVE

The objective of this work is to study the thermal conductivity degradation of new, high thermal conductivity graphites and to compare these results to more standard graphites irradiated at low temperatures.

SUMMARY

Several graphites and graphite composites (C/C's) have been irradiated near 150°C and at fluences up to a displacement level of 0.24 dpa. The materials ranged in unirradiated room temperature thermal conductivity of these materials varied from 114 W/m-K for H-451 isotropic graphite, to 670 W/m-K for unidirectional FMI-1D C/C composite. At the irradiation temperature a saturation reduction in thermal conductivity was seen to occur at displacement levels of approximately 0.1 dpa. All materials were seen to degrade to approximately 10 to 14 % of their original thermal conductivity after irradiation. The effect of post irradiation annealing on the thermal conductivity was also studied.

PROGRESS AND STATUS

Introduction

In recent years graphite has been used in every major tokamak reactor primarily due to its low atomic number, good strength, and high sublimation temperature. Because of the significant advances in C/C processing and fiber development, very high thermal conductivity materials have been recently demonstrated and become attractive for high heat flux applications. The most striking thermal conductivities have been demonstrated for the C/C's made from highly aligned graphite fibers which have intrinsic conductivity approaching that of pyrolitic graphite. One example of such fibers is the vapor grown carbon fibers,[1] which have thermal conductivity of 1950 W/m-K. Along with advances in fiber properties, there have been improvements in both the monolithic graphite and C/C matrix processing areas have occurred which have additionally enhanced thermal conductivities.

Figure 1 gives the thermal conductivity temperature dependence of some C/C composites and two graphites. Inset into the graph are the thermal conductivity of the fibers from which the C/C's were manufactured. The thermal conductivity of copper is included for reference. It is seen that generally the highest thermal conductivity fibers yield composites with the best thermal conductivities. However, in some cases (MKC-1PH), a composite of extremely high conductivity has been fabricated from moderate conductivity fibers. This is attributed to processing improvements which enhance the matrix contribution to the composite conductivity. It has been shown[2] for the MKC-1PH material that matrix graphite planes have aligned themselves radially around the fiber increasing thermal conductivity for the composite. The thermal conductivity in

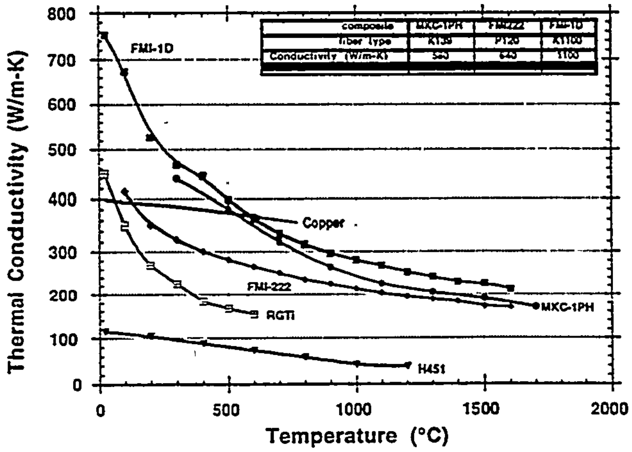

Fig. 1. Thermal conductivity-vs-temperature for some high conductivity graphite materials.

directions normal to the fiber, and thus normal to the matrix graphitic planes, have a correspondingly lower thermal conductivity. For this composite, and others of similar quality, the matrix contribution to thermal conductivity in the high conductivity direction is on the order of the fiber's contribution.

The H451 graphite of Figure 1 represents a standard, high quality, extruded, near isotropic, medium grain graphite which has been in service in the nuclear industry for many years. The second monolithic graphite (RGTi) is one which has been recently developed in Russia. RGTi graphite is prepared from starting materials similar to the H451 material, but includes ~7 weight percent titanium as a recrystallizing agent, yielding large graphitic islands with a preferred orientation perpendicular to the direction of hot pressing. Though the process of metal-induced recrystallization was first observed over twenty five years ago,[3] the demonstration of its effect on the thermal conductivity has been a more recent development.

The irradiation induced degradation in thermal conductivity of graphites is a serious problem for the use of these materials in fusion systems. As with ceramics, graphite thermal conductivity is dominated by phonon transport and is therefore greatly affected by neutron induced defects, such as lattice vacancies and interstitials. For this reason, the extent of the thermal conductivity reduction is directly related to the efficiency of creating and annealing lattice defects and is therefore strongly tied to the irradiation temperature.

The effect of neutron irradiation on the thermal conductivity of graphite has been widely studied. The majority of the literature[4-6] in this area has been in support of the gas cooled reactor program in the U.S. and United Kingdom and has focused on "nuclear" graphites as well as more fundamental work on pyrolitic graphite.[7-8] Over the past several years, the emphasis for radiation effects in graphite has switched to its use as plasma facing components for fusion reactors.[9-12] Because the stress levels anticipated in these applications can be quite high, a growing interest in the radiation effects of C/C composites has occurred. The thermal conductivity of C/C composites has been published for materials of about the same conductivity as nuclear graphites, and shows degradation similar to that expected from the graphite literature. For example, Burchell[11] has shown a saturation thermal conductivity for a good 3-dimensional composite (FMI-222, $K_{unirr.}$ = 200 W/m-K) is reduced to ~40% original room temperature conductivity following fast neutron irradiation at 600°C. However, to this point there has been no published work on the very high (>300W/m-K) thermal conductivity composites.

The purpose of this paper is to present the radiation induced thermal conductivity degradation in several graphites ranging in room temperature conductivity from 114 W/m-K for H-451 graphite, to 670 W/m-K for the unidirectional FMI-1D C/C composite. These materials represent both conventional graphites for reference, as well as the state of the art in high thermal conductivity composites. All materials were irradiated in a range of damage levels from 0.01 dpa to 0.24 dpa at a single irradiation temperature of ~150°C. Such a temperature would represent the lowest service temperature for graphite tile in an ITER-like fusion machine. The effect of postirradiation annealing on the recovery in conductivity is also presented.

Experimental

Six materials were selected for this irradiation study and are listed in Table 1 in order of increasing thermal conductivity. It is important to note that for the high thermal conductivity graphites there is a significant variation in the published values of conductivity even for nominally the same material. This variation can be attributed not only to the method of measurement but also on the manipulation of the measured signal. In general, the values quoted in this paper are lower than the manufacturer's data. Room temperature thermal diffusivity was measured using a xenon thermal flash method. Cylindrical samples of 6 mm diameter were used with thickness ranging from 4 to 10 mm depending on the unirradiated thermal conductivity. As the thermal conductivity degrades substantially following irradiation, sample thickness was chosen to be the thinnest which would yield accurate data in the unirradiated condition. By doing so, measurement complications arising from radial heat loss were minimized. A series of samples of varying thickness were measured and compared to arrive at this minimum value. The thermal conductivity of the material was calculated from the measured thermal diffusivity using the following relation:

$$(1)\quad K = \alpha \rho C_p$$

where α is the measured diffusivity (m^2/s), ρ the density (kg/m^3), and C_p is the specific heat (J/kg-K). The specific heat has not been measured for these materials but was assumed to be the standard value for graphite (684 J/kg-K.) Moreover, it is further assumed that the specific heat of the material is not significantly affected by irradiation. This assumption has been verified in previous studies.[13] For the case of the RGTi material, the specific heat was assumed to be a mass average of graphite and titanium including 7 weight percent titanium.

Table 1. Selected Graphite Information

Material	Manufacturer	Structure	Fiber	Room Temp. Conductivity (W/m-K)
H451	Segri-Great Lakes	Extruded Graphite	–	115
FMI-222	Fiber Materials	3-D Composite	Amoco P-120	200
Hercules 3D	Hercules	3-D Composite	Amoco P-120	345
RGTi	Efremov Institute	Ti Doped Graphite	–	450
MKC-1PH	Mitsubishi Kasei	1D Composite	MKC K-139	555
FMI-1D	Fiber Materials	1D Composite	Amoco K1100	650

The cylindrical graphite samples were stacked axially, wrapped in aluminum foil, and loaded into aluminum capsules for irradiation. The aluminum foil served to contact the inside of the irradiation capsule, which was nominally at reactor coolant temperature, and to conduct the heat generated in the samples to the capsule wall. The temperature of the samples was calculated to be 150°C, though could have been as high as 200°C in the worst case. Capsules were irradiated in the core region of the High Flux Isotope Reactor at the Oak Ridge National Laboratory at a flux of 7.8×10^{18} n/m^2-s (E >0.1 MeV). Total fluences were for 1.26×10^{23} n/m^2, 1.26×10^{24} n/m^2 and 3.22×10^{24} n/m^2. The calculated value of displacements per atom (dpa) for these fluences was 0.01, 0.1, and 0.24 dpa, respectively.

Postirradiation annealing was carried out on each specimen followed by ambient temperature thermal diffusivity measurements. Annealing temperatures were 300, 600, 900, 1200 and 1374°C. Samples were annealed in an argon environment and held at temperature for a period of one hour. The 3-D C/C composite manufactured by Hercules underwent delamination from repeated handling and heating and is not included in the annealing results. This problem stemmed from the need for the small diameter specimen and the large unit cell of the Hercules composite, rather than any radiation-induced degradation.

Results

Shown in Figure 2a and 2b are plots of the absolute and normalized thermal conductivities of the irradiated samples. The normalized data is given as the fraction of original thermal conductivity, K_{irr}/K_{unirr}. Figure 2a also gives the value for dispersion strengthened Glidcop™ copper as reference. All samples in Figure 2 are seen to sharply decrease to less than 40% of their original thermal conductivity by 0.01 dpa. The conductivity is seen to further decrease above this displacement level and approaches an apparent saturation above 0.1 dpa. It is seen from Figure 2b that the conductivity seems to be asymptotically approaching ~10% of original conductivity for all materials studied, irregardless of their initial thermal conductivity. At the highest dose studied (0.24 dpa), the conductivity underwent a very small decrease from the 0.1 dpa values, though there was a small amount of scatter attributable to measurement error.

The effect of isochronal annealing of the irradiated material is demonstrated in Figures 3a and 3b for absolute and normalized thermal conductivity. This figure is for the 0.01 dpa irradiated graphites. In this case, significant recovery in thermal conductivity is seen to occur following the 300°C anneal and increases steadily through the final annealing at 1370°C. It is seen that at this highest annealing temperature, the

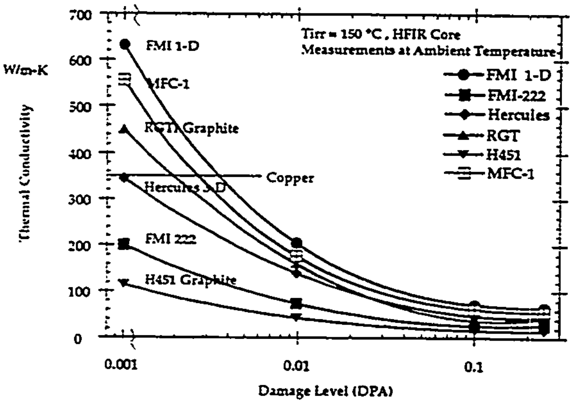

Fig. 2a. Irradiation induced degradation of thermal conductivity.

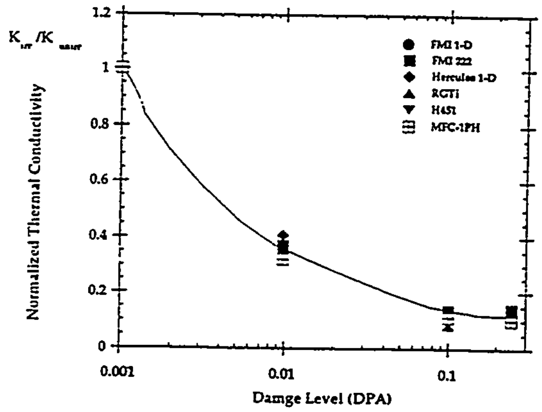

Fig. 2b. Normalized irradiation induced degradation of thermal conductivity.

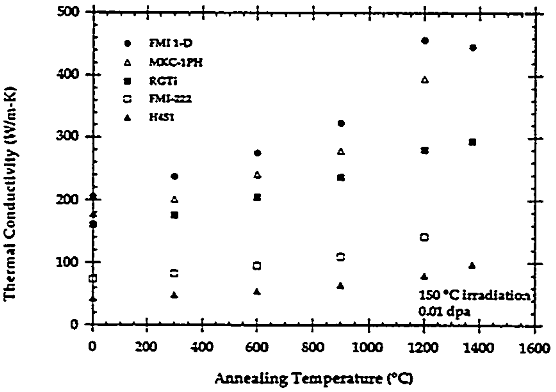

Fig. 3a. Thermal conductivity recovery following isochronal annealing.

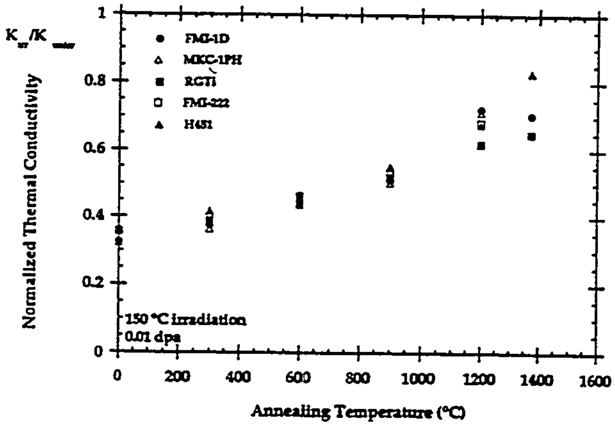

Figure 3b. Normalized thermal conductivity recovery following isochronal annealing.

thermal conductivity has recovered (Figure 3b) to 65-85% of its original value in the various specimens. Two samples (MFC-1PH and FMI 222) from this data set were damaged during a furnace excursion and were not tested at the highest annealing temperature. Shown in Fig. 4 is a compilation of the annealing data for the three fluences. In this case the actual data has been replaced with data-bands for clarity. Two features are of interest from this plot. Firstly, significant recovery has occurred in all the materials for all three fluences. The graphite materials with the lowest fluence (0.01 dpa) recovered to ~75% of their original thermal conductivity, while the highest fluence irradiated materials only recovered to ~45% original conductivity. Secondly, the graphites with the highest dose began thermal annealing at a higher temperature than those with a lighter irradiation.

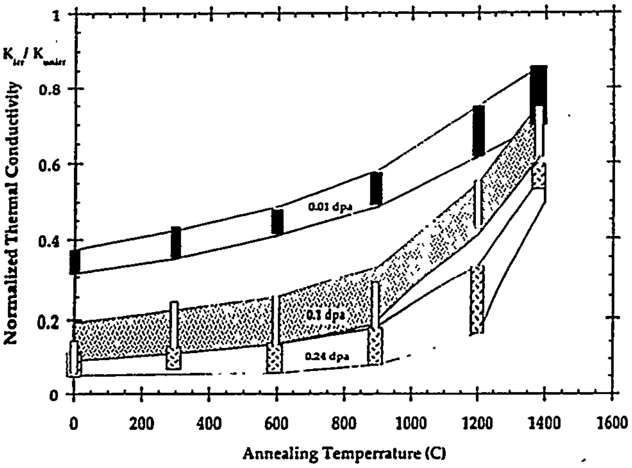

Fig. 4. Normalized thermal conductivity recovery at 0.01, 0.1 and 0.25 dpa.

Discussion

The physical processes governing the thermal conductivity of graphites, as well as the mechanisms responsible for the radiation induced degradation in conductivity, have been well established.[14] For all but the poorest grades of carbon, the thermal conductivity is dominated by phonon transport along the graphite basal planes and is reduced by scattering "obstacles" such as grain boundaries and lattice defects. For graphites with the largest crystallites, i.e. pyrolitic graphite or natural flake, the in-plane room temperature thermal conductivity is approximately 2000 W/m-K.[15]

The thermal conductivity of graphite based material can be written as a summation of the thermal resistance due to scattering obstacles:

$$(2)\quad K(x)=\beta(x)\left(\frac{1}{K_u}+\frac{1}{K_{GB}}+\frac{1}{K_i}\right)^{-1}$$

where the term b(x) is a coefficient which includes terms due to orientation (with respect to the basal plane), porosity and some other minor contributors. This coefficient is in most cases assumed to be constant with temperature, with a value of around 0.6. The first two terms inside the parentheses are the contributions to the thermal conductivity due to the umklapp scattering (K_u) and the grain boundary scattering (K_{gb}). The grain boundary phonon scattering dominates the thermal resistance ($1/K_{gb}$) at low temperatures and is insignificant above a few hundred Celsius, depending on the perfection of the graphite. The umklapp scattering, which defines the phonon-phonon scattering effect on the thermal conductivity, dominates at higher temperatures and scales nearly as T^2. The umklapp scattering therefore defines the upper limit to the thermal conductivity for a "perfect" graphite. Following Taylor's analysis,[16] the umklapp limited thermal conductivity of the graphite crystal would be ~2200 W/m-K at room temperature, which is not far removed from the best pyrolitic graphites or the vapor grown carbon fibers mentioned in the introduction.

The third term in equation (2), K_i, is the contribution to the thermal resistance in the basal plane due to defect scattering. Following neutron irradiation, various types of defects will be produced depending on the irradiation temperature. These defects can be very effective in scattering phonons at flux levels which would be considered modest for most nuclear applications, and would quickly dominate the other terms in equation (2). Several types of defects have been identified in graphite, though at irradiation temperatures less than ~650°C, only simple defects are found in significant quantities. For the 150°C irradiation temperature of this study, simple point defects in the form of vacancies or interstitials along with small interstitial clusters are the predominant defects. It has been further shown[8] that at an irradiation temperature near 150°C, the defect which dominates the thermal resistance is the lattice vacancy.

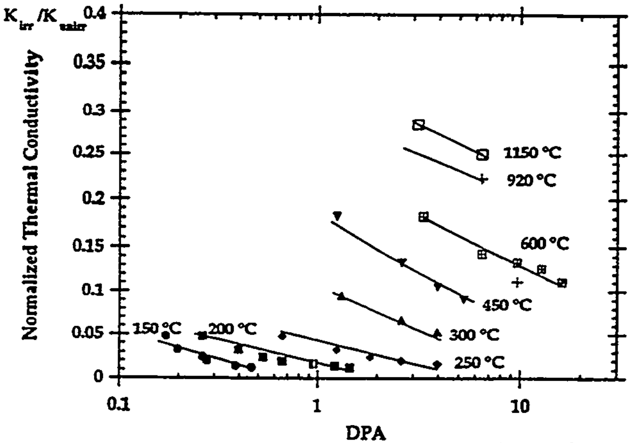

Fig. 5. Normalized thermal conductivity of Pile Grade A graphite.

The temperature at which graphite is irradiated has a profound influence on the thermal conductivity degradation. As an example, Fig. 5 shows one of the most complete sets of irradiation data on Pile Grade A nuclear graphite. This graphite is a medium grained, extruded, anisotropic material with a room temperature thermal conductivity of 172 W/m-K in the extrusion direction. Figure 5 presents the normalized room temperature thermal conductivity for this graphite for various irradiation temperatures. It is seen that as the irradiation temperature is decreased, the degradation in thermal conductivity becomes more pronounced. As an example, following irradiation at 150°C, this graphite appears to approach an asymptotic thermal conductivity of ~1% of original. As the irradiation temperature is increased, and the corresponding interstitial mobility becomes substantial, fewer defects remain in the structure and the thermal conductivity is not significantly reduced.

As mentioned above, at the irradiation temperature of this study, the defect which contributes most to the thermal resistance is the basal plane vacancy.[8] Along with carbon interstitials, these defects can reside as single vacancies, as pairs, or small groups. Upon thermal annealing, interstitial atoms become more mobile and can recombine with the vacancies, restoring the thermal conductivity of the lattice. From Figure 4 it is seen that a significant recovery can occur in the graphites study for annealing temperatures above ~900°C as vacancy mobility becomes substantial. Of particular interest in Figure 4 is that the more heavily irradiated graphite samples exhibited recovery at higher annealing temperatures. One possible explanation for this is that as the fluence is increased, the relative fraction of agglomerated defects compared to single defects is increased leading to less efficient annihilation of basal plane vacancies.

CONCLUSIONS

The thermal conductivity of both standard H451 graphite, high conductivity recrystallized graphite (RGTi) as well as a few high thermal conductivity composites yielded a significant reduction in thermal conductivity near 150°C. Even though the conductivities of these materials varied substantially, the relative rate of degradation in thermal conductivity was very similar. An apparent saturation value of 10-14% original conductivity was achieved above 0.1 dpa for all materials in this study. Isochronal anneals have shown significant recovery in thermal conductivity, with the more heavily irradiated samples requiring a higher temperature before significant recovery began.

ACKNOWLEDGMENTS

This research was sponsored by the Office of Fusion Energy, U.S. Dept. of Energy, under contract DE-AC05-84OR21400 with Martin Marietta Energy Systems, Inc. The authors would like to thank Paul Walsh of the Hercules Corporation and Cliff Baker of Fiber Materials, Inc., for providing materials for this work. We would also like to thank Jeff Bailey and Gary Nelson for their excellent technical assistance.

REFERENCES

1. Heremans, J. and Beetz, C. P., Phys. Rev. B [32] (1985), p. 1981.

2.. Bowers, D. A., Davis, J. W., and Dinwiddie, R. B., "Development of 1-D Carbon Carbon Composites for Plasma Facing Components," J. Nucl. Mater. [212-215] (1994), pp. 1163.

3. Gillot, J., Lux, B., Cornualt, P., and duChaffaut, F., "Katalyse der Graphitierung eines Furfurylalkoholkokses durch Titan and Vanadium," Ber. Deut. Keram. Ges. [45] (1968), pp. 224.

4. Ahlf, L., Conrad, R., Cundy, M., and Scheurer, H. "Irradiation Experiments on High Temperature Gas-Cooled Reactor Fuels and Graphites at the High Flux Reactor Petten," J. Nucl. Mater. [171] (1990), pp. 31.

5. Binkele, L., "The Thermal Conductivity of Neutron-Irradiated Graphites at Temperatures Between 50 and 1000°C," High Temp,-High Pressures, [4] (1972) pp. 401.

6. Price, R. J., "Thermal Conductivity of Neutron-Irradiated Reactor Graphites," General Atomic Report GA-A13157, October 8, 1974.

7. Kelly, B. T. and Brocklehurst, J. E., "High Dose Fast Neutron Irradiation of Highly Oriented Pyrolytic Graphite," Carbon. [9] (1971), pp. 783.

8. Taylor, R., Kelly, B. T., and Gilchrist, K. E., "The Thermal Conductivity of Fast Neutron Irradiated Graphite," J. Phys. Chem. Solids [30] 1969, pp. 2251.

9. Burchell, T. D. , Eatherly, W. P., and Strizak, J. P., "The Effect of Neutron Irradiation on the Structure and Properties of Carbon-Carbon Composite Materials," Effects of Radiation on Materials: Sixteenth International Symposium, ASTM STP 1175, Arvind S. Kumar, David S Gellis, and Randy K. Nandstad, Eds., ASTM, Philadelphia, 1993.

10. Burchell, T. D., and Eatherly, W. P., "The Effects of Radiation Damage on the Properties of GraphNOL N3M," J. Nucl. Mater. [179-181] (1991), pp. 205-208.

11. Wu, C. H., Bonal, J. P., and Thiele, B., "Thermal Conductivity Changes in Graphites and Carbon/Carbon Fiber Materials Induced by Low Neutron Damage," J. Nucl. Mater. [212-215] (1994), in press.

12. Maruyama, T. and Harayama, M., "Neutron Irradiation Effect on the Thermal Conductivity and Dimensional Change of Graphite Materials," J. Nucl. Mater [195] (1992), pp. 44.

13. Simmons, J. H. W., Radiation Damage in Graphite, International Series of Monographs in Nuclear Energy, Vol 102, Pergamon Press, 1965.

14. Kelly, B. T., Physics of Graphite, Applied Science Publishers, 1981.

15. De Combarieu, A., J. Phys. (France), [28] (1968), pp. 931.

16. Taylor, R., Phil. Mag. [13] (1966), pp. 157.

INCUBATION TIME FOR SUB-CRITICAL CRACK PROPAGATION IN SiC-SiC COMPOSITES[1] A. El-Azab and N.M. Ghoniem, University of California, Los Angeles

OBJECTIVE

The objective of this work is to investigate the time for sub-critical crack propagation is SiC-SiC composites at high temperatures.

SUMMARY

The effects of fiber thermal creep on the relaxation of crack bridging tractions in SiC-SiC ceramic matrix composites (CMCs) is considered in the present work, with the objective of studying the time-to propagation of sub-critical matrix cracks in this material at high temperatures. Under the condition of fiber stress relaxation in the bridging zone, it is found that the crack opening and the stress intensity factor increase with time for sub-critical matrix cracks. The time elapsed before the stress intensity reaches the critical value for crack propagation is calculated as a function of the initial crack length, applied stress and temperature. Stability domains for matrix cracks are defined, which provide guidelines for conducting high-temperature crack propagation experiments.

PROGRESS AND STATUS

Introduction

Ceramic matrix fiber composites (CMCs) such as SiC-SiC materials are under consideration for high-temperature structural applications. This class of materials shows non-catastrophic failure behavior which is characterized by fiber bridging of matrix cracks and energy dissipation by debonding and frictional fiber pull-out. These effects qualify CMCs to be classified as high toughness materials. Recent interests in using SiC-SiC composites as structural materials for high heat flux components and blanket in fusion power reactors [1] have raised some questions about the high-temperature toughness issues and high-temperature crack propagation in such materials. At elevated temperatures, creep is expected to influence the stability and propagation of matrix cracks in SiC-SiC composites. In a fusion environment, other inelastic effects such as irradiation creep and swelling are also expected to affect the composite toughness[2-4].

Experimental investigations of high-temperature crack propagation in SiC-SiC composites is underway [5]. Preliminary results have been explained in terms of conventional crack bridging models for fiber composite materials [6], which use simplified bridging relations to study the relaxation of fiber stresses in the bridging zone. In general, the results reported by Henager and Jones [6] have demonstrated that SiC-SiC composites can withstand applied stress intensity factors between 20 and 25MPa-m$^{-1/2}$ without catastrophic crack propagation, at 1100°C. The material, rather, exhibited sub-critical crack growth at speeds in the range 10^{-8}-10^{-7} m-s^{-1} [6]. The reported crack growth speeds were calculated, rather than directly measured, based on the assumption that the specimen compliance change is totally due to crack growth.

A theoretical model was developed to analyze the high-temperature crack propagation data in SiC-SiC composites [6]. Although the model identifies fiber creep in the bridging zone as the growth controlling mechanism, the model details and assumptions did not account for a number of factors, which include the following:

---

[1] This material is based upon work supported by the U. S. Department of Energy under award number DE-FG03-91ER54115.

1. Fiber-matrix interface debonding upon initial crack loading, and the time evolution of the debond profile were not considered. Thus, the effects of the interface bonding and frictional characteristics on the behavior of matrix cracks were ignored.
2. The crack length and the applied load were not included in the developed model.
3. The bridging model was too simple. It considered fiber creep only in a local sense at the matrix crack face, while fiber creep must be considered, at least, over the debond/slip zone.
4. The definition of the bridging stress as given by Henager and Jones [6] was not adequate to find the effective crack tip shielding due to fiber bridging.

The objective of the present work is to analyze the stability of matrix cracks which are bridged by creeping fibers in Nicalon- CVD SiC composites. The creep characteristics of SiC fibers and CVD SiC are reviewed in section 2. An outline of the bridged crack model used in the present analysis is included in sections 3. A brief discussion of the micro mechanical analysis used to obtain the bridging stress is included in section 4. The time-to-crack propagation (incubation time) for a sub-critical bridged matrix crack is investigated. The main results are summarized in section 5, followed by some concluding remarks in section 6.

Creep characteristics of SiC fibers and CVD SiC

CVD SiC have been tested for creep in compression in the temperature range 1550° to 1750°C [7] and in bending in the range 1200° to 1500°C [8]. The latter creep data are considered here, and are shown in Fig. 1. The creep rate of CVD SiC in compression exhibits a power law dislocation mechanism-type creep with a stress exponent of 2.5, while the data of Gulden and Driscoll [8] exhibited a diffusional creep law of the form:

$$\dot{\varepsilon}_c = \frac{13.3\sigma D\Omega_a}{kTd_g^2} \tag{1}$$

where σ is the applied stress, D is the diffusion coefficient for the rate-controlling species, Ω_a is the atomic volume, k is the Boltzmann constant, T is the absolute temperature and d_g is the grain size. An activation energy of 640±88 KJ-mole^{-1} was measured [8].

Creep experiments on SCS-6 SiC fibers were carried out in the temperature range 1000 -1500°C [9-11]. Creep strains were observed to increase logarithmically with time, monotonically with temperature and linearly with tensile stress. Nicalon fibers were also tested for creep [10, 12]. According to Ref. [10], thermal creep strain, ε_c for these two types of fibers is given, as function of stress, time and temperature by

$$\varepsilon_c = A\sigma \exp\left(-\frac{Q}{T}\right)t^p \tag{2}$$

where, for stress in MPa, T in K and t in seconds, $A = 13.112$, $Q = 25800$ and $p = 0.36$ for SCS-6 fibers, and $A = 8.316$, $p = 0.4$ and $Q = 24200$ for Nicalon fibers. The constant Q has the units of temperature. The stress exponent for Nicalon fibers is slightly different from unity [10], but considered to be unity in the present analysis to allow the use of linear viscoelasticity theory.

A comparison of the thermal creep rates of CVD SiC, SCS-6 and Nicalon fibers is shown in Figs. 2 and 3. As can be deduced from these figures, the matrix creep can be totally ignored in comparison to fiber creep. In fact, by using simple rules of mixture, it can be shown that the composites creep rates can be far slower than that of single fibers. This leads to consideration of fiber creep only in the bridging zone of a matrix crack, where fibers are not bonded to the matrix.

Bridged cracks in CMCs

Fig. 4-a shows a continuum representation of a matrix crack which is bridged by fibers. In the present analysis, the singular integral equation method is used to solve the crack problem. Solutions

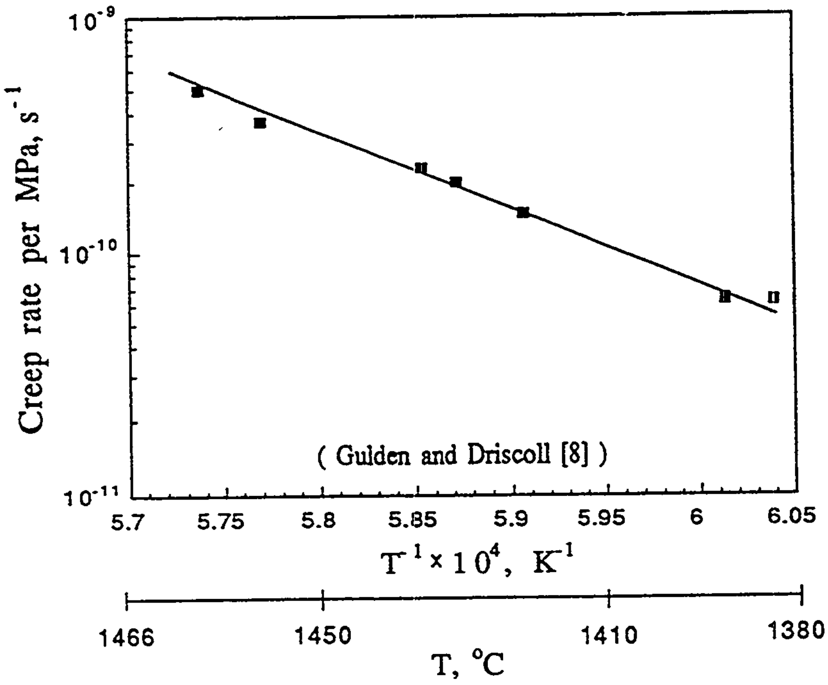

Figure 1: Thermal creep rate of CVD-SiC as function of temperature.

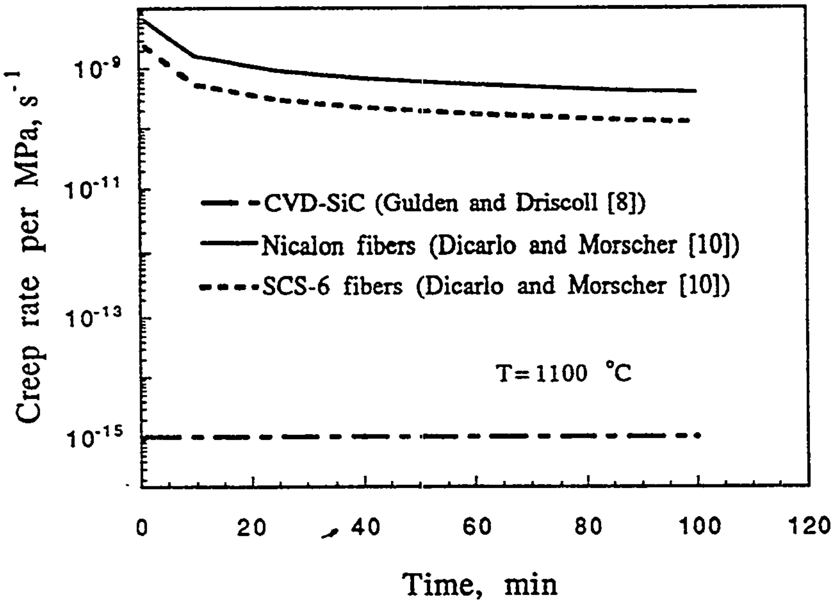

Figure 2: Thermal creep rates of CVD SiC, Nicalon and SCS-6 fibers at 1100°C.

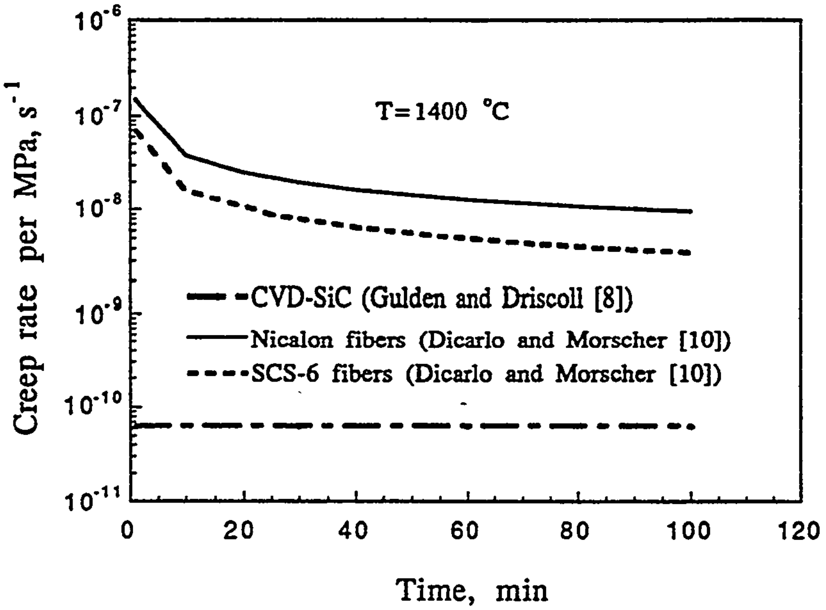

Figure 3: Thermal creep rates of CVD SiC, Nicalon and SCS-6 fibers at 1400°C.

for the crack opening displacement and the stress intensity factor follow directly from the solution of the singular integral equation. The integral equation representing the force equilibrium of a bridged crack perpendicular to the fiber direction in a unidirectional linearly elastic infinite composite, occupying the interval $-c < x < c$, is written as follows:

$$\sigma_a(x) - \sigma_B(x,t) - C_s \int_{-c}^{c} \frac{\delta'(x_o,t)}{x - x_o} dx_o = 0, \qquad |x| < c \tag{3}$$

where $\sigma_a(x)$ is the applied stress and $\sigma_B(x,t)$ is the time-dependent bridging stress. The function $\delta'(x_o,t)$ is the gradient of the crack opening displacement. The constant C_s depends on the elastic compliance constants of the composite, s_{ij}, and is given elsewhere [13]. Singular integral equations similar to equation (3) are usually solved by using the Gauss-Chebyshev integration formula [14]. Due to the presence of a bridging term, which depends non-linearly on the crack opening displacement, an iterative technique is used along with the Gauss-Chebyshev method. Once the singular integral equation (3) is solved for δ', the crack opening displacement $\delta(x,t)$ can then be obtained as follows:

$$\delta(x,t) = -\int_{x}^{c} \delta'(x_o,t) dx_o, \qquad |x| < c \tag{4}$$

The stress intensity factor, $K_I(t)$, ca also be given by:

$$K_I(t) = \lim_{x \to c} \sqrt{2\pi(x-c)}\, C_s \int_{-c}^{c} \frac{\delta'(x_o,t)}{x - x_o} dx_o, \qquad |x| > c \tag{5}$$

It is to be mentioned that the bridging stress in equation (3) is assumed to be time-dependent due to the relaxation of fiber stress by creep at high-temperature. Consequently, the crack opening displacement, $\delta(x,t)$, and the stress intensity factor, $K_I(t)$, are time-dependent.

In order to solve the singular integral equation (3), a definition of the bridging stress, in terms of the crack opening displacement is needed. It is known that, in ceramic matrix composites, the opening of matrix cracks under the influence of external loads is accompanied by fiber debonding and slip on the entire bridging zone. Some energy is dissipated in these two processes, which must

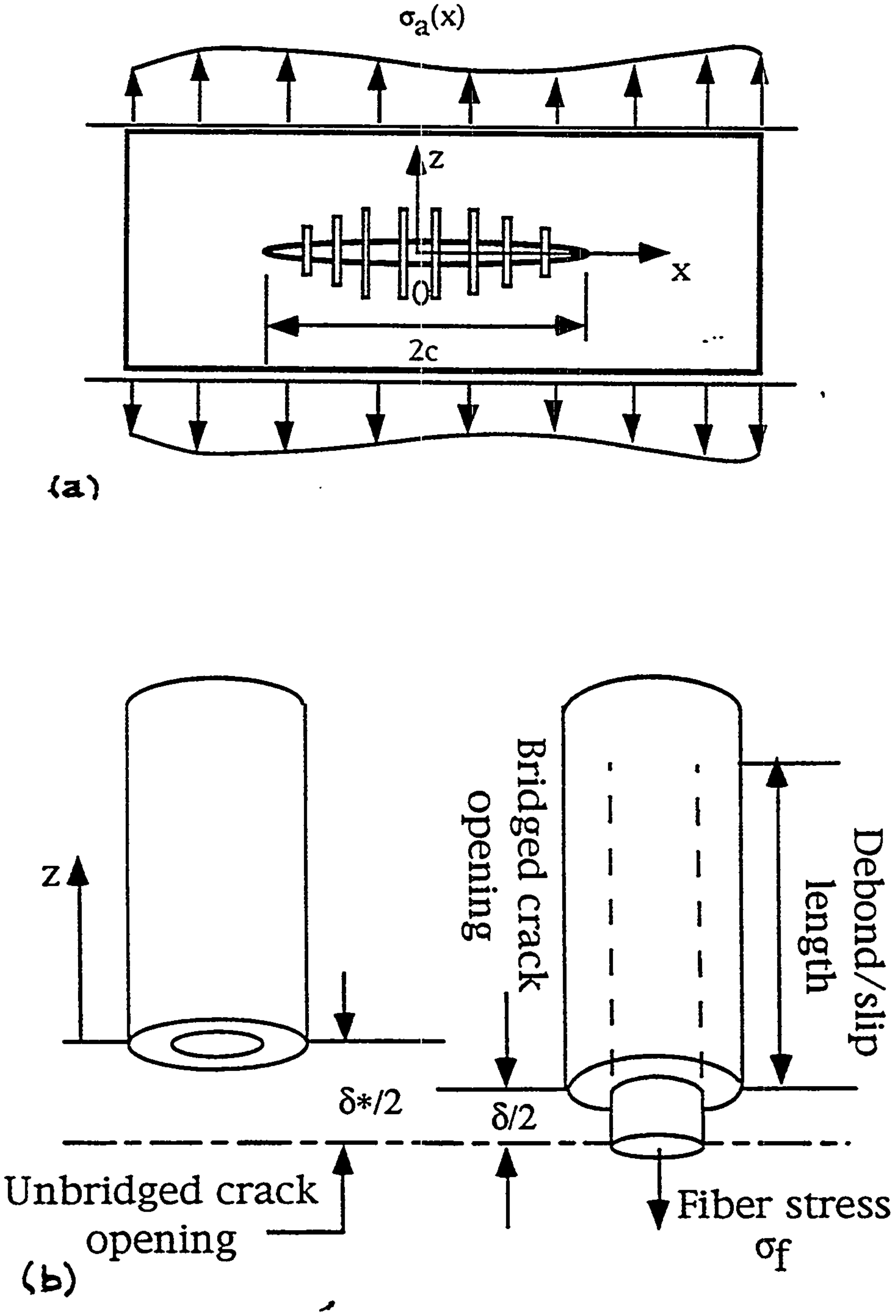

Figure 4: (a) Continuum representation of bridged cracks. (b) Fiber-matrix micro mechanics model.

be supplied the external load. In addition the direct fiber bridging, these effects must be considered. The debonding and frictional slip energy dissipation terms depend on the debond/slip profile around the matrix crack. However, since the latter depends on the crack length, it is expected that these energy terms depend on the crack length.

So far, energy dissipation by friction and debonding has been ignored in the continuum representation of bridged crack in ceramic matrix composites [15-17]. The bridging stress has been defined as the fiber stress averaged over the matrix crack by $\sigma_B = f\sigma_f$, where f is the fiber volume fraction and σ_f is the fiber stress. This definition may be valid, if fiber debonding and slip do not occur. However, since fiber debonding and slip occur during matrix crack opening, the effective bridging stress is generally different from the fiber stress averaged over the crack surface. Also, having considered only the direct effect of fiber bridging, energy dissipation by debonding and slip must be added to the critical matrix strain energy release rate (matrix fracture energy) in defining a fracture criterion. In this case, K_{IC} itself will depend on the crack size and can not therefore be considered a fundamental material property.

In the present analysis, the critical stress intensity factor, K_{IC}, is considered to be a fundamental property and is defined by:

$$K_{IC} = \sqrt{\frac{E_c \mathcal{G}_m}{\Omega}} \tag{6}$$

where $E_c = fE_f + (1-f)E_m$ is the composite modulus in the direction perpendicular to the matrix crack, E_f and E_m are respectively the fiber and matrix moduli and $\mathcal{G}_m$ is the matrix fracture energy. Ω depends on the elastic compliance constants (s_{ij}) and is given by:

$$\Omega^2 = E_c^2 s_{22}\left[2\sqrt{s_{11}s_{22}} + 2s_{12} + s_{66}\right]/4 \tag{7}$$

A simple method to estimate the bridging stress can be illustrated as follows. Consider an *unbridged* matrix crack in which the crack opening displacement is denoted by δ^*, as shown in Fig. 4-b. By applying a distribution of fiber stress $\sigma_f(x)$ on the entire crack to bring fibers from both sides of the matrix crack together, a certain interface debond/slip profile around the matrix crack develops. Also, a reduction of matrix crack opening from the unbridged state δ^* to the bridged state δ takes place. Therefore, as the fiber stress is applied, a work of $\int_{-c}^{c} f\sigma_f(x)\delta^*(x)dx$ is used. Ignoring friction and debonding terms, and considering the matrix crack opening from zero to a level δ against the bridging stress $\sigma_B(x)$, the work done by the bridging stress opposing crack opening is $\int_{-c}^{c}(1-f)\sigma_B(x)\delta(x)dx$, and the factor $(1-f)$ is included since only the matrix faces open. By equating these two terms, and considering only incremental displacements, the following expression for the local bridging stress can be obtained:

$$\sigma_B(x) = \frac{f}{1-f}\sigma_f(x)\frac{d\delta^*}{d\delta} \tag{8}$$

This means that the bridging stress must be defined such that the work done by fiber stress through an incremental displacement $d\delta^*$ which is weighted by fiber volume fraction is equal to the work done by the corresponding bridging stress through an incremental displacement $d\delta$ and weighted by the matrix volume fraction.

El-Azab [13] has used a thermodynamical argument to derive a complete expression for the bridging stress which includes the effect of energy dissipation by debonding and frictional slip in addition to the direct fiber bridging effect. For bridged cracks in which viscoelastic effects are present, this expression is written as:

$$\sigma_B = \frac{f}{1-f}\sigma_f\frac{d\delta_e^*}{d\delta} + \frac{4f}{(1-f)R}\int_0^{\ell}\tau\frac{du_s^e}{d\delta}dz + \frac{8f}{(1-f)R}\mathcal{G}_d\frac{d\ell}{d\delta} \tag{9}$$

in which the δ_e^* is the elastic component of fiber displacement relative to the unbridged crack surface, R is the fiber radius, τ is the interfacial friction stress along the debonded fiber-matrix interface which has a length ℓ. u_s^e is the elastic component of slip displacement along the debonded interface and $\mathcal{G}_d$ is the interface debond energy.

In order to apply the continuum theory of fracture to bridged cracks, the matrix crack must be initially closed and traction free. This is not the case, however, in CMCs due to residual stresses left from the manufacturing step. For example, for composites in which the matrix shrinks more than fibers during cooling from the manufacturing temperature, tensile and compressive stresses exist in the matrix and fibers, respectively, in the fiber direction [13]. Once a matrix crack is formed, and prior to application of external loads, the local residual tensile stress in the matrix is relaxed at the crack face and the matrix crack tends to open. Imagine a hypothetical stress σ_i which is uniformly acting on the composite to nullify the residual matrix stress in the fiber direction. If a matrix crack is then introduced, it will be traction free and closed. In this case, the continuum mechanics of fracture can be applied, and if an external load σ_{ext} is applied to open the crack, the effective applied stress will be given by:

$$\sigma_a = \sigma_{ext} - \sigma_i \tag{10}$$

The stress σ_i is given by:

$$\sigma_i = C_1 \varepsilon_{th} = -C_1 \left(\alpha_m - \alpha_f\right) \Delta T \tag{11}$$

where ε_{th} is the residual misfit strain in the composite, α_f and α_m are the thermal expansion coefficients of fiber and matrix, respectively, and ΔT is the change from the stress-free temperature. The constant C_1 depends on the fiber volume fraction and the elastic constants of fiber and matrix and is given elsewhere [13].

If the combined effect of the thermal misfit, ε_{th}, and pre-loading stress, σ_i, is represented by an effective misfit strain, ε_{eff}, the latter is given by:

$$\varepsilon_{eff} = C_2 \varepsilon_{th} \tag{12}$$

where C_2 depends on the elastic constants of fiber and matrix and the fiber volume fraction. The procedure explained so far means that, the misfit strain ε_{th} will be replaced by ε_{eff} as an initial misfit, which includes the effect of the pre-loading stress σ_i. Also, the crack opening stress will be effectively given by $\sigma_a = \sigma_{ext} - \sigma_i$, as given by equation (10). Fig. 5 shows the magnitudes of ε_{eff} and σ_i versus the magnitude of ε_{th} for Nicalon-CVD SiC composite.

Micro mechanics

Single fiber analysis is carried out in order to implement the definition of σ_B, as given by equation (9). This analysis includes micro mechanical modeling of fiber debonding and slip processes under creep conditions. The fiber/matrix concentric cylinder model depicted in Fig. 4-b is used. Details of the model are found elsewhere [13]. A summary of the basic features of the micro mechanical model are outlined below.

Over the debonded length $0 < z \lesssim \ell$, where z is along fiber direction, axial slip between fiber and matrix is allowed which is resisted by a Coulomb-type friction. In this interval, the model uses an axial equilibrium condition of the form:

$$\frac{d\sigma_f^z(z)}{dz} = \frac{2\mu q(z)}{R} = -\left(\frac{1-f}{f}\right)\frac{d\sigma_m^z(z)}{dz} \tag{13}$$

where $\sigma_f^z(z)$ and $\sigma_m^z(z)$ are the axial fiber and matrix stresses, respectively, $q(z)$ is the interface pressure and μ is the interface friction coefficient. For $z > \ell$, where no axial slip takes place, an equilibrium condition of the form:

$$f\sigma_f^z(z) + (1-f)\sigma_m^z(z) = f\sigma_f \tag{14}$$

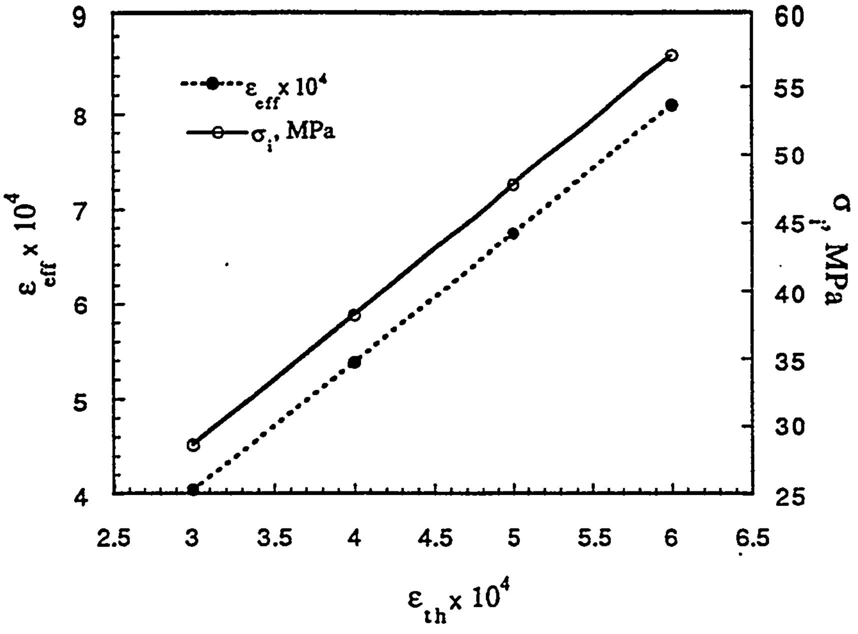

Figure 5: Effective misfit strain, ε_{eff}, and the pre-loading stress σ_i, as functions of thermal misfit, ε_{th}, in Nicalon-SiC composites.

is used, where σ_f is the fiber stress at the matrix crack face. The stress-strain relationships for the matrix are conventional thermoelastic. The fiber stress-strain relationships, however, have the form:

$$\varepsilon_{ij} = \alpha_f \Delta T + \varepsilon^e_{ij} + \varepsilon^c_{ij} \tag{15}$$

where $\alpha_f \Delta T$ is the fiber thermal strain, ε^e_{ij} is the elastic strain component and ε^c_{ij} is the creep strain component. The latter depends on the full history of fiber stresses. Due to fiber creep, all stress and strain components in fiber and matrix are time-dependent.

The crack opening displacement at a particular location along the matrix crack is defined by the net fiber pull-out from the matrix, as given below:

$$\delta = 2 \int_0^\ell [\varepsilon_f - \varepsilon_m] \, dz \tag{16}$$

where ε_f and ε_m are the axial fiber and matrix strains. The elastic fiber displacement component at matrix crack face, δ^*_e, and the elastic slip displacement, u^e_s, which appear in equation (9) are defined by:

$$\delta^*_e = 2 \int_0^\ell \varepsilon^e_f dz,$$

$$u^e_s(z) = \int_z^\ell [\varepsilon^e_f - \varepsilon_m] \, dz \tag{17}$$

where ε^e_f is the elastic component of the axial fiber strain. The fiber debonded length is found by applying energy balance principles to the debond crack, which brings in the effect of interface debonding energy, $\mathcal{G}_d$.

The model solution eventually yields the fiber stress, σ_f, the elastic fiber displacement, δ^*_e, the elastic slip displacement over the debond length, u^e_s, the interfacial friction stress, $\tau = -\mu q$, and the debond length ℓ as functions of the time-dependent crack opening displacement, δ. The relationships between these variables and the crack opening displacement δ are then used to find the bridging stress using equation (9).

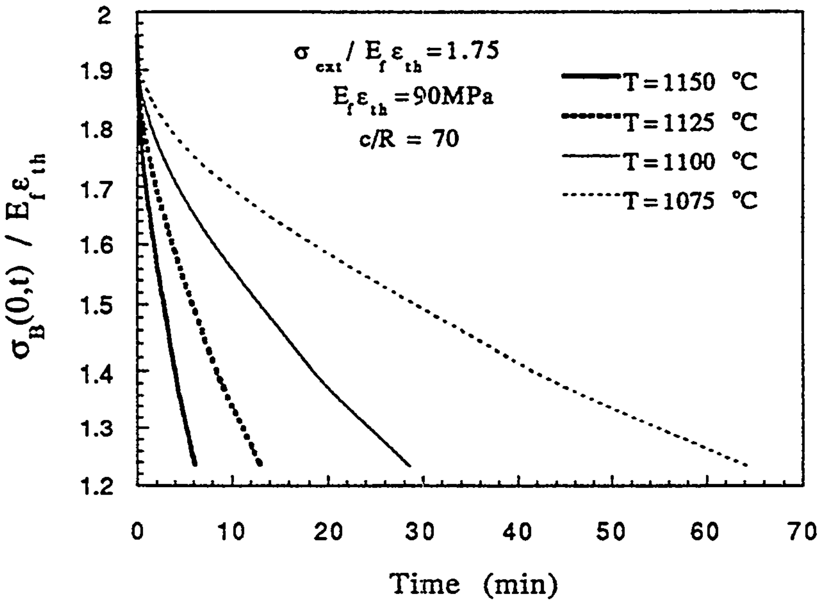

Figure 6: Bridging stress relaxation as function of temperature.

Results and Discussion

The model outlined in the previous sections is applied to sub-critical matrix cracks in one dimensional Nicalon-CVD SiC composites. The fiber and matrix properties used in the present analysis are :$E_f = 180$GPa, $E_m = 380$GPa, $\nu_f = 0.2$ and $\nu_m = 0.18$. The Poisson's ratio of fibers during creep is $\nu_{fc} = 0.45$. The corresponding compliance constants are found to be: $s_{11} = 3.71 \times 10^{-6}\text{MPa}^{-1}$, $s_{22} = 3.44 \times 10^{-6}\text{MPa}^{-1}$, $s_{12} = -6.48 \times 10^{-7}\text{MPa}^{-1}$ and $s_{66} = 8.845 \times 10^{-6}\text{MPa}^{-1}$. A fiber volume fraction of 0.4 is considered. The fiber radius is 7μm. The interface debonding energy of $\mathcal{G}_d$ is assumed to be 5% of the matrix fracture energy $\mathcal{G}_m$. The latter is typically 50J-m^{-2}. The interface friction coefficient μ is assumed to be 0.1. These properties are adopted from El-Azab [13].

Fiber creep in the bridging zone leads to relaxation of the bridging traction that opposes crack opening. Fig. 6 shows the time-dependent relaxation of bridging stress at the center of a bridged crack at different temperatures before the tip stress intensity reaches its critical value, K_{IC}. It is shown that, the bridging relaxation rate is faster at higher temperatures. Due to fiber bridging relaxation, the crack opening displacement and the stress intensity factor are expected to increase with time. Fig. 7 shows the time evolution of the crack opening displacement over the entire matrix crack. Initially, the crack opening profile is fairly flat in the middle section of the crack. This profile, however, approaches the unbridged crack opening as the bridging traction continues to relax by fiber creep. The important aspect to note here is that the increase of the crack opening displacement with time implies that the compliance of the cracked material is increasing although the crack itself does not propagate. This compliance increase may continue for longer times before the crack starts to propagate, depending on the initial crack length, applied stress and temperature. In Henager's experiment [6], however, the increase in compliance was interpreted in terms of crack propagation rather than fiber creep in the bridging zone.

The corresponding behavior of the crack tip stress intensity factor is shown in Fig. 8 for different temperatures. The rate of increase of the crack tip stress intensity is faster at higher temperatures since fiber creep rates are faster. Consequently, the incubation time, which is the time required for $K(t)$ to reach K_{IC}, becomes shorter at higher creep temperatures. The critical tip stress intensity factor K_{IC} is calculated to be 3.77 MPa-m$^{1/2}$ based on matrix fracture energy of 50J-m^{-2} and the composite properties given previously. Although this value is slightly lower than the toughness of

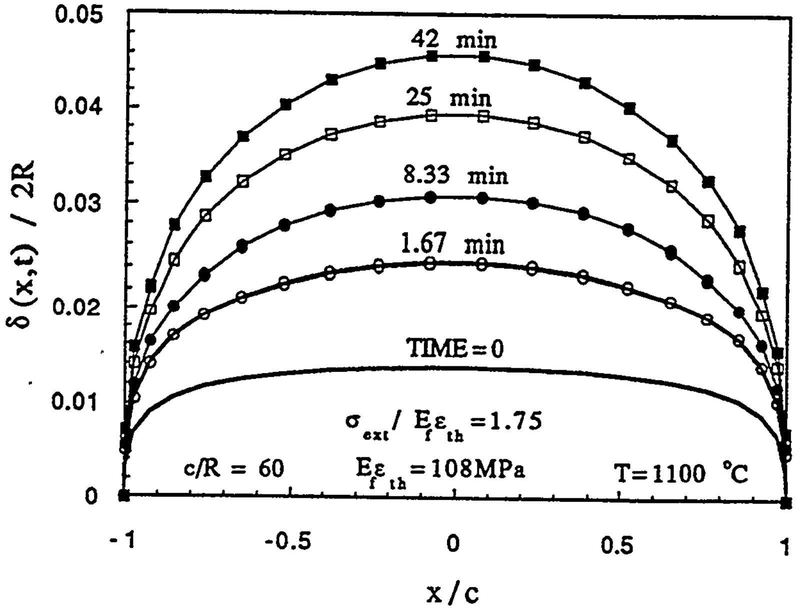

Figure 7: Evolution of crack opening displacement under fiber creep condition.

the monolithic SiC, the applied stresses required to raise the net crack tip stress intensity to K_{IC} may be an order of magnitude higher in case of composites due to fiber bridging. However, under fiber creep the crack tip shielding due to fiber bridging can be gradually lost, which sets restrictions on the high temperature range in which SiC-SiC composites may be used.

The mechanisms of bridging relaxation by fiber creep can be explained by investigating the individual terms in equation (9). The second term (friction term) is a few times higher than the first terms, while the third term is a few orders of magnitude smaller. Creep relaxes the fiber stress, σ_f, leading to partial reduction of the bridging traction (first term). Creep also relaxes the interfacial pressure between fiber and matrix. This interface pressure controls the frictional energy dissipation associated with fiber slip (second term). While the interface pressure relaxes by creep, it actually recovers if the axial fiber stress, σ_f, relaxes due to Poisson's effect. Therefore, the relaxation of σ_f may not have a great influence on the relaxation of the bridging stress.

The debond crack tips at the fiber-matrix interface are shielded by interfacial friction. Relaxation of the interface pressure and, in turn, the interfacial friction stress allows the debond crack to grow. This debond growth depends on the interface debonding energy as well as the friction stress distribution over the debond length. Since the second term in equation (9) increases as the debond length ℓ increases, it may be beneficial to allow growth of debond cracks by lower values of the interface debonding energy and further controlling the interface friction characteristics. An example of the debond growth over the entire matrix crack is shown in Fig. 9.

The time-to-crack propagation (incubation time) has been shown to depend on the temperature (Fig. 8). In Fig. 10, the incubation time is plotted as function of the matrix crack length and temperature. It is observed that, depending on the matrix crack length and temperature, a wide range of incubation times can be obtained. Here we report incubation times between 5min and 1.5 hr, for crack length in the range 120-300 fiber radii, and temperature in the range 1075-1150 °C. Smaller cracks at lower temperatures may exhibit incubation times of several hours or days, depending on the applied loads. The effect of the applied stress is also shown in Fig. 11. It is shown that for the same crack length, the incubation time is longer at lower applied stress.

The effect of the initial misfit strain ε_{th} on the incubation time for sub-critical cracks is shown in Fig. 12. Generally, incubation times becomes longer for higher values of ε_{th}. Based on this figure, it can be argued that a higher level of misfit strain is needed to maintain a higher bridging stress

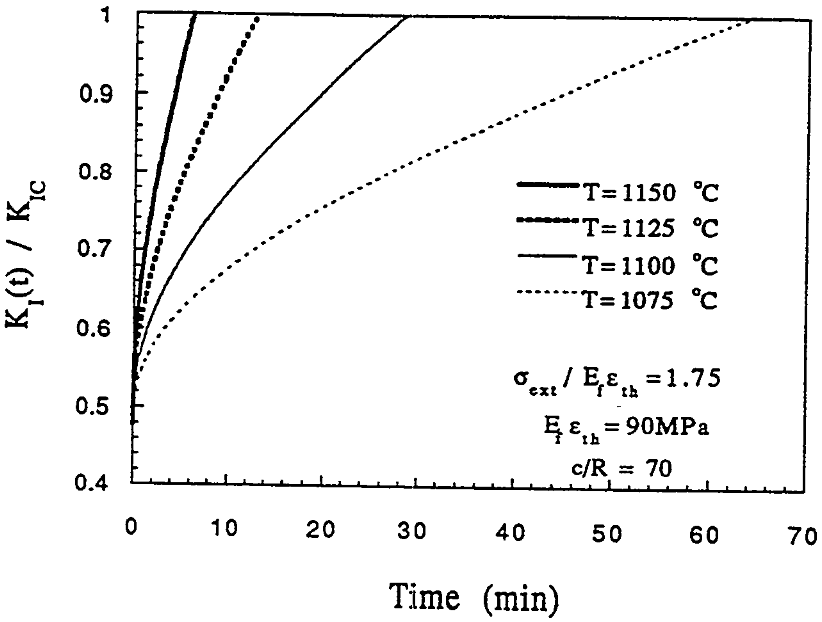

Figure 8: Evolution of the stress intensity factor at different temperatures.

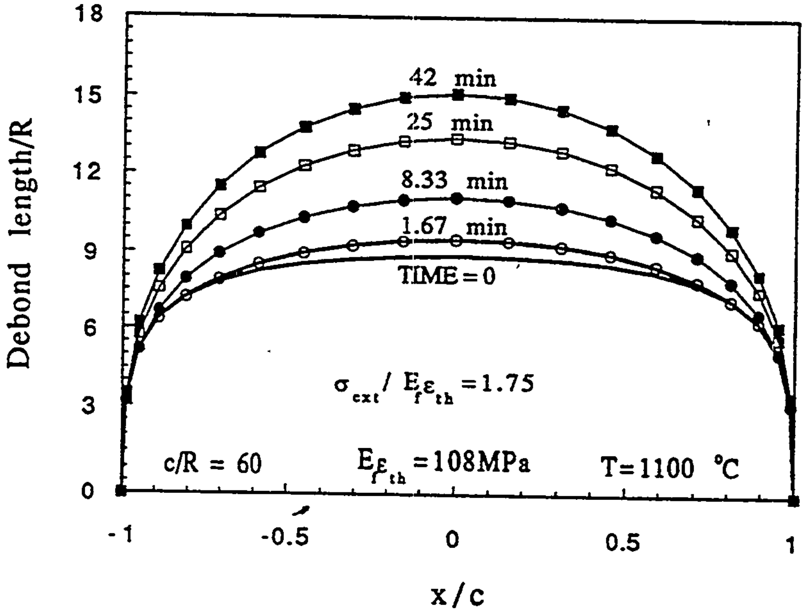

Figure 9: Debond front evolution around matrix crack.

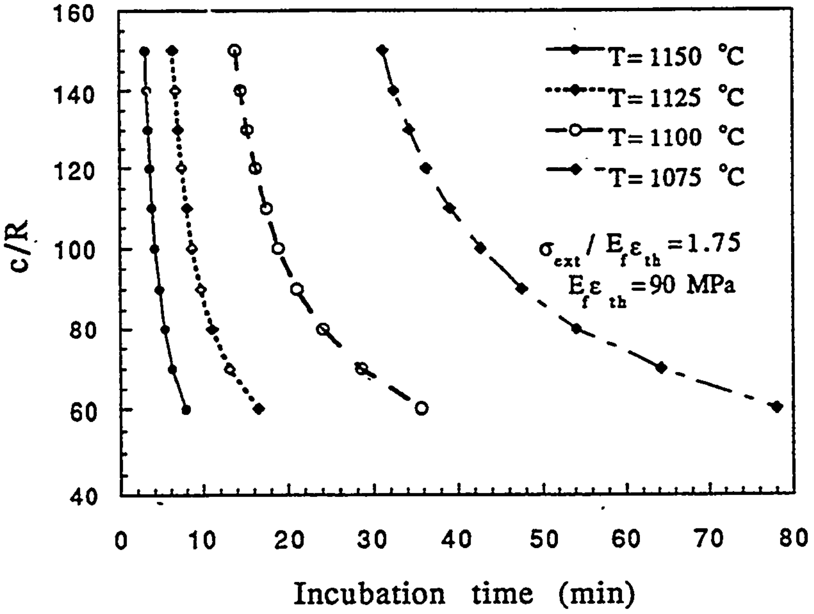

Figure 10: Incubation time for sub-critical crack propagation as function of matrix crack length and temperature.

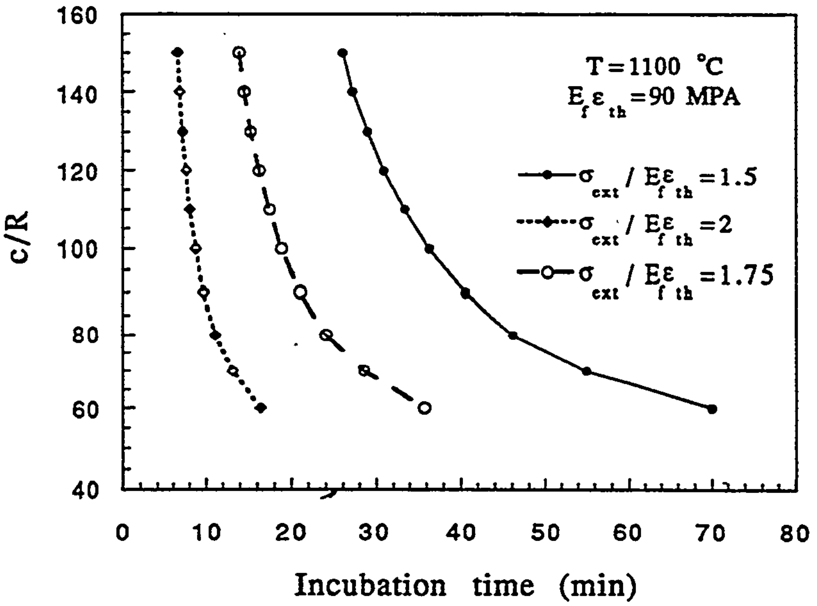

Figure 11: Incubation time for sub-critical crack propagation as function of matrix crack length and external load.

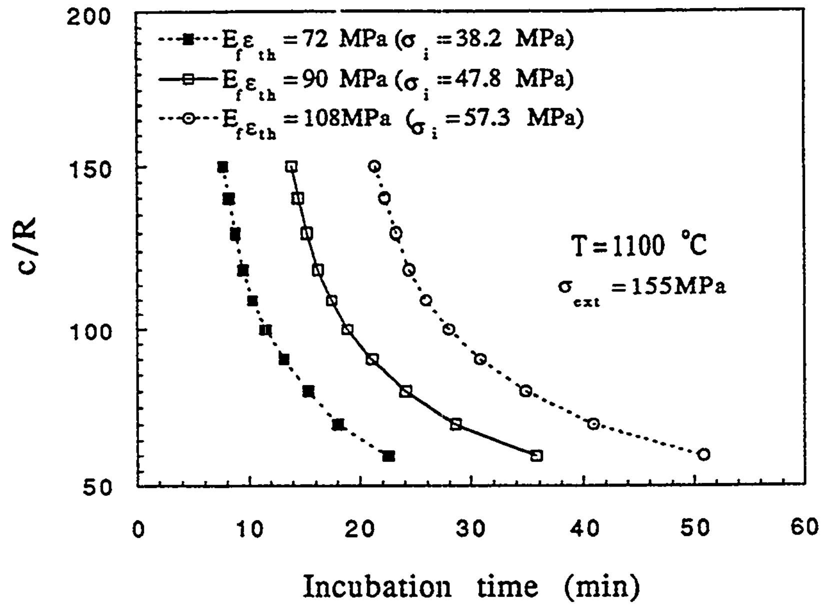

Figure 12: Incubation time for sub-critical crack propagation as function of matrix crack length and thermal misfit strain.

for longer times. This brings in some interesting questions about the expected behavior of SiC-SiC composites in a fusion environment, where irradiation creep is expected to occur once the material is subjected to combined mechanical and irradiation loading, even at temperatures below thermal creep threshold. Swelling rates of the fiber and matrix are expected to control the instantaneous misfit level. Consequently, the relative irradiation creep and swelling rates of the fiber and matrix must be beneficially adjusted to maintain certain levels of misfit between fiber and matrix.

In Figs. 10 through 12, the incubation times for shorter cracks are longer. There is a minimum crack length, which is determined by the effective applied stress alone, below which incubation times must be infinitely long. This limiting value is the length of an unbridged crack which satisfies the condition $K_I = K_{IC}$ at the given applied stress. This means that a horizontal asymptotic line exists for each curve on Figs. 10 through 12. These asymptotes must be the same for the same effective applied stress, σ_a, irrespective the creep temperature. In the large crack length limit, incubation time curves tend to have asymptotic behavior too. Each curve tends to have a vertical asymptote, which means that there exists a minimum incubation time, which depends on the applied stress and temperature, below which large cracks are sub-critical.

The plots shown in Figs. 10 through 12 are useful in two circumstances; studying crack behavior in ceramic matrix composites operating at high temperatures and designing experiments to study crack propagation in such class of materials. In the first case, designers may be interested in allowing for cracks to exist in structural components. If the life time of the component is specified or limited by some factor other than crack growth, then a defect tolerant design can be conducted with the help of incubation charts similar to those given in the present study, by choosing incubation times which are longer than the specified life time of the component. Consequently, an upper defect size limit can be tolerated. In designing crack growth experiments, the incubation charts may help choose the right combination of crack length, applied stress and temperature to run the experiment in a specific time frame.

The present analysis can be advanced to study the time-dependent deformation behavior of structural ceramic matrix composites which contain large numbers of matrix micro-cracks. This can be achieved by using some averaging methodology to predict the global time-dependent load-deformation of the composite using crack solution outlined here as a unit cell solution.

Conclusions

A study of the time-dependent behavior of sub-critical bridged crack in SiC-SiC composites at high temperatures is presented. A new concept of bridging stress is used, which considers the effects of energy dissipation in fiber debonding and frictional slip, in addition to the direct fiber bridging, on the matrix crack opening. A fracture criterion which is based on the matrix fracture energy alone, is used. The effects of the initial residual misfit strains on matrix cracking, and the subsequent crack opening evolution are considered.

It is found that the incubation time for sub-critical bridged cracks is controlled by fiber creep in the bridging zone. Maintaining specific levels of misfit strains may actually delay the relaxation of bridging tractions and, in turn, increase the incubation time of a crack for a given applied stress and creep temperature. For fusion applications, the relative swelling and irradiation creep rates of fibers and matrix will ultimately control the misfit level between fiber and matrix, and particular optimization techniques must be explored to maintain the viability of fiber bridging mechanism of toughening under fusion conditions.

For sub-critical cracks at high temperatures, the incubation time becomes shorter at higher values of applied stress and creep temperature and lower initial misfit strains. The domains of stability of high-temperature bridged cracks can be explored by systematically producing incubation charts of the type shown in Figs. 10 through 12, therefore, a SiC-SiC composite structural element can be designed for reasonably long incubation times for tolerable sizes of matrix cracks, prior to propagation.

FUTURE WORK

The analysis presented here will be advanced to study transient and steady state crack propagation in SiC-SiC composites at elevated temperatures.

References

[1] F. Najmabadi, R. W. Conn and the ARIES Team, ' The ARIES II and ARIES IV Second Stability Tokamak Reactor Study- Final Report,' UCLA-PPG 1461(1994), In press.

[2] A. El-Azab and N. M. Ghoniem, ' Viscoelastic Analysis of Residual Mismatch Stresses in Ceramic-Matrix Composites Under High-Temperature Neutron Irradiation', submitted to Mech. of Materials (1993).

[3] A. El-Azab and N. M. Ghoniem, ' Phenomenological Inelastic Constitutive Equations for CVD SiC and SiC Fibers Under Irradiation', to appear in Fusion Tech. (1994).

[4] A. El-Azab and N. M. Ghoniem, ' Post-irradiation fiber debonding and pull-out in SiC-SiC composites', to appear in J. Nucl. Mater. (1994).

[5] Russell H. Jones, Charles H. Henager and Glenn W. Hollenberg, J. Nucl. Mater.191-194 (1992) 75.

[6] C. H. Henager and R. H. Jones, Mat. Sci. Eng. A166 (1993) 211.

[7] C. H. Carter, Jr., and R. F. Davis, J. Amer. Ceram. Soc. 67 No. 11 (1984) 732.

[8] T. D. Gulden and C. F. Driscoll, Creep of Chemically Vapor-Deposited β-SiC with an Analysis of Creep in Bending, Gulf General Atomic Report, GA-10366, February 16, 1971.

[9] James A. Dicarlo, J. Mater. Sci. 21(1986) 217.

[10] James A. Dicarlo and Gregory N. Morscher, Creep and Stress Relaxation Modeling of Polycrystalline Ceramic Fibers, in Failure Mechanisms in High Temperature Composite Materials, G. K. Haritos, G. Newaz and S. Mall, Eds., ASME AD-Vol. 22, AMD-Vol. 122, 1991, PP. 15-22.

[11] Gregory N. Morscher and James A. Dicarlo, J. Amer. Ceram. Soc. 75 No. 1 (1992) 136.

[12] G. Simon and A. R. Bunsell, J. Mater. Sci.19 (1984) 3658.
[13] Anter A. El-Azab, Time-Dependent High-Temperature Fracture of Ceramic Matrix Composites, Ph. D. Dissertation, University of California, Los Angeles (1994).
[14] F. Erdogan, G. D. Gupta and T .S. Cook, ' Numerical Solution of Singular Integral Equations', in: Fracture Mechanics 1: Methods of Analysis and Solutions of Crack Problems, Editor: G. C. Sih, Noordhoff Int'l Publishing, Leyden (1973) pp. 369-425.
[15] D. B. Marshall, B. N. Cox and A. G. Evans, Acta Metall. 33 No. 11 (1985) 2013.
[16] D. B. Marshall and B. N. Cox, Acta Metall. 35 No. 11 (1987) 2607.
[17] B. N. Cox and D. B. Marshall, Acta Metall. 39 No. 4 (1991) 579.

APPARENT ACTIVATION ENERGY OF SUBCRITICAL CRACK GROWTH OF SiC/SiC COMPOSITES AT ELEVATED TEMPERATURES - Y. S. Chou (Associated Western Universities, NW), M. M. Stackpoole and R. Bordia (University of Washington, Seattle), C. H. Henager, Jr., C. F. Windisch, Jr., and R. H. Jones (Pacific Northwest Laboratory[a]).

OBJECTIVE

The purpose of this study is to investigate the environmental effect of oxygen-containing gases on the subcritical crack growth of continuous fiber (Nicalon "SiC") reinforced ceramic matrix (SiC) composites at elevated temperatures. This is a continuing project and the primary goal for this time period is to obtain an apparent activation energy for SiC/SiC materials with two different interfaces: carbon and boron nitride coatings.

SUMMARY

In the past six months, we have conducted studies of subcritical crack growth on SiC/SiC composite materials in a corrosive (O_2) as well as an inert (Ar) atmosphere for temperatures ranging from 800 to 1100°C. Two materials, one with ~1μm carbon (C) interface and the other with ~0.5 μm boron nitride (BN), were investigated. Apparent activation energies (E_{act}) were determined from both the crack velocity and thermogravimetric analysis. In pure Ar, it was found that the apparent activation energy gradually increased with time, consistent with the development of steady-state bridging zone. The asymptotic value for E_{act} from crack growth data was found to be ~205 kJ/mol and ~234 kJ/mol for BN- and C-interface materials, respectively, in good agreement with published data (~200 kJ/mol) for creep of Nicalon fibers. In the presence of oxygen, E_{act} decreased to ~40-50 kJ/mol for C-interface and ~50-68 kJ/mol for BN-interface. Microstructural characterization of the oxidized samples indicated that the growth rate of the reaction front for BN-interface materials is an order of magnitude lower than for C-interface ones. At higher temperatures, a glassy phase was observed to seal off the BN-interface, whereas the C-interface remained open during all tests.

PROGRESS AND STATUS

Introduction

The brittle nature of monolithic ceramic materials can be greatly improved by incorporating strong continuous fibers into ceramic matrices [1-6]. By carefully controlling the interface and interphases, catastrophic failure can be avoided through progressive interfacial debonding, fiber bridging, and fiber pullout. Fracture toughness values as high as ~30 $MPa\sqrt{m}$ have been reported for continuous fiber reinforced ceramic composites (CFCC) [5]. This allows the fiber-reinforced ceramic materials to be considered as a strong candidate for structural applications at elevated temperatures where monolithic ceramics would not be appropriate.

Recent development of high strength Nicalon (Si-O-C) fibers and Nicalon fiber-reinforced chemical vapor infiltration (CVI) processed SiC matrix composites have offered a great opportunity for structural applications at high temperature as well as for fusion reactor applications [7-10], primarily due to their low activation from irradiation. If, however, CFCCs are to be used in systems where long-term stability is required, a resistance to time-dependent crack growth (e.g., subcritical crack growth (SCG)) would be required. For monolithic SiC ceramics, subcritical crack growth has been studied by Tressler et al. [11-15], Henshall et al. [16], Larsen et al. [17], and Evans and Lange [18]. The high-temperature crack

---

[a] Pacific Northwest Laboratory is operated for the U.S. Department of Energy by Battelle Memorial Institute under Contract DE-AC06-76RLO 1830.

growth mechanism was suggested to be the viscous separation of an amorphous grain-boundary phase [11, 18].

For the CFCC materials such as SiC/SiC composites, Henager and Jones [19-21] have identified a K-independent region for "crack" (damage) propagation at elevated temperatures and attributed this behavior to the development of steady-state bridging zone [19-21]. It needs to be realized that the SiC/SiC fiber composites exhibited multiple cracking damage as well as microcrack damage during the SCG tests rather than the propagation of a single long crack. It would be more appropriate to use the term "damage" in this context rather than crack. The objective of this six-month work is to continue the study of SCG behavior by determining the apparent activation energy for damage growth in argon as well as in oxygen at elevated temperatures. Composites with both 1 μm C- and 0.5 μm BN-interface were examined.

Experimental

Composites consisting of Nicalon fiber cloth (0°/90°) and CVI β-SiC with C- and BN-interfaces were tested. The composites consist of eight plys and are approximately 4 mm in thickness. Interfaces of ~1.0 μm C or ~0.5 μm BN were deposited before the CVI infiltration process. Single-edge-notched-bend bars (SENB) with dimensions of 4 mm x 5.5 mm x 50 mm were tested in a fully articulated SiC bend fixture.

The SCG studies were performed using constant loading tests for times up to 1×10^5 s, giving the velocity of the "damage" zone from the notch root through the specimen for long times. The tests were conducted at temperatures ranging from 800°C to 1100°C in Ar and Ar plus varying O_2 levels. The specimens were typically loaded at an applied stress intensity of 9 to 10 $\mathrm{MPa}\sqrt{\mathrm{m}}$ to begin the test. Activation energy (E_{act}) was determined from the log-log plot of damage velocity versus 1/T. The details of the determination of damage velocity are given in Ref. 19. A typical specimen deflection versus time during one of the SCG tests is shown in Figure 1. The damage velocity at a specific time was determined by differentiating a third-order polynomial equation fit to the deflection versus time data.

Thermogravimetric analysis (TGA) was also conducted on SiC/SiC materials to determine the kinetics of interfacial reaction. TGA tests were conducted using approximately 4 mm x 4 mm x 8 mm bars cut from bend bars with only one exposed surface (area ~0.3 to 0.4 cm^2). Tests were performed at temperatures ranging from 800 to 1100 °C for times from 3 to 24 hours using a Netzsch Analyzer (STA409) with a multi-gas controller (MKS 147) and a O_2 meter (Thermox). Samples after TGA tests were polished and characterized the reaction front using optical microscopy. The growth rate of the reaction front was averaged from the reacted section length divided by the total oxidation time.

Results

Figure 2 shows the apparent activation energy versus time for damage growth in SiC/BN/SiC composites in pure argon environment ($pO_2 < 1 \times 10^{-10}$ ppm). It is interesting to note that the apparent activation energy is not a constant but increases with time. Initially, E_{act} was about 170 kJ/mol and reached approximately 205 kJ/mol in 30000 seconds. Similar behavior was also observed for C-interface composites where E_{act} was found to be ~234 kJ/mol.

In the presence of oxygen, E_{act} was greatly reduced whereas the damage velocity increased appreciably. Figures 3 and 4 show the plots of E_{act} versus time for C-interface materials in Ar plus 5000 ppm pO_2 and for BN-interface materials in Ar plus 20000 ppm pO_2 environments, respectively. The apparent activation energy in oxygen is also not a constant for either interface as in the pure argon environment. In addition, the apparent activation energy tends to decrease at longer times and this decrease in E_{act} was more pronounced for C-interface materials than BN-interface ones. For example, E_{act} almost reached zero at 8000 s before the sample failed whereas BN-interface materials only dropped from 50 kJ/mol to about 42 kJ/mol before the sample failed.

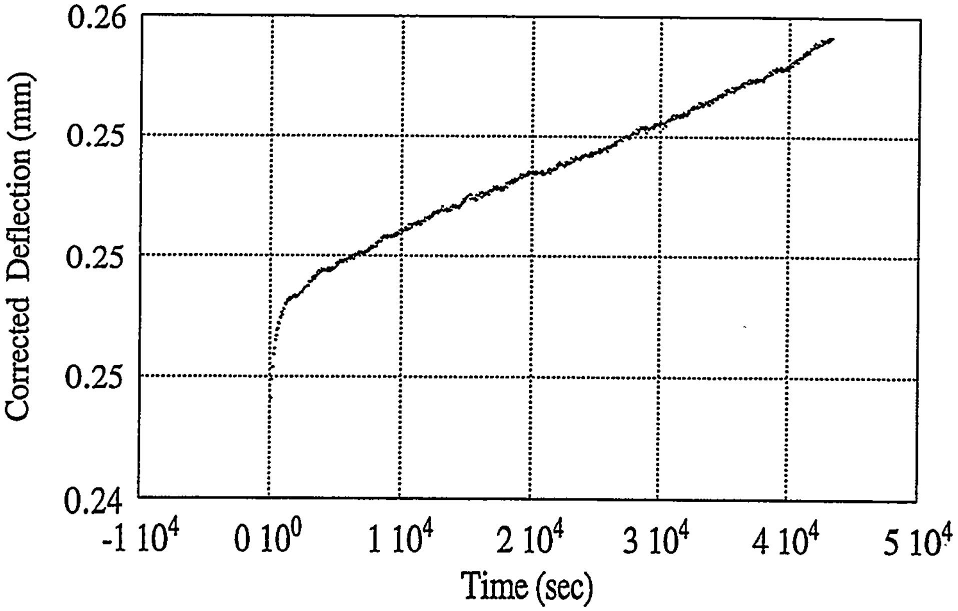

Fig. 1 Typical deflection versus time curve for SiC/SiC composites tested at elevated temperature with constant loading. Note that the damage velocity at a specific time was determined by differentiating the third-order polynomial equation fit to the data.

The apparent activation energy for reactions occurring in the presence of oxygen was also estimated from TGA data for both C- and BN-interface materials. Figures 5 and 6 show a typical plot of weight loss (normalized with respect to exposed area) as a function of time for BN-interface and C-interface materials in Ar with 20000 ppm pO_2 environment, respectively. It is evident that the weight loss is temperature dependent and increases with time. For BN-interface materials, the weight loss initially increases approximately linearly with time and then increases parabolically at longer times. A similar trend was observed for C-interface materials except that the weight loss is more rapid and no distinct parabolic region was observed. For both materials, as temperature increases, so does the weight loss except for the BN-interface materials at 1100°C where the weight loss is less than at 1000°C. By obtaining instantaneous slope (weight loss rate) from Figs. 5 and 6, the apparent activation energy was determined from plots of the slope versus 1/T at specific times. Figures 7 and 8 show the plot of apparent activation energy versus oxidation time for C- and BN-interface materials, respectively. For BN-interface materials, E_{act} was determined from 800 to 1000°C data compared to 800 to 1100°C for C-interface materials. The apparent activation energy versus time from TGA data for both materials exhibited a similar trend as that obtained from the damage growth data for SiC/BN/SiC composite (Figs. 3 and 4), i.e., there exists a maximum E_{act} and E_{act} decreases at longer times. It is worth noting that E_{act} decreases to a minimum value in shorter times at higher oxygen concentrations. Figure 9 shows the average reaction front growth rate as a function of pO_2 for C- and BN-interface materials. The growth rate for the C-interface is approximately an order of magnitude greater than BN-interface.

Discussion

It has been observed by Henager and Jones [19-21] that SiC/SiC composite materials either with a C- or BN-interface exhibited stage-II V-K curves at elevated temperatures in a pure argon environment, i.e., the damage velocity, is independent of applied stress intensity. In the presence of oxygen, the damage velocity increased with increasing oxygen partial pressure, and was attributed to the oxidation of the interface such that the load carrying ability was reduced. For CFCC materials, weak interfaces such as C and BN will lead to debonding as cracks propagate around the fibers leaving behind fibers bridging the crack, which results in non-catastrophic failure. The development of steady-state bridging zones has been modeled successfully to demonstrate the development of stage-II V-K curves [20]. The current measurement of the apparent activation energy of damage velocity for SiC/BN/SiC materials in a pure Ar environment (Fig. 2) seems to be consistent with the development of steady-state bridging zone, such that the fibers behind the crack-tip control the SCG behavior. The asymptotic value for E_{act} in pure Ar is about 205 kJ/mol. Simon and Bunsell [9] have reported an activation energy for Nicalon fibers from tensile creep tests at 1280 to 1320 °C of 370 kJ/mol and 270 kJ/mol in Ar and in air, respectively. DiCarlo [22] recently reported a value of 500 ± 65 kJ/mol for Nicalon fiber creep activation energy using data from bend stress relaxation tests and presented a semi-empirical creep equation for larger creep strain region ($\varepsilon > 1\%$) in which an effective activation energy of 200 kJ/mol was obtained. Our data (234 kJ/mol for C- and 205 kJ/mol for BN-interface materials) are in good agreement with the DiCarlo's data for larger creep strains. It needs to be realized that in addition to fiber creep there are other mechanisms present during the development of the bridging zone, such as fiber-matrix interface creep, time-dependent interface debonding, and roughness-induced stick-slip sliding during fiber pullout. All these processes are expected to play roles in affecting the SCG behavior and need to be further explored. Nevertheless, the current data of E_{act} seems to suggest that fiber creep is the dominant mechanism for SCG behavior in these materials.

In the presence of oxygen, the damage velocities were found to be greater than in the pure Ar environment for both C- and BN-interface materials. In addition, region II in the V-K curves spans a smaller range of stress intensities. The apparent activation energy determined from the measured damage velocity was much smaller than in pure Ar, i.e., ≤ 50 kJ/mol. The oxidation of carbon in the presence of oxygen results in the formation of gaseous carbon oxides, with an overall weight loss, according to the following reactions

$$C + O_2 \rightarrow CO_2 \tag{1}$$

$$C + \frac{1}{2}O_2 \rightarrow CO \tag{2}$$

The activation energy for carbon oxidation varies from 30 to 123 kJ/mol and depends on the way it is formed. The carbon interface in this study was formed by cracking of CH_4 and has the typical laminar microstructure of pyrocarbon [23]. The E_{act} from this study is in reasonable agreement with the published data. It is worth noting that at longer times, E_{act} starts to drop abruptly (Fig. 3 for damage velocity data at pO_2 = 5000 ppm) suggesting that the C-interface was severely damaged (oxidized) such that little load was transferred to the bridging fibers. For very thin C-interfaces, e.g., 0.1 μm, it was found that the interface channels left after the carbon was oxidized were rapidly sealed off by silica at T > 1000°C [23]. In this study, however, the thickness of C-interface is ~1.0 μm and Nicalon fibers, which are not stoichiometric SiC but Si-O-C, are known to release SiO and CO at elevated temperature and shrink. Therefore the interface channel could be kept open for continued oxygen attack. Similar behavior was also observed by Filipuzzi et al. [24] in 1-D SiC/C/SiC materials with a 1 μm thick C-interface. They found that carbon is totally consumed before silica can seal the interface channels. It is interesting to note that E_{act} obtained from the measured damage velocity is in good agreement with TGA tests (Fig. 7) although the stress states are different. The decrease of E_{act} at longer times for TGA tests is likely due to the passive oxidation of SiC matrix and fibers resulting in weight gain, which was attributed to the pore geometry change as well as the localized high concentration of CO_2 [23].

As for BN-interface materials, the measured E_{act} obtained was similar to that of the C-interface materials. The maximum E_{act} is about 50 kJ/mol from the damage velocity data and about 68 kJ/mol from the TGA results. The E_{act} from TGA tests was estimated from data taken from 800 to 1000°C. The oxidation reaction corresponding to this activation energy remains to be identified. However, there are three possible oxidation reactions in SiC/BN/SiC materials

$$2BN + \frac{3}{2}O_2 \rightarrow N_2 + B_2O_3 \tag{3}$$

$$SiC + \frac{3}{2}O_2 \rightarrow CO + SiO_2 \tag{4}$$

$$SiC + O_2 \rightarrow CO + SiO \tag{5}$$

Equation 3 corresponds to oxidation of the BN interface and results in a glassy phase. Equation 4 corresponds to oxidation of the SiC matrix, and could produce glassy as well as crystalline forms of silica [25]. Equation 5 illustrates the active oxidation of SiC resulting in gaseous species and can only occur at low oxygen partial pressures. In addition, Nicalon fibers can also undergo thermal decomposition and gain or lose weight depending on whether oxidation occurs in a passive or active regime. Oxidation reactions (Eqs. 3 and 4) would result in weight gain whereas weight loss is observed for the active oxidation of SiC (Eq. 5). The current TGA results, i.e., weight loss in Fig. 5, suggest that either the SiC matrix undergoes active oxidation or the fibers decompose releasing SiO and CO. It is not clear why weight loss was observed since SiC would be in the passive regime and Nicalon fibers do not decompose below ~1250°C and even higher temperatures when embedded within a matrix. Nevertheless, at longer times and higher temperatures, silica has been observed to seal off the open pores for the BN-interface materials. The formation of a low viscosity glassy phase as well as the thermal decomposition of the interface will all reduce the load carrying capability of bridging fibers and led to lower E_{act} for SCG. In an inert environment, fiber decomposition only occurs around 1400°C and at higher temperature (1500°C) when embedded within SiC matrix [23].

CONCLUSIONS

An apparent activation energy was determined from growth of a damage zone during subcritical crack growth as well as from TGA data for C- and BN-interface materials. In a pure argon environment, the apparent activation energy from damage growth data is consistent with fiber creep results suggesting that the SCG behavior is determined by the creep of bridging fibers. In the presence of oxygen, E_{act} was substantially decreased to ~40-50 kJ/mol and ~50-70 kJ/mol for C- and BN-interface materials, respectively. For C-interface materials, E_{act} is consistent with the oxidation reaction of the interface suggesting the SCG behavior was dominated by the interfacial oxidation reaction. This is unclear for the BN-interface materials. Optically measured reaction front growth rates indicated that C-interface reacts much faster than BN-interface. In addition, a glassy phase was identified for BN-interface materials which sealed off the open pores after long time exposure at elevated temperatures in an oxygen-containing environment.

FUTURE WORK

1. To characterize the BN-interface materials after long time exposure in an oxygen-containing environment.
2. To fit our TGA and optically measured reaction front growth rate data with the existing 1-D model of Filipuzzi [25].

ACKNOWLEDGMENTS

The authors would like to acknowledge J. L. Humason for his testing expertise, and R. A. Adee and N. T. Saenz for microscopy. This work was supported by Basic Energy Sciences under the Department of Energy (DOE) Contract DE-AC06-76RLO 1830 with Battelle Memorial Institute that operates Pacific Northwest Laboratory for DOE.

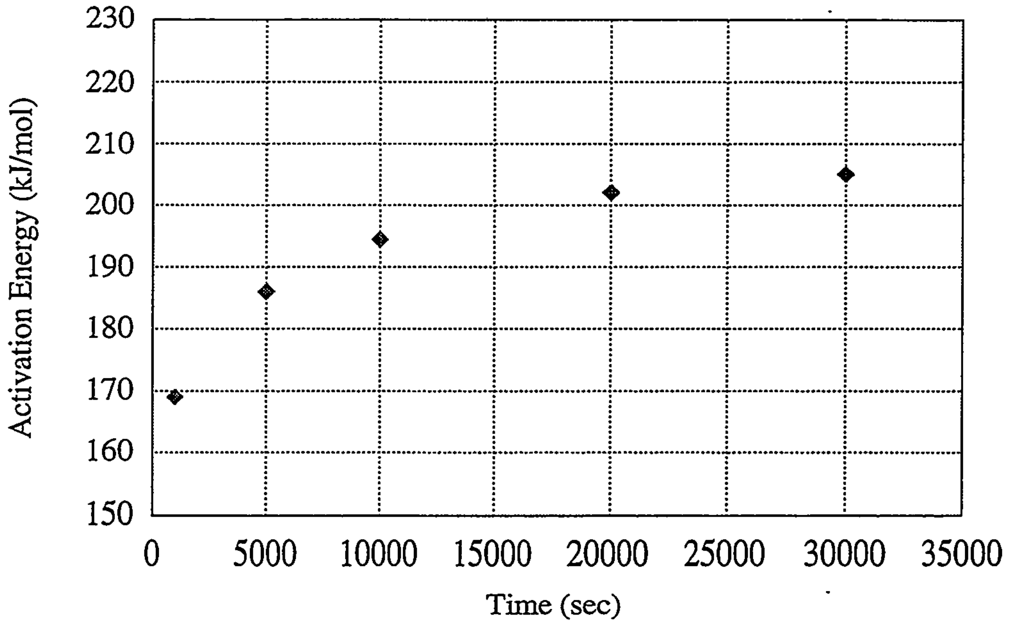

Fig. 2 Activation energy versus time plot for SiC/BN/SiC composites in pure Ar environment.

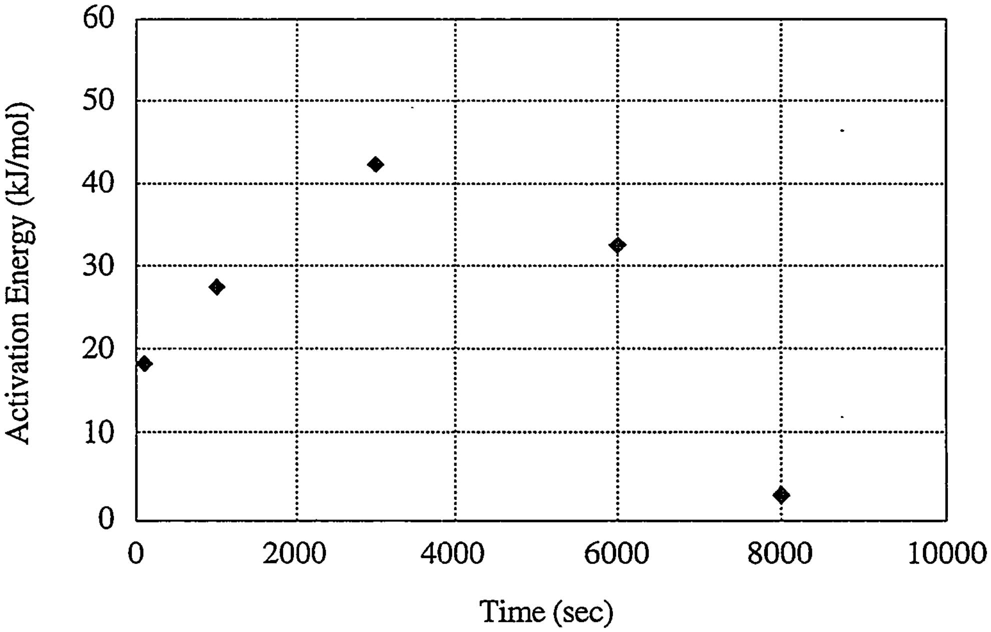

Fig. 3 Activation energy (determined from damage velocity) versus time plot for SiC/C/SiC composites in argon with 5000 ppm pO_2 environment.

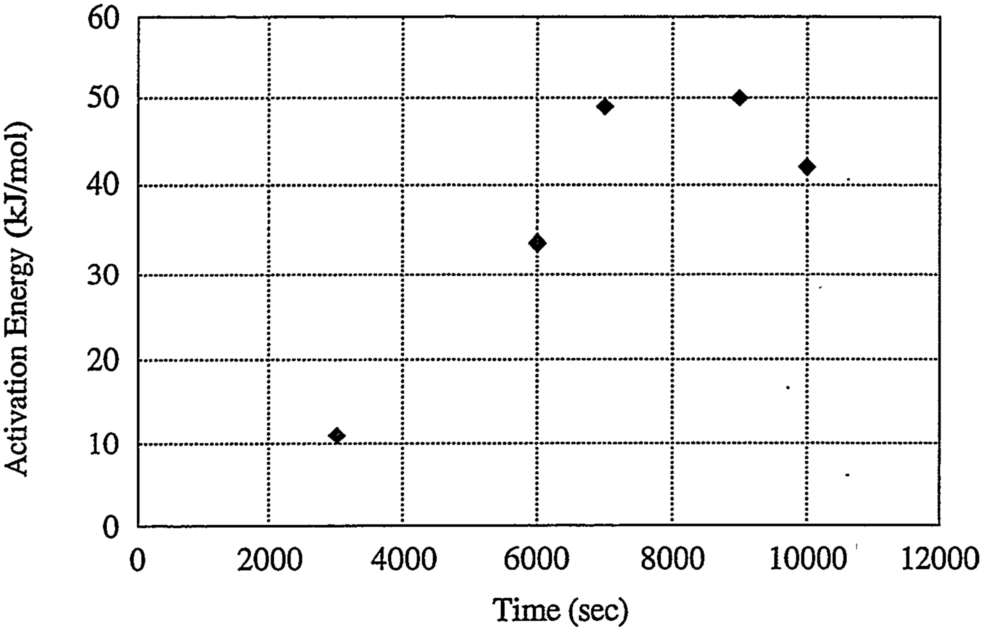

Fig. 4 Activation energy (determined from damage velocity) versus time plot for SiC/BN/SiC composites in argon with 20000 ppm pO_2 environment.

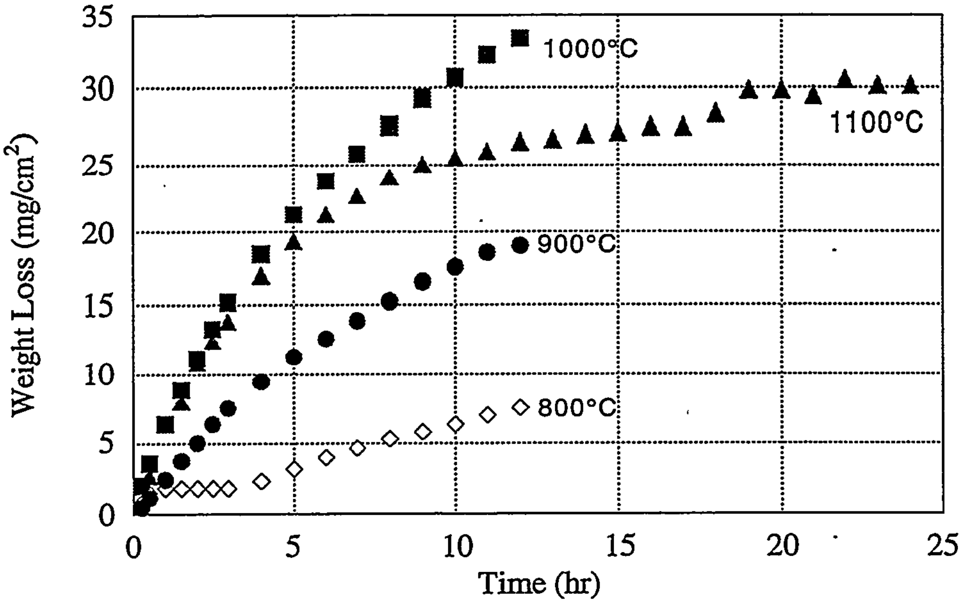

Fig. 5 Weight loss as a function of time for SiC/BN/SiC materials in Ar with 20000 ppm pO_2 environment.

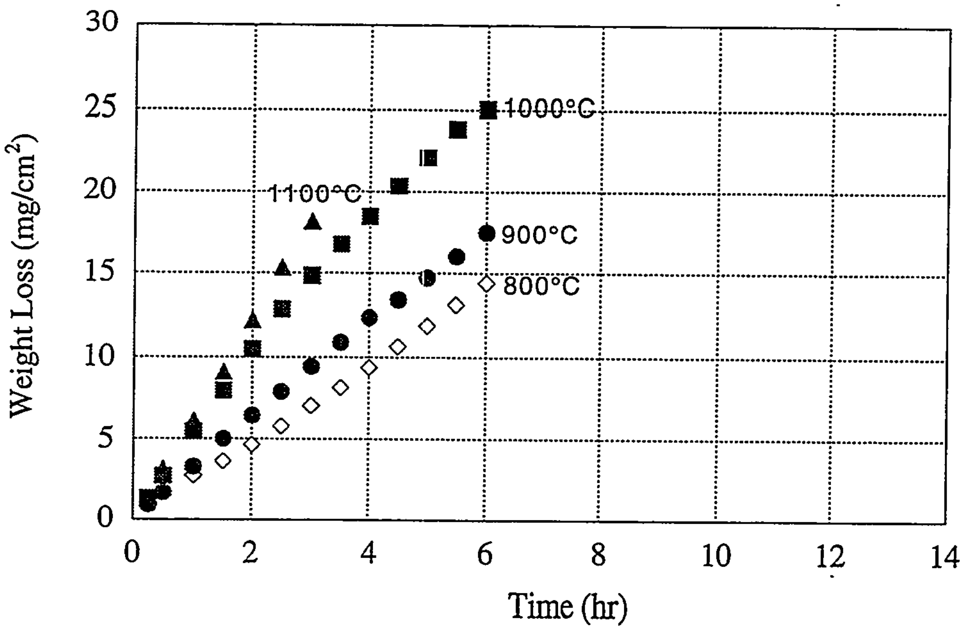

Fig. 6 Weight loss as a function of time for SiC/C/SiC materials in Ar with 20000 ppm pO_2 environment.

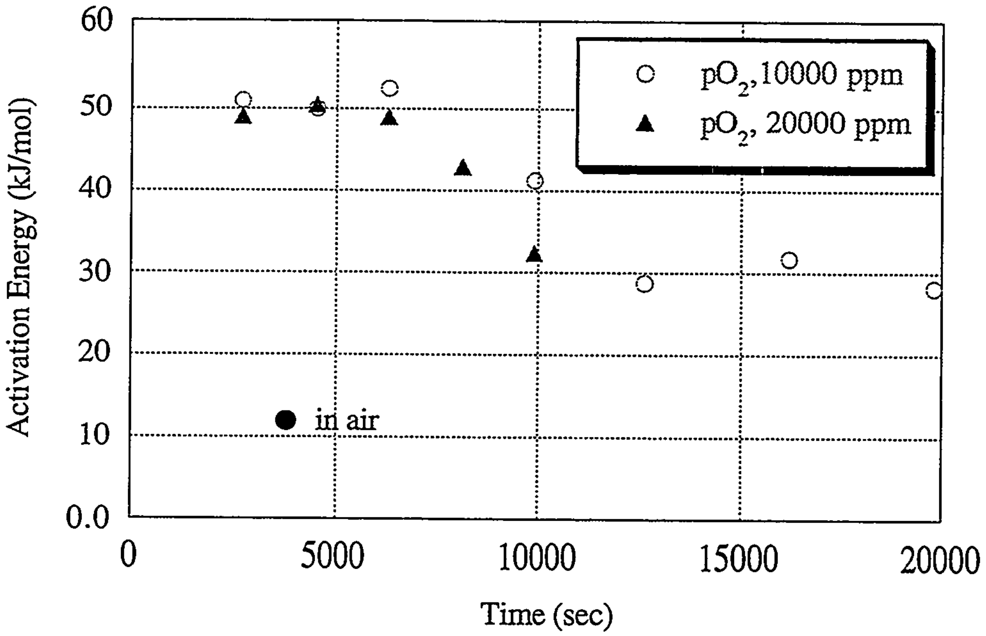

Fig. 7 Activation energy versus time plot obtained from TGA data (800-1100°C) for SiC/C/SiC composites in argon with 10000 ppm and 20000 ppm pO_2 environment.

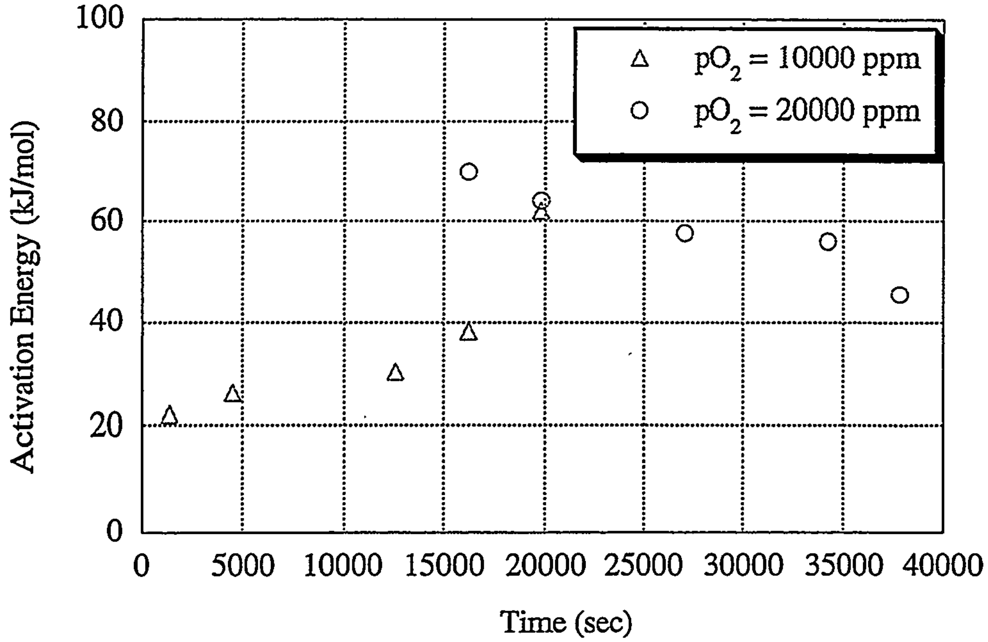

Fig. 8 Activation energy versus time plot obtained from TGA data (800-1000°C) for SiC/BN/SiC composites in argon with 10000 ppm and 20000 ppm pO_2 environment.

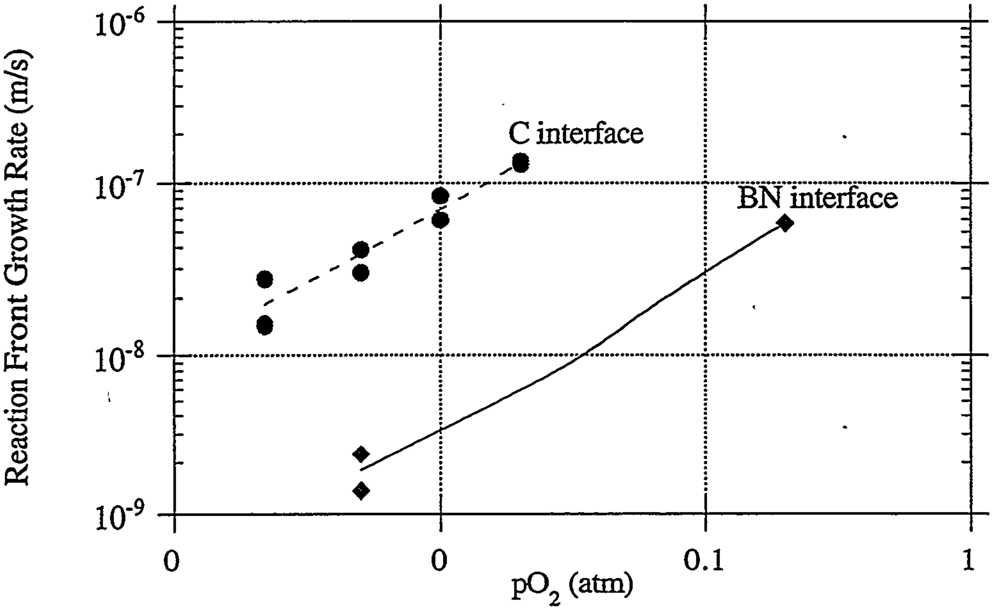

Fig. 9 Average reaction front growth rate (optically measured) versus pO2 for C- and BN-interface materials.

REFERENCES

1. A. G. Evans and R. M. McMeeking, *Acta Metall*, **34** [12] 2435-2441 (1986).
2. K. M. Prewo, *Am. Ceram. Soc. Bull.*, **68** [2] 395-400 (1989).
3. D. B. Marshall and A. G. Evans, *Acta Metall. Mater.*, **37** [10] 2567-2583 (1989).
4. H. C. Cao, E. Bischoff, O. Sbaizero, M. Rühle, A. G. Evans, D. B. Marshall, and J. J. Brennan, *J. Am. Ceram. Soc., 73* [6] 1691-1699 (1990).
5. K. M. Prewo and J. J. Brennan, *J. Mater. Sci.*, **17** 1201-6 (1982).
6. J. B. Davis, J. P. A. Löfvander, A. G. Evans, E. Bischoff, and M. L. Emiliani, *J. Am. Ceram. Soc.*, **76** [5] 1249-57 (1993).
7. T. Mah, N. L. Hecht, D. E. McCullum, J. R. Hoenigman, H. M. Kim, A. P. Katz, and H. A. Lipsitt, *J. Mater. Sci.*, **19** 1191-1201 (1984).
8. G. Simon and A. R. Bunsell, *J. Mater. Sci.*, **19** 3649-3657 (1984).
9. G. Simon and A. R. Bunsell, *J. Mater. Sci.*, **19** 3658-70 (1984).
10. R. H. Jones, C. H. Henager, Jr., and G. W. Hollenberg, *J. Nucl. Mater.*, **191-194** 75-83 (1992).
11. K. D. McHenry and R. E. Tressler, *J. Mater. Sci.*, **12** 1272-1278 (1977).
12. E. J. Minford and R. E. Tressler, *J. Am. Ceram. Soc.*, **66** [5] 338-340 (1983).
13. T. E. Easler, R. C. Bradt, and R. E. Tressler, *J. Am. Ceram. Soc.*, **64** [12] 731-734 (1981).
14. D. E. Carroll and R. E. Tressler, *J. Am. Ceram. Soc.*, **68** [3] 143-146 (1985).
15. K. D. McHenry, T. Yonushonis, and R. E. Tressler, *J. Am. Ceram. Soc.*, **59** [5-6] 262-263 (1976).
16. J. L. Henshall, D. J. Rowcliffe, and J. W. Edington, *J. Am. Ceram. Soc.*, **62** [1-2] 36-41 (1979).
17. D. C. Larsen, J. W. Adams, S. A. Bortz, and R. Ruh, *Fracture Mechanics of Ceramics,* vol. 6, Measurements, Transformations, and High-Temperature Fracture, edited by R. C. Bradt, A. G. Evans, D. P. H. Hasselman, and F. F. Lange, Plenum Press, New York, pp. 571-585 (1986).
18. A. G. Evans and F. F. Lange, *J. Mater. Sci.*, **10** 1659-1664 (1975).
19. C. H. Henager, Jr. and R. H. Jones, *Ceramic Eng. Sci. Proc.*, **13** [7-8] 411-419 (1992).
20. C. H. Henager, Jr. and R. H. Jones, *J. Am. Ceram. Soc.*, **77** [9] 2281-2394 (1994).
21. C. H. Henager, Jr. and R. H. Jones, *Ceramic Eng. Sci. Proc.*, **14** [7-8] 408-415 (1993).
22. J. A. DiCarlo, *Comp. Sci. Tech.*, **51** 213-222 (1994)..
23. L. Filipuzzi, G. Camus, R. Naslain, and J. Thebault , *J. Am. Ceram. Soc.*, **77** [2] 459-66 (1994).
24. L. Filipuzzi and R. Naslain, *J. Am. Ceram. Soc.*, **77** [2] 467-80 (1994).
25. S. Baskaran and J. W. Halloran, *J. Am. Ceram. Soc.*, **77** [5] 1249-55 (1994).

EFFECTS OF NEUTRON IRRADIATION ON DIMENSIONAL STABILITY AND ON MECHANICAL PROPERTIES OF SiC/SiC COMPOSITES - G. E. Youngblood, C. H. Henager, Jr., D. J. Senor, and G. W. Hollenberg (Pacific Northwest Laboratory)[a]

OBJECTIVE

The objective of this work is to assess the development and the performance of continuous fiber SiC_f/SiC composites as a structural material for advanced fusion reactor applications.

SUMMARY

The dimensional stability and some mechanical properties of two similar 2D 0-90° weave SiC_f/SiC composites made with Nicalon™ ceramic-grade (CG) fiber were characterized and compared after neutron irradiation to those properties for ß-SiC. The major difference between these two composites was that one had a thin (150 nm) and the other a thick (1000 nm) graphite interface layer. The irradiation conditions consisted of relatively high doses (4.3 to 26 dpa-SiC) at high temperatures (430 to 1200°C).

Up to about 900°C, swelling of the irradiated SiC_f/SiC composites (< 0.5%) was slightly less than for irradiated monolithic SiC and was relatively independent of dose. The strengths and the modulus of these SiC_f/SiC composites were reduced by about 50% by the irradiation. During irradiation, the Nicalon CG fibers tended to densify and shrink, thus partially decoupling the fibers from the matrix. The decoupling of the fibers from the matrix led to loss of load transfer capability and effectively increased the porosity of the material. Considerable microcracking of the matrix also resulted due to the residual stresses between the shrinking fibers and the expanding matrix.

Synthesis of irradiation resistant SiC_f/SiC composites in the future will require fabrication using improved SiC fibers with better irradiation damage stability. Only then can the fiber/matrix interface thickness and perhaps type be optimized for better performance.

PROGRESS AND STATUS

Introduction

Silicon carbide (SiC) has been considered as a structural material for fusion reactor applications since the 1970s primarily because of its low residual activation and high temperature properties [1,2]. However, except for some special applications, the brittle fracture nature of monolithic SiC limits its use. In the last decade a new class of SiC materials has evolved from the space industry which exhibits a type of inelastic deformation and non brittle failure. These new SiC materials are SiC fiber-reinforced composites (SiC_f/SiC). They consist of continuous fibers, primarily SiC, in a chemically vapor infiltrated (CVI) matrix of ß-SiC. The fibers are coated with a thin interfacial layer, generally graphite, which allows considerable debonding of the fibers from the matrix. Under stress the debonding and associated fiber sliding with strain energy absorption lead to high fracture toughness and high strain-to-failure in these composites, in contrast to the brittle fracture characteristics exhibited by monolithic SiC [3].

Recently, several technical issues were identified which would require further development before the successful application of SiC_f/SiC in a fusion reactor could be realized [4]. This investigation provides an initial effort to address two of these issues: namely, the effects of neutron irradiation on the

---

[a] Pacific Northwest Laboratory is operated for the U.S. Department of Energy by Battelle Memorial Institute under Contract DE-AC06-76RLO-1830.

dimensional stability and on the mechanical properties of SiC_f/SiC composite made with commercially available Nicalon CG fiber.

Experimental Description

A SiC_f/SiC composite, consisting of a Nicalon CG fiber layup in a 2D 0-90° weave pattern with a CVI ß-SiC matrix (manufactured by Dupont Co., Wilmington DE) was examined as the reference material in this work. Nicalon CG is a polymer-derived Si-C-O fiber (12 ±2 wt% O, C:Si = 1.3) that is produced as a textile-grade yarn by Nippon Carbon Co. of Japan. The unirradiated fiber had a mean diameter of 14 µm, a density of 2.54 g/cm^3, and a reported tensile strength of 2.6 GPa and tensile modulus of 190 GPa at room temperature [5]. For comparison, the tested monolithic ß-SiC had a four-point bend strength of 360 MPa and bend modulus of 390 GPa. The reported fiber microstructure consisted of small nano-crystalline (≈2 nm.) ß-SiC grains within a somewhat amorphous Si-C-O matrix [6]. Prior to the CVI process, a uniform 150 nm coating of pyrolytic graphite was deposited onto the Nicalon fibers.

For comparison, data were acquired for a similar 2D 0-90° weave composite fabricated by Oak Ridge National Laboratory. This composite also was made with Nicalon CG fiber, but the graphite interface layer was much thicker (≈1000 nm). In the remainder of this paper the two composite types will be referred to as 2D-150 nm and 2D-1000 nm, respectively. For a more complete picture, some irradiation data from other work [7] for monolithic ß-SiC and Nicalon CG fiber alone and for SiC_f/SiC composites will be combined with this new data.

The composites and fibers were irradiated in either the FFTF or the EBR-II reactors, each a sodium-cooled reactor possessing a fast neutron spectrum with more than 50% of the flux greater than 0.1 MeV. Bend bar specimens and fiber bundles were irradiated at 430, 500, 800, 1000, 1200 and 1500°C to doses of from 4.3 to 26 dpa-SiC. Since it is the high energy neutrons that cause most of the irradiation damage in materials like SiC, the irradiation exposure is given in units of displacements per atom (dpa-SiC) for comparison to other reactor spectrums. The 430°C irradiation was for a weeper capsule at the liquid sodium coolant temperature; all other irradiation temperatures were established for gas-gapped TZM capsules with W ballast for gamma heating. Thermal expansion devices (TED), small vials containing sodium that respond to the sodium thermal expansion, indicated temperatures of 500-505°C and 780-820°C in capsules where the predicted temperatures were 500 and 800°C, respectively. The SiC specimens exhibited only limited activation after irradiation (10 to 200 mR/h at 15 cm), but were highly smearable (18 to 250 cpm/cm^2). Continued precautions during subsequent handling and testing of these materials was necessary. The neutron activation was associated with background contaminants within the SiC ceramics, i.e., ^{54}Mn, ^{58}Co, etc.

All flexural bars, three or four bars for each experimental condition, were cut and diamond machined with 3.18 x 6.35 mm cross sections and 38.1 mm lengths. The 2D fiber weave directions were maintained parallel to the specimen length and width directions. Dimensional measurements of the bars were made before and after irradiation using a DR-25C optical gauge (Bausch and Lomb) with a rounded probe to ensure point contact. Due to a high degree of surface roughness and the tendency for some of the specimens to bow slightly after irradiation, only the length measurements, determined with an accuracy of ± 0.0025 mm, were used as the basis for the linear dimensional changes.

Four-point bend tests were carried out at the temperature of irradiation to measure strength, modulus and fracture energy. Fixtures conforming to MIL-STD-1942 (MR) were manufactured from polycrystalline SiC [8]. The test fixture was fully articulating with a lower universal joint and an upper crossed roller pin design for self alignment. Load was applied to the fixture using an Instron 1125 test machine with a 1000 pound load cell at a strain rate of 1.8×10^{-5} s^{-1}. The upper/lower spans were set at 30/15 mm for the 38.1 mm length bars. Midpoint displacements were monitored via alumina extension rods attached to a strain-gauge extensometer. The specimen deflection and load were corrected to account for the spring constant of the loading bellows and extensometers. Mechanical testing was conducted in flowing, high-purity argon (0.5 cc/hr) contained within a ceramic tube that was sealed by bellows at top and bottom. Test temperatures were monitored with a platinum-30% rhenium/platinum-6% rhenium (Type B) thermocouple placed within 1.6 mm of the specimen centers. The specimens were held for 15 minutes at each test temperature (± 5°C) prior to testing. Exhaust gas, measured with a Thermox oxygen meter, had less than 10 ppm oxygen. Because of the irradiated specimen's smearability, the entire testing apparatus was enclosed within a high air flow hood.

A data acquisition system collected, averaged and recorded 30 data points per second for load, time, displacement, oxygen partial pressure and temperature. Outer surface stresses and strains were calculated using elastic, flexural expressions. The modulus in bending was determined by applying a least squares fit to the linear portion of the stress-strain behavior.

Results and Discussion

Dimensional Stability

Averaged length changes of the irradiated SiC_f/SiC composites (2D-150 nm and 2D-1000 nm) and the monolithic SiC are shown in Figure 1 for the various irradiation temperatures regardless of fluence levels. Standard deviations for the length change measurements varied from 0.01% for the monolithic material up to 0.11% for the composites. For comparison, the swelling data for monolithic SiC determined by Palentine [9] and by Price [10] also are shown in Figure 1.

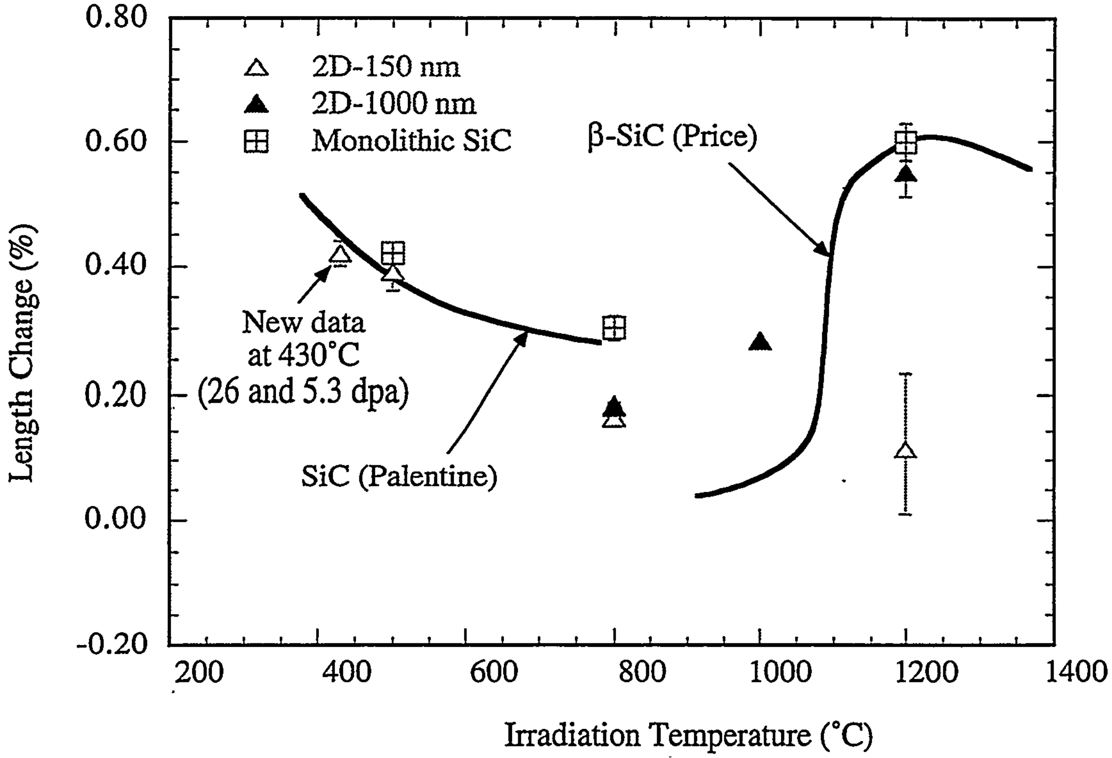

Fig. 1. Macroscopic length change vs. irradiation temperature for monolithic SiC and 2D SiC_f/SiC (2D-150 nm and 2D-1000 nm) composites. The solid lines represent similar measurements for monolithic SiC made by Palentine [7] and by Price [8].

At 430, 500 and 800°C, the swelling of both the monolithic and the 2D-150 nm composite were in close agreement with Palentine's data [7]. At 800°C, the 2D-1000 nm composite exhibited somewhat lower swelling. This new data appears to reflect the steady decline in the swelling with irradiation temperature for SiC-based materials and, as observed by Palentine [7], is relatively independent of dose over this temperature range. Swelling of SiC in this lower temperature range can be attributed to an increase in the lattice constants due to a higher degree of metamictization in the SiC crystal structure [11]. As the temperature increases, the thermal annealing rate increases and the pseudo-equilibrium level of defects decreases. Consequently, the amount of swelling is reduced in the crystalline SiC material.

In contrast, the length of a bundle of Nicalon CG fibers irradiated at 850°C to a dose of 26 dpa contracted and the fiber density increased. The measured relative length change was -4.4 ± 1.1% and the density change, determined by a liquid gradient column technique, was +14.7±0.8%. By assuming isotropic contraction, the length change calculated from the density change is -4.7 ± 0.8%, which is in good agreement with the measured length change value. The Nicalon fiber density change determined here is consistent with density change trends with irradiation dose reported by Okamura et al [12]. During irradiation, the fibers actually shrink as the somewhat amorphous nano-crystalline microstructure of the Nicalon CG fiber becomes more ordered [12].

For irradiation temperatures above about 900°C, the monolithic SiC and the 2D-1000 nm SiC composite exhibited enhanced swelling, in agreement with the data of Price for ß-SiC for comparable doses. However, at 1200°C the swelling of the 2D-150 nm composite was in line with its swelling trend observed at lower temperatures. Price proposed that void formation rather than lattice expansion dominates the swelling mechanism at irradiation temperatures above 1200°C. Consequently, the swelling would be expected to be almost proportional to fluence rather than fluence independent, as was observed for the irradiations at temperatures lower than 900°C.

The macroscopic length change of the irradiated SiC_f/SiC composites can be explained by considering that the fibers were mechanically decoupled from the matrix. The higher composite swelling values near the monolithic swelling values indicate full decoupling while the lower values, observed for the 2D-150 nm composite for instance, suggest only a partial decoupling. It is reasonable to expect some degree of decoupling in these composites as the fiber shrinks away from the matrix during irradiation. The density change data for the Nicalon CG fibers at 850°C indicates that there was considerable diametral shrinkage as well as length shrinkage.

Mechanical Properties

Typical four-point bend stress-strain curves at 430 and 800°C for the SiC_f/SiC composites before and after neutron irradiation are shown in Figure 2. At 800°C, the strengths or maximum stress achieved for the unirradiated 2D-150 nm and 2D-1000 nm SiC_f/SiC composites were about 600 and 300 MPa, respectively. At 430°C for the unirradiated 2D-150 nm specimen, the strength decreased to about 400 MPa. Dupont literature strength values for the 2D-150 nm material also indicate such a temperature dependence with a possible maximum strength near 800°C (quoted values are 300, 400 and 270 MPa at 23, 1000 and 1400°C, respectively [5]). For comparison, similar curves are presented for unirradiated (and irradiated) monolithic SiC at 800°C. At this temperature, the strength of the unirradiated 2D-150 nm composite was greater while the strength of the 2D-1000 nm composite was slightly less than that of the monolithic material. Also, the brittle stress-strain behavior of the monolithic SiC is contrasted with the inelastic-type deformation displayed by the SiC_f/SiC composites in Figure 2. The unirradiated SiC_f/SiC composites achieved strains greater than 1.5% with residual toughness beyond the uniform elongation point (not shown in Figure 2) during bend testing. After bend testing, most of the composite bar specimens were removed from the flexural fixture in one piece.

The effect of irradiation damage on the mechanical properties for both these two composites with different interface thicknesses also is demonstrated by the stress-strain curves in Figure 2. The strengths were reduced by 50% or more at both test temperatures. Nevertheless, the general feature of inelastic deformation with a large strain-to-failure is retained for the irradiated composites.

The explicit dose dependencies of the four-point bend strengths and bend modulus for the SiC_f/SiC composites irradiated at 430, 500, 800 and 1200°C are shown in Figure 3, upper and lower, respectively.

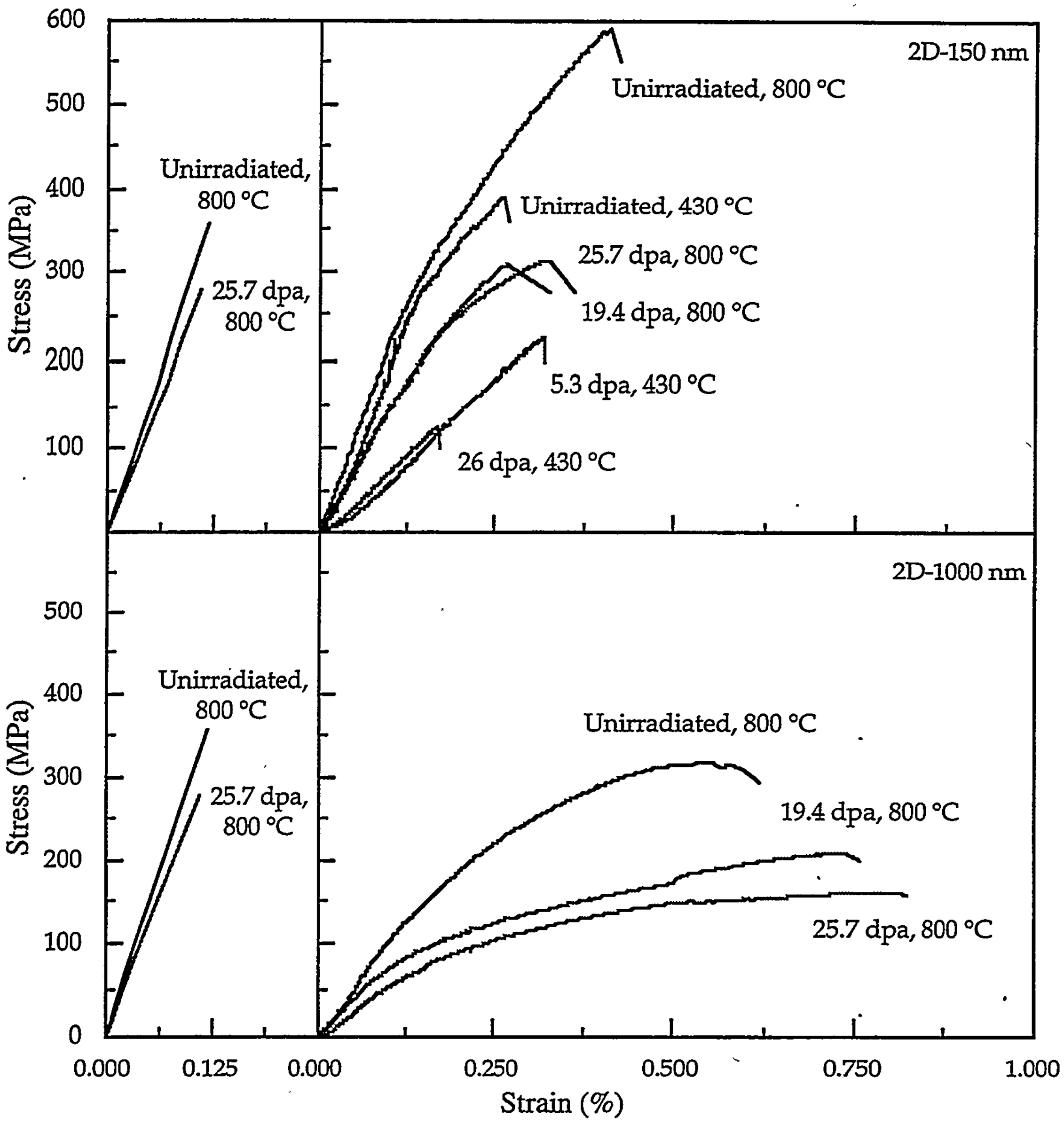

Fig. 2. Typical four-point bend stress-strain curves for SiC_f/SiC composites (2D-150 nm at 430 and 800°C and 2D-1000 nm at 800°C) before and after neutron irradiation. For comparison, similar curves determined for monolithic SiC are shown on the left. Note the improved strength and strain-to-failure (toughness) for the SiC composites compared to monolithic SiC.

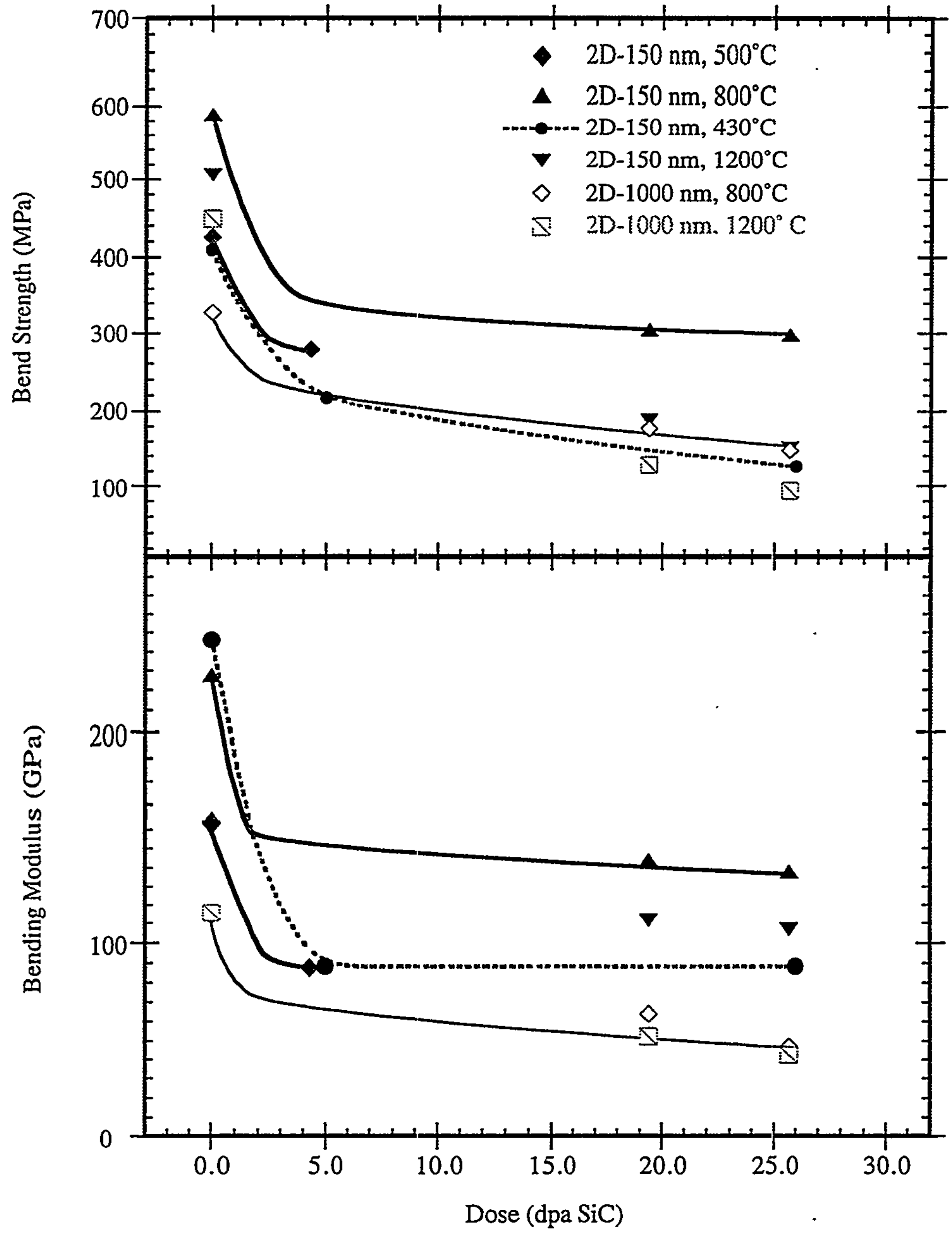

Fig. 3. Dose dependence of the four-point bend strength and modulus for SiC$_f$/SiC composites (2D-150 nm and 2D-1000 nm) neutron irradiated and tested at 430, 500, 800 and 1200°C. The lines indicate saturation of the irradiation effects at relatively low fluence levels [13].

In Figure 3, the dose dependence of these mechanical properties as indicated by solid or dashed lines, which infers an initial transient period followed by saturation with little further effect of exposure. Others have observed low fluence effects in SiC that saturate and then remain relatively unchanged up to higher fluence levels [13]. Likewise, a similar temperature dependence, noted previously for the strengths where optimum performance occurs at about 800°C, is followed for the 2D-150 nm material modulus. The generally lower values of strength and modulus for the 2D-1000 nm material appear to indicate that no such optimum temperature performance exists for the thicker interlayer composite.

In Figure 4, optical micrographs of the unirradiated 2D-150 nm composite and of the same composite irradiated at 500, 800 and 1200°C to doses of 4.3, 25.7 and 25.7 dpa, respectively, depict the microstructural changes after neutron irradiation. In particular, the gap formation around the fibers as well as the gap linking and crack formation, features responsible for the mechanical property changes, are already observed at 4.3 dpa (500°C). These same features appear to be relatively unchanged for further dose to 25.7 dpa (800°C).

By comparing the composite and fiber length change (and fiber density change) data and the microstructural data, the feature that appears to have the most bearing on the mechanical property degradation in irradiated SiC_f/SiC composites (as depicted in Figure 3) is the apparent partial decoupling of the Nicalon CG fibers from the ß-SiC matrix. Fortunately, the decoupling is only partial, and the fibers still contribute to some load bearing (more so in the 2D-150 nm material than in the 2D-1000 nm material) and preservation of the inelastic-type deformation in these irradiated SiC_f/SiC composites as desired.

Typical fracture surfaces of the unirradiated and irradiated 2D-150 nm SiC_f/SiC composite are shown in Figure 5. For the unirradiated fracture (upper views), a singularly directed crack front with limited fiber pullout is observed. In contrast, for this composite irradiated at 800°C (lower views), the crack spreads and propagates in different directions and is accompanied by a significant amount of fiber pullout. Fiber pullout for the unirradiated composite was only ten's of microns, while for the irradiated materials it was millimeters in length. Crack bridging occurred in all these irradiated composites on a macroscopic scale; on a scale much larger than observed for the unirradiated materials. This observation is consistent with the partially decoupled fiber model for these irradiated SiC_f/SiC composites. With the weakened interfacial bonding, the fibers become loaded at distances approaching the weave spacing (millimeters) and fiber fractures occur at varied distances between the weave spacing. Note the crack tracing the weave pattern across the tensile surface view of the irradiated sample in Figure 5.

Fiber shrinkage and decoupling from the matrix during irradiation is an area of concern, but potentially is an area where marked improvement in irradiation performance can be attained. As a more irradiation tolerant fiber is developed, these SiC_f/SiC composites can be optimized for the nuclear application. It appears that the most pressing enabling technology for fabrication of successful composites for the space effort matches that for fusion reactor applications, i.e., the production and use of high-purity (no excess O or C), thermally stable, very fine grain ß-SiC fiber for reinforcement in composites with a ß-SiC matrix.

CONCLUSIONS

Swelling for irradiated SiC_f/SiC composites was only slightly less than for irradiated monolithic SiC. Up to about 900°C, the swelling appeared to be relatively independent of fluence. It is postulated that decoupling of the Nicalon fibers from the SiC matrix occurs during irradiation as these Nicalon CG fibers shrink and densify. The strengths and the modulus of the irradiated SiC_f/SiC composites were reduced by about 50%, which appears to be related to mechanically decoupling of the fibers from the matrix. After initial reductions, the mechanical properties become relatively independent of further neutron dose. Photographic evidence of crack propagation and fiber pull-out for the irradiated composites further support the concept of the Nicalon CG fibers being at least partially mechanically decoupled from the matrix.

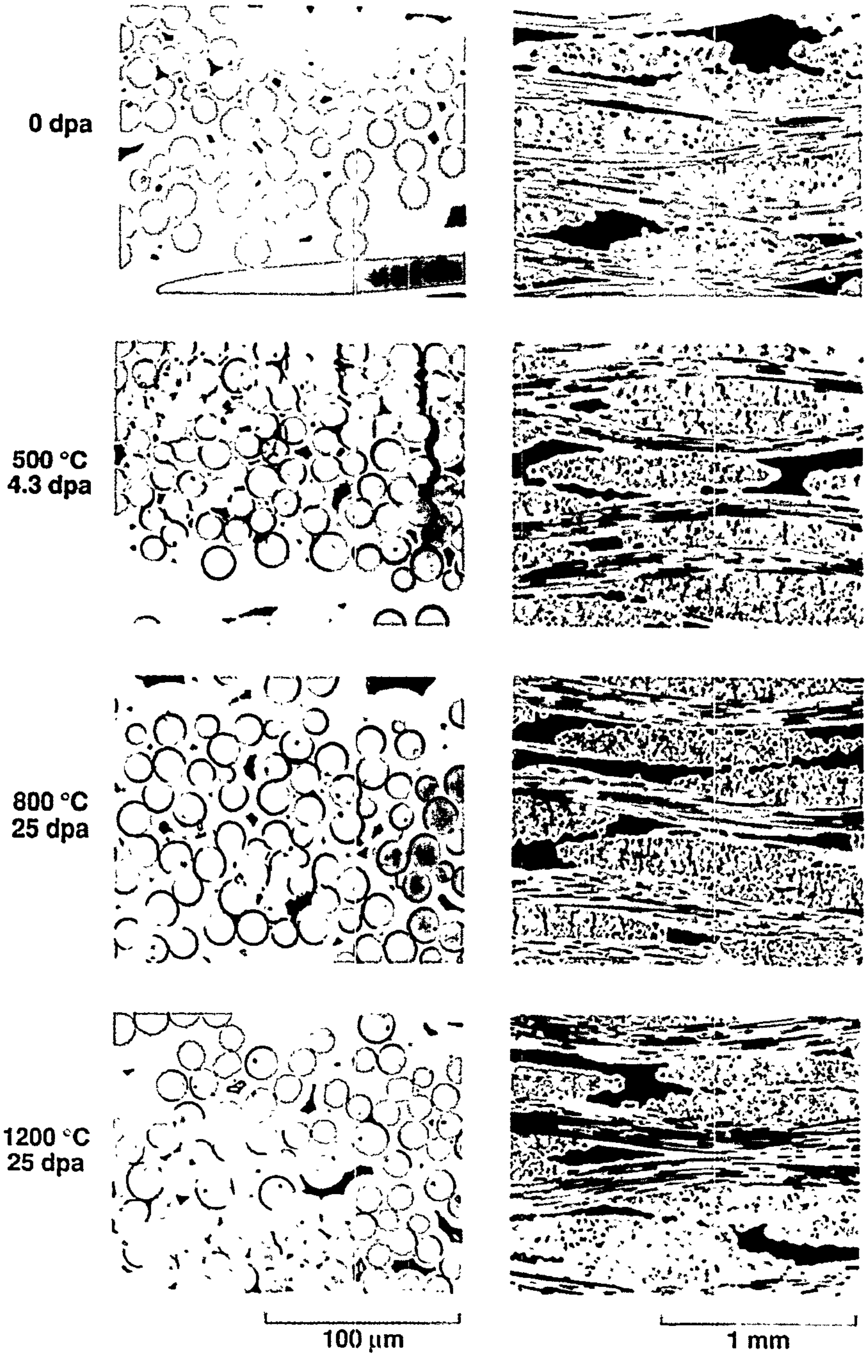

Fig. 4. Optical micrographs of the 2D-150 nm SiC_f/SiC composite depicting microstructural changes due to neutron irradiation at 500, 800 and 1200°C to doses of 4.3, 26 and 26 dpa, respectively. Note the residual macroscopic porosity as a result of the CVI processing in the right-hand views. Also note the gap formation about the fiber cross-sections for all irradiation doses and temperatures as well as the crack formation for the samples irradiated at 500 and 800°C, but not for the sample irradiated at 1200°C.

Synthesis of irradiation resistant SiC$_f$/SiC composites in the future will require: (1) improved SiC fibers with better irradiation damage stability, and then (2) optimization of the fiber/matrix interface layer thickness and perhaps interface type.

FUTURE WORK

Emphasis will be focused on examining the irradiation effects on alternate commercial and developmental SiC-based fibers to identify specific characteristics that might lead to a more radiation tolerant fiber and ultimately to a high performance SiC$_f$/SiC composite suitable for advanced fusion reactor applications..

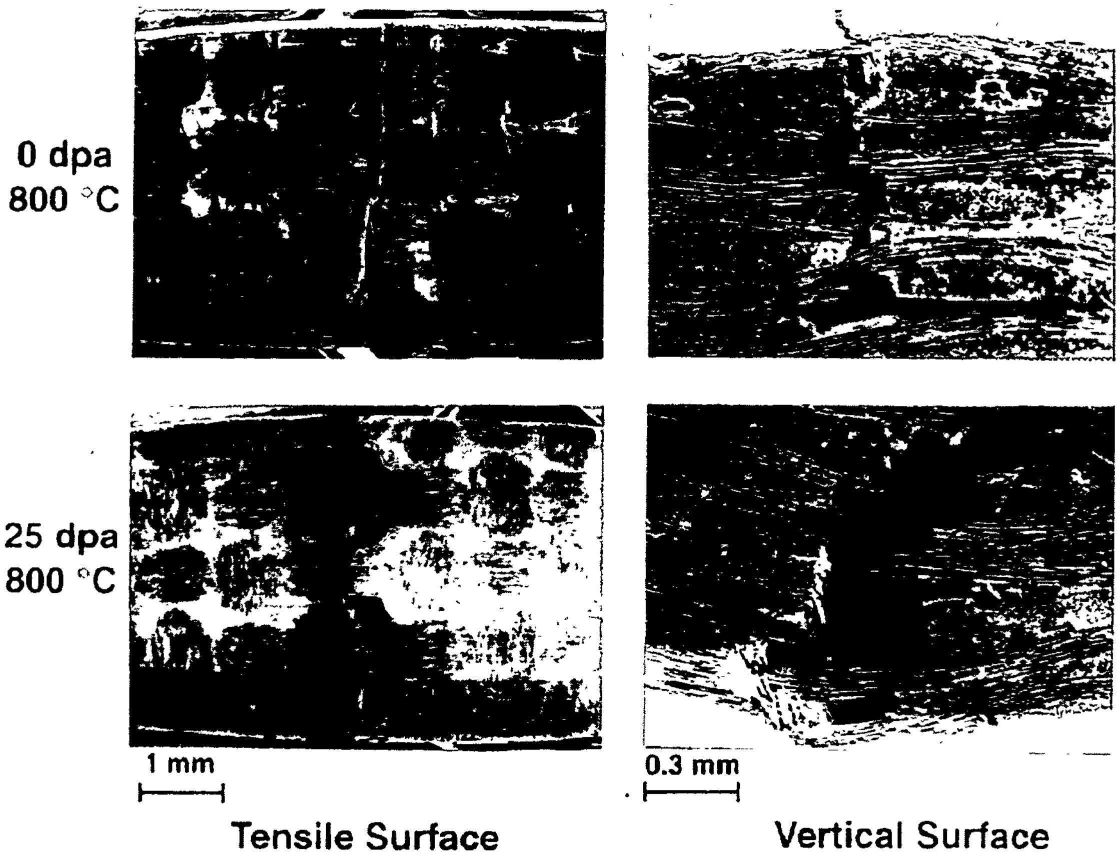

Fig. 5. Crack propagation in unirradiated (upper) and irradiated (lower) 2D-150 nm SiC$_f$/SiC composite after flexure testing at 800°C. Note the extensive amount of fiber pull-out after irradiation.

REFERENCES

1. L. M. Rovner and G. R. Hopkins, "Ceramic Materials for Fusion," *Nuclear Technology 29, 274-302 (1976).*
2. G. G. Trantina, "Ceramics for Fusion Reactors - Design Methodology and Analysis," *J. Nucl. Mater. 85-86, 415-420 (1979).*
3. G. R. Hopkins and J. Chin, "SiC Matrix/SiC Fiber Composite: A High-Heat Flux, Low Activation, Structural Material," *J. Nucl. Mater. 141-143, 148-151 (1986).*
4. G. W. Hollenberg, R. H. Jones and G. E. Lucas, "SiC/SiC Composites for Fusion Applications, Opportunities and Issues - 1990," in Proceedings of the DOE Workshop on Ceramic Matrix Composites for Structural Applications in Fusion Reactors Office of Fusion Energy, Santa Barbara CA (1990). PNL-SA-17843, CONF-9005225.
5. "Ceramic Matrix Composites," Dupont data sheets available from the Dupont Co. Composites Division, Magnolia Run, Wilmington DE.
6. Witold Kowbel (MER Corporation) private communication.
7. G. W. Hollenberg, C. H. Henager, Jr., G. E. Youngblood, D. J. Trimble, S. A. Simonson, G. A. Newsome and E. Lewis, "The Effect of Irradiation on the Stability and Properties of Monolithic Silicon Carbide and SiC_f/SiC Composites up to 25 dpa," accepted for publication in the *J. Nucl. Mater.* (1994).
8. U. S. Department of the Army, Army Materials and Mechanics Research Center, "Flexural Strength of High Performance Ceramics at Ambient Temperature," MIL-STD-1942 (MR), Watertown, MA (1983).
9. J. E. Palentine, "The Calibration of Fast Reactor Irradiated Silicon Carbide Temperature Monitors Using a Length Measurement Technique," *J. Nucl. Mater. 92, 43-50 (1980).*
10. R. J. Price, "Neutron Irradiation Induced Voids in ß-Silicon Carbide," *J. Nucl. Mater. 48, 47-57 (1973).*
11. F. W. Clinard and L. W. Hobbs, "Radiation Effects in Nonmetals." Chapter 7 in Physics of Radiation Effects in Crystals, eds. R. A. Johnson and A. N. Orlov, Elsevier Science Publishers (1986).
12. K. Okamura, T. Matsuzama, M. Sato, H. Kayano, S. Morozumi, H. Tezuka and A. Kohyama, "Effects of Neutron Irradiation on Fine Structure and Strength of SiC Fibers," *J. Nucl. Mater. 155-157, 329-333 (1988).*
13. L. L. Snead, D. Steiner and S. J. Zinkle," Measurement of Effect of Radiation Damage to Ceramic Composite Interfacial Strength," *J. Nucl. Mater. 191-194, 566-570 (1992).*

EFFECT OF IRRADIATION SPECTRUM ON THE MICROSTRUCTURAL EVOLUTION IN CERAMIC INSULATORS - S.J. Zinkle (Oak Ridge National Laboratory)

OBJECTIVE

The objective of this study is to determine examine the effect of variations in the ionizing and displacive radiation environments on the microstructure of oxide ceramic insulators.

SUMMARY

Cross section transmission electron microscopy has been used to investigate the microstructure of $MgAl_2O_4$ (spinel) and Al_2O_3 (alumina) following irradiation with ions of varying mass and energy at room temperature and 650°C. Dislocation loop formation was suppressed in specimens irradiated with light ions, particularly in the case of spinel. An evaluation of the data showed that dislocation loop formation during irradiation at 650°C was suppressed when the ratio of the electronic- to nuclear-stopping power was greater than ~10 and ~1000 for spinel and alumina, respectively. The effect of uniform background levels of ionizing radiation on the microstructural evolution in spinel was investigated by performing simultaneous dual-beam (He^+ and heavy ion) irradiations. The uniform ionizing radiation source did not affect the microstructural evolution of spinel unless the ionization was very intense (average electronic- to nuclear-stopping power ratio >100). These results clearly indicate that light ion and electron irradiations produce microstructures which are not representative of the microstructure that would form in these ceramics during fission or fusion neutron irradiation.

PROGRESS AND STATUS

1. Introduction

Ceramic insulators such as $MgAl_2O_4$ (spinel) or Al_2O_3 (alumina) are required for several key applications in fusion energy systems that are currently being developed. These applications include magnetic diagnostic coils, insulating feedthroughs and windows for the radiofrequency heating components, and blanket insulators (for systems that utilize liquid metal coolants).[1] The 14 MeV neutrons associated with the DT fusion reaction will produce displacement damage and an intense ionizing radiation field in the materials surrounding the confined plasma. At the present time, there are no available sources for bulk irradiations that match the irradiation spectrum and intensity of proposed DT fusion reactors.

Ion irradiation is a convenient method for studying microstructural changes associated with energetic irradiation. In particular, the effect of irradiation spectrum on the microstructural evolution can be examined by changing the mass and energy of the bombarding ion. Recent ion irradiation studies have shown that the microstructure[2] and macroscopic properties[3-6] of insulators such as MgO, Al_2O_3 and $MgAl_2O_4$ are sensitive to variations in the ionizing and displacive irradiation spectra. The published studies indicate that irradiation with energetic light ions causes a large reduction in the density of interstitial dislocation loops and produces less volumetric swelling than irradiation with heavy ions at a comparable displacement damage rate and displacement dose. Several possible physical mechanisms have been proposed for this sensitivity to irradiation spectrum, including enhanced point defect recombination due to ionization-enhanced diffusion (IED), and nuclear stopping power effects.[2,7] The purpose of the present paper is to summarize recent microstructural data obtained on ion-irradiated alumina and spinel which provide further evidence for a strong dependence on irradiation spectrum.

One potential disadvantage associated with ion irradiation is the strong effect of the implanted ions on the microstructural development. As reviewed elsewhere,[2] the implanted ion region of ceramic insulators contains numerous microstructural features that are generally not found in irradiated regions that are isolated from the implanted ions. In addition, defect cluster formation is generally enhanced in the implanted ion regions. In the present study, ion energies ≥1 MeV have been employed to provide sufficient isolation of the implanted ion region from the rest of the irradiated regions.

2. Experimental Procedure

Polycrystalline blocks of Al_2O_3 (GE Lucalox or Wesgo AL995) and $MgAl_2O_4$ (Ceredyne) were sliced into sheets of 0.5 mm thickness, and 3-mm-diameter transmission electron microscope (TEM) disks were ultrasonically cut from the sheets. The grain size of both the alumina and spinel specimens was about 30 μm. The TEM disks were mechanically polished with 0.5 μm diamond paste, and then bombarded in a 3 x 3 target array at room temperature or 650°C in the triple ion beam accelerator facility at Oak Ridge National Laboratory.[8] The irradiation temperature was determined from a thermocouple spot-welded to the face of a stainless steel TEM disk (which has a thermal conductivity comparable to the ceramic specimens) that occupied one of the positions in the 9-specimen array. The temperature of the target holder substrate was also continuously measured during the irradiation. The specimen surface temperature (monitored by the thermocouple on the stainless steel TEM disk) was within 20°C of the substrate temperature for all of the irradiations.

The specimen arrays were exposed to ion beams ranging from 1 MeV H^+ to 4 MeV Zr^+ ions. The ion beam fluxes and fluences on different sets of specimen arrays were systematically varied for a given ion beam in order to gain some knowledge about the relative roles of damage rate and cumulative damage level. In addition, several specimen arrays were exposed to simultaneous dual ion beams in order to study the effect of intense uniform ionization on the microstructural evolution. Table 1 summarizes the range of irradiation conditions that were examined. The TRIM-90 computer code[9] was used to calculate the depth-dependent ionization and displacement damage dose in Al_2O_3. The TRIM calculations were performed using the measured[10] threshold displacement energies of 24 eV and 78 eV in Al_2O_3 for the aluminum and oxygen sublattices, respectively. The damage level in displacements per atom (dpa) was determined from the damage energy calculated by TRIM, using the modified Kinchin-Pease formula[11] and assuming a sublattice-averaged threshold displacement energy of 40 eV. The calculated dpa values for spinel (using an average threshold displacement energy of 40 eV) were similar to those for alumina. The damage rates varied between ~10^{-6} and 10^{-3} dpa/s (with corresponding ionizing dose rates of 0.1 to 30 MGy/s), depending on the ion species and flux. As indicated in Table 1, the calculated ratio of electronic- to nuclear-stopping power (ENSP) at a depth of 0.5 μm varied from about 2.4 for the heaviest ion (4 MeV Zr) to about 2000 for the lightest ion (1 MeV H). A portion of the specimen array in some of the irradiations was coated with a thin layer (~0.1 μm) of conductive carbon prior to irradiation in order to minimize specimen charging. The microstructure of these carbon-coated specimens following irradiation was found to be identical to that of uncoated specimens in the same target holder, which demonstrated that specimen charging did not have a significant effect on the observed microstructure.

Table 1. Summary of ion irradiation conditions

Ion beam	Fluence levels ($10^{20}/m^2$)	Flux levels ($10^{16}/m^2$-s)	Damage parameters at 0.5μm depth		
			dpa	MGy/s	ENSP
1 MeV H	3-170	6-60	0.0005-0.03	0.3-3	2000
1 MeV He	1-100	4-40	0.005-0.5	1-10	800
3 MeV C	0.04-4	0.2-2	0.002-0.2	0.1-1	250
2.4 MeV Mg	8-28	11-38	3-10	8-29	20
2 MeV Al	5-40	11	3-23	7	13
3.6 MeV Fe	0.2-1.2	0.5	0.3-2	0.5	6
4 MeV Zr	0.02-2	0.2-0.3	0.08-8	0.2-0.3	2.4
4 MeV Fe &	0.2-1.2 (Fe)	0.5 (Fe)	0.3-2 (total)	2.5 (total)	28
1 MeV He	3.5-21 (He)	8.5 (He)			
1.8 MeV Cl	0.07-0.4 (Cl)	0.17 (Cl)	0.1-0.7 (total)	4.4 (total)	160
& 1 MeV He	8-40 (He)	18 (He)			

Cross-section TEM specimens were prepared by gluing a mechanically polished nonirradiated specimen to the irradiated surface of each sample, sectioning perpendicular to the irradiation surface, mechanically dimpling, and ion milling either at room temperature or in a liquid nitrogen cooled stage (6 keV Ar ions, 15° sputtering angle) until perforation occurred at the glued interface.[12] The specimens were examined in a Philips CM12 electron microscope operating at 120 kV.

3. Results

Figure 1 shows the depth-dependent damage energy in alumina for the different ions used in this study, as calculated with the TRIM[9] code. The damage energy is directly proportional to the amount of displacement damage created in the ceramic, and is obtained by subtracting the recoil ionization from the nuclear stopping power.[11] For each ion, the damage energy reaches a maximum value at a depth comparable to the ion range. The maximum damage energy increases with increasing ion mass, ranging from ~0.70 eV/nm for 1-MeV H^+ (not shown in Fig. 1) to ~920 eV/nm for 4-MeV Zr^+ ions. The maximum damage energy is 3 to 25 times the damage energy at the surface, with the largest depth dependence occurring for the lightest ions.

Most of the energy lost by the MeV ion beams is due to interactions with the bound valence electrons in the ceramic. These low-energy interactions produce ionization of the lattice atoms by exciting valence electrons into the conduction band. The electronic stopping power of most ions steadily decreases with increasing depth up to the region where the ions are deposited. In the case of energetic light ions such as 1-MeV H^+, the electronic stopping power increases slightly with increasing depth up to the implanted ion region. Figure 2 shows the calculated depth-dependent ratio of the electronic- to nuclear-stopping power (ENSP) in alumina for the different ions used in this study. The ENSP ratio is approximately proportional to the amount of ionization per displaced atom (it is not exactly proportional since displacement damage is only due to the damage energy portion of the nuclear stopping power). Energetic light ions such as 1-MeV H^+ and 1-MeV He^+ have particularly high ENSP ratios. In all cases, the ENSP ratio is greater than one from the irradiation surface up to depths that are comparable to the ion range.

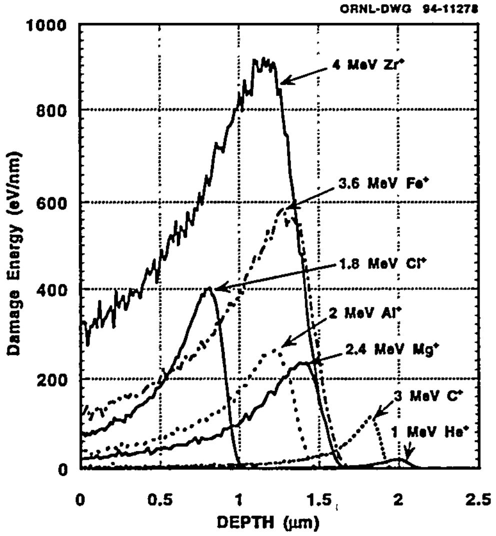

Fig. 1. Calculated depth-dependent damage energy density in Al_2O_3 for various ions.

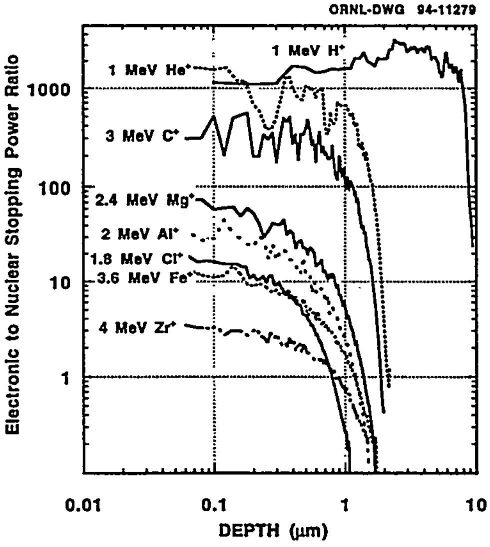

Fig. 2. Calculated ratio of the electronic to nuclear stopping power in Al_2O_3 for various ions.

3.1 Microstructure of irradiated $MgAl_2O_4$

Figure 3 shows the cross-section microstructure of spinel following irradiation with 4-MeV Zr^+ ions at 650°C to a fluence of $2x10^{19}$ Zr^+/m^2. The irradiation produced a moderate density ($8x10^{20}/m^3$) of dislocation loops in the midrange region (~0.5 μm depth), and approximately an order of magnitude higher density of loops in the peak damage region that contained the implanted Zr ions. The dislocation loop density was very low ($<1x10^{19}/m^3$) for regions located within 0.2 μm of the irradiated surface. The average loop diameter was ~15 nm. All of the loops were interstitial in character, with Burgers vectors along <110> directions. Some of the loops were observed to lie on {111} and {110} habit planes. However, most of the loop habit planes were intermediate between {111} and {110} planes. Following the loop sequence outlined by Kinoshita and coworkers,[7,13] this suggests that most of the loops in this specimen have unfaulted and are in the process of rotating from {111} habit planes to {110} habit planes.

ORNL-Photo 6722-93

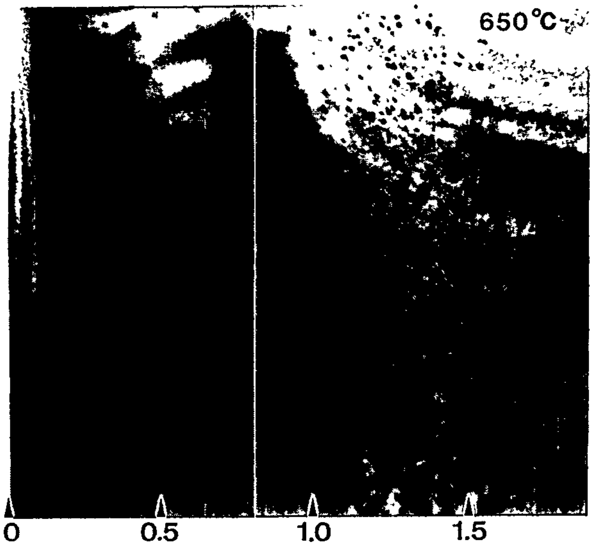

Fig. 3. Depth-dependent microstructure of $MgAl_2O_4$ irradiated with 4-MeV Zr^+ ions to a fluence of $2x10^{19}$ Zr^+/m^2.

Examination of spinel specimens irradiated at lower fluences and with different ions allowed the threshold dose for observable defect cluster formation to be determined.[14] The measured threshold dose for observable defect cluster formation was ~0.1 dpa, which agrees with other ion[15] and neutron[16] irradiation studies performed on spinel.

The microstructure of spinel irradiated with 4-MeV Zr^+ ions at room temperature consisted of a high density ($\sim 5x10^{22}/m^3$) of small defect clusters that were rather uniformly distributed throughout the irradiated region. There was no evidence for a defect-free zone near the irradiated surface in specimens irradiated near room temperature, in contrast to the 650°C results. The loop diameter at intermediate depths (~0.7 μm) increased steadily with increasing fluence, with values of ~3 nm at 1.5 dpa and ~10 nm after a damage level of 10 dpa. Most of the loops were observed to have {110} habit planes after high dose irradiation.

The depth-dependent microstructure of spinel irradiated with 3.6-MeV Fe^+ ions was qualitatively similar to the 4-MeV Zr^+ results. There was no observable defect cluster formation in regions located within ~0.4 μm of the irradiated surface for specimens irradiated with Fe^+ ions at 650°C. The Burgers vector was a/4<110> for most of the dislocation loops analyzed in the specimen irradiated at 650°C to 2 dpa at a depth of 0.5 μm ($1.2x10^{20}$ Fe^+/m^2). The distribution of loops on the different habit planes varied with irradiation depth. In the midrange region (~1 μm depth), about 75% of the loops were located on {110} planes and the remainder were located on {111} planes. The fraction of loops with {111} habit planes increased to ~70% near the peak damage region. The loop density increased and the loop size decreased with increasing depth from the irradiated surface. The measured loop density and average diameter were $5x10^{20}/m^3$ and ~50 nm at a depth of 0.6 μm, and $4x10^{21}/m^3$ and ~20 nm at a depth of 1 μm. Irradiation with Fe^+ ions at room temperature produced a high density ($\sim 5x10^{22}/m^3$) of small defect clusters with an average diameter near 5 nm. The width of the defect-free zone near the irradiated surface was <40 nm in the specimens irradiated at room temperature.

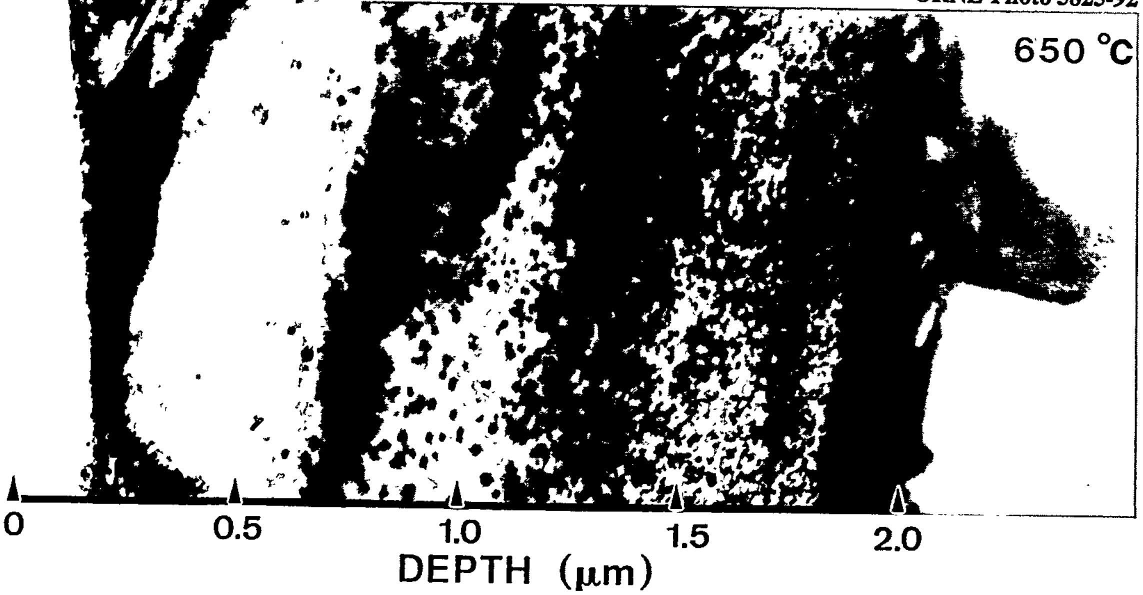
ORNL-Photo 5825-92

Fig. 4. Depth-dependent microstructure of $MgAl_2O_4$ irradiated with 2.4-MeV Mg^+ ions at 650°C to a fluence of $8x10^{20}$ Mg^+/m^2.

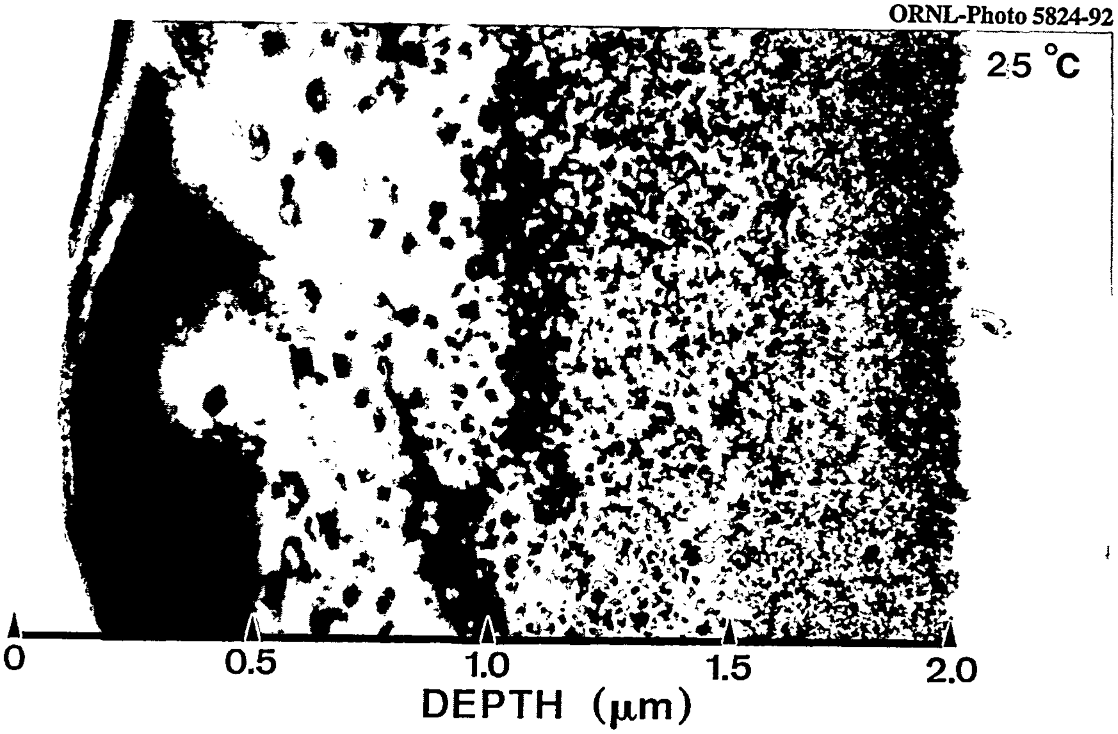
ORNL-Photo 5824-92

Fig. 5. Depth-dependent microstructure of $MgAl_2O_4$ irradiated with 2.4-MeV Mg^+ ions at room temperature to a fluence of $8x10^{20}$ Mg^+/m^2.

The microstructure of spinel irradiated with 2-MeV Al$^+$ ions was similar to that observed following Zr$^+$ and Fe$^+$ ion irradiation. Details of the microstructural analysis have been previously reported.[17,18] A defect-free zone was observed in regions located within ~0.4 μm of the irradiated surface after irradiation with Al$^+$ ions at 650°C. Defect-free zones of comparable width were also observed next to grain boundaries.[17] Irradiation at room temperature reduced the width of this defect-free zone to <50 nm. The fraction of loops with {110} habit planes increased with increasing dose. About 75% of the loops were observed on {110} planes after 3 dpa, and ~90% after 10 dpa. The remaining loops were located on {111} planes. The Burgers vector for almost all of the loops was a/4<110>. A small fraction of the loops on {111} planes had a/6<111> Burgers vectors.

The depth-dependent microstructure of spinel irradiated with 2.4-MeV Mg$^+$ ions at 650°C and room temperature is shown in Figs. 4 and 5, respectively. Microstructural data on spinel specimens irradiated with Mg$^+$ ions at slightly higher fluxes have also been reported elsewhere.[2,14,17,19] In contrast to the heavier ion (Al, Fe and Zr) irradiations, the microstructure in specimens irradiated with Mg$^+$ ions at room temperature was similar to that in specimens irradiated at 650°C. The width of the defect-free region adjacent to the irradiated surface varied between 0.5 and 0.9 μm for both irradiation temperatures. The largest denuded zone width occurred in specimens irradiated at the highest particle flux. The loop density in the midrange region increased with increasing depth. It was generally observed that the loop density was higher in the 650°C specimens compared to the room temperature specimens following irradiation to the same total fluence. As discussed later, this effect may be attributable to the ~50% higher particle flux employed for the room temperature Mg$^+$ irradiations.

Figure 6 shows the microstructure of spinel following irradiation with 3-MeV C$^+$ ions at 650°C to a fluence of 4.6×10^{19} C$^+$/m^2. There was no observable defect cluster formation outside of the implanted ion region (2.1-2.4 μm depth). The damage level at irradiation depths <1.5 μm in this specimen was less than the experimentally-determined threshold level for producing observable defect clusters in spinel (~0.1 dpa) and therefore cannot provide definitive information on possible spectrum effects. On the other hand, the lack of observable dislocation loop formation at depths between 1.5 and 2.1 μm, where the damage level exceeds 0.1 dpa, suggests that C$^+$ ions are not effective at producing defect clusters in spinel. A similar large defect-free zone was observed in spinel irradiated with C$^+$ ions at room temperature to a fluence of 4×10^{20} C$^+$/m^2 (0.2 dpa at 0.5 μm).

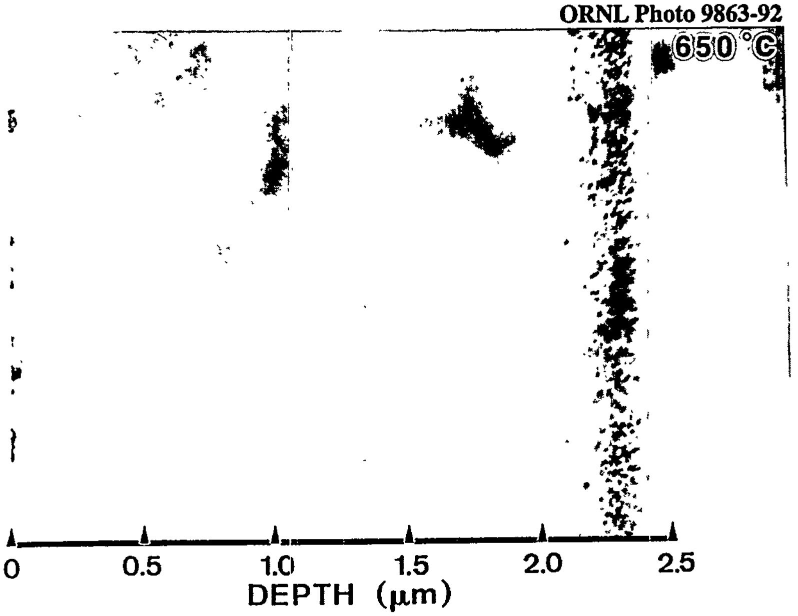

Fig. 6. Depth-dependent microstructure of $MgAl_2O_4$ irradiated with 3-MeV C$^+$ ions to a fluence of 4.6×10^{19} C$^+$/m^2.

ORNL Photo 1080-91

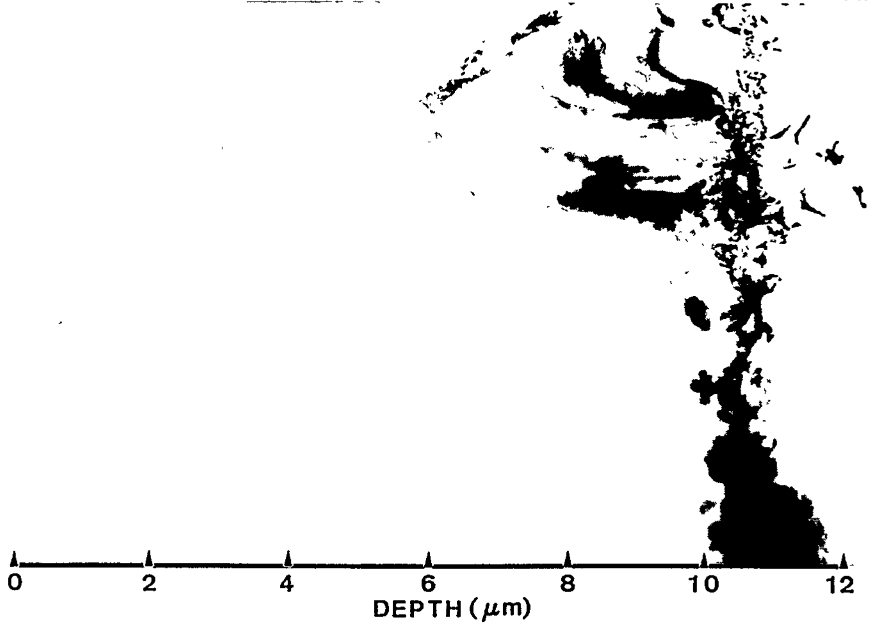

Fig. 7. Depth-dependent microstructure of $MgAl_2O_4$ irradiated with 1-MeV H^+ ions to a fluence of $1.7x10^{22}$ H^+/m^2.

Irradiation of spinel with 1-MeV He^+ or H^+ ions at 650°C did not produce any observable defect cluster formation except in the implanted-ion region. Figure 7 shows an example of the microstructure of spinel following 1-MeV H^+ ion irradiation to a fluence of $1.7x10^{22}$ H^+/m^2. The calculated damage level in this specimen was >0.1 dpa over the latter half of the ion range (5-10 μm depths), but there was no evidence of defect cluster formation in this region (except for the implanted ion region). Similarly, high fluence 1-MeV He^+ ion irradiations that produced midrange damage levels of 0.5 to 3 dpa did not result in any observable defect cluster formation.[2,14,20]

3.2 Microstructure of irradiated Al_2O_3

Alumina was found to be less sensitive than spinel to variations in the irradiation spectrum. Figure 8 shows the microstructure of alumina following irradiation with 2-MeV Al^+ ions at 650°C to a fluence of $9x10^{20}$ Al^+/m^2 (5 dpa at 0.5 μm depth). A high density (~$1x10^{23}/m^3$) of small defect clusters were observed in the irradiated region, without any noticeable depth dependence. An analysis of the dislocation loops indicated that they occurred on both basal (0001) and prism $\{1\bar{1}00\}$ planes, with predominant Burgers vectors of 1/3[0001] and $1/3\langle 1\bar{1}00\rangle$, respectively.[17] The width of the defect-free zones adjacent to the irradiated surface and grain boundaries was <15 nm, which is more than an order of magnitude smaller than that observed in spinel irradiated under comparable conditions.

ORNL Photo 9035-989

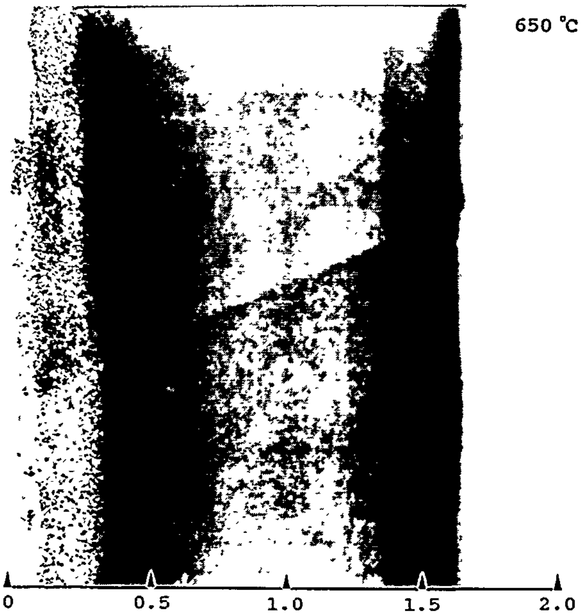

Fig. 8. Depth-dependent microstructure of Al_2O_3 irradiated with 2-MeV Al^+ ions to a fluence of $9x10^{20}$ Al^+/m^2.

The microstructure of alumina irradiated with 3-MeV C^+ ions was similar to that observed following irradiation with heavier ions. Figure 9 shows the microstructure after irradiation to a relatively low fluence of $3x10^{19}$ C^+/m^2 at 650°C (0.015 dpa at 0.5 µm depth). Small dislocation loops were observable throughout the irradiated region in this specimen, indicating that the threshold dose for observable defect cluster formation in alumina at 650°C is ~0.01 dpa. The loop size and density increased with increasing depth for this low-fluence irradiation condition. Low-fluence irradiations of alumina performed with different ions produced a similar threshold dose for observable defect cluster formation of ~0.01 dpa.[14] This threshold dose is an order of magnitude smaller than the threshold dose obtained for spinel at 650°C (Section 3.1).

Defect clusters were formed throughout the irradiated region in alumina irradiated with 1-MeV He^+ ions at 650°C.[2,20] However, the loop density was reduced by about a factor of five and the loop size was increased by about a factor of two compared to specimens irradiated with heavier ions to a similar dose. Irradiation with 1-MeV H^+ produced very few dislocation loops compared to the He, C, Al and Fe irradiations. Figure 10 shows the depth-dependent microstructure of alumina following irradiation with 1 MeV H^+ ions to a fluence of $1.7x10^{22}$ H^+/m^2 at 650°C (0.03 dpa at 0.5 µm depth). Dislocation loops were not observed in the midrange regions of this specimen despite the presence of damage levels that were well above the threshold dose for observable defect cluster formation determined from irradiations with heavier ions (0.01 dpa). A low density of dislocation loops (~$3x10^{20}/m^3$) was observed at intermediate depths (~1 to 3 µm) in another specimen irradiated with 1-MeV H^+ ions at an order of magnitude lower flux and fluence.[2]

ORNL Photo 1242-93

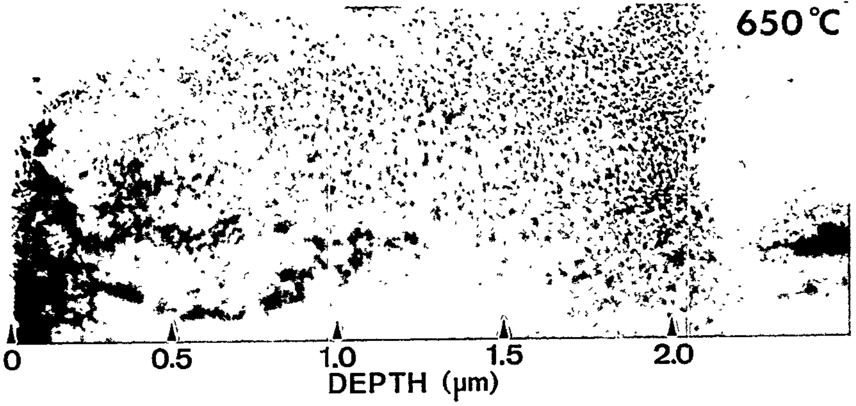

Fig. 9. Depth-dependent microstructure of Al_2O_3 irradiated with 3-MeV C^+ ions to a fluence of $3x10^{19}$ C^+/m^2.

ORNL Photo 1759-91

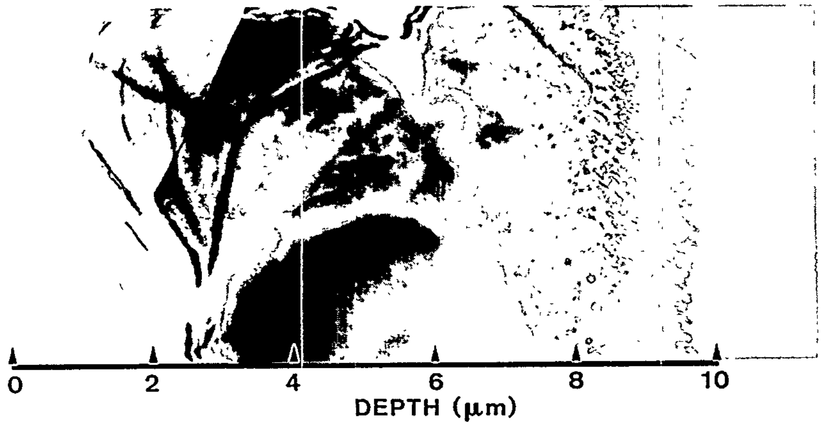

Fig. 10. Depth-dependent microstructure of Al_2O_3 irradiated with 1-MeV H^+ ions at 650°C to a fluence of $1.7x10^{22}$ H^+/m^2. The particle flux was ~$6x10^{17}$ H^+/m^2-s.

3.3 Investigation of the roles of ionizing vs. displacive radiation

The results on ion-irradiated spinel and alumina specimens indicate that the depth-dependent microstructural evolution in both materials is dependent on the mass and energy of the bombarding ion. This sensitivity to irradiation spectrum does not appear to be directly correlated with simple radiation parameters such as damage energy density, average primary knock-on atom recoil energy, displacement damage rate, or ionizing dose rate.[2] Another radiation parameter worth consideration is the electronic- to nuclear-stopping power ratio. As noted in Fig. 2, the ENSP ratio decreases with increasing ion mass and for a given ion is generally highest at the irradiated surface. Since the defect-free zones observed in spinel and alumina are more prominent for the lightest ions and are located adjacent to the irradiated surface, this suggests that the denuded zones may be associated with irradiation conditions which produce a high ENSP ratio.

Figure 11 summarizes the relation between the measured dislocation loop density and the calculated ENSP ratio in spinel and alumina specimens irradiated at 650°C. The data with arrows denote measurements where only upper limits could be estimated due to the extremely low loop densities ($<10^{18}/m^3$). Dislocation loop densities were measured at several different depths in each specimen in order to obtain data at several different ENSP ratios for a given ion (cf. Fig. 2). In the case of spinel, the dislocation loop density was observed to decrease rapidly for ENSP ratios greater than ~3 to 20. The loop density in alumina was observed to decrease rapidly for ENSP ratios greater than ~1000. The data for spinel suggest that the critical ENSP ratio for loop formation depends somewhat on the ion mass, with heavy ions exhibiting the lowest critical ENSP ratio.

ORNL-DWG 94-11307

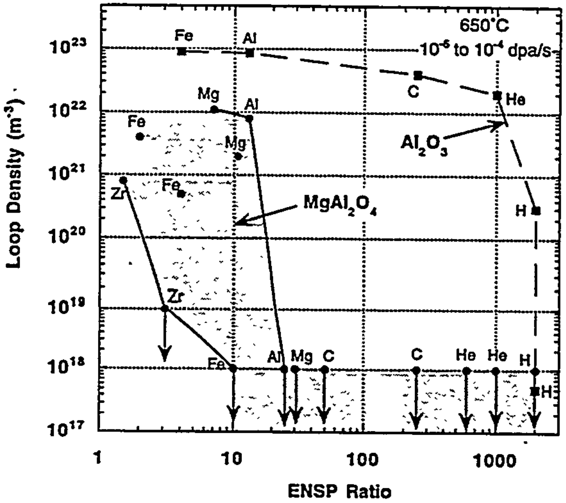

Fig. 11. Effect of electronic to nuclear stopping power on the dislocation loop density in $MgAl_2O_4$ and Al_2O_3 irradiated with single ion beams at 650°C.

The data summarized in Fig. 11 clearly indicate a strong irradiation-spectrum dependence for the microstructure of spinel and alumina. However, these single ion irradiation results cannot easily be extrapolated to fission and fusion reactor environments. In particular, the ionization produced in reactors has two distinct components, which are associated with the primary knock-on atoms (PKAs) and gamma rays, respectively. The PKAs produce intense, spatially localized ionization in the immediate vicinity of the PKA cascade, with most of the ionization in close proximity to the displaced atoms. On the other hand, gamma rays produce a rather uniform background of ionization throughout the material with little or no displacement damage. Table 2 compares the calculated ENSP ratios in a fusion reactor, fast fission reactor, and mixed spectrum (water cooled) fission reactor.[21] The ENSP ratio in each facility was calculated both with and without the gamma ray ionization contribution.

The high flux of gamma rays present in a mixed-spectrum fission reactor has a significant impact on the total (macroscopically averaged) ENSP ratio. On the other hand, gamma rays have a much smaller effect on the calculated ENSP ratio in a fusion reactor due to the higher average PKA energy and the lower gamma ray flux compared to a mixed-spectrum fission reactor. Fast fission reactors exhibit behavior that is intermediate between the mixed-spectrum fission and fusion reactors

Table 2. Calculated ENSP ratio for alumina in the STARFIRE conceptual fusion reactor and the HFIR mixed spectrum and FFTF fast fission reactors[21]

electronic to nuclear stopping power ratio	mixed spectrum reactor	fast reactor	fusion reactor (1st wall)
total	100	4	13
PKA alone	4	2	11

Two scoping dual-ion beam irradiations were performed to experimentally investigate the importance of uniform versus localized ionization effects. Figure 12 compares the depth-dependent microstructure of spinel irradiated at 650°C with a single beam of 3.6-MeV Fe^+ ions and dual beams of 1-MeV He^+ and 3.6-MeV Fe^+ ions. The Fe^+ ion flux was $5x10^{15}$ Fe^+/m^2-s in both specimens. The He^+/Fe^+ particle flux ratio in the dual beam specimen was,[17] which increased the calculated ENSP ratio at a depth of 0.5 μm from ~6 for the single Fe^+ ion beam to 28 for the dual beams (Table 1). The calculated displacement damage from the He^+ ion beam at a depth of 0.5 μm was only 4% of the displacements associated with the Fe^+ ion beam. Both the single- and dual-beam specimen exhibited an identical defect-free zone adjacent to the irradiated surface that extended to a depth of ~0.4 μm. The density of the dislocation loops that were present in the midrange region (0.5 to 1 μm depth) of the two specimens was also similar. These results suggest that moderate levels of uniform ionization (macroscopically averaged ENSP ~28) have only a weak effect on the microstructural evolution in spinel when energetic displacement cascades (mean PKA energy ~10 keV) are produced.

The second scoping dual-ion irradiation used 1.8-MeV Cl^+ and 1-MeV He^+ ion beams, with a He^+/Cl^+ particle flux ratio of 105. This produced a calculated ENSP ratio of ~160 at a depth of 0.5 μm (Table 1). The calculated damage energy and ENSP ratio for 1.8-MeV Cl^+ is similar to that for 3.6 MeV Fe^+ at irradiation depths up to ~0.7 μm (Figs. 1 and 2), and the mean PKA energy for 1.8-MeV Cl^+ ions in spinel (~8 keV) is also comparable to that for 3.6 MeV Fe^+ ions. Figure 13 shows the depth-dependent microstructure of spinel irradiated with dual beams of Cl^+ and He^+ ions at room temperature and 650°C. The calculated damage level at a depth of 0.5 μm was 0.7 dpa in both specimens, with 78% of the displacements associated with the Cl^+ ion beam. There were no observable defect clusters located within ~0.8 μm of the irradiated surface in the specimen irradiated at 650°C. According to the empirical relation established from the single ion irradiations (Fig. 11), the expected denuded zone width for spinel irradiated at 650°C with 1.8-MeV Cl^+ ions alone would have been only ~0.4 μm. Therefore, intense uniform ionizing radiation (macroscopically averaged ENSP ~160) can apparently influence the microstructural evolution in spinel during elevated temperature irradiation. The room temperature dual beam irradiation produced a high density of small defect clusters that were uniformly distributed throughout the Cl^+ ion irradiation region (Fig. 13), which suggests that these levels of uniform ionizing radiation (ENSP~160) do not have a significant impact on the microstructural evolution of spinel during room temperature irradiation.

4. Discussion

The data summarized in Fig. 11 clearly demonstrate that oxide ceramics such as Al_2O_3 and $MgAl_2O_4$ are sensitive to variations in the irradiation spectrum. This dependence on irradiation spectrum was observed in several specimens irradiated with different ion beams at the same calculated displacement damage rate or ionizing dose rate. Therefore, this phenomenon cannot be simply attributed to damage rate or ion beam heating effects. Perhaps the most significant implication of the observed irradiation spectrum dependence is that light ion (e.g. 1-MeV protons) and electron irradiations, which typically have ENSP ratios >1000, cannot be used to "simulate" the behavior of ceramics under fission or fusion neutron irradiation conditions, which have typical ENSP ratios of ~10. Recent electron and light ion irradiation studies performed on oxide ceramics that were irradiated with an applied electric field have found evidence for a permanent radiation-induced electrical degradation (RIED) in the electrical resistance after displacement damage levels of <0.01 dpa.[1,23,24] Extrapolation of these high-ENSP results to fusion reactor conditions would not appear to be warranted, according to the microstructural observations summarized in Fig. 11.

ORNL Photo 6718-93

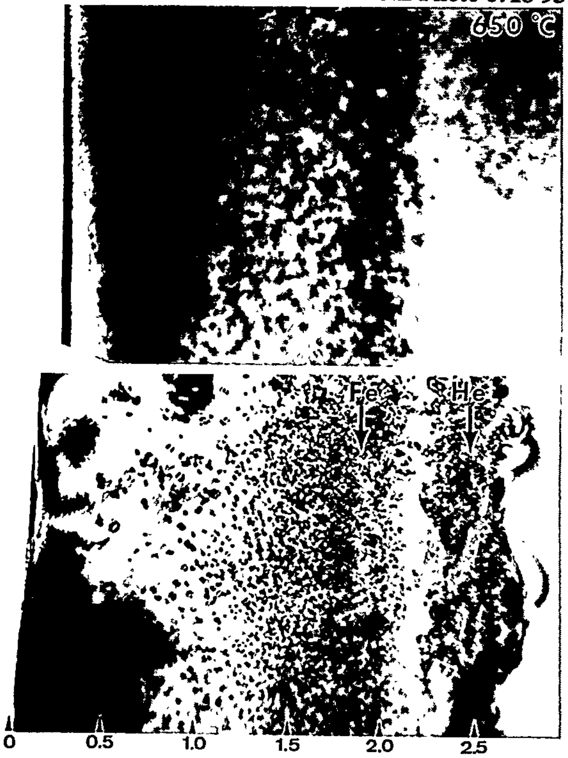

Fig. 12. Comparison of the depth-dependent microstructure of $MgAl_2O_4$ irradiated at 650°C with 3.6-MeV Fe^+ ions (top) and dual beams of 3.6-MeV Fe^+ and 1-MeV He^+ ions (bottom). The dual beam Fe^+/He^+ particle ratio was 17.

ORNL Photo 5258-94

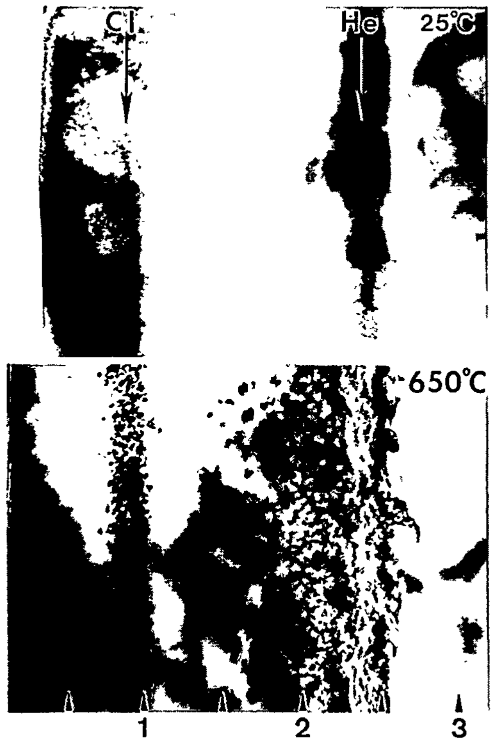

Fig. 13. Depth-dependent microstructure of $MgAl_2O_4$ irradiated at 650°C with dual beams of 1.8-MeV Cl^+ and 1-MeV He^+ ions at a He^+/Cl^+ particle ratio of 105.

It is important to demonstrate that the defect-free regions in the near surface regions of the ion-irradiated ceramics are not an artifact associated with localized ion beam heating effects, particularly since the defect-free zone width for a given ion has been observed to be related to the ion flux. If beam heating effects were significant, then the observed defect-free zone near the surface could be simply due to enhanced thermal diffusion which would promote point defect recombination and the evaporation of point defects from defect clusters. A simple one-dimensional heat transfer calculation shows that the temperature drop in spinel across a 1 μm depth adjacent to the surface would be only ~0.01°C for the maximum beam heating conditions employed in the present experiments (30 MGy/s), assuming a thermal conductivity for irradiated spinel at 650°C of K_{th}=5 W/m-K. Furthermore, the specimen surface temperature during irradiation (monitored by the thermocouple on the stainless steel specimen) was always within 20°C of the heat-sinked substrate temperature for the target array. Additional evidence that the defect-free regions are not due to ion beam heating effects is obtained from observations that the defect-free zone widths for different ions could not be correlated with the beam heating.[2] For example, a high density of small dislocation loops was observed in the near-surface region of Al_2O_3 irradiated at 650°C with 2-MeV Al^+ ions at a beam power of 7 MGy/s (Fig. 8), whereas loops were not observed in alumina irradiated at 650°C with 1-MeV H^+ ions at a lower beam power of 3 MGy/s (Fig. 10).

The suppression of dislocation loop formation in oxide ceramics irradiated with light ions (high ENSP ratio) could in principle be due to two different effects; either a decrease in the defect production rate or an increase in the point defect recombination rate (e.g., due to ionization-enhanced diffusion). However, there is considerable evidence that the low loop density is not due to a low defect production rate. Optical spectroscopy measurements on Al_2O_3 indicate that the defect production rate (relative to the calculated displacement damage rate) of light ions such as protons is equal to or greater than that for heavier ions or neutrons.[25-27] Buckley and Shaibani[28] noted that defect clusters did not form in spinel irradiated with

1 MeV electrons (ENSP ratio ~10,000), but preexisting dislocations climbed readily during the irradiation, indicating the presence of significant concentrations of point defects. Large defect clusters were observed in alumina irradiated with a low flux of protons after a dose of <0.01 dpa in the present study [2]. In addition, the few dislocation loops in spinel that were nucleated in regions with high ENSP ratios grew considerably during irradiation.[2,14] These observations indicate that the suppressed dislocation loop density after light ion irradiation is not associated with a reduction in defect production but is instead due to difficulties in loop nucleation.

As mentioned in the introduction, several previous studies have reported that radiation effects in oxide ceramics are sensitive to the irradiation spectrum. The volumetric swelling in Al_2O_3 and MgO was found to be much lower in specimens irradiated at room temperature with light ions such as H^+ than in specimens irradiated with heavier ions to the same calculated damage level.[3,4] In addition, studies have shown that the volume expansion in Al_2O_3, BeO or MgO induced by heavy ion or fission neutron irradiation may be recovered by subsequent electron or H^+ ion irradiation.[3,4,29] Dislocation loops have not been observed in spinel following electron[28,30,31] or proton[2,20,32] irradiation (ENSP>1000) over a wide range of temperatures and damage levels. Electron irradiation has been shown to cause the disappearance of small dislocation loops produced in $MgAl_2O_4$ by Ar^+ ion or neutron irradiation.[7,31] In the present study, the effect of irradiation spectrum on the microstructural evolution in alumina and spinel was more pronounced at 650°C (~0.4 T_M) than at room temperature (~0.13 T_M). This sensitivity to irradiation temperature implies that the irradiation spectrum effect may be associated with point defect diffusion processes.

It is well established that the migration energy of a defect in semiconductors and insulators is strongly affected by the defect charge state.[33-37] Similarly, it has been demonstrated that the diffusion coefficient (diffusivity) of hydrogen isotopes[38-40] and vacancies[41] in oxide insulators is greatly enhanced by ionizing radiation. Optical absorption measurements performed on oxide insulators have demonstrated that light ion irradiation spectra (high ionizing- to displacive-radiation ratio) preferentially produce a greater fraction of F^+ centers, whereas heavy ions produce a larger proportion of F centers.[4,6,42] In oxide insulators with predominantly ionic bonding, it is expected that the diffusivity of F centers (oxygen vacancy with two trapped electrons) should be significantly less than that of F^+ centers (oxygen vacancy with one trapped electron).[34-36] The precise physical mechanism responsible for ionization-enhanced diffusion in insulators is not known, although several different mechanisms have been proposed.[34] Regardless of the specific mechanism responsible for ionization-enhanced diffusion, the net result is that irradiation sources which produce large amounts of ionization compared to displacement damage are expected to be very effective in enhancing the point defect diffusion in oxide ceramic insulators. According to chemical rate theory calculations, a large increase in the diffusivity of point defects would enhance the amount of point defect recombination and thereby cause a dramatic reduction in the nucleation rate of defect clusters.

An additional possible mechanism for the observed suppression of defect cluster formation in spinel and alumina in highly ionizing irradiation environments may be an ionization-enhanced increase in the point defect recombination volume. Atomistic calculations of F and F^+ centers in Al_2O_3 indicate that F^+ centers exert a strong perturbation on surrounding lattice atoms.[44] It seems plausible that this lattice strain energy could lead to a higher rate of recombination of oxygen interstitials at F^+ centers compared to F centers. The higher concentration of F^+ centers in highly ionizing radiation environments [4,6,42] would therefore result in increased point defect recombination rates.

Further work is needed to identify the most appropriate parameter(s) for characterizing the irradiation spectrum. The electronic- to nuclear-stopping power appears to be a promising correlation parameter for single ion irradiation conditions (Fig. 11). This correlation suggests that dislocation loop formation is suppressed in spinel during irradiation at elevated temperatures (~650°C) at damage rates between 10^{-6} and 10^{-4} dpa/s if the ENSP ratio is greater than about 10. The corresponding critical ENSP ratio for alumina is about two orders of magnitude higher, i.e., 1000. However, dual beam irradiations (e.g. Figs. 12 and 13) have shown that this simple parameter does not accurately predict the microstructural behavior of oxide ceramics that are subjected to moderately intense uniform fields of ionizing radiation. The present results, taken together with recent results obtained by Fukumoto et al.,[13] indicate that homogeneous ionizing radiation fields up to ENSP ratios of ~60 do not have a significant effect on the microstructural evolution in spinel during irradiation at 600 to 650°C when most of the displacement damage is produced by energetic displacement cascades. As demonstrated in Fig. 13, homogeneous ionizing radiation fields apparently can influence the microstructural development in spinel during elevated temperature irradiation if the ionization field is very intense (ENSP~160).

As discussed elsewhere,[2] it is not surprising that the critical ENSP ratio derived from single ion irradiation experiments does not hold for dual beam irradiation experiments. In the single beam experiments, most of the ionization occurs along the bombarding ion path and is therefore in close proximity to the defects produced by displacement damage. On the other hand, the ionization in the dual beam experiments was more uniformly distributed throughout the specimen. Since most of the displacement damage in the dual beam irradiations was produced in spatially discrete collision cascades associated with the heavy ions, the localized ENSP ratio in the vicinity of the heavy ion collision cascades was less than the macroscopic ENSP ratio.

Additional radiation parameters which may be important in the suppression of dislocation loop formation are damage energy and irradiation flux. The nucleation of a stoichiometric dislocation loop in $MgAl_2O_4$ requires the presence of 7 interstitials.[45] Therefore, light ions (which produce diffuse radiation damage due to their low damage energy) might be expected to be less effective in producing dislocation loop nuclei compared to heavy ions (which produce relatively dense displacement cascades). Dalal et al.[42] have concluded that the fraction of F^+ centers compared to F centers in alumina is enhanced as the defect generation rate is increased, due to a suppression of F center formation at high damage rates. According to the previous discussion, this would lead to enhanced defect mobilities (and point defect recombination) at high radiation fluxes. Irradiation flux effects have been observed in several cases in the present set of experiments. As noted in Section 3.1, the defect-free zone adjacent to the irradiated surface in Mg^+-irradiated spinel was found to increase with increasing particle flux. Similarly, the dislocation loop density in proton-irradiated alumina was observed to decrease dramatically when the particle flux was increased by an order of magnitude (Section 3.2 and ref. [2]). Both of these experimental results imply that the point defect diffusivity (or point defect recombination rate) increased with increasing flux.

The present study shows that spinel becomes resistant to defect cluster formation at much lower ENSP ratios compared to alumina (Fig. 11). Previous ion and neutron irradiation studies have found that spinel is significantly more resistant than alumina to void swelling and dislocation loop formation.[2,7,13,15,16,45] Since the ENSP ratio in all of these previous studies was equal to or greater than 4, this provides further confirmation of the empirical correlation between irradiated microstructure and ENSP ratio summarized in Fig. 11. The physical mechanism responsible for the higher sensitivity of spinel to ENSP ratio compared to ceramics such as MgO and Al_2O_3 is uncertain.[2] According to Kinoshita et al.,[16] the most likely mechanisms are effective recombination of interstitials with the high concentration of structural vacancies present in spinel, and the large critical nucleus (7 interstitials) for the formation of a stable dislocation loop. Irradiation-assisted dissolution of small interstitial clusters in spinel has also been suggested to be playing a role.[7] Additional possible mechanisms that would require further study include a high sensitivity to ionization-enhanced diffusion or a strong ionization-induced enhancement of the point defect recombination rate in spinel.

CONCLUSIONS

The microstructural changes in oxide ceramics induced by particle irradiation are dependent on the irradiation spectrum. Spinel is particularly resistant to defect cluster formation over a wide range of irradiation conditions. However, the present study clearly shows that high densities of dislocation loops can be produced in spinel in irradiation environments that produce relatively dense displacement cascades (with an associated low ratio of electronic- to nuclear-stopping power). Data obtained from single ion irradiations performed on spinel and alumina at 650°C at damage rates between 10^{-6} and 10^{-4} dpa/s have been correlated with the electronic- to nuclear-stopping power ratio. Dislocation loop formation is suppressed when the ENSP ratio exceeds ~10 and ~1000 for spinel and alumina, respectively. Due to the sensitivity of spinel and alumina to irradiation spectrum, data obtained on these materials during electron or light ion irradiation is most likely <u>not</u> representative of their behavior in a fission or fusion reactor environment.

Whereas alumina and spinel are sensitive to the localized irradiation spectrum associated with the primary knock-on atoms, they are not as strongly affected by homogeneous ionizing radiation. Moderate background levels of uniform ionizing radiation (averaged ENSP~30) do not significantly affect the microstructural evolution in spinel if most of the displacement damage is produced by energetic displacement cascades. However, high levels of uniform ionization (averaged ENSP~150) can modify the microstructural evolution in spinel, at least at elevated temperatures near 650°C. Since the irradiation spectrum in parts of a fusion reactor that are distant from the first wall are expected to have averaged ENSP ratios >100, this implies that uniform ionizing radiation effects may need to be considered when assessing the suitability of spinel for fusion energy applications.

The physical mechanism responsible for the sensitivity of alumina and spinel to irradiation spectrum is uncertain. The most likely explanation is that ionization enhanced diffusion (associated with high ENSP ratios) increases the amount of point defect recombination and thereby suppresses dislocation loop nucleation. Other possible mechanisms include damage energy effects (subcritical number of interstitials within a "cascade" region) and ionization-enhanced point defect recombination volumes.

ACKNOWLEDGEMENTS

The author thanks S. W. Cook for performing most of the ion irradiations, and A. T. Fisher, J. W. Jones, J. M. Cole and A. M. Williams for specimen preparation. This research was sponsored by the Office of Fusion Energy, U.S. Department of Energy, under contract DE-AC05-84OR21400 with Martin Marietta Energy Systems, Inc.

REFERENCES

1. S.J. Zinkle and E.R. Hodgson, J. Nucl. Mater. 191-194 (1992) 58.
2. S.J. Zinkle, Nucl. Instr. Meth. Phys. Res. B 91 (1994) 234.
3. G.W. Arnold, G.B. Krefft and C.B. Norris, Appl. Phys. Lett. 25 (1974) 540.
4. G.B. Krefft, J. Vac. Sci. Technol. 14 (1977) 533.
5. G.B. Krefft and E.P. EerNisse, J. Appl. Phys. 49 (1978) 2725.
6. R. Brenier, B. Canut, L. Gea, S.M.M. Ramos, P. Thevenard, J. Rankin, L. Romana and L.A. Boatner, Nucl. Instr. Meth. Phys. Res. B 80/81 (1993) 1210.
7. C. Kinoshita, J. Nucl. Mater. 191-194 (1992) 67.
8. M.B. Lewis, W.R. Allen, R.A. Buhl, N.H. Packan, S.W. Cook, and L.K. Mansur, Nucl. Instr. Meth. Phys. Res. B 43 (1989) 243.
9. J.F. Ziegler, J.P. Biersak and U.L. Littmark, The Stopping and Range of Ions in Solids (Pergamon Press, New York, 1985). The calculations in the present paper used the TRIM-90 version.
10. P. Agnew, Phil. Mag. A 65 (1992) 355.
11. M.J. Norgett, M.T. Robinson and I.M. Torrens, Nucl. Eng. Design 33 (1975) 50.
12. S.J. Zinkle, C.P. Haltom, L.C. Jenkins, and C.K.H. DuBose, J. Electron Microsc. Techn. 19 (1991) 452.
13. K. Fukumoto, C. Kinoshita, S. Maeda and K. Nakai, Nucl. Instr. Meth. Phys. Res. B 91 (1994) 252.
14. S.J. Zinkle, in Fusion Reactor Materials Semiannual Prog. Report for period ending March 31, 1993, DOE/ER-0313/14, p. 426.
15. H. Abe, C. Kinoshita and K. Nakai, J. Nucl. Mater. 179-181 (1991) 917.
16. C. Kinoshita, K. Fukumoto, K. Fukuda, F.A. Garner and G.W. Hollenberg, Am. Cer. Soc. Symposium on Fabrication and Properties of Ceramics for Fusion Energy, J. Nucl. Mater., in press.
17. S.J. Zinkle, in 15th Int. Symp. on Effects of Radiation on Materials, ASTM STP 1125, R.E. Stoller, et al., eds. (Amer. Soc. for Testing and Materials, Philadelphia, 1992) 749.
18. S.J. Zinkle, J. Nucl. Mater. 191-194 (1992) 645.
19. S.J. Zinkle, J. Amer. Ceram. Soc. 72 (1989) 1343.
20. S.J. Zinkle, in Fusion Reactor Materials Semiannual Prog. Report for period ending March 31, 1991, DOE/ER-0313/10, p. 302.
21. S.J. Zinkle and L.R. Greenwood, in Fusion Reactor Materials Semiannual Prog. Report for period ending March 31, 1993, DOE/ER-0313/14, p. 74.
23. E.R. Hodgson, J. Nucl. Mater. 179-181 (1991) 383.

24. L.W. Hobbs, F.W. Clinard, Jr., S.J. Zinkle and R.C. Ewing, J. Nucl. Mater. 216 (1994) 291.
25. D.W. Muir and J.M. Bunch, in Radiation Effects and Tritium Technology for Fusion Reactors, CONF-750989, Vol. II, eds. J.S. Watson and F.W. Wiffen (Nat. Tech. Inf. Serv., Springfield, VA, 1976) p. 517.
26. T.F. Luera, J. Appl. Phys. 51 (1980) 5792.
27. P. Agnew, Nucl. Instr. Meth. Phys. Res. B 65 (1992) 305.
28. S.N. Buckley and S.J. Shaibani, Philos. Mag. Lett. 55 (1987) 15.
29. D.G. Walker, J. Nucl. Mater. 14 (1964) 195.
30. S.J. Shaibani, D. Phil. Thesis, Univ. Oxford, UK (1986).
31. Y. Satoh, C. Kinoshita and K. Nakai, J. Nucl. Mater. 179-181 (1991) 399.
32. P.A. Knight, D. Phil. Thesis, Univ. Oxford, UK (1989).
33. J.W. Corbett and J.C. Bourgoin, IEEE Trans. Nucl. Sci. NS-18 , No. 6 (1971) 11.
34. J.W. Corbett and J.C. Bourgoin, Rad. Effects 36 (1978) 157.
35. J.M. Vail, R.J. Brown and C.K. Ong, J. de Phys. 34 (1973) C9-83.
36. N. Itoh, in Dynamic Effects of Irradiation in Ceramics, Los Alamos National Lab. Report LA-UR-92-4400 (1992) p. 3.
37. L. Gea, C.R.A. Catlow, S.M.M. Ramos, B. Canut and P. Thevenard, Nucl. Instr. Meth. Phys. Res. B 65 (1992) 282.
38. Y. Chen, M.M. Abraham and H.T. Tohver, Phys. Rev. Lett. 37 (1976) 1757.
39. Y. Chen, R. Gonzalez and K.L. Tsang, Phys. Rev. Lett. 53 (1984) 1077.
40. Y. Chen and R. Gonzalez, Intern. Mat. Res. Soc. Symp. on Frontiers of Materials Science, Tokyo, 1993, in press.
41. S. Clement and E.R. Hodgson, Phys. Rev. B 36 (1987) 3359.
42. M.L. Dalal, M. Rahmani and P.D. Townsend, Nucl. Instr. Meth. Phys. Res. B 32 (1988) 61.
43. R.E. Stoller and G.R. Odette, J. Nucl. Mater. 141-143 (1986) 647.
44. E.A. Kotomin, A.I. Popov and A. Stashans, J. Phys. Condensed Mat., in press.
45. L.W. Hobbs and F.W. Clinard, Jr., J. de Phys. 41 (1980) C6-232.

DATA ACQUISITION SYSTEM USED IN RADIATION INDUCED ELECTRICAL DEGRADATION EXPERIMENTS – D.P. WHITE (Oak Ridge National Laboratory)

OBJECTIVE

Radiation induced electrical degradation (RIED) of ceramic materials has recently been reported [1-6] and is the topic of much research at the present time. The object of this report is to describe the data acquisition system for an experiment designed to study RIED at the High Flux Beam Reactor (HFBR) at Brookhaven National Laboratory.

SUMMARY

It has been observed [1-6] that some oxide ceramics which have an electric field applied to them while simultaneously being irradiated may undergo a degradation of their insulating properties under certain conditions. An *in-situ* DC conductivity capsule has been constructed to study the effect of neutron irradiation on the electrical conductivity of alumina with an applied electric field at the HFBR. The current capsule differs from a previous design [7,8] in that the current measurements are performed on the low voltage side of the circuit.

The data acquisition system to be described here has been built and will be used to perform the electrical conductivity measurements in an experiment scheduled to begin in October of 1994.

PROGRESS AND STATUS

System Requirements

The phenomenon of RIED is observed to occur at irradiation temperatures within the range 300-600 C [9,10]. Also for RIED to occur it is necessary for the applied electric field to be $\geq 2 \times 10^4$ V/m [9,10]. Under these conditions RIED has been observed to develop at damage doses of from 10^{-5} to 10^{-1} dpa [10].

The capsule to be used at HFBR has three polycrystalline alumina samples. Each sample is supplied with separate high voltage (~100V) coaxial lead lines and separate triaxial return lines. Each sample has a guarded center electrode on the low side necessitating the triaxial return lines. Since an electric field must be applied to the three samples even when no measurements are being made, in this system a matrix switching card (Keithley Instruments model 7153) is used to switch the appropriate sample current to the measurement system.

Alumina which is not in a gamma field has a conductivity of $\sim 10^{-11}(\Omega - m)^{-1}$ at 400 C (the approximate temperature of the samples in this capsule). Conductivities of this order are difficult to measure. However, the gamma dose rate at the HFBR in the V-15 irradiation facility is $\sim 6 \times 10^3$ Gy/s [11]. At this dose rate the conductivity is expected to be $\sim 10^{-7}(\Omega - m)^{-1}$ due to the radiation induced conductivity (RIC) [10,12]. Conductivities of this order are much more easily measured. For the samples in this capsule, which are 0.75 mm thick and have a center electrode diameter of approximately 3 mm and a gap between the center electrode and the guard electrode of 1 mm, this conductivity corresponds to a current through the sample of [13],

$$I = 1.3 \times 10^{-12} V/t \ \ (Amps) \tag{1}$$

where V is the applied voltage (Volts) and t is the sample thickness (meters). As mentioned previously electric fields on the order of $10^5 V/m$ are necessary for the study of RIED. This gives currents on the order of 10^{-7} A for the samples described above which are easily measured with modern picoammeters [14]. For the samples used in this experiment an applied voltage of 75V is necessary to produce an electric field of $10^5 V/m$. The fast neutron flux (E > 0.1 MeV) in the V-15 irradiation facility at the HFBR is $1.5 \times 10^{18} n/(m^2 - s)$ which corresponds to a damage rate in alumina of approximately $1.5 \times 10^{-7} dpa/s$. Thus to obtain doses up to 0.1 dpa will take approximately 8 days of irradiation time. In order to effectively take data over this period of time the data aquistion has been automated.

The data aquisition and control system was required to continuously supply the necessary voltages to the samples and to allow periodic measurements of the conductivity of individual samples via a switching card and the appropriate cable connections. It is also desirable to be able to measure the leakage current of each sample. The leakage current is the surface current which flows from the high voltage side of the sample to the guard electrode. This measurement can be accomplished using the switching card and proper connections to the current measuring unit. The capsule is also supplied with several K-type thermocouples which allow the constant monitoring of the sample temperatures. All of the individual components of the system are controlled via computer over a GPIB bus.

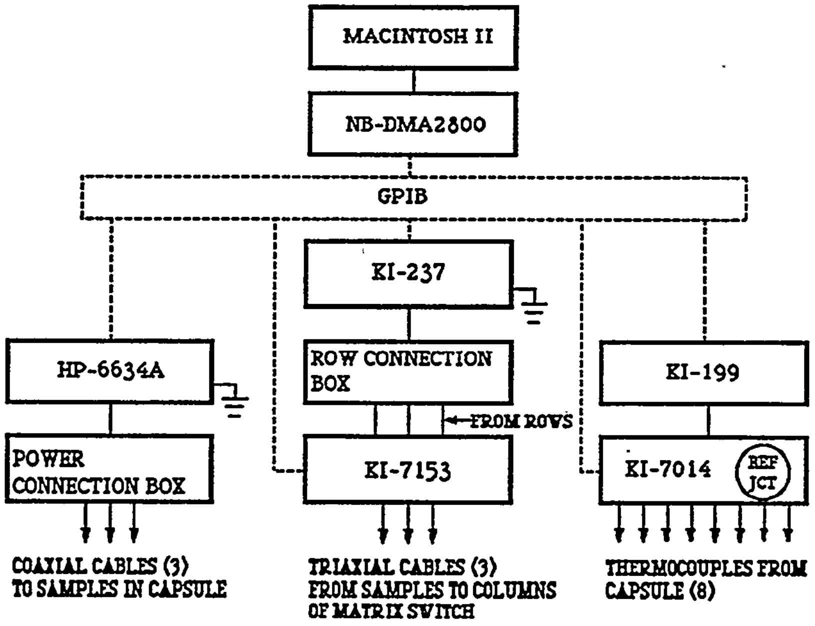

Figure 1: Schematic of data aquisition setup. The dashed lines represent GPIB connections which are used for instrument control and data transfers. Solid lines are cables.

System Details

The power is supplied to the samples by a Hewlett-Packard model 6634A power supply which is capable of supplying up to 120V at 1A. The switching system consists of a Keithley Instruments Model 7001 High Density Switch System with a Model 7153 4×5 high voltage low current matrix card and a Model 7014 thermocouple multiplexer. The current measuring unit is a Keithley Instruments 237 source-measure unit used in measure-only mode. The thermocouple voltages and reference junction voltage are measured using a Keithley Model 199 multimeter. All of these instruments are GPIB (IEEE-488) compatible and are controlled and programmed with a Macintosh IIci computer containing a National Instruments NB-DMA2800 GPIB interface board. This GPIB interface allows data transfers between the computer and the instruments so that all the data are stored on disk. The programming is accomplished using National Instruments LabVIEW II software.

A schematic of the system setup is shown in Fig. 1. The power connection box provides 3 coaxial connections to the power supply for the 3 samples. The 3 triaxial data leads are connected to the columns of the matrix switch card and 3 rows are connected to the row connection box. A schematic of the row connection box is shown in Fig. 2. When the switches on the matrix card are configured to connect the three samples to input 1 of the row connection box the data lines go to ground. This is the configuration used when no measurements are being made. When any one sample is connected to input 2 through the matrix card that data line goes to the KI-237 and a current reading is taken allowing a determination of that sample's conductivity. The guard ring of the sample (which is carrying the leakage current) connected to input 2 is routed directly to ground. When any one sample is connected to input 3 through the matrix card the guard ring current (leakage current) goes to the KI-237 for measurement and the center lead goes to ground. Thus by opening and closing various switches on the KI-7153 matrix card (all switch control is handled by the computer) both bulk current and leakage current for all 3 samples may be measured. This system is also capable of measuring the surface resistance between the center and guard electrode. This is accomplished by using the KI-237 to apply a moderate voltage to the center electrode of a sample (after turning off the HP-6634A) through input 2 of the row connection box and measuring the current. This measurement will have a large uncertainty associated with it due to leakage currents in the triaxial cable.

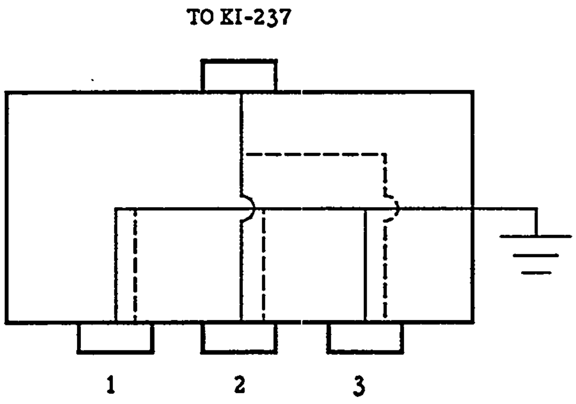

Figure 2: Schematic of row connection box. The solid lines represent the center electrodes of the triaxial cables and the dashed lines represent the guard sheaths.

The data aquisition program is written so that after any set of current readings are taken, the KI-7014 multiplexer steps through each thermocouple and the reference junction and these voltages are read by the KI-199 multimeter and downloaded to the computer whereupon the software converts these readings to temperatures. The cycle period to take measurements on all three samples (both bulk and leakage current measurements) and to measure all the thermocouple voltages is approximately 1 minute.

All of the data which are collected are stored on disk and are also displayed graphically on the computer screen. Thus the experimenter has immediate access to the data in the form of current and temperature plots.

CONCLUSIONS AND FUTURE WORK

The data aquistion system described above will be used in the next several months to take data in an experiment at the HFBR studying the RIED phenomenon. This system will allow the experimenters immediate access to the data and will significantly increase the amount of data and ease the subsequent analysis of this data compared to any non-automated data aquistion system.

ACKNOWLEDGMENTS

This research was performed while the author held a fellowship in the Oak Ridge National Laboratory Postdoctoral Research Program, administered through the Oak Ridge Institute for Science and Education.

REFERENCES

1. E.R. Hodgson, Cryst. Latt. Def. Amorph. Mat., **18** (1989), 169.
2. E.R. Hodgson, J. Nucl. Mater. **179-181** (1991), 383.
3. G.P. Pells, J. Nucl. Mater. **184** (1991), 177.
4. E.R. Hodgson, J. Nucl. Mater. **191-194** (1992), 552.
5. T. Shikama, M. Narui, Y. Endo, T. Sagawa, and H. Kayano, J. Nucl. Mater. **191-194** (1992), 575.
6. X. Zong, C. Shen, S. Liu, Z. Wu, Yi Chen, Y. Chen, B.D. Evans, R. Gonzalez, and C.H. Sellers, Phys. Rev. B **49** no. 22 (1994), 15514.
7. L.L. Snead, D.P. White, S.J. Zinkle, J. Oconor, G. Hartsough, and J. Errante, Fusion Reactor Mater. Semiann. Prog. Rep. DOE/ER-0313/15 (1993), 457.
8. L.L. Snead, D.P. White, and S.J. Zinkle, J. Nucl. Mater., in press.
9. S.J. Zinkle and E.R. Hodgson, J. Nucl. Mater. **191-194** (1992), 58.
10. S.J. Zinkle, Plasma Dev. and Oper. **3** (1992).
11. J.D. Axe and R. Greenberg Eds., *HFBR Handbook BNL 24182* (Brookhaven National Laboratory Associated Universities, Inc., 1992).
12. R.W. Klaffky, B.H. Rose, A.N. Goland and G.J. Dienes, Phys. Rev B **21** (1980) 3610.
13. ASTM D257 *Standard Test Methods for D-C Resistance Or Conductance of Insulating Materials*, (1991).
14. *Low Level Measurements 4th Edition* (Keithley Instruments, Inc. 1992).

CATION DISORDER IN HIGH-DOSE, NEUTRON-IRRADIATED SPINEL - K. E. Sickafus, A. C. Larson, N. Yu, M. Nastasi (Los Alamos National Laboratory); G. W. Hollenberg and F. A. Garner (Pacific Northwest Laboratory); R. C. Bradt (University of Nevada-Reno).

OBJECTIVE

The objective of this effort is to determine whether $MgAl_2O_4$ spinel is a suitable ceramic for fusion applications.

SUMMARY

The crystal structures of $MgAl_2O_4$ spinel single crystals irradiated to high neutron fluences [$>5 \cdot 10^{26}$ n/m^2 ($E_n > 0.1$ MeV)] were examined by neutron diffraction. Crystal structure refinement of the highest dose sample indicated that the average scattering strength of the tetrahedral crystal sites decreased by ~20% while increasing by ~8% on octahedral sites. Since the neutron scattering length for Mg is considerably larger than for Al, this result is consistent with site exchange between Mg^{2+} ions on tetrahedral sites and Al^{3+} ions on octahedral sites. Least-squares refinements also indicated that, in all irradiated samples, at least 35% of Mg^{2+} and Al^{3+} ions in the crystal experienced disordering replacements. This retained *dpa* on the cation sublattices is the largest retained damage ever measured in an irradiated spinel material.

PROGRESS AND STATUS

Introduction

Many studies of neutron irradiation-induced damage in spinel have indicated that spinel is a highly radiation-resistant ceramic.[1-9] Of the mechanisms underlying spinel's radiation resistance, it is known that the vast majority of point defects generated during irradiation annihilate harmlessly by *interstitial-vacancy* recombination rather than condensing into defect aggregates such as dislocation loops and voids.[10] So, the instantaneous displacement damage in spinel, quantified in terms of *displacements per atom* or *dpa*, far exceeds the net or retained displacement damage. In fact, electron microscopy observations indicate that, for total neutron doses ranging from 0.1 - 20 *dpa*,[(a)] dislocation loops accommodate only 0.002 - 0.09% of the total *dpa* induced during an irradiation (depending on neutron fluence and irradiation temperature).[11,14] By contrast, in ceramics more susceptible to radiation damage such as MgO or Al_2O_3, > 0.1% of the total displacements are stabilized in defect aggregates

---

(a) In this report, total *dpa* is estimated based on published or calculated neutron fluences and assuming an equivalence of 1 *dpa* per 10^{25} n/m^2, $E_n > 0.1$ MeV. This estimation factor is within 10% of the total *dpa* calculated using the neutron radiation damage codes SPECOMP & SPECTER[11,12] for irradiations of the compound alumina (Al_2O_3) in typical fission reactor in-core positions, assuming threshold displacement energies $E_d^{Al} = 27$ eV; $E_d^{O} = 30$ eV.[13] Calculations were made for the HFIR, FFTF, and EBR-II reactors, based on available dosimetry data [ibid.].

at similar neutron doses, and vacancy retention can be as high as a few percent.[3] The question raised in the study presented here is this: Is all of the instantaneous *dpa* in spinel truly *lost*, or is some of this *dpa hidden* in disorder on the cation sublattices?

Cation disorder in spinel is defined in terms of the degree of inversion of the cation sublattices. In "normal" spinel, large Mg^{2+} ions occupy tetrahedral (*A*) interstices between oxygen ions, while the smaller trivalent Al^{3+} ions lie in octahedral (*B*) interstices. Ionic radii for magnesium aluminate ions, obtained from Shannon and Prewitt,[15] are shown in Table 1. In an "inverse" spinel, the *A*-sites accommodate only the Al^{3+} ions, while the *B*-sites are occupied by Mg^{2+} and Al^{3+} ions in equal proportions. The general formula for spinel is given by

$$(\mathrm{Mg}_{1-i}^{2+}\ \mathrm{Al}_i^{3+})^{A_{iv}}\ [\mathrm{Mg}_i^{2+}\ \mathrm{Al}_{2-i}^{3+}]_2^{B_{vi}}\ \mathrm{O}_4 \quad \begin{cases} i = 0 & \rightarrow \text{normal spinel} \\ i = 2/3 & \rightarrow \text{random cation arrangement} \\ i = 1 & \rightarrow \text{inverse spinel} \end{cases} \tag{1}$$

Table 1. Ionic radii for tetrahedrally (*IV*) - coordinated Al^{3+}, Mg^{2+}, and O^{2-} ions and octahedrally (*VI*) - coordinated Al^{3+} and Mg^{2+} ions.

$r^{IV}_{Al^{3+}}$	$r^{IV}_{Mg^{2+}}$	$r^{IV}_{O^{2-}}$	$r^{VI}_{Al^{3+}}$	$r^{VI}_{Mg^{2+}}$
0.039 nm	0.049 nm	0.138 nm	0.053 nm	0.072 nm

The quantity in parentheses represents the average occupancy of *A*-sites (coordination *IV*), while the quantity in brackets represents the average occupancy of *B*-sites (coordination *VI*). The variable *i* is the so-called *inversion parameter*, which specifies the fraction of trivalent aluminum ions that occupy *A*-sites. Naturally grown magnesium aluminate spinels exhibit approximately the normal spinel structure, so that $i \sim 0$; the same samples annealed at elevated temperature for a few minutes suffer cation inversion as high as $i = 0.3$.[16] It has been demonstrated that synthetic magnesium aluminate is always partly inverse (e.g., ref. 17); inversion values from about 0.1 - 0.6 have been observed, the latter representing a nearly random cation arrangement.[18,19]

The goal of the experiments described here is to use neutron diffraction to determine the extent of neutron-induced cation disorder in $MgAl_2O_4$, via measurement of the inversion parameter before and after irradiation. Neutron diffraction is superior to X-ray diffraction for disorder measurements in magnesium aluminate because the neutron scattering length (and likewise the cross-section) for a Mg nucleus is sufficiently greater than that of Al, so that their site-occupancies may be distinguished.[20] The X-ray scattering factors for Mg^{2+} and Al^{3+} are too similar to reveal site-occupancy distinctions by X-ray diffraction. Evidence will be presented here for significant accommodation of cation disorder in high dose, neutron irradiated spinel crystals. Specifically, neutron scattering data revealed the highest retained *dpa* (~40% on the cation sublattices) ever measured in spinel with little observed degradation in mechanical properties.[21]

Experimental Procedure

Spinel single crystals with formula MgO• x Al_2O_3 , where x is nearly 1, were obtained from Union Carbide Corporation, San Diego, CA, USA. Details of the crystal purity are given elsewhere.[22] The crystals were cut into cylindrical pellets from transparent, 2-cm long boules, with [001] growth direction. The pellets were approximately 4.8 mm in diameter and 2 - 3 mm in height. Samples were irradiated in the Materials Open Test Facility (MOTA) of the Fast Flux Test Facility (FFTF). The nominal irradiation conditions experienced by the pellets in the FFTF reactor were $24.9 \cdot 10^{26}$ n/m^2 $E_n > 0.1$ MeV) at 658K (249 *dpa*); $5.3 \cdot 10^{26}$ n/m^2 at 678K (53 *dpa*); and $5.6 \cdot 10^{26}$ n/m^2 at 1023K (56 *dpa*). One pellet was not irradiated but stored under ambient conditions as a control sample.

Irradiated crystals were analyzed using the single-crystal diffractometer (SCD) at the Manuel Lujan, Jr. Neutron Scattering Center (*LANSCE*), Los Alamos National Laboratory. The x-y position and time-of-flight (TOF) (the time from the generation of the neutron to detection) are recorded for every neutron detected. The TOF defines the neutron velocity and is directly proportional to its wavelength. The design of the SCD allows for collection of a volume of reciprocal space at each setting of the crystal, in the form of a "histogram." Four histograms were collected to cover the desired portion of reciprocal space, the unique region, $h \geq k \geq l \geq 0$, from each of the samples. The data were collected at ~ 299 K.

The data reduction and structure refinement were carried out using the diffraction code *GSAS* (General Structure Analysis System[23]). The initial values for the atomic positions input into the crystal structure refinement using *GSAS* were obtained from Wycoff.[24] In defining atomic coordinates, two choices for unit cell origin are available in the space group for spinel: the inversion center $\bar{3}m$ or the center $\bar{4}3m$, a translation of $\bar{\tfrac{1}{8}}\,\bar{\tfrac{1}{8}}\,\bar{\tfrac{1}{8}}$ from center $\bar{3}m$. In either case, 24 cations per unit cell are distributed over the equipoints 8(a) and 16(d) (Wycoff's notation), while 32 oxygen anions occupy the equipoint 32(e). In the case of 32(e), the fractional coordinates x, y, and z along the cube axes of the unit cell are the same. They are represented by u, the so-called *oxygen parameter*. The significance of u will be discussed later.

During the structure refinement, atomic positions, temperature and occupancy factors, extinction, and individual histogram scale factors are varied in a least-squares procedure. Refinement proceeds until calculated reciprocal-space intensities, based on the structure model, best match observed intensities. Because neutrons are scattered from atomic nuclei, which act as point scatterers, the scattering length of an atom does not vary with d-spacing. Thus, the scattering length for a site is the weighted linear sum of the scattering lengths of the atoms occupying that site.

The model structure was tested for convergence using the following unweighted and weighted definitions for the residual index:[25]

$$R = \sqrt{\frac{\sum_j \left(|F_{jo}| - |F_{jc}|\right)}{\sum_j F_{jo}}} \quad (a) \qquad R_w = \sqrt{\frac{\sum_j W_j \left(|F_{jo}| - |F_{jc}|\right)^2}{\sum_j W_j F_{jo}^2}} \quad (b) \qquad (2)$$

where F_{jo} and F_{jc} are proportional to the observed and calculated scattering factors at reciprocal-space position j, respectively; w_j is the weight assigned to the intensity at position j, equal to the inverse of the counting error (i.e., the square root of the observed intensity) at position j.

Results

1. Scattering Power and Cation Inversion.

Table 2 shows the results of the crystal structure refinements, based on the neutron diffraction data obtained from unirradiated and irradiated spinel samples. The only constraint in these refinements is that oxygen sites are fully occupied by oxygen anions. Normalized, average scattering powers are shown for *A*- and *B*-site cations and for oxygen anion sites. Also indicated in Table 2 are the residual indices from the crystal structure refinement for each sample. The *A*-site (8(a)) scattering power, $\hat{f}_A$ is normalized by the coherent neutron scattering length for magnesium, b_{Mg} = 5.375 fm. Similarly, the scattering power $\hat{f}_B$ for the *B*-site (16(b)) is normalized by b_{Al} = 3.449 fm, while $\hat{f}_O$ for the oxygen-site (32(e)) is normalized by b_O = 5.805 fm. Coherent neutron scattering lengths (which are analogous to the atomic form factors f in X-ray scattering) were obtained from Koester *et al.*[26]

Table 2. Scattering power of tetrahedral and octahedral cation sites, and oxygen anion lattice sites, in unirradiated and neutron irradiated spinel crystals. Also tabulated are the residual indices from the crystal structure refinement for each crystal.

	Scattering Power (normalized)			Residual Index	
Sample	$\hat{f}_A$ A-Site 8(a)	$\hat{f}_B$ B-Site 16(d)	$\hat{f}_O$ O-Site 32(e)	R	R_W
Unirradiated	0.862	1.001	1.000	0.076	0.065
56 *dpa*/1023 K	0.765	1.167	1.000	0.095	0.099
53 *dpa*/678 K	0.756	1.123	1.000	0.112	0.103
249 *dpa*/658 K	0.687	1.086	1.000	0.107	0.096

It is readily apparent in Table 2 that the scattering powers of both *A*- and *B*- cation sites in spinel are changed following neutron irradiation. It is observed that the average scattering power of an *A*-site diminishes following irradiation, while the scattering power of a *B*-site increases. Since the scattering length for Mg is much larger than for Al, these results suggest that the higher scattering power Mg atoms are replaced by Al atoms on *A*-sites and vice versa on *B*-sites, during neutron irradiation.

To determine the extent of inversion in each crystal, an additional *constrained* least-squares refinement procedure was performed. The initial condition for this refinement procedure was a normal spinel lattice. The refinement required that (i) all *A* and *B* sites be occupied by a Mg or Al atom; (ii) occupancy of an *A*-site by an Al atom required simultaneous occupancy of a *B*-site by a Mg ion; (iii) the Al:Mg atom ratio in the crystal was fixed at 2:1. A summary of the results is presented in Table 3. Fig. 1 shows schematically the inversion parameter results; here, i is seen to increase from $i \sim 0.24$ in

Table 3. Least-squares refinement results for inversion parameter, oxygen parameter, and residual indices for unirradiated and neutron irradiated spinel single crystals.

Sample	Inversion Parameter (i)	Oxygen Parameter (u)		Residual Index	
		$\bar{3}m$	$\bar{4}3m$	R	R_w
Unirradiated	.237 ± .020	.237371 ± .000049	.387629 ± .000049	0.074	0.066
56 *dpa*/1023 K	.644 ± .016	.241627 ± .000049	.383373 ± .000049	0.093	0.072
53 *dpa*/678 K	.592 ± .026	.241924 ± .000077	.383076 ± .000077	0.115	0.092
249 *dpa*/658 K	.692 ± .026	.241845 ± .000073	.383155 ± .000073	0.109	0.099

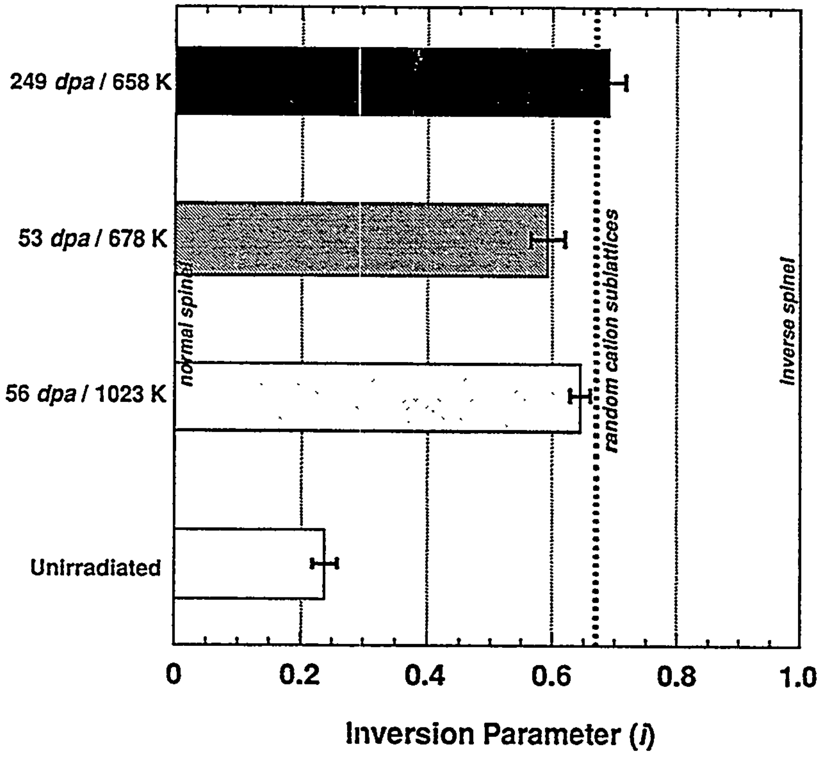

Fig. 1. Plot of the cation inversion parameter i for unirradiated and irradiated spinel single crystals, as determined from least-squares structure refinements of neutron diffraction data.

the unirradiated sample to inversion values ranging from 0.59 to 0.69 in the neutron irradiated samples. In fact $i \sim 0.69$ for the highest fluence sample (249 *dpa*) exceeds the value of i pertaining to randomized cation sublattices ($i = 0.67$).

These results suggest that in all neutron irradiated spinel samples, at least 35% of the *A*-sites (or equivalently, ~ 17% of the *B*-sites) in the irradiated spinel crystals have experienced Al^{3+} for Mg^{2+} disordering replacements. This retained *dpa* on the cation sublattices is the largest retained *dpa* ever measured in an irradiated spinel material (as discussed earlier, only 0.002 - 0.09% of the instantaneous *dpa* has ever been observed in the microstructure of irradiated spinel).

2. The Oxygen Parameter

Additional, indirect evidence for cation disorder in irradiated spinel crystals is obtained from determination of the oxygen parameter, *u*, in the crystal structure refinement. The following discussion refers to the schematic diagram in Fig. 2. Here are shown two interpenetrating tetrahedra that make up the basic structural unit in the spinel crystal lattice. One tetrahedron consists of an *A*-site cation coordinated by four oxygen anions. The second tetrahedron consists of an oxygen anion, coordinated by one *A*-site and three *B*-site cations.

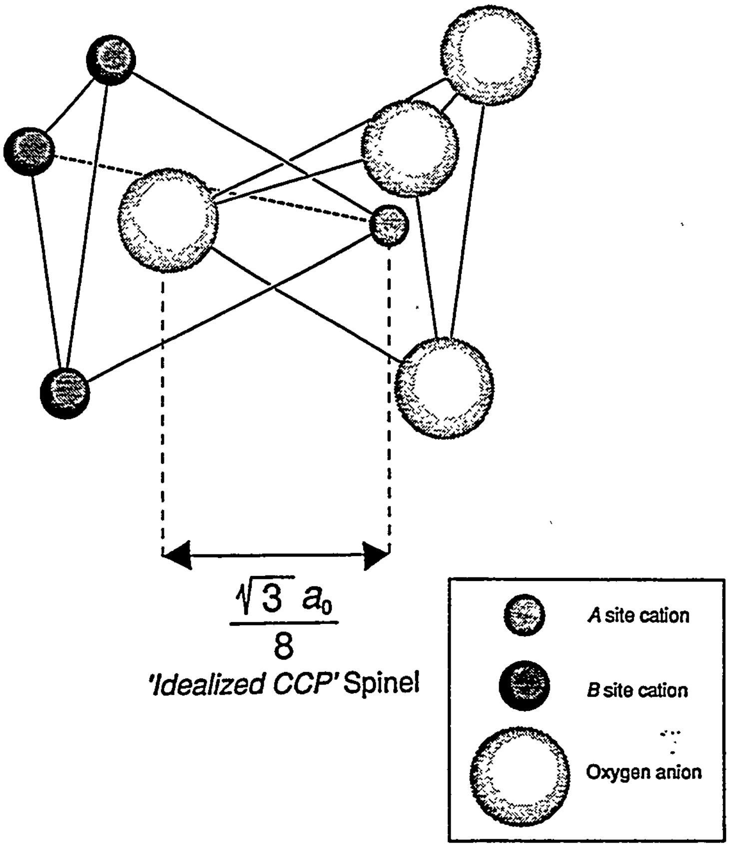

Fig. 2. Schematic diagram of the fundamental structural unit in spinel: two interpenetrating tetrahedra. One tetrahedron consists of an *A*-site cation coordinated by four oxygen anions. The second tetrahedron consists of an oxygen anion, coordinated by one *A*-site and three *B*-site cations. All ions are drawn smaller than their actual radii. *B*-site cations are drawn slightly larger than their *A*-site counterparts, as in Fig. 1. Also shown is the Oxygen - to - *A*-site bond length for a "perfect cubic close-packed" anion sublattice.

The oxygen parameter arises because, in real spinel crystals, the oxygen lattice is not "idealized *CCP* (cubic close-packed)." This is attributable in part to the fact that each divalent cation (Mg^{2+}) in the lattice is too large to fit into one of the comparatively small tetrahedral *A* interstices; consequently the surrounding O^{2-} ions expand outwards by equal displacements along the body diagonals of the cube. If this dilatation did not take place, the bond length between an O^{2-} anion and an *A*-site cation would be precisely 1/8 of the body-diagonal of the unit cell; i.e., $0.125 \bullet \sqrt{3}\, a_0$, where a_0 is the lattice parameter. In crystal structure refinements of $MgAl_2O_4$, a significant oxygen dilatation is always observed (Wycoff[24]). This dilatation is usually reported in terms of the oxygen parameter, u: u is the fraction of the cubic unit cell edge defining the position of the oxygen ion at fractional coordinates u, u, u. For idealized *CCP* oxygen packing, $u = 0.375$ for unit cell origin at $\bar{4}3m$; $u = 0.250$ for unit cell origin at $\bar{3}$m. Wycoff[24] reports $u(\bar{4}3m) = 0.387$ or $u(\bar{3}m) = 0.262$ for natural $MgAl_2O_4$. This represents an O-to-*A*-site bond length of $0.137 \bullet \sqrt{3}\, a_0$. In the crystal structure refinements for the unirradiated spinel samples in this study, similar values were obtained: $u(\bar{4}3m) = 0.3876$ or $u(\bar{3}m) = 0.2626$; O-to-*A*-site bond length $= 0.1376 \bullet \sqrt{3}\, a_0$.

Now, consider the case in which a divalent Mg^{2+} ion exchanges places with a trivalent Al^{3+} ion. This positions a much smaller cation in the *A* interstice than before ($r^{IV}_{Al^{3+}} = 0.039$ nm; $r^{IV}_{Mg^{2+}} = 0.049$ nm; Table 1). This, in turn, should relax the dilatation previously imposed on the surrounding oxygen ions. If, by irradiation for instance, one induces a significant number of Mg^{2+}/Al^{3+} site exchanges within the crystal lattice, the O-to-*A*-site bond length should relax toward the idealized *CCP* value of $0.125 \bullet \sqrt{3}\, a_0$. This is precisely what is found in the neutron irradiated samples. Fig. 3 shows crystal structure refinement results for the O-to-*A*-site bond length and the oxygen parameter u for all of the spinel crystals measured in this study. It is clear that the O-to-*A*-site bond length and u shift toward their idealized *CCP* values after neutron exposure. Also, changes in these parameters apparently saturate with neutron fluence. For instance, both the 53 and 249 *dpa* samples irradiated at ~670K show the same value for the O-to-*A*-site bond length ($0.1330 \bullet \sqrt{3}\, a_0$). These results indicate, in accordance with the scattering power results presented earlier, that Mg^{2+} ions increasingly occupy *B*-sites and Al^{3+} ions increasingly occupy *A*-sites as irradiation progresses.

3. Interstitial Sites

Some evidence was found for occupied interstitial sites in the irradiated spinel single crystals. This was determined by examining Fourier transform *difference* maps of the neutron diffraction data. Four such maps are shown in Fig. 4, where the unirradiated sample (Figs. 4a and 4c) is compared to the 53 *dpa*/678 K neutron irradiated sample (Figs. 4b and 4d). These maps are equivalent to a display of the difference between $|F_{jo}|$ and $|F_{jc}|$ at each reciprocal lattice position j. Contours in these maps represent real-space regions of nuclear *density* (i.e., neutron scattering length) which produce scattered intensity in the observed diffraction pattern that is not accounted for in the calculated or model structure factor. In Fig. 4, the model structure factors are obtained from the *unconstrained* least-squares refinement presented earlier. The maps in Fig. 4 represent slices along the <111> crystallographic axis. The center of Figs. 4a and 4b is at unit cell fractional coordinates 3/24, 3/24, 3/24, relative to a $\bar{3}m$ origin. The center of Figs. 4c and 4d is at unit cell fractional coordinates 5/24, 5/24, 5/24, relative to a $\bar{3}m$ origin.(a) These layers are special because in an idealized spinel structure, they are empty interstitial layers. No atoms should be located in these planes.

(a) A different convention for the occupation of equipoints by cations is used in Fig. 4 than described earlier. Cations here are distributed over equipoints 8(b) and 16(c) rather than 8(a) and 16(d).

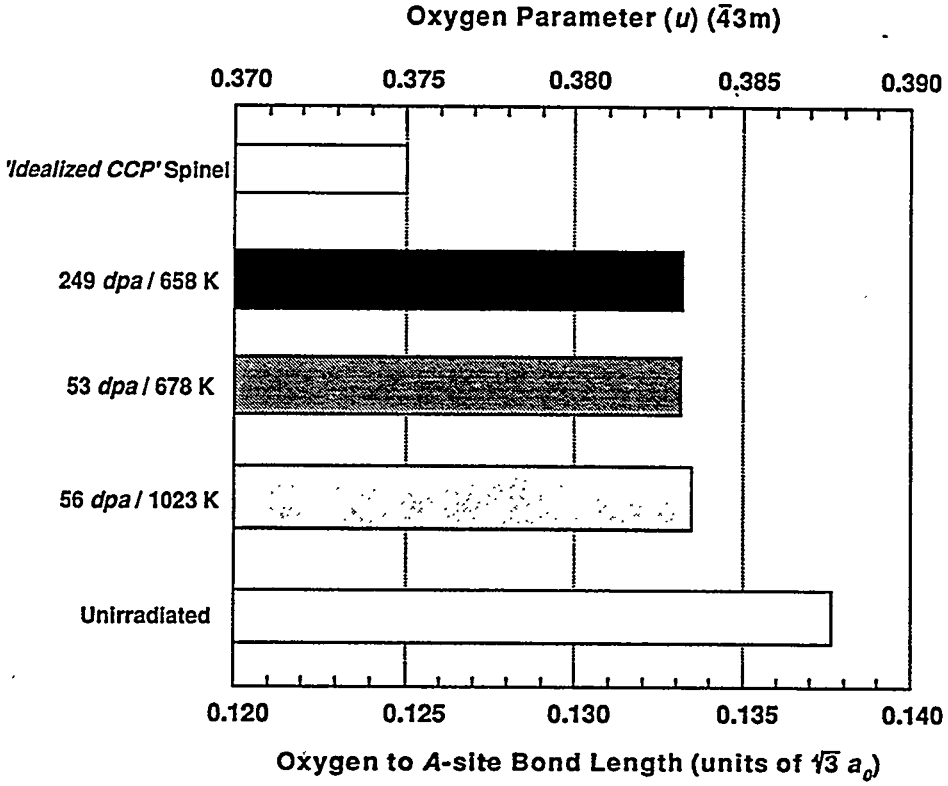

Fig. 3. Histogram showing the Oxygen to *A*-site bond length and oxygen parameter u (for the $\bar{4}3m$ origin) for unirradiated and irradiated spinel single crystals. Values were determined from the crystal structure refinement using *GSAS*. Also shown is the Oxygen-to-*A*-site bond length and u for an "idealized cubic close-packed" anion sublattice.

In the case of the unirradiated sample, almost no neutron scattering length is present in the Fourier difference maps of Fig. 4, at least in terms of a statistically appreciable quantity. However, in the irradiated sample, regions are observed where statistically significant nuclear densities reside. These are indicated by arrows in Figs. 4b and 4d. The symmetry of these locations in the maps is highly suggestive of at least partial occupancy of these interstitial sites by cations following irradiation. Work is in progress to quantify the retained *dpa* at these sites. Fourier difference maps were also obtained from other layers along <111> that contain cations in some, but not all, cation interstitial sites for a given layer. Evidence was also found for the partial occupation of interstitial sites following neutron irradiation. However, this effect is easiest to see in the completely vacant layers, as demonstrated in Fig. 4.

CONCLUSIONS

In this study, it was found by neutron diffraction that the average scattering power of an occupied, tetrahedral (*A*) site diminished by ~20% while increasing by ~8% on octahedral (*B*) sites at the highest neutron fluence investigated (~250 *dpa*). By least-squares refinement of the diffraction

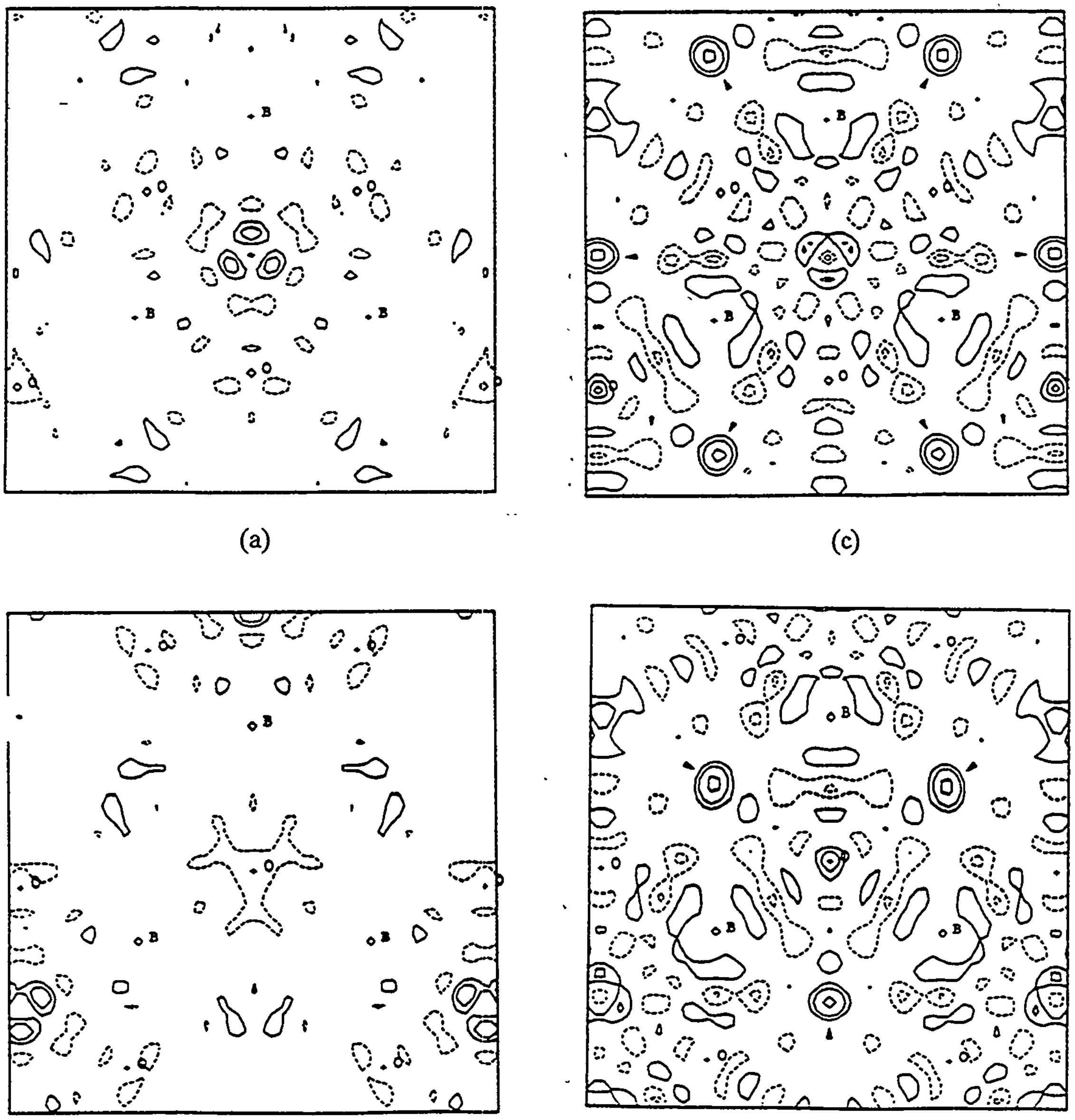

(a)

(c)

(b)

(d)

Fig. 4. Fourier transform *difference* maps of the neutron diffraction data for the unirradiated sample (a,c) compared to the 53 *dpa*/678 K neutron-irradiated sample (b,d). Maps represent real space slices along the <111> crystallographic axis. The dimensions of each map are 0.6 nm by 0.6 nm. The center of (a) and of (b) is at unit cell fractional coordinates 3/24, 3/24, 3/24, relative to a $\bar{3}m$ origin. The center of (c) and of (d) is at unit cell fractional coordinates 5/24, 5/24, 5/24, relative to a $\bar{3}m$ origin. See text for discussion.

data, the inversion parameter, *i*, was found to increase from $i \sim 0.24$ (unirradiated) to $i \sim 0.6$ to 0.7, in the neutron-irradiated samples (> 50 *dpa*). From these measurements, it is estimated that ~35% of the cation sites have experienced Mg^{2+} for Al^{3+} or Al^{3+} for Mg^{2+} ion exchange. This retained *dpa* on the cation sublattices is the largest retained *dpa* ever measured in an irradiated spinel material (only 0.002 - 0.09% of the instantaneous *dpa* has ever been observed in irradiated spinel crystal microstructure). Measurements of O-to-*A*-site bond length and the oxygen parameter *u* provide additional indirect evidence for cation disorder in irradiated samples. Also, the latter measurements indicate that, upon neutron exposure in excess of ~50 *dpa*, cation disorder effects are saturated (for irradiations at ~670K). The cation disorder measured in this study likely represents the majority of the retained damage in irradiated spinel.

The results cited here indicate that interstitial-vacancy recombination is a highly efficient point defect annihilation mechanism in spinel, even when it leads to disorder on the cation sublattices of the crystal. Due to the high efficiency of interstitial-vacancy recombination, the condensation of point defects into aggregates such as dislocation loops and voids is of little consequence in irradiated spinel. The ability of spinel to accept cation sublattice disorder suggests that additional radiation-resistant ceramics may be found in multicomponent oxides where cation disorder is easily accommodated.

Acknowledgments

This work was performed for the U.S. Department of Energy (DOE), Office of Basic Energy Sciences, Division of Materials Sciences; and also supported by DOE under Contract DE-AC06-76RLO 1830. Pacific Northwest Laboratory is operated for DOE by Battelle Memorial Institute.

Expected Achievements in the Next Reporting Period

This segment of the work is complete.

References

1. G. F. Hurley and J. M. Bunch, Am. Ceram. Soc. Bull. **59** (1980) 456.

2. G. F. Hurley, J. C. Kennedy, F. W. Clinard Jr., R. A. Youngman, and W. R. McDonell, *J. Nucl. Mater.* **103/104** (1981) 761.

3. F. W. Clinard, Jr., G. F. Hurley, and L. W. Hobbs, "Neutron Irradiation in MgO, Al_2O_3, and $MgAl_2O_4$ Ceramics," *J. Nucl. Mater.* **108/109** (1982) 665-670.

4. F. W. Clinard, Jr., G. F. Hurley, and R. W. Klaffky, Res. Mech. **8** (1983) 207.

5. F. W. Clinard, Jr., G. F. Hurley, L. W. Hobbs, D. L. Rohr, and R. A. Youngman, *J. NuclMater.* **122/123** (1984) 1386.

6. F. W. Clinard, Jr., G. F. Hurley, R. A. Youngman, and L. W. Hobbs, *J. Nucl. Mater.* **133/134** (1985) 701.

7. C. A. Parker, L. W. Hobbs, K. C. Russell, and F. W. Clinard, Jr., *J. Nucl. Mater.* **133/134** (1985) 741.

8. Y. Fukushima, T. Yano, T. Maruyama, and T. Iseki, *J. Nucl. Mater.* **175** (1990) 203.

9. H. Suematsu, T. Iseki, T. Yano, Y. Saito, T. Suzuki, and T. Mori, *J. Am. Ceram. Soc.* **75** (1992) 1742.

10. L. W. Hobbs and F. W. Clinard, Jr., "Faulted Defect Aggregates in Neutron-Irradiated $MgAl_2O_4$ Spinel," *Journal de Physique* **41** (1980) C6-232-236.

11. L. R. Greenwood, "SPECOMP Calculations of Radiation Damage in Compounds," in *Reactor Dosimetry: Methods, Applications, and Standardization, ASTM STP 1001*, Harry Farrar IV and E. P. Lippincott, Eds., American Society for Testing and Materials, Philadelphia (1989) 598-602.

12. L. R. Greenwood and R. K. Smither, "SPECTER: Neutron Damage Calculations for Materials Irradiations," Argonne National Laboratory Report ANL/FPP/TM-197, 1985.

13. L. R. Greenwood, private communication (1994).

14. C. Kinoshita, K. Fukumoto, and K. Nakai, "Electron-, Ion-, and Neutron-Irradiation Damage in Ceramics," *Ann. Chim. Fr.* **16** (1991) 379-389.

15. R. D. Shannon and C. T. Prewitt, "Effective Ionic Radii in Oxides and Fluorides," Acta. Cryst. **B25** (1969) 925-946.

16. U. Schmocker, H. R. Boesch, and F. Waldner, "A Direct Determination of Cation Disorder in $MgAl_2O_4$ Spinel by ESR," Phys. Lett. **40A(3)** (1972) 237-238.

17. E. Brun, S. Hafner, P. Hartmann, and F. Laves, "Elektrische Quadrupolwechselwirkung von ^{27}Al und Kationenverteilung in Spinell ($MgAl_2O_4$)," Naturwissenschaften **47** (1960) 277.

18. E. Stoll, P. Fischer, W. Hälg, and G. Maier, "Redetermination of the Cation Distribution of Spinel ($MgAl_2O_4$) by Means of Neutron Diffraction," *J. Physique*, Paris **25** (1964) 447-448.

19. U. Schmocker and F. Waldner, *J. Phys.* C9 (1976) L235-237.

20. G. E. Bacon, "A Neutron-Diffraction Study of Magnesium Aluminum Oxide," Acta Cryst. **5** (1952) 684-686.

21. C. A. Black, F. A. Garner, and R. C. Bradt, "Influence of High Dose Neutron Irradiation at 385 and 750°C on the Microhardness of $MgAl_2O_4$ Spinel," Fusion Reactor Semiannual Progress Report DOE/ER-0313/15, Oak Ridge, Tennessee (1994) 508-514.

22. F. A. Garner, G. W. Hollenberg, J. L. Ryan, Z. Li, C. A. Black, and R. C. Bradt, "Dimensional Stability, Optical and Elastic Properties of $MgAl_2O_4$ Spinel Irradiated in FFTF to Very High Exposures," Fusion Reactor Semiannual Progress Report DOE/ER-0313/15, Oak Ridge, Tennessee (1994) 502-507.

23. A. C. Larson and R. B. VonDreele, "General Structure Analysis System (GSAS)," LA-UR 86-748, Los Alamos National Laboratory, Los Alamos, New Mexico (1990).

24. R.W.G. Wycoff, *Crystal Structures V. 3: Inorganic Compounds* $R_x(MX_4)_y$, $R_x(M_nX_p)_y$, *Hydrates and Ammoniates*, 2nd ed., John Wiley & Sons, New York (1965) 76.

25. J. E. Post and D. L. Bish, "Rietveld Refinement of Crystal Structures Using Powder X-ray Diffraction Data," in *Reviews in Mineralogy, Vol. 20: Modern Powder Diffraction*, Eds. D. L. Bish and J. E. Post, Mineralogical Society of America (Bookcrafters, Inc. Chelsea, Michigan) (1989) 333-367.

26. L. Koester, H. Rauch, and E. Seymann, Atomic Data and Nuclear Data Tables **49** (1991) 66.

ELASTIC STABILITY OF HIGH DOSE NEUTRON IRRADIATED SPINEL

- Z. Li and S.-K. Chan (Argonne National Laboratory), F. A. Garner (Pacific Northwest Laboratory)[c], and R.C. Bradt (University of Nevada-Reno)

OBJECTIVE

The objective of this effort is to identify ceramic materials that are suitable for fusion reactor applications.

SUMMARY

Elastic constants (C_{11}, C_{12} and C_{44}) of spinel ($MgAl_2O_4$) single crystals irradiated to very high neutron fluences have been measured by an ultrasonic technique. Although results of a neutron diffraction study show that cation occupation sites are significantly changed in the irradiated samples, no measurable differences occurred in their elastic properties. In order to understand such behavior, the elastic properties of a variety of materials with either normal or inverse spinel structures were studied. The cation valence and cation distribution appear to have little influence on the elastic properties of spinel materials.

PROGRESS AND STATUS

Introduction

Magnesium aluminate spinel ($MgAl_2O_4$) has been considered as a potential fusion reactor candidate material for service as dielectric windows in radio frequency heating systems or as insulators for magnetic coils[1]. This spinel has demonstrated a remarkable insensitivity to neutron irradiation to levels as high as $2x10^{26}n/m^2$ (E>0.1 MeV)[2,3]. An extensive irradiation program using high purity $MgAl_2O_4$ spinel was conducted in the Fast Flux Test Facility (FFTF) reaching exposure levels an order of magnitude or more larger than those of all previous studies[4]. A series of non-destructive and destructive tests was performed on these highly irradiated samples. In particular the results of a neutron scattering study show that significant levels of cation disorder occurred in these samples during irradiation to high dose levels[5]. These specimens were therefore changed from normal spinel to a rather randomized spinel. In this paper the elastic properties of the irradiated spinel are reported and the effects of the cation distribution on its elastic properties are then discussed.

Experimental Procedures

The preparation and irradiation history of irradiated samples have been reported previously[4]. Both [100] and [111] oriented single crystals were used for elastic property measurements. The single crystal specimens were in the form of ~4.8mm diameter cylindrical pellets with a height of ~4.3mm for [111] and of ~2.8mm for [100] oriented specimens. The flat surfaces of the cylindrical pellets were parallel to the (100) and (111) planes for the [100] and [111] oriented specimens, respectively. The orientation error was much less than 2°, as determined from x-ray Laue patterns.

Sound velocities through the specimens were measured by the phase comparison method[6,7] in the 20-60 MHz carrier frequency range. Four sets of measurements were made for the longitudinal and transverse acoustic modes (V_L and V_T) in the directions normal to the (100) and (111) faces of the specimens.

---

[1] Pacific Northwest Laboratory is operated for the US Department of Energy by Battelle Memorial Institute under Contract DE-AC06-76RLO

The three independent elastic constants of cubic spinel, C_{11}, C_{12}, and C_{44}, were derived from those sound velocities as:

$$\rho V^2_L = C_{11} \tag{1a}$$

and

$$\rho V^2_T = C_{44} \tag{1b}$$

for the [100] oriented samples and

$$\rho V^2_L = (C_{11} + 2C_{12} + 4C_{44})/3 \tag{2a}$$

and

$$\rho V^2_T = (C_{11} - C_{12} + C_{44})/3 \tag{2b}$$

for the [111] oriented samples, where L and T denote the longitudinal and transverse vibration modes, respectively, and ρ is the sample density, which was measured at 3.55 g/cm^3. The measurements were carried out at room temperatures varying from 21 to 23°C. "Nonaq" stopcock grease was used to achieve the longitudinal acoustic coupling between the sample crystal and the fused silica buffer rod, whereas solid salol was used for the coupling during the transverse acoustic wave measurements.

Results and Discussion

Tables 1 and 2 summarize the measured sound velocities and the elastic stiffness moduli of the spinel specimens at each irradiation level. The compressive modulus C_{11} and shear modulus C_{44} were directly determined from [100] oriented samples using Equations 1a and 1b. The values of C_{12} were obtained from [111] oriented samples by using either Equation 2a or 2b. The C_{12} listed in Table 2 are the average values determined from these equations. The errors in the velocity and elastic moduli are estimated to be less than 1% and 3%, respectively. The largest uncertainties arise from the measurement of the sample

Table 1. Measured sound velocities of the irradiated Mg

	[100]		[111]	
	V_L(Km/sec.)	V_T(Km/sec.)	V_L(Km/sec.)	V_T(Km/sec.)
Unirradiated	8.875	6.625	10.674	5.125
24.9*/385°C	9.007	6.510	10.602	5.106
5.3/404°C	8.967	6.559	10.628	5.075
5.6/750°C	8.930	6.647	10.672	5.125
13.7/750°C	8.932	6.540	10.616	5.161
21.7/750°C	8.842	6.553	10.554	5.118

*Neutron Fluence in units of 10^{26} n/m^2 (E>0.1 MeV)

Table 2. Elastic properties of the irradiated $MgAl_2O_4$

	C_{11} (GPa)	C_{12} (GPa)	C_{44} (GPa)	E (GPa)	G (GPa)	ν
Unirradiated	280	155	156	274	108	0.27
24.9/385°C	288	157	150	274	108	0.27
5.3/404°C	285	158	153	273	108	0.27
5.6/750°C	283	156	156	276	109	0.27
13.7/750°C	283	154	152	273	108	0.27
21.7/750°C	278	151	152	271	107	0.27

thickness and sample density. The error range was confirmed by the cross-check of the C_{12} values calculated from Equations 2a and 2b. For example, the values of C_{12} were 150 and 151 calculated from equations 2a and 2b, respectively, for samples treated at 750°C to $21.7 \times 10^{26} n/m^2$ (E>0.1MeV). These values are in good agreement with each other. Table 2 also lists the calculated polycrystalline elastic moduli, Young's modulus, shear modulus, and Possion's ratio from the single crystal elastic constants based on the Voigt-Reuss-Hill averaging scheme.

The primary structural effect of neutron irradiation is to produce atomic displacement by direct momentum transfer. Such displacements depend on the binding energies of the atoms relative to the maximum energy transfer. In the unit cell of $MgAl_2O_4$, there are 32 oxygen ions with 32 corresponding octahedral interstitial sites and 64 tetrahedral interstitial sites. Of these interstitial sites, 8 of the tetrahedral ones (A sites) are filled by Mg^{2+} and 16 of the octahedral ones (B sites) are filled by Al^{3+}. In general, the binding energies of the divalent and trivalent ions in spinels are relatively small, as indicated by their tendency at high temperature towards random distribution on the A and B sites, respectively, and also between the A and B sites.

The crystal structures of the irradiated spinel specimens were examined by neutron scattering at Los Alamos National Laboratory[5]. The results show that at least 35% of the cation sites had experienced Mg^{2+} for Al^{3+} or Al^{3+} for Mg^{2+} ion exchange. It is therefore reasonable to assume that the effects of the neutron irradiation are, in the order of decreasing probability of occurrence, (1) disordering in the occupancy of A and B interstitial sites by Mg^{2+} and Al^{3+}, (2) creation of oxygen vacancies (and corresponding interstitials) and (3) nucleation and growth of dislocation loops and voids. Each of these changes can affect the elastic properties.

For example, on disordering the A and B cation sites, the contraction or expansion of the tetrahedral and octahedral oxygen cages creates corresponding structural elastic dipole fields. The incoherent components of these random fields interfere destructively in the short range. Over a longer range (much larger than the dimensions of a unit cell), the coherent components of the random fields collectively produce about the same total effect as before disordering had taken place, when the A and B sites were occupied as in a normal spinel. Therefore the expected outcome is no change in the elastic properties associated with long wavelength acoustic phonons.

The creation of oxygen vacancies, particularly if a sufficient number of them occur locally to allow precipitation to take place, can produce a much more dramatic effect on elastic properties. Although there exists some evidence for the formation of dislocation loops and voids, they occur at such small densities[8] that it is not surprising that their effect on microhardness is relatively small[9]. It has been suggested[10] that most of the oxygen vacancies generated by irradiation are annihilated by vacancy-interstitial recombination so that dislocation loops account for no more than 0.01% of the total displacements per atom in the irradiated spinel. The results of our ultrasonic study are consistent with the concept of redistribution of Mg^{2+} and Al^{3+} ions on both the A and B sites. The elastic constants remained unchanged for different levels of neutron irradiation as shown in Table 2. The polycrystalline elastic properties were also found to be independent of irradiation level.

The elastic properties of unirradiated single crystals with both the normal and inverse spinel structures have previously been studied[7,11,12]. Table 3 lists the elastic constants of three normal aluminate spinel single crystals, $MgAl_2O_4$, $CoAl_2O_4$ and $FeAl_2O_4$, three inverse spinel ferrites, $NiFe_2O_4$, $CoFe_2O_4$ and Fe_3O_4, one normal spinel ferrite, $ZnFe_2O_4$ and one mixed spinel ferrite, $MnFe_2O_4$, listed in their order of increasing lattice parameter, a_o. The C_{11} values decrease gradually with increasing of a_o, whereas the C_{44} values of the ferrites are 30% to 40% smaller than those of the aluminate spinels. It is of particular interest to note that, although the $ZnFe_2O_4$ has the normal spinel structure, its C_{44} value is nearly the same as those of the inverse spinel ferrites. For $MnFe_2O_4$, it is known that 80% of the tetrahedral sites are occupied by Mn^{2+}, leaving only 20% of the Mn ions to occupy octahedral sites[13]. The C_{44} value of the $MnFe_2O_4$ is also within the same range as those of the inverse spinel ferrites. It therefore appears from Table 3, that the elastic constants, especially C_{44}, of the different spinel structures are not significantly affected by the details of cation occupation of the various sites. This is in agreement with the recent results for the irradiated spinel specimens.

Table 3. Elastic properties of single crystals with different spinel structures [7]

Formula	Type	a_o (nm)	ρ (g/cm^3)	C_{11} (GPa)	C_{12} (GPa)	C_{44} (GPa)
$MgAL_2O_4$	normal	0.8083	3.578	282.5	154.9	154.7
$CoAl_2O_4$	normal	0.8103	4.416	290.5	170.3	138.6
$FeAl_2O_4$	normal	0.8119	4.280	266.0	182.5	133.5
$NiFe_2O_4$	inverse	0.8339	5.368	273.1	160.7	82.3
$CoFe_2O_4$	inverse	0.8392	5.304	257.1	150.0	85.3
Fe_3O_4	inverse	0.8396	5.163	267.6	105.6	95.3
$ZnFe_2O_4$	normal	0.8441	5.324	250.5	148.4	96.2
$MnFe_2O_4$	mix	0.8499	5.0	213.0	135.0	86.0

CONCLUSIONS

The elastic properties of high purity stoichiometric $MgAl_2O_4$ spinel appear to be remarkably resistant to neutron irradiation at temperatures in the range 385 - 750°C. The large level of cation disordering associated with high displacement levels appears to have little influence on the elastic properties of spinel materials. Comparison of these results with results of other non-irradiation studies on various spinels leads to the conclusion that such an insensitivity is not unexpected.

ACKNOWLEDGEMENTS

This work was supported by the U.S.Department of Energy, BES-Materials Sciences, under Contract #W-31-109-ENG-38 and also by the Office of Fusion Energy, under contract DE-AC06-76RLO 1830.

REFERENCES

1. F. W. Clinard Jr, G. F. Hurley and R. W. Klaffky, Res Mech. 8 (1983) 207.

2. G. F. Hurley and J. M. Bunch, Am. Ceram. Soc. Bull. 59 (1980) 456.

3. H. Suematsu, T. Iseki, T. Yano, Y. Saito, T. Suzuki and T. Mori, J. Am. Ceram. Soc. 75 (1992) 1742.

4. F. A. Garner, G. W. Hollenberg, F. D. Hobbs, J. L. Ryan, Z. Li, C. A. Black and R. C. Bradt, J. Nucl. Mater. (1994) in press.

5. K. E. Sickafus, A. C. Larson, M. Nastasi, N. Yu, G. W. Hollenberg, F. A. Garner and R. C. Bradt, in this issue.

6. E. S. Fisher and H. J. McSkimin, J. Appl. Phys. 29 (1958) 1473.

7. Z. Li, E. S. Fisher, J. Z. Liu and M. V. Nevitt, J. Mater. Sci. 26 (1991) 2621.

8. C. Kinoshita, K. Fukumoto, K.Fukuda, F. A. Garner and G.W.Hollenberg, in this issue.

9. C. A. Black, F. A. Garner and R. C. Bradt, J. Nucl Mater. (1994) in press.

10. F. W. Clinard, Jr, G. F. Hurley and L. W. Hobbs, J. Nucl. Mater. 108 & 109 (1982) 655.

11. Z. Li and E. S. Fisher, J. Mater. Sci. Lett. 9 (1990) 759.

12. V. Askarpout, M. H. Manghnani, S. Fassbender and A. Yoneda, Phys. Chem. Minerals 19 (1993) 511.

13. F. S. Galasso, Structure and Properties of Inorganic Solids, (Pregamon Press, New York, 1970) 218.

RADIATION-INDUCED ELECTRICAL DEGRADATION EXPERIMENTS IN THE JAPAN MATERIALS TESTING REACTOR -- Eugene Farnum and Kent Scarborough (Los Alamos National Laboratory), Tatsuo Shikama, Minoru Narui and Tsutomu Sagawa (The Oarai Branch, Institute for Materials Research, Tohoku University)

OBJECTIVE

The objective of this experiment is to determine the extent of degradation during neutron irradiation of electrical and optical properties of candidate dielectric materials. The goals are to identify promising dielectrics for ITER and other fusion machines for diagnostic applications and establish the basis for optimization of candidate materials.

SUMMARY

An experiment to measure radiation-induced electrical degradation (RIED) in sapphire and MgO-insulated cables was conducted at the JMTR light water reactor. The materials were irradiated at about 260 °C to a fluence of 3×10^{24} n/m^2 (E>1 MeV) with an applied DC electric field between 100 kV/m and 500 kV/m. No degradation was observed in the sapphire sample: instead, radiation-induced conductivity (RIC) seemed to decrease slightly during the experiment. Substantial degradation, that increased with applied electric field, occurred in the MgO-insulated cables. The physical degradation apparently remained in the material while the reactor was off, but did not increase conductivity. This effect is different from the RIED effect reported by Hodgson but is similar to previous results reported by Shikama et. al. However, it was not possible to determine explicitly whether the observations were caused by degradation in the cable insulation or by some deterioration at the cable termination. Experimental conditions and resistance measurements were made and reported in accordance with agreements developed at the Sixth International Conference on Fusion Reactor Materials.

PROGRESS AND STATUS

Introduction

Radiation-induced electrical degradation (RIED) and radiation-induced conductivity (RIC) have been identified as the major electrical effects caused by radiation in ceramics. RIC is an electronic effect caused by excitation of electrons into the conduction band during ionizing radiation (Klaffkey et al.[1] and Farnum et al.[2]). RIED is characterized by an increase in conductivity during irradiation that remains, or partially remains, after irradiation has ceased. The origin of RIED is still unknown, but the effect has been observed during electron irradiation by Hodgson[3] during proton irradiation, by Pells[4], and during neutron and gamma irradiation in a light-water reactor by Shikama et al.[5] . In the previous work, the presence of an applied electric field of more than 20 V/mm is necessary to observe RIED as well as temperature above 250 °C and radiation with both ionizing and displacive components. The onset of the RIED effect occurred at about 10^{-5}, 10^{-3} and 10^{-2} dpa for the electron, proton, and reactor irradiations respectively. Thus, RIED seems to depend on the amount of ionization, or perhaps, as suggested by Zinkle and Kesternich[6] , the ratio of ionization to displacement energy deposited. Higher amounts of ionization make the effect begin at lower fluences. Moroño and Hodgson[7] have also reported that the onset is inversely related to the square root of the flux. However, RIED has not always been observed. Farnum et al. did not see RIED in Wesgo AL995 alumina irradiated to a maximum fluence of 0.03 dpa.[8] In addition, Zinkle and Kesternich[6] reported that RIED-like behavior can also be created by low surface conduction that depends on the atmospheric conditions, being observed in He-ion irradiations at low vacuum conditions but not at high vacuum conditions. Finally, Shikama[9] reported an RIED-like effect that showed high conductivity only during irradiation. At the Sixth International Conference on Fusion Reactor Materials (ICFRM-6), Kesternich suggested that the cause of observed RIED in previous experiments could be surface conductivity increases from contamination deposited during the experiment. Kesternich's results were discussed in depth by the international community at the ICFRM-6 meeting and a number of recommendations for future experiments were developed. These included making surface conductivity, sample temperature, and lead resistance measurements as well as controlling atmosphere and recording specimen history. Wesgo AL995 polycrystalline Al_2O_3 was again identified as the standard comparison material.

The experiment reported here was conducted at the Japan Materials Testing Reactor in Oarai, Japan. The conditions were chosen to be within the boundaries of temperature and electric field known to cause RIED (240 to 280 °C and 100 kV/m), but were at the lower end of those boundaries. The flux was about a factor of two lower than the maximum available flux in JMTR and the irradiation was carried out over two 25-day reactor cycles to increase the fluence. The measurement techniques recommended from the ICFRM-6 workshop were made, and we tried to adhere to all the ICFRM-6 recommendations.

Experimental Procedure

The experiment contained one sapphire disk sample and 3 MgO-insulated 316-stainless-steel- or inconel-sheathed coaxial cables. All electrical leads out of the reactor core area were mineral-insulated (MI) cables. A DC voltage was applied continuously to the samples during the irradiation except for short periods during switching operations. An atmosphere of static helium gas at a pressure between 30 kPa and 130 kPa was maintained around all the samples during the experiment. This pressure was controlled and was changed during the experiment to measure the effect of gas pressure on sample temperature and on the electrical conductivity measurements. The reactor fast flux (E > 1 MeV) was 7.1×10^{17} n/m^2s during the first cycle and 7.9×10^{17} n/m^2s during the second cycle. Thermal neutron (E < 0.683 eV) fluxes for the two cycles were 2.0×10^{18} n/m^2s and 2.7×10^{18} n/m^2s respectively. The gamma heating rate at the irradiation location was 5.0 W/g or 5000 Gy/s (iron) when the reactor was operating at full power (50 MW), and about 300 Gy/s gamma background radiation after the reactor was shut down.

Techniques

The samples were measured with Keithley 2001 Digital Multimeters (DMM) and the experiment was controlled with a Macintosh computer using a Labview® program and GPIB control. A Keithley 7002 matrix switching unit was used with Model 7153 matrix cards to change samples and measurement. These cards use triaxial shielded cables. In addition, a Hewlett Packard 4194A Impedance Analyzer was used to measure AC impedance from 100 Hz to 1 MHz periodically during the irradiation.

Sample 1: Sample 1 was a 10-mm-diameter by 1-mm-thick disk of sapphire. The material was Crystal Systems Hemex-Ultra (VUV-grade) with (0001) orientation (c-axis normal to the surface). A platinum electrode and guard ring were attached to the surface of the low side and a 10-mm platinum disk was attached to the high side of the sample with platinum paste heated to 800 °C. The low-side center electrode was 5 mm in diameter. The center-electrode lead was a chromel-alumel coaxial MgO-insulated thermocouple cable, and the high voltage lead was a single-conductor coaxial MgO-insulated cable as shown in figure 1a. The guard ring was connected to the reactor ground at the capsule. The center lead thermocouple was attached to a platinum post on the center electrode approximately 2 mm above the sample surface.

Sample 2: Sample 2 was an MgO-insulated, 1.6-mm-OD, chromel-alumel thermocouple cable with dimensions shown in figure 1b. The end of this cable and the ends of the other MI cables were terminated with an alumina cap that insulated the center conductor from the sheath. The ends were not sealed with glass, but were open to the capsule atmosphere through the seams in the alumina cap. The chromel and alumel leads were not connected to each other in the reactor but were both connected to the high voltage supply during the experiment.

Samples 3 and 4: These samples were terminated the same as sample 2. Each was a single conductor MgO-insulated coaxial cable with dimensions shown in figure 1b. Sample 3 had a diameter of 1.6 mm and sample 4 had a diameter of 2.3 mm. The cables were exposed in the high flux region for approximately 300 mm of their length.

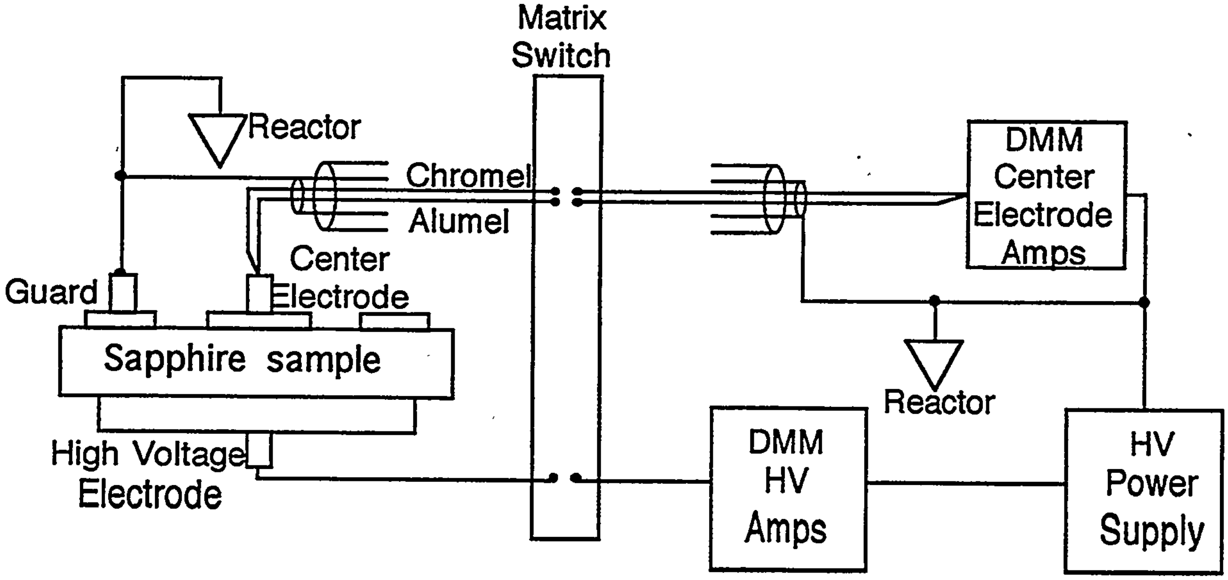

Figure 1 a: Schematic diagram of sapphire sample number 1 with electrical connections. (DMM = digital multimeter, HV = high voltage)

Measurements

Five experiments were programmed into the control computer and were run sequentially on each of the samples as appropriate. In each experiment, one thermocouple representing reactor power was measured and archived along with the data. These measurements are described below.

Experiment 1 -- DC electrical conductivity: Two DMMs were used to measure both the current from the power supply to the high voltage electrode and the current from the center electrode to ground. The guard ring in sample 1 was connected to the measurement system electrical ground (the triaxial cable guard sheath) at the first junction box outside the reactor containment vessel. An electrical schematic of the measurement system with known resistances is shown in figure 2. The Keithley 2001 DMM has an internal resistance of 1250 ohms during current measurements in the micro amp range. The MI cable measurements used the same arrangement, but only the current from the high voltage supply was measured because no electrodes were used. The cable sheath was grounded at the capsule, and the center conductor, open-ended in the capsule, was maintained at the high voltage.

During this experiment, the current of both the high voltage and low sides was measured several times as a function of voltage from +100 V to -100 V. This measurement was made both at reactor full power and at reactor shut down (in the ~300 Gy/s gamma background). For the MI cables, only the center conductor current was measured. No case showed ohmic behavior in the voltage/current curves, the negative voltages showing greatly reduced leakage currents as shown, for example, in figure 3 for the thermocouple cable. We attribute these results to ejection of photoelectrons from the capsule walls that are attracted to the electrode wires in the part of the capsule where the wires are not shielded. Thus this current, measured at low fluence, is a leakage current through the capsule gas and is dramatically lower with negative voltages. When we discovered this effect, after a fluence of about 0.7 x 10^{23} n/m^2, we changed the voltage from its initial value of +100 V to -100 V and kept it at -100 V for the duration of the experiment. Thus in the first reactor cycle, only about 50% of the fluence was at negative voltage, the remainder being at positive voltage. Negative voltage was applied during all of the second cycle.

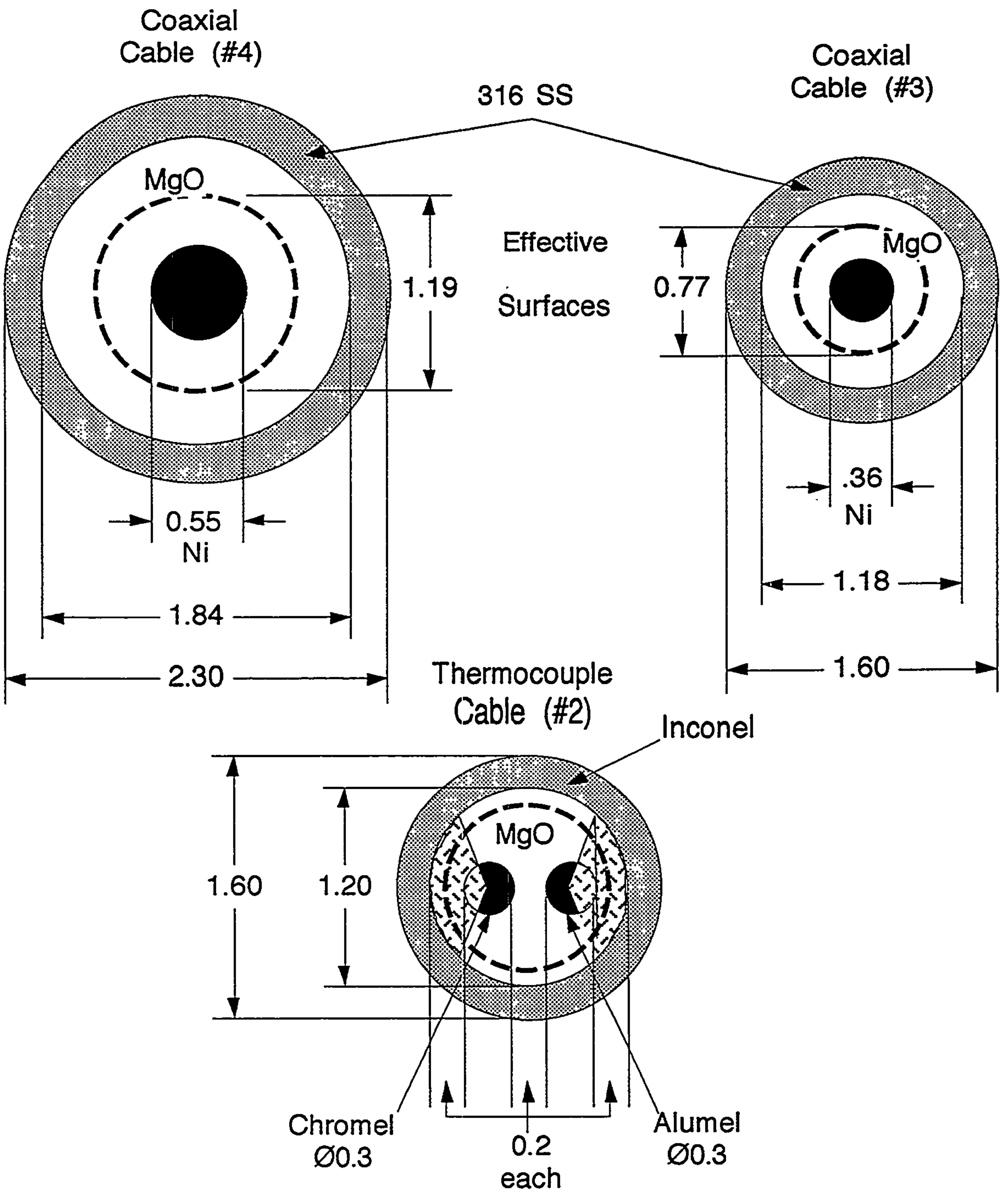

Figure 1 b: Cross-section diagrams of the three mineral-insulated cables, samples #4, #3, and #2.

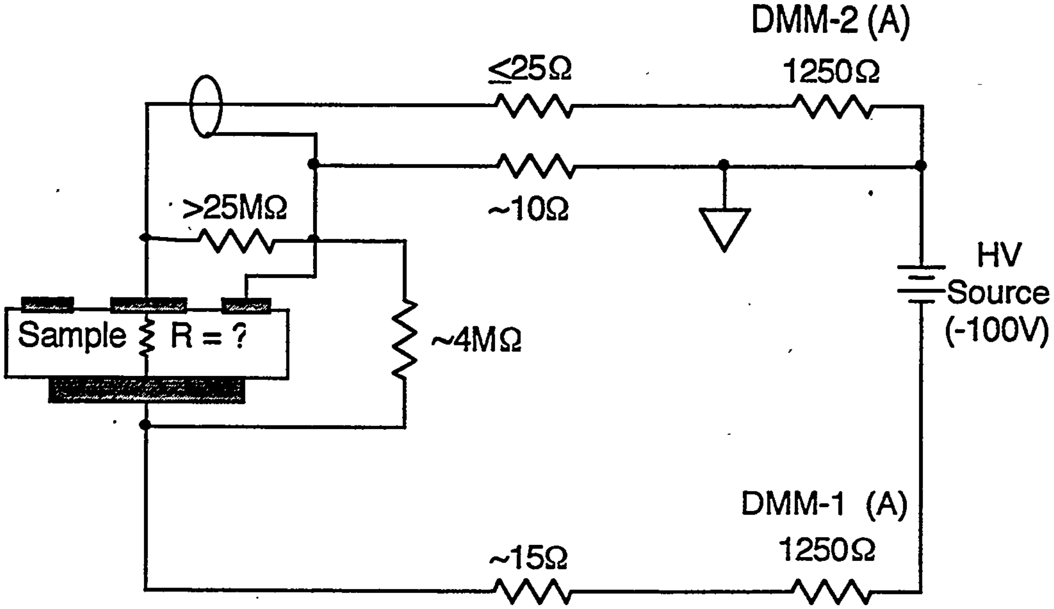

At +100 V, DMM-1 = +100μA and DMM-2 = +1.55 μA
At -100 V, DMM-1 = -8 μA and DMM-2 = +0.25 μA

Figure 2: Electrical schematic of the known resistances in the electrical conductivity measurement of the sapphire disk sample. Currents shown were measured with the reactor at full power and at a fluence of 0.3 x 10^{24} n/m^2. Resistances were measured at -100 V.

Experiment 2 -- Center electrode temperature. The center electrode leads, consisting of a chromel alumel thermocouple pair, were used as a thermocouple to directly measure specimen temperature for sample 1. The reference junction temperature at the reactor pressure boundary was also measured with a separate chromel alumel thermocouple and was used by the DMM to measure true temperature at the sample.

Experiment 3 -- Center electrode to guard electrode resistance. The center-electrode-current DMM was used with its internal voltage source to measure the surface resistance between the center and guard electrodes. During this measurement, the high voltage was switched off. Only sample 1 was measured in this experiment.

Experiment 4 -- Center electrode lead resistance. Since the center electrode lead of sample 1 was a thermocouple pair, we were able to measure the round trip lead resistance of this pair. This measurement gave some assurance that both leads remained connected to the center electrode pin and, because the lead resistance is temperature sensitive, also gave us another measure of the changes in reactor power. Coupled with the measurements in experiment 2, any disconnection from the center electrode would be detectable.

Experiment 5 -- AC impedance. We connected the Hewlett Packard 4194A Impedance Analyzer directly to sample 1, using the guarded electrode as low, and measured impedance from 100 Hz to 1 MHz. The high voltage was disconnected during this experiment.

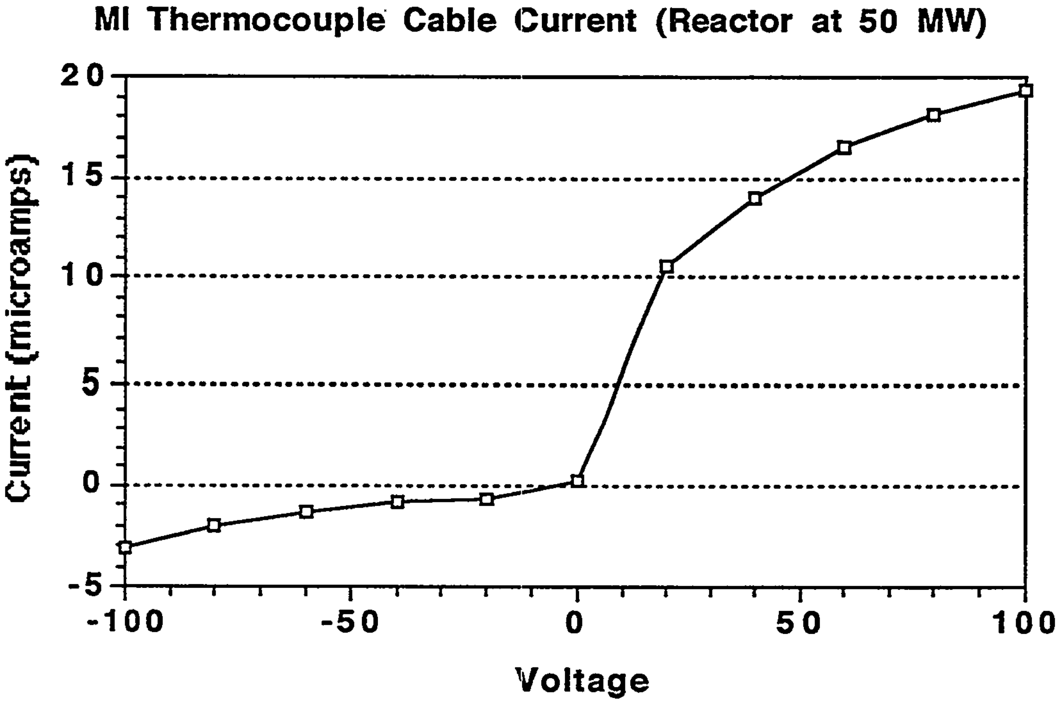

Figure 3: Plot of current vs. voltage in the MgO-insulated thermocouple cable with the reactor at 50 MW power. The temperature was 285 °C and the fast neutron flux was 8.5×10^{17} n/m^2 s (E>1.0 MeV) at a fluence of about 0.1×10^{24} n/m^2.

Results

No permanent post irradiation degradation was observed in any of the samples. The sapphire disk sample with negative voltage applied showed a slightly positive current, indicating that other resistances in the circuit had more effect on the current than the sample resistance. This positive current increased slightly during the experiment. We conclude that the conductivity of the sapphire sample either remained constant or, more likely, decreased with increasing fluence.

However, the current into the MI cables (samples # 2, #3, and, #4) increased quite dramatically with fluence after an incubation fluence of about 10^{24} n/m^2. The amount of increase was highly dependent on the electric field applied. This current increase was not permanent as has been observed in previous RIED experiments, but decreased to nearly the initial value when the reactor was shut down (and temperature returned to 26 °C). The high voltage lead of the sapphire disk sample also showed increased current, presumably due to a similar degradation.

Figure 4 shows the results from the sapphire sample electrical conductivity measurement (sample 1, experiment 1). Only the data with -100 V applied are shown. The data at 0.3×10^{24} n/m^2 were obtained from a short period during the first cycle when the voltage was reversed to -100 V. At about 0.7×10^{24} n/m^2 the reactor had an unplanned shut down and remained off for about 12 days. Irradiation was resumed with -100 V applied. At 1.35×10^{24} n/m^2 the second irradiation cycle began after being off for about 42 days. The reactor completed the second cycle at 3.05×10^{24} n/m^2. (A complete temperature/time history is shown in figure 6.) All of the above reactor-off measurements show a return to approximately zero conductivity. This reactor off conductivity is very close to the noise level in the experiment (on the order of 10^{-10} $(\Omega m)^{-1}$), so no permanent degradation could be measured. Figure 4a and b are the center-electrode and high-side electrode currents respectively of the sapphire sample. The increase in high-side current at 2.4 x 10^{24} n/m^2 closely correlates with an increase in reactor power and an associated 3 °C increase in sample temperature.

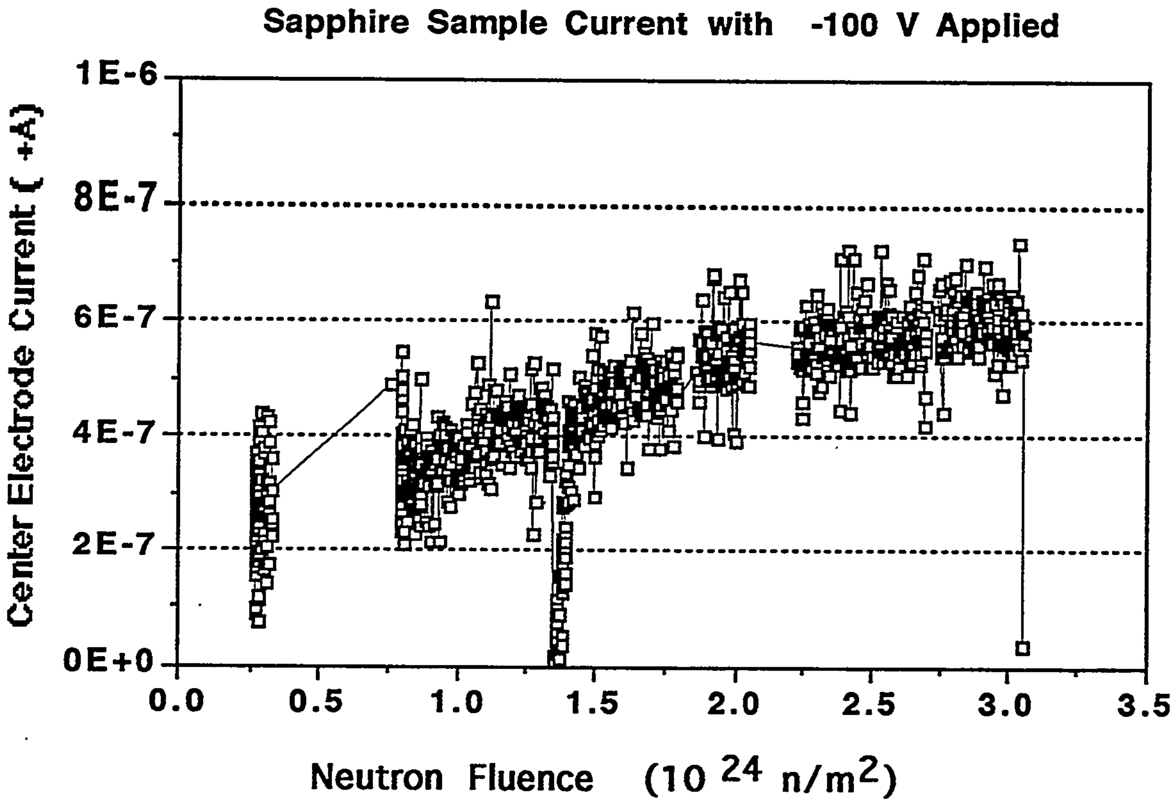

Figure 4 a: Center-electrode current vs. fluence for the sapphire sample with the reactor at full power and an applied electric field of 100 kV/m. The data at a fluence of 1.35 and 3.05 are with the reactor off.

Figure 5a shows the leakage current from the three MI cables vs. fluence. The electric field shown was calculated by dividing the applied voltage by the insulator thickness shown in figure 1b and represents a kind of average field. The actual field varies within the insulator as the inverse radius. The final effective resistance to ground of these cables was calculated from the applied voltage and the leakage current. After a fluence of 3.05 x 10^{24} n/m^2, and with the reactor at full power, the resistances were 2.9 MΩ, 5.0 MΩ, and 33 MΩ for the thermocouple, small diameter and large diameter cables respectively. For the large-diameter cable, about half of the current was caused by the initial RIC and half was degradation from the initial RIC value.

As with the sapphire sample, all the MI cables showed radiation-induced conductivity (RIC) when the reactor was on, but returned to near unirradiated conductivity (below our measurement threshold) when the reactor was off. However, the MI cables showed substantial and increasing degradation that depended strongly on the electric field across the insulator. While the measurable current disappears when the reactor is turned off, the physical degradation apparently remains, because when the reactor is restarted, the current quickly returns to the degraded value observed prior to reactor shut-down. Figure 5b shows the leakage current from the Thermocouple cable (sample 2) prior to and after the inter-cycle shut-down.

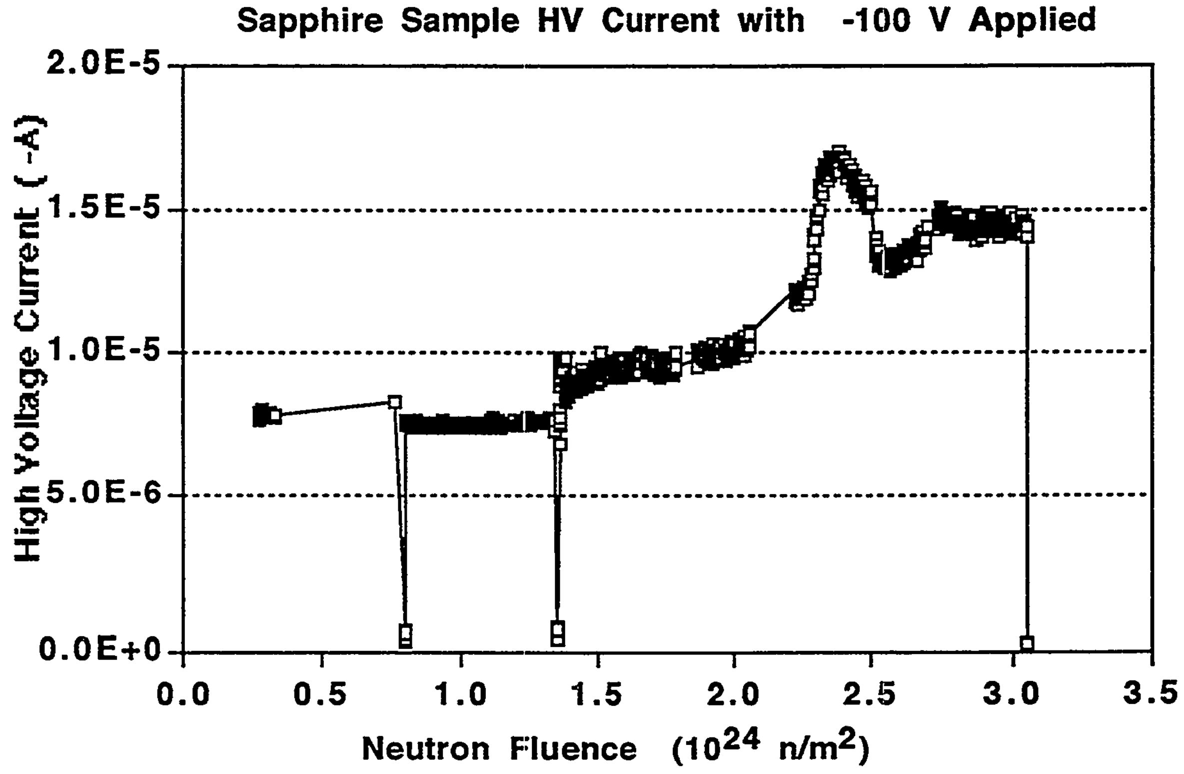

Figure 4 b: high-side electrode current vs. fluence for the sapphire sample.

Experiment 2 measured the sapphire sample temperature near the center electrode. The temperature history of the sample for the entire experiment vs. experiment time is shown in figure 6. The first cycle, from 4 x 10^4 s until about 3.1 x 10^6 s was interrupted by the reactor shut down. The second cycle begins at about 7.1 x 10^6 s and ends at about 9.2 x 10^6 s. The average temperature during reactor full power operation is 247 ± 5 °C during the first cycle and decreases from about 284 to 268 °C during the second cycle. Temperature with the reactor off was about 26 °C. The higher temperature in the second cycle is attributable to a reduction in other experiments that caused higher neutron flux at this experiment's location. The variations in temperature during the second cycle are caused by variations in reactor power. These variations can be correlated directly with changes in the high voltage current in all the MI cables. The current into the high side of sample 1 was the most sensitive to variations in reactor power as can be seen in figure 4b. This sensitivity is higher than would be predicted from classical RIC considerations.

Experiment 3 measured the resistance between the center electrode and ground with the high side disconnected from the high voltage. This resistance increased slowly from 25 MΩ to 40 MΩ during the experiment, but was never less than 25 MΩ.

The center lead resistance measurements (experiment 4) showed variation with temperature as expected but showed no effect of radiation. The round trip resistance of the chromel alumel thermocouple leads was about 99 Ω at the reactor-full-power temperature.

The results of the AC impedance measurements have not yet been fully analyzed and will be reported elsewhere, but these measurements were consistent with the DC measurements and showed no unexpected results. The AC electrical conductivity of the sapphire sample decreased by about 65% during the irradiation. The AC measurements were also affected by gas pressure.

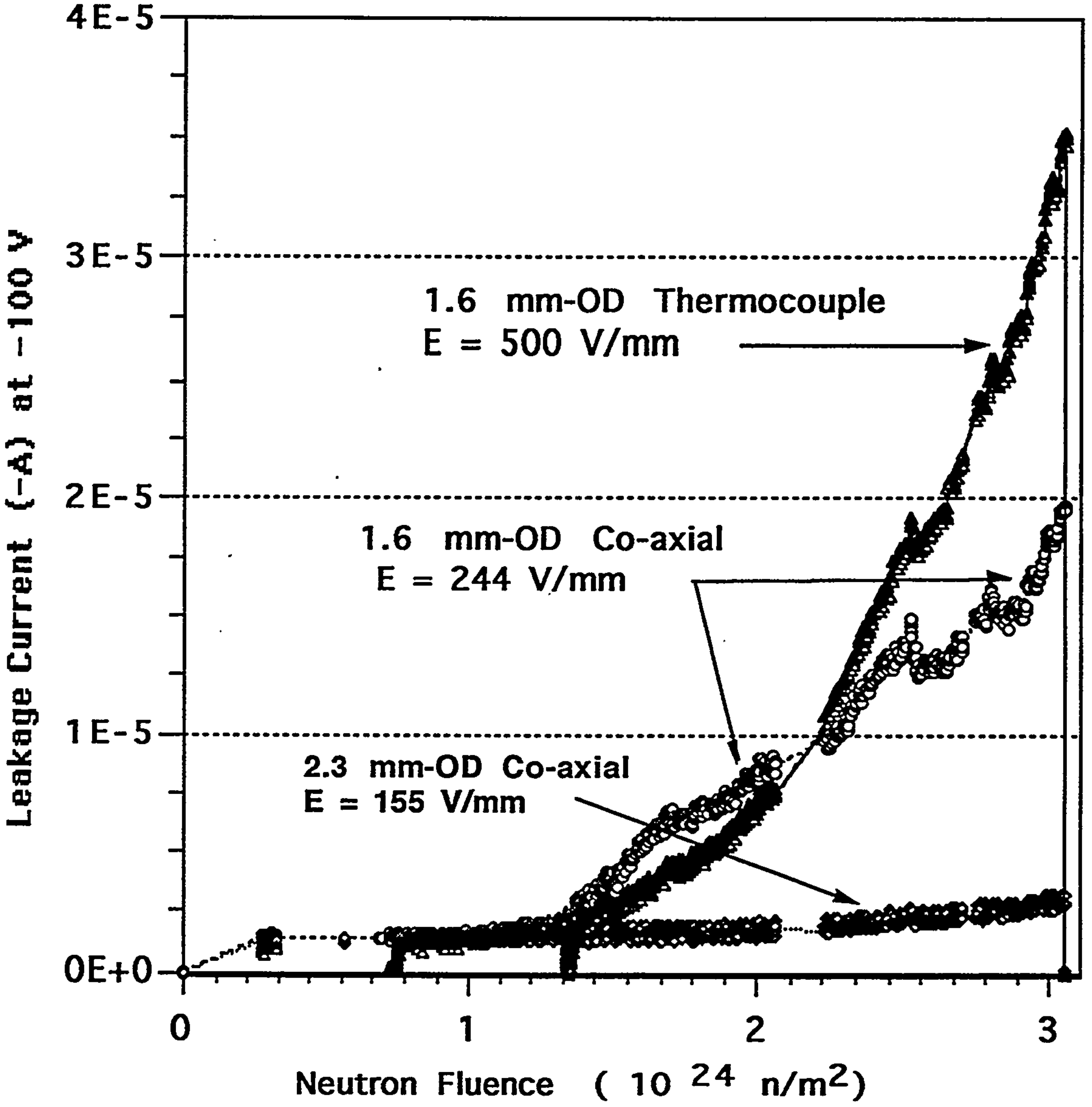
Leakage current in MgO-insulated Cables with -100 Volts Applied, at Reactor Full Power and at ~260 C.

Figure 5a: Leakage current at -100 V for the three MgO-insulated MI cables vs. fluence.

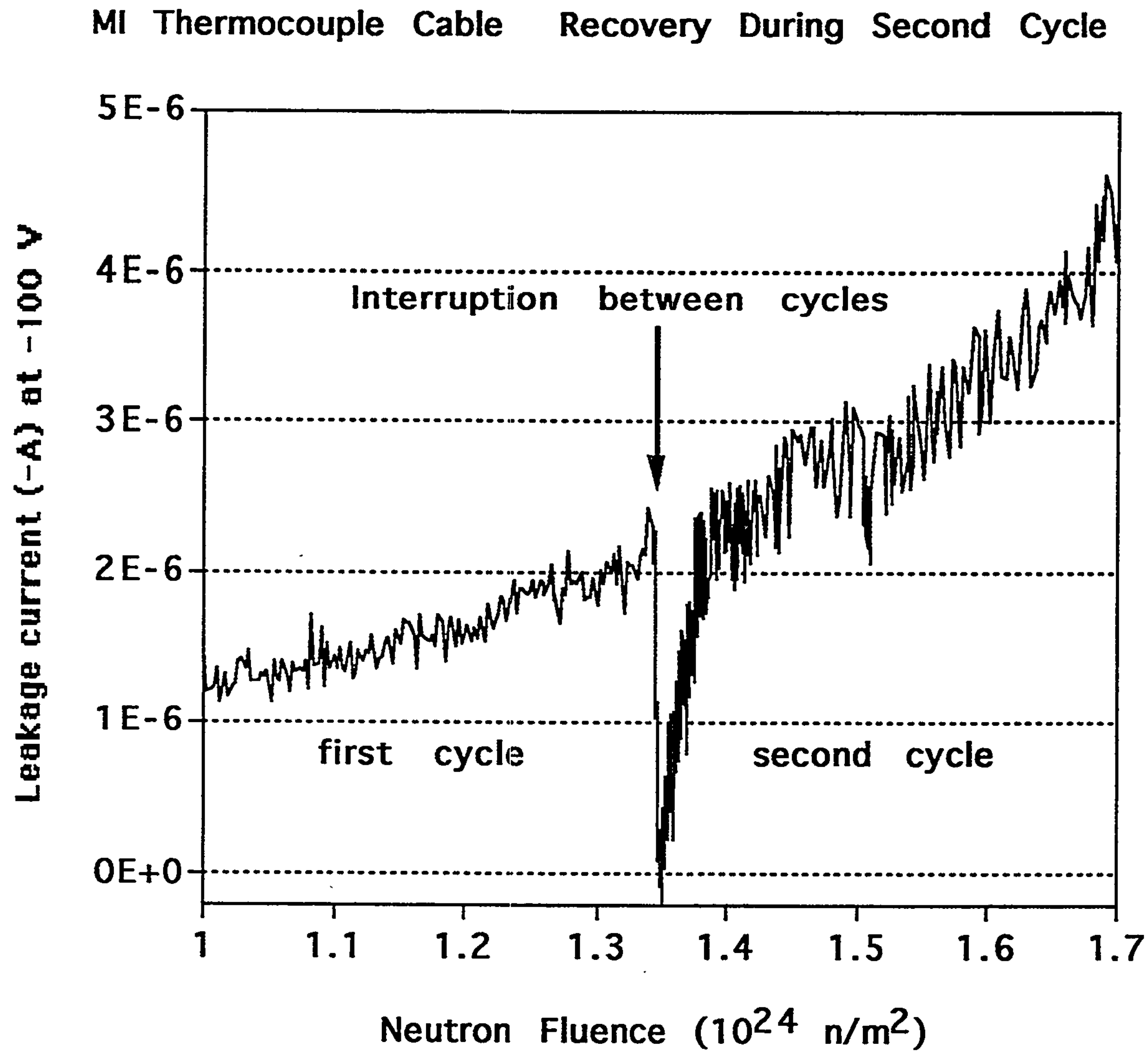

Figure 5b: Leakage current in the Thermocouple MI cable before and after the inter-cycle break.

Discussion

Even though the temperature of this experiment was only between 250 and 280 °C, we expected to observe RIED in the sapphire sample. Moroño and Hodgson[7] speculate that the lower limit for RIED is 150 °C. In this experiment we saw no measurable permanent degradation in either the sapphire sample or the MI cables. Therefore, we saw no RIED up to the final damage level of about 0.3 dpa.

The slight apparent decrease in conductivity with time in the sapphire sample is consistent with previous results[2,8,9]. This effect is different than RIED. At the doses reached in this experiment, the activation energy for conductivity in RIED-degraded materials has been reported by Pells[10] and by Möslang et al.[11] to be greatly reduced from unirradiated values. If the degradation observed in the MI cables is similar to RIED, the temperature reduction from 280 °C to 26 °C would not be sufficient to explain the loss of current on reactor shut down. However, Möslang et al.[11] also reported that the activation energy of Wesgo alumina, that did not show RIED under helium-ion irradiation, did not decrease substantially, while the activation energy of Vitox alumina, that did show RIED, was dramatically reduced. Since the degradation we observed is different from the RIED that Möslang reported, we cannot say from our data whether the return to low conductivity upon reactor shut down is caused by reduced temperature or reduced ionization.

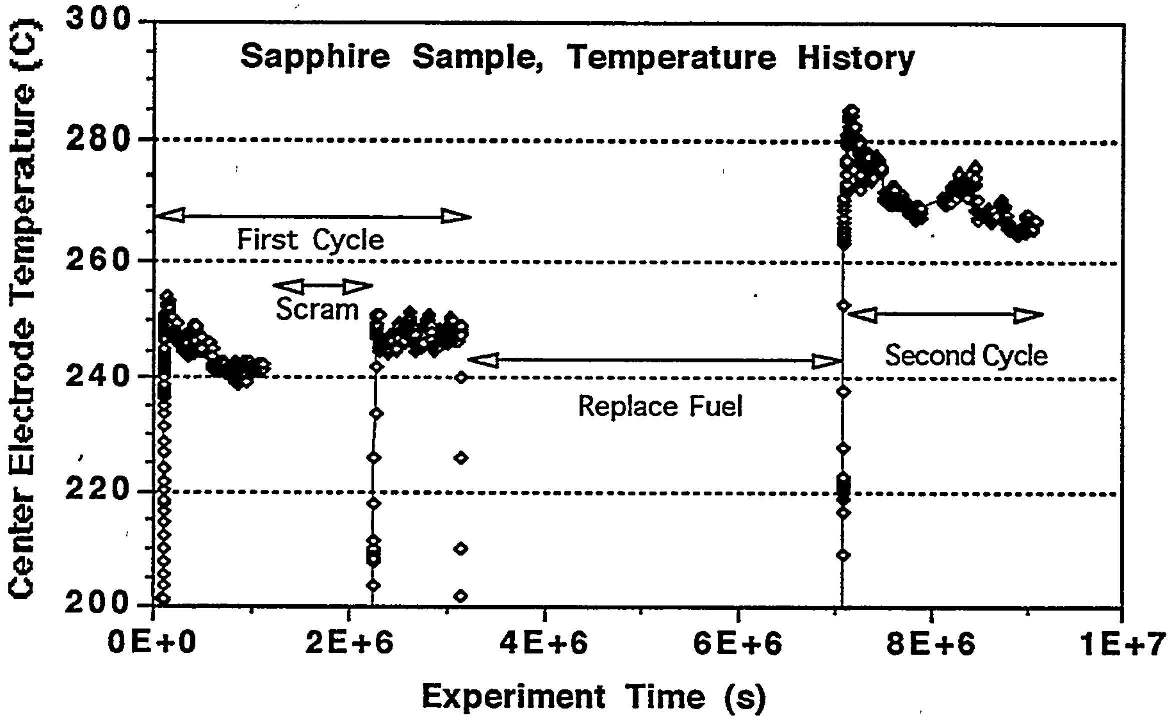

Figure 6: Temperature history of the sapphire sample 1 for the entire experiment.

Although the degradation in the MI cables is different from RIED, some permanent degradation clearly took place. This type of permanent degradation was also observed in Shikama's earlier work[9]. We cannot determine from this experiment whether the effect is related to bulk properties of the MgO, intergranular surface conduction within the MgO, conductivity in the gas that has leaked into the cable through the open end, or conduction through some surface coating at the open cable end. Close comparison of the data at the end of the first cycle and the beginning of the second (figure 5b) shows that the cause of the degradation is permanent, even though it does not affect conductivity after reactor shut down. The fact that the effect is strongly dependent on the applied electric field rather than the voltage suggests either a mechanism with some restricted carrier motion such as ionic conduction or vacancy migration, or, alternatively, a conductive coating whose rate of formation is field dependent. Clearly ionization is needed to provide carriers for the current (at least at room Temperature), and apparently these carriers disappear when the irradiation is stopped.

It is not possible to rule out unknown effects from the gas environment or alumina termination cap in explaining the cable degradation. Helium gas was free to permeate the cable insulator and certainly provided some leakage paths from the cable center conductors to ground. The purity of the He gas, after remaining in the capsule for many hours of high-temperature irradiation is also questionable. However, we would not expect gas effects to be permanent, have an incubation time, or increase uniformly with time.

Certainly, some field-dependent surface-coating process could have taken place that caused surface conduction at the cable termination. Zinkle and Kesternich[6] suggested that formation of a carbon-film from vacuum gasses could explain RIED-like behavior in poor vacuum conditions. However, It is questionable whether such a mechanism could occur in the He gas environment. In Addition, measurements of surface conductivity on the alumina sample (in the same capsule) showed only increasing resistance with time.

If the effect is in the bulk MgO, it is interesting to speculate on the possible origin of the degradation. The migration of defects to make divacancies or vacancy clusters could explain the field dependency. Pells and Shikama[12] suggested that V_n centers are mobile in the RIED temperature range and may contribute to enhanced vacancy motion. Zinkle[13] also suggested that defect mobility is dependent on the degree of ionization concurrent with displacements. If ionization-enhanced vacancy diffusion were contributing to the degradation in the cables, then one might expect that the lower ionization to displacement ratio of the reactor irradiation relative to the electron irradiations of Hodgson, would require higher temperatures for RIED in the reactor experiments, putting the experiment reported here below the lower temperature limit for RIED. However, degradation was not observed in either bulk alumina or MgO-insulated MI cables during neutron irradiations at 615 and 655 °C to damage levels up to 2.2×10^{-2} dpa (Farnum et al.[8]).

FUTURE WORK

Part of the goal of this experiment was to develop improved methods for measuring in situ conductivity in fission reactor sources. It is the first in a planned series of experiments in JMTR and is a preliminary experiment to one planned for HFIR in May, 1995. All of the experiments will try to determine the environmental conditions under which RIED may be a problem for fusion reactors and to determine the degree of degradation expected with neutron irradiation.

ACKNOWLEDGMENTS

The authors would like to thank D.P. White of ORNL for his assistance with the data acquisition programming.

REFERENCES

[1] R.W. Klaffky, B.H. Rose, A.N. Goland, and G.J Dienes, Phys. Rev. B 21 (1980) 3610.
[2] E. H. Farnum, J. C. Kennedy, F. W. Clinard and H. M. Frost, J. Nucl. Mat. 191-194 (1992) 548-551.
[3] E.R. Hodgson, J. Nucl. Mater. 179-181 (1991) 383-386.
[4] G.P. Pells, J. Nucl. Mater. 184 (1991) 177-182.
[5] T. Shikama, M. Narui, Y. Endo, T. Sagawa and H. Kayano, J. Nucl. Mater. 191-194 (1992) 575.
[6] S. Zinkle and W. Kesternich, Fusion Reactor Materials Semi-Annual Progress Report for the Period Ending March 31, 1993, DOE/ER-0313/14.
[7] A. Moroño and E. R. Hodgson, J. Nucl. Mater. 212-215 (1994) 1119.
[8] Eugene H. Farnum, Frank W. Clinard, Jr., Walter F. Sommer, James C. Kennedy III, and Tatsuo Shikama. J. Nucl Mater. 212-215 (1994) 1128.
[9] Tatsuo Shikama, Minoru Narui, Hideo Kayano and Tsutomu Sagawa, J. Nucl Mater. 212-215 (1994) 1133.
[10] G. P. Pells, Radiation Effects, 97 (1986) 199-207.
[11] A. Möslang, E. Daum and R. Lindau, Proceedings of the 18th Symposium on Fusion Technology, Karlsruhe, August 22-26, 1994, in press.
[12] Tatsuo Shikama and G. Phillip Pells, J. Nucl. Mater. 212-215 (1994) 80.
[13] S. J. Zinkle, REI-7 Proceedings, Nucl. Instr. Meth. B, in press.

OPTICAL ABSORPTION AND LUMINESCENCE IN NEUTRON-IRRADIATED, SILICA-BASED FIBERS -- D. W. Cooke, E. H. Farnum, F. W. Clinard, Jr., B. L. Bennett, B. Sundlof and W. P. Unruh (Los Alamos National Laboratory)

OBJECTIVES

The objectives of this work are to assess the effects of thermal annealing and photobleaching on the optical absorption of neutron-irradiated, silica fibers of the type proposed for use in ITER diagnostics, and to measure x-ray-induced luminescence of unirradiated (virgin) and neutron-irradiated fibers.

SUMMARY

ITER plasma performance will be monitored by fiber optics cables capable of transmitting light of various wavelengths in the ultraviolet, visible, and near infrared regime. The fibers must retain their optical integrity under extreme conditions of elevated temperature and mixed neutron and γ-ray exposure. Previous research has shown that fibers composed of pure silica cores and fluorine-doped cladding might be appropriate candidates for this application. Optical absorption and emission on commercially-available silica fibers containing both low (< 1 ppm) and high (600 - 800 ppm) OH concentrations, that had been irradiated at the Los Alamos Spallation Radiation Effects Facility (LASREF) to a fluence of 10^{23} n-m^2, were measured in the wavelength interval 200 - 800 nm. Generally the low-OH fiber performance was superior, although neither fiber exhibited the optimum optical integrity required for ITER diagnostic applications. Both unirradiated fibers showed good transmissivity in the region of 400 - 800 nm; however, following irradiation each exhibited strong absorption over the entire wavelength region except for a small interval around 400 to 500 nm. Attempts to thermally anneal or photobleach the radiation-induced damage were only partially successful. In addition to the poor transmission properties of the irradiated fibers in the 200 - 800 nm region, there was intrinsic luminescence near 460 nm that occurred during exposure to *continuous* x irradiation at room temperature. This emission, if induced by neutrons and γ rays of the ITER environment, would interfere with optical diagnostic measurements.

PROGRESS AND STATUS

Introduction

Fiber optics will be an integral part of the diagnostics utilized in the operation of ITER. Information on plasma performance, in the form of light signals of 200 - 1500 nm wavelength, will be transmitted via fiber optics over several tens of meters. Stringent requirements will be placed on these fibers and diagnosticians must have information on their optical properties as a function of neutron and γ dose, temperature, etc., for design considerations. Accordingly, experiments have been undertaken to assess the optical performance of various silica-based fibers subjected to mixed neutron and γ radiation fields.

Experimental Procedures

Test materials and irradiation facility

Two types of optical fibers consisting of a pure fused silica core with fluorine-doped (~ 4 mole %) cladding were obtained from Fiberguide Industries, Inc. [1] and tested in the as-received state. Anhydroguide and Superguide fibers contained less than 1 ppm and 600 - 800 ppm of OH, respectively. The fibers were supplied with either nylon (for low fluence exposure) or aluminum (for high fluence exposure) jackets. After the irradiation, 50-cm sections of irradiated fibers were excised from longer coils and subjected to optical absorption and luminescence measurements at room temperature. Effects of thermal annealing (up to 600°C) and photobleaching on the absorption were investigated.

All fibers were irradiated at LASREF (Los Alamos Spallation Radiation Effects Facility) over a two and one-half month period and subjected to either a low fluence or high fluence environment. The high fluence region contained both high energy neutrons and γ rays, whereas shielding limited the neutron energies and virtually eliminated γ rays in the low fluence region. The fluence encountered by fibers in the high fluence region was calculated to be $2.79 \times 10^{23} \pm 8.89$ n m^{-2}, with 94.5% having energy less than 1.0 MeV and 0.32% with energy greater than 20 MeV.

Results

Optical absorption

A comparison of the optical absorption of irradiated and unirradiated silica fibers [Anhydroguide (*A*) and Superguide (*S*)] are shown in Fig. 1. Unirradiated *A* and *S* fibers exhibit good transmissivity above about 400 nm with *A* being slightly better than *S*. Absorption peaks below 400 nm have been thoroughly discussed in the literature and are generally related to E′ centers and peroxy radicals (for a review see Ref. [2]). Following low-fluence irradiation both *S* and *A* fibers exhibit intense absorption below 400 nm. In fact, the optical absorption unit (HP 8452A) cannot detect any optical emission above the background level in this region as shown by the flat top in Fig. 1. Additionally, there is a radiation-induced absorption band near 620 nm for both *A* and *S* fibers. This is the well-known absorption attributed to non-bridging oxygen hole centers (NBOHC) in silica [3]. Absorption peaks near 350 nm in the virgin samples may be associated with the presence of chlorine as reported in Refs. [4] and [5], although at present the Cl content of fibers *A* and *S* is unknown. Moreover, samples displaying this band usually contain <200 ppm OH and >300 ppm Cl. Recall that fiber *S* contains ~600 - 800 ppm OH.

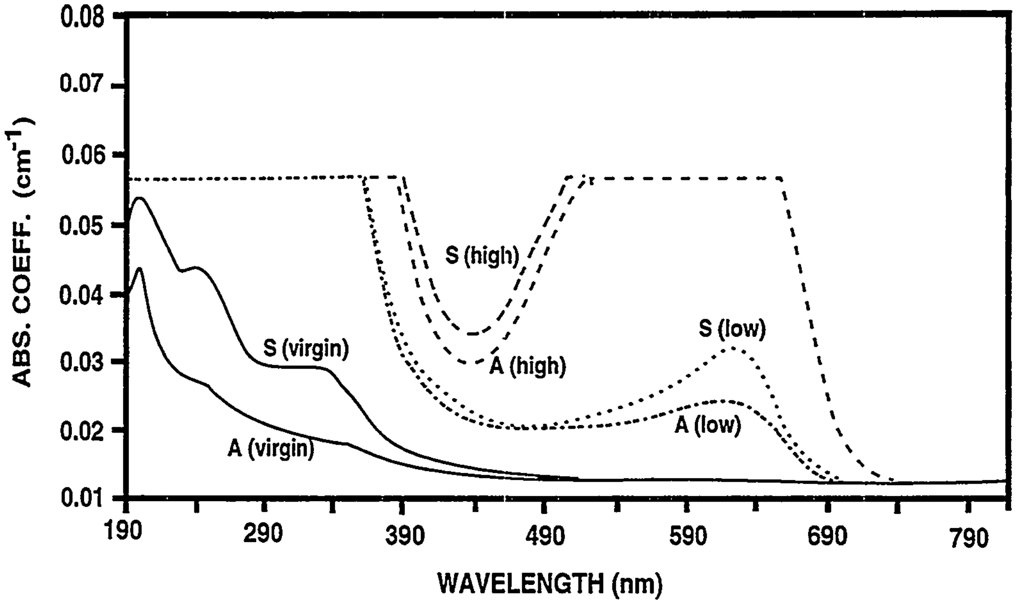

Fig. 1. Optical absorption of virgin and irradiated (high and low fluence) Anhydroguide (A) and Superguide (S) silica fibers.

Thermal annealing

Results of thermal annealing experiments on *A* fibers exposed to high fluence radiation are shown in Fig. 2. The fiber was heated from room temperature (25°C) to 600°C in steps of 100°C (beginning at 100°C) except for an additional point at 550°C. Typically the fiber was ramped to the desired temperature in 20 min. and held for 2 hr. before furnace cooling to room temperature. Temperature soaks at 400°C and above were reduced to 1 hr. duration. Thermal annealing of the broad absorption near 620 nm is clearly evident. Interestingly, results from a similar experiment on *S* fiber showed no evidence of thermal annealing up to 600°C. Given the large OH content of *S* fiber compared to *A* fiber, these results suggest that OH is responsible for stabilizing the radiation-induced NBOHCs rendering them impervious to thermal annealing. Previous work on γ-radiation induced NBOHCs has suggested that OH stabilizes the defect by forming a hydrogen bond of the type $\equiv \mathrm{Si}-\mathrm{O}\bullet --- \mathrm{H}-\mathrm{O}-\mathrm{Si}\equiv$ or $\equiv \mathrm{Si}-\mathrm{O}\bullet --- \mathrm{H}-\mathrm{Si}\equiv$, as reported in Ref. [3]. Of course the strong absorption between 500 and 700 nm may be due to multiple radiation-induced centers [6] that cannot be resolved with the present system. The effect of the F-doped cladding on the growth and thermal annealing properties of the 620-nm band must also be investigated. Previous work on γ-ray induced absorption near 630 nm has demonstrated that this band grows much faster in fibers composed of pure silica cores with a F-doped cladding than in fibers with a silicone cladding, for example [7].

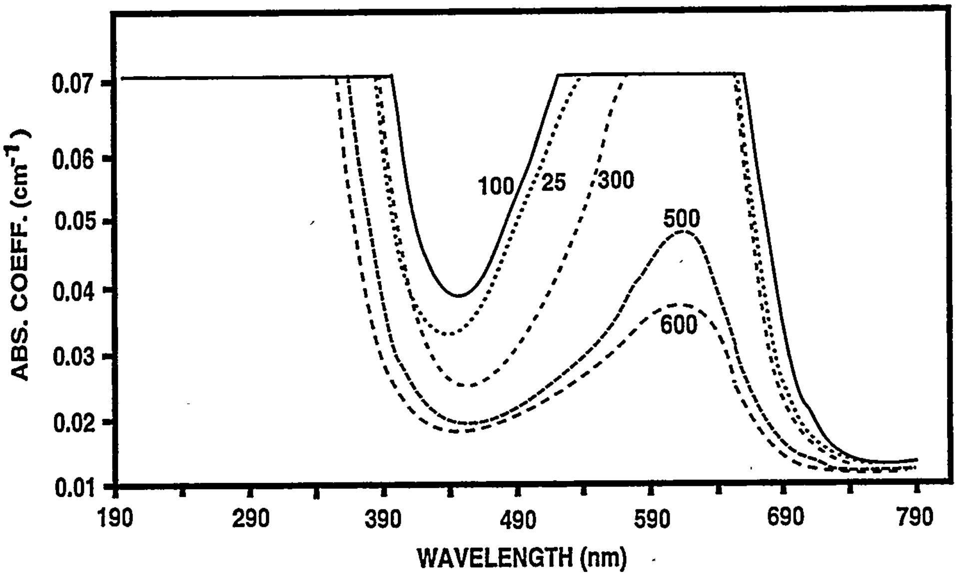

Fig. 2. Optical absorption of the low-OH content fiber (*A*) as a function of thermal annealing temperature (°C).

Photobleaching

Radiation-induced optical absorption in *A* fibers subjected to high-fluence radiation can be partially reduced by thermal annealing as shown in Fig. 2. A similar experiment was done to assess the effect of photobleaching on these fibers; the results are shown in Fig. 3. An unfiltered 200W Hg lamp was used to illuminate the fiber for up to six hours duration at room temperature. Although not shown in the graph, it was found that photobleaching for one hour resulted in the same magnitude of optical bleaching as that observed after six hours. Due to experimental limitations it was not possible to clearly observe the bleaching effect on the 620-nm peak. It is clear, however, that there is reduced absorption near 450 nm due to photobleaching. The magnitude of optical photobleaching in *A* fibers is very small compared to thermal annealing and it is evident that long exposures would be required to significantly reduce the radiation-induced absorption. It should be noted, however, that photobleaching with light of wavelengths corresponding to the radiation-induced absorption peaks should be much more effective than illumination with a broadband source. Further experimental work is required to assess the effects of photobleaching on *A* fibers. Hayashi et al. [8] have shown that photobleaching γ-irradiated silica fibers with selected wavelengths can reduce radiation-induced attenuation. Moreover, they demonstrated a three-fold decrease in attenuation when the photobleaching was done at 70°C rather than 28°C.

No photobleaching was attempted on *S* fibers because it had already been determined that thermal annealing was ineffective in reducing the radiation-induced absorption and it was assumed that photobleaching would be equally ineffective.

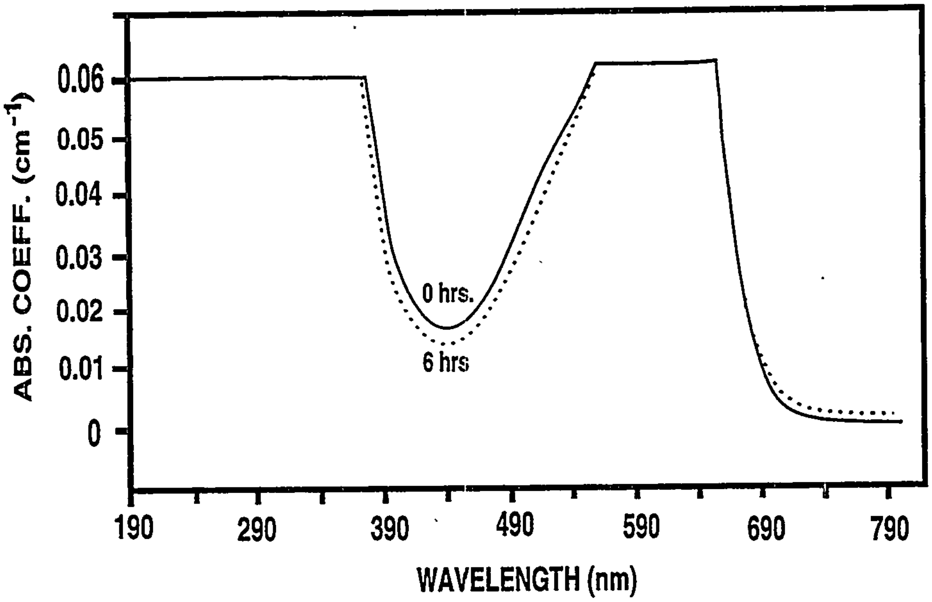

Fig. 3. Optical absorption of the low-OH content fiber (*A*) as a function of photobleaching time.

Radiation-induced luminescence

Luminescence obtained from *S* and *A* fibers that had been exposed to the high fluence region and subsequently excited by low-energy x rays at room temperature is shown in Fig. 4. It is characterized by band emission peaking near 450 nm. Gaussian deconvolution of the emission shows two bands (not shown in Fig. 4) with maxima at 445 and 475 nm. This x-ray-induced luminescence (also referred to as radioluminescence) is obtained during *constant* x-ray excitation. Both irradiated and unirradiated fibers were examined and it was found that each exhibited band emission near 450 nm except for the unirradiated *S* fiber, which showed no measurable luminescence. This absence of luminescence in the virgin fiber was surprising because *S* fibers exhibited the most intense luminescence after neutron irradiation. Compared to the unirradiated *A* specimen, the x-ray luminescence for the high-fluence-exposed sample is three times more intense.

The nature of the defect responsible for the luminescence near 450 nm is unclear. Previous work has suggested that it results from the recombination of holes at E′ centers [9]. More recent *ab-initio* molecular-orbital calculations conclude that 450-nm luminescence is attributable to a triplet-to-ground state transition of a neutral oxygen-vacancy defect [10]. Regardless of origin, its presence during exposure of diagnostic fibers to the ITER plasma will interfere with real-time measurements.

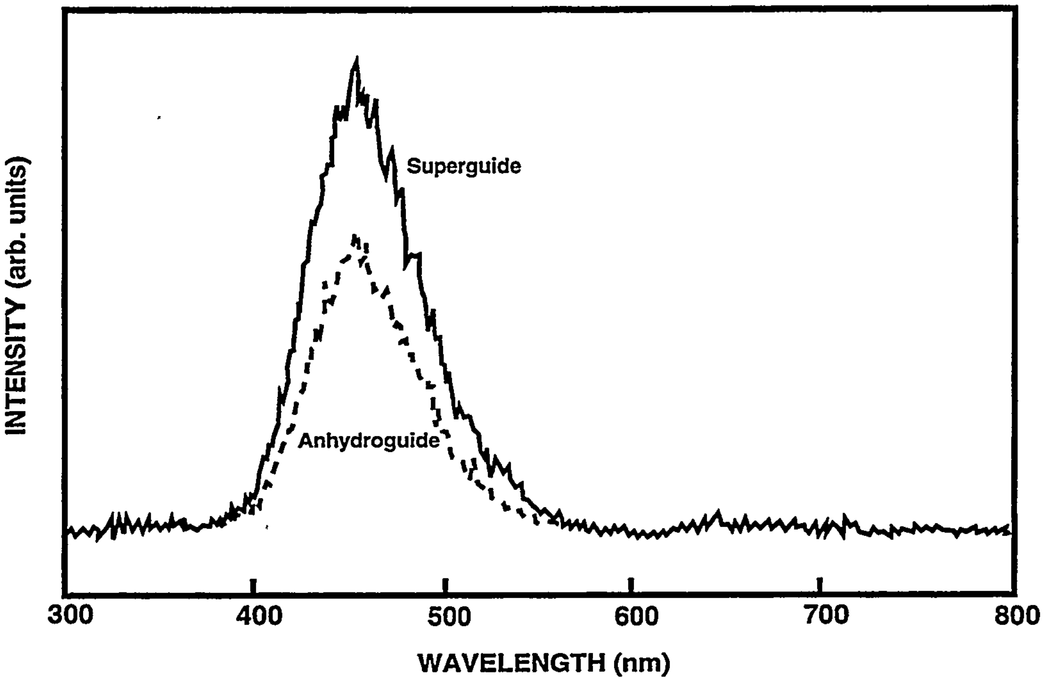

Fig. 4. X-ray-induced luminescence from neutron-irradiated, low- and high-OH content silica fibers.

Discussion and Conclusions

Silica-based fibers containing small (Anhydroguide) or large (Superguide) amounts of OH exhibit strong optical absorption when exposed to low- and high-fluence radiation fields. *A* fibers exhibit better performance than *S* fibers because 1) they are less susceptible to radiation-induced absorption, 2) the radiation-induced absorption can be partially thermally annealed, and 3) they exhibit weaker luminescence under continuous excitation. However, neither of the fibers in their present form are ideal for ITER diagnostic applications in the 200 - 800-nm regime. Strong radiation-induced optical absorption occurs for all wavelengths except approximately 400 to 500 nm, which, unfortunately, is the spectral region where radiation-induced luminescence occurs.

Additional research on the effects of high fluence neutron radiation on the optical properties of silica-based fibers is clearly needed to understand the radiation-induced defects. Although a good data base presently exists for silica-based fibers that have been exposed to low fluences of neutrons and γ rays, the requirements for ITER diagnostics mandate a new regime of high fluence exposures with *in-situ* and post-irradiation testing that have not been previously undertaken [11].

REFERENCES

[1] Fiberguide Industries, Inc., 1 Bay Street, Stirling, NJ 07980.
[2] D. L. Griscom, SPIE **541** (1985) 38.
[3] K. Nagasawa, Y. Hoshi, Y. Ohki and K. Yahagi, Jpn. J. Appl. Phys. **25** (1986) 464.
[4] K. Awazu and H. Kawazoe, J. Appl. Phys. **68** (1990) 3584.
[5] H. Nishikawa, R. Tohmon, Y. Ohki, K. Nagasawa and Y. Hama, J. Appl. Phys. **65** (1989) 4672.
[6] D. L. Griscom, J. Ceram. Soc. Jpn. **99** (1991) 923.
[7] K. Nagasawa, R. Tohmon and Y. Ohki, Jpn. J. Appl. Phys. **26** (1987) 148.

[8] S. Hayashi, Y. Wada, Y. Chigusa, K. Fujiwara, Y. Hattori and Y. Matsuda, Influence of Radiation on Material Properties: 13th International Symposium (Part II), ASTM STP 956, F. A. Garner, C. H. Henager, Jr., and N. Igata, Eds., American Society for Testing and Materials, Philadelphia, 1987, pp. 647 - 653.
[9] G. H. Sigel, Jr., J. Non-Cryst. Solids **13** (1973/74) 372.
[10] R. Tohmon, Y. Shimogaichi, H. Mizuno, Y. Ohki, K. Nagasawa and Y. Hama Phys. Rev. Lett. **62** (1989) 1388.
[11] See, for example, E. J. Friebele, K. J. Long, C. G. Askins, M. E. Gingerich, M. J. Marrone and D. L. Griscom, SPIE **541** (1985) 70; J. K. Partin, ibid., 97; G. H. Miley, O. Barnouin, J. Nadler, W. Williams and A. Procoli, Fusion Engineering and Design **18** (1991) 341; Radiation Effects in Materials for Fusion Diagnostic Systems Workshop, Princeton Plasma Physics Laboratory, Princeton, NJ, March 1991. (Available from E. H. Farnum, Los Alamos National Laboratory).

Distribution

1-15. Argonne National Laboratory, 9700 South Cass Avenue, Argonne, IL 60439
M. C. Billone
O. K. Chopra
H. M. Chung
D. R. Diercks
A. K. Fisher
J. Gazda
A. B. Hull
C. E. Johnson
F. Kassner
R. F. Mattas
L. A. Niemark
J. H. Park
D. L. Smith
S. W. Tam
H. C. Tsai

16-17. Argonne National Laboratory, EBR-II Division, P.O. Box 2528, Idaho Falls, ID 83403-2528
H. P. Planchon
D. L. Porter

18. Auburn University, Department of Mechanical Engineering, 201 Ross Hall, Auburn, AL 36849
B. A. Chin

19-32. Battelle-Pacific Northwest Laboratory, P.O. Box 999, Richland, WA 99352
J. L. Ethridge
F. A. Garner (5)
D. S. Gelles
L. R. Greenwood
M. L. Hamilton
H. L. Heinisch
G. W. Hollenberg
R. H. Jones
W. W. Laity
O. D. Slagle

33. Carnegie Institute of Technology, Carnegie-Mellon University, Schenley Park, Pittsburgh, PA 15213
W. M. Garrison, Jr.

34. Commissariat à l'Energie Atomique, Direction des Technologies Advancées, M2R1/DECM Cen-Saclay, Gif Sur Yvette, Cedex, France
F. Tavassoli

35-38. General Atomics, P.O. Box 85608, San Diego, CA 92138
T. A. Lechtenberg
D. I Roberts
K. R. Schultz
C. Wong

39. General Dynamics Corp., 5001 Kearny Villa Rd., San Diego, CA 92138
T. L. Cookson

40. Georgia Institute of Technology, Fusion Research Center, 0225, Atlanta, GA 30332
W. M. Stacey

41. Grand Canyon University, Department of Natural Science, 3300 W. Camelback Rd., Phoenix, AZ 85017
W. A. Coghlan

42-44. Idaho National Engineering Laboratory, Fusion Safety Program, P.O. Box 1625, Idaho Falls, ID 83415-3523
G. Longhurst
K. McCarthy
D. Petti

45-46. Lawrence Livermore National Laboratory, P.O. Box 808, Livermore, CA 94550
E.C.N. Dalder
J. Perkins

47-55. Los Alamos National Laboratory, P.O. Box 1663, Los Alamos, NM 87545
J. L. Anderson
F. W. Clinard
D. W. Cooke
E. H. Farnum
H. M. Frost
J. C. Kennedy
R. E. Siemon
W. F. Sommer
K. E. Sickafus

56. Manlabs, Inc., 231 Erie Street, Cambridge, MA 02139
D. Tognarelli

57-59. Massachusetts Institute of Technology, Department of Metallurgy and Materials Science, Cambridge, MA 02139
L. W. Hobbs
K. C. Russell
N. J. Grant

60-61. Massachusette Institute of Technology, Plasma Fusion Center Headquarters, Cambridge, MA 02139
H. D. Becker
D. B. Montgomery

62-63. McDonnell-Douglas Aerospace, Mail Code 306 4204, P.O. Box 516, St Louis, MO 63166
J. W. Davis
G. W. Wille

64. M. J. Schiff & Associates, 1291 N. Indian Hill Blvd., Claremont, CA 91711-3897
G.E.C. Bell

65-67. National Institute of Standards and Technology, Boulder, CO 80302
F. R. Fickett
R. P. Reed
H. I. McHenry

68-69. Naval Research Laboratory, Code 6506, Washington, DC 20375
D. L. Gibson
J. A. Sprague

70-112. Oak Ridge National Laboratory, P.O. Box 2008, Oak Ridge, TN 37831
Central Research Library
Document Reference Section
Laboratory Records Department (2)
Laboratory Records-RC
Patent Section
D. J. Alexander
J. Bentley
E. E. Bloom
T. D. Burchell
G. M. Goodwin
R. H. Goulding
M. L. Grossbeck
A. N. Gubbi
J. F. King
E. A. Kenik
R. L. Klueh
E. H. Lee
L. K. Mansur
P. J. Maziasz
M. C. Osborne
J. E. Pawel
T. C. Reuther
T. K. Roche
A. F. Rowcliffe (10)
M. J. Saltmarsh
J. Sheffield
L. L. Snead
R. E. Stoller
K. R. Thoms
P. F. Tortorelli
R. L. Wallace
D. P. White
S. J. Zinkle

113. Oregon Graduate Institute, Dept. of Materials Science & Engineering, 19600 N.W. Von Neumann Drive, Beaverton, OR 97006
J. M. McCarthy

114-116. Princeton University, Princeton Plasma Physics Laboratory, P.O. Box 451, Princeton, NJ 08540
R. C. Davidson
D. M. Meade
Long-Poe Ku

117-118. Rensselaer Polytechnic Institute, Troy, NY 12181
D. Steiner
David Duquette

119. Rockwell International Corporation, NA02, Rocketdyne Division, 6633 Canoga Avenue, Canoga Park, CA 91304
D. W. Kneff

120-122. Sandia National Laboratories, Fusion Technology Dept., Dept. No 6531, P.O. Box 5800, Albuquerque, NM 87185-5800
M. J. Davis R. D. Watson
M. Ulrickson

123-125. Sandia National Laboratories, Livermore Division 8316, Livermore, CA 94550
W. Bauer W. G. Wolfer
K. Wilson

126. San Diego State University, Mechanical Engineering Dept., San Diego, CA 92182-0191
L. D. Thompson

127. TSI Research, 225 Stevens Ave., #110, Solana Beach, CA 92075
E. T. Cheng

128-129. University of California at San Diego, U.S. ITER Project Office, 9500 Gilman Drive, Bldg. 302, La Jolla, CA 92093-0035
C. C. Baker T. R. James

130-131. University of California, Dept. of Mechanical, Aerospace, and Nuclear Engineering, Santa Barbara, CA 93106
G. E. Lucas G. R. Odette

132-134. University of California, Dept. of Chemical, Nuclear , and Thermal Engineering, Los Angeles, CA 90024
M. A. Abdou S. Sharafat
N. M. Ghoniem

135. University of Michigan, Dept. of Nuclear Engineering, Ann Arbor, MI 48109
T. Kammash

136. University of Missouri, Department of Nuclear Engineering, Rolla, MO 65401
A. Kumar

137-138. University of Wisconsin, Nuclear Engineering Dept., 1500 Johnson Drive, Madison, WI 53706
J. B. Blanchard G. L. Kulcinski

139-142. Westinghouse Hanford Company, P.O. Box 1970, Richland, WA 99352
R. E. Bauer F. M. Mann
A. M. Ermi R. J. Puigh

143-145. Hokkaido University, Faculty of Engineering, Kita 13, Nishi 8, Kita-ku, Sapporo 060, Japan
Heischichiro Takahashi Akira Okada
Somei Ohnuki

146-147. Japan Atomic Energy Research Institute, Tokai Research Establishment, Tokai-mura, Naka-gun, Ibaraki-ken 319-11, Japan
Akimichi Hishinuma K. Noda

148. Kyushu University, Dept. of Nuclear Engineering, Faculty of Engineering, Kyushu University 36, Hakozaki, Fukuoka 812, Japan
C. Kinoshita

149-150. Muroran Institute of Technology, Dept. of Metallurgical Engineering, 27-1 Mizumoto-cho, Mororan 050, Japan
Toshihei Misawa Akihiko Kimura

151. Nagoya University, Dept. of Nuclear Engineering, Furo-Cho, Chikusa-ku, Nagoya 464-01, Japan
Michio Kiritani

152-155. National Institute for Fusion Science, Furo-cho, Chikusa-ku, Nagoya 464-01, Japan
Osamu Motojima
Chusei Namba
Takeo Muroga
Nobuaki Noda

156-158. National Research Institute for Metals, Tsukuba Branch, Sengen, Tsukuba-shi, Ibaraki-ken, 305, Japan
Fujio Abe
Josei Nagakawa
Haruki Shiraishi

159. Osaka University, Dept. of Nuclear Engineering, 2-1 Yamadaoka, Suita, Osaka 565, Japan
Tetuo Tanabe

160. PNC Oarai, 4002 Narita, Oarai, Ibaraki 311-13, Japan
Itaru Shibasaki

161. Science University of Tokyo, Dept. of Materials Science & Technology, 2641 Yamazaki Noda City, Chiba Prefecture 278, Japan
Naohira Igata

162. Teikyo University, Otsuka, Hachioji, Tokyo 192-03, Japan
Akira Miyahara

163. Tohoku University, Institute for Materials Research, Katahira 2-2-1, Sendai 980, Japan
Hideki Matsui

164-165. Tohoku University, Institute for Materials Research, Oarai Branch, Oarai, Ibaraki 311-13, Japan
Hideo Kayono
Tatsuo Shikama

166. Tohoku University, Dept. of Nuclear Engineering, Tohoku University, Aoba, Aramaki, Sendai 980, Japan
Katsunori Abe

167. Tohoku University, Dept. of Machine Intelligence and Systems Engineering, Aramaki, Aoba-ku, Sendai 980, Japan
Tatsuo Kondo

168. Tokai University, Dept. of Nuclear Engineering, 1117 Kitakaname, Hiratsuka-shi, Kanagawa-ken 259-12, Japan
Shiori Ishino

169. University of Tokyo, Dept. of Nuclear Engineering, 3-1, Hongo 7-Chome, Bunkyo-Ku, Tokyo 113, Japan
Naoto Sekimura

170-171. University of Tokyo, Dept. of Materials Science, 3-1, Hongo 7-Chome, Bunkyo-ku, Tokyo 113, Japan
Akira Kohyama
Yutaka Kohno

172. Commission of European Communities, Directorate-General for Research Science and Education, Fusion Programme RUE De La Loi 200, B-1049 Brussels, Belgium
J. Darvas

173-174. Chalk River Nuclear Laboratories, Atomic Energy of Canada, Ltd., Chalk River,
Ontario KOJ 1J0, Canada
I. J. Hastings D. P. Jackson

175. Southwestern Institute of Physics, P.O. Box 432, Chenedu 610041, Sichuan, P.R. China
J. P. Qian

176. Institute of Atomic Energy, Academia Sinica, P.O. Box 275-51, Beijing, P.R. China
J. Yu

177. Riso National Laboratory, Materials Dept., P.O. Box 49, DK-4000, Roskilde, Denmark
B. N. Singh

178. Centre d'Etudes Nucleaires, Saclay, DLPC/SMCM, Commissariat a l'Energie Atomique,
91191 Gif-Sur-Yvette, Cedex, France
N. Roux

179. Commission for European Communities, Joint Research Centre, I.A.M. Ispra Establishment
21020 Ispra (Varese), Italy
P. Fenici

180. EURATOM/CIEMAT Fusion Association, Avenida Complutense 22, 28040, Madrid, Spain
E. R. Hodgson

181. Paul Scherrer Institute, CH-5232 Villigen, Wuerenlingen PSI, Switzerland
M. Victoria

182. Harwell Laboratory, B393, Radiation Damage Dept., Oxfordshire, OX11 ORA, United Kingdom
C. A. English

183. Metallurgical and Nuclear Consultant, 9A Cumnor Rise Road, Cumnor Hill, Oxford OX2 9HD,
United Kingdom
D. R. Harries

184. Hahn-Mietner-Institut fur Kernforschung Berlin, Postfach 390128, Glienicker Str. 100, D-14109,
Germany
H. Wollenberger

185. Institut fur Festkorperforschung Forschungszentrum Jülich, Postfach 1913, D-52425 Jülich,
Germany
H. Ullmaier

186-189. ITER Garching Joint Work Site, Max-Planck-Institute für Plasmaphysik, Boltzmannstrasse 2,
D-85748 Garching bei München, Germany
B. Barabash G. Kalinin
Y. Gohar R. Parker

190-191. ITER Naka Joint Work Site, 801-1 Mukouyama, Naka-machi, Naka-gun, Ibaraki-Ken,
311-01, Japan
M. Huguet (2)

192-195. ITER San Diego Joint Work Site, 11025 N. Torrey Pines Road, La Jolla, CA 92037
V. Chuyanov F. Puhn
S. J. Piet P. Smith

196-197. Kernforschungszentrum Karlsruhe, Postfach 3640, 75 Karlsruhe 1, Germany
M. Dalle-Donne (INR) K. Ehrlich (IMF-II)

198. Max-Planck-Institut für Plasmaphysik, Boltzmannstrasse 2, D-85748 Garching bei München, Germany
Patrick Lorenzetto

199. A. A. Baikov Institute of Metallurgy, USSR Academy of Sciences, Leninsky Prospect 49, Moscow, Russia
L. I. Ivanov

200. CRISM "Prometey," Naberezhnava r. Monastyrick 1, 193167, St. Petersburg, Russia
V. V. Rybin

201. D. V. Efremov Institute of Electro-Physical Apparatus, 189631, St. Petersburg, Russia
S. A. Fabritsiev

202. Kharkov Institute of Physics & Technology, Radiation Damage and Materials Dept., Akademicheskaya 1, 310108 Kharkov, Ukraine
I. M. Neckludov

203-205. V. I. Lenin Research Institute of Atomic Reactors, 433510 Dimitrovgrad-10, Ulyanovsk Region, Russia
V. Kazakov V. K. Shamardin
A. S. Pokrovsky

206. Department of Energy, DOE Oak Ridge Field Office, P.O. Box 2008, Oak Ridge, TN 37831-6269
Assistant Manager for Energy Research and Development

207. Department of Energy, DOE Oak Ridge Field Office, P.O. Box 2008, Oak Ridge, TN 37831-6269
S. D. Frey

208. Department of Energy, Office of Basic Energy Sciences, Washington, D.C. 20585
R. J. Gottschall

209-216. Department of Energy, Office of Fusion Energy, Washington, D.C. 20585
S. E. Berk W. F. Dove R. E. Price
M. M. Cohen R. McKnight F. W. Wiffen
N. A. Davies W. Marton

217. Department of Energy, Richland Operations Office, Federal Bldg., MS-A590, Richland, WA 99352
D. Segna

218-247. Department of Energy, Office of Scientific and Technical Information, Office of Information Services, P.O. Box 62, Oak Ridge, TN 37831
For distribution as shown in DOE/TIC-4500, Distribution Categories UC-423 (Magnetic Fusion Reactor Materials) and UC-424 (Magnetic Fusion Energy Systems)